AD-A170 393 DIGEST - INTERNATIONAL CONFERENCE ON OPTICAL AND MILLIMETER WAVE PROPAGAT..(U) OREGON GRADUATE CENTER BEAVERTON DEPT OF APPLIED PHYSICS AND E.. R A ELLIOTT 1/6

UNCLASSIFIED MAY 86 ARO-23498.1-EL-CF DAAL03-86-G-0088 F/G 4/1 NL

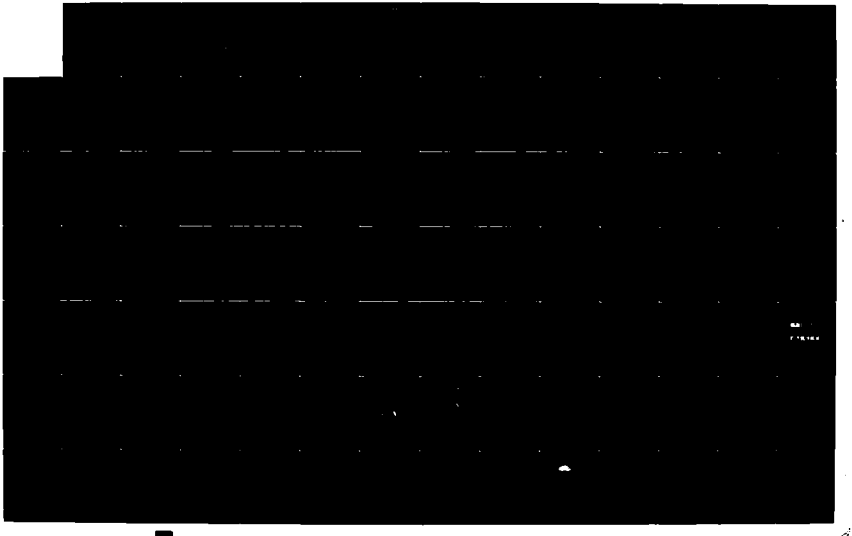

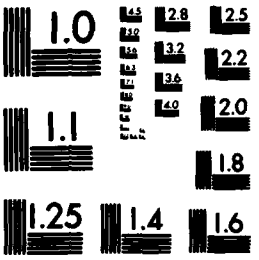

DIGEST

International Conference on
Optical and Millimeter Wave Propagation and Scattering in the Atmosphere

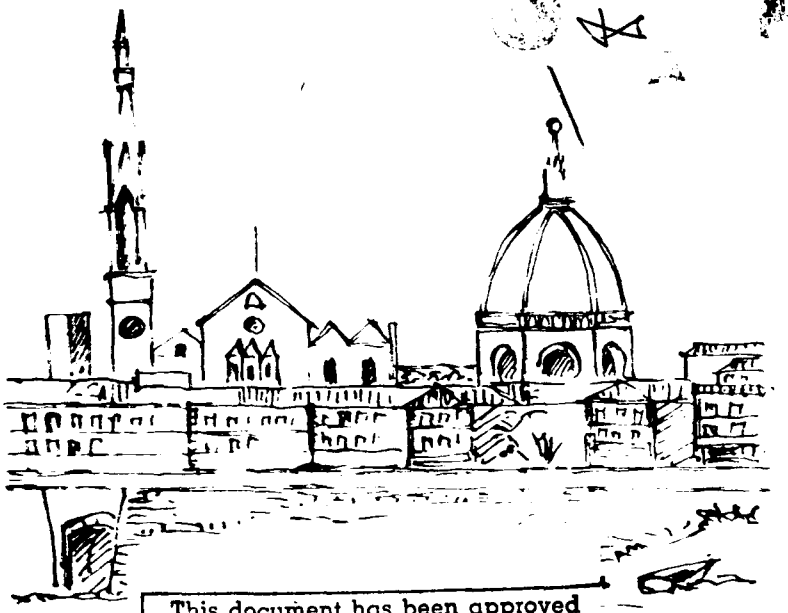

FLORENCE, ITALY

May 27-30, 1986

DIGEST

International Conference on
Optical and Millimeter Wave Propagation and Scattering in the Atmosphere

FLORENCE, ITALY

May 27-30, 1986

ORGANIZED BY

- Department of Physics, University of Florence
- Oregon Graduate Center

SPONSORED BY

- University of Florence
- Fondazione Ugo Bordoni, Rome
- Optical Society of America
- CNR - Consiglio Nazionale delle Ricerche, Italy
- IROE-CNR, Florence
- U.S. Army Research, Development, and Standardization Group, U.K.
- U.S. Army Research Office

UNDER THE AUSPICES OF

- Radiation Commission, International Association of Meteorology and Atmospheric Physics
- URSI - International Union of Radio Science
- Italian Commission for Optics
- CNR National Groups: Elettromagnetismo, Elettronica Quantistica e Plasmi (GNEQP), Fisica dell'Atmosfera e dell'Oceano (GNFAO)

ADVISORY COMMITTEE

Giuliano Toraldo di Francia,
University of Florence, Italy
Charles H. Townes,
University of California, Berkeley, USA
Emil Wolf,
University of Rochester, USA

ORGANIZING COMMITTEE

Anna Consortini, *General Cochair*,
University of Florence, Italy
Richard A. Elliott, *General Cochair*,
Oregon Graduate Center, USA

TECHNICAL PROGRAM COMMITTEE

Reginald J. Hill, *Program Cochair*, NOAA, USA
Ronald L. Phillips, *Program Cochair*,
University of Central Florida, USA
Tito F. Arecchi, University of Florence, Italy
Roy S. Cole, University College, U.K.
Ronald L. Fante, AVCO Systems Division, USA
Francesco Fedi, Fondazione Ugo Bordoni, Italy
Giorgio Flocco, University of Rome, Italy
Walter A. Flood, Army Research Office, USA
Dieter H. Höhn, FFO, West Germany
Akira Ishimaru, University of Washington, USA
Gerard Megie, CNRS, France

LOCAL ORGANIZING COMMITTEE

Mario Carnevale, Fondazione Ugo Bordoni, Roma
Giuliano Conforti, IROE-CNR, Firenze
Giovanni d'Auria, Università di Roma "La Sapienza"
Francesco Mencaraglia, IROE-CNR, Firenze
Giuseppe Molesini, Istituto Nazionale di Ottica, Firenze
Luca Pantani, IROE-CNR, Firenze
Giancarlo Righini, GNEQP-CNR, Firenze
Nicola Rubino, IROE-CNR, Firenze
Domenico Solimini, Università di Roma "Tor Vergata"

UNCLASSIFIED
SECURITY CLASSIFICATION OF THIS PAGE (When Data Entered)

REPORT DOCUMENTATION PAGE		READ INSTRUCTIONS BEFORE COMPLETING FORM
1. REPORT NUMBER ARO 23498.1-EL-CF	2. GOVT ACCESSION NO. N/A AD-A178 515	3. RECIPIENT'S CATALOG NUMBER N/A
4. TITLE (and Subtitle) Digest - International Conference on Optical and Millimeter Wave Propagation and Scattering in the Atmosphere		5. TYPE OF REPORT & PERIOD COVERED 22 Apr 86 - 21 Apr 87 Final Report 6. PERFORMING ORG. REPORT NUMBER
7. AUTHOR(s) Richard A. Elliott		8. CONTRACT OR GRANT NUMBER(s) DAAL03-86-G-0088
9. PERFORMING ORGANIZATION NAME AND ADDRESS Oregon Graduate Center Beaverton, OR 97006-1999		10. PROGRAM ELEMENT, PROJECT, TASK AREA & WORK UNIT NUMBERS
11. CONTROLLING OFFICE NAME AND ADDRESS U. S. Army Research Office Post Office Box 12211 Research Triangle Park, NC 27709		12. REPORT DATE May, 1986 13. NUMBER OF PAGES 404
14. MONITORING AGENCY NAME & ADDRESS (if different from Controlling Office)		15. SECURITY CLASS. (of this report) Unclassified 15a. DECLASSIFICATION/DOWNGRADING SCHEDULE

16. DISTRIBUTION STATEMENT (of this Report)

Approved for public release; distribution unlimited.

17. DISTRIBUTION STATEMENT (of the abstract entered in Block 20, if different from Report)

NA

18. SUPPLEMENTARY NOTES

The view, opinions, and/or findings contained in this report are those of the author(s) and should not be construed as an official Department of the Army position, policy, or decision, unless so designated by other documentation.

19. KEY WORDS (Continue on reverse side if necessary and identify by block number)

Optical Wave Propagation
Millimeter Wave Propagation
Surface Scattering
Atmospheric Particles
Particle Scattering

20. ABSTRACT (Continue on reverse side if necessary and identify by block number)

The conference was held as scheduled. Topics covered include scintillation theory, two-frequency scintillation, imaging and scintillation, coherence theory, lidar, surface scattering, nonlinear effects, transmission remote sensing, particle scattering and scintillation.

DD FORM 1 JAN 73 1473 EDITION OF 1 NOV 65 IS OBSOLETE

UNCLASSIFIED
SECURITY CLASSIFICATION OF THIS PAGE (When Data Entered)

INDEX

SCINTILLATION THEORY

H.T. Yura: An Elementary Derivation of the Saturation of Optical Scintillation 7

S.M. Flatté: The Path-Integral Technique in Wave Propagation through Random Media 11

R. Mazar, L.B. Felsen: Coherence Functions Evaluated Along Ray Paths in the Inhomogeneous Background of a Weakly Random Medium 15

V.E. Zuev, V.A. Banakh, V.L. Mironov: Retroflected Laser Radiation in the Turbulent Atmosphere 19

J. Gozani: Regularized 2-Scale Solution for a Wave Propagation in a Random Medium 23

A.M. Whitman: A New Derivation of Uscinki's Approximate Solution of the Fourth-Moment Equation 27

C.D.V. Thomas: Computations of the Effect of Atmospheric Turbulence on Laser Beam Propagation 31

TWO-FREQUENCY SCINTILLATION

M. Tur, Z. Azar, E. Azoulay: Temporal and Spectral Correlations of Two-Wavelength Optical Propagation in the Turbulent Atmosphere 35

N. Ben-Yosef, E. Goldner, A. Weitz: Two Color Correlation of Scintillations 39

K.S. Gochelashvili, T.S. Radjabov, I.M. Uzunov, V.I. Shishov: Beam Wave Frequency Correlation in Turbulent Atmosphere 43

IMAGING AND SCINTILLATION

J.C. Dainty: Speckle Interferometry and Speckle Imaging 51

C. Aime: Recovery of Astronomical Images from a Dichromatic Analysis of Speckles 55

D.M. Winker: Zernike Decomposition for a Kolmogorov Turbulence Spectrum with Finite Outer Scale 59

G.J.M. Aitken, R. Johnson, R. Houtman: Stellar Speckle-Image Reconstruction from Phase Gradients 63

J. Wang, U. Merlo, E. Fionda: Variability of Amplitude Scintillations Observed in Beijing and Rome on SIRIO Satellite Links . 67
P. Basili, P. Ciotti, G. d'Auria, U. Merlo, P. Ferrazzoli, D. Solimini: Scintillation on High- and Low-Elevation Satellite Propagation Paths 71

COHERENCE THEORY
E. Wolf: Some Recent Developments in Optical Coherence Theory 77
M. Nieto-Vesperinas: Classical Radiometry: a Short Wavelength Limit for a General Mapping of Cross-Spectral Densities in Second-Order Coherence Theory 79

LIDAR
T.D. Wilkerson: Lidar Profiling of Atmospheric Properties that Influence Propagation 85
G. Megie: Remote Sensing of Meteorological Parameters: Effects of Atmospheric Transmission and Scattering Properties on Dial Measurements 89
H. Edner, B. Galle, A. Sunesson, S. Svanberg, L. Uneus, S. Wallin, W. Wendt: Atmospheric Pollution Monitoring Using Optical Remote Sensing Techniques 93
W. Büchtemann, R. Ebert: CO_2-Laser Radar: Environmental Effects and System Approaches 97
G. de Leeuw: Lidar Measurements in the Marine Atmosphere 101

SURFACE SCATTERING
C.S. Gardner: Target Induced Speckle Effects in Picosecond Laser Ranging and Altimetry 107
K. Furutsu: Transport Theory of Random Planar Waveguide with a Fixed Scatterer - Mode Theory 111
H. Essen, E.P. Baars: Measurements on Multipath Propagation at 94 GHz over Snow Covered Terrain 115
E.R. Mendez, K.A. O'Donnell, A.S. Harley: Resonant Light Scattering from Rough Conducting Surfaces 119
R. Schiffer, K.O. Thielheim: Light Scattering by Composite Rough Surfaces 123

NONLINEAR EFFECTS
V.E. Zuev, A.A. Zemlyanov, Yu.D. Kopytin, A.A. Pogodaev: Nonlinear Optics of Atmospheric Aerosol 129
V.E. Zuev, A.A. Zemlyanov, V.V. Kolosov, S.N. Sinev: The

Transfer Equation Method in the Problems of Wave Beams Self-Action 133
R.K. Chang: Nonlinear Optical Interactions in Liquid Droplets During High Intensity Laser Irradiation 137
R.L. Armstrong: Propagation of Intense Light Beams in the Presence of Hydrodynamic Aerosol-Beam Interactions 143
M. Lax, B. Yudanin: Early-Time Hydrodinamic Response to Pulsed Laser Radiation 147
K.S. Gochelashvili, A.M. Prokhorov, A.N. Starodumov, V.I. Shishov: Pulse Propagation in a Nonlinear Randomly Inhomogeneous Medium 151
L. Crescentini, G. Fiocco: Interferometric Detection of Convective Instabilities Induced in Air by Energetic Beams 153

SCINTILLATION
R.S. Cole: Amplitude and Phase Scintillations in the Oxygen Absorption Region 157
E.P. Baars: Experimental Investigation of Millimeter Wave Propagation in the Atmosphere 161
M. Bertolotti, C. Sibilia: Coupled Mode Theory of Propagation through the Turbulent Atmosphere 165
E. Jakeman: Ray Propagation through Sub-Fractal Media 171
S.P. Petracca, I.M. Pinto: Functional Representations of the EM Field in Inhomogeneous Possibly Stochastic Media 175
L.C. Andrews, R.L. Phillips: A Statistical Model for the Intensity and Phase of Random Optical Fields 179
J.H. Churnside, R.J. Hill, G.R. Ochs: Yet Another Probability Distribution for Intensity Fluctuations in Strong Turbulence .. 185

TRANSMISSION
A. Kohnle, R. Neuwirth, W. Steffens, H. Jundt: Experimental Investigations of Atmospheric IR-Propagation over Land and Sea 191
A. Paraboni: The Role of Tropospheric Propagation in the Earth-Space Telecommunication Systems at Millimeter Waves 195
H.J. Liebe: Modeling Millimeter Wave Propagation in Moist Air . 203
J. Costales, G. De Amici, S. Levin, H. Pascalar, G. Smoot, C. Witebsky: Correlated Measurements of Atmospheric Signals at 10,33 and 90 GHz 207

POSTER PAPERS
P1 - E. Azoulay, Z. Azar: Aperture-Averaged Statistics of Laser Intensity Fluctuations in Strong Turbulence 211

P2 - R. Barbini, A. Ghigo, M. Giorgi, K.N. Iyer, A. Palucci, S. Ribezzo: Preliminary Results from the ENEA Lidar System 215
P3 - H.G. Booker, H.O. Vats: Laser Propagation through the Atmosphere near Ground Level 219
P4 - R.H. Clarke, P. Kara, N-Y.E. Ng: Statistics of Laser Beam Propagation through a Turbulent Atmosphere 223
P5 - A. Consortini, G. Conforti: Strong Scintillation Measurements Corrected for the Apparatus Saturation 227
P6 - A. Consortini, M. Mantovani, G. Conforti: Beam Wandering Due to a Thick Turbulent Layer Along the Path 231
P7 - A.D. Devir, A. Ben-Shalom, S.G. Lipson, U.P. Oppenheim, E. Ribak: Long Path Atmospheric Transmittance Measurement: Technique,Instrumentation and Results 235
P8 - T. Duracz, N.J. McCormick: Analytical Error Estimates for the Time-Dependent Radiative Transfer Inverse Method for Estimating Single-Scattering Parameters 239
P9 - R.A. Elliott, N.J. McCormick, T. Duracz: Preliminary Experimental Tests of the Time-Dependent Radiative Transfer Inverse Method for Estimating Single-Scattering Parameters ... 243
P10 - D.A. Erasmus: Variations in Atmospheric Refractive Index Associated with Ground Turbulence at the Mauna Kea Observatory 247
P11 - R.L. Fante: Effect of a Phase Screen on Imaging with Light of Arbitrary Spatial Coherence 251
P12 - F.F. Forbes: National New Technology Telescope Site Survey Instrumentation 255
P13 - R.J. Hill, S.F. Clifford, J.T. Priestley, R.A. Bohlander, R.W. McMillan: Millimeter-Wave Scintillation Due to Atmospheric Surface-Layer Turbulence 259
P14 - R.J. Hill, J.H. Churnside: Measurements of Laser Scintillation in Strong Turbulence Relevant to Laser Eye Safety 263
P15 - W. Kohsiek: On the Use of CO_2 Laser Scintillometer for the Investigation of Heat Transfer between a Sea Surface and the Atmosphere 267
P16 - I.N. Kolev, O.P. Parvanov, R.P. Avramova, V.N. Naboko, B.K. Kaprielov: Lidar Determination of the Horizontal Air Motion Velocity in the Atmospheric Boundary Layer 271
P17 - I. Last, Y. Weissman: Angular Resolution of an Optical Receiver in a Turbulent Atmosphere for a Wide Range of the Apertures 275
P18 - H. Leelavathi, J.P. Pichamuthu: The Propagation of Optical Pulses through Dense Scattering Media 279
P19 - I. Maignial, J.L. Brenguier, P.F. Combes, C. Pouit: In Cloud Temperature Measurement by Microwave Radiometry 283
P20 - R.J. Millington, M.J. Goodspeed: An Approach to the

Optical Measurement of Humidity Flux 287
P21 - G.R. Ochs: Some Observations of Spherical-Wave Covariance in Strong Refractive-Index Turbulence 293
P22 - A.J. Patitsas: Scattering from Randomly Oriented Fibers in the Rayleigh-Debye-Gans Approximation 297
P23 - I. Porceddu, V. Quesada: Stochastic Model for Turbidimetric Parameters Evaluation against Observed Values 301
P24 - S.B.S.S. Sarma, P.K. Pasricha: Atmospheric Turbulence Measurements with a Microwave Refractometer 303
P25 - J.B. Smyth: Atmospheric Optics 307
P26 - C.C. Wackerman, J.R. Fienup: Minimum Variance Estimator of Fourier Intensities Degraded by Atmospheric Turbulence 311
P27 - S. Zhengfang: Behaviors of Beam Wander in the Turbulent Near-Earth Atmosphere 315

REMOTE SENSING
J.F. Holmes: Optical Remote Wind Measurement Using Speckle-Turbulence Interaction 321
S.F. Clifford, J.H. Churnside: Synthetic Aperture Spatial Filtering of Scintillation: a New Technique for Measuring Optical Refractive Turbulence Profiles 325
W. Kohsiek: Remote Sensing of Heat and Moisture Fluxes by Optical and Millimeter Wave Scintillation 329
J. Vernin, J.L. Caccia: Remote Sensing of Atmospheric Turbulent Layers 333
G. Ortgies: Meteorological Parameters Derived from Scintillation Measurements 337
W. Porch, L. Rosen: Comparisons of Meteorological and Structure Parameters in Complex Terrain 341
C.J. O'Brien, L. Uphoff, R. Saint-Denis, M. Lapinskas: A Remote Sensing Application for a Spaced Based Laser Communication System 345
R.G. Isaacs, G. Deblonde, R. Worsham, L.D. Kaplan, V.J. Falcone: Remote Sensing of Atmospheric Water Vapor Profiles from Simulated Millimeter Wave Moisture Sounder Data 349
D.J. McCleese, D.M. Rider, J.S. Margolis, J.T. Schoefield: Remote Sensing of Wind by Electrooptic Phase Modulation of Atmospheric Emission 353

PARTICLE SCATTERING
A. Zardecki, S.A.W. Gerstl: Multiple Scattering Effects in the Off-Axis Propagation of Laser Radiation 359
V.V. Varadan, V.K. Varadan: Effects of Multiple Scattering and

non-Spherical Statistics in Discrete Random Media 363
L.R. Bissonnette: Model and Laboratory Simulation of Multiple Scatter Effect on Laser Forward-and Backscattering 367
C.L. Rino: A Multiple Scattering Layer Model for Propagation in Discrete Random Media 371
G. Zaccanti, P. Bruscaglioni, P. Pili: Multiple Scattering Effects on the Propagation of a Light Beam in an Inhomogeneous Medium 375
A. Mugnai, W.J. Wiscombe: Scattering from Nonspherical "Chebyshev Particles" 379
M. Kleiman, A. Cohen, I. Ariel, S. Egert: Light Scattering by Multi-Layered Particles 383
A.K. Majumdar: Higher-Order Temporal Moments of Picosecond Optical Pulses in a Laboratory-Simulated Multiple Scattering Atmosphere 387
F. Prodi, V. Levizzani, G. Casarini: Determination of the Optical Characteristics of Atmospheric Particles Separated by Size 391
G. Lee, J. Rockway, B. Speer, G. Moradian: Optical Propagation and Communication through Clouds 393
H.M. Gupta: Monte-Carlo Simulation of an Optical Scatter Channel: Use of Variance Reduction Techniques 397

Authors' Index 401

TIME-TABLE

	Tuesday, May 27	Wednesday, May 28	Thursday, May 29	Friday, May 30
	GREEN ROOM			
8.45				REMOTE SENSING
9.00	SCINTILLATION THEORY	COHERENCE THEORY	SCINTILLATION	
9.40				
9.45		LIDAR		
11.55				
12.00				
12.05				
13.30	TWO-FREQUENCY SCINTILLATION	SURFACE SCATTERING	TRANSMISSION	PARTICLE SCATTERING
14.25				
14.30	IMAGING AND SCINTILLATION			
14.50				
15.00			POSTER SESSION	
15.05				
15.10		NONLINEAR EFFECTS		
16.40				
17.00				
17.05				CLOSING STATEMENT
18.05				

SCINTILLATION THEORY

An Elementary Derivation of the Saturation of Optical Scintillation

H. T. Yura
Electronics Research Laboratory
The Aerospace Corporation
P. O. Box 92957
Los Angeles, CA 90009

(invited)

Although the literature abounds with many papers dealing with saturation of scintillation and related phenomena, these works tend to be very mathematical in nature and difficult to understand the underlying physical phenomena that causes this effect. The purpose of this paper is to present an elementary derivation of this phenomena which physically elucidates the underlying causes of saturation of optical scintillation. As will be shown, saturation of optical scintillation is obtained from a straightforward generalization of Tatarskii's geometrical opticals model[1] to one that includes the progressive loss of transverse spatial coherence of the wave as it propagates through the turbulent medium.

The physical mechanism through which turbulence induces beam breakup is the focusing produced by the inhomogeneities in the path of the wave. The simplest model of this effect that retains the essential physics is a plane wave incident upon a series of closely packed refractive spheres. Consider the scalar plane-wave field with wave number k incident on a single sphere of radius a and refractive index n_1 relative to the surrounding medium (where the refractive index is assumed unity). The scattering for the range of parameters of interest, $n_1 \lesssim 10^{-6}$, $ka \gg 1$, is primarily in the forward direction. In the geometric approximation, the condition $n_1 \ll 1$ implies negligible reflection at the surface of the sphere and that each ray (the normal to the wavefront) will pass into and out of the sphere virtually unperturbed in direction (the refraction angle at the surface is $\approx n_1$).

In this so-called paraxial approximation, it is well known that a sphere can act as a lens with a focal length $f = a/2n_1$. For $n_1 > 0$, the lens is converging; for $n_1 < 0$, there is a virtual focal point behind the lens at $a/2|n_1|$, and the lens is divergent. For $a = 10$ cm and $n_1 = 10^{-6}$, the focal range $f = 50$ km. Hence, for most applications we are much closer to this spherical lens than its focal plane (except for the smallest of spheres), and the focusing power of the lens will not be very effective. The fractional

intensity increase (or decrease, for $n_1 < 0$) induced per sphere will then be small.

We can estimate the irradiance fluctuation induced by a single sphere being swept past the line of sight between the source and observation point as follows: In the absence of the sphere, the (plane-wave) irradiance is $I_o = A_o^2$ at all ranges, where A_o is the initial amplitude. With the sphere present, the energy incident upon the sphere is brought to a focus at range f along the optic axis (neglecting diffraction). If we pass a plane perpendicular to the optic axis at a distance z from the sphere, the energy will be confined to an area $(1 - (z/f))^2 \pi a^2$, and conservation of energy implies that the mean square relative amplitude fluctuation at z due to a single sphere is

$$\left\langle \left(\frac{\delta A}{A_o}\right)^2 \right\rangle = \frac{(z/f)^2}{(1 - \frac{z}{f})^2} \tag{1}$$

Assuming the mean number of (closely packed) spheres of radius a along the path is z/a and the contribution from each sphere to the resulting amplitude fluctuations are independent we conclude that the resulting mean square relative amplitude fluctuation from the multiple spheres is given by multiplying Eq. (1) by z/a.

This geometrical optics result should provide a reasonable estimate of irradiance fluctuations when diffraction effects are small. Hence for $z \ll ka^2$ we obtain the estimate (for $z \ll f \sim n_1/a$, and neglecting factors of order unity)

$$\langle (\delta A/A_o)^2 \rangle \sim \left[\langle n_1^2 \rangle \frac{z^2}{a^2}\right] \frac{z}{a} \sim \langle n_1^2 \rangle (z/a)^3, \; z \ll ka^2 \tag{2}$$

To relate this result to the Kolmogorov "continuum model" we note that in the inertial subrange we have the estimate $\langle n_1^2 \rangle \sim C_n^2 \, a^{2/3}$ for $\ell_o \ll a \ll L_o$, where C_n^2, ℓ_o and L_o are the index structure constant, inner and outer scale, respectively. Substituting this into Eq. (2) and summing over all scale sizes yields

$$\langle (\delta A/A_o)^2 \rangle \sim \sum_{a=\ell_o}^{L_o} \left[C_n^2 \, a^{2/3}\right](z/a)^3 \sim z^3 \, C_n^2/\ell_o^{7/3}, \; z \ll k\ell_o^2 \tag{3}$$

In the geometric optics regime, the amplitude fluctuations increase as the cube of the distance, are dominated by the smallest eddies, and are independent of wavelength.

The effect of diffraction by the spheres can be included by noting for $z > ka^2$ the diffracted energy at range z will now be confined to an area of the order the square of diffraction spot size $\sim a^2(1 - (z/f))^2 + (z/ka)^2$ rather than the square of the geometric spot size $\sim a^2(1 - (z/f))^2$. Hence, diffraction effects are obtained from Eq. (1) as

$$\langle(\delta A/A_o)^2\rangle = \frac{(z/f)^2}{(1 - \frac{z}{f})^2} \left[\frac{\text{Geometric Spot Area}}{\text{Diffraction Spot Area}}\right] \tag{4}$$

$$= \frac{\langle n_1^2\rangle z^3}{a^3} \left[1 + (z/ka^2)^2\right]^{-1}$$

$$+ \sum_{a=\ell_o}^{L_o} \left[C_n^2 a^{2/3}\right](z/a)^3\left[1 + (z/ka^2)^2\right]^{-1} \tag{5}$$

For large z, the main contribution to the sum occurs for $a \sim (z/k)^{1/2}$ and thus we obtain that $\langle(\delta A/A_o)^2\rangle \sim C_n^2 z^{11/6} k^{7/6}$, in agreement with the Born-Rytov results[1].

Although diffraction effects due to the eddies has slowed down the growth (from a z^3 to a $z^{11/6}$ range dependence) of amplitude fluctuations it does not result in a saturation of scintillation. This effect is obtained by including in the analysis the loss of transverse coherence of the initially coherent wave as it propagates through the medium. The ability of a turbulent eddy to focus a partially coherent wave can be considerably less than for a coherent wave, implying reduced amplitude fluctuations. Now it has been shown[2] that the spot size area resulting from an obstacle of radius a is of the order

$$\text{Diffraction Spot Area} \sim a^2\left(1 - \frac{z}{f}\right)^2 + \left(\frac{z}{ka}\right)^2 + \left(\frac{z}{k\rho_o}\right)^2, \tag{6}$$

where ρ_o is the lateral coherence length of the wave[3]. The third term on the right side of Eq. (6) gives the effects of diffraction due to a partial coherent wave and will result in saturation.

Substituting Eq. (6) into Eq. (4) yields

$$\langle(\delta A/A_o)^2\rangle = \langle n_1^2\rangle\, k^2 a z \frac{1}{1 + \left(\frac{ka^2}{z}\right)^2 + \left[\frac{a}{\rho_o}\right]^2}$$

$$+ \sum_{a=\ell_o}^{L_o} \frac{C_n^2 z^3}{a^{7/3}} \frac{1}{1 + \left(\frac{z}{ka^2}\right)^2 \left(1 + \frac{a^2}{\rho_o^2}\right)} \qquad (7)$$

For sufficiently large z and $\rho_o < (z/k)^{1/2}$ the main contribution to the sum in Eq. (7) occurs for $a \sim \rho_o$ and thus we obtain the estimate

$$\langle(\delta A/A_o)^2\rangle \sim C_n^2 z^3 \rho_o^{-7/3} (z/k\rho_o^2)^{-2} \sim C_n^2 k^2 z \rho_o^{5/3} \qquad (8)$$

Now for the Kolmogorov spectrum in the inertial subrange we have that[3] $\rho_o \sim (k^2 C_n^2 z)^{-5/3}$ and hence Eq. (8) yields $\langle(\delta A/A_o)^2\rangle \sim 1$. That is, including the effects of partial coherence in the diffraction analysis results in saturation of amplitude fluctuations.

References

1. V. I. Tatarskii, "The Effects of the Turbulent Atmosphere on Wave Propagation," National Technical Information Service, U. S. Dept. of Commerce, Springfield, VA (1971).

2. Lutomirski, R. F., and H. T. Yura, Appl Opt. 10, 1652 (1971).

3. R. E. Hufnagel and N. R. Stanley, J. Opt. Soc. Am. 54, 52 (1964).

The Path-Integral Technique in Wave Propagation through Random Media

Stanley M. Flatté
Physics Department, University of California
Santa Cruz, CA 95064 U.S.A.
(invited)

Application of the Feynman path integral to pulse propagation through a random medium is described, with examples involving seismic, acoustic, and optical waves.

High frequency ($\gtrsim$ 1cpd) variations in travel time of acoustic transmissions over ocean mesoscale distances are known to be dominated by the effects of internal wave displacements of the sound speed stratification (Flatté, 1983). Variations in the difference in travel time between transmissions in opposite directions along the same path (reciprocal transmissions) are dominated by internal-wave currents (Munk, Worcester, and Zachariasen, 1981). A typical application involves 10-ms-wide pulses travelling over 300 km. It has been demonstrated that this type of data can be inverted for internal-wave strengths. Information can be obtained about range-averaged mean energy level and about energy distribution in the vertical. Data from the 1983 Tomography Experiment (Worcester, Spindel, and Howe, 1985), consisting of 41 days of one-way and 21 days of reciprocal transmissions between two moorings 300 km apart, have been used to observe the statistical field strength of internal waves (Flatté and Stoughton, 1986; Stoughton, Flatté and Howe, 1986). One-way travel-time variances are in the range 5-15 ms^2. Measurements of travel time in opposite directions (reciprocals) measure the field of velocity in the medium rather than refractive index. Reciprocal variances in the 1983 experiment are about 1.5 ms^2 above the 1-ms^2 measurement noise. It is shown that the accuracy of measurement of these variances is not strongly affected by the partially saturated nature of the sound propagation.

Application of the path-integral method of wave propagation through random media to the analysis of seismic-wave propagation through the earth's mantle is underway. Seismic waves with periods of 1 to 10 Hz received at 100-km-square arrays on the surface of the earth exhibit paradoxical wave-front properties involving small phase (or travel time) fluctuations combined with large amplitude fluctuations. A description of these observations will be given.

Application of the path-integral technique to atmospheric problems will be discussed the context of the Stellar Horizon Atmospheric Dispersion (SHAD) program. The SHAD system is a satellite-based star tracker that will measure the vertical gradient of atmospheric density, integrated along a line (the tangent line) that is perpendicular to a radius vector of the earth and whose point of closest approach is at an altitude between 20 and 60 km above the surface of the earth. The system was suggested by Fred Quelle of the Office of Naval Research, who is now involved in the planning for the development of the system.

A SHAD tangent line through the atmosphere remains within an atmospheric scale height of its tangent point over a horizontal distance of about 600 km. In the atmosphere, the gradient of refractive index is proportional to the density gradient, which is proportional to the temperature gradient. Therefore, a SHAD system measures the temperature gradient integrated along a straight line whose length is roughly 600 km and whose lowest (tangent) point varies from 20 to 60 km altitude. The tangent point of one star observation slices down through the atmosphere along an 'observation line' in a time that varies from twenty seconds to several minutes, and during one star observation as many as 100 point observations along this observation line may be made.

Any atmospheric process, such as planetary waves or gravity waves, that has a vertical scale size larger than the light-ray-bundle size, which is on the order of one meter or less, will contribute to the refraction being measured by a SHAD system. If the horizontal scale size of the atmospheric phenomenon is smaller than 600 km, then a statistical average needs to be done to find its effective contribution. In addition to measuring the differential refraction of a star, a SHAD system has the capability of measuring the image size of the star, and hence the spreading of the image due to the atmosphere. This spreading is proportional to the rms temperature gradient fluctuation within the width of the light bundle being detected. Hence image spreading is a measure of atmospheric turbulence.

On July 22-23, 1985, a workshop was held at the La Jolla Institute Center for Studies of Nonlinear Dynamics to provide a forum for middle-atmosphere scientists to discuss the impact of future data from the Stellar Horizon Atmospheric Dispersion (SHAD) system on fundamental research questions in atmospheric dynamics.

The workshop at La Jolla Institute included discussions on the usefulness of SHAD data for the investigation of the phenomena of global climate, tides, planetary waves, gravity waves, and turbulence. It was concluded that all

these areas of middle-atmospheric research would benefit substantially from data supplied by an ongoing SHAD program. In most cases the SHAD data would be unique; that is, no other comparable measurements are available. Brief explanations of the application of SHAD data to various areas will be given, and the appropriate questions related to the theory of wave propagation through random media will be raised.

References

S.M. Flatté, "Wave propagation through random media: Contributions from ocean acoustics," *Proc. IEEE*, vol. 71, pp. 1267-94, 1983.

W. Munk , P. Worcester, and F. Zachariasen, *J. Phys. Ocean.*, vol. 11, pp. 442-54, 1981.

P. Worcester, R. C. Spindel, and B. Howe, "Reciprocal acoustic transmissions: Instrumentation for mesoscale monitoring of ocean currents," *IEEE Journal of Oceanic Engineering*, vol. 123-37, 1985.

S.M. Flatté and R.B. Stoughton, "Theory of acoustic measurement of internal-wave strength as a function of depth, horizontal position, and time," *submitted for publication*, 1985.

S.M. Flatté, R.B. Stoughton, and B. Howe, "Acoustic measurements of internal-wave *rms* displacement and *rms* horizontal current off Bermuda in late 1983," *submitted for publication*, 1985.

Coherence Functions Evaluated Along Ray Paths in the Inhomogeneous Background of a Weakly Random Medium

R. Mazar and L.B. Felsen
Dept. of Electrical Engineering and Computer Science/Weber Research Institute
Polytechnic University, Farmingdale, NY 11735 USA

(invited)

I. Introduction

The propagation properties of high frequency waves in a medium with gradual inhomogeneities are conveniently charted along the geometric optical rays. When weak fluctuations are superimposed on this background environment, on a scale large enough so as not to violate the geometric optical conditions, the rays are randomly perturbed, and the physical properties of the resulting wave field are specified by its various statistical moments. Instead of constructing these moments at each field point by performing the averaging there, it is physically more incisive and analytically more convenient to propagate the moments directly, from the source to the observer, by deterministic propagation equations. For high frequency fields and large scale, weak fluctuations, this strategy has been implemented by extracting from the wavefunctions the rapidly varying plane wave phase exp(ikz) along the (straight) direction of propagation and constructing the moment equations for the resulting "parabolically approximated" remainder fields [1,2]. By one procedure [1,2], the moment equations have been reduced to first order partial differential form and then solved by the method of characteristics, the allowable characteristic trajectories being paraxial with respect to z. Solutions for the second moment generated by this technique were found to have enough spectral content to describe phenomena near caustics if the background refractive index is weakly focusing and supports ray fields with small angular deviations from z [3].

In a medium with general, though gradually varying, background profile, the rays may follow trajectories deviating markedly from the z-direction, thereby making extraction of an exp(ikz) phase inadequate. It is then suggestive to extract the phase accummulation along each curved ray trajectory, and to attempt construction of the moment equations for the reduced fields in the random medium in ray centered coordinates [4,5]. It has been shown that this is indeed possible [6], and that the resulting equations bear strong resemblance to those pertaining to propagation along a straight coordinate. As we shall demonstrate (so far in two dimensions), we can solve these equations for the average field, the second moment, and the multifrequency higher moments by adapting the techniques employed for the homogeneous background locally to each ray.

Before describing the solution method, we may anticipate the possibility of even further generalization by basing the construction of the high-frequency moment equations in very general randomly varying propagation, reflection, and diffraction environments on the various categories of rays in the geometrical theory of diffraction (GTD) [7]. This would require the consideration of canonical problems that model the statistical counterparts of the deterministic building blocks of GTD. We shall attend to this task, being encouraged by the success of the first generalization, to the arbitrarily inhomogeneous background, reported here.

II. The Two-Point Coherence Function

A. Propagation equation

A scalar time-harmonic two-dimensional wave field $\hat{u}(\underline{r})$ is assumed to propagate in a medium characterized by the inhomogeneous real squared index of refraction $n^2(r)[1 + 2\tilde{n}(\underline{r})]$, where $n(r)$ is the deterministic background portion and $\tilde{n}(\underline{r})$ is a weak random perturbation. Introducting for each ray trajectory in the background medium the ray-centered coordinates $\underline{r} = (r,\tau)$, where τ measures length along the ray and r measures transverse distance away from the ray, and extracting the phase accumulation $\exp[ik\int_0^\tau n_0(\zeta)d\zeta]$, where k is a reference wave number and $n_0(\tau) \equiv n(0,\tau)$, one generates the reduced field $u(r,\sigma)$, which satisfies approximately a ray-centered stochastic parabolic equation. Then in the sum and difference coordinates

$$p = \frac{r_1 + r_2}{2} \quad , \quad s = r_1 - r_2 \quad , \tag{1}$$

the two point coherence function

$$\Gamma(\bar{p},\bar{s},\bar{\sigma}) = \langle u(\bar{p} + \frac{\bar{s}}{2},\bar{\sigma})u^*(\bar{p} - \frac{\bar{s}}{2},\bar{\sigma})\rangle \tag{2}$$

with * denoting the complex conjugate, can be shown to satisfy a deterministic propagation equation of the form

$$E\Gamma(\bar{p},\bar{s},\bar{\sigma}) = 0, \text{ subject to } \Gamma(\bar{p},\bar{s},0) \equiv \Gamma_a(\bar{p},\bar{s}) \quad . \tag{3}$$

Here, $\bar{p} = p/\ell$, $\bar{s} = ks$, $\bar{\sigma} = \sigma/\ell$ are scaled coordinates, with ℓ representing the characteristic length, over which the background refractive index varies appreciably. The operator E has the functional dependence

$$E = E(\bar{p},\bar{s},\bar{\sigma}, \frac{\partial}{\partial\bar{p}}, \frac{\partial}{\partial\bar{s}}, \frac{\partial}{\partial\bar{\sigma}}, \varepsilon_1, \varepsilon_2) \tag{3a}$$

wherein $\varepsilon_{1,2}$ are perturbation parameters $\varepsilon_1 = (k\ell)^{-2/3}$, $\varepsilon_2 = (k\ell_n)^{-1}$, and ℓ_n is the correlation length of the refractive index fluctuations. These length scales are ordered so that $(2\pi/k) << \ell_n << \ell$. The fluctuations are assumed to be statistically homogeneous, isotropic, and delta correlated along the ray coordinate τ.

B. Zeroth order solution

To effect a solution, the propagation equation (3) is subjected to a succession of spectral forward and inverse transforms, multiple scalings of derivative operators, rescalings of variables and, finally, expansion with respect to the perturbation parameters ε_1 and ε_2 [8a] to yield an equation for the propagation of the intensity spectra. Its simplified form corresponding to the zeroth order term in the expansion is solved by the method of characteristics along the background rays. The solution strategy depends on whether the observer is reached by one or more isolated (widely separated) rays, or by two closely adjacent rays. In the former (regular ray) domain, the individual ray fields are uncorrelated because their separation exceeds the scale ℓ_s; a quadratic, two-scale expansion (see [8a]) is adequate in this case. In the latter (transitional ray) domain, near a caustic, the two ray fields must be treated together by a cubic, three-scale expansion that yields a result in the following form:

$$\Gamma(\bar{p},\bar{s},\bar{\sigma}) = \frac{1}{(2\pi)^2\bar{n}_0(\bar{\sigma})}\iint_{-\infty}^{\infty} d\bar{v}d\bar{\rho}\tilde{\Gamma}_a(\bar{v}_a,\bar{\rho}_a)\cdot\exp\{-\int_0^{\bar{\sigma}} d\zeta Q_0(\bar{v},\bar{\rho},\zeta)\}\exp(i\bar{\rho}\bar{s})$$

$$\cdot\int_{\infty}^{\infty} d\bar{\eta}\exp[i\bar{\eta}(\bar{v}-\bar{\rho})]\exp\{\frac{i(\epsilon_1\alpha_0\bar{\eta})^3}{3} - \beta\int_0^{\bar{\sigma}} d\zeta G_0(\bar{v},\epsilon_2\bar{\eta}\bar{s},\zeta)\}\quad , \tag{4}$$

where the subscript"a"identifies quantities evaluated in the source plane $\bar{\sigma}=0$, $\tilde{\Gamma}_a$ is a spectral transform of Γ_a in (3), and $\bar{s}$ is a rescaled $\bar{s}$ coordinate. The functions Q_0 and α_0 are related to the background ray geometry, whereas the effect of fluctuations is expressed by the terms β and G_0, which contain the refractive index correlation function in the transverse (r) coordinates. For isolated ray fields away from the caustic, the quadratic approximation results on setting $\epsilon_1 = 0$. In the absence of fluctuation, $\beta = 0$. In that case, and for an initial condition appropriate to line source excitation, the resulting deterministic intensities near and away from the caustic agree completely and continuously with the respective expressions obtained from uniform and isolated ray theory [9]. This check suggests strongly that our approximate solution in (4) has enough spectral content to accommodate the corresponding averaged wave phenomena with comparable quality when fluctuations are included.

We have shown elsewhere [8b] that the solution strategy outlined above can be extended to evaluation of the m-frequency, 2mth moment

$$\Gamma_{2m}(p_i,s_i,\sigma;k_i|i=1\ldots m) = <\prod_{j=1}^{m} u(p_j+\frac{s_j}{2},\sigma;k_j)u^*(p_j-\frac{s_j}{2},\sigma;k_j)> \tag{5}$$

where p_j and s_j are the sum and difference coordinates defined in (1) for each frequency constituent having a wavenumber k_j.

The solution for Γ_{2m} is synthesized by integration over $\bar{v}_j,\bar{\rho}_j,\bar{\eta}_j$, $j=1\ldots m$, of the m-fold product of spectral elements as in the integrand of (4), with coupling between individual j-contributions residing solely in the generalized functions G_0 indicative of the fluctuations. In the absence of fluctuations ($\beta=0$) and for a deterministic source, Γ_{2m} separates into the product of m second order coherence functions,each being associated with a frequency ω_j and coordinates $(\bar{p}_j,\bar{s}_j,\bar{\sigma})$.

Acknowledgement

This work has been sponsored by the Rome Air Development Center, Hanscom AFB, USA, through the Joint Services Electronics Program, Contract No. F-49620-85-C-0078, and through the Office of Naval Research under Contract No. N-00014-79-C-0013.

References

1. V.I. Tatarskii and V.U. Zavorotnyi, "Strong Fluctuations in Light Propagation in Randomly Inhomogeneous Medium", in "Progress in Optics", Vol. XVIII, E. Wolf (Ed.). (North-Holland Publishing Co., Amsterdam 1980).

2. M.J. Beran, "Coherence Equations Governing Propagation Through Random Media", Radio Science, 10 (1), pp. 15-24, (1975).

3. S. Frankenthal, M.J. Beran and A.M. Whitman, "Caustic Corrections Using Coherence Theory", J. Acoust. Soc. Am. 71 (2), pp. 348-358, (1982).

4. V.A. Babich and N.J. Kirpichnikova, "Boundary Layer Method in Diffraction Problems" (translated from the Russian by Springer-Verlag, 1980).

5. V. Červeny, M.M. Popov and I. Pšenčik, "Computation of Wave Fields in Inhomogeneous Media - Gaussian Beam Approach", eophys. J. Astr. Soc. 70, pp. 109-128, (1982).

6. R.J. Hill, "A Stochastic Parabolic Wave Equation and Field-Moment Equations for Random Media having Spatial Variations of Mean Refractive Index", J. Acoust. Soc. Am., 77 (5), pp. 1742-1752, (1985).

7. Geometric Theory of Diffraction, Edited by R.C. Hansen, IEEE Press, (J. Wiley & Sons, New York, 1981).

8. R. Mazar and L.B. Felsen, "High Frequency Coherence Functions Propagated Along Ray Paths in the Inhomogeneous Background of a Weakly Random Medium
a. I. Formulation and Evaluation of the Second Moment
b. II. Higher Moments", submitted to J. Acoust. Soc. Am.

9. R.M. Lewis, N. Bleistein and D. Ludwig, "Uniform Asymptotic Theory of Creeping Waves", Comm. Pur. Appl. Math., XX pp. 295-328, (1967).

RETROREFLECTED LASER RADIATION IN A TURBULENT ATMOSPHERE

V.E. Zuev, V.A. Banakh, V.L. Mironov

The Institute of Atmospheric Optics, Siberian Branch
USSR Academy of Sciences, Tomsk, USSR (invited)

The peculiarities of the problems on wave propagation along the paths with reflection in randomly inhomogeneous media are connected with correlation of incident and reflected waves passing during their propagation through the same medium inhomogeneities. They were considered in Refs. [1-7].

1. The Effect of the Backscattering Amplification

In paper [3] the relation between the statistical moments of intensities of direct and reflected from a point reflector spherical waves was found

$$\langle (I^R(x_0,0))^n \rangle = I_0^{-n} \langle I^{2n}(x,0) \rangle, \qquad (1)$$

where $I_0 = |u_0|^2$ is the initial intensity of an irradiating wave, $\langle I^{2n}(x,0) \rangle$ are the moments of the direct wave in the reflector's plane $x' = x$, $\langle (I^R(x_0,0))^n \rangle$ are the moments of the wave reflected in the source plane $x' = x_0$.

For the mean intensity (n = 1) we have [3]

$$\langle I^R(x_0,\vec{\rho}) \rangle = (|u_0|^2/(k\mathcal{L})^4)\,(1 + B_{I,S}(x,\vec{\rho})), \qquad (2)$$

where $\mathcal{L} = x - x_0$, $k = 2\pi/\lambda$, $B_{I,S}$ is the normalized correlation function of the spherical-wave intensity in the reflector's plane.

It follows from Eqs. (1), (2) that in the strictly backward direction (r = 0) there occurs amplification of the reflected wave intensity by the value determined by variance of the direct spherical wave intensity $\sigma_{I,S}^2 = B_{I,S}(x,0)$. In the region of weak fluctuations, when the parameter $\beta_0^2 = 1{,}23\, C_n^2 k^{7/6} \mathcal{L}^{11/6} < 1$ (C_n^2 is the structure characteristics of the refractive index fluctuations) $\sigma_{I,S}^2 = 0{,}4\,\beta_0^2$ and $\langle I^R(x_0,0) \rangle$ increases, in comparison with propagation in a homogeneous medium, by the value $0{,}4\,\frac{|u_0|^2}{(k\mathcal{L})^4}\,\beta_c^2$ [1]. However in the general case the value of amplification depends on the sizes of exit apertures of the source 2a and the reflector $2a_r$. Moreover, the correlation of direct and backward waves can lead to the opposite effect: the mean intensi-

ty attenuation, if $\Omega_{эфф} \simeq 1$ [7] ($\Omega_{эфф}^{-1} = \Omega^{-1} + \Omega_z^{-1}$, $\Omega = \frac{ka^2}{\mathcal{L}}$, $\Omega_z = ka_z^2/\mathcal{L}$.

In region of strong fluctuations ($\beta_c^2 \gg 1$) $\sigma_{I,S}^2 = 1 + 2{,}74\,\beta_o^{-4/5}$, and the intensity of a spherical wave reflected from the point scatterer ($\Omega, \Omega_z \ll \beta_o^{-12/5}$) increases by a factor of more than two. If $\Omega \gg \beta_o^{-12/5}$ then the amplification of mean intensity is small. In this case it is determined by the value of asyptotically small terms of the order of $\beta_c^{-4/5}$ [2, 3].

2. The Effect of Long-Range Correlations

The analysis of the reflected-wave field coherence function shows that it is represented at $\beta_o^2 \gg 1$ as two terms one of which describes propagation along the doubled-length path, and the second is responsible for the correlation of counter waves. In the case of scattering of a spherical wave the second term makes approximately the same contribution to the intensity of the reflected wave as the first one (Section I) and for a plane wave this term appears to be asymptotically small. In the latter case its value is determined by so-called "long-range" correlations of the field [1] caused by coherence of the rays propagating in opposition between the source and the reflector along the spaced paths. The scale of decrease of this term is $\sqrt{\mathcal{L}/k}\;\beta_c^{6/5}$, and when $\beta_o^2 \gg 1$ it is large. This circumstance allows the effective focusing of the reflected plane wave to be made using a receiving lens if its sizes $2a_t$ satisfy the condition $ka_t^2/\mathcal{L} = \Omega_t \gg \beta_o^{12/5}$. In fact, in focus of such a lens the mean intensity increases by a factor of two in comparison with propagation along the doubled-length path [1].

Thus, if in the plane of the lens there is no effect of amplification of the plane wave backscattering, then such amplification arises in the lens focus. On the contrary, when the reflected spherical wave is focused by a lens with sizes $\Omega_t \gg \beta_o^{12/5}$ the effect of backscattering amplification occurring in the plane of the lens disappears in the plane of a sharp lens image [6].

3. Amplification of Intensity Fluctuations

Correlation of counter waves also results in the increase of the reflected-radiation intensity fluctuations. In particular, when $\beta_0^2 < 1$, the relative variance of the spherical-wave intensity scattered by a point reflector takes the value $\sigma_{I,R}^2 = 1{,}6\beta_0^2 = 4\sigma_{I,S}^2$, that is, increases by a factor of four in comparison with the direct propagation [1]. In the general case the value of amplification of weak intensity fluctuations depends on sizes of the source transmitting aperture and of the reflector [2,3].

The significant amplification of strong intensity fluctuations ($\beta_0^2 >> 1$) occurs only when reflection from a point ($\Omega_t \ll \beta_0^{-12/5}$) reflector does not depend on diffraction parameters of the transmitting wave. In this case the saturation level of the relative variance of the reflected-radiation intensity is five, if the irradiating wave is spherical, and is three, if it is plane [2,3].

The long-range correlations of the reflected field also appear in the behavior of the reflected radiation intensity fluctuations. In particular, the saturation level of intensity fluctuations of a plane wave scattered with a point reflector increases from the value $\sigma_{I,R}^2 = 3$ in the plane of the lens to the value $\sigma_{I,F}^2 = 5$ in its focus [4].

If the spherical-wave source field is focused after the reflection, then the saturation level of intensity variance in the lens focus turns out to be lower than in the plane of the lens [3,4].

However, these variations are of the local character. When the observation plane is displaced from the focus along the optical axis of a lens ($l \neq F_t$), the relative variance of the reflected-radiation intensity takes eventually the same values as in the plane of the lens itself [5].

REFERENCES

1. Yu.A.Kravtsov, A.I.Saichev. Usp. Fiz. Nauk, 1982, v.137, ed.3, p.501-527.
2. Signals and Noises in Laser Sounding /Orlov V.M. et al. Moscow, Radio i Svyaz', 1985.
3. V.P.Aksenov, V.A.Banakh, V.L.Mironov. - J. Opt. Soc. Am. A, 1984, v.1, N3, p.263-274.
4. V.P.Aksenov, V.A.Banakh, V.M.Buldakov et al. - Optics Letters, 1984, v.10, N4, p.107-109.
5. V.P.Aksenov, V.A.Banakh, V.M.Buldakov et al. - Kvant. Elektron., 1985, v.12, N10, p.2136-2140.
6. V.A.Banakh, V.L.Mironov, I.N.Smalikho. - In: VIII All-Union Symposium on Laser and Acoustic Sounding of the Atmosphere. Abstracts of the Papers, Part I, Tomsk, 1984, p.41-44.
7. V.A.Banakh, V.M.Buldakov, I.N.Smalikho. - In: IX All-Union Symposium on Diffraction and Propagation of Waves. Abstracts of Papers, Part I, Tbilisi, 1985, p.410-413.

Regularized 2-Scale Solution for a Wave Propagation in a Random Medium

Joseph Gozani
Tel Aviv University,Faculty of Engineering,Tel Aviv, Ramat Aviv 69978,Israel.

1. Introduction

The fourth moment coherence function (MCF4) is defined by $\Gamma_4=\langle U_1\, U_2^*\, U_3^*\, U_4\rangle$. The wave function $U_i = U(\underline{\rho}_i,Z)$ is the envelope of a quasi-monochromatic wave with wave number k. The transverse position vectors are denoted by $\underline{\rho}_i = (x_i, y_i)$, i=1,2,3,4, and Z is the forward propagation range. The symbols $\langle\ \rangle$ and * denote ensemble average and complex conjugation respectively.

We use the Two Scale Expansion (TSE) - an extended uniformity perturbation method. It was successfully applied to solve problems of wave propagation in inhomogeneous random media [1-7]. TSE analytic expressions produce results comparable to those of other numerical and analytical methods [6-10]. In this paper we resolve the loss of symmetry of the solution and obtain a more general exact correction term.

2. Theory

The partial differential equation governing the propagation of MCF4 is

$$\left[\partial_Z - \frac{i}{k}\left[\partial_{\underline{P}}\cdot\partial_{\underline{S}} + \partial_{\underline{Q}}\cdot\partial_{\underline{R}}\right]\right]\Gamma_4 = k^2\, F\left[\underline{P}/\ell\ ,\ \underline{S}/\ell\ ,\ \underline{Q}/\ell\right]\Gamma_4, \tag{1}$$

with the initial condition (IC), $\Gamma_4(\underline{P},\underline{S},\underline{Q},\underline{R},Z=0) = \Gamma^0\ (\underline{P},\underline{S},\underline{Q},\underline{R})$. The transverse variables $\underline{P},\underline{S},\underline{Q},\underline{R}$ are a combination of sum and difference of $\underline{\rho}_i$. The operator $\partial_{\underline{\rho}} = (\partial/\partial\rho_x\ ,\ \partial/\partial\rho_y)$ is a two dimensional gradient. The scattering function F is a linear combination of structure functions $D(\underline{\rho})$ of the random medium:

$$F(\underline{P},\underline{S},\underline{Q}) = \frac{1}{2}\left[D(\underline{S}+\underline{P}) + D(\underline{S}-\underline{P}) - D(\underline{S}+\frac{\underline{Q}}{2}) - D(\underline{S}-\frac{\underline{Q}}{2}) - D(\underline{P}+\frac{\underline{Q}}{2}) - D(\underline{P}-\frac{\underline{Q}}{2})\right]. \tag{2}$$

$D(\underline{\rho})$ depends on a dimensionless variable $\underline{\rho}/\ell$ where ℓ is a typical characteristic scale. Defined in the following equation, it is also related to its isotropic spectrum $\phi(\alpha)$ by

$$D(\underline{\rho}) = \int_{-\infty}^{\infty} \left\langle\left[\tilde{n}(\underline{R}) - \tilde{n}(\underline{R}+\underline{\rho})\right]^2\right\rangle ds_Z = 2\pi\int_{-\infty}^{\infty} d^2\alpha\ \phi(\alpha)\left[1-\cos(\underline{\alpha}\cdot\underline{\rho})\right], \tag{3}$$

and $\tilde{n}(\underline{r})$ is the random deviation of the refractive index from the mean $\langle n\rangle=1$.

TSE expresses MCF4 using slow and fast variables. The procedure has several stages denoted by a subscript. For clarity, a slow variable appears under the original one.

a. Obtain a dimensionless integro-differential equation

Equation (1) is rendered dimensionless by:

$$\underline{p} = \underline{P}/\ell\ ,\ \underline{s} = k\,\underline{S}\ ,\ \underline{q} = \underline{Q}/\ell\ ,\ \underline{r} = \underline{R}/\ell\ ,\ z = Z/\ell,\ D(\cdot) = \bar{\sigma}(0)\, d(\cdot), \tag{4}$$

where ℓ $\propto$ the smallest scale of the random medium. Then the Fourier Transform is used on $\underline{p}$ and $\underline{r}$, to obtain an integro-differential equation,

$$\left[\partial_z + \underline{\eta}\cdot\partial_{\underline{s}} + \underline{\omega}\cdot\partial_{\underline{q}}\right]\Gamma_a = \frac{\ell}{\ell_F}\int_{-\infty}^{\infty} d^2\eta'\ f_a(\underline{\eta}',\varepsilon\underline{s},\underline{q})\ \Gamma_a(\underline{\eta}-\underline{\eta}',\underline{s},\underline{q},\underline{\omega},z). \tag{5}$$

The coefficient $\ell/\ell_F \ll 1$. Here $\ell_F^{-1} = k^2\bar{\sigma}(0)$ is the mean free path. Our small

parameter $\varepsilon = (\kappa\ell)^{-1}$, measures the narrow forward single scattering angle.

Throughout the paper extensive use of the shift operator,

$$\exp(\underline{a}\cdot\partial_{\underline{\rho}})\, g(\underline{\rho}) = g(\underline{\rho}+\underline{a}), \qquad \text{if } \partial_{\underline{\rho}}\cdot\underline{a} = 0, \tag{6}$$

substantially cuts the procedure. Its formal application can be shown using Taylor's expansion of the operator. By using Eq.(6) the convolution on the right-hand side (RHS) of Eq.(5) becomes:

$$\text{RHS} = \frac{i}{\ell_F}\int_{-\infty}^{\infty} d^2\eta'\, f_a(\underline{\eta}', \varepsilon\underline{s}, \underline{q})\, \exp\left[-\underline{\eta}'\cdot\partial_{\underline{\eta}}\right] \Gamma_a(\underline{\eta},\underline{s},\underline{q},\underline{\omega},z). \tag{7}$$

b. Two Scale Expansion

We expand $\underline{\eta}$ and $\underline{s}$ in two scales, thus imbedding MCF# in a higher dimensional space:

$$\Gamma_b\left[\begin{matrix}\underline{\eta}_1 & \underline{s}_1 \\ \underline{\eta}_2 & \underline{s}_2\end{matrix}, \underline{q}, \underline{\omega}, z\right]_{\substack{\eta_1=\eta \\ \eta_2=\varepsilon\eta}}^{\substack{s_1=s \\ s_2=\varepsilon s}} = \Gamma_a(\underline{\eta},\underline{s},\underline{q},\underline{\omega},z). \tag{8}$$

In light of the assumption in Eq.(8) a change of derivative

$$\partial_{\underline{\eta}} \to \partial_{\underline{\eta}_1} + \varepsilon\partial_{\underline{\eta}_2}, \qquad \partial_{\underline{s}} \to \partial_{\underline{s}_1} + \varepsilon\partial_{\underline{s}_2}, \tag{9}$$

transforms Eq.(5) into

$$\left[\partial_z + \underline{\eta}_1\cdot\partial_{\underline{s}_1} + \underline{\eta}_2\cdot\partial_{\underline{s}_2} + \underline{\omega}\cdot\partial_{\underline{q}}\right]\Gamma_b$$

$$= \frac{i}{\ell_F}\int_{-\infty}^{\infty} d^2\eta'\, f_b(\underline{\eta}', \underline{s}_2, \underline{q})\, \Gamma_b\left[\begin{matrix}\underline{\eta}_1 - \underline{\eta}' & \underline{s}_1 \\ \underline{\eta}_2 - \varepsilon\underline{\eta}' & \underline{s}_2\end{matrix}, \underline{q}, \underline{\omega}, z\right]. \tag{10}$$

The convolution in Eq.(10) is obtained by using the shift operator.

c. Obtain an exact Integral Equation

We Fourier transform both sides of Eq.(10) with respect to the $\underline{s}_1$ and $\underline{\eta}_1$, to obtain

$$\left[\partial_z + \underline{\xi}\cdot\partial_{\underline{\nu}} + \underline{\eta}_2\cdot\partial_{\underline{s}_2} + \underline{\omega}\cdot\partial_{\underline{q}}\right]\Gamma_c = \frac{i}{\ell_F} f_c(\underline{\nu} + i\varepsilon\partial_{\underline{\eta}_2}, \underline{s}_2, \underline{q})\,\Gamma_c\,. \tag{11a}$$

The RHS is formally obtained as follows:

$$\text{RHS} = \frac{i}{\ell_F}\int_{-\infty}^{\infty}\int_{-\infty}^{\infty} d^2\eta' d^2\eta_1\, f_b(\underline{\eta}', \underline{s}_2, \underline{q})\,\Gamma_b\left[\begin{matrix}\underline{\eta}_1 - \underline{\eta}' & \underline{\xi} \\ \underline{\eta}_2 - \varepsilon\underline{\eta}' & \underline{s}_2\end{matrix}, \underline{q}, \underline{\omega}, z\right]\exp\left[i\,\underline{\nu}\cdot\underline{\eta}_1\right]$$

$$= \frac{i}{\ell_F}\int_{-\infty}^{\infty}\int_{-\infty}^{\infty} d^2\eta'\, d^2\eta_1\, f_b(\underline{\eta}', \underline{s}_2, \underline{q})\exp\left[i\underline{\eta}'\cdot(\underline{\nu} + i\varepsilon\partial_{\underline{\eta}_2})\right]\Gamma_b\,. \tag{11b}$$

Here $f_c(\underline{\nu}+i\varepsilon\partial_{\underline{\eta}_2})$ can be understood as a convolution if we use a Fourier

transform, or as a complicated differential operator according to Taylor's series expansion. Equation (11) is solved with IC Γ_c^0, the result of Γ^0 after the above mentioned Fourier transforms. Once the formal form of the RHS is obtained, Eq.(11) can be transformed into an exact Volterra integral equation (IE). The RHS of Eq.(11a) is split into a dominant term and a small perturbation.

$$\left[\partial_z + \underset{\sim}{\xi}\cdot\partial_{\underset{\sim}{y}} + \underset{\sim}{\eta}_2\cdot\partial_{\underset{\sim}{s}_2} + \partial_{\underset{\sim}{q}}\right]\Gamma_c - \frac{\ell}{\ell_F} f_c(\underset{\sim}{y},\underset{\sim}{s}_2,\underset{\sim}{q})\,\Gamma_c = \frac{\ell}{\ell_F} h(\underset{\sim}{y},i\,\epsilon\partial_{\underset{\sim}{\eta}_2},\underset{\sim}{s}_2,\underset{\sim}{q})\,\Gamma_c \quad ,(12a)$$

$$h(\underset{\sim}{y},i\,\epsilon\partial_{\underset{\sim}{\eta}_2},\underset{\sim}{s}_2,\underset{\sim}{q})\,\Gamma_c = \left[f_c(\underset{\sim}{y}+i\,\epsilon\partial_{\underset{\sim}{\eta}_2},\underset{\sim}{s}_2,\underset{\sim}{q}) - f_c(\underset{\sim}{y},\underset{\sim}{s}_2,\underset{\sim}{q})\right]\Gamma_c$$

$$= \sum_{\ell=1}^{\infty}\frac{(i\epsilon)^\ell}{\ell!}\left[\partial_{\underset{\sim}{x}}\cdot\partial_{\underset{\sim}{y}}\right]^\ell f(\underset{\sim}{x},\underset{\sim}{s}_2,\underset{\sim}{q})\,\Gamma_c\left[\begin{matrix}\underset{\sim}{y} & \underset{\sim}{\xi}\\ \underset{\sim}{y} & \underset{\sim}{s}_2\end{matrix},\ \underset{\sim}{q},\ \underset{\sim}{\omega},\ z\right]_{\underset{\sim}{x}=\underset{\sim}{y},\ \underset{\sim}{y}=\underset{\sim}{\eta}_2} . \qquad (12b)$$

We now solve the homogeneous Eq.(12a) by the method of characteristics to obtain the fundamental solution Ψ, with IC $\Psi = 1$ at $t = 0$. The RHS of Eq.(12a), $h\Gamma_c$, is treated as a source term. The final expression of Ψ is

$$\Psi\left[\begin{matrix}\underset{\sim}{y} & \underset{\sim}{\xi}\\ \underset{\sim}{\eta}_2 & \underset{\sim}{s}_2\end{matrix},\ \underset{\sim}{q},\underset{\sim}{\omega},z\right] = \exp\left[\frac{\ell}{\ell_F}\int_{t=0}^{t=z} d\tau\ f\left[\underset{\sim}{y}-\underset{\sim}{\xi}\tau,\ \underset{\sim}{s}_2-\underset{\sim}{\eta}_2\tau,\ \underset{\sim}{q}-\underset{\sim}{\omega}\tau\right]\right]. \qquad (13)$$

The fundamental solution is used to solve the inhomogeneous equation. Interpreting $f_a(\underset{\sim}{y}+i\epsilon\partial_{\underset{\sim}{\eta}_2})$ as a convolution from Eq.(11b), the IE for Γ_c is

$$\Gamma_c\left[\begin{matrix}\underset{\sim}{y} & \underset{\sim}{\xi}\\ \underset{\sim}{\eta}_2 & \underset{\sim}{s}_2\end{matrix},\ \underset{\sim}{q},\underset{\sim}{\omega},z\right] = \Gamma_c^0\left[\underset{\sim}{y}-\underset{\sim}{\xi}z,\ \underset{\sim}{\xi},\underset{\sim}{q}-\underset{\sim}{\omega}z,\underset{\sim}{\omega}\right]\Psi(z)$$

$$+ \frac{\ell}{\ell_F}\int_0^z d\tau\,\exp\left[\frac{\ell}{\ell_F}\int_\tau^z du\, f\left[\underset{\sim}{y}-\underset{\sim}{\xi}u,\underset{\sim}{s}_2-\underset{\sim}{\eta}_2u,\underset{\sim}{q}-\underset{\sim}{\omega}u\right]\right]$$

$$\times\left\{\int_{-\infty}^{\infty} d^2\alpha\ 2\phi(\underset{\sim}{\alpha})\,\sin\left[\frac{\underset{\sim}{\alpha}}{2}\cdot\left[\underset{\sim}{s}_2+\frac{\underset{\sim}{q}}{2}-\left[\underset{\sim}{\eta}_2+\frac{\underset{\sim}{\omega}}{2}\right](z-\tau)\right]\right]\right.$$

$$\left.\times\sin\left[\frac{\underset{\sim}{\alpha}}{2}\cdot\left[\underset{\sim}{s}_2-\frac{\underset{\sim}{q}}{2}-\left[\underset{\sim}{\eta}_2-\frac{\underset{\sim}{\omega}}{2}\right](z-\tau)\right]\right]\exp\left[i\underset{\sim}{\alpha}\cdot\left[\underset{\sim}{y}-\underset{\sim}{\xi}(z-\tau)\right]\right]\right.$$

$$\left.\times\,\Gamma_c\left[\begin{matrix}\underset{\sim}{y}-\underset{\sim}{\xi}(z-\tau) & \underset{\sim}{\xi}\\ \underset{\sim}{\eta}_2-\epsilon\underset{\sim}{\alpha} & \underset{\sim}{s}_2-\underset{\sim}{\eta}_2(z-\tau)\end{matrix},\ \underset{\sim}{q}-\underset{\sim}{\omega}(z-\tau),\underset{\sim}{\omega},\tau\right]\right\}$$

$$-\frac{1}{2}\left[d\left[\underset{\sim}{s}_2+\underset{\sim}{y}-\left[\underset{\sim}{\eta}_2+\underset{\sim}{\xi}\right](z-\tau)\right]+d\left[\underset{\sim}{s}_2-\underset{\sim}{y}-\left[\underset{\sim}{\eta}_2-\underset{\sim}{\xi}\right](z-\tau)\right]\right]\otimes d\left[\underset{\sim}{y}+\frac{\underset{\sim}{q}}{2}-\left[\underset{\sim}{\xi}+\frac{\underset{\sim}{\omega}}{2}\right](z-\tau)\right]$$

$$- d\left[\underline{v} - \frac{\underline{q}}{2} - \left[\underline{\xi} - \frac{\underline{\omega}}{2}\right](z-\tau)\right]\Big] \Gamma_c\left[\begin{matrix}\underline{v}-\underline{\xi}(z-\tau) & \underline{\xi} \\ \underline{\eta}_2 & , \ \underline{s}_2-\underline{\eta}_2(z-\tau)\end{matrix}, \ \underline{q}-\underline{\omega}(z-\tau), \underline{\omega}, \tau\right]. \qquad (14)$$

In terms of iterated kernel the complete solution is

$$\Gamma_c = \sum_{\ell=0}^{\infty} \Gamma^{(\ell)}, \qquad \Gamma^{(0)} = \Gamma_d^{\circ}\left[\underline{v}-\underline{\xi}z, \underline{\xi}, \underline{q}-\underline{\omega}z, \underline{\omega}\right] \Psi(z). \qquad (15)$$

The Neumann series of Eq.(15) converge absolutely and uniformly in ε and z. Successive substitutions for the first two terms luckily give us sufficient accuracy, since higher iterates are difficult to compute. The first order iterate is of $O(\varepsilon)$ due to the leading term in Eq.(12b). Previously used TSE variants, expanded the solution in powers of ε perturbation series. The ε^0 term coincides with our $\Gamma^{(0)}$ but our correction term is new. Furthermore our formulation shows that these are convergent series.

d. Return to original space

Before assembling all spectral contributions, we must insert the value of $\underline{s}_2 = \varepsilon \underline{s}$ and $\underline{\eta}_2 = \varepsilon \underline{\eta}$ from Eq.(8), and apply the inverse of the above mentioned Fourier transform. A return to the dimensional variables by Eq.(2), is the final step.

e. Symmetrization

The original exact solution exhibits a symmetry i.e. $\Gamma_s(\underline{p},\underline{s},\cdot) = \Gamma_s(\underline{s},\underline{p},\cdot)$, which Eq.(14) does not. Since we judiciously applied at first the Fourier transform to $\underline{p}$, TSE procedure is an asymmetric process. TSE could be exactly repeated on $\underline{s}$. Therefore the final **symmetric solution** should be

$$MCF4 = \frac{1}{2}\left[\Gamma_d(\underline{p}, \underline{s}, \underline{q}, \underline{r}, z) + \Gamma_d(\underline{s}, \underline{p}, \underline{q}, \underline{r}, z)\right]. \qquad (16)$$

3. Conclusion

We presented expressions for the propagation of MCF4 in terms of a convergent series. We applied TSE with a parameter ε whose smallness is independent of the turbulence strength. We have shown how to symmetrize the solution. Thus the two main problems of TSE: the significance of correction terms and the loss of symmetry - are regularized.

References

1. S. Frankenthal, A.M. Whitman, and M.J.Beran, J.Acoust.Soc.Am., **71**(2), 848-858 (1982).
2. M.J. Beran, A.M. Whitman, and S. Frankenthal, J.Acoust.Soc.Am., **71**(5), 1124-1130 (1982).
3. R. Mazar and M.J. Beran, J.Acoust.Soc.Am.,**72**(4), 1269-1275 (1982).
4. C. Macaskill, Proc.Roy.Soc.London, A**386**, 461-474 (1983).
5. R. Mazar, J.Acoust.Soc.Am., **75**(6),1748-1759, (1984).
6. R. Mazar, J. Gozani, and M. Tur, J.Opt.Soc.Am., Dec. (1985).
7. B.J. Uscinski and C. Macaskill, Optica Acta, **32**(1), 71-89 (1985).
8. S. Frankenthal, A.M. Whitman, and M.J. Beran, J.Opt.Soc.Am. A, **1**,(6), 585 - 597 (1984).
9. A.M Whitman, and M.J. Beran, J.Opt.Soc.Am., Dec. (1985).
10. J. Gozani, J.Opt.Soc.Am., Dec. (1985).

A New Derivation of Uscinski's Approximate Solution Of The Fourth-Moment Equation

Alan M. Whitman
Tel-Aviv University
Faculty of Engineering
Tel-Aviv, Israel

In the recent past an approximate solution to the fourth-moment equation has been obtained [1],[2]. This has been shown to provide an accurate solution to the atmospheric scintillation problem for all propagation ranges [3], and holds the promise of being applicable to other outstanding fluctuation problems. However the two-scale method used in the derivation has been criticized as being physically and mathematically obscure. Furthermore, Uscinski's original calculation of the dominant order term [4] is also difficult to follow because of the plethora of computational steps and the profusion of approximations. In the present article we will present a simpler derivation of this result.

The fourth-moment equation for two-dimensional, plane wave propagation is [3]

$$\frac{\partial L}{\partial \varsigma} = i \frac{\partial^2 L}{\partial \bar{x} \partial \bar{p}} + \gamma\, h(\bar{x}, \bar{p})\, L \qquad L = 1 \;@\; \varsigma = 0 \qquad (1)$$

We write this as an integrodifferential equation by means of

distributions

$$\frac{\partial L}{\partial \varsigma} = \int\int \left\{ i\,\delta'(\bar{x}-\bar{x}')\,\delta'(\bar{p}-\bar{p}') + \gamma\, h(x',p')\,\delta(\bar{x}-\bar{x}')\,\delta(\bar{p}-\bar{p}') \right\} L(\varsigma, x', p')\, dx'\, dp'$$

Approximating the derivative by the difference $[L(\varsigma+\Delta\varsigma, \bar{x}, \bar{p}) - L(\varsigma, \bar{x}, \bar{p})]/\Delta\varsigma$ and again using distributions, this time for $L(\varsigma, \bar{x}, \bar{p})$ we obtain

$$L(\varsigma+\Delta\varsigma, \bar{x}, \bar{p}) \sim \int\int \left\{ \delta(\bar{x}-\bar{x}')\,\delta(\bar{p}-\bar{p}') + \Delta\varsigma \left[i\,\delta'(\bar{x}-\bar{x}')\,\delta'(\bar{p}-\bar{p}') + \gamma\, h(x',p')\,\delta(\bar{x}-\bar{x}')\,\delta(\bar{p}-\bar{p}') \right] \right\} L(\varsigma, x', p')\, dx'\, dp'$$

which is accurate to order $\Delta\varsigma^2$. Now we insert the Fourier transforms of δ and δ', so that

$$L(\varsigma+\Delta\varsigma, \bar{x}, \bar{p}) \sim \frac{1}{(2\pi)^2} \int\int\int\int\int e^{i\sigma(\bar{x}-x')}\, e^{iu(\bar{p}-p')} \left\{ 1 + \Delta\varsigma \left[i\sigma u + \gamma\, h(x',p') \right] \right\} \times L(\varsigma, x', p')\, dx'\, dp'\, du\, d\sigma$$

The crucial step in the derivation is to expontiate the term in curly brackets. Thus

$$1 + \Delta\varsigma \left[i\sigma u + \gamma\, h(x',p') \right] = e^{\Delta\varsigma \left[i\sigma u + \gamma h(x',p') \right]} + O(\Delta\varsigma^2)$$

Subsequent integration with respect to σ produces

$$L(\varsigma+\Delta\varsigma, \bar{x}, \bar{p}) \sim \frac{1}{2\pi} \int\int\int \delta(\bar{x}-x'+\Delta\varsigma u)\, e^{iu(\bar{p}-p')}\, e^{\gamma\Delta\varsigma h}\, L(\varsigma, x', p')\, dx'\, dp'\, du$$

At this point we can do either the u integration or the x' integration. The former gives the result

$$L(\varsigma+\Delta\varsigma, \bar{x}, \bar{p}) \sim \frac{1}{2\pi\,\Delta\varsigma} \int\int e^{-i(\bar{x}-x')(\bar{p}-p')/\Delta\varsigma}\, e^{\gamma\Delta\varsigma h(x',p')}\, L(\varsigma, x', p')\, dx'\, dp'$$

This formula, in which the symmetry of $\bar{x}$ and $\bar{p}$ has been preserved,

could serve as a numerical algorithm for marching the L field. Indeed such a proceedure has been used successfully on a factorized wave equation [5]. Furthermore it can be viewed as a numerical approximation of the formal, path integral solution of Eq (1) [6]. The second alternative produces

$$L(\varsigma+\Delta\varsigma,\bar{x},\bar{p}) \sim \frac{1}{2\pi}\iint e^{i\nu(\bar{p}-p')} e^{i\Delta\varsigma h(\bar{x}+\Delta\varsigma\nu,p')} L(\varsigma,\bar{x}+\Delta\varsigma\nu,p')\,dp'd\nu \quad (2)$$

Although the symmetry between $\bar{x}$ and $\bar{p}$ has been destroyed, this equation is correct to the same degree as the former. If we set $\varsigma = 0$ here, use the initial condition, and note that

$$\Delta\varsigma\, h(\bar{x}+\Delta\varsigma\nu,p') = \int_0^{\Delta\varsigma} h(\bar{x}+\nu t,p')\,dt + O(\Delta\varsigma^2)$$

we can write Eq (2) in the form

$$L(\Delta\varsigma,\bar{x},\bar{p}) \sim \frac{1}{2\pi}\iint e^{i\nu(\bar{p}-p')} e^{i\Delta\varsigma\int_0^1 h(\bar{x}+\Delta\varsigma\nu t,p')\,dt}\,dp'd\nu \quad (3)$$

Iterating Eq (2) backward to the plane $\varsigma-\Delta\varsigma$ and setting $\varsigma = \Delta\varsigma$ gives

$$L(2\Delta\varsigma,\bar{x},\bar{p}) \sim \frac{1}{(2\pi)^2}\iiiint e^{i\Delta\varsigma[h(\bar{x}+\Delta\varsigma\nu,p')+h(\bar{x}+\Delta\varsigma\nu+\Delta\varsigma\nu_1,p_1)]} \times e^{i\nu(\bar{p}-p')} e^{i\nu_1(p'-p_1)}\,d\nu d\nu_1\,dp'dp_1$$

Taylor expanding $h(\bar{x}+\Delta\varsigma\nu+\Delta\varsigma\nu_1)$ about $\bar{x}+\Delta\varsigma\nu$, and neglecting terms of order $\Delta\varsigma^2$ allows two integrals to be evaluated. The resulting expression can then be manipulated into the form of Eq (3) with $2\Delta\varsigma$ replacing $\Delta\varsigma$ everywhere. Continuing in this way we can arrive at an expression for $L(n\Delta\varsigma,\bar{x},\bar{p})$, and on doing the double limit $n\to\infty$, $\Delta\varsigma\to 0$, such that $n\Delta\varsigma = \varsigma$, we obtain the

dominant order two-scale result [3]

$$L(\varsigma,\bar{x},\bar{p}) = \frac{1}{2\pi}\int_{-\infty}^{\infty} e^{iu(\bar{p}-p')}\, e^{i\varsigma\int_0^t h(\bar{x}-\varsigma u t, p')\,dt}\, du\,dp' + O(f(\varsigma))$$

Although we cannot determine $f(\varsigma)$ from the rather crude argument presented here, we know from previous work that $f(\varsigma) = o(1)$ both for $\varsigma \to 0$, and $\varsigma \to \infty$ for a variety of structure functions.

References

[1] C. Macaskill, Proc. R. Soc. London, Sec. A 386, 461-474 (1983)

[2] S. Frankenthal, A.M. Whitman, and M.J. Beran, J. Opt. Soc. Am. A 585-597 (1984)

[3] A.M. Whitman and M.J. Beran, J. Opt. Soc. Am. A, Dec 1985

[4] B.J. Uscinski, Proc. R. Soc. London, Sec. A 380, 137-169 (1982)

[5] L. Fishman and J.J. McCoy, Geophys. J. R. Astr. Soc., 80, 439-461 (1985)

[6] J.J. McCoy, personal communication

COMPUTATIONS OF THE EFFECT OF ATMOSPHERIC TURBULENCE ON LASER BEAM PROPAGATION

C.D.V. Thomas
Royal Armament Research and Development Establishment, Fort Halstead, Sevenoaks, Kent TN14 7BP

The computations reported in this paper refer to scintillations at optical wavelengths for a beam propagated through atmospheric turbulence with moderate to high values of the refractive index structure constant. Various cases, including multiple scattering, were included. The spectrum of refractive index fluctuations was taken as modified Von Karman spectrum: Ishimary, 1978. The covered two main areas:

1. Numerical computations of the scintillation index and spatial spectrum using the solution to the fourth order moment equation derived by Uscinki, 1982 and Macaskill, 1983.
2. Computations of the probability of exceeding given threshold irradiances at various distances from a laser producing an initially gaussian beam.

The solution of the fourth moment equation derived by Uscinky (1982) for plane waves and Macaskill (1983) for spherical waves was used to calculate the scintillation index vs range. Calculation of the scintillation index involved multidimensional numerical integration using a Cray-1 computer. It is hoped to present the results of some calculations for the three dimensional case.

The results of these calculations of the scintillation index, along with calculations of the mean irradiance and probability distribution of the irradiance fluctuations were also used to calculate the probability of exceeding a given threshold irradiance at any point in a beam which has passed through atmospheric turbulence.

The mean intensity was calculated by evaluating the solution to the second order moment equation. This solution was derived by Ishimaru: 1978, and is valid for both single and multiple scattering.

The probability distribution of the irradiance fluctuations was assumed to be log-normal in the case of weak scintillation, however for other cases including the transition to saturation and beyond, the fluctuations were assumed to be K-distributed, Parry, 1979.

These calculations have implications for laser safety procedures.

Results of the computations will be presented at the conference, and it is hoped to publish a full account of this work shortly.

REFERENCES.

1. Macaskill C. (1983) Proc. Roy. Soc. A386, 461.

2. Ishimaru A. (1978) "Wave Propagation and Scattering in Random Media", Academic Press, N.Y.
3. Uscinki B.J. (1982) Proc. Roy. Soc. A380, 137.
4. Parry G. (1979) J. Optical Soc. America Vol. 69, 796.

TWO-FREQUENCY SCINTILLATION

Temporal and Spectral Correlations of Two-Wavelength Optical Propagation in the Turbulent Atmosphere

M. Tur
School of Engineering, Tel-Aviv University, Tel-Aviv, ISRAEL 69978

Z. Azar and E. Azoulay
Soreq Nuclear Research Center, Department of Atmospheric Optics
Yavne 70600, ISRAEL

(invited)

An optical beam, propagating through a randomly inhomogeneous medium, experiences both phase and intensity fluctuations which are the result of random scattering and diffraction from the refractive index inhomogeneities in the random medium. While these fluctuations severely limit the performance of surveillance, communication and lidar systems that use the random medium as their channel, study of the statistical properties of the received fluctuations may also reveal useful information about the nature and structure of the random medium and/or the optical source (the inverse problem).

Space diversity (simultaneous measurements of the received radiation at several spatially separated points) and time diversity (measuring the time correlation of the fluctuations) not only add important data to ease the solution of the inverse problem, but their incorporation in practical devices also significantly improve the signal to noise ratio in the above mentioned electro-optic systems.

Recently, a new degree of freedom has been investigated, namely, spectral diversity; or the bichromatic intensity correlation of two optical beams with different wavelengths, propagating through the same channel (The somewhat related subject of pulse spreading has been extensively studied in the past using the second order statistical moment of the propagating amplitudes of two very closely spaced optical frequencies[1]). Here, comparisons between experimentally determined bichromatic correlations and their theoretically calculated counterparts will refine the models used to describe the refractive index correlation function of the medium. In system design, a small value of the bichromatic correlation coefficient increases the chances that whenever signal fading takes place at one wavelength, good reception will occur at the other wavelength[2]. If on the other hand, the bichromatic correlation coefficient is high, one wavelength from a cheap and weak optical source can be used to probe the medium and momentarily locate high transmission, short-lived, time windows for a stronger, and inevitably more expensive source to successfully transmit the information through the highly transmissive channel.

Early measurements by Gurvich et al[3]. were limited to one set of fairly close wavelengths: 0.44μm, 0.63μm. Also, theoretical treatments could only handle the weak scattering regime. Last year, new theoretical studies[4,5] of the two-frequency fourth moment equation in the strong multiple scattering regime, have resulted in a closed form, though approximate and difficult to evaluate expression for the bichromatic covariance function,

$$C(z;\ \vec{\rho}_1,\ \vec{\rho}_2;\ k_1,\ k_2,\ \tau=t_1-t_2)$$

$$= \frac{\left[\langle I(z,\ \vec{\rho}_1,\ k_1,\ t_1)\rangle - \langle I(z,\ \vec{\rho}_1,\ k_1,\ t_1)\rangle\right]\left[\langle I(z,\ \vec{\rho}_2,\ k_2,\ t_2)\rangle - \langle I(z,\ \vec{\rho}_2,\ k_2,\ t_2)\rangle\right]}{\langle I(z,\ \vec{\rho}_1,\ k_1,\ t_1)\rangle\langle I(z,\ \vec{\rho}_2,\ k_2,\ t_2)\rangle}$$

κ_1 and κ_2 are the two wavenumbers ($\kappa_i = 2\pi/\lambda_i$), z is the range, $\vec{\rho}_i$ are two spatial transverse coordinates, either in the receiver plane-where detectors are located, or in the transmitter plane, signifying the location or directions of the transmitters, τ is the time delay between measurements taken at the two different wavelengths, I(·) is the fluctuating intensity and <> denote ensemble averaging. The range dependence of $C(z; \vec{\rho}_1, \vec{\rho}_2; \kappa_1, \kappa_2)$ for either a plane or cylindrical waves, propagating in a two-dimensional random medium, has been studied in some detail in Refs. [4]-[5] for both a single and double scale correlation functions. The results show that independent of the refractive index spectrum of the medium, $C(z; \rho_1, \rho_2; \kappa_1, \kappa_2)$ decreases fairly rapidly with both Z and $\Omega=(k_2-k_1)/(k_1+k_2)$, as Ω departs from zero. Oceanographic measurements of $C(z; \rho_1, \rho_2; k_1, k_2)$ for acoustic propagation[6] revealed higher values for C(·) than those predicted by the present theory[4].

Optical experiments in the atmosphere[3,7] result in even higher values for the bichromatic correlation than in the ocean. The experimental setup is shown in Fig. 1.

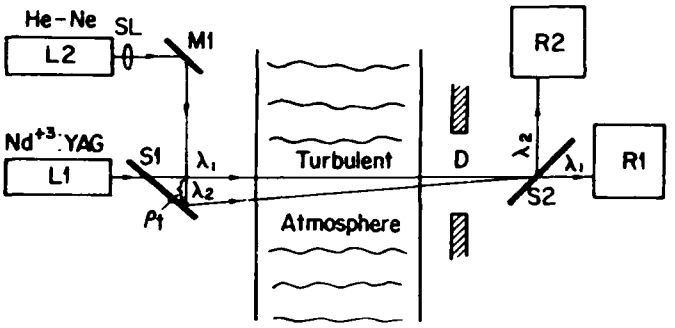

Fig. 1 - Experimental setup. L1, L2, lasers; SL - beam forming lens; M1, plane mirror; S1, S2 dichroic beam splitters; D, variable circular aperture; R1, R2 receivers.

The transmitter incorporates two CW lasers, both operating at their TEM_{oo} modes with initial beam diameters of ≈1.2mm. L1 is a 120mW, 1.064μm Nd^{+3} : YAG laser, emitting with a divergence angle of 3 mrad. L2 is a 16mW, 0.6328μm He - Ne laser, having an initial divergence of 1 mrad which is then transformed by the lens SL to a 3 mrad beam. The emission from L2 is combined with the emission from L1 by the plane mirror M1 and beam splitter S1, whose position determined the distance ρ_t, and hence the angle between the two beams. The receivers were described in details elsewhere[7].

Fig. 2a depicts the measured normalized time-autocovariance function $Cov(z=1300m, \vec{\rho}_1-\vec{\rho}_2=0, \lambda_{1.06}, \lambda_{1.06}, \tau)$ and the normalized time-crosscovariance function $Cov(z=1300m, \vec{\rho}_1-\vec{\rho}_2=0, \lambda_{1.06}, \lambda_{0.63}, \tau)$ as a function of the time delay for an aperture size of 15mm. Thus, in spite of the strong turbulence conditions (σ_1^2(Rytov) > 5) and the high value of Ω(=0.25), the correlation coefficient exceeds 0.8. Similar measurements with smaller apertures or longer ranges (≈3000m) still gave correlation coefficients in excess of 0.7. The dependence of the two functions on τ are nearly the same, and the time

correlation at FWHM≈4msec.

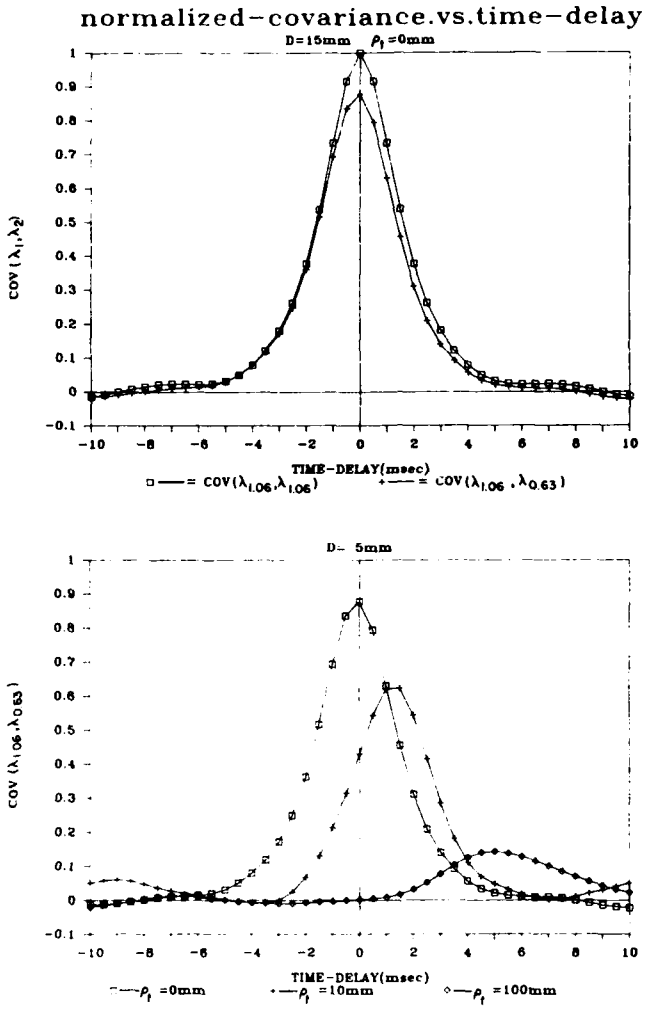

Fig. 2 - Measured normalized time-autocovariance and crosscovariance function as a function of the time delay for z=1300m, D=15mm, and $C_n^2 = 10^{-13}m^{-2/3}$. (a) $\vec{\rho}_t$=0; (b) $\vec{\rho}_t$=0, 10, 100mm.

Fig. 2b depicts the measured normalized, time-crosscovariance function $Cov(z=1300m, \vec{\rho}_t=\vec{\rho}_1-\vec{\rho}_2, \lambda_{1.06}, \lambda_{0.63}, \tau)$ as a function of the time delay for an aperture size of 15mm, and $\vec{\rho}_t$=0,10,100mm. The correlation between the two beams decreases as $\vec{\rho}_t$ increases and it is evident that the correlation strongly depends on the initial condition of the experiment. The shift of the peak is due to the cross wind along the path[8].

Unlike the underwater acoustic experiment, where the propagation is essentially two dimensional in character[6], the optical experiments described above, require a three dimensional theory. The basic theoretical formulation[4,5] is three dimensional but we are unaware of any published results for this case for $\Omega \neq 0$ and therefore, direct comparison between theory and experiment is not possible at this time. Even when these results become available, the agreement between the theory and the experiment may not be too good, since, as pointed out in Ref. [4], a major expected reason for the discrepancy between the theory and the experiment in the acoustical case, can be attributed to insufficient accuracy of the theoretical result. In particular, all mentioned results are a zero order approximation in a certain asymptotic expansion. While for $\Omega=0$, this approximation is accurate enough, $\Omega \neq 0$ probably requires more terms in the expression to be evaluated.

In conclusion, measurements of space-time spectral crosscorrelations are challenging the current theoretical solutions of the fourth moment equation. The high measured values of the bichromatic correlation coefficient should also prove useful in various system designs.

References

1. R.L. Fante, "Two-position, two-frequency mutual-coherence function in turbulence", J. Opt. Soc. Am., 71, 1446(1981)
2. B.G. King, P.J. Fitzgerald, and H.A. Stein, "An experimental study of atmospheric optical transmission", BSTJ, 62, 607(1983)
3. A.S. Gurvich, V. Kan, and V. Pokasov, "Two-frequency fluctuations of light intensity in a turbulent medium" OPTICA ACTA, 26, 555(1979)
4. B.J. Uscinski and C. Macaskill, "Frequency cross-correlation of intensity fluctuations in multiple scattering", OPTICA ACTA, 32, 71(1985)
5. R. Mazar, J. Gozani, and M.Tur, "A two scale solution for the intensity fluctuations of two-frequency wave propagation in a random medium", J. Opt. Soc. Am. A, 2, 2152(1985)
6. T.E. Ewart, C. Macaskill, and B.J. Uscinski, " The MATE acoustic frequency cross correlations of intensity", J. Acoust. Soc. Am., 77, 1732(1985)
7. Z. Azar, H.M. Loebenstein, G. Appelbaum, E. Azoulay, U. Halavee, M. Tamir, and M. Tur, "Aperture averaging of the two-wavelength intensity covariance function in atmospheric turbulence", Appl. Opt., 24, 2401(1985)
8. Ting-i Wang, G.R. Ochs, and R.S. Lawrence, "Wind measurements by the temporal cross-correlation of the optical scintillations", Appl. Opt., 20, 4073(1951)

TWO COLOR CORRELATION OF SCINTILLATIONS

N. Ben-Yosef, E. Goldner, and A. Weitz
Applied Physics Division, Graduate School of Applied Science and Technology,
The Hebrew University of Jerusalem, Jerusalem, ISRAEL

Introduction

The correlation between the scintillations of two waves, at different wavelengths, propagating in the same turbulent medium were not measured extensively. At the case where it was measured [1], no complete agreement with theory was obtained. The present set of measurements show that there is a loss of correlation with increasing turbulence level.

The simple, weak turbulence theory, predicts that the correlation of the intensity fluctuations of two waves propagating in the same medium is independent of turbulence strength and depends only on the wavelengths. This conclusion is reached using the Rytov approximation and the Kolmogorov turbulence spectrum. The use of thsi spectrum means that all the relevant path integrals depend on the refractive index structure constant as a multiplier and thus its elimination from the correlation coefficient is obvious. It will be shown that by using the Von-Karman spectrum and the Rytov approximation the two color correlation coefficient is dependent on the inner scale size parameter which can be dependent on turbulence strength [2-4]. Most of the experimental results can be so explained.

Experimental Results

The present experiment consisted of two laser beams (at 0.632 μmeter and 1.06 μmeter) propagating along the same 150 meters long path. The intensity of each at the end of the path was measured separately.

The correlation coefficient was measured as a function of turbulence strength by measuring continuously along the day. A "point" was represented by analyzing the proper averages over a time interval of about 40 sec.. In order to check the accuracy of the measurements and the validity of the use of weak and moderate strength turbulence approximations, figure 1 shows the plot of $\sigma^2_{I_1}$ (He-Ne) vs. $\sigma^2_{I_2}$ (Nd-Yag). The solid line is the weak turbulence approximation.

One observes that a fair agreement exists. The slight deviations at low and intermediate values are due to the ripple noise in the Nd-Yag laser.

The two color correlation coefficient, as defined in [1] as a function of $\sqrt{\sigma_{I_1}\sigma_{I_2}}$ is shown in figure 2. The parameter $\sqrt{\sigma_{I_1}\sigma_{I_2}}$ was chosen to represent the measure of turbulence intensity. The five points at $\sqrt{\sigma_{I_1}\sigma_{I_2}} < 0.2$ show low correlation due to the fact taht at this region the noise is significant compared to the optical scintillation, as the noise in the two channels is not correlative the low correlation is not surprising, these points will not be considered further.

Disregarding the noise dominant region one observes that the correlation coefficient obtains the value of about 0.875 and decreases monotonously with increasing turbulence level.

The Theoretical Correlation Coefficient

Following the well known theories [5,6,8] one can write the two point log-amplitude coherence function using the proper turbulence spectrum. The use of the Kolmogorov spectrum is justified if $\ell_o \ll \sqrt{\lambda L}$ (the outer scale size parameter is of no importance in the present case). In our experiment $\sqrt{\lambda L} \approx 10$ millimeters so that the dissipation range is of importance. In order to account for this region (the region of small size turbulent eddies) the Von-Karman spectrum has to be used. One should remember that this spectrum reduces to the Kolmogorov one for $\ell_o = 0$. Using this spectrum one obtains the family of the solid lines in figure 2 with 1 serving as parameter.

By comparing the experimental results with the family of curves one concludes that the present theory with a constant value for the inner scale parameter cannot account for the results. On the other hand, the results can be completely understood by stipulating that the turbulence spectrum changes with increasing turbulence strength. The change is such that as the turbulence becomes stronger the inner scale size parameter decreases. This conclusion means that increasing the turbulence strength increases the relative weight of the small turbulent eddies. This stipulation has some indirect evidence in direct measurements of ℓ_o as reported by [2-4] which show that values of ℓ_o down to 3 m'm were measured.

Discussion

The results show that the two color correlation decreases faster than predicted by theory assuming a fixed functional shape of the turbulence spectrum. Assuming a varying spectrum the results are quite consistent with theory.

In any case, the fast loss of correlation indicates that the small turbulent eddies increase their relative weight as turbulence becomes stronger.

References

1. Gurvich, A.S., Kan, V. and Pokasov, V.V., "Two Frequency Fluctuations of Light Intensity in a Turbulent Medium", Optica Acta, 26, p.555 (1979).

2. Zubrovsky and Karpov, Izv. Akad. Nauk. SSSR, Fiz. Atmos. Okeana. 6, p. 989 (1970).

3. Hill, R.T., "Theory of Saturation of Optical Scintillation by Strong Turbulence", J.O.S.A. 72, p. 212 (1982).

4. Coles, W.A. and Frehlich, R.G., "Simultaneous Measurements of Angular Scattering and Intensity Scintillations in the Atmosphere", J.O.S.A., 72, p. 1042 (1982).

5. Ishimaru, A., "Temporal Frequency Spectra of Multifrequency Waves in Turbulent Atmosphere", IEEE Trans. AP-20, p. 10 (1972).

6. Fante, R., "Electromagnetic Beam Propagation in Turbulent Media", Proc. IEEE, 63, p. 1669 (1975).

7. Ben-Yosef, N., Tirosh, E., Weitz, A. and Pinsky, E., "Refractive Index Structure Constant Dependence on Height", J.O.S.A. 69, p. 1616 (1979).

8. Ishimaru, A., "Wave Propagation and Scattering in Random Media", Vol. 2, Academic Press, New-York (1978).

Figure Captions

Figure 1. The normalized intensity standard deviation at 0.6328 μmeter, $\sigma^2_{I_1}$, vs. the normalized intensity standard deviation at 1.06 μmeter, $\sigma^2_{I_2}$. The solid line is the weak turbulence approximation.

Figure 2. The two color cross correlation coefficient vs. $\sqrt{\sigma_{I_1} \cdot \sigma_{I_2}}$ (proportional to turbulence intensity). The solid lines represent the moderate turbulence approximation using the Von-Karman turbulence spectrum with ℓ_0, the inner scale size parameter, as parameter.

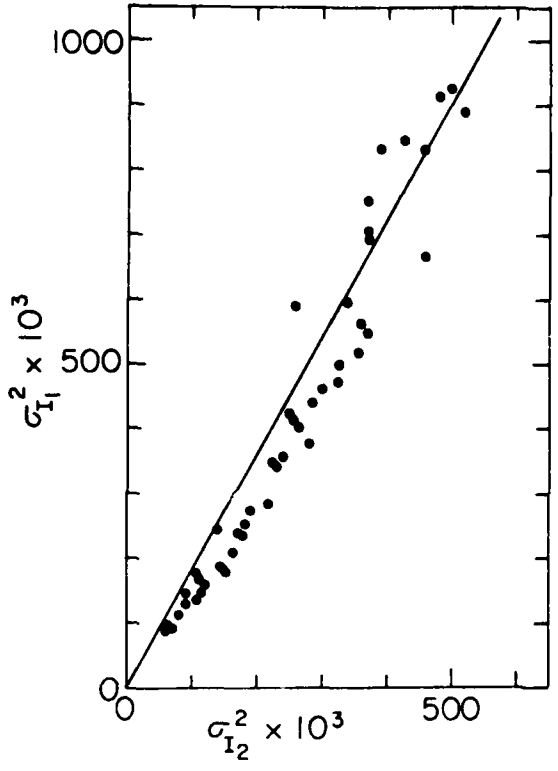
1000
500
0
0
500
$\sigma_{I_1}^2 \times 10^3$
$\sigma_{I_2}^2 \times 10^3$

Fig. 1

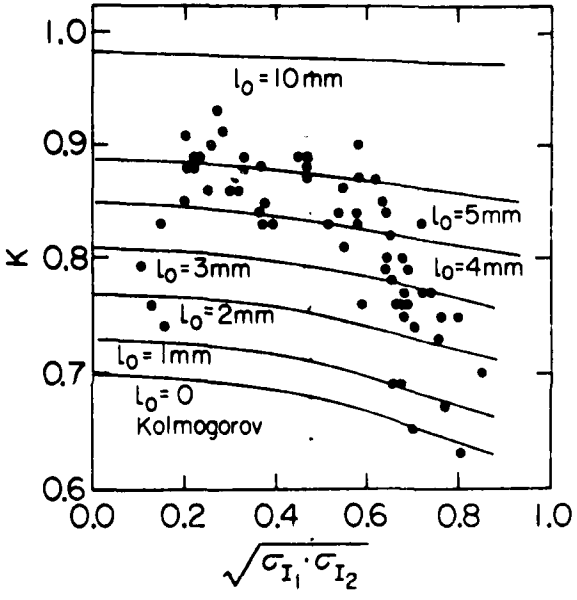
1.0
0.9
0.8
0.7
0.6
K
0.0
0.2
0.4
0.6
0.8
1.0
$\sqrt{\sigma_{I_1} \cdot \sigma_{I_2}}$
l_0 = 10mm
l_0=5mm
l_0=4mm
l_0=3mm
l_0=2mm
l_0=1mm
l_0= 0
Kolmogorov

Fig. 2

BEAM WAVES FREQUENCY CORRELATION IN TURBULENT ATMOSPHERE

K.S.Gochelashvily
General Physics Institute, Moscow, USSR
T.S.Radjabov
Institute of Astrophysics, Tadjik Academy of Sciences, Dushanbe, USSR
I.M.Uzunov
Institute of Electronics, Bolgarian Academy of Sciences, Sofia, Bulgaria
V.I.Shishov
P.N.Lebedev Physical Institute, Moscow, USSR

The properties of frequency correlation of saturated intensity fluctuations are required in many applications, in which laser beams emanating from independent sources with different wavelengths are used in propagation experiments in turbulent atmosphere, i.e. in two-wavelength remote sensing of atmospheric aerosole [1].

At present, there exists a consistent correlation theory of propagation of monochromatic wave beams in random media with large-scale index of refraction inhomogeneities based on moment equations for the field of radiation [2] . This theory predicts the results for the fourth moment of the field, that are in good agreement with experimental evidence, in case of both week and saturated fluctuations of intensity.

In the paper we generalize the theory to the case of two-frequency wave beams propagation in turbulent media.

The evolution of spectral and correlation characteris-

tics of intensity of irradiances with wave numbers k_1 and k_2 propagating in the z direction in a random medium is described by the equation for the fourth moment of the complex amplitude of the field:

$$W(\vec{\rho}_1'; \vec{\rho}_1''; \vec{\rho}_2', \vec{\rho}_2''; z; k_1; k_2) =$$

$$\langle E(\vec{\rho}_1'; z, k_1) E^*(\vec{\rho}_1''; z, k_1) E(\vec{\rho}_2'; z; k_2) E^*(\vec{\rho}_2''; z; k_2) \rangle \quad (1)$$

The analysis of the iteration series built on the integral equation for the spectrum $\check{\check{W}}$ shows that in the region of small distances of propagation the first iteration $\check{\check{W}}_{(1)}$ gives the results, that coincide with obtained by the Obuchov-Rytov method.

The spectrum of intensity fluctuations is broadened as the distance z is increased. In the region of small Fresnel numbers of the radius of coherence of the field the iteration series is summed with the use of the results of the theory of limiting laws of distribution of sums of large numbers of independent random variables [5]. Here the spectrum is represented by the sum of two components - the low frequency (L.F.) and high frequency (H.F.) in spatial frequencies domain. The low frequency component of the spectrum is represented by the Fourier transform of the product of monofrequency (for $k_1 = k_2 = k$) second moments, the exact solution for the equation for which is known. This component describes large frequency detuning in frequency correlation function of intensity fluctuations.

The high-frequency component of the spectrum is represented as the Fourier transform of the product of two-fre-

quency (for $k_1 \neq k_2$) second moments, the equation for which can be solved only approximately, in the region of small frequency detunings.

The solution of the integral equation for the spectrum of two-frequency mutual coherence function $\overset{\vee\vee}{B}_E(\vec{\rho}; \vec{q}; z)$ can be written in the form

$$\overset{\vee\vee}{B}_E(\vec{\rho}; \vec{q}; z) = \{ \overset{\vee\vee}{B}_{(0)}(\vec{\rho}; \vec{q}; z) + \overset{\vee\vee}{B}_{(1)}(\vec{\rho}; \vec{q}; z) \} \times \exp\{ i q_m^{-2} (q^2 + \tfrac{1}{4} \rho^2) \},$$

where $\overset{\vee\vee}{B}_{(0)}(\vec{\rho}; \vec{q}; z)$ is the exact solution for $\Delta k = 0$. $\overset{\vee\vee}{B}_{(1)}(\vec{\rho}; \vec{q}; z)$ - the first approximation for small frequency detuning $(\Delta k/k) \ll 1$; $q_m^{-2} = (z/k)(\Delta k/2k)$.

By introducing

$$V_{(0)}(\Delta k; z) = \int d^2\vec{q}\, d^2\vec{\rho} \exp\{ i q_m^{-2} (q^2 + \tfrac{1}{4} \rho^2) \} \overset{\vee\vee}{B}_{(0)}(\vec{\rho}; \vec{q}; z),$$

$$V_{(1)}(\Delta k; z) = \int d^2\vec{q}\, d^2\vec{\rho} \exp\{ i q_m^{-2} (q^2 + \tfrac{1}{4} \rho^2) \} \overset{\vee\vee}{B}_{(1)}(\vec{\rho}; \vec{q}; z),$$

we obtain

$$W^{(2)}_{(0)}(0; 0; 0; 0; z) =$$

$$|V_{(0)}(\Delta k; z)|^2 + 2 \mathrm{Re} \{ V_{(0)}(\Delta k; z) V^*_{(1)}(\Delta k; z) \};$$

where

$$W^{(4)}_{(0)}(\vec{\rho}_+; \vec{\rho}; \vec{\rho}_1; \vec{\rho}_2; z) =$$

$$\int d^2\vec{\rho}\, d^2\vec{q}\, \overset{\vee\vee}{W}{}^{4.F.}_{(0)}(\vec{\rho}, \vec{\rho}; \vec{\rho}_1, \vec{\rho}_2; z) \exp\{ i\vec{\rho}\vec{\rho}_+ + i\vec{q}\vec{\rho}_1 \}.$$

The described treatment enables one to deduce the correlation properties of intensity fluctuations for arbitrary boundary conditions. In the case of initial plane wave, propagating in a turbulent medium with power law index of

refraction spectrum

$$\Phi_n(\varkappa) = A\,\varkappa^{-(\alpha+2)} \exp\left(-\varkappa^2/\varkappa_m^2\right);$$

$$A = (2\pi)^{-2}\,\Gamma(\alpha+1)\sin\left[(\pi/2)(\alpha-1)\right]\,C_n^2,$$

$$W_{(1)}^{(1)\,P.W.}(0;0;0;0;z) = B(\alpha)\left\{D_s\left(\sqrt{z/k}\right)\right\}^{-(2/\alpha)(2-\alpha)} \times$$

$$\left\{\left(1+\frac{\Delta k}{2k}\right)^{(2-\alpha)} + \left(1-\frac{\Delta k}{2k}\right)^{(2-\alpha)}\right\}^{-(1/\alpha)(4-\alpha)};$$

$$D_s(\rho) = 4\pi k^2 z \int d^2\vec{q}\,\Phi_n(q)\left\{1-\cos(\vec{q}\,\vec{\rho})\right\};$$

$$B(\alpha) = \left\{(2-\alpha)\,2^{(4/\alpha+\alpha-3)}\,\Gamma(4/\alpha-1)\,\Gamma(1+\alpha/2)\right/$$

$$\left.(\alpha-1)\,\Gamma(2-\alpha/2)\right\}\,{}_2F_1\left\{4/\alpha-1,\ \alpha-1,\ \alpha;\ \alpha/(\alpha+1)\right\};$$

$$W_{(1)}^{(1)\,P.W.}(\vec{\rho}_+;\vec{\rho};\vec{\rho}_1;\vec{\rho}_2;z) =$$

$$\int d^2\vec{\rho}\,d^2\vec{q}\,\exp\left\{i\vec{\rho}\,\vec{\rho}_+ + i\vec{q}\,\vec{\rho}_1\right\}\,\overset{\vee\vee}{W}_{(1)}^{L.F.}(\vec{\rho};\vec{\rho};\vec{q};\vec{\rho}_2;z)$$

For $\alpha = 5/3$ this result coincides with the result obtained in [4],

$$W_{(2)}^{(2)\,P.W.}(0,0;0;0;z) = 1 + C(\alpha)\,D_s\left(\sqrt{z/k}\right)\left(\Delta k/2k\right)^{(\alpha/2)};$$

$$C(\alpha) = \left\{\alpha\,2^{\alpha}/(\alpha+2)\right\}\cos(\alpha\pi/4)\,\Gamma(1+\alpha/2).$$

The results of computations for the frequency correlation of aperture averaged intensity fluctuations of irradiances at 1,06 μm and 0.63 μm in the regime of strong fluctuations show good agreement with experiment [5].

References

I. V.E.Zuev. Laser irradiance propagation in the atmosphere. Moscow Radio i Sviaz, I98I (in Russian)

2. K.S.Gochelashvili, V.I.Shishov. Waves in Random Media, VINITI, Moscow, I98I (in Russian)

3. I.A.Ibragomov, Yu.V.Linnik. The independent and stationary dependent quantities, Moscow, Nauka, I965 (in Russian).

4. V.U.Zavorotni. Izv.VUZ Radiofizika, 24, 60I (I98I) (in Russian)

5. Z.Azar et al. Proceedings of CLEO-85, Baltimore, Maryland, USA.

IMAGING AND SCINTILLATION

SPECKLE INTERFEROMETRY AND IMAGING

J C Dainty
Blackett Laboratory,
Imperial College,
London SW7 2BZ, UK
(invited)

Introduction

It is well known that time averaged stellar images are degraded by atmospheric turbulence or 'seeing'. At the very best observing sites, angular resolutions as small as 1 arc second can be obtained, compared to the limit λ/D set by diffraction of approximately 0.025 arc second for a 4m diameter telescope at a wavelength of 400 nm. The technique of speckle interferometry, which was invented by A Labeyrie[1], enables diffraction limited resolution to be achieved routinely and with proper calibration yields the autocorrelation of the object intensity or, equivalently, its Fourier modulus. A variety of techniques, which we shall call 'speckle imaging', attempt to produce an object map (i.e. the object intensity) from short-exposure speckle data. Although no totally satisfactory method of speckle imaging has yet been implemented routinely in astronomy, several proposed techniques look very promising.

Speckle Interferometry

Let $o(x,y)$ denote the object intensity and $O(u,v)$ denote its Fourier transform. When imaging through the turbulent atmosphere, the instantaneous image intensity is simply the object intensity convolved with the instantaneous point spread function, assuming isoplanatic imaging: the Fourier transform of the image intensity, $I(u,v)$, is therefore given by

$$I(u,v) = O(u,v)\, T(u,v) \quad , \qquad (1)$$

where T(u,v) is the instantaneous transfer function of the telescope/atmosphere combination.

In speckle interferometry, the average energy spectrum of the image is found:

$$\langle |I(u,v)|^2 \rangle = |O(u,v)|^2 \langle |T(u,v)|^2 \rangle . \qquad (2)$$

Thus the Fourier modulus of the object can be determined if the speckle transfer function, $\langle |T(u,v)|^2 \rangle$, is known. The key feature of speckle interferometry is that this transfer function has a component that is proportional to the diffraction-limited transfer function of the telescope - even if the telescope has (small) aberrations. Moreover, the average energy spectrum of the object can be measured with good signal-to-noise ratio using only a few detected photons per frame[2] and the limiting magnitude for simple objects is on the order $m_v = 18$. The technology of detectors and computers now allows the theoretical limits of speckle interferometry to be achieved in practice.

Speckle Imaging

There are basically two different approaches to the problem of restoring the object intensity o(x,y), or, equivalently, the magnitude and phase of the object spectrum, from a set of instantaneous image intensities {i(x,y)}. The first is to use the Labeyrie technique to obtain the Fourier modulus |O(u,v)| and then somehow deduce the Fourier phase from it. The second is to process the speckle data {i(x,y)} in such a way as to extract information that is additional to the Fourier modulus and that allows reconstruction of the object o(x,y): several methods of achieving this aim have been proposed.

(i) Reconstruction from the Fourier Modulus

In one dimension, it has been known for some time that a unique phase cannot be found from the Fourier modulus even for positive objects of

finite support. Considering a sampled object with N values, there are up to 2^{N-1} possible objects all of which have exactly the same Fourier modulus. Thus, in one dimension, given only the Fourier modulus, it is impossible to reconstruct uniquely the original object except in very special cases of no practical importance.

However, the situation appears to be quite different in two (or more) dimensions, as first demonstrated by Fienup[3] and explained by Bruck and Sodin[4] for sampled objects. The ambiguity of the one dimensional case stems from the factorisability of all one variable polynomials, whereas factorisable two variable polynomials are a set of measure zero. It is, of course, easy to construct artificial cases for which the two dimensional problem is not unique: these cases appear to involve objects with a high degree of symmetry. The question of uniqueness is the subject of current investigation and debate[5].

The iterative algorithm[6] of Fienup for finding the Fourier phase from the Fourier modulus has been quite successful on laboratory data with realistic noise. The algorithm involves the successive application of object and Fourier domain constraints until convergence is obtained. Convergence is not guaranteed, however, and the algorithm can get stuck in local minima. Developments in array processors are likely to bring further refinements to this algorithm.

(ii) Reconstruction from Speckle Data {i(x,y)}

Of the many techniques that have been proposed[7], we shall review three of the most promising: (a) expontential filter method[8], (b) cross-spectrum method[9] and (c) triple correlation method[10].

(a) Exponential Filter Method. The image data are multiplied by an exponential function exp(-ax) and the average energy spectrum of this modified data set $\langle|I'(u,v)|^2\rangle$ is combined with the average energy spectrum of the original data $\langle|I(u,v)|^2\rangle$. It can be shown that these two energy spectra can yield a unique reconstruction of the object intensity. However, the best available algorithm for this method,

which uses a modification of the Fienup algorithm, is not guaranteed to converge to this unique solution.

(b) Cross-spectrum Method. The cross-spectrum $\langle I(u,v)I^*(u+\delta u, v+\delta v)\rangle$ of the data is computed. This yields phase difference information in the Fourier plane, from which the Fourier phase can be computed.

(c) Triple Correlation Method. The average triple correlation $\langle \int_{-\infty}^{\infty} I(x)\, I(x+x_1)\, I(x+x_2)\, dx \rangle$ or bispectrum $\langle I(u_1)I(u_2)I(-u_1-u_2) \rangle$ is computed. The Fourier phase can be reconstructed from the bispectrum. The full implementation of this method requires a large amount of computer memory ($\sim N^4/8$ words for an N x N reconstruction).

The main obstacle to speckle imaging at present is the cost of the technology required to implement the above ideas in (near) real time - this cost is falling and routine speckle imaging should be feasible in the next few years.

References

1 A Labeyrie, Astron. Astrophys, 6, 85-87 (1970).
2 J C Dainty and A H Greenaway, J Opt Soc Am, 69, 786-790 (1979).
3 J R Fienup, Opt Lett, 3, 27-29 (1978).
4 Yu M Bruck and L G Sodin, Opt Commun, 30, 304-308 (1979).
5 See eg Image Recovery: Theory and Application, H Stark, Ed, Academic Press, 1986.
6 J R Fienup, Appl Opt, 21, 2758-2768 (1982).
7 J C Dainty and J R Fienup, Ch 7 of Ref 5.
8 J G Walker, Appl Opt, 21, 3132-3137 (1982).
9 K T Knox and B J Thompson, Astrophys J, 193, L45-L48 (1974).
10 A W Lohmann et al, Appl Opt, 22, 4028-4037 (1983).

RECOVERY OF ASTRONOMICAL IMAGES FROM A DICHROMATIC ANALYSIS OF SPECKLES

Claude AIME

Département d'Astrophysique de l'I.M.S.P. Université de Nice
U.A. 709 DU C.N.R.S. - Parc Valrose - 06034 Nice Cedex France
(invited)

Abstract. - A technique is proposed for recovering images degraded by atmospheric turbulence. It is based upon the analysis at two close wavelengths of the speckle pattern formed at the telescope focus.

I - Introduction

Speckle interferometry techniques take advantage of the fact that the instantaneous monochromatic point spread function $S(\lambda,\alpha)$ of an unresolved star is a random function which shows small features called speckles whose characteristic size is close to the width of the Airy function of the telescope aperture. The point spread function is given by the Fourier transform of the complex amplitude of the wave Ψ on the telescope aperture P :

$$S(\lambda,\alpha) = |\Psi(\alpha/\lambda) * P(\alpha/\lambda)|^2 / (A\lambda^2) \qquad (1)$$

where bold letters denote Fourier transform, * stands for convolution, λ is the light wavelength, α the vector of angular position and A the lens area . For an astronomical object $O(\lambda,\alpha)$ of small angular extent, isoplanatism is assumed, and the image observed in the focal plane is the random function $I(\lambda,\alpha)$ given by the convolution relation :

$$I(\lambda,\alpha) = O(\lambda,\alpha) * S(\lambda,\alpha) \qquad (2)$$

In the Fourier transform plane, this expression becomes :

$$\mathbf{I}(\lambda,f) = \mathbf{O}(\lambda,f) \cdot \mathbf{S}(\lambda,f) \qquad (3)$$

It has been shown [1-3] that $\mathbf{S}(\lambda,f)$ countains information speckled all over the transform plane up to the cutt off frequency D/λ of the telescope. However, this information at high angular frequencies cannot be readily obtained from $\mathbf{I}(\lambda,f)$ by any integrative process because $\mathbf{S}(\lambda,f)$ becomes a zero-mean-value complex-function for angular frequencies higher than r_o/λ, r_o being the parameter of Fried [4].

Many proposals [5-8] have been made to use the high angular information present in $\mathbf{S}(\lambda,f)$ to perform the recovery of $O(\lambda,\alpha)$. We shall examine briefly here the techniques of Labeyrie and of Knox and Thompson [9] from which the dichromatic technique we propose is derived.

II - The techniques of Labeyrie and Knox and Thompson .

Labeyrie's technique makes it possible to obtain the modulus of the Fourier transform of the intensity distribution in the observed object. It consists of computing the image energy spectrum :

$$\langle|\mathbf{I}(\lambda,f)|^2\rangle = |\mathbf{O}(\lambda,f)|^2 \langle|\mathbf{S}(\lambda,f)|^2\rangle \qquad (4)$$

where the symbol < > denotes an ensemble average. Labeyrie [5] has shown that $\langle |I(\lambda,f)|^2 \rangle$ has a high frequency component extending up to the telescope cut-off frequency.

The observation of a near-by unresolved star gives the necessary calibration for the determination of $|O(\lambda,f)|^2$ from the observed value of $\langle |I(\lambda,f)|^2 \rangle$.

Algorithms have been developed to reconstruct an image from the modulus alone of its Fourier transform [8], but this information is not enough in principle, and soon after the first speckle observations Knox and Thompson proposed a generalization of Labeyrie's technique which makes it possible to obtain directly the phase information from the speckle data. It consists of computing the image cross-spectrum defined by :

$$K(\lambda,f,\Delta f) = \langle I(\lambda,f).\ I^*(\lambda,f+\Delta f) \rangle = O(\lambda,f)\ O^*(\lambda,f+\Delta f).\ \langle S(\lambda,f)\ S^*(\lambda,f+\Delta f) \rangle \qquad (5)$$

where the symbol * indicates a complex conjuguate. For $\Delta f = 0$, Eq.(5) reduces to Eq.(4) of Labeyrie's technique.

Knox and Thompson have shown that, for Δf small compared with r_0/λ, the term $S(\lambda,f)\ S^*(\lambda,f+\Delta f)$ is a complex value which jitters around the real value $\langle |S(\lambda,f)|^2 \rangle$. It can be shown [10] that, for $f >> r_0/\lambda$:

$$\langle S(\lambda,f)\ S^*(\lambda,f+\Delta f) \rangle \sim \langle |S(\lambda,f)|^2 \rangle\ .\ H(\lambda\Delta f/r_0) \qquad (6)$$

where $H(\lambda.\Delta f/r_0)$ is a constant value given by the autocorrelation function of Fried's coherence function of the wave [4]. If, for the sake of simplicity, we assume that $H(\lambda\Delta f/r_0) \sim 1$ for Δf small enough, then Labeyrie's technique makes it possible to obtain the modulus and phase of $O(\lambda,f)O^*(\lambda,f+\Delta f)$. If moreover we allow the approximation $|O(f+\Delta f)| \sim |O(\lambda,f)|$, then we obtain the differences in phase of $O(\lambda,f)$ for the frequency shift Δf. A summation technique allows the retrieval of the phase over the whole transform plane.

III - <u>Proposal for an image reconstruction technique making use of the analysis of the speckle image at two close wavelengths.</u>

The technique we propose is basically a generalization to the speckle case of a technique proposed by Koechlin [10,12] for Michelson stellar interferometry. It requires a simultaneous analysis of the speckle image at two close wavelengths λ and $\lambda+\Delta\lambda$, and it takes advantage of the deterministic dependance of the point spread function size on λ as shown by Eq.1. For $\Delta\lambda$ small, it is expected that the instantaneous transfer functions at λ and $\lambda+\Delta\lambda$ will be similar one to the other, and that $S(\lambda+\Delta\lambda,f)$ will equal $S(\lambda,(\lambda+\Delta\lambda)f/\lambda)$.

In order to take advantage of this deterministic behavior, it is proposed to compute the dichromatic cross-spectrum $M(\lambda,\Delta\lambda,f)$ defined by :

$$M(\lambda,\Delta\lambda,f) = \langle I(\lambda+\Delta\lambda,f)\ \ I^*(\lambda,(\lambda+\Delta\lambda)f/\lambda) \rangle \qquad (7)$$

which can be interpreted as the "achromatized" cross-spectrum of the image intensity.

If we use the notation :

$$\delta f = f\ \Delta\lambda/\lambda \qquad (8)$$

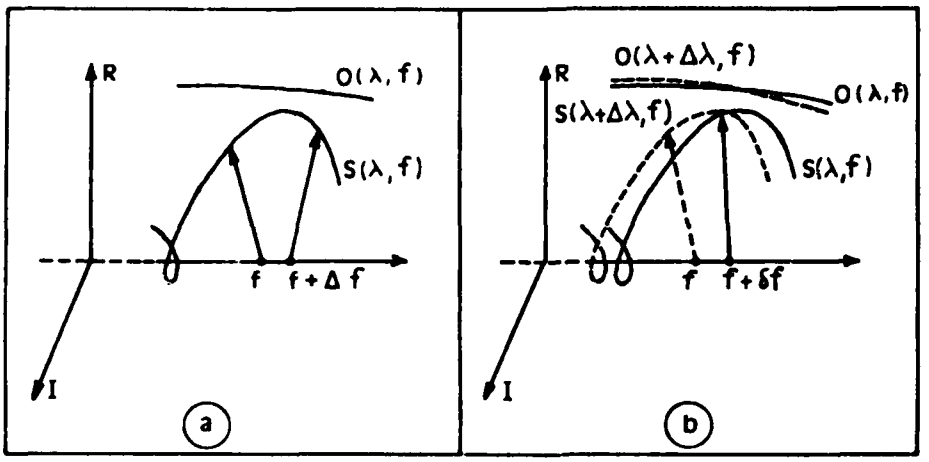

Figure. Schematic representation of complex functions $O(\lambda,f)$, $O(\lambda+\Delta\lambda,f)$ $S(\lambda,f)$ and $S(\lambda+\Delta\lambda,f)$ which appear in equations (5) and (7) of Knox Thompson (a) and dichromatic (b) techniques. Curves are drawn for one-dimensional signals and a region of the Fourier plane limited to a spatial frequency difference which corresponds to about one speckle. R = real part. I = imaginary part. Knox Thompson technique assumes small phase differences in $S(\lambda,f)$ for Δf small with regard to ro/λ. Dichromatic technique assumes a similarity relation between $S(\lambda,f)$ and $S(\lambda+\Delta\lambda,f)$ so that $S(\lambda,f+\delta f) \sim S(\lambda+\Delta\lambda,f)$ with $\delta f = f\Delta\lambda/\lambda$. It is also assumed that $O(\lambda+\Delta\lambda,f) \sim O(\lambda,f)$.

expression (7) can be written as :

$$M(\lambda,\Delta\lambda,f) = O(\lambda+\Delta\lambda,f)\ O^*(\lambda,f+\delta f).\langle S(\lambda+\Delta\lambda,f)\ S^*(\lambda,f+\delta f)\rangle \quad (9)$$

This expression is very similar to that of Knox and Thompson in Eq.(5). In a recent chromatic study of speckle patterns, we have shown that, for $f>>r_o/\lambda$, the term between bracketts of equation (9) is a real term in the form of :

$$\langle S(\lambda+\Delta\lambda,f)\ S^*(\lambda,f+\delta f)\rangle \sim \langle |S(\lambda,f)|^2\rangle \ .\ B^2(\lambda,\Delta\lambda) \quad (10)$$

where $B(\lambda,\Delta\lambda)$ is a spectral coherence term [13] which accounts for the wavelength dependance of the wave perturbation Ψ at the telescope pupil. Using the same reasoning as in Knox and Thompson's technique, we shall assume for simplicity that, for $\Delta\lambda$ small enough, the term $B^2(\lambda,\Delta\lambda)$ is almost equal to one.

Moreover, we shall assume that the intensity of the object is wavelength independant. This will be true for most of the astronomical objects provided that the observations are performed in the continuum of the spectrum. Under these assumptions, $M(\lambda,\Delta\lambda,f)$ gives :

$$M(\lambda,\Delta\lambda,f) = O(\lambda,f)\ O^*(\lambda,f+\delta f)\ \langle |S(\lambda,f)|^2\rangle \quad (11)$$

Here also, Labeyrie's technique will permit the determination of the modulus of $O(\lambda,f)$ $O^*(\lambda,f+\delta f)$. The derivative of the phase of $O(\lambda,f)$ will be obtained from this analysis and the retrieval of $O(\lambda,\alpha)$ could be performed.

A schematic comparison between the dichromatic technique and the Knox and Thompson's one is made in the figure.

IV - Discussion.

The technique presented here takes advantage of the analysis of the speckle image at two close wavelengths. The technique can readily be generalized to multiple wavelength analysis, in a speckle-spectroscopy type experiment [14] or in a one-dimensional space-wavelength analysis [15].

The signal to noise ratio S.N.R. of the experiment will highly depend upon the spectral coherence term $B(\lambda,\Delta\lambda)$ and astronomical seeing [16] . Although a detailed study of the S.N.R. is yet to be done, a good value is expected since experimental tests on spectral coherence of speckles [10] revealed to be more favorable than theoretical predictions[13].

References

[1] Labeyrie (A.) - Progress in Optics, vol XIV, E. Wolf ed., 1976.
[2] Dainty (J.C.) - Topics in Applied Optics, vol IX, J.C. Dainty ed., 1975.
[3] Roddier (F.) - Progress ir Optics, vol XIX, E. Wolf ed., 1981.
[4] Fried (D.L.) - J. Opt. Soc. Am., 1966, 56, 1372.
[5] Labeyrie (A.) - Astron. Astrophys., 1970, 6, 85.
[6] Weiglt (G.) - Opt. Commun., 1977, 21, 55.
[7] Lynds (C.R.), Worden (S.P.), Harvey (J.W.) - Astrophys. J., 1976, 207, 174.
[8] Fienup (J.R.) - Optic Letters, 1978, 3, 27.
[9] Knox (K.T.), Thompson (B.J.), Astron. J. - 1974, 193, L 45.
[10] Aime (C.), Petrov (R.G.), Martin (F.), Ricort (G.), Borgnino (J.)-S.P.I.E. Proceedings 556, 297.
[11] Koechlin (L.) - E.S.O. Proceedings - Geneva, 1977, 475.
[12] Koechlin (L.) - Thesis Nice University, France, 1985.
[13] Roddier (F.) - E.S.O. Proceedings - Garching, 1981, 5.
[14] Weigelt (G.) - S.P.I.E. Proceedings 332, 284.
[15] Martin (F.), Bijaoui (A.), Touma (H.), Aime (C.) - S.P.I.E. Proceedings 546,1985.
[16] Coulman (C.E.) - Ann. Rev. Astron. Astrophys., 1985, 23, 19.

Zernike Decomposition for a Kolmogorov Turbulence Spectrum with Finite Outer Scale

D.M. Winker
Air Force Weapons Laboratory
AFWL/ARBA, KAFB
Albuquerque, NM 87117 USA

The use of Zernike polynomials to represent phase distortion in image-forming optical systems is well established, whether the distortions arise from the system itself [1] or from propagation through the atmosphere lying between the object and the optical system [2,3]. Research in optical propagation generally relies on Kolmogorov turbulence theory to describe atmospheric turbulence. The Kolmogorov theory predicts an inertial range of turbulence having an energy spectrum which follows a simple power law for spatial scales lying between some large scale where the turbulence is created and some (much) smaller scale where the turbulent motion is dissipated by the viscosity of the air. The turbulence within this inertial range is assumed to be isotropic. Kolmogorov theory predicts a power spectrum for refractive index fluctuations following an 11/3 power law in the inertial range. Previous studies of the contribution of atmospheric turbulence to wavefront distortion have assumed the large-scale limit of the inertial range (the outer scale, L_o) to be infinite. Although this assumption is non-physical, as the spectrum then contains infinite energy, it has been assumed that the size of the outer scale has little influence on phasefront statistics, and that the inertial range may in fact be extended to infinitely large scales with no significant error.

In recent years, the astronomical community has proposed a 'next generation' of telescopes using apertures significantly larger than any existing telescope [4]. It seems possible that for optical systems on the scale of the 8 and 10 meter apertures now being proposed for these telescopes, outer scale effects might become significant. For this reason a study was undertaken to quantify the importance of any possible effect. In this paper, the Zernike decomposition of Kolmogorov turbulence derived by Noll [3] will be rederived for the case of a Kolmogorov spectrum modified by the presence of a finite outer scale. Since the nature of the integrals encountered in computing this decomposition resist evaluation by numerical techniques, the computations have been performed analytically whenever possible.

For the case of Kolmogorov turbulence, the index of refraction structure function $D_n(r)$ is given by:

$$D_n(r) = C_n^2 r^{2/3}$$

This gives the familiar Kolmogorov spectrum for index of refraction fluctuations [5]:

$$\Phi_n(k) = 8.16\, C_n^2\, k^{-11/3}$$

where k is the spatial wavenumber. This spectrum contains infinite energy, leading to an infinite phase variance. In the past, this difficulty has been handled by working with the piston-removed phase variance, which is finite. If we assume a flat spectrum for $k < 2\pi/L_o$ the phase variance will also be finite. We will assume a spectrum of the form:

$$\Phi_n(k) = 8.16\, C_n^2\, (k^2 + k_o^2)^{-11/6}$$

where $k_o = 2\pi/L_o$. In order to write the spectrum in terms of a scalar, k, rather than a vector, we have assumed that turbulence at scales larger than the outer scale is isotropic. The phase fluctuation spectrum has the same form:

$$\Phi_\phi(k) = B\, (k^2 + k_o^2)^{-11/6}$$

where the normalization constant, B, may be determined from a comparison of the representation of the phase structure function, $D_\phi(r)$, in terms of the index of refraction fluctuation spectrum, Φ_n:

$$D_\phi(r) = \frac{\kappa^2}{\pi} \int\int dz\, k dk\, \Phi_n(k,z)\, [1 - J_0(kr)]$$

and in terms of the phase fluctuation spectrum, Φ_ϕ:

$$D_\phi(r) = \frac{1}{\pi} \int_0^\infty k dk\, \Phi_\phi(k,z)\, [1 - J_0(kr)]$$

where $\kappa = 2\pi/\lambda$. The Zernike decomposition may then be performed in the same manner as in [3], by replacing the Kolmogorov spectrum with the modified spectrum in the expression:

$$\langle a_j^* a_{j'} \rangle = \int\int d\vec{k}\, d\vec{k}' Q_j^*(k) \Phi_\phi(k/R, k'/R)\, Q_{j'}(k')$$

where a_j is a Zernike coefficient, Q_j is the Fourier transform of the jth Zernike polynomial, and the

phase spectrum is scaled by R, the aperture radius.

This last expression contains integrals of the form:

$$\int_0^{\infty} dk \frac{J_\nu(ak)\, J_\mu(ak)}{k\,(k^2+k_0^2)^{-11/6}}$$

which may be evaluated following an approach suggested by Watson [6]. The product of the two Bessel functions is converted to a single Bessel function using Neumann's function. This Bessel function is then expressed in terms of a contour integral using:

$$J_\nu(x) = \frac{1}{2\pi i} \int_{-\infty i}^{+\infty i} ds\, \frac{\Gamma(-s)\,(x/2)^{\nu+2s}}{\Gamma(\nu+s+1)}$$

After reversing the order of integration, the evaluation is straightforward. The final expression for the magnitude of the Zernike polynomial coefficients is a complicated expression involving a sum of two terms containing hypergeometric functions of the type ${}_3F_4$. The hypergeometric functions are readily evaluated numerically. Results and scaling laws will be discussed.

1. Bezdid'ko, S.N., 1974: The Use of Zernike Polynomials in Optics. Soviet Journal of Optical Technology, 41, 425-429.
2. Fried, D.L., 1965: Statistics of a Geometric Representation of Wavefront Distortion. J. Optical Society of America, 55, 1427-1435.
3. Noll, R.J., 1976: Zernike Polynomials and Atmospheric Turbulence. J. Optical Society of America, 66, 207-211.
4. Burbidge, G. and L.D. Barr, ed., 1982: Advanced Technology Optical Telescopes. Proceedings SPIE, v332.
5. Fried, D.L., 1966: Limiting Resolution Looking Down Through the Atmosphere. J. Optical Society of America, 56, 1380-1384.
6. Watson, G., 1944: A Treatise on the Theory of Bessel Functions, 2nd ed., Cambridge University Press, New York, NY.

Stellar Speckle-Image Reconstruction From Phase Gradients

G.J.M. Aitken, R. Johnson and H. Houtman
Queen's University, Kingston, Ontario, Canada

Introduction.

The estimation of the phase function is a major problem in the reconstruction of a stellar object's complex spatial spectrum from a set of speckle images. The Knox-Thompson[1] approach measures a 2-D array of phase differences between adjacent spatial-frequency components, the phase function being determined either by summing outward from the origin or fitting a function to the array of phase differences. However, the estimation of a phase difference in a given spatial-frequency interval is simply an estimation of the gradient of the phase. In this paper a process is described which estimates the true phase gradient directly from the speckle images. An important property of the phase-gradient process described here is that the noise biases at low photon levels are less troublesome than in the K-T process and, in principle, can be systematically removed during data reduction.

Phase-Gradient Estimtor

Let i_n be the n^{th} speckle image in a set of N, o the object and s_n the time-varying point-spread function of the atmosphere-telescope combination. Their respective Fourier transforms are I_n, O and S_n. For each of the speckle images compute

$$D_{nx} = \mathrm{Im}\{I'_{nx}\, I_n^*\}, \tag{1}$$

where Im{.} indicates the imaginary part, $I'_{nx} = j2\pi\ \mathrm{F.T.}\{x\ i_n\} = dI_n/df_x$ from the Fourier differentiation theorem, f_x is the x-component of spatial frequency, and the primed symbol denotes differentiation with respect to the spatial-frequency components indicated by the subscripts x or y.

If α and θ_n are the angles of O and S_n, respectively, the expected value of (1) reduces to

$$\langle D_{nx}\rangle = |O|^2\ \langle |S_n|^2\rangle\ \alpha'_x = \langle |I_n|^2\rangle\ \alpha'_x\ , \tag{2}$$

where the fact that $\langle \theta_n \rangle = \langle \theta'_{nx} \rangle = 0$ has been used. Similarly, $D_{ny} = I_m\{I'_{ny}\ I_n^*\}$ and $\langle D_{ny} \rangle = \langle |I_n|^2 \rangle\ \alpha'_y$. Thus, the estimator for the gradient of object phase is

$$\hat{\nabla\alpha} = \sum_{n=1}^{N} \mathrm{Im}\{I'_{nx}\ I_n^*\ \mathbf{x} + I'_{ny}\ I_n^*\ \mathbf{y}\} \ / \ \sum_{n=1}^{N} |I_n|^2 \qquad (3)$$

where $\mathbf{x}$ and $\mathbf{y}$ are unit vectors in the f_x and f_y directions, respectively.

The phase estimate is found by integrating $\hat{\nabla\alpha}$ outward from the origin over multiple paths in order to determine the gross tilt, then by function fitting to establish local features.

Bias and Noise

When the photon-effect model described by Nisenson and Papaliolios[2] is applied to the calculation of D_{nx}, the bias term is

$$B_x = |P|^2\ \bar{N}_p\ \langle I'_{nx}(o) \rangle / \langle I_n(o) \rangle\ , \qquad (4)$$

where P is the Fourier transform of the recording system's response to a single photon event and $\bar{N}_p$ is the average number of photons per image. The long exposure image gives $\langle I'_{nx}(o) \rangle / \langle I_n(o) \rangle$, white $|P|^2$ and $\bar{N}_p$ can be evaluated for the specific system. B_y has the same form.

Since for real objects only $I_m\{\langle I'_{nx}(o) \rangle\}$ comes into play, objects whose centroids are located at the centre of the field will have zero bias. In fact, if the centroid of each speckle image is shifted to the centre of the field, the bias terms will be eliminated. The information lost is the true position of the source; however, averaging of the shifts imposed on the individual images would re-establish the position.

The variance of D_{nx} due to atmospheric fluctuations reduces to

$$\langle N_x^2 \rangle = \langle |I_n|^2 \rangle^2 [2\langle (\theta'_x)^2 \rangle + (\alpha'_x)^2]\ , \qquad (5)$$

Therefore, the phase-gradient error for N images is

$$\Delta\alpha'_x = 2[\langle (\theta'_x)^2 \rangle + (\alpha'_x)^2]^{1/2} / N^{1/2} \qquad (6)$$

When $\langle (\theta'_x)^2 \rangle$ is very small the terms contributing α'_x in (5) disappear. The error in α'_y is of the same form.

The quantities θ'_x and θ'_y are not readily accessible from analytic expressions for S. However, a computer simulation using 100 instantaneous atmosphere-telescope transfer functions corresponding to a 1m telescope and r_o = 12.5 cm yielded a value of 2×10^{-5} radians²/cycle for $\Delta\alpha'_{x,y}$. Other estimates confirm that the value would be of the order of 10^{-3} to 10^{-4}. For a 1m telescope and a 128 x 128 sample field the maximum rate of change of phase, α'_{max}, would be 2×10^{-4} rad²/cycle. These figures indicate that with N=100 the effects of the atmosphere will be reduced adequately to allow good estimates of $\hat{\nabla}\alpha$ as is demonstrated in the example described below.

Demonstration

Fig. 1(a) shows a test object as seen through the telescope with no atmosphere. Fig. 1(b1) and (b2) show two examples of the 100 speckle images generated by random phase masks in the 128 x 128 pixel computer simulation. A long exposure image is shown in (c). The reconstructed image in (d) was obtained by Fourier inversion of the spectrum whose modulus was calculated by the conventional speckle interferometry processing and whose phase is the integrated phase gradient estimate. Finally, in Fig. 1(e) Fienup's process[3] is applied with the constraints that the object must be real and positive.

The authors wish to acknowledge the support of this work by the Natural Sciences and Engineering Research Council of Canada.

REFERENCES

1. K.T. Knox, J. Opt. Soc. Am. 66 (1976) 1236.
2. P. Nisenson and C. Papaliolios, Optics Commun. 47 (1983) 91.
3. J.R. Fienup, Appl. Opt. 21 (1982) 2758.

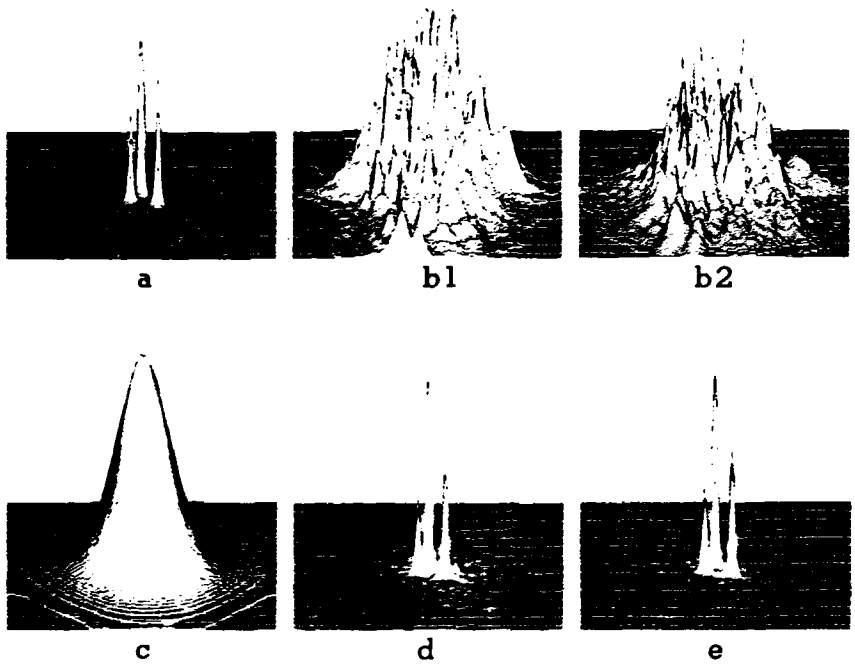

Fig. 1. (a) The diffraction limited image. (b1) and (b2) Typical speckle images. (c) The long-exposure image. (d) The reconstructed image. (e) The image of (d) after application of Fienup's algorithm.

Variability of Amplitude Scintillations Observed in Beijing and Rome on SIRIO Satellite Links.

J. Wang (*), U. Merlo (**), E. Fionda (**)

(*) MOA/CAST, P.O. Box 5106, Beijng, China
(**) Fondazione U. BORDONI, viale Europa 160, 00144 Rome, ITALY

Amplitude scintillation measurements have often to deal with natural events subject to intrinsic non-stationarities, such as solar heating or clouds. In these cases, particular care should be paid in performing spectral, variance and parameter estimations.
In the present contribution we report some scintillation measurements over two links with SIRIO satellite and we refer a simple but effective evaluation of the diurnal evolution of turbulence induced by solar heating.

Measurements.

During the period June 1983-February 1985, SIRIO satellite was in a geostationary orbit over the Indian ocean and trasmitted at 11.5 GHz with circular polarization. Propagation and telecommunication experiments were held in cooperation between Italy and People's Republic of China. Amplitude scintillations have been measured in two stations placed in Beijing (CHINESE ACADEMY OF SPACE) and Rome (ISTITUTO SUPERIORE DELLE POSTE E TELECOMUNICAZIONI). The stations were identical and were equipped with 3 m Cassegrain antennas with mean axis elevation of 20.5° in Beijing and 20.0° in Rome. Diurnal drifting of satellite was compensated by automatic tracking. Data were recorded on magnetic tapes (sampling rates 1-10 Hz) and analogic strip chart. The intensity of scintillations has been estimated by using records of 30 minutes length for Beijing and 25 minutes for Rome.
Data during rain events were excluded from analysis, but cloud effects have not yet been separated from those of clear sky convective turbulence. Meteorological ground recordings were gathered by observatories situated near the vertical projection of atmospheric propagation path.
The intensity of scintillations has been evaluated by scintillation index defined as $SI = ((Pmax - Pmin) / (Pmax + Pmin)) \times 100$ where Pmax and Pmin are respectively the third peak down from the maximum and third peak up from minimum during each estimation interval /1/. The use of this simple index may be justified by remembering that the log-amplitude of each scintillation event follows a normal distribution /2/ and that the standard deviation could be estimated by means of scintillation index.

Synthesis of results.

Measurements of mean SI taken in Rome and Beijing and corresponding mean ground temperature are shown in Fig. 1. These values represent the mean of hourly samples taken over the same summer month. It appears that the four curves present noticeable similarities.

The largest part of data has been collected during clear sky conditions but some variations of SI (particulary for Beijing) may be caused by cumulus clouds . Daily cyclical behavior of mean SI has been noted through all summer months (e.g. Fig. 2), while in winter it is less noticeable. Comparison between mean ground temperature and mean SI by regression analysis in Fig. 3 confirms the strong similarity of the behavior of these quantities for different climates of Rome and Beijing. Correlation coefficients are respectively 0.920 for Rome and 0.905 for Beijing. Results shown are valid through wavelengths where direct effect of temperature over structure parameter C_n^2 is negligible in respect of humidity /3/. Apparent relationship between power and ground temperature may be explained noting that intensity of turbulence and absolute humidity could be enhanced by ground temperature increments and remembering that scintillation power is proportional to the refractive index structure parameter C_n^2, after the well known relationship:

$$C_n^2 = a^2 C_T^2 + b^2 C_q^2 + 2ab\, C_{Tq}$$

where the parameters in the second term depend on atmospheric pressure, temperature, absolute humidity and the wavelength of radiation. Behaviors shown have been obtained from monthly mean quantities. The spread of indidual samples is shown for Beijing and Rome in Fig. 4, by means of the standard deviation of mean (hourly) values of SI versus mean (hourly) scintillation intensity for each month.
For further deepening of the relationship between scintillations and temperature, cross-correlation analyses of SI versus ground temperature are reported in Fig. 5 and Fig. 6. In Fig. 5 it is shown the short-term cross-correlation index between mean SI and mean ground temperature in Beijing. It may be remarked a tendency of SI to anticipate about 0.5 hour ground temperature variations. This tendency is confirmed by the long-term cross-correlation between hourly samples for Rome in Fig.6. This behavior could be explained by approximately modelling the observed turbulence as partly related to the varying of ground temperature and partly to the actual value of the same temperature. Higher variability of mean SI has been found from 09 to 12 and from 16 to 19 hours, local time.

Concluding Remarks.

Analysis of amplitude scintillations during summer in the different climates of Beijing and Rome has shown that mean scintillation intensity follows a diurnal cycle. A noticeable variability of mean scintillation intensity index has been found, particularly around 10.30 and 17.30, local time. It has been noted that this behavior could be approximately related to the cycle of ground temperature. Scintillation intensity has been found to be slightly anticipating ground temperature variations. Relationships found may be useful for scintillation modeling and simulation.

References

/1/ U. Merlo,E. Fionda,P.G.Marchetti, Electr. Lett..Vol.21.p.1094(1985).
/2/ A.Ishimaru,"Wave Propagation and Scattering in Random Media", (Academic Press, New York, 1978).
/3/ R.J.Hill,S.F.Clifford,R.S.Lawrence, J.Opt.Soc.Am..Vol.70.p.1192(1980).

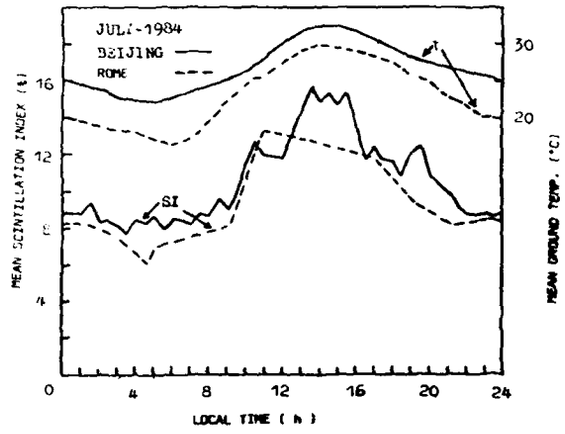

Fig. 1 DIURNAL VARIATION OF MEAN SCINTILLATION INDEX AND MEAN GROUND TEMPERATURE IN ROME AND BEIJING.

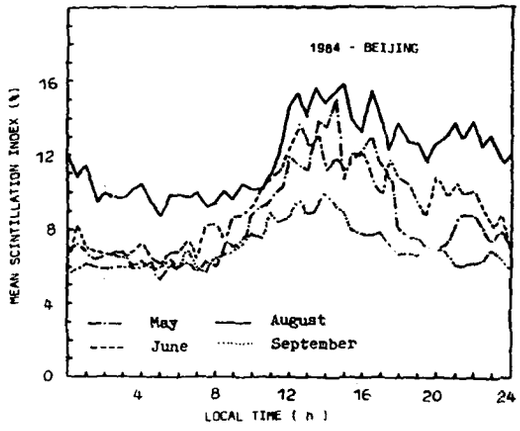

Fig. 2 DIURNAL VARIATION OF MEAN SCINTILLATION INDEX IN BEIJING DURING HOT SEASON.

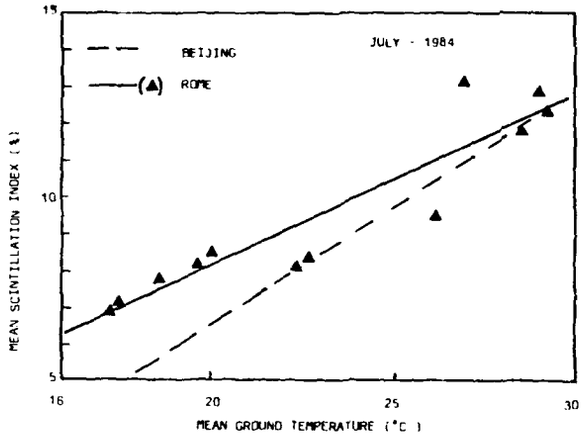

Fig. 3 VARIABILITY OF MEAN SCINTILLATION INDEX AND MEAN GROUND TEMPERATURE FOR ROME AND BEIJING.

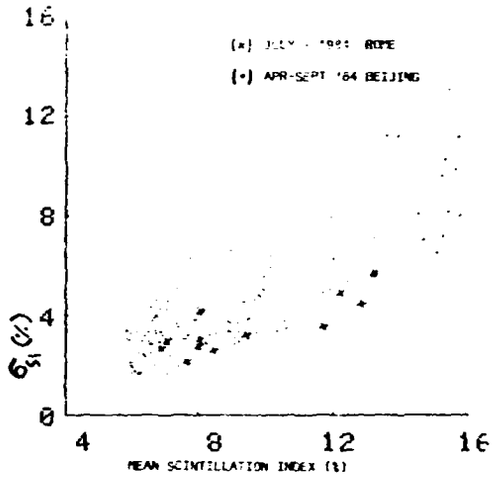

Fig. 4 VARIABILITY OF HOURLY MEAN SCINTILLATION INDEX IN ROME AND BEIJING.

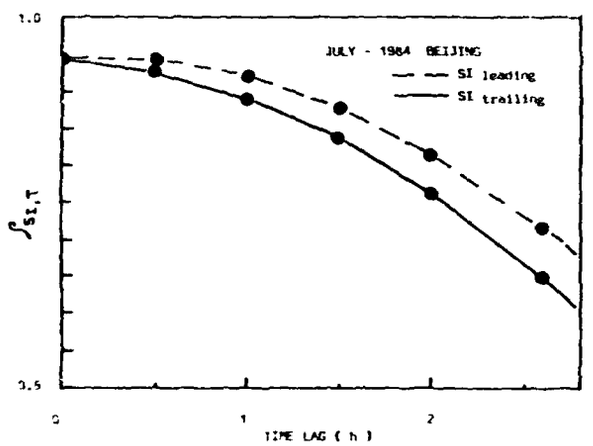

Fig. 5 SHORT-TERM CROSS CORRELATION BETWEEN HOURLY MEAN SCINTILLATION INDEX AND MEAN GROUND TEMPERATURE IN BEIJING.

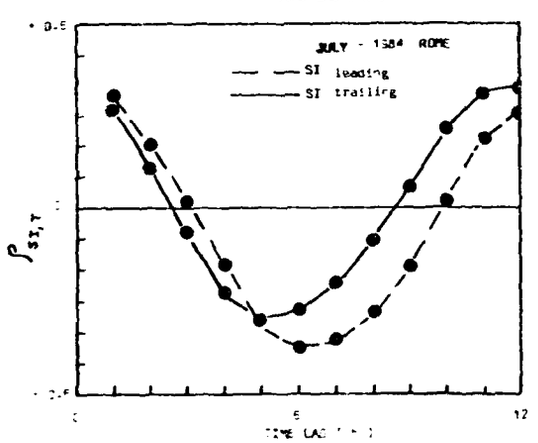

Fig. 6 LONG-TERM CROSS CORRELATION BETWEEN HOURLY SAMPLES OF SCINTILLATION INDEX AND GROUND TEMPERATURE IN ROME

SCINTILLATION ON HIGH- AND LOW-ELEVATION SATELLITE PROPAGATION PATHS

Patrizia Basili, Piero Ciotti, Giovanni d'Auria
Dipartimento di Elettronica, Università di Roma "La Sapienza"
Via Eudossiana 18, 00184 Rome, Italy

Ugo Merlo
Fondazione Ugo Bordoni, Viale Europa 160, 00144 Rome, Italy

Paolo Ferrazzoli, Domenico Solimini
Dipartimento di Ingegneria Elettronica, Università di Roma "Tor Vergata"
Via Orazio Raimondo, 00173 Rome, Italy

SUMMARY

Introduction.

In 1983 the SIRIO satellite was shifted from its original location 15°W on the Atlantic Ocean to a new position 65°E on the Indian Ocean for a cooperative Italian-Chinese experiment. A decrease of the elevation of the satellite with respect to the Italian stations resulted from the shift. Therefore the displacement offers a peculiar opportunity of analyzing the propagation characteristics of two earth-space propagation paths involving the atmospheric layers to a different extent. In this paper the statistical properties of the fluctuations of the field amplitude on the two paths are analyzed for a number of selected events for which enhancement of the peak-to-peak value was observed. Particular emphasis is placed on the spectral properties, which are discussed with reference to other observations and theory.

The experiment.

The SIRIO experiment was designed to investigate the propagation characteristics of an earth-space path at the frequencies of 11.5 and 17.75 GHz. The amplitude of the circularly polarized field of the down-link at 11.5 GHz was recorded at the earth station of Fucino, Italy, nearly 700 m above the sea level, and subsequently, after the displacement of the satellite, in Rome, Italy, about 50 m above the sea level. The two stations are about 100 Km apart. The elevation of the propagation path was 33°30' for the first location and slightly less than 20° for the second one. The Fucino station used a 17-m shaped Cassegrain antenna, while the Rome Cassegrain antenna had a diameter of 3 meters. The sampling frequency was 10 Hz and data were recorded on digital magnetic tapes.

Analysis of the intensity of fluctuations points out the seasonal and diurnal variability already observed in analogous experiments (1, 2). In addition, occasional enhancement of fluctuations are observed, which are usually accompanied by an average attenuation and occur in concurrence with rain or in adjacent periods. The analysis of two of such events is presented in this summary, one referring to the low-elevation propagation path and the other to the initial link with the satellite seen

at 33°30' above the horizon.

Results.

Observations taken by the Italian Air Force Meteorological Service at Fiumicino Airport, about 20 Km from the Rome ground station, reported 2/8 of cumulus clouds at 12:00 GMT on August 17, 1984. Fig.1 reports the amplitude of the 11.5 GHz received field for a period starting at 12:30 p.m. local time. The mean level of the field is nearly constant and quite close to its value for clear sky conditions. The corresponding spectrum (Fig.2), evaluated by an FFT routine, is slowly decreasing at the lower frequencies and falls off with a slope close to -8/3 beyond the corner frequency near 0.2 Hz. About one hour later a moderate mean attenuation can be observed in the record of the field amplitude (Fig. 3). The attenuation appears to produce an enhancement of the low frequency part of the spectrum (Fig.4), whereas the high frequency behavior remains almost unchanged. When a rain cell develops across the propagation path, a noticeable attenuation is observed (Fig.5). Three regions can now be observed in the spectrum (Fig.6): a low frequency zone where the spectrum decreases with a slope that seems to be consistent with both the theoretically predicted (3) and experimentally observed (4) -8/3 slope for propagation in an absorbing medium; a rather flat intermediate zone between the low corner frequency about 0.01 Hz and the high corner frequency about 0.2 Hz; a high frequency zone which falls off with the expected -8/3 slope.

The existence of a low frequency spectral region with a -8/3 slope when the path attenuation is not negligible confirms previous observations (5). Indeed, although the frequency of the electromagnetic wave does not fall within an absorption band of the atmospheric gases, the presence of liquid water on the path makes the global refractive index complex. The random space-time variations of the liquid water density due to turbulence in the clouds produces random fluctuations of the complex refractivity. The effect on the amplitude spectra of waves propagating in such a random absorbing medium is analogous to the one theoretically predicted by Ott and Thompson (3).

To clarify this point, several additional events have been analyzed, taking also into account concurrent radiometric measurements. Amplitude fluctuations and the radiometric signal have been recorded at the Fucino ground station where, as said, the satellite had a local elevation different from that at the Rome station. The obtained results appear to be consistent, at least within the natural variability of experimental data, and with regard to the differences in the propagation path. As an example, Fig.7 reports the time series of a long (1h 26') attenuation event and Fig.8 the corresponding spectrum. In this case the low frequency region which is attributed to absorption extends to about 0.02 Hz, thus somewhat reducing the flat portion of the spectrum, according, again, to the theory. Of course, statistical nonstationarities and possibly highly variable atmospheric conditions along the slant earth-space path introduce disturbing effects which are to be carefully considered.

References.

1- F. Rucker, and F. Dintelmann, "Effect of antenna size on OTS signal scintillation and their seasonal dependence", Electron. Lett., vol. 19, pp. 1032-1034, 1983.

2- D. Vanhoenacker, and A. Vander Vorst, "Experimental evidence of a correlation between scintillation and radiometry at centimeter and millimeter wavelengths", IEEE Trans. Antennas Propag., vol. AP-33, pp.40-47, 1985.

3- R.H. Ott, and M.C. Thompson, Jr., "Atmospheric amplitude spectra in an absorption region", IEEE Trans. Antennas Propag., vol. AP-26, pp. 329-332, 1978.

4- F.C. Medeiros Filho, D.A.R. Jayasuriga, and R.S. Cole, "Spectral density of amplitude scintillations on a 55 GHz line of sight link", Electron. Lett., vol. 17, pp. 25-26, 1981.

5- P. Basili, P. Ciotti, G. d'Auria, A. Silbermann, D. Solimini, and E. Matricciani, "Amplitude scintillation in propagation paths above 10 GHz", Proc. URSI Comm. F Symp., Louvain-La-Neuve, Belgium, ESA SP-194, pp. 95-101, 1983.

Acknowledgments.

This work has been partially supported by Ministero della Pubblica Istruzione and C.N.R.

SIRIO data recorded at Fucino have been kindly supplied by Politecnico di Milano, C.S.T.S., Milan, Italy.

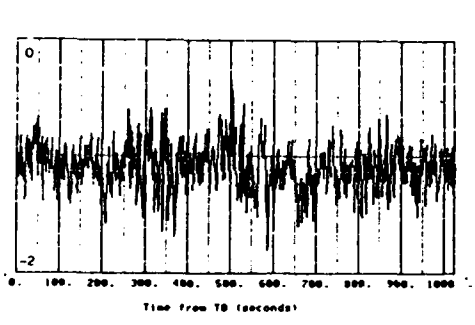

Fig.1 Field log-amplitude recorded in Rome, Italy, on 17 Aug. 1984, starting 12:30 local time.

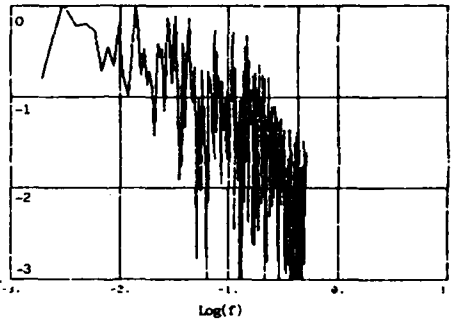

Fig.2 Spectrum (log scale) of log-amplitude record of Fig.1.

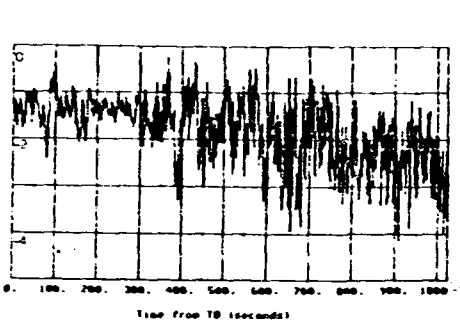

Fig.3 Field log-amplitude recorded in Rome, Italy, on 17 Aug. 1984, starting 13:36 local time.

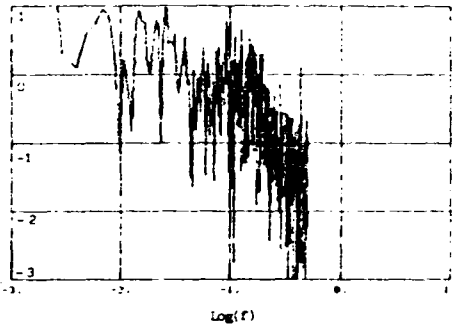

Fig.4 Spectrum (log scale) of log-amplitude record of Fig.3.

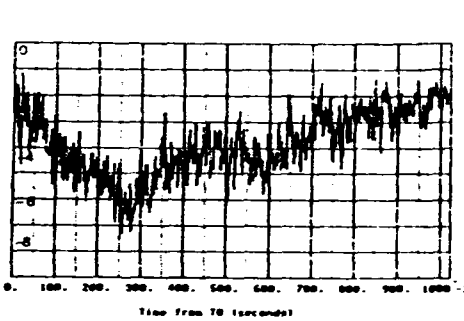

Fig.5 Field log-amplitude recorded in Rome, Italy, on 17 Aug. 1984, starting 13:54 local time.

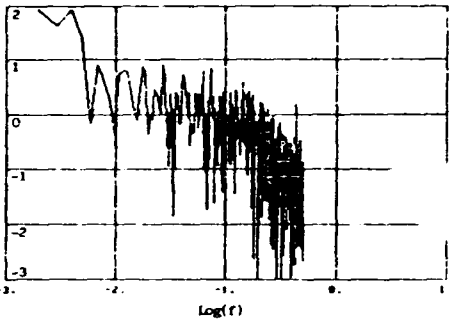

Fig.6 Spectrum (log-scale) of log-amplitude record of Fig.5.

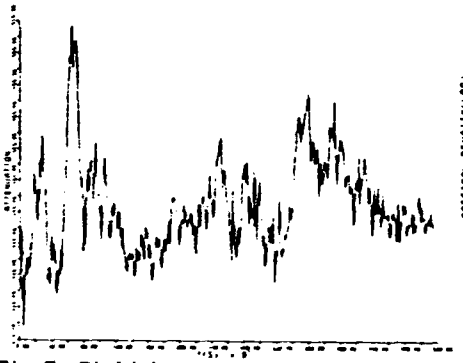

Fig.7 Field log-amplitude recorded at Fucino, Italy, on 17 Jul. 1979, starting 15:35 local time.

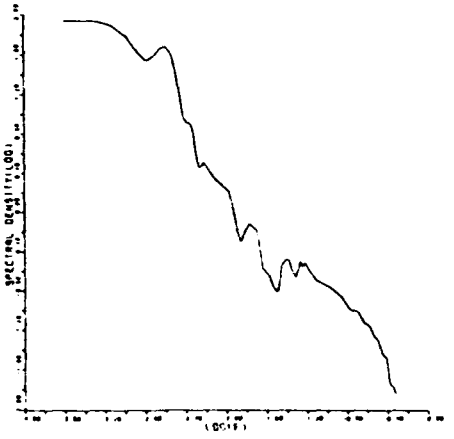

Fig.8 Spectrum (log scale) of log-amplitude record of Fig.7.

COHERENCE THEORY

Some Recent Developments in Optical Coherence Theory[+]

Emil Wolf[*]

Department of Physics and Astronomy
University of Rochester
Rochester, NY 14627 USA

(invited)

A review will be presented of some recent researches relating to partially coherent wavefields. These include the clarification of the relationship between space-time correlation functions employed in the traditional description of partial coherence and the single-frequency correlation functions frequently used in the analysis of problems relating to atmospheric propagation and to speckle patterns. Second-order as well as higher-order correlations will be considered.

Progress towards the clarification of the foundations of the theory of radiative energy transfer will also be described and some of the important unsolved problems in this area will be noted.

+ Supported by the National Science Foundation

* Also at the Institute of Optics, University of Rochester

Classical radiometry: a short wavelength limit for a general mapping of cross-spectral densities in second-order coherence theory

by

M. Nieto-Vesperinas
Instituto de Optica, C.S.I.C.
Serrano, 121
28006 Madrid, Spain.

In the last years there has been much effort in the attempt to derive the empiric laws of radiometry from the statistical theory of wave fields[1-3]. In this context, expressions for the so-called generalized radiance were proposed in terms of the cross-spectral density of the optical field. It has also been shown[4] that it is not possible to build a generalized radiance that depends linearly on the cross-spectral density of the optical field and that satisfies the three requisites of radiometry. In general[5], all the generalized radiance functions proposed in the literature can be mathematically

derived as particular cases of a general mapping, between the cross-spectral density and the generalized radiance, originally propond in Quantum Statistical Mechanics by Cohen[6].

The difficulties mentioned above can be, however overcomed when one considers the limit of short wavelengths for the radiated field. This was recently put forward for quasi-homogeneous sources, and for a particular case of generalized radiance, (the established in Ref. 3) in Ref. 7. In fact, the sources for which traditional radiometry was applied are of dimensions very large compared to the radiation wavelength and are quasihomogeneous (e.g. blackbody sources).

In this communication it is shown that for this class of sources, in the short wavelength limit, all generalized radiance functions obtained from Cohen's mopping reduce to the ordinary radiance and thus satisfies the three conditions of classical radiometry. Also, the associated specific intensity, that characterizes 3-D propagation of the field, is shown to satisfy the radiative transfer equation in free space.

(*) This Work has been supported by the National Science Foundation and CAICYT.

References

1. A. Walther, J. Opt. Soc. Am. 58, 1256 (1968).

2. V.I. Tatarskii, The Effect of the Turbulent Atmosphere an Wave Propagation (V.S. Department of Commerce, National Technical Information Service, Springfield, Va, 1971). Sec. 63.

3. E. Wolf, Phys Rev. D 13, 869 (1976).

4. A. T. Friberg, J. Opt. Soc. Am. 69, 192 (1979).

5. M. S. Zubairy, A Study an the Foundation of the Theory of Radiative Energy Transfer (Ph. D. Theris Univ. of Rochester, 1978). Sec. 2.2.

6. L. Cohen, J. Math. Phys. 7, 781 (1966).

7. J. T. Foley and E. Wolf, Opt. Comm. 55, 236 (1985).

LIDAR

Lidar Profiling of Atmospheric Properties that Influence Propagation

THOMAS D. WILKERSON

Institute for Physical Science and Technology
University of Maryland
College Park, MD USA 20742
(invited)

During the past 20 years, many lidar techniques have been devised and demonstrated for quantitative, remote measurements of the atmosphere.[1-4] Such measurements have been carried out even at ranges exceeding 100 km. Ground-based, airborne, and balloon borne lidar probes measure stratospheric particulates,[5,6] ozone,[7,8] and free[9] OH. Remarkable observations of atmospheric structure have been made using the mapping capabilities of lidar. These include tropospheric folds,[10] convection and advection in the planetary boundary layer,[11,12] and gravity waves in the upper atmosphere.[3,13] This paper describes the lidar technology now available for profiling the atmosphere's thermodynamic variables: temperature T, pressure p, density n, and humidity [H_2O]. The latter is included here because the typical H_2O latent heat content is important dynamically and water vapor has strong effects on optical propagation. It will be seen that several accurate lidar methods can be used to monitor the state of atmosphere during propagation measurements, or as operational support for propagation devices such as radars and high intensity lasers.

Table I lists lidar techniques by the physical effects and molecules employed. Entries in the table indicate the altitude zones of the atmosphere in which the methods provide direct measurements of T, p, n, and [H_2O]; in this order, available accuracies are nominally 1°K, 3 mb, 0.3%, and 3%. Most of the methods are based on optical transitions involving discrete energy levels of the atoms or molecules (absorption, fluorescence, Raman scattering); exceptions are #12 and #13 that employ gas refractivity and Rayleigh scattering.

Differential absorption lidar (DIAL) techniques are available for all four types of profiling, using near infrared lines of H_2O (720, 820, 940 nm) and O_2 (690, 770 nm). Two laser pulses are transmitted, one tuned onto an absorption line, the other tuned into a nearby portion of the spectrum where there is little or no absorption. Time-resolved analysis of the ratio of the two lidar returns provides a range-resolved profile of the amount of

absorber.[1-4,14,15] For certain lines of H_2O this yields the concentration $[H_2O]$ (or its mixing ratio in air) directly.[16-21] For other lines, the absorber in question consists of excited state molecules whose abundance in the atmosphere is related to temperature or pressure as well as sheer material quantity. The O_2 molecule has been singled out for this work particularly.[3,22-26] The laser requirements for DIAL (and fluorescence lidar) are stringent, including emission linewidth and frequency stability of order 0.01-0.03 cm^{-1} (300-900 MH_2). Groundbased and airborne DIAL observations based on the near IR spectra of H_2O and O_2, while still undergoing refinements, are part of the developed technology for atmospheric profiling.

Raman lidar[27-37] employs the backscattered lidar returns at different frequencies corresponding to the Raman spectra of atmospheric constituents such as N_2, H_2O, CH_4, etc. With sufficient care in blocking out backscatter from the primary laser transmission (and, in some cases, daylight[33,35]), the water vapor mixing ratio $[H_2O]/[N_2]$ and the nitrogen density profile $[N_2]$ can be determined without using the spectrally pure lasers required for DIAL. The countervailing fact is that Raman scattering coefficients are 3-4 orders of magnitude smaller than for Rayleigh scattering; so the lidar returns are faint, and one requires a favorable combination of large telescope, high laser power, and discrimination against background light. Relatively recent developments include high spatial resolution in vertical $[H_2O]$ profiles,[35] measurements to high altitude,[36] and temperature profiling to altitudes of order 2 km using rotational Raman scattering[34,37] by N_2.

For higher altitudes, it has been suggested[38,39] that stratospheric temperature and pressure can be measured by means of a variation of the OH fluorescence technique[9] already employed for OH density. The ambient temperature in the altitude range 80-100 km is measured from the ground by means of sodium D-line fluorescence lidar;[40-44] recently the sodium temperature near 90 km has been measured with 2°K accuracy and 1 km altitude resolution.[45] To cover a broader range of altitudes, Rayleigh scattering of high energy laser pulses (e.g., Nd:YAG) is used to obtain the relative density and absolute temperature of the atmosphere between 30 and 100 km.[3,13,46-48]

To summarize, a host of lidar methods is now available to support measurements of optical and millimeter wave propagation, even to great distances from the lidar station and to high altitudes above the earth.

REFERENCES

1. E. D. Hinkley (editor), Laser Monitoring of the Atmosphere, Springer Verlag (1976).
2. A. I. Carswell, Canad. J. Phys. 61, 378 (1983).
3. D. K. Killinger and A. Mooradian (editors), Optical and Laser Remote Sensing, Springer-Verlag (1983).
4. R. M. Measures, Laser Remote Sensing: Fundamentals and Applications, John Wiley (1984).
5. M. P. McCormick, Opt. Eng. 21, 340 (1982).
6. M. P. McCormick, T. J. Swissler, W. H. Fuller, W. H. Hunt, and M. T. Osborn, Geof. Int. 23, 187 (1984).
7. O. Uchino, M. Maeda, H. Yamamura, and M. Hirono, J. Geophys. Res. 88, 5273 (1983).
8. G. J. Megie, G. Ancellet, and J. Pelon, Appl. Opt. 24, 3454 (1985).
9. W. S. Heaps and T. J. McGee, J. Geophys. Res. 90, 7913 (1985).
10. S. T. Shipley, E. V. Browell, D. S. McDougal, B. L. Orndorff, and P. Haagenson, Environ. Sci. & Tech. 18, 749 (1984).
11. S. H. Melfi, J. Spinhirne, S.-H. Chou, and S. Palm, J. Clim. Appl. Met. 24, 806 (1985).
12. J. T. Sroga and E. W. Eloranta, J. Appl. Meteor. 19, 598 (1980); K. E. Kunkel, E. W. Eloranta, and J. A. Weinman, J. Atmos. Sci. 37, 978 (1980).
13. M.-L Chanin and A. Hauchecorne, J. Geophys. Res. 86, 9715 (1981).
14. R. M. Schotland, "Some Observations of the Vertical Profile of Water Vapor by a Laser Optical Radar", Proc. 4th Symp. on Remote Sensing of Environment, University of Michigan, Ann Arbor (1966).
15. R. M. Schotland, J. Appl. Meteor. 13, 71 (1974).
16. V. V. Zuev, V. E. Zuev, Y. S. Makushkin, V. N. Maricher, and A. A. Mitsel, Appl. Optics 22, 3742 (1983).
17. E. V. Browell, T. D. Wilkerson, and T. J. McIlrath, Appl. Optics 18, 3474 (1979).
18. E. V. Browell, A. F. Carter, and T. D. Wilkerson, Opt. Eng. 20, 84 (1981).
19. C. Cahen, G. Megie, and P. Flamant, J. Appl. Meteor. 21, 1506 (1982).
20. R. M. Hardesty, Appl. Optics 23, 2545 (1984); R. M. Hardesty, "Measurement of Range-Resolved Water Vapor Concentration by Coherent CO_2 Differential Absorption Lidar", NOAA Tech. Memo. ERL/WPL-118 (March 1984).
21. T. D. Wilkerson and G. K. Schwemmer, Opt. Eng. 21, 1022 (1982).
22. J. B. Mason, Appl. Optics 14, 76 (1975).
23. G. K. Schwemmer and T. D. Wilkerson, Appl. Optics 18, 3539 (1979).
24. C. L. Korb and C. Y. Weng, J. Appl. Meteor. 21, 1346 (1982).
25. C. L. Korb and C. Y. Weng, Appl. Optics 22, 3759 (1983).
26. J. E. Kalshoven, C. L. Korb, G. K. Schwemmer, and M. Dombrowski, Appl. Optics 20, 1967 (1981).
27. D. A. Leonard, Nature 216, 142 (1967).
28. J. A. Cooney, Appl. Phys. Lett. 12, 40 (1968).
29. S. H. Melfi, J. D. Lawrence, and M. P. McCormick, Appl. Phys. Lett. 15, 295 (1969).
30. R. G. Strauch, V. E. Derr, and R. E. Cupp, Appl. Optics 10, 2665 (1971).
31. S. H. Melfi, Appl. Optics 11, 1605 (1972).
32. J. C. Pourny, D. Renaut, and A. Orszag, Appl. Optics 18, 1141 (1979).
33. D. Renaut, J. C. Pourny, and R. Capitini, Optics Lett. 5, 233 (1980).
34. J. A. Cooney, Opt. Eng. 22, 292 (1983).
35. J. Cooney, K. Petri, and A. Salik, Appl. Optics 24, 104 (1985).

36. S. H. Melfi and D. Whiteman, Bull. Am. Meteor Soc. 66, 1288 (1985).
37. Y. F. Arshinov, S. M. Bobrovnikov, V. E. Zuev, and V. M. Mitev, Appl. Optics 22, 2984 (1983).
38. T. J. McIlrath, Opt. Eng. 19, 494 (1980).
39. T. J. McGee and T. J. McIlrath, Appl. Optics 18, 1710 (1969).
40. J. E. Blamont, M.-L. Chanin, and G. Megie, Ann. Geophys. 28, 833 (1972).
41. G. Megie, F. Bos, J. E. Blamont, and M.-L. Chanin, Planet. Space Sci. 26, 27 (1978).
42. A. J. Gibson, L. Thomas, and S. K. Bhattacharyya, Nature 281, 131 (1979).
43. L. Thomas and S. K. Bhattacharyya, Proc. 5th ESA-PAC Symp. on European Rocket and Balloon Programmes and Related Research, ESA-SP-152 (1980).
44. K. H. Fricke and U. von Zahn, J. Atmos. Terrest. Phys. 47, 499 (1985).
45. U. von Zahn, private communication (1986).
46. A. Hauchecorne and M.-L. Chanin, J. Atmos. Terrest. Phys. 44, 577 (1981).
47. G. B. Heckly, A. Hauchecorne, and M.-L. Chanin, Comptes Rendu, Serie II 295, 997 (1982).
48. A. Hauchecorne and M.-L. Chanin, J. Geophys. Res. 88, 3843 (1983).

Table I. Applicability of Meteorological Lidar Methods

Method	T	p=nkT	n	$[H_2O]$
1. H_2O DIAL - 1 line	—	—	—	trop. lower strat.
2. H_2O DIAL - 2 lines	trop.	—	—	trop.
3. O_2 DIAL - 1 line	trop.	—	—	—
4. O_2 DIAL - 2 lines	trop.	—	—	—
5. O_2 DIAL - troughs	—	trop.	trop.	—
6. H_2O Raman - vibrat.	—	—	—	trop. lower strat.
7. N_2 Raman - vibrat.	—	—	trop. strat.	—
8. N_2 Raman - rotat.	trop.	—	—	—
9. OH fluor. - 2 lines	strat. meso.	—	—	—
10. OH fluor. - 2 bands	—	strat. meso.	—	—
11. Na fluor.	meso.	—	meso.	—
12. Laser altimetry - multi-color	—	trop.	—	—
13. Air scatt. - Rayleigh	trop. strat. meso.	—	trop. strat. meso.	—

REMOTE SENSING OF METEOROLOGICAL PARAMETERS : EFFECTS OF ATMOSPHERIC TRANSMISSION AND SCATTERING PROPERTIES ON DIAL MEASUREMENTS

G. MEGIE
Service d'Aéronomie du CNRS
B.P. 3
91371 Verrières-le-Buisson

(invited)

High vertical resolution measurements of the physical parameters of the lower atmosphere (temperature, pressure, humidity) will allow significant progress in various areas of atmospheric research (meteorology, climatology, pollution studies). Such measurements have recently became feasible due to the development of tunable, narrow bandwith laser sources in the near infrared (720-760 nm) - i.e. Nd Yag excited dye lasers or solid state Alexandrite lasers. The differential absorption laser technique (DIAL) forms the basis for these high accuracy determinations of state variables in the atmosphere : it uses two laser pulses, one located on a resonant absorption line of the species to be measured (ν_L) and a second one at a nearby reference frequency (ν_R). The energy $E_{L/R}$ backscattered at each frequency by aerosols and molecules in the atmosphere is measured as a function of time using a range gated receiver which allows the atmospheric absorption $\bar{K}$ of a particular species to be measured over a known path ΔR :

$$\bar{K} = \frac{1}{2\Delta R} \ln \frac{E_L(R) / E_R(R)}{E_L(R + \Delta R) / E_R(R + \Delta R)} \qquad (1)$$

The absorption is then used to determine the species concentration as in the case of water vapor. Furthermore, if the species concentration is known in the atmosphere as for molecular oxygen, the measurement of the absorption at the center of a line will lead to the determination of the temperature (Mégie, 1980 ; Korb and Weng, 1982). Similarly, measurement in a far line wing can be used for the determination of pressure in order to obtain a maximum sensitivity of the absorption coefficient (Korb, 1977 ; Mégie, 1980).

Analysis of the various error sources in such measurements shows that, besides stringent requirements on laser frequency stability and bandwith and knowledge of spectroscopic parameters, propagation of the laser beam through the atmosphere leads to various systematic errors which have to be accounted for to improve the measurement accuracy.

a) Atmospheric scattering and extinction :

Equation (1) is only an approximation of the general formula which relates the atmospheric absorption $\bar{K}$ to be the backscattered energy. Effects related to differential extinction due to molecular and Mie scattering have to be accounted for, whereas their relative magnitude is less than 10^{-3} in the near infrared due to the sharp structure of the absorption features which allows a small frequency interval between the absorbed and reference frequencies. Spatial and temporal correlations between successive range cells will also influence the retrieval of $\bar{K}$ depending on the time interval between successive laser shots. Experimental results show that the decorrelation time for backscatter returns by aerosols particles is of the order of a few microseconds (Hardesty et al., 1981). Successive pulses separated by time intervals greater than this will thus appear as uncorrelated over the period during which the atmosphere can be considered as frozen. This period is of the order of 10 msec and corresponds roughly to the coherence time of atmospheric turbulence. This means also that, taking into account the non stationary nature of the atmospheric attenuation, a point might be reached where variations in the attenuation level over the integrated interval will dominate the averaging process.

b) Atmospheric absorption :

These effects are related to the spectral characteristics of the laser emission. A special attention should be payed to the contribution of the amplified spontaneous emission (ASE) which results in a broadband spectrum superposed to the narrow linewidth laser emission. To limit the resulting systematic error at values below a few percent, spectral purity of the laser emission - i.e. ratio between emission in the narrow peak to the total emitted energy - should be better than 99 %. Whereas such values are easily attainable with solid state laser sources, difficulties in the

system design arise when using Nd Yag excited dye lasers.
The problem of the finite linewidth of the laser emission has also to be addressed. Cahen and Mégie (1981) have shown that the spatial distribution of absorption coefficients in the atmosphere measured with the DIAL technique is restored, in the case of a pulsed laser system, only if the emission is monochromatic. Due to the finite linewidth of the laser line, a systematic error is introduced which can be as large as 5 % if the ratio of the laser to the absorption linewiths exceeds 0.5. Furthermore, due to the scattering process in the atmosphere itself, the backscattered line always corresponds to a Doppler broadened line (Rayleigh Scattering) superposed with a narrower peak due to Mie scattering by aerosol particles. To account for the residual dependence on the transmission properties of the atmosphere within the laser propagation path, special algorithms should be developed, to reduce the residual errors down to 0.05 K for laser bandwiths of 0.04 cm (Korb et al. 1982).

All these effects have been demonstrated or accounted for in various experiments which have shown that the overall accuracy which can be expected from DIAL measurements can be better than 5 % for humidity retrieval (Cahen et al., 1981 ; Browell et al., 1979), 0.5 to 1 K for temperature and 2-3 mb for pressure profiling (Korb et al., 1983 b). Both ground based and airborne systems have been developed which have been used for the study of local scale convective activity or mesoscale processes such as cyclogenesis or disturbances associated with the occurence of cold or warm fronts. Further directions in this field will include developments of automated systems either for ground based monitoring or airborne experiments and feasibility studies of space borne active systems for global measurements.

REFERENCES

1) E.V. Browell, T.D. Wilkerson, T.J. Mc Ilrath (1979), Appl. Opt., 18, 3774.

2) C. Cahen, G. Mégie (1981), J. Quant. Spectrosc. Radiat. Transfer., 25, 151.

3) C. Cahen, P. Flamant, G. Mégie (1982), J. Appl. Meteor., 21, 1506.

4) R.M. Hardesty, R.J. Keeler, M.J. Post and R.A. Richter (1981), Appl. Opt., 20, 3763.

5) C.L. Korb, C.Y. Weng (1982), J. Appl. Meteor., 21, 1346.

6) C.L. Korb, C.Y. Weng (1983), Appl. Opt., 22, 3759.

7) C.L. Korb, C.K. Schwemmer, M. Dombrovski, C.Y. Weng (1983 b) in Optical and Laser Remote sensing, 39, 120, D.K. Killinger and A. Mooradian eds., Springer Verlag, Berlin, Heidelberg.

ATMOSPHERIC POLLUTION MONITORING USING OPTICAL REMOTE SENSING TECHNIQUES

H. Edner, B. Galle*, A. Sunesson, S. Svanberg,
L. Unéus, S. Wallin and W. Wendt

Department of Physics, Lund Institute of Technology
P.O. Box 118, S-221 00 Lund, Sweden
*IVL, P.O. Box 5207, S-402 24 Göteborg, Sweden
(invited)

The problems connected with atmospheric pollutants are being more and more widely recognized. Soil- and lake acidification have been long discussed while reports on widespread damage to forests are more recent. Air pollutants constitute a threat to public health both directly through inhalation and indirectly through possible long-term influences on the atmospheric environment. The need for powerful actions and international cooperation is becoming evident. Clearly, efficient methods for measuring local, regional and global pollution are much needed. Optical remote sensing techniques provide powerful means for studying atmospheric pollutants. Most techniques utilize differential optical absorption of radiation that is transmitted to probe the air. Regular light sources as well as lasers can be efficiently applied in pollution monitoring. A good review of the field is provided by Ref. [1].

In optical remote sensing of atmospheric pollutants wavelength regions relatively free from major species absorption (eg by CO_2 and H_2O) have to be utilized. For obtaining a high sensitivity to minor constituents, molecular transitions with high absorption coefficients are selected. Frequently the accuracy of an optical absorption measurement is not limited by photon statistics but rather by noise due to atmospheric turbulence. In a long-path absorption measurement, the turbulence will cause the light beam to walk over the receiver aperture. If the beam is first directed towards a remote retro-reflector, the beam will instead walk over the reflector causing strong variations in the intensity reflected back. In measurements employing laser light back scattering (lidar: light detection and ranging) the wavelength tuning of the laser is frequently changed between the resonant wavelength and the close-lying off-resonance (reference) wavelength between subsequent pulses. Again, atmospheric fluctuations in the individual volume elements will cause the elastically backscattered intensity to vary. The remedy for these detrimental effects of atmospheric turbulence is to measure the absorption on the resonance and reference wavelengths simultaneously, or at least at such short time separations that the atmosphere can be considered to be "frozen". The time scales of atmospheric turbulence have been extensively investigated; of particular interest is an investigation using CO_2 lasers by Menyuk and Killinger [2]. The conclusion is that most of the noise can be eliminated by working on time scales below 10 ms.

Most practical Nd:YAG lasers, that are used for pumping tunable dye lasers operate with a repetition rate of about 10

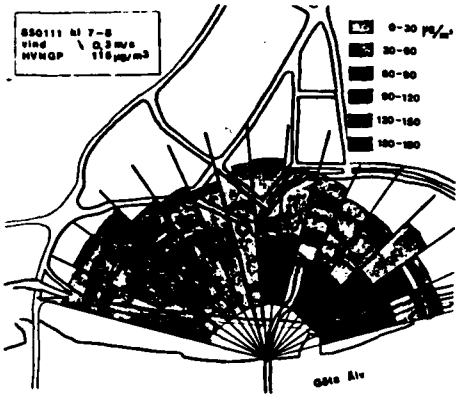

Fig.1. Charting of NO_2 distribution by the dial technique [4].

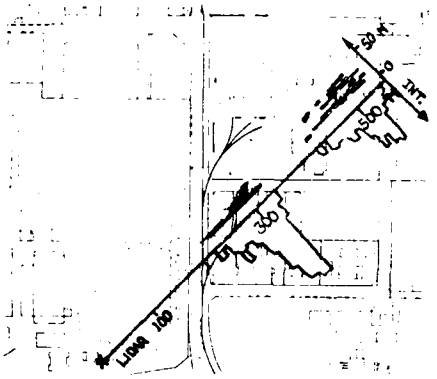

Fig.2. Charting of particles by the lidar technique [5]

Hz. Although wavelength changes between pulses still does not fulfil the temporal requirements just stated, quite satisfactory results can be obtained in range resolved dial (differential absorption lidar) measurements at the price of some extra signal averaging. Using the mobile system described in Ref. [3] we have recently studied the NO_2 dynamics at temperature inversion situations. In Fig. 1 the NO_2 distribution over the central part of the city of Göteborg during a winter morning is shown [4]. The data are obtained in successive horizontal scans during a total time of 1 hour. An easier task for such a system is to map the relative particle distribution in industrial areas. An example from such measurements is shown in Fig. 2 [5]. A new, larger and more versatile mobile system for lidar and other optical atmospheric measurements has recently been completed. A lay-out of this system is shown in Fig. 3 [6]. When fast data taking and a high precision are needed a laser system generating two sharp wavelengths simultaneously or at very short time intervals is desirable. In airborne dial measurements it is mandatory because of swift changes is the aerosol backscattering. If the pulses are transmitted at sub-millisecond intervals the signal returns can be detected through a common detection channel using a single transient digitizer. Simultaneous transmission from a two-wavelength laser normally requires very sharp wavelength separation into two individual detection channels. Different more or less complex schemes for circumventing the problems of atmospheric fluctuations have been introduced.

We have recently proposed a different approach using a rather broad-band laser and utilizing the spectral separation obtained by gas filtering. [7]. The principle of the gas correlation lidar scheme is shown in Fig. 4. The laser emission covers both on- an off resonance wavelengths for the species to be studied. The spectral contents in the backscattered radiation is unscrambled by comparing the intensity received directly and

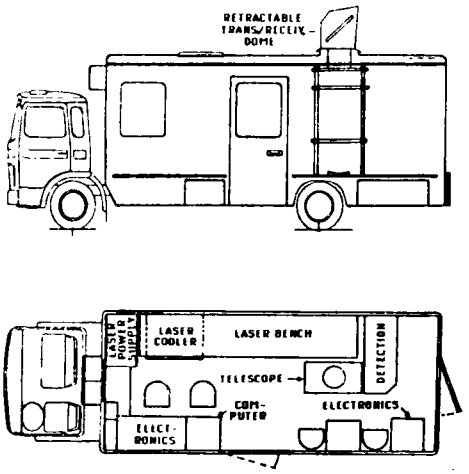

Fig.3. Mobile laboratory for atmospheric remote sensing [6]

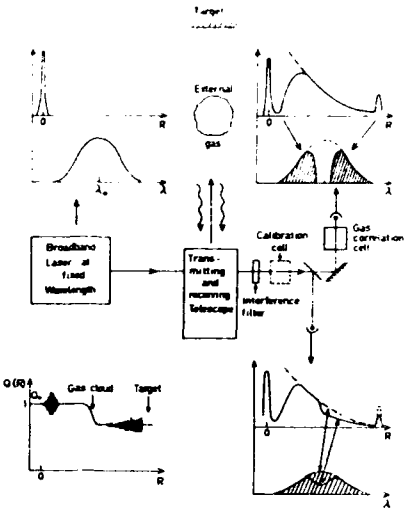

Fig.4. The principle of gas correlation lidar [7].

through a cell filled with the gas to be studied in sufficient concentration to cause strong or complete absorption on resonant wavelengths. The spectral and temporal signals occurring in the detection of a remote gas cloud are illustrated in the figure. The technique has been tested for the case of an artificial Hg cloud. Since the gas can handle many spectral features in parallel a very simple laser with little wavelength control might be used. A normal flashlamp can also be employed for path average measurements using a topographic target or a simple retro-reflector. This technique is now being tested for SO_2 [8]. The gas correlation lidar technique has the potential of allowing very simplified equipment to be employed in certain measurement situations. However, it should be pointed out that the sensitivity is lower than in normal, narrowband dial since the spectral separation is incomplete. Calibration of the instrument using gas cells is also necessary. Since the information is obtained from ratios of the two channel signals for the same light pulse immunity to atmospheric turbulence and other fluctuations is largely granted.

Continous conventional light sources provide possibilities in atmospheric long-path absorption measurements as shown by Platt and Perner (See Ref. 9 for a review). In their doas (differential optical absorption spectroscopy) scheme a high-pressure xenon lamp mounted in front of a reflector is used to transmit a beam over a distance of up to several kilometers before reaching the optical telescope receiver. Clearly, atmospheric turbulence will cause the received intensity to fluctuate strongly. However, by performing a swift spectral scan covering on- and off-resonance wavelengths in a time interval of "frozen" atmospheric conditions even very small intensity variations due to specific absorptions can be monitored. The low photon statistics is

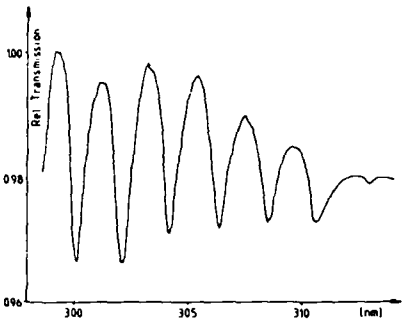

Fig.5. Doas monitoring of ambient SO_2 over a 600 m urban pathlength (MV: 22 ppb [10].

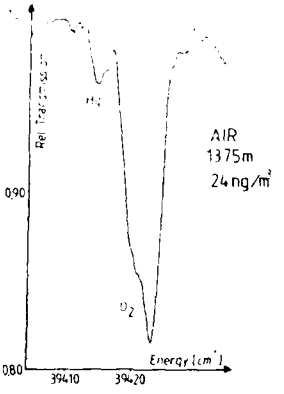

Fig.6. Doas recordings of Hg in air [11].

compensated by adding a large number of scans. We have constructed a high-resolution doas system with a new wavelength scanning principle. Measurements have been performed for SO_2, NO_2 and Hg [10]. The excellent signal to noise ratio obtained in measurements of this kind is illustrated in Fig. 5. For the first time it was also possible to measure the local Hg background concentration in the ppt ($1 : 10^{12}$) range. The system has also been used for assessing the Hg emissions from refuse disposal sites and chlorine-alkali industry [11]. A measurement example is shown in Fig. 6.

This work was supported by the Swedish Board for Space Activities (DFR), the Swedish National Environmental Protection Board (SNV) and the Air and Water Pollution Research Institute (IVL).

REFERENCES:

1. D. A. Killinger and A. Mooradian (Eds.), Optical and Laser Remote Sensing (Springer, Heidelberg 1983).
2. N. Menyuk and D. A. Killinger, Opt. Lett. 6, 301 (1981).
3. K. Fredriksson, B. Galle, K. Nyström and S. Svanberg, Appl. Opt. 20, 4181 (1981).
4. B. Galle, A. Sunesson, and W. Wendt, to appear.
5. A. Sunesson and L. Unéus, Lund Reports on Atomic Physics LRAP-54 (1985).
6. H. Edner, K. Fredriksson, A. Sunesson, S. Svanberg, L. Unéus and W. Wendt, to appear.
7. H. Edner, S. Svanberg, L. Unéus and W. Wendt, Opt. Lett. 9, 493 (1984).
8. H. Edner, S. Montán, A. Sunesson, S. Svanberg, L. Unéus and W. Wendt, to appear.
9. U. Platt and D. Perner, in Ref. 1
10. H. Edner, A. Sunesson, S. Svanberg, L. Unéus and S. Wallin, Appl. Opt., February 1986.
11. B. Galle, Å. Iverfelt, L. Unéus and S. Wallin, to appear.

CO_2-Laser Radar:

Environmental effects and system approaches

W. Büchtemann, R. Ebert

Forschungsinstitut für Optik
Schloss Kressbach
74 Tübingen, F.R. Germany
(invited)

Introduction

CO_2-laser radars, as understood here, are systems using the reflection of solid targets for the purpose of ranging, imaging, tracking etc., and are using in general heterodyne detection to achieve sensitivity or to exploit the optical phase information. Such systems experience interactions with the atmosphere and reflection by diffuse or specular targets. The interactions tend to degrade the signal, but can be used sometimes to measure atmospheric quantities. This talk gives a comprehensive overview over more recent theoretical and experimental results, mainly obtained at our laboratory, both with respect to describe atmospheric and target effects as well as system approaches.

Atmospheric effects

Apart from atmospheric extinction, /1/, radiation will suffer predominantly from turbulence which causes intensity, phase, and angle of arrival fluctuations. For the case of the CO_2- laser radar the situation is simplified by the fact that for most practical applications scintillation is not saturated which leads for homogeneous turbulence to a well understood behaviour /2/. One has a complication by the reflection geometry with possible path correlation effects.

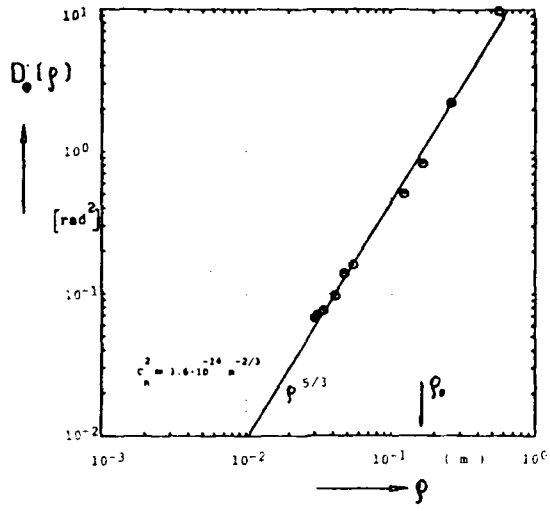

Fig. 1: Phase difference fluctuations between two points of separation ϱ due to turbulence.

Measured phase fluctuations for moderate path lengths and moderate to strong turbulence in a reflective geometry show good agreement with theory, see Fig. 1, which indicates that the maximum aperture for near ground applications is about 100 mm. Fig. 1 shows as solid line the predicted $\varrho^{5/3}$ behaviour.

Rain will affect the phase in quite a different way /3/, see Fig. 2. In this case, the mutual coherence function, which describes the phase fluctuations as function of lateral separation, drops already at very small separations, but remains at a constant level up to very large separations. The level itself depends on the rain rate. Further depicted in Fig. 2 is the effect of turbulence for a pathlength of 1200 m and several levels of turbulence strength. Also different is the frequency behaviour: For rain, the spectrum is expected to be flat out to several hundreds of Hz and drops then with a f^{-7}-law. Fig. 3 shows a measured example. This frequency behaviour gives the opportunity to separate phase fluctuations caused by turbulence and rain and makes it possible to use phase fluctuations to measure path averaged rain rates, as it was done recently /4/.

Heterodyne efficiency also is affected by turbulent phase fluctuations. Heterodyne efficiency is 1 if a complete phase match exists between signal and local oscillator (L.O.), both being focused totally onto the detector. Fig. 4 shows the computed heterodyne efficiency for a focused signal spot being slightly smaller (factor of 0.8) than the L.O. as a function of detector size for various angle of arrival fluctuations ε, ε =2 corresponding to strong turbulence over a distance of some km.

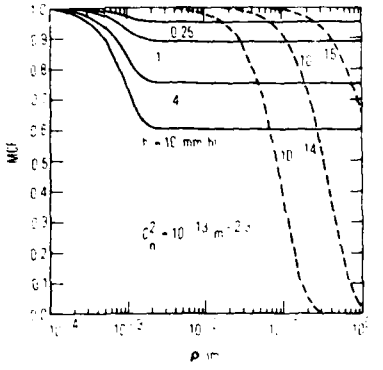

Fig. 2: The mutual coherence function at 10.6 µm for a path of 1200 m and various rain rates h (solid curves). Dashed curves: Clear air turbulence, different values of the index structure constant C_n.

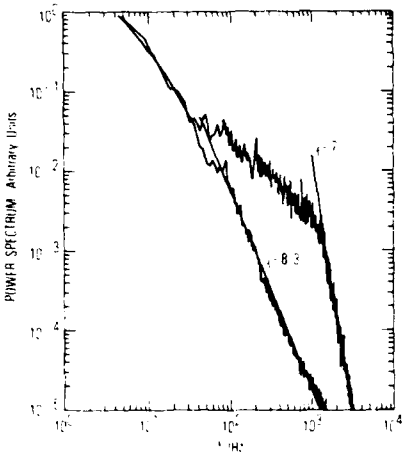

Fig. 3: Experimentally obtained phase-difference power spectrum measured during drizzlelight-rain conditions (upper trace) and a few minutes after the rain stopped (lower trace).

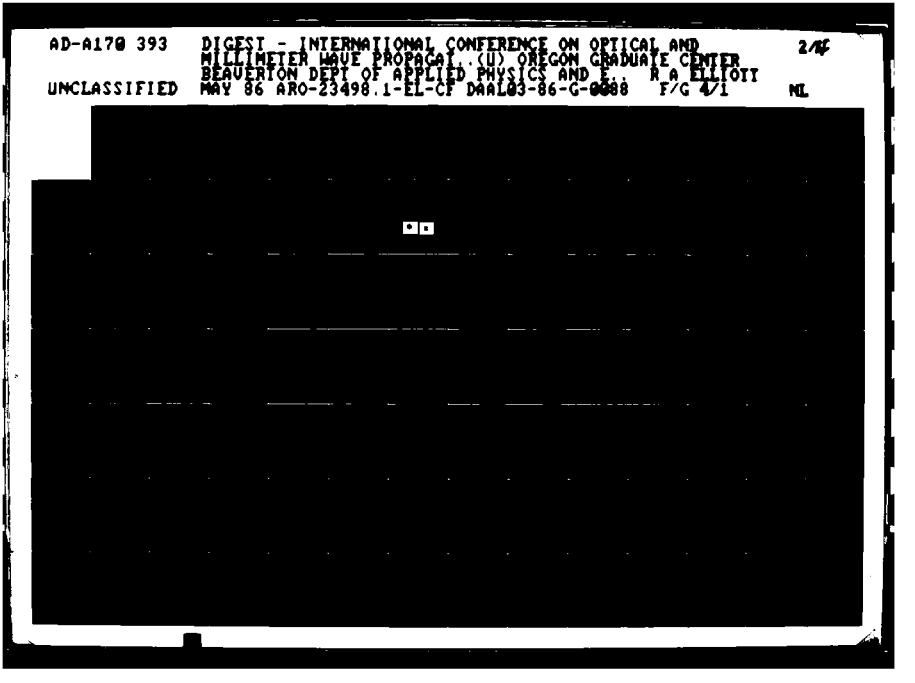

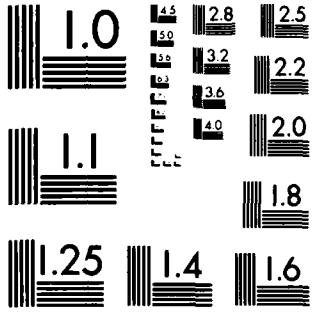

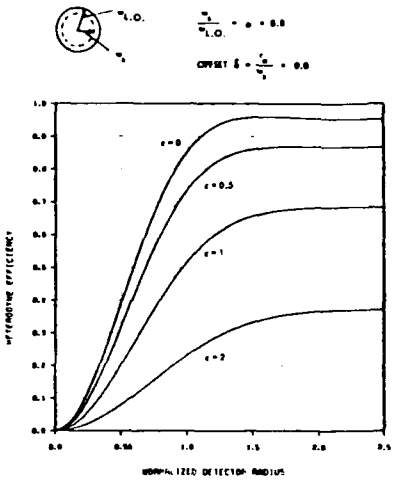

Fig. 4: Heterodyne efficiency as a function of normalized detector radius, the signal spot size w_s being slightly smaller than the L.O. ($w_{L.O.}$), for various levels of angle of arrival fluctuations ϵ , $\epsilon = 2$ corresponding to strong turbulence and a path of several km.

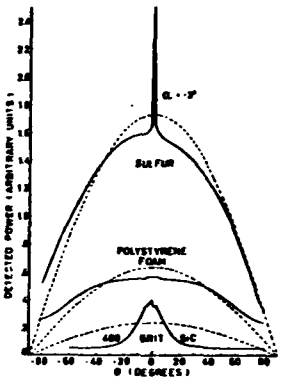

Fig. 5: Backscattered power as a function of target aspect angle θ. Detector viewing angle $\alpha = 3°$. For each curve the dashed line is least-squares best fit to a cosine /5/.

Target effects

For active systems targets are described by their reflectivity, apart from effects of coherence. Reflectivity should be used in the definition of the radiance factor which is unity for a Lambertian reflector, i.e. a reflector which reflects all incoming radiation in such a way that the apparent radiance is constant for all aspect angles. There is an urgent need for standard reflectors which enable system assessment and calibration. Fig. 5 shows candidates for standard reflectors /5/.

An additional property of targets, when illuminated by a laser, is speckle. The signal characteristics of a diffuse reflector are described by the negative exponential distribution which leads to a normalized signal variance of 1. The generalized theory is quite intricate /6/, but many practical objects can be discribed as diffuse targets whose reflective properties are described as multiplicative factor with a variance of one or near one.

False alarm and detection probability: Binary imaging

Atmospheric and speckle effects make it impractical to use an imaging laser radar in the conventional way where the information is extracted from the strength of the return signal (grey scale imaging). More practical system approaches use e.g. a threshold to determine if a target element is present or not: Binary imaging. Such systems determine range or range rate, e.g. in an 3-D-system which analyses relief images.

It is still necessary to optimise binary systems with respect to signal statistics, e.g. by using multiple channels, where the signal of several channels is added incoherently, that is after squaring. This leads to much improved signal statistics regarding false alarm probability and signal detection compared to a single channel system. Four channels are adequate to obtain signal statistics close to incoherent systems /7/.

System aspects

The heterodyne technique in the IR region is well established and the necessary components are available. With cw CO_2-laser radars the problem of frequency stabilisation of the transmitter with respect to the L.O. is overcome by the use of a high efficiency acousto-optical frequency shifter. The high efficiency of the A.O. (up to 80%) allows the use of the diffracted, frequency shifted beam as transmitter. The unshifted beam has a cleaner frequency characteristic, suitable for L.O. operation. For pulsed CO_2-laser radars the frequency stabilisation between transmitter and L.O. can be done with a Stark cell technique /8/. Advances in thermoelectrically cooled detectors will frequently eliminate the necessity of liquid nitrogen cooling. An NEP of $\sim 2 \cdot 10^{-19} WHz^{-1}$ at 60 MHz has been measured /9/.

References

1. A. Kohnle, Opt. and mm Wave Prop., Florence, May 86
2. R.L. Fante, Proc. IEEE vol. 68, 1424-1443 (1980)
3. H.T. Yura et al., J. Opt. Soc. America, vol. 73, 1574-1580 (1983)
4. R.L. Schwiesow, Appl. Optics, vol. 24, no.24 (1985)
5. H. Henshall et al., Proc. of 3rd Topical Meeting on Coherent Laser Radar, Gt. Malvern, UK (1985)
6. J.H. Shapiro, Appl. Optics, vol. 21, 3398-3407 (1982)
7. W. Büchtemann, FfO-Report 1985/98
8. W. Büchtemann et al., Proc. of 1st Top. Meeting. Coh. Laser Radar, Aspen, USA (1981)
9. M. C. Wilson et al., Proc. of CLEO, Baltimore, USA,(1985)

Lidar Measurements in the Marine Atmosphere

G.de leeuw, TNO Physics and Electronics Laboratory,
P O Box 96864, 2509 JG The Hague,
The Netherlands

1. INTRODUCTION

Propagation losses in the marine atmosphere are hard to determine directly. Apart from the usual problems associated with transmission measurements, the difficult accessibility of the oceans makes it almost impossible to measure transmission reliably. To achieve this, two stable platforms are required. At coastal transmission sites the results are often influenced by aerosols produced by breaking waves in the surf zone. Therefore alternative methods are used to investigate the transmission of the marine atmosphere. The most common method is measuring aerosol particle size distributions and calculation of the extinction coefficients by Mie theory (cf. refs. 1-4). Direct measurements are required, however, to verify the results. A promising technique to do this is remote sensing with lidar (LIght Detection and Ranging). With a monostatic lidar system, which uses the aerosol as a diffuse scatterer, range-resolved extinction and backscatter coefficients can in principle be measured.

In this contribution some results are presented of vertical extinction profiles measured with a 1.06 μm lidar system. In addition to the lidar measurements, aerosol particle size distributions and meteorological parameters were recorded. Empirical relations between the lidar-measured extinction and backscatter coefficients and the meteorological and aerosol parameters were derived from a statistical approach. Some preliminary results of this analysis are presented.

The measurements were performed in May/June 1983 in the North Atlantic at Station Lima (57°N, 20°W), aboard the Dutch weathership MS Cumulus

2. EXPERIMENTS

A small calibrated lidar system was used to measure vertical profiles of extinction from the sea surface up to a maximum altitude of 1000 m. The emitter was a Nd Glass laser (wavelength 1.06 μm) with an energy of 100 mJ in a 30 ns pulse. The receiver system consisted of a Cassegrain telescope with a main mirror of 74 mm diameter. The intensity of the received radiation was detected with a fast photodiode. The whole system was contained in a box of 20x20x30 cm. Aboard MS Cumulus this instrument was mounted on an actively stabilized platform to correct the roll and pitch of the ship.
Vertical profiles of extinction were measured with this system according to the method described by Kunz [5], from signals recorded under elevations of -0.9, 0, 10, and 30 degrees.

Aerosol particle size distributions were measured with PMS optical particle counters in the size range from 0.16 to 32 µm, and with a Rotorod inertial impactor in the size range from 10 to 100 µm. Visibility was measured with an AEG point visibility meter. Information on airmass history was obtained from Rn measurements and airmass trajectory analyses. Meteorological parameters, including radiosonde soundings, were obtained from the crew of the weathership, MS Cumulus.

3. RESULTS

3.1 Vertical extinction profiles

A total number of 281 extinction profiles were measured in a purely marine atmosphere. Visual inspection of the profiles showed that in 63% of the measurements a vertically homogeneous layer existed near deck level (12 m). The depth of this homogeneous layer was generally some hundreds of meters, although in some cases it only amounted to some tens of meters. Above the homogeneous layer the extinction decreased in 22% (cf. fig. 1, profiles 1, 3, 6, 7 and 9), and increased in 48% due to clouds (profiles 4 and 5). In the remaining 30% the homogeneous layer extended up to the maximum altitude probed by the lidar (profile 10).

In those cases where the extinction was not vertically homogeneous, the extinction was monotonously decreasing in 35% (profile 11), in 37% the extinction decreased until a homogeneous layer was encountered (profile 8), and in 28% the extinction was increasing from deck level (profile 2).

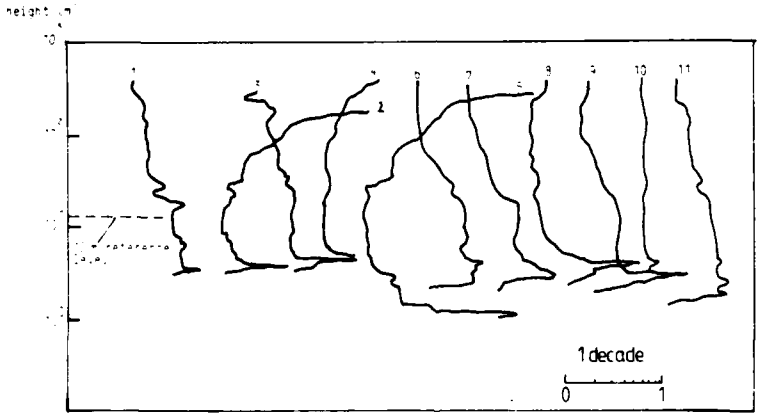

Figure 1. Examples of extinction profiles (see text).

The quoted figures include all measured profiles. It is noted that during practically all measurements the sky was (partly) clouded. This may have had influence on the profiles, also in those cases where they were measured between the clouds. As described by Blanchard and Woodcock [6], a sea-salt inversion may exist just below cloud base which extends beyond the clouds due to wind shear. The difference in particle size distributions in the sea-salt inversion and in the lower layer will affect the extinction profile near cloud base heights, also between the cloud patches. In a small number of cases the influence of the clouds extended to the sea surface, causing extinction profiles that increased fast with altitude (cf. fig. 1, profile 2). During the larger part of the measurements cloud base was so high that cloud effects were not observed in the range where extinction profiles could be measured reliably.

3.2 Influence of meteorological and aerosol parameters

The shapes of the extinction profiles will be strongly influenced by the vertical variation of particle size distributions. In cloud-free skies and when cloud base is so high that they do not affect the surface layer, particle size distributions are determined by vertical mixing, relative humidity and mixing layer height. Vertical mixing is induced by convective forces due to thermal instability, and by mechanical stirring due to windspeed. Gravitational forces drag the particles down. Obviously, vertical mixing velocities vary with particle weight (size). Furthermore the weight of the hygroscopic sea-salt particles is very sensitive to changes in relative humidity. Variations in mixing layer height affect the overall concentrations by its dilution effect. Things are complicated by the presence of a source (the sea), of which the intensity varies strongly with windspeed. Another source is the entrainment of particles from the layer capping the marine inversion. This discussion shows that a strong interaction exists between the micro-meteorological climate and aerosol particle size distributions, which in turn have a strong effect on the extinction and backscatter coefficients. A statistical approach is applied to analyse these interactions and to derive empirical relations between extinction and backscatter coefficients on the one side and meteorological and aerosol parameters on the other side. Fits were applied to e.g. windspeed, relative humidity, particle concentrations for specific diameters, integrated particle number, area and volume concentrations, and combinations of these parameters. In future analyses other parameters will be included as well.

As an example, the variation of lidar-measured extinction and backscatter coefficients at 12 m (deck level) with windspeed are shown in fig. 2. Extinction appears to be only weakly dependent on windspeed (if at all). The correlation between these two parameters is very low. A much better correspondence is observed between backscatter and windspeed. The relation between these two parameters depends on relative humidity. For humidities between 70 and 80% (fig. 2b) we derived:

$$\beta = 1.6\ 10^{-3}\ u^{0.67}\ ,$$

where β is the backscatter coefficient (/km) and u is windspeed (m/s). This behaviour of backscatter can be understood from consideration of the aerosol properties. It is well established [7] that the production of marine aerosol particles (having a spectral mode near 3 μm) increases strongly with windspeed. Therefore it is not surprising that good correlations were also found between backscatter and aerosol total area and volume concentrations.

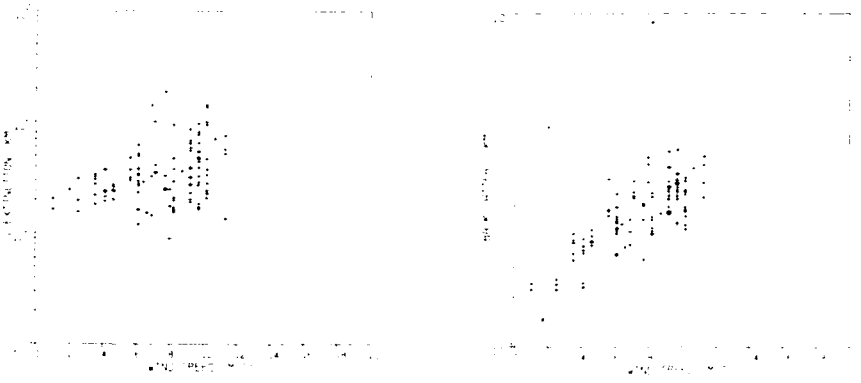

Figure 2. Windspeed dependence of lidar-derived extinction and backscatter coefficients (70% < RH < 80%).

4. CONCLUSION

Good correspondence was observed between lidar-derived backscatter and aerosol and meteorological parameters. For extinction this correspondence is less clear. Hopefully a multiparameter fit, including more parameters than used sofar, will provide a better description of extinction properties of the marine atmosphere. This subject is under continuous study at our institute.

REFERENCES

1. Hughes, H.G. and Richter, J.H., Opt. Eng. 19 (1980), 616.
2. Hughes, H.G., J. Appl. Meteor. 19 (1980), 803.
3. Noonkester, V.R., Appl. Opt. 20 (1981), 1275.
4. Fairall, C.W., Davidson, K.L. and Schacher, G.E., Opt. Eng. 21 (1982), 847.
5. Kunz, G.J., Appl. Opt. 22 (1983), 1955.
6. Blanchard, D.C. and Woodcock, A.H., Ann. N. Y. Ac. Sci. (1980), 330.
7. Exton, H.J., Latham, J., Park, P.M., Perry, S.J., Smith, M.H., and Allan, R.R., Quart. J. R. Met. Soc. 111 (1985), 817.

SURFACE SCATTERING

Target Induced Speckle Effects in Picosecond Laser Ranging and Altimetry

by

Chester S. Gardner
Department of Electrical & Computer Engineering
1406 W. Green St.
University of Illinois at Urbana-Champaign
Urbana, IL 61801

(invited)

Mode-locking and Q-switching techniques are now used routinely to generate laser pulses of a few picoseconds in duration. These short pulses provide higher accuracies in applications such as remote sensing and ranging. In practice, many targets, such as the ocean surface, the ground and man-made objects, have range spreads that far exceed the widths of the picosecond laser pulses. The reflected pulses are broadened to about twice the range spread of the target, while the pulse shape is related to the target geometry. If the range spread of the target is larger than the transmitted pulse width, the width of the received pulse will be longer than the correlation length of the speckle-induced fluctuations. As a consequence, speckle will cause random small-scale fluctuations within the received pulse that will distort its shape. This phenomenon is called time-resolved speckle. Similar phenomena can also occur for extended flat diffuse targets, in which the broadening of the received pulse is due to the wave-front curvature of the laser beam, and for continuously distributed targets in the atmosphere.

Target surface characteristics significantly influence the statistics of the reflected pulses. Speckle induced by diffuse targets is fully developed so that the reflected field follows circular Gaussian statistics. The reflected signal from a cube corner reflector (CCR) array consists of the coherent addition of the reflected electric-field components from CCR's at various ranges within the array. For targets such as the LAGEOS satellite, the number of CCR's contributing to the received signal at any given time will be small (i.e. < 10). Consequently, the speckle is only partially developed because the statistics of the reflected field will not be Gaussian.

The severity of speckle is characterized by the speckle signal-to-noise ratio parameter, K, which can be regarded as the number of speckle correlation

cells averaged by the receiver aperture. K is equal to or greater than 1 and typically is much larger than 1 for diffuse targets but usually is less than 10 for CCR arrays. K is defined as

$$K = \frac{\langle N \rangle^2}{\mathrm{Var}(N) - \langle N \rangle} ,$$

where N is the total photocount in the detected pulse.

The effects of time-resolved speckle are illustrated in Figure 1 where the received pulse shape is plotted for the case where a 30 ps FWHM laser pulse has been reflected from a tilted CCR array. The array consisted of 4 CCR's spaced 4 cm apart and tilted so that the range separation between adjacent CCR's was 4 mm. The target range was 389 m and the detector was a streak-camera with a 2 ps response time[1,2]. The speckle fluctuations within the pulse are clearly evident. The mean pulse shape was computed by averaging 50 pulses and is plotted in Figure 2. The structure in the mean pulse is caused by the range spread of the target and corresponds to reflections from individual CCR's within the array. Similar effects are seen in Figure 3 where a typical ocean reflected laser pulse is plotted. The two dominant peaks are reflections from the crest and trough of a capillary wave on the ocean surface. The laser altimeter was in an aircraft flying over Chesapeak Bay at an altitude of appoximately 330 m[1,3].

For applications such as target identification and remote sensing of sea states, the waveform of the received pulse is used to characterize the target. Therefore knowledge of the statistics of the time-resolved speckle is important. For applications such as laser distance ranging, estimation of the arrival time of the target-reflected pulse in the presence of time-resolved speckle is the problem of interest. In this paper, the theoretical descriptions of target signatures and target-induced speckle are reviewed and compared with recent picosecond laser ranging and altimeter experiments. Speckle effects in laser remote sensing and ranging are discussed.

References

1. J. B. Abshire and J. E. Kalshoven, Jr., "Multicolor Laser Altimeter for Barometric Measurements over the Ocean: Theoretical," Appl. Opt., 22, 2578 (1983).

2. J. B. Abshire, J. F. McGarry, H. E. Rowe and J. J. Degnan, "Streak Camera-Based Laser Receiver Development," Proc. 5th International Workshop on Laser Ranging Instrumentation," Royal Greenwich Observatory, Herstmonceux, UK, September 24-28, 1984.

3. K. E. Im and C. S. Gardner, "Theoretical and Experimental Analysis of the Performance of Two-Color Laser Ranging Systems," EOSL Report No. 85-006, August 1985.

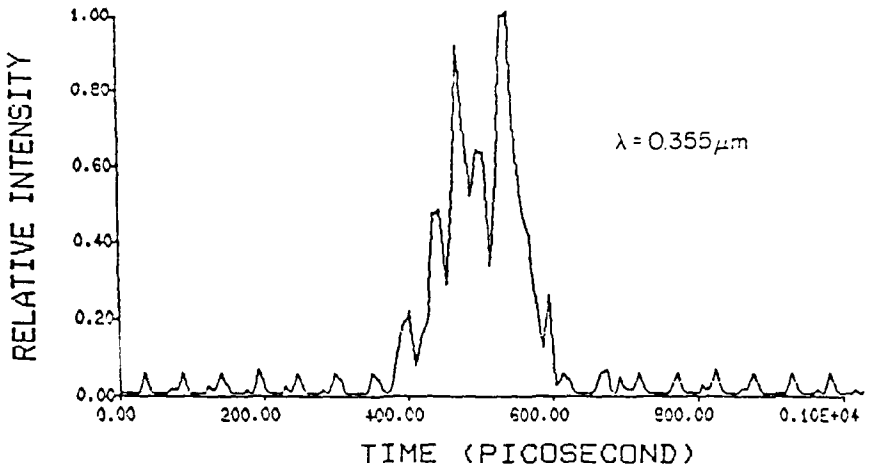

Figure 1. Typical waveform of a 30 ps FWHM Nd:YAG laser pulse that was reflected from a tilted CCR array target. The wavelength was 0.355 μm and target range was 389 m. The target consisted of 4 CCR's spaced 4 cm apart and tilted so that the range separation between adjacent CCR's was 4 mm. The structure within the pulse is due to speckle noise.

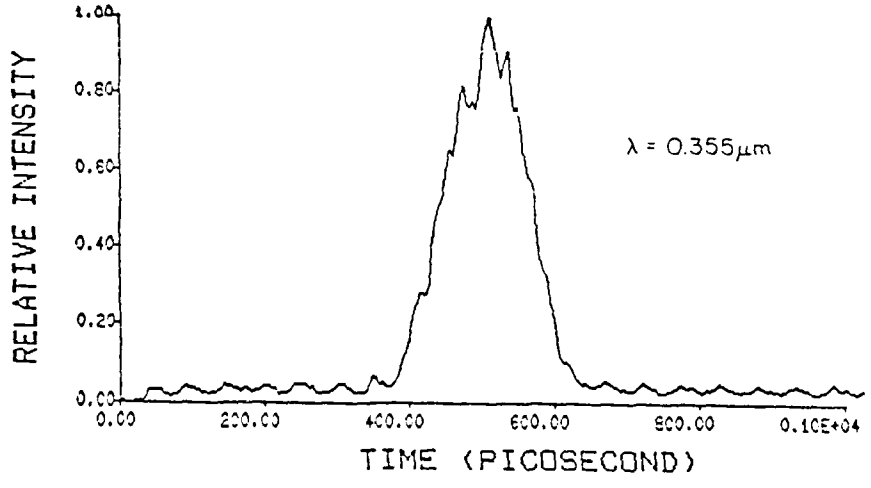

Figure 2. Average waveform of 50 pulses reflected from the tilted CCR array target described in Figure 1. The structure within the average pulse is due to the range spread of the target and corresponds to reflections from individual CCR's within the array.

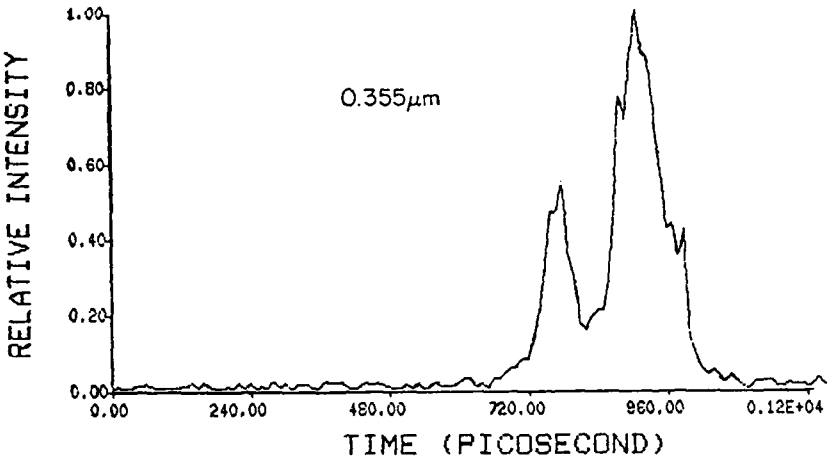

Figure 3. Typical ocean reflected laser pulse. The two dominant peaks are reflections from the crest and trough of a capillary wave on the ocean surface. The laser altimeter was in an aircraft flying over Chesapeake Bay at an altitude of 330 m.

Transport theory of random planar waveguide with a fixed scatterer - Mode theory

K. Furutsu

Nakato 187-6, Musashi-Murayama, Tokyo 190-12, Japan

(invited)

Transport equations have been investigated also for a waveguide with either random wall [1] or random medium characteristics [2], to the approximation of using the coupled power equation , neglecting the interference effects at all. In a recent paper [3], a unperturbative transport theory has been developed typically for a random layer with two rough boundaries allowing both reflection and transmission of waves, and the results can naturally be applied also to the present waveguide, as illustrated in the figure below:

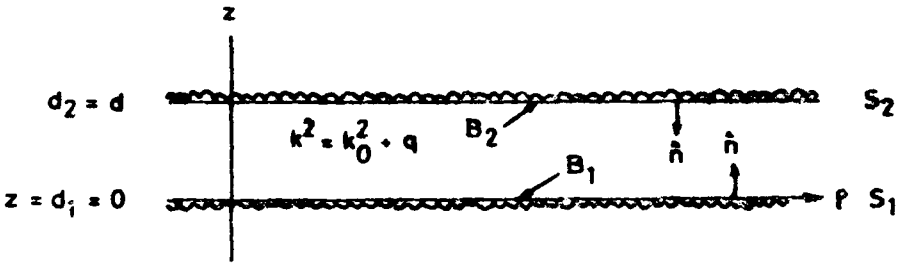

With the space coordinate vector $\hat{x} = (x_1, x_2, x_3) = (\underline{\rho}, z)$ in terms of the horizontal coordinate vector $\underline{\rho} = (x_1, x_2)$ and $z = x_3$, the wave equation for a scalar wave function $\psi(\hat{x})$ may be written, as:

$$[\, L - q(\hat{x}) \,]\, \psi(\hat{x}) = j(\hat{x}), \qquad L = -\left(\frac{\partial}{\partial \hat{x}}\right)^2 - k_0^2 , \tag{1}$$

with two effective boundary conditions of the form

$$-\partial_n \psi \Big|_{S_i} = B_i \psi \Big|_{S_i} = \int d\underline{\rho}'\, B_i(\underline{\rho} \mid \underline{\rho}')\, \psi(\underline{\rho}', d_i), \qquad i = 1, 2, \tag{2}$$

that are transferred from the real boundaries onto reference boundary planes S_1 and S_2, chosen at $z = d_1 = 0$ and $d_2 = d$, respectively. Here, $q(\hat{x})$ ($q^*(\hat{x})$) is the random part of the nondissipative medium, $j(x)$ is a source term, and $\partial_n = \hat{n} \cdot \partial / \partial \hat{x}$; and B_i has been obtained in an explicit operator form for given boundary change [4]. Here, the wave equation and the two boundary conditions can be written by one coordinate matrix equation, as

$$[\, L - q - B_1 - B_2 \,]\, \psi = j ,$$

with the new boundary conditions that $\partial_n \Psi$ be zero in the outsides of S_1 and S_2, $z < 0$ and $z > d$. Here B_j is regarded as a $\hat{x}$ matrix with the elements $B_j(\hat{x}|\hat{x}') = \delta(\eta - d_j) B_j(\xi|\xi') \delta(\eta' - d_j)$, as well as g is with the diagonal elements $g(\hat{x})\delta(\hat{x}-\hat{x}')$. Hence, for the Green function of Eq. (3), say g, the governing equation is given by

$$[L - v]\, g = 1, \qquad v = g + B_1 + B_2, \tag{4}$$

which has exactly the same form as that in a random medium v; and therefore enables the statistical Green functions to be obtained with a well-established procedure, on treating the medium and the boundaries on exactly the same footing [3].

Thus, the first-order Green function, $G = \langle g \rangle$, is the solution of $(L - M)G = 1$, with the effective medium-boundary matrix M, defined by $\langle vg \rangle = MG$; and the second-order Green function defined by $I(x_1; x_2 | x_1'; x_2') = \langle g^*(x_1|x_1') g(x_2|x_2') \rangle$, or, in matrix form, by $I(1;2) = \langle g^*(1) g(2) \rangle$ is the solution of a Bethe-Salpeter equation of the form

$$I(1;2) = U^{(c)}(1;2)\,[\,1 + K(1;2)\, I(1;2)\,]. \tag{5}$$

Here, $U^{(C)}(1;2) = G^*(1)G(2)$, and $K(1;2)$ can be divided into two major parts $K^{(q)}(1;2)$ and $K^{(B)}(1;2)$ of the medium and the boundaries, respectively. Specific expressions of $K(1;2)$ were given for both a slightly random medium-boundaries and a particulate medium and/or embossed boundaries [3], [4]. The solution of B-S Eq. (5) can be given by

$$I(1;2) = U^{(c)}(1;2) + U^{(c)}(1;2)\, S(1;2)\, U^{(c)}(1;2), \tag{6}$$

in terms of the incoherent scattering matrix S(1;2), defined by [4]

$$S = K\,[\,1 + U^{(c)} S\,] = [\,1 - K U^{(c)}\,]^{-1} K \tag{7}$$

similar to the Lippmann-Schwinger scattering matrix.

The Fourier transform of $G(x|x') = G(z|\xi - \xi'|z')$ with respect to $\xi - \xi'$, say $\tilde{G}(z|\lambda|z')$, can be expanded in a mode series, as

$$\tilde{G}(\eta|\lambda|\eta') = \sum_{\alpha} [\,\lambda^2 - \kappa_\alpha^2\,]^{-1} \phi_\alpha(\lambda, \eta)\, \bar{\phi}_\alpha(\lambda, \eta'). \tag{8}$$

Here, the $\phi_\alpha(\lambda, \eta)$'s are a set of eigenfunction, defined by the eigenvalue equation

$$-\left(\frac{\partial}{\partial\eta}\right)^2 \phi_\alpha(\underline{\lambda},\eta) - \int d\eta'' \tilde{M}^{(q)}(\eta|\underline{\lambda}|\eta'')\,\phi_\alpha(\underline{\lambda},\eta'') = a^2(\underline{\lambda})\,\phi_\alpha(\underline{\lambda},\eta), \qquad (9)$$

with the boundary conditions

$$\left[-\partial_n - \tilde{M}^{(j)}(\underline{\lambda})\right]\phi_\alpha(\underline{\lambda},\eta)\Big|_{S_j} = 0, \qquad j = 1, 2, \qquad (10)$$

where $a^2(\underline{\lambda})$ is the eigenvalue, $\kappa_\alpha^2 = k_0^2 - a^2(\underline{\lambda})$, $\mathrm{Im}[\kappa_\alpha] < 0$, and $\tilde{M}^{(j)}$ and $\tilde{M}^{(q)}$ are the Fourier transforms of $M^{(j)}(\underline{\rho})$ and $M^{(q)}(z|\underline{\rho}-\underline{\rho}'|z')$, respectively; equations of $\bar{\phi}_\alpha(\underline{\lambda},\eta)$ are the transpose of Eqs. (9) and (10). The Fourier inversion of Eq. (8) can be given in terms of the residue values at the poles $\underline{\lambda}^2 = \kappa_\alpha^2$, say $\underline{\lambda} = \underline{k}_\alpha = k_\alpha \underline{a}$ with the two-dimensional unit vector $\underline{a}$, since the integrand has no other singularity as the whole; hence,

$$G(\hat{x}|\hat{x}') = \sum_\alpha G_\alpha(\underline{\rho}-\underline{\rho}')\,\phi_\alpha(\eta)\,\bar{\phi}_\alpha(\eta'), \qquad (11)$$

where $\phi_\alpha(\eta)$ designates $\phi_\alpha(\underline{\lambda},\eta)$ at the poles. With $k_{ab} = (k_a^q + k_b)/2$, a corresponding horizontal power-flux vector at $\hat{x}$, say $\underline{W}(\hat{x}|\hat{x}')$, is

$$\underline{W}(\hat{x}|\hat{x}') = \sum_{ab}{}' \sum_{cd}{}' \int_{2\pi} d\underline{a}\, d\underline{a}'\, k_{ab}\,\underline{a}\, N_{ab}(\eta)\, I_{ab;cd}(\underline{a}|\underline{\rho}-\underline{\rho}'|\underline{a}')\, \bar{N}_{cd}(\eta'). \qquad (12)$$

Here, Σ' means the summation only over the propagative mode waves, $N_{ab}(z) = \phi_a^*(\eta)\,\phi_b(\eta)$, $\Delta_{ab} = \int d\eta\, N_{ab}(\eta) \sim \delta_{ab}$; and, from Eq. (6),

$$I_{ab;cd}(\underline{a}|\underline{\rho}-\underline{\rho}'|\underline{a}') = U_{ab}^{(c)}(\underline{\rho}-\underline{\rho}')\,\delta_{ac}\,\delta_{bd}\,\delta(\underline{a}-\underline{a}')$$

$$+ \int d\underline{\rho}'' \int d\underline{\rho}'''\, U_{ab}^{(c)}(\underline{\rho}-\underline{\rho}'')\, S_{ab;cd}(\underline{a}|\underline{\rho}''-\underline{\rho}'''|\underline{a}')\, U_{cd}^{(c)}(\underline{\rho}'''-\underline{\rho}'), \qquad (13)$$

where, from Eq. (7), $S_{ab;cd}$ is the solution of the integral equation

$$S_{ab;cd}(\underline{a}|\underline{\rho}-\underline{\rho}'|\underline{a}') = K_{ab;cd}(\underline{a}|\underline{a}')\,\delta(\underline{\rho}-\underline{\rho}')$$

$$+ \sum_{ij}{}' \int d\underline{\rho}'' \int d\underline{a}''\, K_{ab;ij}(\underline{a}|\underline{a}'')\, U_{ij}(\underline{\rho}-\underline{\rho}'')\, S_{ij;cd}(\underline{a}''|\underline{\rho}''-\underline{\rho}'|\underline{a}'), \qquad (14)$$

and $K_{ab;cd}(\underline{a}|\underline{a}')$ is given in terms of the mode transform of $K(x_1;x_2|x_1';x_2') = K(\underline{r},z_1,z_2|\underline{\rho}-\underline{\rho}'|\underline{r}',z_1',z_2')$. The solution of Eq. (14) may be obtained by various means, including the matrix doubling method by using an addition formula of scattering matrices [3] and also the eigenvalue method by constructing a set of eigenfunctions of $K_{ab;cd}$ [5].

When a fixed scatterer $q_\alpha(\hat{x})$, say, is embedded in the medium, the equation for the Green function $g^{(\alpha)}(\hat{x}|\hat{x}')$, say, is given in matrix form, by

$$[\, L - v - \mathcal{g}_\alpha \,]\, \mathcal{g}^{(\alpha)} = 1 , \qquad v = \mathcal{g} + B_1 + B_2 . \tag{15}$$

Hence, the equation of $G^{(\alpha)} = \langle g^{(\alpha)} \rangle$ becomes, by introducing the effective medium-boundary matrix M_α, defined by $\langle v g^{(\alpha)} \rangle = M_\alpha G^{(\alpha)}$ and also setting $M^{(\alpha)} = M + \Delta \mathcal{g}_\alpha$, as

$$[\, L - M - \mathcal{g}_\alpha' \,]\, G^{(\alpha)} = 1 , \qquad \mathcal{g}_\alpha' = \mathcal{g}_\alpha + \Delta \mathcal{g}_\alpha , \tag{16}$$

whose solution is given, in terms of a scattering matrix $T^{(\alpha)}$ of q_α', by

$$G^{(\alpha)} = G + G\, T^{(\alpha)} G , \qquad T^{(\alpha)} = [\, 1 - \mathcal{g}_\alpha' G \,]^{-1} \mathcal{g}_\alpha' . \tag{17}$$

Here, to the second order of q, $\Delta \mathcal{g}_\alpha = \langle \mathcal{g}\, G\, T^{(\alpha)} G\, \mathcal{g} \rangle$ and is generally very small compared with $\mathcal{g}_\alpha$, letting $\mathcal{g}_\alpha' \sim \mathcal{g}_\alpha$. The same is also for the second-order Green function $I_\alpha(1;2) = \langle g^{(\alpha)*}(1)\, g^{(\alpha)}(2) \rangle$, which is still the solution of the B-S Eq. (5) with the replacement of $U^{(C)}(1;2) \to G^{(\alpha)*}(1) G^{(\alpha)}(2) = U^{(C)} + U^{(C)} V^{(\alpha)} U^{(C)}$ and $K(1;2) \to K_\alpha(1;2) = K(1;2) + \Delta K_\alpha(1;2)$, where $V^{(\alpha)}$ and ΔK_α are the changes caused by the scatterer. The solution is given by

$$I_\alpha(1;2) = I(1;2) + I(1;2)\, V^{(\alpha/K+\Delta K)}(1;2)\, I(1;2) , \tag{18}$$

in terms of an effective scattering matrix $V^{(\alpha/K+\Delta K)}$ of $\mathcal{g}_\alpha$, given by

$$V^{(\alpha/K+\Delta K)} = V^{(\alpha/K)} + [\, 1 + V^{(\alpha/K)} I \,]\, S_\alpha^{(\Delta K/K)} [\, I\, V^{(\alpha/K)} + 1 \,] . \tag{19}$$

Here, the first term $V^{(\alpha/K)} = [\, 1 - V^{(\alpha)} U^{(cc)} S\, U^{(cc)} \,]^{-1} V^{(\alpha)}$ is the leading term, and $S_\alpha^{(\Delta K/K)} = [\, 1 - S^{(\Delta K)} I\, V^{(\alpha/K)} I \,]^{-1} S^{(\Delta K)}$ where $S^{(\Delta K)}$ is given by the same equation as $S(1;2)$ with $K \longrightarrow \Delta K_\alpha$. The mode transformed version of $V^{(\alpha/K+\Delta K)}$ is given by the elements $V^{(\alpha/K+\Delta K)}_{ab;cd}(\underset{\sim}{\Omega}|\underset{\sim}{\Omega}')$, which is subject to the important optical relation

$$\sum_a{}' \int_{2\pi} d\underset{\sim}{\Omega}\; V^{(\alpha/K+\Delta K)}_{aa;cd}(\underset{\sim}{\Omega}|\underset{\sim}{\Omega}') = 0 , \tag{20}$$

meaning that the scattering cross section $V^{(\alpha/K+\Delta K)}_{aa;cd}$ has negative values in the shadow direction and its neighborhood.

[1] F.G. Bass, V.D. Freulicher, and I.M. Fuks, IEEE Trans. AP-22, 278; 288 (1974).
[2] For example, L.B. Dozier and F.D. Tappert, J. Acoust. Soc. Am. 63, 353 (1978).
[3] K. Furutsu, J. Opt. Soc. Am. A2, 913; 932 (1985).
[4] K. Furutsu, IEE Proc. 130(London), Part F, 601 (1983); J. Math. Phys. 26, 2352 (1985); for electromagnetic waves, J. Opt. Soc. Am. A2, to be published (Dec., 1985).
[5] K. Furutsu, J. Math. Phys. 21, 765 (1980).

MEASUREMENTS ON MULTIPATH PROPAGATION AT 94 GHZ

OVER SNOW-COVERED TERRAIN

H.Essen, E.P. Baars

FGAN - Forschungsinstitut für Hochfrequenzphysik
Neuenahrer Straße 20
D-5307 Wachtberg-Werthhoven
Germany

1. INTRODUCTION

The adverse weather capabilities of millimeterwave radars for surveillance and guidance applications especially in comparison with IR systems are rather well established. One of the more critical environmental conditions for a millimeterwave radar sensor is snow covered terrain. Not only clutter from the snow surface may impose problems but also the possibility of performance degradation due to multipath propagation has to be considered. In comparison with lower frequencies, however, the smaller wavelength in comparison with a given surface roughness should result in a less pronounced interaction between direct and indirect path. This should lead to a better low angle tracking and guidance performance if compared with classical radar frequencies.

2. MEASUREMENT APPROACH

2.1 OBJECTIVE

Some results on multipath propagation in the millimeterwave region are published for a bistatic measurement configuration and different type of terrain or a maritime environment [1]. With the intention to study the multipath effect representative for a millimeterwave radar under snow conditions monostatic transmission measurements have been performed at 94 GHz.
The influence of multipath propagation on the angle sensing performance of a millimeterwave monopulse radar should be investigated.

2.2 MEASUREMENT SET-UP AND EQUIPMENT

Geometry
The radar was positioned at a height of 3 m above ground and was operated over a folded transmission path against a corner reflector of 100 m^2 nominal cross section at a range of 700 m. The corner reflector was mounted at a sliding ladder contraption to allow a variation of the corner reflector height. It was as well possible to vary the height continuously as in steps of 12.5 cm.
For the main measurement approach the radar antenna was fixed at different elevation angles while the reflector height was altered from bottom to the top of the ladder during the measurement run.
For an additional approach the reflector was fixed in height and the reflector and its vicinity was scanned by the antenna beam.

Measurement Radar

The block diagram of the 94 GHz coherent monopulse radar involved in the measurements is shown in Figure 2.1. The first stage of the transmitter branch is a CW Gunn oscillator which is phase locked to the master crystal reference. This Gunn oscillator synchronizes the 2-stage IMPATT amplifier chain which in a short pulse mode drives the output stage tube. In a long pulse mode the tube is driven by a CW IMPATT oscillator and the pulse length determined by the modulator pulse. The polarization of the transmitted signal can be manually switched by feeding one of the two ports of an orthomode transducer in front of the 2-feet transmitting antenna. The receiving antenna is a 2-feet dual plane monopulse antenna. The monopulse comparator feeds the input ports of the mixers for the sum and the elevation and traverse channels. All mixers are pumped by a common Gunn oscillator which is again phase locked to the master reference.
The performance data are tabulated in Table 2.1. The radar front end is mounted on a KRUPP 2000 pedestal to allow scanning and tracking modes.

Antennas :			
Transmitter		Receiver	
3 dB Beamwidth	0.4 dB	Monopulse Antenna in El and traverse	
Gain	53 dB	3 dB Beamwidth	0.4 dB
		Gain	53 dB
		Null Depth (rel. to Sum Peak)	-25 dB
		Isolation between Sum and Difference Ports	20 dB
Transmitter :		Receiver :	
Phase locked to Crystal Reference		Three identical Channels for Sum, Elevation Difference and traverse	
Frequency	94 GHz	Dynamic Range	60 dB

Table 2.1: Performance Data of 94 GHz Coherent Monopulse Radar

3. RESULTS

3.1 ENVIRONMENTAL CONDITIONS

The environmental conditions under consideration here may be described as typically wintery for west and northwest Germany. The snow cover over the measurement terrain, which was a plane wheat field, had a depth of about 10 cm. The seedlings were well covered by the snow, the snow surface was structured by wind erosion with a rms height of the structure of up to 2 cm. The air temperature was around - 5°C over day and considerably lower during nights. The liquid water content of the snow was 4 % by volume.

3.2 INTERFERENCE DIAGRAMS

As indicated in paragraph 2.2 patterns due to interference between direct and indirect ray were gained from the variation of the backscatter amplitude during variation of the reflector height. Measurement runs have been performed for different fixed elevation angles of the antenna. Figure 3.1 gives an example for an antenna elevation of -0.3°. The patterns are not corrected by the antenna characteristic.
This pattern, representative for snow covered terrain can be compared with that measured with the same geometry over the same terrain without snow cover. Figure 3.2 shows the respective graph.
From the interference patterns the ratio between maximum and minimum can be extracted. Under consideration of the antenna diagram this leads directly

to the specular reflection coefficient R. The reflection coefficient of the surface is given by the product of R and the reflection coefficient of a smooth surface r_0.
Model calculations /2/ lead to a theoretical dependence of the specular reflection coefficient R on the effective roughness parameter P which is given by the equation $R = \exp -4\pi^* P$ where P is defined as $P = \Delta h^* \sin \Psi / X$
During the experiments under consideration the effective roughness parameter P was varied by changing the antenna elevation and thereby the grazing angle Ψ. The graph of Figure 3.3 shows the good conformity of the experimental values and the theoretical curve.

3.3 BEAM SCANNING APPROACH

As mentioned in Paragraph 2.2 the radar employed during the measurements allowed a beam scanning mode. To take advantage of this possibility the reference reflector was positioned at a height of 2 m above ground and together with the surrounding terrain scanned in elevation over azimuth by the antenna beam. In the evaluation process the radar return for each resolution cell was calibrated in dBm^2 and colour coded leading to a pseudo colour representation of the antenna diagram. Figure 3.4 shows a grey shade version of this representation. The figure shows a deformation of the antenna diagram which is obviously due to the multipath propagation.
Figures 3.5 gives the corresponding response in the elevation monopulse difference channel. Comparison with the undisturbed diagrams shows that there is no influence on the position of the center of gravity due to the multipath effect.

4. CONCLUSIONS

It could be demonstrated, that for very low grazing angles multipath effects can be observed. The dependence of the specular scattering coefficient on the effective roughness of the underlying ground is well described by the existing theory /2/. It shows up that snow covered terrain under snow conditions which are representative for 80 % of the snow periods occurring in northwest Germany do not impose additional problems if compared with agricultural conditions of the terrain which can be met over 3/4 of the year. Moreover show the results of monopulse investigations that at least under geometrical preconditions similar to those during our experiments there will not be a significant amount of disturbance in tracking performance for a monopulse system.

REFERENCES

/1/ Beard, C.I. "Coherent and Incoherent Scattering of Microwaves from the Ocean", IRE Transactions on Antennas and Propagation, pp. 470 - 483, Sep. 1961

/2/ Beckmann, P., Spizzichino, A. "The Scattering of EM Waves from Rough Surfaces", New York, Pergamon Press, 1963

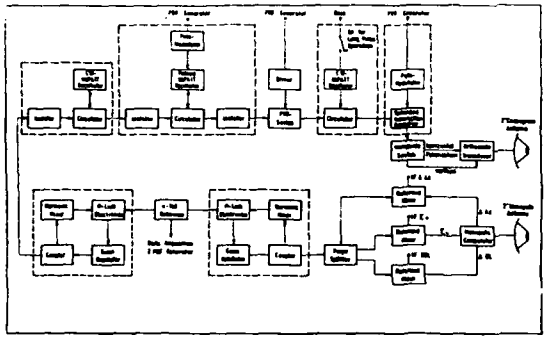

Fig. 2.1: Block Diagram of Measurement Radar

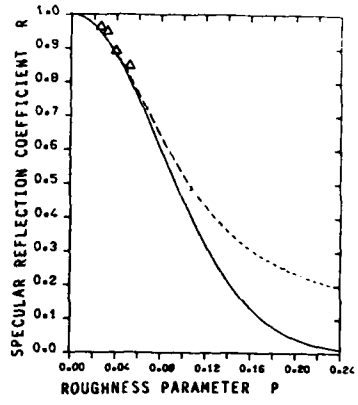

Fig. 3.3: Dependence of the Specular Scattering Coefficient on the Roughness Parameter

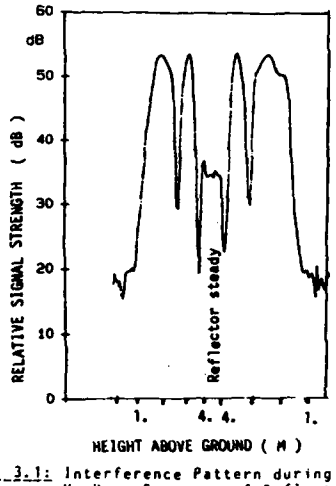

Fig. 3.1: Interference Pattern during Up-Down Sequence of Reflector Field covered with Snow

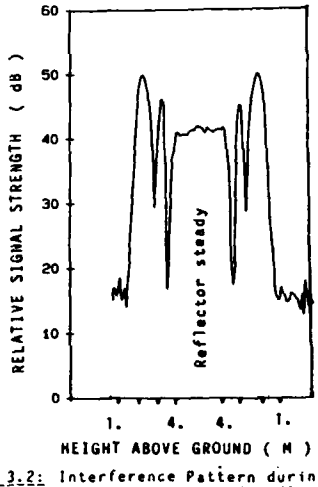

Fig. 3.2: Interference Pattern during Up-Down Sequence of Reflector. Field without Snow

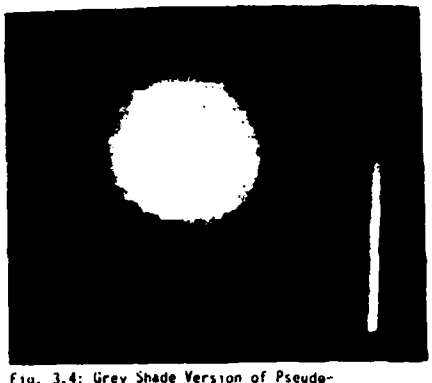

Fig. 3.4: Grey Shade Version of Pseudo-Colour Representation of the RCS of the Reflector in the El/Az Plane for Monopulse Sum Channel

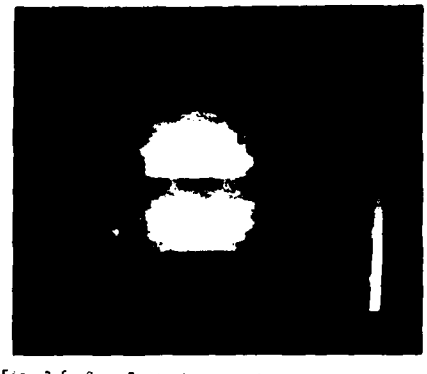

Fig. 3.5: Grey Shade Version of Pseudo-Colour Representation of the RCS of the Reflector in the El/Az Plane for Monopulse Elevation Difference

Resonant Light Scattering from Rough Conducting Surfaces

E R Mendez, K A O'Donnell and A S Harley

Optics Section
Blackett Laboratory
Imperial College
LONDON SW7 2BZ

The scattering of electromagnetic waves from rough surfaces is a subject that has been widely studied in the literature. A number of methods have been used to describe the complex interactions between the wave and the surface and to predict the properties of the scattered light. These include the Kirchhoff method [1], the Rayleigh approach [2], and more recently the extinction theorem [3]. All these methods have their well known limitations. For example, theories based on the Kirchhoff approximation break down when the surface has structure comparable to or smaller than the wavelength λ. Also, at least in their simplest form, these theories do not take into account the effects of multiple scattering and shadowing. The Rayleigh approach has limitations in that it does not converge for deterministic surfaces with non-analytic profiles or large slopes: to our knowledge its range of validity for random rough surfaces has not been established. In principle, only the extinction theorem method puts no restriction on the surface properties and correctly takes account of multiple scattering. However, the method of solution is perturbative and hence limited in that sense. The approximations involved in the various scattering theories have been recently compared and discussed by Brown [4].

In the present work we discuss the various solutions that have been obtained with the extinction theorem for the special case of a perfectly conducting surface whose height statistics are jointly Gaussian to all orders. A perturbation solution for the case of scalar waves has been given by Nieto-Vesperinas and Garcia [5], and also by Shen and Maradudin [6]. The solution of Shen and Maradudin is particularly interesting in that it is valid for surfaces of roughness comparable to the wavelength, and, under some circumstances, it predicts rather dramatic departures from the Kirchhoff theory. In the

Figure we show the predictions of this theory for the scattered specular intensity $\langle I \rangle_s$ as a function of angle for different values of the parameter T/λ where T is the lateral correlation length of the height fluctuations. This plot is for the case of a diffuser with $k\sigma = 1/\sqrt{2}$, where k is the wavenumber and σ is the standard deviation of the surface height. It is apparent that when $T < \lambda$, the surface may reflect much more specular light than the Beckmann [1] theory (dotted curve in the figure) would predict. Under similar conditions, the diffuse component also departs significantly from the Beckmann theory. However, in the limit $T >> \lambda$, the Beckmann results are, essentially, recovered from those of Shen and Maradudin. A vectorial theory based on the extinction theorem has also been developed [7], although the analysis is limited to rather smooth diffusers.

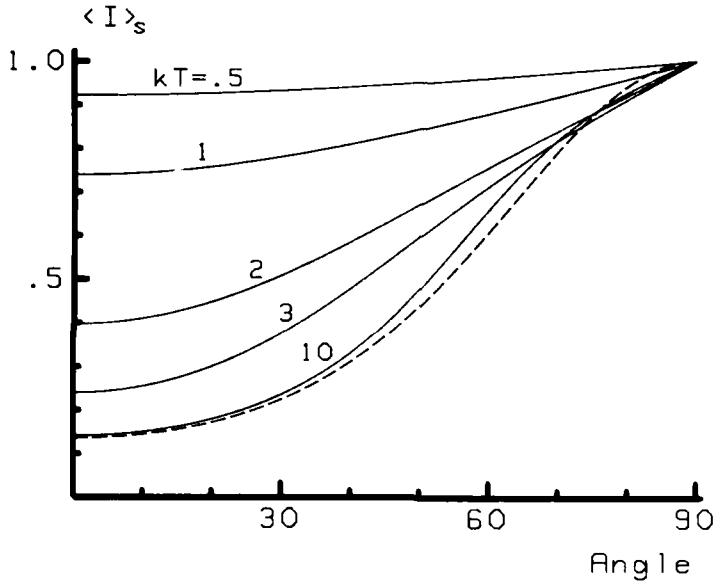

In spite of the theory that is available, to our knowledge there has not yet been an experimental test of these theories with a surface that was known a priori to have Gaussian statistics. Diffusers that have been used by other workers include metal coated ground glass, ground metal surfaces, polycrystalline surfaces, and gold coated sandpaper. None of these surfaces have well-defined statistics that are necessary to accurately test the theory. On the other hand, Gray [8] has developed a method of producing rough surfaces by exposing photoresist

to a large number of speckle patterns. It may be shown that such a surface will ideally have joint Gaussian statistics and a correlation function that can be controlled. We have constructed such surfaces with correlation lengths of the order of a few microns.

Of particular interest for us is the resonance region (i.e. $T \sim \lambda$) where significant departures from the Kirchhoff theory should be observed. To experimentally investigate scattering in this region with our diffusers, we have used a CO_2 laser (λ = 10.6 μm) and a nitrogen cooled HgCdTe detector. In our set up, the angles of incidence and detection are varied under software control from an LSI 11/23 computer which also controls a bank of attenuators and the rotation of an analyser.

Data will be presented for the specular reflection as a function of angle with s polarised light, which should correspond most closely to the scalar wave case of the Figure. If possible, preliminary data will also be presented for the diffuse component and for depolarisation. Finally, conclusions will be drawn as to which theory is most suitable to explain the experimental results.

References

[1] Beckmann, P and Spizzichino, A, 'The Scattering of Electromagnetic Waves from Rough Surfaces', Pergamon, New York (1963).

[2] Millar, R F, Radio Science 8, 785-796 (1973).

[3] Winebrenner, A and Ishimaru, A, Radio Science 20, 161-170 (1985).

[4] Brown, G S, Wave Motion 7, 195-205 (1985).

[5] Nieto-Vesperinas, M and Garcia, N, Optica Acta 28, 1651-1672, (1981).

[6] Shen, J and Maradudin, A, Phys Rev B 22, 4234-4240 (1980).

[7] Nieto-Vesperinas, M, J Opt Soc Am 72, 539-547 (1982).

[8] Gray, P F, Optica Acta 25, 765-775 (1978).

LIGHT SCATTERING BY COMPOSITE ROUGH SURFACES

R. Schiffer and K.O. Thielheim
Institut für Reine und Angewandte Kernphysik
Olshausenstr. 40, 2300 Kiel, FRG

Calculating the light scattering properties of statistically rough surfaces is in general a rather difficult task, and only two limiting cases can be treated in a straight-forward analytical manner and lead to simple results. The first limit, the case of strong roughness, is the geometrical optics case, where the surface undulations are assumed to vary slowly on the scale of the incident wavelength: here the slope distribution $P(\beta)$ of the surface structure enters - β is t e inclination angle of a local surface normal vector. In the second limiting case, the case of slight roughness, the surface height deviations are assumed to be small compared to the wavelength, and here a perturbation approach, the "Rayleigh-Rice-method", can successfully be applied; the decisive quantity in this case is the correlation function $\varrho(\tau)$ of the roughness structure defined as follows: representing the rough surface by $z = \zeta(x,y)$ we have

$$\langle \zeta(x,y) \rangle = 0$$

$$\langle \zeta(x,y)\, \zeta(x+\Delta x, y+\Delta y) \rangle = h^2 \varrho\left(\sqrt{(\Delta x)^2+(\Delta y)^2}\right) \qquad (\varrho(0) = 1)$$

where the brackets denote the average over (x,y). Both limiting cases are discussed extensively e.g. in Chap. 9 of the Radar Cross Section Handbook [1].

As most natural surfaces do not fall within the scope of one of these limiting cases, the construction of a surface model with composite roughness looks promising, a surface described as a superposition of both roughness types. Surfaces of this kind have been considered by several authors [2-8], and our model follows their general lines.

As we are especially interested in the spectral reflectance of rough surfaces, we first concentrate on the wavelength dependence of light scattered from a surface of the second type, the slightly rough surface. Most authors applying the Rayleigh-Rice-approach are only interested in the incoherent scattering, because the coherent cross section - resulting from the second order perturbation terms - only describes the diminution of the zero order specularly reflected intensity. The widely accepted result for this diminution, the factor $\exp(-4h^2k^2\cos^2\psi_i)$ (k: wavenumber, ψ_i: angle of incidence), is, however, only correct, if the tangent plane approximation is valid, i.e. if the correlation length of the roughness structure is much larger than wavelength. In the general case Valenzuela's "effective reflection coefficients" [9] have to be applied for calculating the

coherent contribution - the only composite roughness model including these modified coefficients appears to be that by Wu and Fung [4] , who, though, only study the backscattered radiation.

The resulting modified coherent reflectances for linear polarization states perpendicular and parallel to the scattering plane are

$$R_{\perp}^{COH}(\vartheta_i) = \left(\frac{\cos\vartheta_i - \sqrt{\varepsilon - \sin^2\vartheta_i}}{\cos\vartheta_i + \sqrt{\varepsilon - \sin^2\vartheta_i}} \right)^2 \left[1 - H_{\perp}(\vartheta_i) \right]$$

$$R_{\parallel}^{COH}(\vartheta_i) = \left(\frac{\varepsilon\cos\vartheta_i - \sqrt{\varepsilon - \sin^2\vartheta_i}}{\varepsilon\cos\vartheta_i + \sqrt{\varepsilon - \sin^2\vartheta_i}} \right)^2 - \frac{(\varepsilon-1)(\varepsilon\cos\vartheta_i - \sqrt{\varepsilon - \sin^2\vartheta_i})}{(\varepsilon\cos\vartheta_i + \sqrt{\varepsilon - \sin^2\vartheta_i})^3} H_{\parallel}(\vartheta_i)$$

where ε is the dielectric constant of the material in the half space $z \leq 0$, and $H_{\perp/\parallel}$, being proportional to h^2k^2, is defined in a recent paper [10] . The resulting curves show that slight surface roughness in general reduces the reflectance, and the angle of maximum polarization (Brewster angle) is shifted to a smaller value.

For discussing the spectral reflectance of the surface the total incoherent intensity has to be accounted for, too; it results from integrating the incoherent differential scattering cross section [1] over all scattering directions. The general result is, for most angles of incidence, a reddening of the integrated scattered radiation. So a slight surface roughness of dielectric material in general leads to a reflection loss and to reddening effects - this phenomenon has recently been discussed in connexion with light scattering from interplanetary dust [11] .

Now the composite surface can be constructed by superposing both roughness types; the following results apply in the special case that the incident and scattered beams lie in a plane perpendicular to the surface. For the coherent cross section per unit area we obtain an expression resulting from the strong roughness alone but containing the modified reflectances defined above:

$$Q_{\perp/\parallel}^{COH}(\vartheta_i, \vartheta_r) = S(\vartheta_i, \vartheta_r) \frac{1}{4} \frac{P\left(\frac{|\vartheta_r - \vartheta_i|}{2}\right)}{\cos\left(\frac{\vartheta_r - \vartheta_i}{2}\right)} R_{\perp/\parallel}^{COH}\left(\frac{\vartheta_i + \vartheta_r}{2}\right),$$

where S is a shadowing factor [12] and ϑ_r is the scattering angle defined such that $\vartheta_r = \vartheta_i$ for specular reflection. The incoherent scattering cross section is

$$\sigma_{pq}^{cc}(\vartheta_i,\vartheta_r) = S(\vartheta_i,\vartheta_r)\int_0^{\frac{\pi}{2}} d\beta' \sin\beta' \, w\left[2k\sin\left(\tfrac{\vartheta_i+\vartheta_r}{2}\right)\sin\beta'\right]$$

$$\cdot \int_0^{2\pi} d\eta \, |\beta_{pq}|^2 \frac{P(\alpha)}{\cos\alpha} \, \Theta(\cos\alpha)\,\Theta(\cos\theta_i)\,\Theta(\cos\theta_r)$$

with $$w(K) = \frac{2h^2}{\pi}\int_0^{\infty} d\tau \, \tau \, \varrho(\tau) \, J_0(K\tau) \quad ,$$

$$\cos\alpha = \cos\tfrac{\vartheta_r-\vartheta_i}{2}\cos\beta' + \sin\tfrac{\vartheta_r-\vartheta_i}{2}\sin\beta'\sin\eta$$

$$\cos\theta_i = \cos\tfrac{\vartheta_i+\vartheta_r}{2}\cos\beta' + \sin\tfrac{\vartheta_i+\vartheta_r}{2}\sin\beta'\sin\eta$$

$$\cos\theta_r = \cos\tfrac{\vartheta_i+\vartheta_r}{2}\cos\beta' - \sin\tfrac{\vartheta_i+\vartheta_r}{2}\sin\beta'\sin\eta \quad ,$$

and

$$\Theta(x) = \begin{cases} 1 & \text{for } x > 0 \\ 0 & \text{for } x < 0 \end{cases}$$

the β_{pq} are polarization factors [10], where p and q represent the indices $\perp$ and $\parallel$, referring to the polarization states of the scattered and incident beams.

The numerical results show that our surface model with composite roughness can in fact reproduce many observed properties of real surfaces. We not only obtain a reduced and reddened reflectance, but also a depolarization of the backscattered intensity and off-specular peaks, which are discussed e.g. by Gasvik [13]. Some of the plots closely resemble curves obtained by Sung and Eberhardt [14,15], who start from the geometrical optics result and take into account the finite radii of curvature by a perturbation technique.

References

[1] G.T. Ruck, D.E. Barrick, W.D. Stuart, C.K. Krichbaum, Radar Cross Section Handbook, Plenum, New York (1970)
[2] J.W. Wright, IEEE Trans. Antennas Propag. AP-16, 217 (1968)
[3] A.K. Fung, IEEE Trans. Antennas Propag. AP-17, 590 (1969)
[4] S.T. Wu, A.K. Fung, J. Geophys. Res. 77, 5917 (1972)

[5] J.C. Leader, J. Opt. Soc. Am. 66, 536 (1976)
[6] J.C. Leader, Radio Sci. 13, 441 (1978)
[7] G.S. Brown, IEEE Trans. Antennas Propag. AP-26, 472 (1978), AP-28, 943 (1980)
[8] F.T. Ulaby, F. Kouyate, A.K. Fung, A.J. Sieber, IEEE Trans. Geosci. Remote Sens. GE-20, 518 (1982)
[9] G.R. Valenzuela, IEEE Proc. 58, 1279 (1970)
[10] R. Schiffer, K.O. Thielheim, J. Appl. Phys. 57, 2437 (1985)
[11] R. Schiffer, Astron. Astrophys. 148, 347 (1985)
[12] M.I. Sancer, IEEE Trans. Antennas Propag. AP-17, 577 (1969)
[13] K. Gasvik, Opt. Acta 27, 965 (1980); 28, 131 (1981)
[14] C.C. Sung, W.D. Eberhardt, J. Appl. Phys. 49, 994 (1978)
[15] C.C. Sung, W.D. Eberhardt, J. Opt. Soc. Am. 68, 323 (1978)

NONLINEAR EFFECTS

NONLINEAR OPTICS OF ATMOSPHERIC AEROSOL

V.E. Zuev, A.A.Zemlyanov, Yu.D.Kopytin, V.A.Pogodaev
The Institute of Atmospheric Optics, Siberian Branch
USSR Academy of Sciences, Tomsk, 634055, U S S R
(invited)

Introduction

The object of investigation in nonlinear optics of atmospheric aerosol is the effects appearing at interaction of high-power laser radiation with an aerosol component of the atmosphere, as well as radiation propagation under the action of these effects[1]. Among the known effects, the effects of vaporization, sublimation, combustion have the lowest energy thresholds, while those of explosion and breakdown have the highest ones.

In the present paper the explosion, combustion and breakdown of aerosols have been chosen as the objects for investigation.

I. Laser Beam Propagation through an Explosively Evaporating Water-Droplet Aerosol

The explosion of droplets heated by radiation causes an essential nonlinearity in the interaction of high-power laser radiation with aerosols. The explosion of an absorbing droplet is caused by the phase transition from a liquid to a vapor in regions where the electromagnetic wave energy is dissipated in the form of heat.

The authors have carried out the experimental study of explosive droplet vaporization initiated by high-power laser radiation for a wide range of droplets sizes from 1 to 10^3 μm, covering the range of droplets sizes found in natural meteorological objects. Both cw and pulsed laser sources with wavelengths λ , λ = 10.6, 2.36, 1.06, and 0.69 μm were used in the experiments. The power density in the region of the droplets varied from 10^2 to 10^8 Wcm^{-2}.

Figure 1 presents experimental data describing water droplet explosions caused by CO_2 laser radiation The depen-

dence of the characteristic intensity of radiation (either the mean or the peak power, according to the situation) on the particle's radius is presented in this figure and is characteristic for a given experiment. Open circles are the authors' and their colleagues' data, dark circles are the results of the other authors. The threshold intensities calculated theoretically for various explosion regimes are also presented in this figure. These curves have the following meanings. Curve I corresponds to a stationary regime of particle heating to its temperature of explosion vaporization. In the region between the curves II and III the transition from fragmentation regime of droplet explosion to the gasdynamic regime takes place. The level III characterizes the limit for the supercritical explosion of the super heated region.

The investigations made concerned the study of the dynamics of extinction of radiation in the volume occupied by small optical depth water aerosols ($\tau \sim 0.1$) irradiated by TEA CO_2 laser pulses with an intensity of up to 30 Jcm^{-2}.

Figure 2 shows the dependence of the extinction coefficient (when $\lambda = 0.63$ μm) in the irradiated zone on the high-power radiation density. The results show that the possibility of the complete clearing of a small-droplet fog by TEA CO_2 laser radiation pulses with microsecond duration exists.

II. Laser Radiation Transfer in Combustible Aerosols

This paper presents the results of the experimental investigations into the nonlinear distortions of the sounding beam ($\lambda = 0.63$ μm) taking place in the beam of a high-power ND glass laser ($\lambda = 1.06$ μm, W = 1000 J, t_p = 1 ms). A suspension in air of sooty particles (exponential size spectrum from 2 to 50 μm radii) was used in the experiment.

Figure 3 shows the data relating to the dynamics of the aerosol's optical depth obtained from the oscillograms of the Nd-glass laser pulses. (Curve 1 corresponds to the ener-

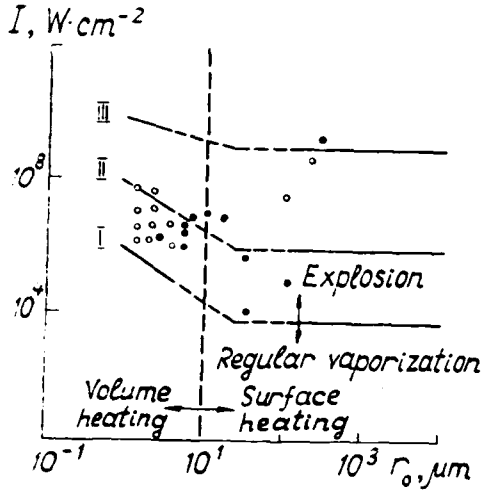

Fig. 1

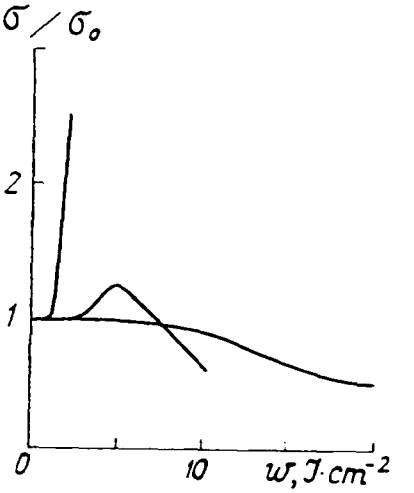

Fig. 2

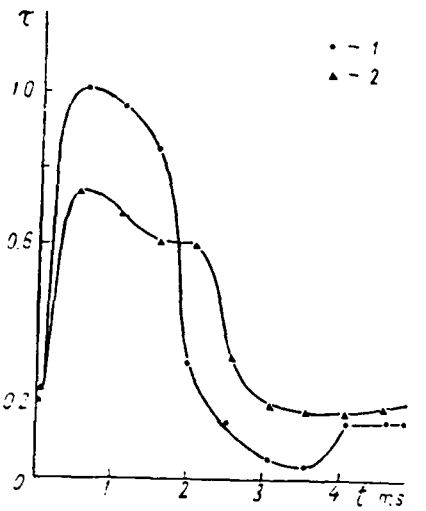

Fig. 3

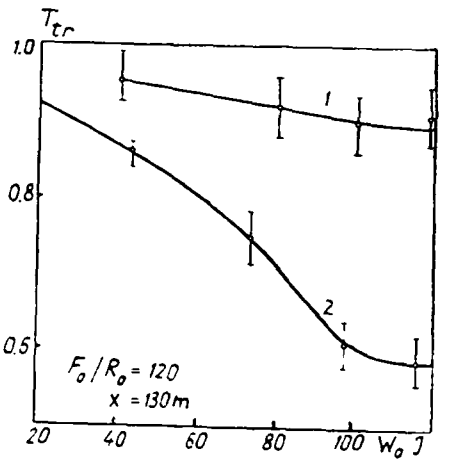

Fig. 4

gy density per pulse 150 J/cm^2, 2 - 100 J/cm^2). The decrease in aerosol transmission occurring during the laser pulse is due to the joint effect of the scattering of light by thermal and mass aureoles around the burning particles and fragmentation of large particles into smaller ones. The partial "clearing" of the medium occurring just after the cessation of the high-power pulse can be related to the relaxation of the thermal and mass aureoles, which makes, as a consequence, the effect of particles burning the dominating factor.

III. Ionization and Optical Breakdown in Aerosol Media

The particles of condensed matter play important roles as prime centers of ionization and centers of initiation of the shock wave following the optical breakdown. Optical breakdown causes nonlinear energetic attenuation of light and provides the principle limitation to the beam power that is transportable through the atmosphere.

Figure 4 presents the experimental results on the dependence of the integral (over the pulse duration) transmission of the beam channel path $T_{tr} = W/W_o$ on the pulse energy W_o. Here, W is the pulse energy at the end of the path. The curves presented in this figure illustrate two meteorological situations which differ in intensity of atmospheric turbulence Cn^2 by more than one order of magnitude (Curve 1 - $Cn^2 = 10^{-14} cm^{-2/3}$, Curve 2 - $Cn^2 = 4 \cdot 10^{-15}$ $cm^{-2/3}$).

Experiments on initiating optical breakdown in natural fogs and rains have been realized and proved that in the atmosphere aerosol formations such as fog and rain caused weakening of the atmospheric turbulence, thus improving the conditions for laser beam focusing and, as a consequence, for laser sparking in the natural atmosphere. The washing-out of atmospheric aerosols was also observed in field experiments, but only after a long period of precipitation, what caused an increase in the breakdown threshold by one order of magnitude.

1. V.E.Zuev, A.A.Zemlyanov et al. High-Power Laser Radiation in Atmospheric Aerosols. D.Reidel Publ.Company, 1984.

THE TRANSFER EQUATION METHOD IN THE PROBLEM OF WAVE BEAMS SELF-ACTION

V.E. Zuev, A.A. Zemlyanov, V.V. Kolosov, S.N. Sinev
The Institute of Atmospheric Optics SB USSR Acad.Sci.,
Tomsk, 634055, USSR

The investigations of focusing phenomena, partially-coherent beam propagation, the methods for improving the beam quality in nonlinear media are urgent problems in the theory of wave--beams self-action. To solve these problems [1] the transfer equation method is used in the given paper.

Transparent media are investigated in the paper, and the problem of the beam self-action in the transfer equation method is formulated as follows:

$$\left[\frac{\partial}{\partial x} + \vec{n}\nabla_{\vec{R}} + \frac{1}{2}\nabla_{\vec{R}}\tilde{\varepsilon}(W)\nabla_{\vec{n}}\right] I(x,\vec{R},\vec{n},t) = 0 ; \qquad (1)$$

$$I(x=0,\vec{R},\vec{n},t) = I_0(\vec{R},\vec{n},t); \qquad (2)$$

$$W(x,\vec{R},t) = \iint_{-\infty}^{\infty} d^2n\, I(x,\vec{R},\vec{n},t). \qquad (3)$$

Here I is the brightness, W is the beam intensity; x, $\vec{R}$ are the longitudinal and transverse coordinates, respectively; t is the time, $\vec{n}$ is the vector of direction in the plane perpendicular to the distance of propagation; $\tilde{\varepsilon} = \tilde{\varepsilon}(W)$ is the dielectric-constant perturbation in the beam channel depending on its intensity.

To solve the transfer equation (1) the method of characteristics has been used. This enables one to extract peculiarities of integrated solution which are of great importance for the problems with sharp intensity gradients in the beam channel. In the method of characteristics the beam intensity is associated with initial brightness by an integral formula

$$W(x,\vec{R},t) = \iint_{-\infty}^{\infty} d^2n\, I_0(\vec{R}'(x'=0),\vec{n}'(x'=0),t), \qquad (4)$$

where $\vec{R}'(x')$, $\vec{n}'(x')$ are the characteristics of Eq.(1).

The following type of beams is considered

$$I(x=0,\vec{R},\vec{n},t)=I_0(t)\exp\{-S(\vec{R},\vec{n})\},$$

which allows one to use the Laplacian method and its modifications for calculating the integral (4). In this case at a space point the direction $\vec{n}^*(x,\vec{R})$ is determined where the beam brightness is maximum. The direction of brightness maximum coincides with the normal to the beam wave front at a point x, $\vec{R}$. The coordinate of maximum is sought from solution of equation $\nabla_{\vec{n}} S(\vec{n}^*) = 0$.

Then, in the vicinity of directions $\vec{n} = \vec{n}^*$ the Taylor-series expansion of the function S is carried out, and the integral (2) is calculated. At large nonlinearity parameters $P^2 = L_d^2/L_N^2$, where L_d is the diffraction length, and L_N is the self-action length, the focal points forming a caustic can appear in the region of the beam.

The appearance of a caustic implies intersection of infinitely close characteristics and vanishing of determinant of the S-form stability matrix at a point $\vec{n}^*$ $\det[\partial^2 S/\partial n_i \partial n_j]=0$; i,j =y,z.

Under this condition the S-function expansion at a point n^* is determined by appropriate statements of the catastrophes theory [2].

This method is effective for describing partially-coherent beams with "little" coherence time.

Figure 1 presents the results of solution of the problem on partially-coherent beam self-action in the Kerr defocusing medium. The nonlinearity parameter for a partially coherent beam is connected with the corresponding parameter of a coherent beam by the relation $P_{pc}^2 = P_c^2/(1+N)$, where N is the number of spatial inhomogeneities in the cross section of a partially coherent beam.

The figure indicates a significant difference in solutions in the vicinity of large and "moderate" nonlinearity parameters. At large nonlinearity parameters a limiting intensity level is formed to which the solution tends with the parameter P increase.

The transfer equation method allows the investigation of wave-beam self-action in randomly inhomogeneous media with large scale fluctuations of a complex dielectric constant of the medium to be made [1]. It is effective for analyzing the integral quality of the beams in nonlinear media. The method enables one

to obtain phase-correction algorithms for nonlinear laser beam distortions.

The effect of the initial beam profile on the character of its nonlinear distortions has been investigated in the paper.

Figure 2 presents the results of calculating the ring-beam propagation under the conditions of wind nonlinear refraction. It follows from the calculations that regulating the initial intensity distribution in the beam, one can attain significant growth of peak intensity at the end of the path. In so doing the shift of intensity maximum to an optical axis of radiation propagation is provided.

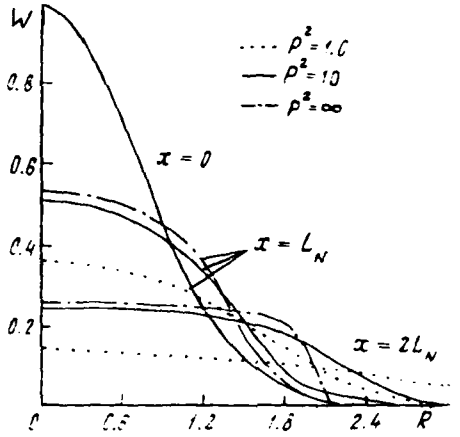

Fig. 1

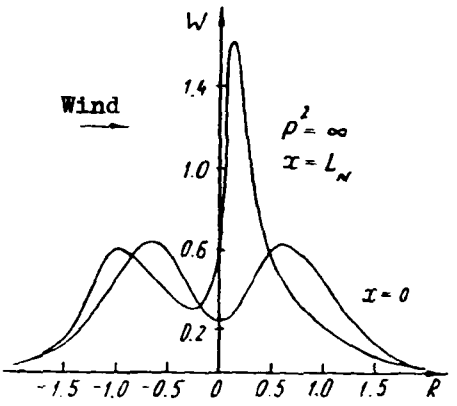

Fig. 2

References

1. V.E. Zuev et al. High-Power Radiation in Atmospheric Aerosols. D. Reidel Publishing Company, 1984.
2. Gilmore R. Catastrophe Theory for Scientists and Engineers. John Wiley & Sons, 1981.

Nonlinear Optical Interactions in Liquid Droplets during High Intensity Laser Radiation

Richard K. Chang

Yale University
Section of Applied Physics and Center for Laser Diagnostics
New Haven, Connecticut 06520, USA

(invited)

When a liquid is irradiated with a high intensity laser beam, the induced polarization is no longer linearly (L) proportional to the electric field at the incident frequency ω_i, i.e., $P^L \neq \chi^{(1)}E(\omega_i)$, where $\chi^{(1)}$ is the linear optical susceptibility. The first nonvanishing nonlinear (NL) polarization in a liquid is $P^{NL} = \chi^{(3)}E\ E\ E$, where $\chi^{(3)}$ is the 3rd-order susceptibility of rank four and the E's are the electric field amplitudes at specific frequencies.[1] The P^{NL} can be treated as the "source term" in the standard Maxwell wave equation within a polarizable medium described by $\chi^{(1)}$.

For liquid droplets, weak laser beam interactions are generally treated by the Lorenz-Mie scattering theory, where the droplet is assumed to be a sphere with an index of refraction $n = [1 + 4\pi\chi^{(1)}]^{1/2}$. The size parameter ($x = 2\pi a/\lambda$, where a is the droplet radius and λ is the wavelength) and n determine the elastic scattering at the far field and optical absorption within the droplet which has a nonzero absorption coefficient [i.e., $\mathrm{Im}\chi^{(1)} \neq 0$]. Several facts based on the Lorenz-Mie calculations involving only P^L are well established and will be important to nonlinear optical considerations when P^{NL} is included: (1) at specific x values, morphology-dependent resonances (MDR's) result, giving rise to large internal fields confined near the droplet interface and causing increased elastic scattering and, for liquids with $\mathrm{Im}\chi^{(1)} \neq 0$, increased absorption; (2) when x does not

correspond to MDR's, the spherical interface focuses the incident plane wave at one point just within the exit face and, for some ranges of x values, at another point just within the entrance face (i.e., at one or two spots within the droplet). A droplet with $x > 1$ and $n > 1$ can be envisioned as an optical cavity for specific x values ($x_{n,\ell}$) corresponding to MDR's of mode number n and mode order ℓ. By solving for the poles of the Lorenz-Mie scattering coefficients,[2] the effective Q-factor for a droplet cavity is proportional to Re $x_{n,\ell}$/Im $x_{n,\ell}$ or inversely proportional to the linewidth of $x_{n,\ell}$ when the scattering coefficients or the internal field coefficients are plotted as a function of x.

The MDR's occurring within the inelastic emission profile (e.g., fluorescence or Raman linewidth) can be envisioned as "trapping" the internally generated inelastic radiation. Thus, should the amplification of the fluorescence or spontaneous Raman emission be greater than the radiation leakage from the droplet, lasing or stimulated Raman oscillations can occur.

Dyed liquid droplets undergoing lasing and pure liquid droplet undergoing stimulated Raman oscillations have been detected spectrally[3,4] and photographed.[5] Spectrally, these oscillations consist of sharp peaks corresponding to different MDR's which provide feedback at specific wavelengths within the fluorescence and spontaneous Raman profiles. Photographically, the lasing and stimulated Raman fields are noted to be confined within the droplet interface.

Stimulated Raman scattering (SRS) from a single micrometer-size pure water droplet is intense and can be readily detected with one Q-switched laser pulse of less than 1 GW/cm^2. In fact, the SRS of the O-H stretching mode at $\omega_s = \omega_i - \omega_{O-H}$ (where $\omega_{O-H} \simeq 3450$ cm^{-1}) is so intense that this 1st Stokes SRS can act as the pump for another 1st-order SRS process at

$\omega_s = \omega_i - 2\omega_{O-H}$ and possibly $\omega_s = \omega_i - 3\omega_{O-H}$. Should the water droplets contain some anions (e.g., NO_3^-), the spontaneous Raman emission of the ν_1 anion mode will be amplified by the incident wave at ω_i, i.e., proportional to $[Im\chi^{(3)}_{\nu_1}]|E(\omega_i)|^2$ or amplified by the SRS wave of water at ω_s, i.e., proportional to $[Im\chi^{(3)}_{\nu_1}]|E(\omega_s)|^2$, where $[Im\chi^{(3)}_{\nu_1}]$ is related to the spontaneous Raman profile and cross section of the ν_1 anion mode.[6] Our multi-order SRS experiments indicate that intense fields exist at ω_i and at ω_s within the droplet. In addition to elastic scattering at ω_i, a sizable fraction of the incident radiation is converted to other frequencies at $\omega_s = \omega_i - m\omega_{O-H}$ (where m = 1, 2, 3) for pure water droplets. Furthermore, ω_i is converted to additional frequencies at $\omega_s = \omega_i - m2\pi\nu_1$ and $\omega_s = \omega_i - \omega_{O-H} - 2\pi\nu_1$ for water droplets containing large concentrations of anions (e.g., greater than 0.2 M of NO_3^-). Intense inelastic scattering at ω_s via the SRS process can be a significant fraction of the overall electromagnetic scattering from single droplets.

In the wavelength region where there is no optical absorption by pure water [i.e., $Im\chi^{(1)} = 0$], high intensity laser beams can still induce droplet heating via several nonlinear optical mechanisms related to $\chi^{(3)}$: (1) two-photon absorption, i.e., proportional to $[Im\chi^{(3)}]|E(\omega_i)|^2$, inducing an electronic transition to the excited state (reachable by $2\omega_i$) which upon non-radiative relaxation gives rise to droplet heating, and (2) the SRS process, i.e., proportional to $[Im\chi^{(3)}]E(\omega_i)E^*(\omega_s)$, can coherently excite the vibrational modes from v = 0 to v = 1 and upon relaxation to the vibrational ground state (v = 0) give rise to droplet heating. The SRS process does not involve real transitions to excited electronic states and hence there is no requirement for the coincidence between these states and the photon energies as in the case of two-photon absorption ($2\hbar\omega_i$) or linear absorption ($\hbar\omega_i$).

Furthermore, the SRS process does not require the coincidence of the infrared or near infrared photon energies and the vibrational modes, overtones, or combinations, as in the case of linear absorption. The SRS induced heating does require the presence of an intense field at $E(\omega_i)$ to provide gain for $E(\omega_s)$. Together these two fields can coherently induce vibronic transitions from v = 0 to v = 1. Such SRS induced heating ultimately limits the irradiation level of the high intensity beam with the droplet before the droplet is vaporized, starting from the focal spots within the droplet.

Other nonlinear processes also describable by $\chi^{(3)}$ can limit the irradiation level of a high intensity beam with the droplet before the droplet is shattered. Although not yet demonstrated in the laboratory, stimulated Brillouin scattering from a droplet should be considered. Through the electrostrictive pressure [proportional to $\chi^{(3)}E(\omega_i)E^*(\omega_B)$, where $\omega_B = \omega_i - \omega_{acoustic}$], intense pressure (acoustic) waves can be generated within the liquid. The stimulated Brillouin scattering induced sound waves require the presence of an intense field at $E(\omega_i)$ to provide gain for $E(\omega_B)$, which is initially generated from spontaneous Brillouin waves. These two intense waves, $E(\omega_i)$ and $E(\omega_B)$, can create such an intense pressure wave that they can shatter a single droplet into many fragments. We have achieved laser-induced shattering of water droplets which causes the destruction of the droplet morphology and is accompanied by a sound.

In conclusion, nonlinear optical interactions within a single micrometer-size droplet must be considered in high intensity laser propagation in the atmosphere containing water droplets. Several such nonlinear optical interactions have been observed in the laboratory using lasers in the sub-GW/cm^2 range to irradiate a single droplet flowing in a linear stream. Our results suggest that the stimulated Raman process (which is known to coherently

induce vibronic transitions) may lead to droplet vaporization and that the stimulated Brillouin process (which is known to coherently induce pressure waves) may lead to droplet shattering.

This work was done in collaboration with Shi-Xiong Qian and Johannes Eickmans. We gratefully acknowledge the partial support of this work by the Army Research Office (Contract No. DAAG29-85-K-0063).

REFERENCES

1. Y.R. Shen, The Principles of Nonlinear Optics (Wiley, New York, 1984).
2. C.F. Bohren and D.R. Huffman, Absorption and Scattering of Light by Small Particles (Wiley, New York, 1983).
3. H.-M. Tzeng, K.F. Wall, M.B. Long and R.K. Chang, Opt. Lett. 9, 499 (1984).
4. J.B. Snow, S.-X. Qian, and R.K. Chang, Opt. Lett. 10, 37 (1985).
5. S.-X. Qian, J.B. Snow, H.-M. Tzeng, and R.K. Chang, "Lasing Droplets: Highlighting the Liquid-Air Interface by Laser Emission," Science, in press.
6. J. Eickmans, S.-X. Qian, and R.K. Chang, "Detection of Water Droplet Size and Anion Species by Nonlinear Optical Scattering," to be published in the Proceedings of the First World Congress on Particle Technology, Nuremberg, Federal Republic of Germany, April 16-18, 1986.

PROPAGATION OF INTENSE LIGHT BEAMS IN THE PRESENCE OF HYDRODYNAMIC AEROSOL-BEAM INTERACTIONS

by

R. L. Armstrong

Physics Department, Applied Laser Optics Group,
New Mexico State University, Las Cruces, NM 88003, USA

(invited)

The propagation of a light beam through the atmosphere is generally accompanied by interactions with aerosols along the beam path. For the case of weak or moderate beams[1] (e.g., for irradiances $\lesssim 10^6$ W/cm^2 for 10 μm water aerosols), diffusive evaporation and conductive heat transfer are the dominant aerosol-beam interactions. In this regime, aerosol heating and enhanced vaporization[2] may result in thermal blooming effects,[3] and pronounced spatio-temporal distortion in the propagating beam.[4] With increasing beam irradiance, explosive vaporization,[5] aerosol ablation,[6] and enhanced aerosol breakdown[7] are included in the wide circle of allowed phenomena.

No single theoretical model exists for this high-flux aerosol behavior. The concept of developed vaporization regimes[8,9] may be

exploited to provide insight into high aerosol heating rates, and steady-state temperature conditions. Internal aerosol heat transfer,[10] when combined with a kinetic description of the boundary condtions at the aerosol surface, lead to a description of explosive aerosol behavior. Radiation-induced vaporization provides the basic mechanism for a model of aerosol-enhanced breakdown.[7,9] Finally, in work discussed in this presentation, hydrodynamics in the surrounding medium leads to a description of explosive vaporization and shock wave-related phenomena accompanying intense aerosol irrdiation.[11]

In this talk, we present the results of theoretical modeling calculations of irradiated aerosols in the convective mass transport regime.[1] In this regime, copious aerosol vaporization together with marked hydrodynamic (shock-wave) - related effects occur in the medium surrounding intensely irradiated aerosols. This regime is bounded at low irradiances by the diffusive mass flux regime treated earlier,[4] and at high irradiances by the emergence of internal aerosol hydrodynamic effects such as ablation and shattering, and by the occurance of aerosol-enhanced air breakdown.[1]

In the convective mass flux regime, the multi-component hydrodynamic equations (for the aerosol vapor and the ambient atmosphere) must be solved subject to appropriate boundary conditions at the aerosol interface. Boundary conditions may be specified using the concept of a Knudsen layer, an interface region a few mean free path lengths in thickness, across which equilibrium is established. These boundary conditions take the form of "jump conditions" expressing the conservation of mass, momentum and energy

across the Knudsen layer. The jump conditions result in relations between the aerosol vapor pressure, density and temperature across this layer.

Numerical solutions to the hydrodynamic equations have been obtained using an extension of the CONID hydrodynamics code.[12] This code has been modified by the inclusion of a high irradiance source term, and by the addition of jump conditions at the aerosol boundary. The results of these calculations will be presented for both liquid and solid aerosols irradiated by high-flux laser beams. The phenomena to be discussed include aerosol vaporization and heating, shock and rarefaction wave behavior, interacting shocks, and beam propagation characteristics. A survey of recent experimental results related to high-flux atmospheric propagation will also be given.

REFERENCES

1. T. P. Reilly, Proc. Soc. Photo-Opt Instrum. Eng. 410, 2 (1983).

2. R. L. Armstrong, Appl. Opt. 23, 148 (1984).

3. F. G. Gebhardt, Proc. Soc. Photo-Opt. Instrum. Eng. 195, 162 (1979).

4. R. L. Armstrong, S. A. W. Gerstl and A. Zardecki, J. Opt. Soc. Am. 2, 1739 (1985).

5. P. Kafalas and A. P. Ferdinand, Jr., Appl. Opt. 12, 29 (1973).

6. B. Steverding, J. Appl. Phys. 45, 3507 (1974).

7. D. C. Smith, J. Appl. Phys. 48, 2217 (1977).

8. V. A. Batanov, F. V. Bunkin, A. M. Prokhorov and V. B. Federov, Sov. Phys. JETP 36, 311 (1984).

9. R. L. Armstrong, J. Appl. Phys. 56 2142 (1984).

10. A.V. Kuzikovskii, Sov. Phys. J. 10, 615 (1973).

11. R.L. Armstrong, P. J. O'Rourke and A. Zardecki, submitted to Physics of Fluids.

12. R.D. Janssen and P. J. O'Rourke, Los Alamos National Laboratory Report No. LA-10269-MS, December, 1984.

Early-Time Hydrodynamic Response To Pulsed Laser Radiation

Melvin Lax and Boris Yudanin

Physics Department, City College of New York, New York, NY 10031

(invited)

An implicit numerical Galerkin approximation using splines for the case of spherically symmetric shock and rarefaction waves is compared to an approximate (scaling) analytic solution.

If an intense beam of high-energy laser radiation propagates through an atmosphere containing absorbing aerosol particles, the aerosols will respond by altering their temperature, density, pressure, and by evaporation from the surface. As a result, the refraction index will change markedly. Such an interaction involves the solution of a system of coupled equations for the electromagnetic waves and for the matter. Solution of this complete time-dependent coupled problem does not appear feasible at present. Some simplifications can be made based on the difference in the interaction mechanisms at different time intervals as proposed by Armstrong [1] The first two stages involve absorption of the laser energy, and a hydrodynamic response to the heated, pressurized fluid. If the pulse length is short compared to the hydrodynamic response time (droplet radius divided by the velocity of sound) these two steps occur separately: first the energy is absorbed with essentially no motion. Then there will be a hydrodynamic response with no absorption. Moreover, for pulses short compared to thermal relaxation times the hydrodynamic response will be essentially complete before thermal effects become important. (The pulse repetition period is assumed long compared to all these times.)

This means that there exists a time interval, perhaps $10^{-9} < t < 10^{-7}$ sec. in which we can assume purely a purely hydrodynamic response of the water droplet to the elevated temperature and pressure induced in the droplet relative to the surrounding air during the first stage. The solution of this short-time hydrodynamic problem provides an initial condition to later events which are influenced by thermal processes.

For simplicity we assume a uniform distribution of temperature and pressure in the droplet (which is a good approximation when the droplet radius is small compared to the wavelength). This assumption makes the problem spherically symmetric. The simplified problem can now be formulated as follows: at time t = 0 a droplet of radius R_0 starts in the hydrodynamic state

$$T=T_0 \,,\quad P=P_0 \,,\quad \rho=\rho_0 \,,\quad v=0 \tag{1a}$$

and the surrounding air starts in the state

[1] R.L. Armstrong, "Interaction of absorbing aerosols with intense light beams", J. Appl. Phys. 56, (7), 1984, (2142-2153).

$$T = T_a\ ,\quad P = P_a\ ,\quad \rho = \rho_a\ ,\quad v = 0. \tag{1b}$$

where $T_w > T_a$; $P_w \gg P_a$; $\rho_w \gg \rho_a$

At time t = 0 the hydrodynamic interaction between the water and the air begins. If we neglect the surface tension, then the resulting evolution can be described by the set of equations:

$$\frac{\partial \rho}{\partial t} + \rho \frac{\partial v}{\partial r} + v \frac{\partial \rho}{\partial r} + \frac{2v\rho}{r} = 0 \tag{2}$$

$$\frac{\partial v}{\partial t} + v \frac{\partial v}{\partial r} + \frac{1}{\rho} \frac{\partial P}{\partial r} = 0 \tag{3}$$

$$\frac{\partial P \rho^{-\gamma_i}}{\partial t} + v \frac{\partial P \rho^{-\gamma_i}}{\partial r} = 0 \tag{4}$$

where γ_i equal 1.4 for the air, 3.0 for the water. In deriving these equations a gas-like equation of state was assumed (for simplicity) for both water and air, but the method of solution does not depend on this assumption.

We use as dependent variables P, ρ, v : pressure, density and velocity. If we neglect the surface tension on the water-air boundary, then the pressure and the velocity will be continuous across it. This is not the case for the density, which undergoes a discontinuous jump at that surface. In the spline integration procedure, continuity is determined by the specification of the multiplicity of the mesh points. To treat all equations with the same mesh specification, over all space, it is convenient to make all functions continuous. For this purpose, we replace the original density function, ρ_{orig}, by

$$\rho = \rho_{orig} + \Delta(t)\ H(r - R_b(t)) \tag{5}$$

where

$$\Delta(t) = \rho_{orig}(r = R_b(t) - \epsilon) - \rho_{orig}(r = R_b(t) + \epsilon) \tag{6}$$

is the negative of the jump in ρ_{orig} and H(x) is a Heaviside function. In this way, the jump is canceled and ρ is continuous.

The above equations require a set of boundary and initial conditions which we are going to discuss now. If the time we are concerned with is smaller then that which the rarefaction wave takes to reach the center of the droplet then the hydrodynamical parameters at the center will remain at their undisturbed values. Thus at $r = 0$ we have the boundary condition

$$P = P_w\ ;\ v = 0\ ;\ \rho = \rho_w\ ;$$

The analogous boundary condition at infinity is

$$P = P_a\ ;\ v = 0\ ;\ \rho = \rho_a$$

But in order to reach this outer boundary the solution experiences a discontinuous transition across a shock, which propagates through the air from the expanding surface of the droplet and for a sufficiently large difference of initial pressure starts immediately when the interaction

begins.

In order to get a numerical solution for such a shock containing problem without introducing an artificial viscosity, we consider our spatial region only to the instantaneous position of the shock, and instead of the b.c. at infinity we use Hugoniot conditions at the shock front:

$$v(r=R_s(t)-\epsilon)=\frac{2}{\gamma_a+1}U_s\,;\;\rho(r=R_s(t)-\epsilon)=\rho_a\,\frac{\gamma_a+1}{\gamma_a-1}\,;\;P(r=R_s(t)-\epsilon)=\rho_a\,U_s^2\,\frac{2}{\gamma_a+1} \quad (7)$$

Here $R_s(t)$ is the shock position, and U_s is the shock velocity. The unknown position of the shock can be found from:

$$E_0=4\pi\int_0^{R_s}\left\{\frac{\rho v^2}{2}+\frac{P}{\gamma-1}\right\}r^2dr \quad (8)$$

which represents conservation of total energy of the water-gas system within the sphere bounded by the shock wave.

In deriving Eq. (8) we have neglected the pressure of the undisturbed air which means that we neglect the original energy of the air in comparison with the energy acquired by the droplet due to the laser irradiation. As to initial conditions, the obvious ones, Eqs. (1a,b) are difficult to employ, because of the jump at $r = R_0$ in pressure and density which at the next instant of time will result in a nonzero velocity distribution and jumps on the emerged shock. This suggests that we use as a set of initial conditions, the pressure, density and velocity distributions shortly after the surface of the droplet was released (e.g. at time t=0+η).

In order to find the latter conditions we will note, that for sufficiently small time "η", the shock and the rarefaction waves will propagate the negligible distances $U_{shock}\eta$ and $-U_{sound}\eta$ respectively. These distances are much smaller than the radius of the droplet $R_0 + U_b\eta$ which means that the spherical geometry effects will not be of importance at that time. In other words we can use the exact analytical solution of a one dimensional shock-tube problem to generate our initial conditions. For the one-dimensional case, the shock and boundary velocities are time-independent. In the air the 1D solution is:

For: $R_s = R_0 + U_s t_0 \geq r \geq R_b = R_0 + U_b t_0$

$$\frac{U_s}{c_\infty}=\frac{\gamma_a+1}{2}\left\{1-G\right\}\,;\;\frac{v}{c_\infty}=\frac{U_b}{c_\infty}=1-G\,;\;\frac{P}{P_\infty}=G^{\gamma_\infty}\left\{1-2G\right\}\,;\;\frac{\rho}{\rho_\infty}=\frac{\rho_a}{\rho_\infty}\,\frac{\gamma_a+1}{\gamma_a-1} \quad (9)$$

In the water the 1D solution is:

For: $R_0 - c_\infty t_0 \leq r \leq R_b + (U_b\,\frac{\gamma_\infty+1}{2}-c_\infty)t_0$

$$\frac{2}{\gamma_\infty-1}\left\{1-\left|\frac{P(x)}{P_\infty}\right|^{\frac{\gamma_\infty-1}{2\gamma_\infty}}\right\}=\frac{2}{\gamma_\infty-1}\left\{1-\left|\frac{\rho(x)}{\rho_\infty}\right|^{\frac{\gamma_\infty-1}{2}}\right\}=\frac{v(x)}{c_\infty}=\left\{1+\frac{x-1}{\tau}\right\}\frac{1-G}{2-G} \quad (10)$$

For: $R_b + (U_b \frac{\gamma_w + 1}{2} - c_w) t_0 \leq r \leq R_b$

$$\frac{v}{c_w} = 1 - G \qquad \frac{P}{P_w} = G^{\gamma_w}\left\{1 - 2G\right\} \qquad \frac{\rho}{\rho_w} = G\left\{1 - G\right\}^{\frac{1}{\gamma_w}} \tag{11}$$

and initial undisturbed values for $r \leq R_0 - c_w t_0$ and $r > R_s$. Here, the dimensionless position, time, and G are given by:

$$x = \frac{r}{R_0}; \qquad \tau = \frac{c_w t_0}{R_0}; \qquad G = \left\{\frac{\rho_a}{\rho_w} \frac{\gamma_w(\gamma_a + 1)}{2}\right\}^{\frac{1}{\gamma_w}} \tag{12}$$

Finally we have a set of hydrodynamical equations (2) - (4) in an expanding spatial region $0 < r < R_{shock}$ with the set of boundary and initial conditions specified by Eqs.(7-12). The problem is solved by the use of a partial differential equation solver POST (in one spatial and one time dimension) written by N. Schryer.[2]

We will transform the original equations into Lagrangian form in order to split the problem into several regions with fixed boundaries. The transformations are not known, a priori, but are found by solving a set of ordinary differential equations along with the partial differential equations (a facility provided by POST). In each of these regions the solution (for pressure, density, velocity) is continuous. The regions are: water (from the origin to the water-air boundary), air (from the surface of the drop to the position of the shock). Corresponding equations, which describe the water-air and shock boundaries respectively are:

$$\frac{dR_b}{dt} = v(r = R_b \pm \epsilon) \qquad \frac{dR_s}{dt} = v(r = R_s - \epsilon)\frac{\gamma_a + 1}{2} \tag{13}$$

In order to make these boundaries stationary we use the transformation (for water and air regions respectively):

$$\xi = \frac{r}{R_w(t)} \quad 0 \leq \xi \leq 1 ; \quad \text{and} \quad \xi = 1 + \frac{r - R_b(t)}{R_s(t) - R_b(t)} \quad 1 \leq \xi \leq 2 \tag{14}$$

Viewgraphs depicting the solution of this transformed system of hydrodynamical equations in the spatial region [0,2] will be presented at the conference.

[2] N. Schryer, "POST - A Package for Solving Partial Differential Equations in One Space Variable" A T&T Bell Laboratories report

PULSED IRRADIANCE PROPAGATION NI RANDOM NONLINEAR MEDIA

GOCHELASHVILI K.S., PROKHOROV A.M., STARODUMOV A.N., SHISHOV V.I.*

General Physics Institite, Moscow, USSR

*P.N.Lebedev Physical Institute, Moscow, USSR

(invited)

The scattering of laser irradiance in turbulent atmosphere leads to development of phase-amplitude distortions in the beam. Under the conditions of self-action the atmospherically induced distortions are exhibited together with the nonlinear blooming effects.

The blooming effects may be minimized by the use of short pulses and large aperture. The development of phase-amplitude distortions in the process of propagation of irradiance in turbulent atmosphere is determined by two fact the accumulation of fluctuations due to linear processes of scattering, and the growth of perturbations as a result of development of instabilities. The character of instability depends upon the nature and sign of the nonlinearity. In the medium with noninertial nonlinearity the beam is stable in defocusing media and unstable in focusing media. In the medium with inertial (heating) nonlinearity the instability develops for arbitrary sign of nonlinearity for values of the self-induced phase increament

(k is the wave number, z - the distance of propagation, I_0 - irradiance intensity, t_p - pulse length, α is proportional to the absorption coefficient). We have investigated the regimes of instabilities of long pulses ($a/v < t_p < a/v_1$, where a - is the beam width, v - is the

speed of sound in the medium, $V_\perp$ - the transverse component of the wind speed).

The growth of amplitude fluctuations in turbulent nonlinear medium is analyzed by the method of smooth perturbations. It is shown, that in the region $S_\perp \gg 1$ amplitude fluctuations grow up exponentially with small oscillations.

Although the initial stage of growth of perturbations ($\sigma_A^2 \ll 1$) is emenable to linearized theory approach, the analysis of propagation of randomised field demands the full account of nonlinear interaction of spatial harmonics. The stage of stochastization of the field is characterized by saturation of amplitude fluctuations $\sigma_A^2 \simeq 1$. The equations for the mutual coherent fluctuations of the second order in nonlinear media are derived. The analysis of these equations is carried out, and the laws of evolution of the scales of the field in the do ain of saturated amplitude fluctuations are obtained. The cases of stationary and moving media are considered.

INTERFEROMETRIC DETECTION OF CONVECTIVE INSTABILITIES INDUCED IN AIR BY ENERGETIC BEAMS

L. Crescentini and G. Fiocco

Dipartimento di Fisica, Universita' "La Sapienza",
00185 Roma, Italy

In this note a laboratory simulation of the effects expected by the passage of relatively powerful laser beams in the atmosphere is reported. The purpose of the experiments is, among others, to establish how the coherence of the beam is degraded by self-induced modifications of the refractive index and in a more general perspective to study the transition regimes between diffusion and convection at low Rayleigh numbers.

While a vast amount of literature exists on the effects of thermal blooming in a powerful laser beam, the asymmetries induced in the refractive index of air by self-induced convection appears to have received less attention; the onset of convection in an absorbing gas and the related effects on the propagation of the beam have been studied mainly using numerical techniques, e.g. by Gerasimov et al., 1978; Gerasimov et al., 1979; Petrishchev et al., 1981.

On the other hand, interferometric measurements of the refractive index fields in fluids have been carried out at least since the early sixties (e.g. J. Gille and R. Goody, 1964).

Preliminary experiments for the detection of convective instabilities induced in an initially motionless volume of air by the in-situ deposition of heat will be described here.

The experiments are carried out with a Michelson interferometer operating at visible wavelengths; the light source is either an Ar+ or a He-Ne laser. The arms length of the interferometer is about 50 cm. One of the mirrors can be moved piezoelectrically for the purpose of scanning.

A horizontal 30-cm long and 0.3-mm diameter constantane wire is placed along the axis of one of the interferometer arms: the wire, and subsequently the surrounding air can be heated by the flow of an adjustable current.

The interferometer fringe patterns and their changes are observed with a video detector connected to a microprocessor. Solutions of different complexity, and cost, for the detection and further analyses have been utilized. Rather simple is the association of a 256x128 pixel video detector made by Micron Tech. [illegible]

Inc. with an Apple II personal computer. Somewhat more elaborate is a successive version including a vidicon camera, hardware for the digital acquisition of the signal, an array processor hosted by an IBM PC XT for subsequent processing of the acquired signal. The software which has been developed allows some degree of correction for the misalignments and impertections in the optical elements of the interferometer.

The effect of heating of the gas induced by the current flow in the wire is made evident by changes in the fringe pattern. By comparing the fringes obtained in the presence and absence of the source, the bidimensional perturbation of the temperature field is obtained.

Preliminary experiments, carried out with the first version of the instrument, indicate that differences in temperature of the order of 0.01 K can be detected for a heat dissipation of a few mW/m in steady state conditions. Such temperature field displays a strong vertical asymmetry, indicative of the presence of convection. These experiments were limited by the sensitivity and resolution of the detector. Progress with the more advanced version of the instrument will be reported.

References.

Gerasimov B.P., V.M. Gordienko, and A.P. Sukhorov, Numerical investigation of light-absorbent convection in horizontal tube. 1. Steady convection states in the field of continuous laser radiation, Inzh.-Fiz. Zh., 33, 709-718, 1978.

Gerasimov B.P., V.M. Gordienko, and A.P. Sukhorov, Numerical investigation of photoabsorption convection in a horizontal tube. 2. Unsteady-state convection, Inzh.-Fiz. Zh., 34, 331-336, 1979.

Gille J., and R. Goody, Convection in a radiating gas, J. Fluid Mech., 20, 47-79, 1964.

Petrishchev V.A., L.V. Piskunova, V.I. Talanov, and R.E. Erm, Numerical modeling of thermal self-action in the presence of induced convection, Radiophys. and Quantum Electron., 24, 107-115, 1981.

SCINTILLATION

AMPLITUDE AND PHASE SCINTILLATIONS IN THE OXYGEN ABSORPTION REGION

R.S. COLE

Department of Electronic & Electrical Engineering, University College London, Torrington Place, London, WC1E 7JE. (invited)

Introduction

It has been shown that the theoretical work of Tatarski[1] on the effect of atmospheric turbulence at optical frequencies can be applied to millimetre wavelengths[2]. To take absorption into account a complex refractive index must be included in Tatarski's analysis. It was Ott and Thompson[3] who first predicted an enhancement at the low frequency end of the amplitude scintillation spectral density function due to the absorption mechanism, subsequently observed by Medeiros, et al[4]. Ishimaru[5] has theoretically examined the phase scintillations for the lossless case. This paper summarizes the theoretical predictions for both the amplitude and phase scintillations in the 60 GHz absorption region and compares them with the experimentally observed results on a 4 Km line of sight path across central London.

Theoretical Model

Use is made of the two dimensional spatial spectral density of the log amplitude fluctuations in a plane perpendicular to the propagation path at a distance L from the transmitter. This function was obtained by Gurvich[6] for the plane wave case and is given by

$$F_x(K) = \pi^2 k^2 L \left[f_{xR}(K)\phi_R(K) - f_{xRI}(K)\phi_{RI}(K) + f_{xI}(K)\phi_I(K) \right] \qquad (1)$$

where $f_{xR}(K)$, $f_{xI}(K)$ and $f_{xRI}(K)$ are filter functions, K is the spatial wavenumber and $k = 2\pi/\lambda$, where λ is the wavelength of the electromagnetic wave. $\phi_R(K)$ and $\phi_I(K)$ are the three dimensional Kolmogorov spectral density functions of the real and imaginary parts of the refractive index fluctuations and $\phi_{RI}(K)$ the cospectral density function between them. The term $f_{xR}(K)\phi_R(K)$ describes signal fluctuations due to variations in the real part of the RI (scattering), $f_{xI}(K)\phi_I(K)$ due to variations in the imaginary part of the RI (absorption) and $f_{xRI}(K)\phi_{RI}(K)$ due to the interaction between these mechanisms.

The corresponding spatial spectral density for phase fluctuations is

$$F_s(K) = \pi^2 k^2 L \left[f_{sR}(K)\phi_R(K) + f_{sRI}(K)\phi_{RI}(K) + f_{sI}(K)\phi_I(K) \right] \qquad (2)$$

Here $f_{sR}(K) = f_{xI}(K)$, $f_{sI}(K) = f_{xR}(K)$, $f_{sRI}(K) = f_{xRI}(K)$.

i.e. the roles of the filter functions between the phase and amplitude cases has been interchanged.

Temporal rather than spatial characteristics are easier to measure experimentally. Using Taylor's hypothesis of "frozen turbulence" the temporal spectral density of the amplitude and phase scintillations $W_x(\omega)$, $W_s(\omega)$ can be related to $F_x(K)$, $F_s(K)$ respectively. Analytic asymptotic expressions can then be obtained for the extremes of the scintillation spectra.

Low Frequency Region $\left[\frac{\omega}{v}\sqrt{\frac{L}{K}} < 1\right]$

Here $f_{xI}(K)$, $f_{sR}(K)$ can be approximated to two whereas $f_{xR}(K)$, $f_{sI}(K)$ are negligible. The cospectrum can be neglected provided that the refractive index structure parameter $C_{nI}^2 << C_{nR}^2$. In practice $C_{nI}^2 \approx 10^{-6} C_{nR}^2$. Hence

$$W_x(\omega) = W_{xR}\left[1 + 5.15\,\frac{C_{nI}^2}{C_{nR}^2}\,\left(\frac{k}{L}\right)^{4/3}\left(\frac{\omega}{v}\right)^{-8/3}\right] \tag{3}$$

where $W_{xR} = 0.85 C_{nR}^2 \frac{L}{v} k^2 \left(\frac{L}{k}\right)^{4/3}$, v is transverse wind velocity.

The spectral density starts departing from the expected scattering shape (given by W_{xR}) for frequencies below a "lower corner frequency" defined by $W_x(\omega) = 2W_{xR}$, i.e.

$$f_{c_1} = 0.74\left[\frac{C_{nI}^2}{C_{nR}^2}\right]^{3/8}\frac{v}{\sqrt{\lambda L}}\ \text{Hz} \tag{4}$$

The corresponding expressions for phase are

$$W_s(\omega) = W_{sR}\left[1 + 5.15\,\frac{C_{nR}^2}{C_{nI}^2}\,\left(\frac{k}{L}\right)^{4/3}\left(\frac{\omega}{v}\right)^{-8/3}\right] \tag{5}$$

Here $W_{sR} = 0.85 C_{nI}^2 \frac{L}{v} k^2 \left(\frac{L}{k}\right)^{4/3}$

Unlike the amplitude case no lower cut-off frequency will exist since the frequency independent term W_{sR}, associated with C_{nI}^2, is very small compared with the frequency dependent term. Hence

$$W_s(\omega) = 4.38 C_{nR}^2 \left(\frac{L}{v}\right) k^2 \left(\frac{\omega}{v}\right)^{-8/3} \tag{6}$$

and again, unlike the amplitude case, the lower scintillation frequency phase fluctuations are due to the real part of the refractive index.

High Frequency Region $\left[\frac{\omega}{v}\sqrt{\frac{L}{k}} > 1\right]$

In this case $f_{xR}(K) = f_{xI}(K) = f_{sR}(K) = f_{sI}(K) \sim 1$. Again neglecting the cross term

$$W_x(\omega) = W_s(\omega) = 2.19\,\frac{L}{v} k^2 C_{nR}^2 \left(\frac{\omega}{v}\right)^{-8/3} \tag{7}$$

i.e. the amplitude and phase scintillation spectral densities are both due to the real part of the RI and are identical. These results are summarized in Figure 1.

Differential Phase Spectra

In order to avoid equipment related phase noise masking the effect of the turbulence induced phase fluctuations, the spectra of the phase difference fluctuations between two neighbouring frequencies on the side of the oxygen absorption peak were measured. These two phase related signals were obtained by narrow band frequency modulating a Gunn oscilator. In this case, the phase difference between signals with wave numbers k_1, k_2 can be written as

$$\phi_d(t) = \phi_{k_1}(t) - \phi_{k_2}(t) \tag{8}$$

The spectral density function can then be written as

$$W_{\phi d}(\omega,k_1,k_2) = W_s(\omega,k_1,k_1) - 2W_s(\omega,k_1,k_2) + W_s(\omega,k_2,k_2) \tag{9}$$

Here $W_S(\omega,k,k)$, are the signal frequency spectral density functions ($k = k_1$ or k_2) corresponding to equations (6) and (7). Again using Taylor's hypothesis an asymptotic expression for the cross term $W_s(\omega,k_1,k_2)$ can be found and hence also for $W_{\phi d}(\omega,k_1,k_2)$.

Low Frequency Region $\left[\frac{\omega}{v}\sqrt{\frac{L}{k}} < 1\right]$

Here $W_s(\omega,k_1,k_2) = 4.38C_{nR}^2\, k_1k_2\, \frac{L}{v}\left(\frac{\omega}{v}\right)^{-8/3}$. Combining with equation 9

$$W_{\phi d}(\omega,k_1,k_2) = 4.38C_{nR}^2\,(k_1 - k_2)^2\,\frac{L}{v}\left(\frac{\omega}{v}\right)^{-8/3} \tag{10}$$

High Frequency Region $\left[\frac{\omega}{v}\sqrt{\frac{L}{k}} > 1\right]$

Here, provided $W_s(\omega,k_1,k_2)$ can be neglected, substituting equation 7 in 9,

$$W_{\phi d}(\omega,k_1,k_2) = 2.19C_{nR}^2\,(k_1^2 + k_2^2)\,\frac{L}{v}\left(\frac{\omega}{v}\right)^{-8/3} \tag{11}$$

when $k_1 = k_2$, as in the present experiments, this is a factor of two greater than the corresponding expression for the phase scintillation spectrum at a single frequency.

Hence the asymptotes to the low and high frequency ends of the differential phase spectrum will be expected to show a -8/3 slope with a ratio between them of $(k_1^2 + k_2^2)/2(k_1 - k_2)^2$ (12)

The assumption that $W_S(\omega,k_1,k_2)$ is zero in this case does depend on the relevant filter function, which arises in the differential phase shift case, being zero in the wavenumber range of interest. In fact when k_1 and k_2 are very close as in the current experiment this is not always the case. For large wavenumbers (small outer scale of turbulence of L_o) it can be neglected but for smaller wavenumbers (large L_o) it can no longer be neglected and the ratio (equation 12) is reduced.

Results

Figure 2 shows an example of an experimental amplitude scintillation spectrum and clearly exhibits the -8/3 slopes. The lower cut-off frequency

f_c compares well with equation". A differential phase spectrum is shown in Figure 3. The ratio between the asymptotes (equation 12) is 45 dB comparing well with a predicted value 47 dB (k_1 = 1160 m^{-1}, k_2 = 1165 m^{-1}).

References

1. TATARSKI, V.I.: "Wave propagation in a turbulent medium", N.Y., Dover, 1961.
2. CLIFFORD, S.F. & STROHBEHN, J.W., IEEE Trans., AP-18, pp 264-274, 1970.
3. OTT, R.H. & THOMPSON, M.C., IEEE Trans. AP-26, pp 329-332, 1978.
4. MEDEIROS FILHO, F.C., JAYASURIYA, D.A.R., COLE, R.S., & HELMIS, C.G., IEEE Trans., AP-31, pp 672-676, 1983.
5. ISHIMARU, A., IEEE Trans., AP-20, pp 10-19, 1972.
6. GURVICH, A.S., Radio Eng. Electron. Phys., 13, pp 1687-94, 1968.

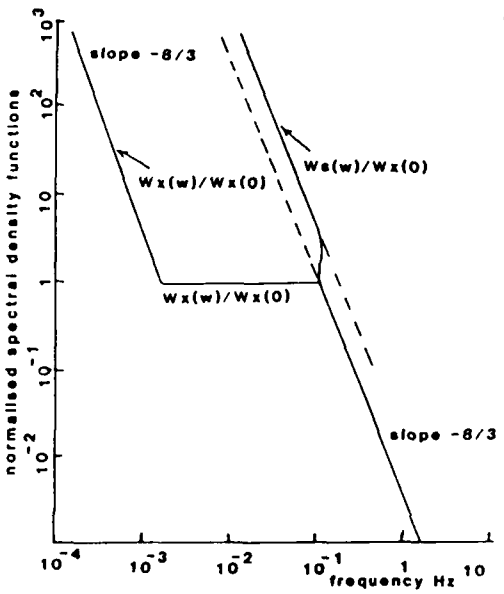

Figure 1.

Spectral density function of log amplitude fluctuations $W_x(\omega)$ and phase fluctuations $W_s(\omega)$ normalised to $W_x(0)$.

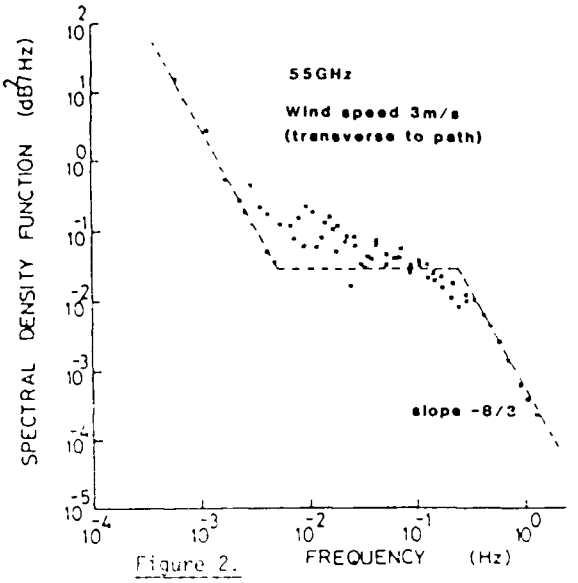

Figure 2.

Amplitude scintillation spectrum.

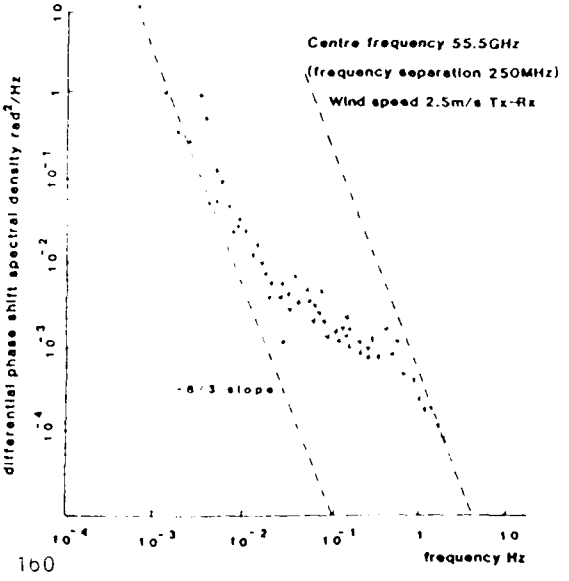

Figure 3.

Differential phase scintillation spectrum.

EXPERIMENTAL INVESTIGATION OF MILLIMETER WAVE PROPAGATION IN THE ATMOSPHERE

Ernst Peter Baars
FGAN - Forschungsinstitut für Hochfrequenzphysik
D-5307 Wachtberg-Werthhoven
Federal Republic of Germany

(invited)

1. INTRODUCTION

The importance of the millimetre wave region for radar remote sensing and guidance and for communication has grown considerably during the las decade due to the increasing demands on higher angular resolution, wider bandwidth, improved jamming resistance and covertness of operation. As a consequence an intensive investigation of the environmental constraints for system performance in this frequency band became necessary.
One aspect, the characterisation of the propagation effect for the terrestrial line-of-sight path will be discussed here.
Starting with short survey on its general characteristics our measurement approach, instrumentation and examples of results will be given.

2. CHARACTERISTICS OF THE TERRESTRIAL LINE OF SIGHT PATH

On a terrestrial path the propagated electromagnetic wave interacts with the atmospheric gases, the terrain (or sea) surface and, if present, with particulates as from precipitation, smoke, dust or sand clouds. This interaction effects the parameters of the wave mainly by three mechanisms: Absorbtion, refraction and scattering.

For the c l e a r a t m o s p h e r e, i.e. in the absence of particulates, Oxygen and watervapor are the primary gases causing propagation attenuation due to molecular absorption in the millimetre wave region.
This effect varies with radiated frequency, temperature and atmospheric pressure. A plot of the attenuation due to atmospheric gases versus frequency or wavelength, ranging from the centimeter wave region to the visible, is given in Fig. 1 for the 'normal' atmosphere.
The macro-structure of the atmospheric refractivity influences the millimetre wave in a similar extent as the longer microwaves. However, for short slant ranges (10 km) as envisaged for most applications ray bending and increased time delay can be neglected for the normal atmosphere.
The fine structure of the refraction index may cause amplitude and phase scintillation by a stochastic refraction process on inhomogenities.
Scattering may occure if the refraction inhomogenities are in the order of the wavelength. For the usual line-of-sight path the scattered field, however, is negligible small.
Scattering on the terrain or water surface may constitute indirect paths and an interaction of the direct and indirect waves. This phenomenon, known as multipath propagation, depends on the geometry of the propagation path and the reflectivity and roughness of the surface relative to the wavelength.
For the millimetre waves specular multipath is only possible if the antenna beam illuminates partly the surface at very low grazing angles.

The primary p a r t i c u l a t e s effecting millimetre waves are rain drops due to the significance of their influence and their frequency of occurance. Absorption and scattering can be calculated by expressions derived by MIE, provided size, shape and density of the droplets are known in the statistical sense.
The influence of other particulates on millimetre waves is either small as for

fog, hail, dry snow, smoke, dust and sandclouds or occurs less frequently as sleet and wet snow.

3. MEASUREMENT APPROACH AND INSTRUMENTATION

Our experimental investigations were concentrated on the atmospheric window at 94 GHz. In most propagation measurements parallel observations at 47 GHz have been performed for comparison reasons.
A typical measurement set-up in a bistatic transmit/receive configuration is outlined in Fig. 2:
At 94 GHz the transmitted signal can be switched between vertical and horizontal polarization. An orthomode transducer at the output of the receiving antenna splits the incoming wave into its co- and crosspolarized components. The two channel superheterodyne receiver and the associated data recording allows the parallel registration of both components. Transmitter and receiver are phase coherent locked to crystal references permitting short term phase measurements. For long term phase measurements a reference signal has to be transferred.
The 47 GHz system is a one channel amplitude only system. Transmitter and receiver polarization are linear/circular switchable.
To arrive at comparable path geometries for both frequencies the antenna beamwidths and positions have to be nearly identical. 2 feet and 1 feet diameter antennas usually have been selected for the 47 and 94 GHz systems respectively providing a beam width of about 0.7 degrees and a gain of 47 dB at both wavelength. A solid state IMPATT oscillator as the transmitting source providing a CW power of 100 mW and a receiver sensitivity of -90 dBm results in a system dynamic range of greater then 45 dB for a slant range up to 10 km.
To avoid unintentional multipath effects the antenna positions have to be carefully selected. A good indication for the absence of multipath is a constant receiving level for a variation of either transmitter or receiver height.
For a monostatic measurement configuration transmitter and receiver are collocated with either two seperate antennas or with a transmit/receive switch and a common antenna. A folded path is constituted by operating against a calibrated reflector at the required range. Unwanted reflections will be minimized by pulse modulating the transmitter signal and gating the received signal at a time corresponding to the propagation time to and from the reflector.
This monostatic radar approach allows in a simple way to assess propagation inhomogenities by using multiple reflectors and multiple range gates.
It is obvious that the experimental investigation of the millimetre wave propagation requires a comprehensive characterization of the respective environment. As an example the meteorological instrumentation accompanying our long term rain measurements over a 500 m path is given in lower part of Fig. 2.

4. MEASUREMENT RESULTS

In the passed seven years several measurement campaigns have been performed to assess the propagation characteristics in both measurement configurations over land and in the maritime environment.
The main results may be summarized as:

- Multipath propagation could be observed for one-way and folded near horizontal line-of-sight paths over Land /2/ and over sea. An interference diagram resulting from pathlength changes by tidal variations is given in Fig. 3.
- Clear air scintillations up to about 2 dB occured occasionally on a 500 m path when solar flux varied due to fast changing cloud cover. A quantitative investigation is required.
- Rain attenuation at 47 and 94 GHz is well described by the MIE theory, if the calculation is based on the actual measured dropsize distribution, larger deviations have been observed on particular rain events, if the dropsize dis-

tribution is derived from the rainrate (Marshall-Palmer or Joss et.al.)/3/.
- Rain attenuation is general higher at 94 GHz then at 47 GHz /3/.
- Rain attenuation at 94 GHz is comparable to those at the two main IR-windows /4/, /5/.
- Attenuation due to sleet and wet snow is lower than for rain at a comparable water equivalent.
- Other particulates (dry snow, hail, haze, fog, smoke, dust) have no significant influence on millimetre wave transmission but cause severe restrictions on IR transmission /3/, /6/, /7/.

References

/1/ Altshuler, E.E. 'Millimeter Wave Propagation Handbook' NATO AC/243 (Panel III) RSG8, Document AC/243-D/916 AC/243 (Panel III) D/220, May, 1984

/2/ Essen, H. Baars, E.P. 'Measurements on Multipath Propagation at 94 GHz over Snow-Covered Terrain' Optical and Millimeter Wave Propagation and Scattering in the Atmosphere, Florence, 27.-30 May, 1986

/3/ Keizer, W.P. Fuchs, H.H. Makaruschka, R. 'Propagation Measurements at Millimetre Waves at Ypenberg Airfield, NL and Birkhof, GE' Report of NATO Ac/243 (Panel III) RSG8

/4/ Neuwirth, R. 'Simultane Messungen der atmosphärischen Extinktion über See für sichtbare, infrarote und mm-Wellen-Strahlung über Entfernungen bis 12 km' FGAN-FfO 1985/50 FGAN-FHP 4-85, Lfd.Nr. 235

/5/ Neuwirth, R. Fuchs, H.H. 'Extinction Properties of visible-, Ir- and mm-Propagation (94 GHz)' submitted to III. Int. Conf. on Advanced Infrared Detectors and Systems (IEEE), London, 3-5 June 1986

/6/ Baars, E.P. Essen, H. '94 GHz Transmission Measurements at SNOW ONE-A' Snow Symposium II, Hanover, N.H., Aug. 1982

/7/ Essen, H. Baars, E.P. 'Millimeter Wave Transmission through Man-Made Obscurations in a Battlefield Environment' AGARD AVP-Symposium, Toulouse, Oct. 1985

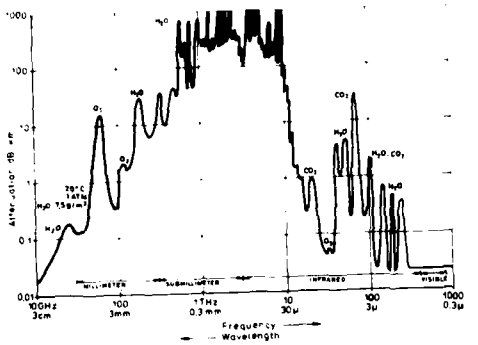

Fig.1: Attenuation of Electromagnetic Wave Propagation in the Clear Atmosphere in Dependence of the Wavelength

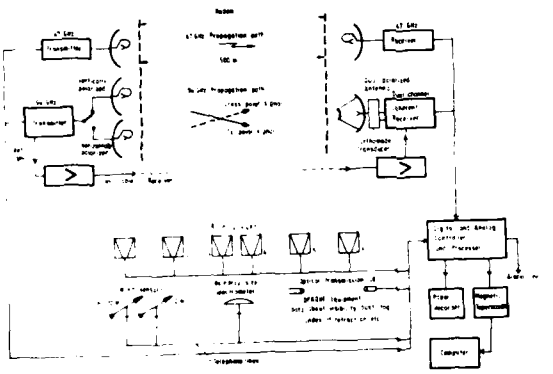

Fig.2: Typical Set-up for Bistatic Transmission Measurements

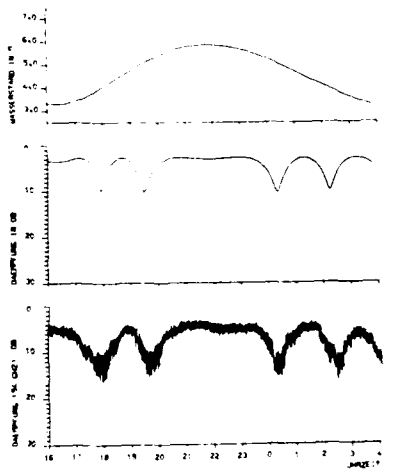

Fig.3: Interference Diagram for Multipath Propagation at 94 GHz
Upper Curve: Tidal Variation, Medium Curve: Calculated Interference Pattern, Lower Curve: Measured Pattern

COUPLED MODE THEORY OF PROPAGATION THROUGH THE TURBULENT ATMOSPHERE

M.Bertolotti and C.Sibilia - Dipartimento di Energetica
Sezione Fisica- Università di Roma "La Sapienza"
ROMA, ITALY (invited)

Coupled mode theory is an alternative way to usual methods (1) to derive correlation functions of electromagnetic fields transmitted in the turbulent atmosphere (2).The measurement of correlation functions has been the object of a numer of investigations.

In Italy in particular, phase and angle of arrival fluctuations have been studied (3) together with intensity fluctuations (4).

Basically the coupled mode method consists of adapting the formalism of coupled-mode theory, usually employed for describing electromagnetic propagation and mode coupling in an imperfect optical fiber (5), to the case of propagation in an unbounded random medium.

The description of propagation of a monocromatic field in an unbounded random medium is achieved by choosing as ideal normal modes the ones pertaining to a homogeneous medium possessing a constant refractive index n_1,

$$E_\chi(\vec{\tau}, z) = \frac{1}{2\pi}\,\hat{e}(\chi)\exp\left(-i\vec{\chi}\cdot\vec{\tau} - i\beta_\chi z\right), \qquad (1)$$

where

$$\beta_\chi = \left(\kappa^2 - \chi^2\right)^{1/2}, \qquad (2)$$

with $\kappa = \omega n_1/c$, $\vec{r} \equiv (x, y)$, and $\hat{e}(\chi)$ is the unit polarization vector.

For linear polarized ($E_y = E_z = 0$) wave one can then write

$$E(\vec{r}, z, t) = \int d\chi \, E_\chi(\vec{r}, z) e^{i\omega t} c_\chi(z), \tag{3}$$

where the expansion coefficients $c_\chi(z)$ are derived solving the set of coupled equations

$$\frac{dc_{\chi'}(z)}{dz} = \iint d\vec{\chi}' \exp\left[i(\beta_\chi - \beta_{\chi'})z\right]\left(-\frac{i\kappa_0}{4\pi^2}\right) d\vec{r}\, \delta n(\vec{r}, z) \exp\left[i(\vec{\chi} - \vec{\chi}')\cdot\vec{r}\right] c_\chi(z), \tag{4}$$

where $\kappa_0 = \omega/c$ and

$$n(\vec{r}, z) = n_1 + \delta n(\vec{r}, z). \tag{5}$$

The correlation functions

$$\Gamma_{\chi\chi'}(z) = \langle c_\chi(z) c^*_{\chi'}(z) \rangle, \tag{6}$$

are then found to obey a diffusione equation in the χ -space

$$\frac{\partial \chi_{\chi,\chi+\eta}}{\partial z} - D\left(\frac{\partial^2}{\partial \chi_x^2} + \frac{\partial^2}{\partial \chi_y^2}\right)\chi_{\chi,\chi+\eta} = 0, \quad (7)$$

where the diffusion coefficient D assumes a particularly simple expression for Gaussian refractive-index fluctuations

$$D = \sqrt{\pi}\, \kappa^2 \langle \delta n^2 \rangle / d \,. \quad (8)$$

The solutions of eq.(7) permit to evaluate the mutual coherence function and compare it with results obtained by the moments of the field.
The coupled mode method can be extended to the propagation of a nonstationary and non-monochromatic field, with the hypothesis that the refractive index fluctuations are not time-dependent during the inverse-band width or pulse time.
In this sense the coupled equations for the field amplitudes are a little bit more complicated and now the significant quantity is:

$$\chi_{\chi\chi'}(z,\omega,\omega') = \langle c_\chi(z,\omega)\, c^*_{\chi'}(z,\omega') \rangle \,. \quad (9)$$

For a stationary nonmonochromatic field the equation for $\chi_{xx'}(z,\omega,\omega')$ is

$$\frac{\partial \chi_{xx'}}{\partial z} = -D\left\{\frac{\partial^2 \chi_{xx'}}{\partial^2 \chi} - \frac{\partial^2 \chi_{xx'}}{\partial \omega^2}(\omega-\omega_0)^2\right\} + \tag{10}$$

$$-2D'(\omega-\omega_0)\frac{\partial \chi_{xx'}}{\partial \omega}\Big\},$$

which is of the same form of the Fokker-Planck equation for the field propagation in a nonlinear optical material .

A discussion of this case will be also provided.

1. V.I.Tatarski - The effects of the Turbulent Atmospere on wave Propagation, NTIS, Springfield, Va.1971

   A.Ishimaru - Wave Propagation and Scattering in Random Media - Academic, New York 1978

   J.W.Strohbehn - in Laser Beam Propagation in the Atmosphere, J.W.Strohbehn, ed., Springer-Verlag, Berlin, 1978 .

2. B.Crosignani and P.Di Porto - J.Opt.Soc.Am.73, 1581 (1983).

3. s.f.e. P.Burlamacchi,A.Consortini,L.Ronchi - Appl.Opt. 6, 1273 (1967).

   M.Bertolotti,M.Carnevale,L.Muzii and D.Sette - Appl. Opt.7, 2246 (1968)

   A.Consortini,P.Pandolfi,C.Romanelli and R.Vanni - Opt. Acta 27, 1221 (1980)

   A.Consortini,G.Fidanzati, A.Mariani,L.Ronchi - Appl. Opt.11, 1229 (1972)

   A.Consortini,L.Ronchi,L.Stefanutti - Appl.Opt.9,2543 (1970).

4. A.Consortini,G.Conforti - J.Opt.Soc.Am.A1, 1075 (1984)
A.Consortini,E.Briccolani, G.Conforti - J.Opt.Soc.Am.
A3, 401 (1986).

5. D.Marcuse - Theory of Dielectric Optical Waveguides
Academic, New York, 1974.

RAY PROPAGATION THROUGH SUB-FRACTAL MEDIA

by E Jakeman

Royal Signals & Radar Establishment

Malvern, Worcestershire, WR14 3PS, UK

(invited)

Although a great deal of attention has been devoted over the years to diffraction and interference effects associated with the propagation of coherent light through the turbulent atmosphere, effects visible to the naked eye are generally geometrical in origin and associated with the scattering of incoherent light. Thus the performance of many simple optical instruments which are used to enhance our natural eyesight is limited by the refraction of rays. Even in the case of coherent light, strong scattering regimes exist where geometrical optics effects assume an important if not dominant role. It is therefore of interest to investigate the statistical properties of rays propagating through refracting media, both from the point of view of noise modelling and in the context of remote sensing.

In many calculations of the atmospheric propagation of light it has been assumed that the refractive index spectrum is an inverse power law based on the Kolmogorov model for the inertial range velocity spectrum [1]. For example, in the case of phase screen scattering, the structure function corresponding to such an unmodified power law would be

$$\langle(\phi(0) - \phi(\underline{r}))^2\rangle \quad |\underline{r}|^{5/3} \tag{1}$$

Following the work of Mandelbrot [2] this can be identified as a fractal model with $\emptyset(\underline{r})$ containing a heirarchy of structure down to arbitarily small length scales. Though continuous, the initial wavefront is not differentiable and on both physical and mathematical grounds it is unreasonable to expect such a model to generate geometrical optics effects associated with rays or wavefront normals. Although models belonging to the same class as (1) may find applications in scattering problems involving rigid structures, such as rough surfaces [3], in the case of fluid media there will generally be some effect such as an inner scale cut-off in the velocity spectrum, capillarity, or thermal diffusion, which will smooth the wavefront over distances which are considerably larger than the optical wavelength [4].

It is well known, however, that the use of single scale smoothly varying models, which are differentiable to all orders, leads to the prediction of focussing, caustics and other higher order geometrical singularities in the propagating wave field [5]. These render the ray density statistics infinite beyond the point where focussing starts to occur. In practice these divergencies are smoothed by diffraction in coherent configurations, and by finite source and detector size in the incoherent case. Moreover there are many situations of interest where the light is detected at propagation distances which are much less than those where focussing begins to take place.

When the above considerations are added to the mathematical difficulty of investigating full diffraction limited geometrical optics, it is evident that what is required is a multiscale model which will generate ray effects, but not geometrical singularities. Such are the properties of the class of sub-fractal or fractal slope models. These can be interpreted as fractal models subjected to elementary smoothing and exhibit a more rapid power law spectral cut-off at high frequencies [6]. The class of structure functions corresponding to equation (2) are given by [7].

$$\langle(\phi(0) - \phi(\underline{r}))^2\rangle \quad Ar^2 - B|r|^P \quad 2<P<4 \tag{2}$$

Wavefronts with this property are only once differentiable and may be thought of as heirarchical constructions of different sized facets. Although this remains a crude model for the properties of real turbulent media it has led to a number of predictions in agreement with experimental data and is remarkable for the reduction in complexity which it brings to both analytical work and numerical calculations [8]. Thus earlier work has shown its close relationship with K distributed noise, often observed in propagation experiments [7], and it also appears to provide a good model for the intensity statistics observed in phase screen scattering into the far field [9]. In more recent work numerical ray tracing has been used to simulate propagation beyond a sub-fractal diffuser [10], see figure 1.

This investigation is being extended to include the presence of simple optical components and additional scattering layers. At the same time laboratory experiments to measure the phase structure functions of turbulent layers are being undertaken in order to examine the validity of the model.

In this paper a brief review of the subject will be followed by presentation of recent results.

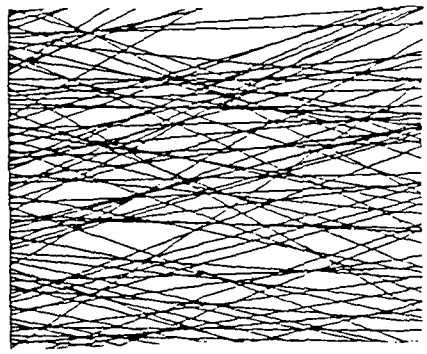

Figure 1. Ray propagation key on a subfractal diffuser

References

[1] V I Tatarski, Wave Propagations in a Turbulent Medium, McGraw Hill New York, 1961.

[2] B B Mandelbrot, The Fractal Geometry of Nature (Freeman, San Francisco 1982).

[3] D L Jordan, R C Hollins & E Jakeman, Appl Phys, B31, 179-186 (1983).

[4] R J Hill & S F Clifford, J Opt Soc Am 68, 892-899 (1978).

[5] M V Berry, J Phys A 10, 2061-2081 (1977).

[6] C L Rino, Radio Sci, 14, 1135-1155 (1979).

[7] E Jakeman, J Opt Soc Am, 72, 1034-1041 (1982).

[8] E Jakeman & J H Jefferson, Optica Acta, 31, 853-865 (1984).

[9] J G Walker & E Jakeman, Optica Acta, 31, 1185-1196 (1984).

[10] E Jakeman, Proceedings of the 6th Trieste International Symposium on Fractals in Physics, (North Holland, Amsterdam 1985).

FUNCTIONAL REPRESENTATIONS OF THE EM FIELD IN INHOMOGENEOUS POSSIBLY STOCHASTIC MEDIA

S.P. Petracca, I.M. Pinto
Dip. di Elettronica, Università di Napoli
(invited)

Electromagnetic fields and potentials in non-homogeneous media are nonlinear functionals of the refractive index distribution. Accordingly, several functional representation tools (alternative, though possibly related) do naturally suggest themselves. In this Communication we shall attempt to survey them briefly, paying special attention to computational accuracy and ease.

In the *weak* inhomogeneity assumption, viz.:

$$n(\underline{r}) = n_0 + \delta n(\underline{r}) \quad ; \quad \frac{\delta n(\underline{r})}{n_0} \ll 1 \tag{1}$$

the Volterra functional series [1] :

$$\underline{E}(\underline{r},\omega) = \sum_{m=1}^{\infty} \underline{E}^{(m)}(\underline{r},\omega) \tag{2}$$

$$\underline{E}^{(m)}(\underline{r}) = \int d\underline{r}_1 \cdots \int d\underline{r}_m \, \underline{\Gamma}^{(m)}(\underline{r}-\underline{r}_1, \cdots, \underline{r}-\underline{r}_m) \frac{\delta n(\underline{r}_1)}{n_0} \cdots \frac{\delta n(\underline{r}_m)}{n_0}$$

will be rapidly convergent. The kernels $\underline{\Gamma}^{(m)}(\cdot)$ can be systematically found by letting (2) together with:

$$\frac{\delta n(\underline{r})}{n_0} = A_1 \delta(\underline{r}-\underline{r}_1) + A_2 \delta(\underline{r}-\underline{r}_2) + \cdots + A_k \delta(\underline{r}-\underline{r}_k) \quad , \quad k=1,2,\cdots,m \tag{3}$$

successively into the wave equation:

$$\Box^2 \underline{E} + \nabla\nabla\cdot\underline{E} \cdot \nabla \ln[n^2(\underline{r})] = j\zeta_0\beta_0 \underline{J} + j\zeta_0\beta_0^{-1}\nabla\left[\frac{\nabla\cdot\underline{J}}{n^2}\right] \tag{4}$$

wherein ζ_0 and β_0 are the *free-space* ($n = n_0$) characteristic impedance and wavenumber, respectively, and $\underline{J}$ is the impressed source-term. Differentiating the resulting identity with respect to $A_1, A_2, \cdots, A_k$ and then setting $A_1 = A_2 = \cdots = A_k = 0$ gives a hierarchy of linear *space-invariant* wave equations in the unknown $\underline{\Gamma}^{(k)}(\cdot)$, $k=1,2,\cdots,m$ [2] .

The Volterra series is especially useful when dealing with random inhomogeneities. A simple but relevant example is that of a quasi-ergodic zero-mean gaussian-uncorrelated random medium, viz.:

$$< \delta n(r_1) \ldots \delta n(r_{2M-1}) > = 0$$

$$n_o^{-2M} < \delta n(r_1) \ldots \delta n(r_{2M}) > = W_o \sum \prod \delta(\underline{r}_i - \underline{r}_j) \tag{5}$$

wherein the sum runs over the $(2M-1)!!$ unordered partitions of $\{\underline{r}_1, \underline{r}_2, \ldots, \underline{r}_M\}$ into pairs. For this case, the EM field average and self-coherency matrix (including field intensity and polarization) are easily found [2] :

$$< E(r) > = W_o \int d\underline{r}_1 \, \underline{\Gamma}^{(2)}(\underline{r}-\underline{r}_1, \underline{r}-\underline{r}_1) + \ldots \tag{6}$$

$$< E(\underline{r}) E^*(\underline{r}) > = W_o \int d\underline{r}_1 |\underline{\Gamma}^{(1)}(\underline{r}-\underline{r}_1)|^2 + W_o^2 \int d\underline{r}_1 \int d\underline{r}_2 \cdot$$
$$\cdot \{ \underline{\Gamma}^{(2)}(\underline{r}-\underline{r}_1, \underline{r}-\underline{r}_1) \underline{\Gamma}^{*(2)}(\underline{r}-\underline{r}_2, \underline{r}-\underline{r}_2) + 2 \, |\underline{\Gamma}^{(2)}(\underline{r}-\underline{r}_1, \underline{r}-\underline{r}_2)|^2 \} + \ldots$$

The standard Volterra series, being a *singular* perturbation method [3] can exhibit secular terms. The latter can be removed by using *renormalization* (eigenvalue straining) schemes, where, e.g., the formal eigenvalues' expansions:

$$k_i = k_i^{(o)} + \sum_{m=1}^{N-1} \chi_i^{(m)}(k_i) \tag{7}$$

($k_i^{(o)}$ being the *unperturbed* problem's eigenvalues, and $\chi_i^{(m)}(\cdot)$ unknown, $m = 1,2, \ldots, N-1$) are *telescopically* inserted into the N-order truncated Volterra series solution, and the $\chi_i^{(m)}(\cdot)$ are then determined by comparison with the *complete* (secular) solution [1]. Alternatively, a (prerenormalized) solution *à la Rytov* [3] can be sought, whose exponent is expanded into a Volterra series.

Conceptual extensions of the Volterra functional power series include the (functional) Lagrange-Bürmann expansion and Padé approximants.

The former [4] is nothing but a Volterra series, whose argument is a properly chosen functional of $\delta n(\underline{r})/n_0$, instead of $\delta n(\underline{r})/n_0$. A skillful choice of the argument functional may result in a dramatic convergency improvement, compared to standard Volterra series.

Rational (Padé [5]) functional approximants can be easily obtained from truncated Volterra series solutions [6]. They have been the key to non-perturbative QED and QCD [5], and could reasonably yield accurate solutions of Maxwell equations in strongly inhomogeneous, possibly stochastic media.

We turn now briefly to other functional representations based on functional integration [7].

Path-integral representations of the EM propagator in inhomogeneous media [8,9] can be evaluated in closed form only in a very few cases [10]. Remarkably, the Feynman expansion of the EM path-integral gives back the Volterra series solution [2].

Solving Maxwell equations in inhomogeneous media using the Cameron Martin orthogonal functional expansion [11] (functional analogue of L^2 approximants, infinite-dimensional Fourier-Hermite series) meets the difficulty of evaluating Wiener integrals [7]. This task deserves further study, to be accomplished efficiently.

As a conclusion, we suggest that functional methods may provide a general, systematic framework for studying EM wave propagation in inhomogeneous, possibly stochastic media. It is important to note that the whole machinery of Volterra series and Padé approximants can be fully implemented, using symbolic manipulation codes such as, e.g., MACSYMA, SMP, REDUCE, etc., to obtain automatically analytical solutions as well as their numerical evaluation.

References

1] G. Franceschetti, I. Pinto, J.O.S.A., A2, 887, 1985.

2] S. Petracca, doctoral dissertation, Dep.t of Physics, University of Naples, 1985.

3] A. Nayfeh, Perturbation Methods, Wiley-Interscience, New York, 1973.

4] D. Gorman J. Zaborsky, IEEE Trans. AC-11, 498, 1966.

5] P.R. Graves Morris (ed.), Padé Approximants, The Institute of Physics, London and Bristol, 1973.

6] S. Petracca, I. Pinto, work in progress, 1986.

7] I.M. Gel'fand, A.M. Yaglom, J. Math. Phys., 1, 48, 1960.

8] G. Eichmann, J.O.S.A., 61, 161, 1971.

9] D. Eve, Proc. Roy. Soc. (London), A347, 405, 1976.

10] L.S. Schulman, Techniques and Applications of Path Integration, J. Wiley & Sons, New York, 1979.

11] R.H. Cameron, W.T. Martin, Ann. Math., 48, 385, 1947.

A STATISTICAL MODEL FOR THE INTENSITY AND PHASE OF RANDOM OPTICAL FIELDS

L. C. Andrews
Department of Mathematics, University of Central Florida
Orlando, Florida 32816

R. L. Phillips
Department of Electrical Engineering and Communication Sciences
University of Central Florida, Orlando, Florida 32816

(invited)

1. INTRODUCTION

To date, the most useful models for the intensity and phase fluctuations of an optical wave propagating through atmospheric turbulence are those which have been heuristically derived. Although the approach is not from first principles, some of these empirically derived models show good quantitative agreement with experimental data. For example, the class of K distributions has been found to provide excellent models for predicting intensity statistics in a variety of experiments involving radiation scatscattered by turbulent media [1 - 4]. However, the K distribution is not satisfactory for all such experimental data and is not theoretically applicable in weak scattering regimes [3,5]. The universal scattering model (USM) appears applicable under all conditions of atmospheric turbulence, but it is mathematically complicated for certain computations [6,7]. The I-K distribution for intensity fluctuations was developed as an attempt to find a more tractable version of the USM distribution [8,9]. Like the USM, the I-K distribution is theoretically applicable under all conditions of atmospheric turbulence.

In this paper we wish to discuss the underlying mathematical basis that leads to the I-K distribution and develop a corresponding model for phase fluctuations [10].

2. SCATTERING MODEL OF THE OPTICAL FIELD

By assuming a discrete scattering model, the field of the optical beam at a given detection point and time is of the form

$$U(t) = e^{i\omega t}\left(Ae^{i\theta} + Re^{i\phi}\right), \tag{1}$$

where ω is the carrier frequency of the optical wave. The term $Ae^{i\theta}$ is a constant amplitude component while the second term is the resultant of one or more scatterers with combined amplitude R and phase ϕ. We make the assumption that the scattered portion of the field is a zero-mean, doubly-stochastic, circular complex Gaussian variate where the mean

intensity $b = \langle R^2 \rangle$ is a fluctuating quantity governed by the gamma distribution. This is comparable to making the assumption that the number of terms contributing to the scattered portion of the field is a random variable (independent of the amplitudes and phases of the individual scatters) that is governed by the negative binomial distribution [4,9].

The conditional joint probability density function (PDF) of R and Φ is given by

$$p_1(R,\Phi|b) = \frac{R}{\pi b} e^{-R^2/b}, \tag{2}$$

which is simply the product of a Rayleigh distribution and a uniform distribution over 2π radians. The gamma distribution for b has the functional form

$$p_2(b) = \frac{\alpha(\alpha b/b_o)^{\alpha-1}}{\Gamma(\alpha) b_o} e^{-\alpha b/b_o}, \quad b > 0, \tag{3}$$

where b_o is the mean value of b and α is a positive parameter related to the effective number of independent scatterers that contribute to the average intensity b of the scattered portion of the field. The unconditional joint PDF of R and Φ is recovered by calculating

$$p_3(R,\Phi) = \int_o^\infty p_2(b) p_1(R,\Phi|b) db = \frac{\alpha(\alpha/b_o)^{\alpha-1}}{\Gamma(\alpha)\pi b_o} \int_o^\infty b^{\alpha-2} e^{-\alpha b/b_o} Re^{-R^2/b} db. \tag{4}$$

By making the change of variable $b = b_o R^2/x$, we find that Eq. (4) becomes

$$p_3(R,\Phi) = \frac{1}{\Gamma(\alpha)\pi b_o} \int_o^\infty \left(\frac{\alpha}{x}\right)^\alpha e^{-x/b_o} R^{2\alpha-1} e^{-\alpha R^2/x} dx, \tag{5}$$

which we choose to leave in integral form at this point.

3. THE I-K DISTRIBUTION

The total intensity of the optical field (1) is

$$I = |U(t)|^2 = A^2 + R^2 + 2AR\cos(\Phi - \Theta). \tag{6}$$

Our approach to finding the PDF of I will be to first calculate the characteristic function of I defined by the expectation

$$C(u) = E[e^{iuI}] = \int_o^\infty \int_{-\pi}^{\pi} e^{iuI} p_3(R,\Phi)\, d\Phi\, dR. \tag{7}$$

Substituting (5) into (7) and performing the integration with respect to only Φ and R, we obtain the characteristic function representation

$$C(u) = \frac{1}{b_o} \int_0^\infty \left(\frac{\alpha}{x}\right)^\alpha \frac{e^{-x/b_o - \alpha A^2/x}}{\left(\frac{\alpha}{x} - iu\right)^\alpha} \exp\left(\frac{-\alpha^2 A^2/x}{\frac{\alpha}{x} - iu}\right) {}_1F_1\left(1-\alpha; 1; \frac{A^2 u^2}{\frac{\alpha}{x} - iu}\right) dx, \quad (8)$$

where ${}_1F_1$ denotes the confluent hypergeometric function [11].

The direct inversion of (8) for arbitrary values of α is very difficult. However, for $\alpha = 1$ the confluent hypergeometric function is approximately unity. If we set ${}_1F_1 = 1$ in (8), the inversion of the resulting expression leads to the family of I-K distributions [8]

$$p_4(I) = \begin{cases} \frac{2\alpha}{b_o}\left(\frac{\sqrt{I}}{A}\right)^{\alpha-1} K_{\alpha-1}(2A\sqrt{\frac{\alpha}{b_o}}) I_{\alpha-1}(2\sqrt{\frac{\alpha I}{b_o}}), & I < A^2 \\ \frac{2\alpha}{b_o}\left(\frac{\sqrt{I}}{A}\right)^{\alpha-1} I_{\alpha-1}(2A\sqrt{\frac{\alpha}{b_o}}) K_{\alpha-1}(2\sqrt{\frac{\alpha I}{b_o}}), & I > A^2. \end{cases} \quad (9)$$

Eq. (9) is exact for $\alpha = 1$, but represents an approximation to the PDF of intensity associated with (1) for other values of α. We have found, however, that α can be restricted to values near unity for almost all conditions of atmospheric turbulence except in the saturation regime. Moreover, the normalized moments of (9) appear to fit experimental data very accurately for all conditions of turbulence, even in the saturation regime.

A particularly advantageous value of α to use in (9) is the value 1/2, since in this case the Bessel functions reduce to exponential functions. A comparison of the normalized moments of (9) when $\alpha = 1/2$ with experimental data of Parry and Pusey [2] is shown in Fig. 1.

4. THE PHASE DISTRIBUTION

To develop a corresponding expression for the phase distribution of the optical field (1), we start by introducing the complex phasor

$$Ve^{i\psi} = Ae^{i\Theta} + Re^{i\phi}, \quad (10)$$

where V and ψ denote the amplitude and phase, respectively, of the field U(t). From (10) we obtain the equations of transformation

$$\begin{aligned} R^2 &= A^2 + V^2 - 2AV\cos\gamma \\ \sin\phi &= \frac{V}{R}\sin\gamma, \end{aligned} \quad (11)$$

where $\gamma = \psi - \Theta$ and the Jacobian of transformation is V/R. By substituting (11) into (2), we get the conditional joint PDF

$$p_5(V,\psi|b) = \frac{V}{\pi b}\exp\left[-\frac{1}{b}(A^2 + V^2 - 2AV\cos\gamma)\right], \quad (12)$$

where $0 \leq V < \infty$ and $-\pi < \gamma \leq \pi$. The unconditional phase distribution is then determined by evaluating the double integral

$$p_6(\psi) = \int_0^\infty \int_0^\infty p_2(b) p_5(V,\psi|b) \; dV \; db, \tag{13}$$

where $p_2(b)$ is given by (3).

Performing the integration in (13) with respect to V leads to

$$p_6(\psi) = \frac{(\alpha/b_o)^\alpha}{2\pi\Gamma(\alpha)} (A\sqrt{\pi} \cos\gamma \; L + M), \tag{14}$$

where

$$L = \int_0^\infty b^{\alpha-3/2} \exp(-\frac{\alpha b}{b_o} - \frac{A^2}{b}\sin^2\gamma) \; db \tag{15}$$

and

$$M = \int_0^\infty b^{\alpha-1} \exp(-\frac{\alpha b}{b_o} - \frac{A^2}{b}\sin^2\gamma) \, {}_1F_1(-1/2;1/2;-\frac{A^2}{b}\cos^2\gamma) \; db. \tag{16}$$

The evaluation of (15) is immediate but (16) requires an application of Kummer's transformation and then expressing the resulting ${}_1F_1$ function by its series representation [11]. Termwise integration finally leads to the result $(-\pi < \gamma \leq \pi)$

$$p_6(\psi) = \frac{(\sqrt{\alpha\rho})^{\alpha+1/2}}{\Gamma(\alpha)\sqrt{\pi}} \cos\gamma \, |\sin\gamma|^{\alpha-1/2} K_{\alpha-1/2}(2\sqrt{\alpha\rho}\,|\sin\gamma|) + \frac{(\sqrt{\alpha\rho})^\alpha}{\Gamma(\alpha)\sqrt{\pi}} \sum_{n=0}^{\infty} \frac{(\alpha\rho)^{n/2}\cos^{2n}\gamma}{\Gamma(n+1/2)} K_{\alpha-n}(2\sqrt{\alpha\rho}), \tag{17}$$

where $\rho = A^2/b_o$ is the power ratio of mean intensities of the constant amplitude component to the random component of the field.

REFERENCES

1. E. Jakeman and P. N. Pusey, IEEE Trans. Antennas Propag. AP-24, 806-814 (1976).

2. G. Parry and P. N. Pusey, J. Opt. Opt. Opt. Soc Opt. Soc. Am. 69, 796-798 (1979).

3. G. Parry, Opt. Acta 28, 715-728 (1981).

4. E. Jakeman, J. Phys. A 13, 31 - 48 (1980).

5. R. L. Phillips and L. C. Andrews, J. Opt. Soc. Am. 71, 1440 - 1445 (1981).

6. R. L. Phillips and L. C. Andrews, J. Opt. Soc. Am. 72, 864-870 (1982).

7. A. K. Majumdar, J. Opt. Soc. Am. A 1, 1067 - 1074 (1984).

8. L. C. Andrews and R. L. Phillips, J. Opt. Soc. Am. A 2, 160 - 163 (1985).

9. L. C. Andrews and R. L. Phillips, "A mathematical genesis of the I-K distribution for random optical fields," (submitted).

10. D. J. Link, R. L. Phillips, and L. C. Andrews, "A theoretical model for optical wave phase fluctuations," (submitted).

11. L. C. Andrews, Special Functions for Engineers and Applied Mathematicians, (Macmillan, New York, 1985).

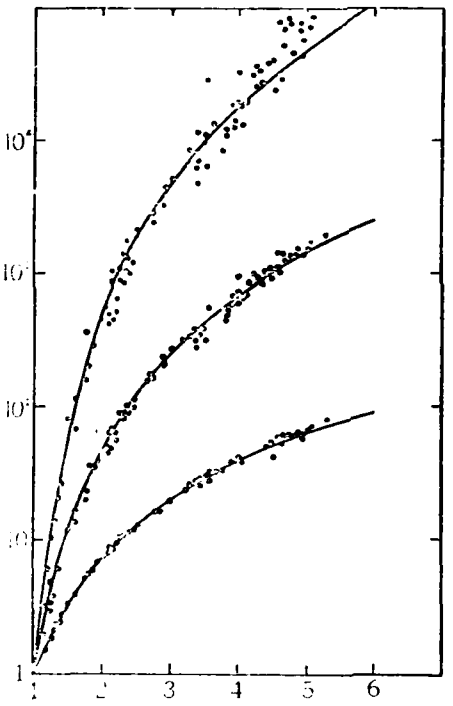

Fig. 1 Comparison of experimental data with I-K distribution for the special case $\alpha=1/2$.

YET ANOTHER PROBABILITY DISTRIBUTION FOR INTENSITY FLUCTUATIONS IN STRONG TURBULENCE

James H. Churnside, Reginald J. Hill, and Gerard R. Ochs
NOAA/ERL/Wave Propagation Laboratory
Boulder, Colorado 80303

INTRODUCTION

It is generally accepted that the fluctuations of an optical signal caused by propagation through weak turbulence will have a lognormal probability density function. For propagation through strong turbulence, no such concensus exists. A number of density functions have been considered, including Rician,[1] lognormal,[2,3] and K[4,5] distributions, and others that cannot be described by simple analytic formulas.[6,7] Of these, the K distribution has probably been the most successful at describing data.[4,5,8] It also reduces to the generally accepted limit of a negative exponential density function for extremely high turbulence levels. Using an argument similar to that leading to the K distribution, we arrive at a probability density function that consists of a negative exponential whose mean value is a lognormally distributed random variable. This is shown to agree well with experimental results.

THEORY

It has long been noted by one of us (GRO) that for strong scintillation the probability distribution of intensity departs significantly from an exponential distribution because of the slowly varying intensity underlying the spikes of intensity. The spikes of intensity have a small spatial scale of order the wave coherence length ρ_o, whereas the temporally slowly varying part has the large spatial scale of order $\lambda L/\rho_o$, where λ and L are wavelength and path length. As asymptotically strong turbulence is approached the small-scale scintillations give intensity variance approaching unity whereas the large-scale contribution to the variance decreases to zero. It therefore seems reasonable to assume that

in the approach to asymptotically strong turbulence the small-scale intensity fluctuations have an exponential distribution which is modulated by the large-scale intensity fluctuations. It remains to determine the probability distribution of the large-scale intensity fluctuations.

A method of measuring only the large-scale intensity fluctuations is to aperture average using an aperture size $\sqrt{\lambda L}$, which is the geometric mean of the small-scale ρ_o and large scale $\lambda L/\rho_o$. This takes advantage of the gap in the spatial power spectrum of intensity between the small-scale (high wavenumber) and large-scale (low wavenumber) contributions to the intensity variance. This gap is more pronounced for plane waves than for spherical waves and most pronounced for strongest turbulence. Note that the corresponding gap in the temporal spectrum of intensity is not well defined because strong turbulence measurements in the atmosphere usually imply light and variable winds. We hypothesize that the large-scale contribution to the scintillation is lognormally distributed, and our measurements of aperture-averaged scintillation tends to support this hypothesis.

The two-scale model is appealing since intensity covariance in strong turbulence clearly shows the effects of two scale sizes.[3,10] Another two scale model applied to speckle by Newman[9] gives the K distribution.

The probability density function of intensity that results from a lognormally modulated exponential distribution is given by

$$p(I) = \frac{1}{\sqrt{2\pi}\,\sigma} \int_0^\infty \frac{dz}{z^2} \exp\left[-\frac{I}{z} - \frac{(\ell nz + \frac{1}{2}\sigma^2)^2}{2\sigma^2}\right] \qquad (1)$$

where σ^2 is the log-intensity variance of the large-scale process, z is the modulation depth due to that process, and I is the observed intensity normalized by its mean value.

The moments of Eq. (1) are easily found to be

$$\langle I^n \rangle = n! \exp\left[\frac{1}{2} n(n-1)\,\sigma^2\right] , \qquad (2)$$

which agrees with the asymptotic approach to exponential statistics given by Dashen.[11] Equation (2) can be written in terms of the normalized variance of irradiance σ_N^2 as

$$\langle I^n \rangle = n! \left(\frac{\sigma_N^2 + 1}{2}\right)^{\frac{1}{2}n(n-1)} . \quad (3)$$

The lognormal-exponential moments are seen to lie between those of the lognormal and the K density functions. Previously published experimental moments seem also to lie between the lognormal and K values.[4,5,8]

EXPERIMENT

The experimental source was a He-Ne laser producing about 20 mW of 0.633 μm radiation with a beam divergence of about 1 mrad. This light was propagated across 1 km of flat grassland at a height of about 1.5 m to the receiver. At the receiver, the light was passed through a 1 mm aperture, a narrow-band interference filter, and into a photomultiplier tube. The photomultiplier tube current was amplified using a high gain transimpedance amplifier, and the resulting signal was digitized using a 12 bit A to D converter. The digitized signals were stored on magnetic tape for later processing.

The intensity signal was sampled at a rate of 5000 samples/second for 10,833 samples; sampling was then stopped while these values were recorded. Each data set consisted of 50 of these blocks of data and took about 3.5 minutes to collect. The probability density function of a typical data set is plotted in Fig. 1. Also plotted in the figure are the K and lognormal-exponential distributions that have the same normalized variance ($\sigma_N^2 = 4.32$). Although the two distributions are very similar, the data suggest that the lognormal-exponential distribution might be a better approximation to the probability density function of intensity than either the lognormal or the K distributions.

REFERENCES

1. J. W. Strohbehn, Ting-i Wang and J. P. Speck, Rad. Sci. 10, 59 (1975).
2. G. R. Ochs and R. S. Lawrence, J. Opt. Soc. Am., 59, 226 (1969).
3. S. F. Clifford, G. R. Ochs and R. S. Lawrence, J. Opt. Soc. Am. 64, 148 (1974).
4. G. Parry and P. N. Pusey, J. Opt. Soc. Am. 69, 796 (1979).
5. G. Parry, Opt. Acta 28, 715 (1981).

6. Ting-i Wang and J. W. Strohbehn, J. Opt. Soc. Am. 64, 994 (1974).

7. R. L. Phillips and L. C. Andrews, J. Opt. Soc. Am. 72, 864 (1982).

8. R. L. Phillips and L. C. Andrews, J. Opt. Soc. Am. 71, 1440 (1981).

9. D. Newman, J. Opt. Soc. Am. A 2, 22 (1985).

10. W. A. Coles and R. G. Frehlich, J. Opt. Soc. Am. 72, 1042 (1982).

11. R. Dashen, Opt. Lett. 9, 110 (1984).

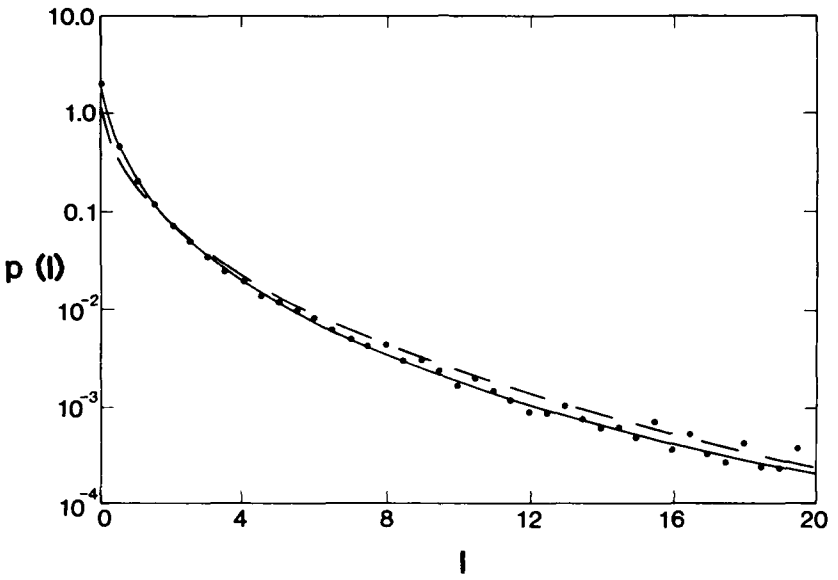

Figure 1. Plot of probability density function vs. intensity for K (dashed line) and lognormal-exponential (solid line) models along with experimental values (points).

TRANSMISSION

Experimental Investigations of Atmospheric IR-Propagation over Land and Sea

A.Kohnle, R.Neuwirth, W.Steffens, H.Jundt

Forschungsinstitut für Optik (FGAN-FfO)
Schloß Kreßbach
D-7400 Tübingen 1 (invited)

Introduction

The performance of electro-optical (EO) sensors is often severely limited by atmospheric transmission characteristics. This limitation results from the complex interaction of electro-magnetic radiation with atmospheric particles and molecules. For proper EO systems performance assessment the atmospheric process must be quantified and related to easily measurable meteorological and (for a maritime environment) oceanographic parameters.
Experimental and theoretical investigations of infrared (IR) atmospheric propagation in the past have permitted to establish transmission models and codes like LOWTRAN /1/ and others /2/, which are extended and updated depending on the availability of new relevant scientific results.

The need for sensors with better "all weather" capability raised the interest on mm-wave propagation (35-300 GHz). It is well established that with increasing wavelength the all weather capabilty of a sensor increases, whereas the geometrical resolution decreases. Therefore, "multisensor systems" are being envisaged to account for this fact.
As a part of multisensor assessment studies simultaneous atmospheric transmission experiments at visible, IR (3.4-5.0 µm, 8.25-13.0 µm) and mm-waves (94 GHz) over ranges of 4.35 km, 6.5 km and 11.91 km over sea and 500 m and 5.4 km (also at 10.6 µm) over land with relevant meteorological measurements and measurements of the size distribution of aerosol- and raindrop particles (0.15 µm - 10 mm diameter) were performed. The mm-part of these investigations has been performed by scientists of the FGAN-FHP.*)
These measurements have produced time series of extinction values for the wavelengths (bands) mentioned above under different meteorological conditions, extinction correlations, statistics, aerosol extinction, aerosol-scattering-functions and rain extinction. As a part of this large effort basic results concerning IR-propagation are reported here.

---

*) FGAN-FHP: Forschungsinstitut für Hochfrequenzphysik
principal investigator: Dr.H.H.Fuchs

1. Kneizys, F.X., et al., Report AFGL-TR-83-0187, 1983
2. Jessen, W., et al., Report FfO 83/79, 1983

IR/mmW-Extinction in Rain /3/

As a part of the analysis of the experiments mentioned above, correlations of IR- and mmW-extinction in rain over sea for ranges from 4 to 12 km have been made and compared with theoretical calculations based upon model rain-drop size-distributions and Mie's theory. The scatter plots of experimental values (measurements every 10 sec, integration time 150 sec) show good correlation with the measured values for medium ranges. The deviations increase with range. This is basically caused by the different sensitivities of IR- and mm-waves against

- change in rain-drop size-distribution,
- change in molecular (continuum) attenuation,
- change in background aerosol distributions (IR),
- multipath interference (mmW).

Fig.1 presents an example of such a scatter plot for a range of 6.58 km. It does not only show a rain- but also a fog-situation. Both cases can be clearly separated because of the fact that IR is much more affected by fog than mm-waves.

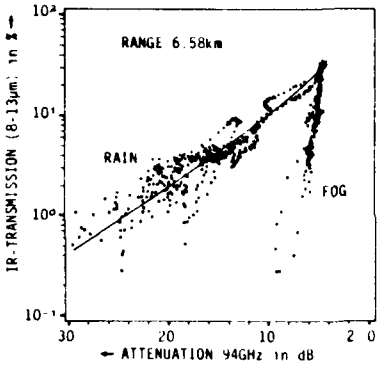

Fig.1: Correlation of IR-transmission and mmW-attenuation for a range of 6.58km.

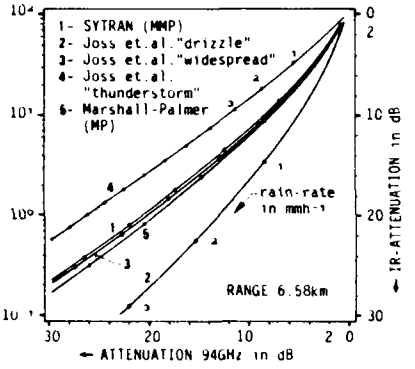

Fig.2: Correlation of calculated rain-attenuation for IR and mmW for different rain models and rain-rates and for a range of 6.58km

Comparisons of calculated pure rain extinction values based on calculations with different rain-models reported in the literature /4,5,6/,s.Fig.2 with measurements (corrected for molecular absorption) show that the Joss et al. "drizzle"- and "thunderstorm"-models are good upper and lower bounds for the experimental data at all ranges.

3. Neuwirth,R.,Fuchs,H.H., Rep.FfO 85/50, FHP4-85/Lfd.Nr.235
4. Joss, J., Waldvogel, A., J.Atm. Sci., Vol.26, 1969
5. Marshall, I.S., Palmer, W.M.K., J.Met., 5, 1948
6. Van de Vrie, Phys.Lab.TNO, Rep.No.PHL.,1976-07, 1976

Algorithm to Convert Broad-Band to Laser-Line Extinction /7/

Another interesting analysis aspect for the above mentioned experiments (and others) is the question how exactly 10.6 μm (CO_2)-laser extinction coefficients can be calculated from measured broad-band (8-13 μm) transmission values. The theoretical results can be compared with simultaneous measurements over a range of 5.4 km over land mentioned above.

The laser extinction coefficient σ for a certain laser-line is given by a sum of scattering(β) and absorption (α) coefficients (molecular (m) and aerosol (a) part) by

$$\sigma = \beta_m + \alpha_m + \beta_a + \alpha_a \quad . \tag{1}$$

The mean band aerosol transmission $\bar{\tau}_a$ over the experimental range R_0 for a transmissometer with blackbody source temperature T_B and relative sensitivity R_n can be expressed as

$$\bar{\tau}_a \simeq \frac{\bar{\tau}}{\bar{\tau}_m} \tag{2}$$

with $$\bar{\tau}_m = \int_{\Delta\lambda} \tau_m(\lambda,R_0)R_n(\lambda)L(\lambda,T_B)d\lambda \Big/ \int_{\Delta\lambda} R_n(\lambda)L(\lambda,T_B)d\lambda \quad .$$

$\bar{\tau}$ is the measured transmission, $L(\bar{\tau},T_B)$ the Planck function at wavelength λ. Equation (2) holds within about 2% accuracy. The band aerosol extinction can then be expressed as

$$\bar{\sigma}_a = \frac{-\ln(\bar{\tau}_a)}{R_0} \quad . \tag{3}$$

It can be shown that for a wide range of environmental conditions and a variety of aerosol models a unique conversion factor $Q \approx 0.8$ exists to convert 8-13 μm aerosol extinction $\bar{\sigma}_a$ to 10.6 μm laser extinction σ_a by

$$\sigma_a(\lambda) \approx \bar{\sigma}_a(\Delta\lambda)Q \quad . \tag{4}$$

To determine the laser extinction coefficient σ from a broad-band measurement, the molecular part σ_m in Eq.(1) has to be calculated using a transmission code, e.g. FASCODE /8/.

Experimental results (to be shown at the oral presentation) show good agreement with calculated values using this algorithm.

7. Tamir,M., et al., Report FfO 1980/124, 1980
8. Smith, H.J.P., et al., Report AFGL-TR-78-0081, 1978

Aerosol Extinction and Phase-Functions

A third area of investigation is the development of aerosol-models based on in situ aerosol size distribution measurements and validation of these models by comparison of calculated and measured transmission values. New dynamic aerosol models have been developed recently and were published (U.S.Navy Maritime Aerosol Model , FfO Maritime and Rural Aerosol Model etc.) /1,9,10/. For special applications not only extinction but also the whole scattering function is essential. The impact of a size distribution change of the FfO Maritime Aerosol Model (caused by different relative humidities) on the corresponding phase-function for 10.6 µm laser radiation is indicated in Figs.3,4.

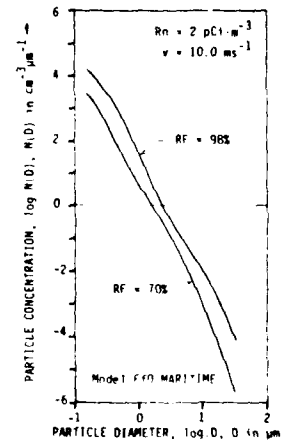

Fig.3: Dynamic of the FfO-MARITIME Aerosol Model size distribution with increasing relative humidity

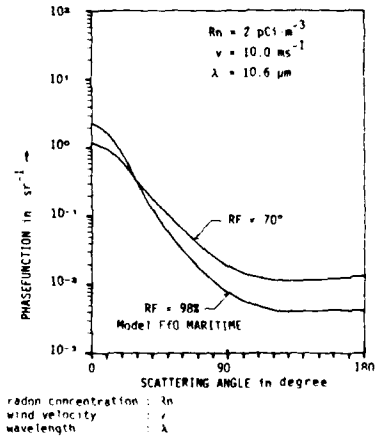

Fig.4: Change of calculated phase-function with increasing relative humidity

A comparison of a number of phase-functions calculated from aerosol size distributions measured over sea (North and Baltic Sea) and over land (Southern Germany) with FfO aerosol model calculations show a fairly good agreement for visibilities $V_N \gtrsim 2$ km. Comparisons with other models e.g. LOWTRAN 6 aerosol models will be shown at the oral presentation.

Concluding Remarks

There are other analysis aspects of these measurements which are pursued presently, e.g. absorption fluctuation, range extrapolation of transmission data.

9. Halavee,U., et al., Reports FfO 82/50, 1982
and FfO 83/49, 1983
10.Höhn, D.H., et al., Infrared Physics, Vol.25, No1/2, 1985

THE ROLE OF TROPOSPHERIC PROPAGATION IN EARTH-SPACE TELECOMMUNICATION SYSTEMS AT MILLIMETER WAVES

Aldo PARABONI

Dipartimento di Elettronica del Politecnico di Milano,
Centro di Studio per le Telecomunicazioni Spaziali del
Consiglio Nazionale delle Ricerche (CSTS-CNR)

ABSTRACT

The future telecommunication satellites will operate in the 20, 30, 40 and 50 GHz bands, where propagation is seriously impaired by tropospheric effects.

This paper deals with these effects and their impact on the system design.

1 - Introduction

In the first half of the 80's the exploitation of the 12/14 GHz bands for routinary Telecommunication services (second generation satellites) has become a reality.

The continuous growth in demand for transmission capability however is bound to bring also these new bands to saturation quite soon; for this reason the World Administrative Radio Conference (WARC) in 1979 and 1985 has proceeded to the assignement of new frequancy bands in the millimeter waves range.

With this allocation, considerable bandwidths are assigned to satellite telecommunication and broadcasting services in the 20/30, 40 and 50 GHz bands, even though in sharing with terrestrial services.

The exploitation of these new bands poses extraordinary problems to the technology world as well as to the bodies responsible of planning these advanced systems (third generation satellites), whose operational phase is envisaged to start in the second half of the next decade.

It must be said however that this challenge is well worth facing, since problems like the bandwidth shortage, the geostationary orbit congestion and the electromagnetic interference should be alleviated for a fairly long time; one must consider in fact that the efficient exploitation of the spectrum, together with the use of very sofisticated antennae systems (viable only at millimeter waves), will allow the reuse of the same frequency several times within the same terrestrial area (with a gain much greather than the mere increment of the allocated bandwidth), the increase in the number of satellites within the usable geostationary arc and the decrease of the "respect distances" to be observed between terrestrial transmitting terminals, which will no longer be installed in remote shielded sites, as presently is, but will be possibly located at the use premises.

It is obviously very difficult to draw the scenario of satellite telecommunications in the next 10-15 years, even by restricting ourselves to what can be envisaged simply by projecting the actual

trends; infact, apart from the new applications, even the bare configuration of the future telecommunication systems will be quite different from the actual one: different integration and role of the satellite with respect to the terrestrial network, different proportion of the local business networks with respect to the public ones, new services such as high capacity data transmission, electronic mail, fac-simile newspaper transmission, teleconferencing etc.

Finally it is worth mentioning the breakthrough of direct TV or audio broadcasting, for which the feeder-links will be frequently choosen within the millimeter waves frequency range.

2 - From centimeter to millimeter wavelengths

Moving from the 4/6 GHz to the 12/14 GHz bands a lot of problems appeared due to the fact that the wavelength (inside the water medium) and the raindrop circumference became comparable thus causing some resonance-like phenomena which resulted in a remarkable increase of absorption and scattering.

In order to gather the information needed to evaluate the required system margins, a number of propagation experiments were set up in the last decade; common objective of these experiments was the compilation of statistical Cumulative Distribution Functions (CDFs) giving the fraction of the total time during which given fade levels were exceeded; some of these experiments were conducted in terrestrial paths, others in inclined paths; among these latter same utilized satellite links thus performing direct measurements whereas others estimated attenuation indirectly by means of radiometers or meteorological radars.

Table 1 gives the satellites employed for thse experiments /1, 2, 3, 4, 5, 6/.

Fig. 1, taken from /5/, gives an example of CDF measured with the satellite SIRIO in the Italian station of Fucino; the ordinate gives the percentage of the observation time during which the attenuation value was exceeded. Assuming this curve as a long term probability distribution, a hypothetical link should be designed with a margin equal to the abscissae corresponding to the given (tolerated) outage in ordinate.

Despite the enormous effort which single countries or groups of countries had to sustain to partecipate in these experiments, it became soon apparent that a limited number of stations such as the ones actually eployed was far from enough to allow the complete characterization of the region in which future plants were planned; moreover little was known, even after long measuring campaigns, about the possibility of extending the results to frequencies, polarisations and elevations different from the ones directly involved. Finally it was noted that a very large variability existed from one year to the other and that, even in short distances, attenuation varied both on an instantaneous and statistical basis.

A great effort was then devoted in the assessment of what are called "prediction methods" or "scaling methods", which, in a sense, completely overturn the previous phylosophy according to which measurements are primarily a means to achieve the information directly needed by system designers. In the new viewpoint the measurements are rather

intended as a tool for checking procedures which allow us to connect what is "known" in a certain site (meteorological data, measurements in different conditions etc.) to what is actually "needed".

For the future applications our ability to devise significant propagation experiemnts will be seriously defied as important differences with respect to the actual conditions, will need consideration.

These differences arise from the following peculiarities of the future systems:

- very high attenuations at 20 and 30 GHz (see Fig. 1) due to rain for time percentages as low as 0.01%, which are the ones tc the considered in many CCIR regulations concerning the availability and quality requirements for telecom. and TV feeder-links. This constraint compels us to consider alternative and more cost-effective system philosophies which require more information about propagation and characterization of the transfer channel.
- advanced technologies allowing the satellite and terrestral network to be considered as a global system, in which many functions traditionally performed by the network (exchanges, rigeneration, routing, etc.) will be assigned to the satellite. The full exploitation of this flexibility also requires complex information about attenuation and depolarisation jointly reached in places at large distance.

3 - Attenuation

The prediction of the Co-Polar-Attenuation (CPA) still remains the major problem to be tackled when designing the radiolink margin (i.e. the excess fading the system can stand before reaching a specified signal-to-noise ratio).

The most common input-information for this prediction is the "point rain intensity" CDF; nowadays it is however rather frequently the case that attenuation CDFs are available but at a different frequency, elevation or polarisation.

Considering first the case of the rain intensity, two sources of uncertainty exist: the non perfect knowledge of the local long-term CDF of rain intensity and the possible errors in making allowance for factors such as the horizontal and vertical structure of the rain, the raindrop size distribution of the particles and the nature of the phenomena encountered along the path (melting snow, ice, temperature profile, absorption by gaseous tropospheric components, etc.).

Despite these latter difficulties, reasonably accurate methods to predict CPA statistics from given rain intensity statistics have been recently established and tested against a very large amount of CPA and rain data collected concurrently /7/; as a result of this test it was demonstrated that accuracies of the order of some 25% (RMS error) can be reached by means of simple procedures (among which is the one proposed by CCIR /8/); better values (lower than 20%) can be also reached by sacrificing semplicity or by inserting some auxiliary information typical of the site (local data).

Unfortunately these data are only at 11,14 and 18 Ghz (SIRIO and

OTS satellites), so that we can not be sure that the same confidence applies also in the 30,40 and 50 GHz bands.

The future activity in Europe with the satellites OLYMPUS /9/ and ITALSAT /10/ will be devoted to filling in this gap.

As fot the uncertainty due to the unawareness of the rain statistics, of course the situation varies considerably from site to site; the CCIR world map of rain intensity exceeded for typical fractions of time /8/ is probably accurate in areas where many measurements are available but it can not be elsewhere.

Extensive tests /11/ have been conducted in the recent past on some prediction methods utilizing as input information the raint CDFs given by the CCIR climatic maps.

As expected a much greather uncertainty was found (of the order of 50-60%); unfortunately it is impossible to distinguish the contribution due to the input data from that due to the higher frequencies (30 GHz), longer paths involved (20 deg. elevations) etc. even if the major source of uncertainty is certainly the first one.

A more refined rain intensity climatic map stil remains an objective of many countries or research bodies.

As for the frequency scaling formulae, a good accuracy can be achieved in the range 11-18 GHz (less than 10%) over and extended attenuation range (2 to 10 dB @ 11.6 GHz) /12/.

There are however different aspects to be considered when moving from the centimeter waves (second generation satellites) to the millimeter waves (third generation satellites).

A first difference concerns the different time percentages that probably will be taken as reference. For services other than telephony and/or in case of private business networks it is perfectly possible that outage time percentages much greather than 0.01% will be tolerated. Moreover even in the case of ordinary telephonic services outages longer than some minutes could be considered as equipment failures (even though caused by propagation) and assigned to the higher time percentages allowed by the present CCIR Regulations for this cause of outage.

These higher percentages imply a completely different scenario as regards the physical phenomena which dominate propagation: indeed when passing to percentages of the order of 0.1% or greater, the widespread stratified rain is to be considered instead of the convective one.

The spatial and temporal structure of such rainfall still remains to be understood satisfactorily: the melting layer, the distribution and dynamics of the small drops, the horizontal and vertical profile etc. are only a few examples of large research areas to be explored in the near future.

A second important difference is constituted by the topology of the novel systems which will be characterized by a large number of (possibly) small earth terminals with a margin of a few dBs. In order to avoid the very frequent outages which would be implied thereby, many types of countermeasures are now being studied by several administrations; one of these could consist of a stearable spot beam on board, to be pointed toward one (or a few) earth terminal(s) undergoing severe wheather conditions (large scale diversity). In other cases particular beams at different frequencies or particular forms of redundancy could be reserved for these "unlucky" earth terminals /13/.

When few dB margins are considered, many new problems, previously considered marginal, become of great importance: the scintillations, the so called "clear air" plateau due to the absorption of water vapour and oxygen, the contribution to the total CPA due to the above mentioned melting layer, the interference due to depolarisation (in case of dual frequency links) or any other type of interference.

Moreover the design of common on-board resources as mentioned before, requires the knowledge of two-dimensional statistics giving the probability of simultaneous exceedance of CPA in two separate sites, since this could constitute outage in the event of this resource being required simultaneously by two or more earth stations.

4 - Depolarisation

The major source of depolarisation (XPD) is the anisotropy of the medium, which, being constituted by non-spherical particles, presents a different propagation constant in the various polarisation planes. Since the transmitted polarisation can not be always parallel to the symmetry planes (if existing) of the medium, a depolarisation arise; its entity depends on the degree of asymmetry of the particles and on the angle formed by the transmitted polarisation and the symmetry planes.

These factors, in turn, depend on frequency, on the dynamic phenomena governing the drop-air interaction (turbolence, up draft, wind shear) and on the electrostatic field sustained by the charges carried by the couds, which tend to align the ice needles.

Fig.2, taken from /14/ gives an example of probability of depolarisation at 11.6 GHz conditioned to attenuation (median value and extreme deciles- Sirio data).

Despite the greath effort in measuring the XPD in many earth stations, up to 30 GHz, our present ability to predict this parameter is far less than the one concerning the attenuation.

5 - Scintillations and multipath

The phenomenon of scintillations is well known in its physical background and technical consequences; it is due to the presence of irregularities in the structure of the refractive index, whose scattering causes a series of paths (or scattering chains) which interfere to each other whithin the receiving antenna. The mechanism is not conceptually different from the one better known in the terrestrail pahts as multipath; the only difference consist in the different spatial configuration of the tropospheric irregularities (of layered type in terres trial paths) which produces secondary waves of higher intensity.

Effects of these phenomena are, besides the well known amplitude scintillations, the phase scintillations and possible spectral distortions.

Out present ability to predict these effects at millimetric waves is certainly very low.

6 - REFERENCES

/1/ L. Ippolito "Radio Propagation for Space Communication Systems" IEEE Proc. Vol. 69 N. 6, June 1981

/2/ D.Cox, H.W. Arnold "Results from the 19- and 28- GHz COMSTAR Satellite Propagation Experiment at Crawford Hill" IEEE Proc. Vol. 70 N. 5, May 1982

/3/ J. Fugono et al. "ETS-II Experiments" IEEE Trans. on Aerospace and Electronics Systems Vol. 16 N. 5, Sept. 1980

/4/ P.A. Watson, F. Dintelmann, N.J. Mc Ewan "Propagation Experiments with the OTS Satellite" Interim Eutelsat Rep. P/Tec 83/1 Feb. 1983

/5/ "Programma SIRIO' Tech. Rep. of Consiglio Nazionale delle Ricerche Italy Feb. 1983.

/6/ H. Fukuchi et al. "Centimeter Wave Propagation Experiments Using the Beacon Signal of CS and BSE Satellites" IEEE Trans. on Antennas and Propagation Vol. AP-31 N. 4 July 1983

/7/ "COST 205: Prediction of rain attenuation statistics from point rainfall intensity data" Alta Frequenza Vol. LIV N. 3 May-June 1985

/8/ "Recommendations and Reports of the CCIR" Vol. 5 Propagation in non-ionized media, XVth Plenary Assembly Geneva 1982

/9/ "OLYMPUS user's guide" Report of the European Space Agency UG-6-1 Nov. 1983.

/10/ B. Giannone, E. Saggese, E. Matricciani, A. Paraboni "The ITALSAT Propagation Experiment" Space Communication and Broadcasting Vol. 3 N.3, Sept. 1985

/11/ W.L. Stutzman, W.K. Dishman, "A simple model for the estimation of rain-induced attenuation along earth-space paths at millimeter wavelenghts" "Radio Science Vol. 17 N. 6 Nov.-Dec. 1982.

/12/ "Project COST 205: Frequency and polarisation scaling of rain attenuation" Alta Frequenza Vol. LIV N. 3 May-June 1985

/13/ F. Carassa "Adaptive methods to counteract rain attenuation effects in the 20/30 GHz band" Space Communication and Broadcasting Vol. 2 N. 3, Sept. 1984.

/14/ M. Mauri, A. Paraboni, D. Tarducci "Depolarization Measurements at 11.6 GHz in Earth-Space Paths using the SIRIO Satellite" IEEE Trans. on Antennas and Propagation March 1986.

TABLE 1

Satellite	launch date	Frequencies (GHz)
ATS-5 (USA)	8/69	15.3
ATS-6 (USA)	5/74	20-30
CTS (Canada)	1/76	11.7-12.2
COMSTARs (USA)	5/76 7/76 6/78	19-28
ETS-II (Japan)	2/77	1.7-11.5-34.5
SIRIO (Italy)	8/77	11.6-17-17.8
CS (Japan)	12/77	17.7-20.3
BSE(Japan)	4/78	11.7-12.2
OTS(Europe)	5/78	11.6-11.8-14.5

FIGURE CAPTIONS

Fig. 1 Cumulative distributions of Attenuation (CPA): ordinate give the probatility of the value in abscissae being exceeded-SIRIO Data @ 11.6 and 17.8 GHz /5/.

Fig. 2 Conditional quantiles (i.e. values exceeded for 10,50,90% of the time) of depolarisation (XPD) against attenuation (CPA) /14/.

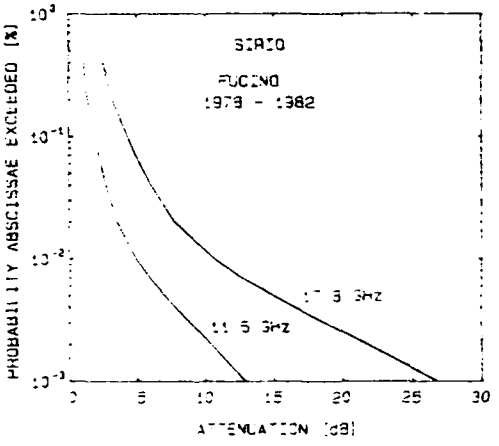

Fig. 1

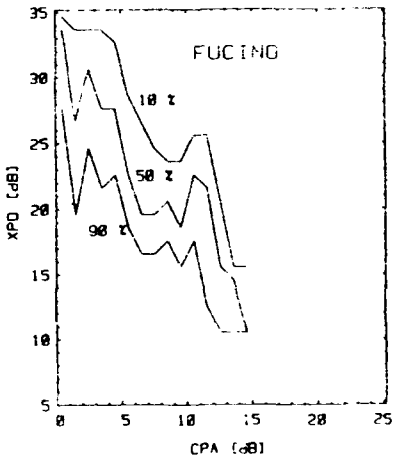

Fig. 2

MODELING MILLIMETER-WAVE PROPAGATION IN MOIST AIR*

Hans J. Liebe

National Telecommunications and Information Administration
Institute for Telecommunication Sciences (ITS)
Boulder, Colorado 80303, U.S.A.

A model that describes accurately atmospheric millimeter-wave properties in terms of easily available meteorological data has been the goal of ITS's computer program MPM [1]. There are four atmospheric "windows" W1-W4 in the molecular absorption by O_2 and H_2O over the frequency range f=30 to 300 GHz. For the nonprecipitating atmosphere, it is water vapor and its conversion into suspended droplets (that is, haze, fog, cloud) that degrades the window transmission. Characteristics of the propagation medium (see [1]) can be expressed in terms of barometric pressure P in kPa, temperature T in K, relative humidity RH in %, and suspended droplet concentration w in g/m³, all assumed known along the path length L in km.

Specific attenuation and dispersive delay rates

$$\alpha = \alpha_d + \alpha_v + \alpha_w \quad \text{dB/km}, \tag{1a}$$

$$\beta - \beta_o = \beta_d + \beta_v + \beta_w \quad \text{ps/km}, \tag{1b}$$

are separated into contributions from dry air $(\alpha,\beta)_d$, water vapor $(\ )_v$ and suspended droplets $(\ )_w$, while β_o is the total refractive delay. A typical example of (1) is displayed in Figure 1, as obtained with the program MPM. Sea level conditions were simulated by a P-T data pair and RH = 0 to 100% for eight cases, allowing a maximum absolute humidity of v(100%RH) = 6.80 g/m³ (e_s = 0.872 kPa). A 9th case was added to the 100%RH condition in order to simulate a fog with w = 0.1g/m³, representative of about 0.3km optical visibility.

Corroborative experimental data of sufficient quality to seriously test predictions are scarce. Reliability, precision, and limited scope of supporting meteorological data often compromise the accuracy of results deduced from field observations. Generally, laboratory experiments provide more precise tests by simulating controlled electromagnetic and atmospheric conditions crucial to model validations. In this paper we present and discuss:

- two sets of field data (Figure 2 and Table 1) supporting MPM predictions, and
- preliminary results from on-going laboratory studies of moist air absorption.

Attenuation rates $\alpha(v)$ reported at f_1 = 31.84 and f_2 = 245.80 GHz together with data on the associated differential dispersion $\Delta N = \Delta\beta/3.336 - N(f_2 - N(f_1)$ [2] are compared with MPM predictions in Figure 2. A nonlinear dependence of $\alpha(v)$ and a linear dependence of $\Delta N(v)$, both on absolute humidity v, can be observed.

---

*Work was supported in part by ARO 187-82 and by NOSC RW 59-501-8.

AD-A170 393 DIGEST - INTERNATIONAL CONFERENCE ON OPTICAL AND MILLIMETER WAVE PROPAGAT..(U) OREGON GRADUATE CENTER BEAVERTON DEPT OF APPLIED PHYSICS AND E.. R A ELLIOTT 3/4

UNCLASSIFIED MAY 86 ARO-23498.1-EL-CF DAAL03-86-G-0088 F/G 4/1 NL

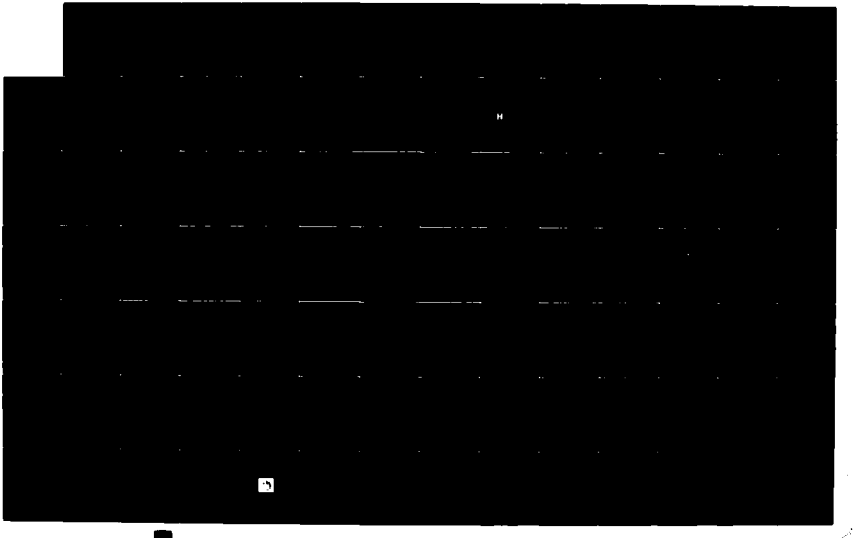

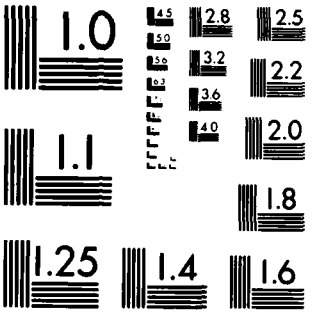

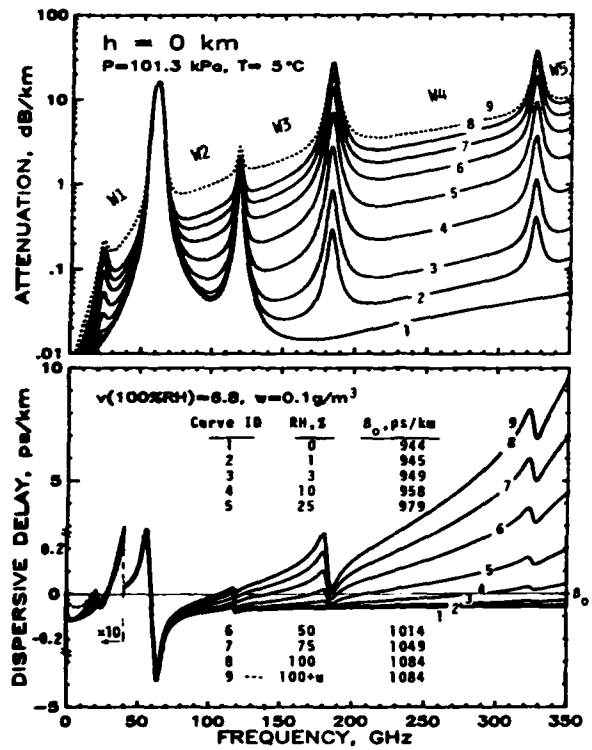

Figure 1. Specific attenuation (α) and dispersive delay (δ) for 9 (see ID) humidity cases of sea level air as predicted by the MPM program for a frequency range, f=1 to 350 GHz [1].

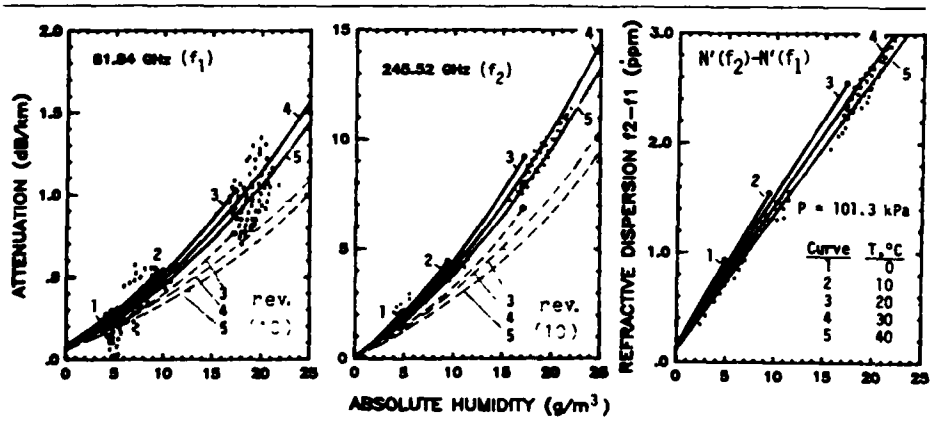

Figure 2. Specific attenuation α and refractive dispersion $\Delta N = N'(f_2) - N'(f_1)$ for air at temperatures ranging from 0° to 40°C measured in Tokyo, Japan over a line-of-sight path (L = 0.81 km): rectangles, data clusters [2]; lines, MPM; circles, RH = 100%.

Table 1. MPM Predictions of Atmospheric Emission Measurements [3] Taken at 10, 33, and 90 GHz from Two Separate Elevations ($h_{1,2}$) in California

EXPERIMENT*			MPM PREDICTIONS †								
			Dry Air*				Water Vapor*			Cloud Droplets*	
f	T_X		A_d	T_d	a_v	b_v	A_v	T_v	a_v+b_vV (100%RH)	a_W	x_W
GHz	K	V(mm)=	0	0	0 to 58.2		14		58	W = 0 to 5 mm	
h_1 = 0.25 km:			dB $\cdot10^{-3}$	K	$\cdot10^{-3}$	$\cdot10^{-5}$	dB	K	dB/mm $\cdot10^{-3}$	dB/mm	
10	2.5 (3)		35.3	2.10	0.47	0.29	0.0072	0.46	0.64	0.098	154
33	12.4 (3)		112.1	6.63	5.56	3.19	0.0841	5.43	7.41	0.990	134
90	34.3 (5)		195.6	11.5	22.80	23.10	0.365	22.8	36.20	4.830	133
		V(mm)=	0	0	0 to 13.3		4.7		13		
h_2 = 3.80 km:											
10	1.11 (4)		17.5	1.05	0.30	0.90	0.0016	0.10	0.42	0.098	233
33	4.48 (18)		56.5	3.36	3.86	8.00	0.0199	1.29	4.90	0.990	202
90	11.0 (1)		90.5	5.36	15.50	55.40	0.0851	5.50	22.70	4.830	213

*) Clear, dry weather conditions (W = 0), $V(h_2)/V(h_1)$ = 1/3
h_1 : 15 - 24°C, 99.5 kPa; h_2 : 2 - 10°C, 65.3 kPa

†) San Francisco, CA Mean July height profile
h_1 : 17°C, 99 kPa } Cloud between 4.4 and
h_2 : 6.5°C, 65 kPa } 5.1 km, $x_W = a_W/[a_v+b_vV(100\%RH)]$

*) $A = A_d + A_v + A_W$ dB , $A_v = a_vV + b_vV^2$[revised MPM - see (10)], $A_W = a_WW$
$T_X = T_d + T_v$ K , $T_d = 260\cdot(1-10^{-0.1Ad})$, $T_v = 283\cdot(1-10^{-0.1Av})$

A series of 10/33/90 GHz radiometer experiments at two elevations (0.25 and 3.80 km) was reported in [3]. A typical set of zenith brightness results T_X for clear conditions is given in Table 1. The MPM program was applied to a mean July climate for the general area specifying P(h), T(h) and v(h) profiles over the range h = 0 to 30 km. By numerical integration, dry air zenith attenuation A_d, water vapor attenuation A_v, and cloud attenuation A_W have been calculated for various vapor (V) and droplet (W) path contents (see Table 1). By assuming average medium temperatures of 260(dry)/283(vapor)K and vapor contents of V = 14 and 4.7 mm, it was possible to reproduce in consistent manner all six reported T_X values. The factor x_W indicates the enormous increase in attenuation should a small amount of V convert into W [7,8]. Predictions by MPM have been tested with a variety of reported cases [1]. Fairly good agreement was found over a wide range of parameter choices; frequencies varied between 2.5 and 430 GHz and meteorological conditions as follows: P = 70 to 101 kPa, T = -10 to 35°C, v = 0 to 20 g/m^3 and V = 0 to 30 mm.

In an effort to improve the MPM program, we conducted quantitative laboratory studies of pressure and temperature dependencies of water vapor (e) and moist air (P) attentuation α in the W3 frequency range [4]. Recently, with improved instrumentation, pressure scans of α (e,P) were repeated at 137.9 GHz and T = 286 to 315 K for e ($\leq$ 90% RH) and P $\leq$ 110 kPa. A first fit of the extensive parametric data set yielded the following preliminary result:

$$\alpha = (15\ e\theta^{0.8} + 0.44\ ep\theta)\ 10^{-2} \quad \text{dB/km}, \qquad (2)$$

where e and p = P-e are in kPa and θ = 300/T(K).

The local H_2O line base (30x) of MPM employs a VanVleck-Weisskopf shape function and makes a contribution to (2) that is represented by

$$\alpha_\ell = (0.816\ e^2\theta^3 + 0.174\ ep\theta^3)\ 10^{-2} \quad dB/km. \qquad (3)$$

A continuum term $\alpha_c = \alpha - \alpha_\ell$ must be formulated to account for the measured attenuation α. The MPM continuum reads

$$\alpha_c = (14.2\ e^2\theta^{9.0} + 0.27\ ep\theta^{1.9})\ 10^{-2} \quad dB/km. \qquad (4)$$

All three results (2)-(4) follow the analytical form [4]

$$\alpha_{Th} = k_S\ e^2 + k_f\ ep \quad \text{and} \quad m = k_S/k_f, \qquad (5)$$

as is expected from self- and airbroadened contributions of the rotational spectrum of H_2O, where m indicates the broadening efficiency of H_2O with respect to AIR. The rotational spectrum extends beyond 15 THz, displaying many lines which are stronger than those falling with their center frequencies below 1 THz (local line base of MPM). Hence (3) is not a full account of H_2O line contributions. From line center studies it is known that m_1 (H_2O/AIR) = 4.80 and m_2 (H_2O/N_2) = 4.41, proving nitrogen more effective (m_1/m_2 = 1.088) than air in broadening H_2O lines. When the experiment leading to (2) was repeated using nitrogen, it yielded at θ = 1 (300 K):

$$k_f\ (N_2))/k_f(AIR) = 1.09(2). \qquad (6)$$

This surprising result indicates that foreign-gas-broadening is the same in far-wing ranges and at line cores. Now, if a similar behavior for self-broadening is assumed, one can write

$$k_S = m_1\ k_f\ \theta^{2.5} = 2.11 \times 10^{-2}\ \theta^{2.5}, \qquad (7)$$

which leaves the substantial amount

$$k_S^x = 0.15\ \theta^{8.8} - 0.021\ \theta^{2.5} = 0.13\ \theta^{9.6} \quad dB/km(kPa)^2 \qquad (8)$$

to an unidentified absorber. An Arrhenius plot ($\ln k_S^x$ - vs - 1/T) determines a characteristic energy of 5.90 kcal/mole. Based on (7) and (8), the observed attenuation α (2) can be separated into three terms

$$\alpha = (2.11\ e^2\theta^{2.5} + 0.44\ ep\theta)10^{-2} + 0.13\ e^2\theta^{9.6} \quad dB/km \qquad (9)$$

Equation (9) confirms findings in the 30 THz window by Loper et al. [5], who identified the additional absorber to be a dimer $(H_2O)_2$. On the other hand, there is a line shape theory capable of predicting, with empirically adjusted parameters, far-wing behavior of the H_2O spectrum, leading to comparable results [6].

The laboratory result (2) calls for a revision of the Millimeter-Wave Propagation Program, MPM. An experimental water vapor absorption term is formulated on the basis of (4). It follows with f in GHz that

$$N_e''(f) = \alpha_c/0.182f = f(41\ e^2\theta^9 + 0.78\ ep\theta^{1.9})\ 10^{-6} \quad ppm. \qquad (10)$$

Equation (10) replaces the continuum contribution (14a) in [1], predicting lower water vapor attenuation rates at warm temperatures (high absolute humidites e or v). The laboratory studies are still in progress and (10) should be viewed as an interim solution. We like to emphasize that (4), (10) are only valid in conjunction with the local H_2O line base of MPM described in [1].

REFERENCES

[1] H. Liebe, Radio Sci., 20(5), 1069-1089, 1985.
[2] T. Manabe et al., Int'l. J. IR & MM Waves, 6(4), 313-322, 1985.
[3] J. Costales et al., Radio Sci., 21(1), 47-55, 1986.
[4] H. Liebe, Int'l J. IR & MM Waves, 5(2), 207-227, 1984.
[5] G. Loper et al., Aerospace Coop. Report SD-TR-84-14, May 1984.
[6] M. Thomas and R. Nordstrom, Appl. Optics, 24(21), 3526-3530, 1985.
[7] H. Gerber, NRL Report 8956, December 1985.
[8] S. Gathman, Opt. Eng., 22(1), 57-62, 1983.

CORRELATED MEASUREMENTS OF ATMOSPHERIC SIGNALS AT 10, 33 AND 90 GHZ

J. Costales, G. De Amici*, S. Levin, H. Pascalar**, G. Smoot, and C. Witebsky
Lawrence Berkeley Laboratory and Space Sciences Laboratory
University of California Berkeley, CA 94720

Coordinated ground-based measurements of atmospheric emission have been made at several different frequencies (10, 31.4, 33, and 90 GHz) and several different angular scales, at altitudes of 250 m and 3800 m. These measurements have produced results important for both ground-based and space-based observations of and through the atmosphere. In particular, these results provide statistics about atmospheric fluctuations on time scales ranging from seconds to days.

As part of a larger effort to measure the cosmic microwave background radiation spectrum, we have made frequent simultaneous measurements of the microwave thermal emission from the atmosphere at 10 GHz, 33 GHz, and 90 GHz in Berkeley, CA and at the Barcroft laboratory of the White Mountain Research Station in California. Typical good weather values of the atmospheric antenna temperature measured in Berkeley (250 m) are 3.18±0.29 K, 12.3±0.3 K and 34.4±0.5 K at 10, 33, and 90 GHz respectively. Corresponding values at White Mountain (3800m) are 1.11±0.04 K, 4.48±0.18 K, and 11.0±0.1 K. Correlations among the different frequencies are well explained by a simple model in which $T_a = a_\nu + b_\nu W$, where a_ν is the oxygen term, b_ν is the water coefficient, and W [mm] is the precipitable water content. Linear correlations were seen among the atmospheric antenna temperatures at the three different frequencies, and the slopes of these relations place restrictions on models which predict the values of a_ν and b_ν.

Using the three radiometers mentioned above, as well as a parabolic dish system operated at 31.4 GHz, we have observed atmospheric fluctuations from the Berkeley site by measuring the atmospheric antenna temperature difference between two zenith angles. We sampled various angular scales. The dish system was used to sample angular scales of a few degrees, while the other radiometers were employed at larger angular separations. A typical measurement consisted of a sequence of 4096 consecutive 1-second samples from each of several radiometers comparing the same two patches of sky. These measurements show strong correlations among the different frequencies, and are consistent with the hypothesis that water fluctuations dominate other effects.

Taking the fluctuations to be due entirely to atmospheric water, we find the RMS variation (cm) for atmospheric water to be $(5.0 \pm 2.5) \times 10^{-3} t^{1.3\pm0.3}$ for times from 1–10^3 seconds. The Kolmogorov turbulence theory predicts a power spectrum given by

$$|P(H_2O)| = Cf^{-(\alpha+1)/2} D^{\alpha/2}$$
$$= Cf^{-1.33} D^{0.83} \quad \text{for} \quad D < 5.6 \text{ km}.$$

Data taken at a variety of different zenith angles with the radiometer systems mentioned above are consistent with the Kolmogorov theory, but do not place stringent limits on the spatial dependence.

*On leave from Istituto di Radioastronomia/CNR, Bologna, Italy
** Aerojet ElectroSystems

POSTER PAPERS

Aperture-Averaged Statistics of Laser Intensity Fluctuations In Strong Turbulence

P1

E. Azoulay, Z. Azar: Soreq Nuclear Research Center, Department of Atmospheric Optics, Yavne 70600, Israel; and M. Tur: School of Engineering, Tel-Aviv University, Tel-Aviv, Israel.

The statistics of intensity scintillations of a laser beam, propagating through atmospheric turbulence, has been extensively studied in recent years for point receivers. While the log-normal distribution is fairly adequate in the weak turbulence regime[1-2], quite a few distributions have been suggested to describe strong optical scintillations: from the Rayleigh distribution (for very strong turbulence), through the Γ- K- and the recently introduced I - K distributions[2-6]. Most practical applications, however, use detectors with finite apertures, rather than point receivers, and the statistics of the aperture-averaged scintillations is vital for system analysis. Fried et. al.[1] measured the cumulative distribution function of P_Σ, as a function of the aperture diameter, under weak scattering conditions, and found it to be very close to log-normal for all aperture sizes.

If $I(\vec{r})$ is the random (point) spatial intensity distribution over the aperture, then the aperture-averaged power is

$$P_\Sigma = \int_\Sigma I(\vec{r})d\vec{r} = \sum_{i=1}^{n} I(\vec{r}_i)\Delta\vec{r}_i \qquad (1)$$

where the aperture was divided into n cells, with dimensions smaller or equal to the correlation length. Thus, to evaluate the probability distribution function of P_Σ one needs to know the multi-dimensional joint probability distribution of $I(\vec{r})$ (up to order n), along with the different correlations distances, and to have the capability to carry out the required n-dimensional integration. Bearing in mind that the analytical forms of the Γ- K- or I - K distributions are fairly complicated, the above mentioned two requirements render any such attempt virtually impossible.

In this paper we propose an empirical, Monte-Carlo approach to evaluate the probability distribution function of the aperture-averaged power, P_Σ, for at least a certain class of point probability distributions.

For simplicity, we shall approximate the intensity normalized spatial covariance by[2]

$$Cov_I(\vec{r}) = \begin{cases} 1 & |\vec{r}| \le \rho_p \\ b_T & L_o > |\vec{r}| > \rho_p \\ 0 & |\vec{r}| \ge L_o \end{cases} \qquad (2)$$

$\rho_p = 0.36\sqrt{\lambda L}/\sigma_1^{6/5}$ is the transverse correlation distance, b_T is the height of the correlation tail and L_o is the outer scale, normally much bigger than the aperture size. The point probability distribution function of $I(\vec{r})$, is now decomposed into two random components, satisfying the following conditions: (a) $I = I_1 + I_2$; (b) I_1 is independent of $\vec{r}$ and $Var(I_1) = b_T \cdot Var(I)$; (c) I_1 and I_2 are statistically independent.

Consider the often used Γ distribution function[3], which is the characteristic distribution of a random walk in one dimension and thus characterizes the power fluctuations of an incoherent source. It is a fair approximation to a laser beam propagating over distances much longer than

its coherence length. Its characteristic function is easily expressed as a product

$$\Phi(u) = \left[1 - i\frac{u}{\beta}\right]^{-\alpha} = \left[1 - i\frac{u}{\beta}\right]^{-\alpha_1}\left[1 - i\frac{u}{\beta}\right]^{-\alpha_2} = \Phi_1(u)\cdot\Phi_2(u) \qquad (3)$$

I_1 and I_2 will be both Γ-distributed variates with $\beta_{I_1} = \beta_{I_2} = \beta$ and $\alpha_{I_1} = b_T/\mathrm{Var}(I)$ and $\alpha_{I_2} = (1-b_T)/\mathrm{Var}(I)$. We now divide the aperture into n small squares, each of length ρ_p. We further assign random intensities to the various cells according to the following rule: we draw, at random, a number from the I_1 distribution and assign it to all cells. Then, numbers are drawn from the I_2 distributions, and randomly assigned to the different cells. The intensity at each cell is the sum of I_1 and I_2. Under the above mentioned conditions and by repeating this drawing procedure many times, it can be readily shown that the resulting $I(\vec{r})$ is Γ-distributed with the assumed correlation function, where α and β are determined by the mean and variance of the distribution.

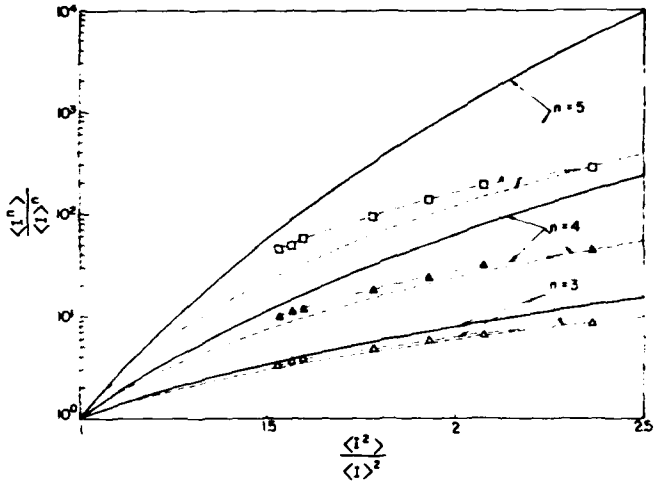

Fig. 1: Computed values of the aperture averaged normalized moments $\langle I^n \rangle / \langle I \rangle^n$ for n=3-5 are compared with the values expected from various model distributions, having the same second moments $\langle I^2 \rangle / \langle I \rangle^2$. The continuous lines indicate the moments obtained from log-normally distributed intensity fluctuations. The dashes lines indicate moments from Γ-distributed intensity fluctuations. Data were computed for $\sigma_I^2 = 20$

Using this scheme we were able to perform multiple iterations, each yielding one realization of $I(\vec{r})$ at the receiver's plane and the total power, collected by the receiver's aperture, P_I , was calculated from Eq. (1). The

first five statistical moments of P_Σ were then evaluated as a function of the integrated turbulence and the aperture's diameter.

Figure 1 depicts the results obtained for aperture diameters in the range 2mm-10mm. The results show gradual departure from the point receiver distribution function toward the log-normal distribution function, so that for rather small apertures one can use the log-normal function as a good approximation even in the strong turbulence regime.

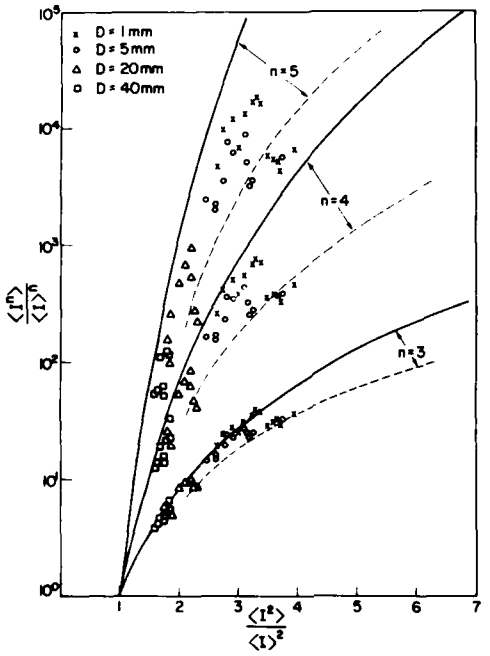

FIG. 2. Measured values of the aperture averaged normalized third, fourth, and fifth moments are compared with the values predicted by the various model distributions, having the same normalized second moments as the experimental data. The continuous lines indicate the moments expected from log-normally distributed intensity fluctuations and apply to all values of normalized second moment. The dashes lines indicate moments expected from K-distributed fluctuations and apply to values of the normalized second moment greater than 2.

Measurements of the same moments of the aperture-averaged intensity distribution function were obtained using a set-up, described elsewhere[7]. The measurements were made with 3mrad He-Ne laser beam propagated through 1000m of a fairly homogeneous, 1.8m high, atmospheric layer. Simultaneously with the probability distribution measurements, we also recorded the index-of-refraction structure constant C_n^2, by monitoring the normalized variance σ_I^2 of a second He-Ne laser beam propagating over a short path length[8].

During the experiments, the index-of-refraction structure constant attained values in the range $10^{-13} - 10^{-11}$ $m^{-2/3}$, which correspond to strong turbulence conditions.

After the subtraction of the dc background level the corrected digitized records of the received signal was used to compute the first five statistical normalized moments of the beam intensity $< I^n >/< I >^n$. This normalization process permits us to discern the inherent statistics of the scattering process independently of the power of the laser beam.

Figure 2 depicts the measured values of the normalized moments $< I^n >/< I >^n$ for n=3-5 as a functions of the normalized second moment $< I^2 >/< I >^2$, for four aperture sizes (D=1,5,20,40mm). For purposes of comparison with theoretical models, we also show the log-normal and K-distribution curves for those normalized moments. Many of the data obtained with the point receiver (D=1mm) correlate well with previously published results[4-5], for values of $< I^2 >/< I >^2 < 3.5$ the data indeed substantiate the log-normal model while showing big discrepancies with this model for large values of the mean-square fluctuations. The K-distribution appears to fit many of the point receiver data for values of $< I^2 >/< I >^2 \geq 3.5$. The aperture averaged (D=5,20mm) normalized moments clearly shows early trend toward the log-normal model, i.e. the passing level from log-normal model to the K-distribution decreases (for D=20mm the passing level is 2.2). The data obtained with the larger aperture size D=40mm remain log-normally distributed for all values of the mean-square fluctuations that were obtained in the experiment, so that even in the deep-saturation regime the aperture-averaged intensity distribution function can be adequately described by the log-normal distribution function. While data scatter increases with the order of the displayed moment, plotting of the different order normalized moments of an unknown distribution, as a function of $< I^2 >/< I >^2$, is often advantageous to the plotting of the cumulative distribution, since it delineates the subtle differences between statistical distributions, particularly in the tails. Anyway, scattering can be reduced somewhat by taking more sample points from which the calculation are made.

In summary, the proposed method enabled us to show that under strong scattering conditions the point receiver power statistics is considerably different from the aperture averaged power distribution function. Moreover, the aperture-averaged intensity distribution function can be adequately described by the log-normal distribution function. The described method is empirical in nature. Its mathematical justification and validity, as well as generalizations to probability distribution functions other than the K-distribution is under current investigation.

References

1. D. L. Fried et. al., J. Opt. Soc. Am., 57, 787 (1967)
2. R. Fante, Proc IEEE, 63, 1669 (1975)
3. E. Jakeman, J. Phys. A., 13, 31 (1980).
4. R.L. Phillips and L.C. Andrews, J. Opt. Soc. Am., 71, 1440 (1981)
5. G. Parry and P. N. Pusey, J. Opt. Soc. Am., 69, 795 (1979)
6. R.L. Phillips and L.C. Andrews, J. Opt. Soc. Am., 2, 160 (1985)
7. Z. Azar et. al., J. Appl. Opt., 24, 2401 (1985)
8. R.J. Hill and S.F. Clifford, J. Opt. Soc. Am., 68, 892 (1978)

PRELIMINARY RESULTS FROM THE ENEA LIDAR SYSTEM P2

R. Barbini, A. Ghigo[+], M. Giorgi, K.N. Iyer[o], A. Palucci [+] and S. Ribezzo
ENEA, TIB, Divisione Fisica Applicata, P.O. Box 65, 00044 Frascati (Rome), Italy

INTRODUCTION

The remote sensing of gaseous species in the atmosphere using Differential Absorption Lidar (DIAL)[1] is well recognized as a very sensitive and long range technique [2]. Since most of the atmospheric pollutants have specific absorption bands between 8 and 12 μm, this is a very promising spectral window for atmospheric DIAL. Employing coherent (heterodyne) detection technique CO_2 Lidar is best suited for accurate wind measurements [3]. Hence a CO_2 Lidar system is being developed at the ENEA Centre at Frascati (Rome) with the primary objective of atmospheric pollution monitoring.

PRINCIPLE AND RELEVANT LIDAR EQUATION

In the DIAL technique the laser transmits at a high and a low absorption frequency of the species under investigation. The two wavelengths are so chosen as to minimize the interference effects by other gases such as water vapour. In the range resolved DIAL the return signal is provided by the naturally occurring aerosols in the atmosphere. The average gas concentration in the range cell ΔR [4] is given by

$$\bar{n}(R) = \frac{1}{2\,\Delta\sigma\,\Delta R} \ln \frac{P_1(R)\,P_2(R+\Delta R)}{P_2(R)\,P_1(R+\Delta R)} \qquad (1)$$

where P_1 and P_2 are the received powers at the high and low absorption frequencies respectively, normalized to the corresponding transmitted powers, $\Delta\sigma$ is the differential absorption cross section, R the range and ΔR the range resolution . For sensitive and high range resolution measurements over long ranges the LIDAR transmitter should have high power output and narrow pulsewidth.

THE ENEA LIDAR FACILITY

The dual laser DIAL system under development is schematically shown in Fig. 1 and its characteristics are listed in Table I.

The laser head with the required characteristics has been developed using a SFUR (Self Filtering Unstable Resonator)[5] TEA CO_2 laser cavity, which emits a single transverse mode (TEM_{oo}) radiation with low divergence employing a limiting intracavity aperture at the confocal point which also

serves as the output coupler [6] (Fig. 2). Single Longitudinal Mode (SLM) locking is achieved by injecting a CW CO_2 into the laser cavity. The measured performance of this cavity is included in Table I.

The return signals from either the target or naturally occurring aerosols are collected by a telescope (Fig. 2) and focussed onto the HgCdTe detector cooled to lN_2 temperature. The detected signal is preamplified, digitized and stored pulse by pulse in a PDP 11/24 Computer via the CAMAC interface which also controls the measurement cycle, the time delay between the two laser shots, the movement of the telescope and stores other housekeeping system parameters.

PLANNED CALIBRATION EXPERIMENTS

a) Differential absorption

The value of σ, the differential absorption cross section, to be used in eq. (1) is very critical and depends on the laser line shape, the pressure broadening effect and the interference by other species. Therefore, actual measurement for the given laser parameters using laboratory absorption cells of the gas under investigation is necessary rather than employing the widely varying values quoted in the literature.

The transmission of laser radiation with power P_o through an absorption cell of length L may be expressed as

$$P_c = P_o \exp(-\sigma N_c L) \qquad (2)$$

where N_c is the concentration of absorbing gas molecules in the cell, P_c is the power after transmission through the cell. Using eq.(2) for the high absorbing line and a similar equation with P_c' and σ' for corresponding quantities in the low absorption line, we can write

$$\Delta\sigma = \frac{1}{N_c L} \ln\left(\frac{P_c}{P_c'}\right) \qquad (3)$$

which can be used in eq. (1). We propose to make the measurements of $\Delta\sigma$ for the different lines of the CO_2 laser in the 10 μ region and these results will be reported.

b) Measurements using targets

Before undertaking actual DIAL measurements of atmospheric gases, it is necessary to employ remote calibration targets and the laser return from these targets should be quantitatively analyzed as a necessary part of Lidar performance estimate. Uncertainties are introduced by strong signal fluctuations due to speckle, glint and atmospheric turbulence effects. We

intend to make measurements of the laser returns at different CO_2 wavelengtns using standard calibration targets such as polyethylene foam, 400 grit Silicon carbide sandpaper and topographic targets such as treetops. From a study of the normalized variance of the received intensity the probability density functions (PDF) can be estimated, which gives a measure of the uncertainty of the measurement for different types of targets.
Furthermore the effect of signal averaging on reducing these uncertainties will be investigated. A study of the temporal correlation of the normalized laser returns would give an estimate of the effect of changes of the background atmospheric absorption which is neglected in eq. (1).

REFERENCES AND FOOTNOTES

1) Baumgartner R.A. and Byer R.L.: Opt.Lett. 2, 163 (1978)
2) "Optical and Laser Remote Sensing", Killinger D.K. and Mooradian A. eds. Springer-Verlag , Berlin 1983
3) Brown D., Callan R. et al.: Proc.3rd Topical Meeting on Coherent Laser Radiation: Technology and Applications, Great Malvern (UK), July 1985, pp. 30
4) Schotland R.M.: J.Appl.Meteorol. 13, 71 (1974)
5) Gobbi P.G. and Reali G.C.: Opt.Comm. 52, 195 (1984)
6) R. Barbini et al.: LXXI SIF Annual Congress, Trieste, October 1985, p. 143; Lasers'85, Las Vegas (USA), December 1985; and submitted for publication.

(+) ENEA Guest

(°) ENEA Guest. Permanent address: Phys.Dept., Saurashtra University, 360005 Rajkot (India).

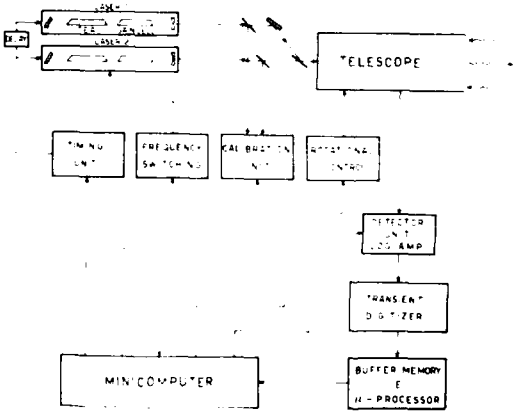

Fig. 1 - Layout of the LIDAR/DIAL facility

TABLE I

CO_2 LIDAR/DIAL SYSTEM

LASER	
CO_2 source grating tuned	λ = 9 ÷ 12 um
Pulse energy	E = 2.7 J TEM_{00}
Pulsewidth	T = 80 ns
Pulse repetition rate	f = 1 ÷ 5 Hz
Beam divergence (half angle)	$\theta \approx 0.65$ mrad
RECEIVER	
Telescope	d = 33 cm
Newton with spherical mirror	f # = 3
FOV (adjustable)	FOV = 1 mrad
Detector: HgCdTe @ 77°K	
Area = 1 x 1 mm^2	
NEP 10^{-8} - 10^{-12} W	
TRANSIENT DIGITIZERS	
Dynamic range	8 bits, 9 bits
Sampling rate	100 MHz, 1 GHz

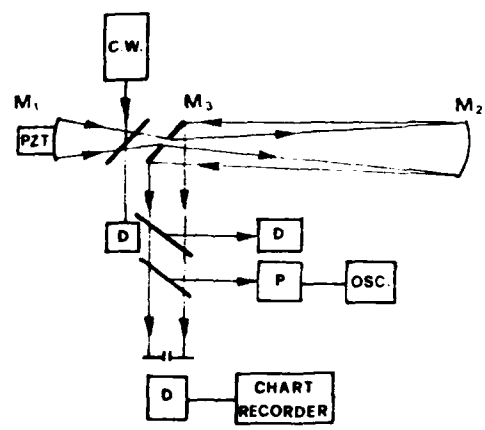

Fig. 2 - The CO_2 SFUR resonator: M_1, M_2, M_3 are mirrors; D = pyroelectric detector; P = photon drag detector; C.W. = CO_2 injection laser; PZT = piezo-transducer.

Henry G. Booker
Department of Electrical Engineering and Computer Sciences
University of California San Diego
La Jolla, CA. 92093, USA

and

Hari Om Vats
Physical Research Laboratory
Ahmedabad-380009, India

Introduction. Based on the work of Booker et al (1985), and of Booker and MajidiAhi (1981), Booker and Vats (1985) (Hereafter referred as BV) have investigated the laser propagation near ground level for divergent terminals at equal height (2 meters) above a curved earth in an atmosphere possessing rms fluctuations of temperature from 0.03^0 C to 3^0 C. These rms fluctuations of temperature correspond to rms refractive index variations of 10^{-7} to 10^{-5}. Four propagation ranges namely 1, 2, 4 & 8 Kms were considered. Here we shall summarize the main results of BV. Reader may refer BV for details about the procedure used in the calculations.

Results and discussions. Intensity spectra and scintillation index S_4 were calculated for several distances between Transmitter and receiver. The value of S_4^2, the square of scintillation index, are shown in Table 1.

Figure 1 shows intensity spectra for range of 1 kilometer. The scale of the irregularities (wavelength/2π) is shown along the upper abscissa, and the values of the outer scale Lo, the inner scale Li and the Fresnel Scale F are marked. Spectra are shown for values of $\overline{(\Delta\phi)^2}$ from 10 to 10^8 radian^2. For sufficiently small values of $\overline{(\Delta\phi)^2}$, the intensity spectra show a maxima at approximately the Fresnel scale. In these circumstances the important phenomenon is difractive scattering by irregularities whose size is of the order of the Fresnel scale and less. The intensity correlation scale in the reception plane is then of the order of F, and scattering is through angles of the order of $(\lambda/2\pi F)$. However, when $\overline{(\Delta\phi)^2}$ exceeds unity, refractive scattering by large-scale irregularities comes into play, involving deviations through angles of the order of $(\lambda/2\pi Lo)$.

Table 1. Values for S_4^2, the square of the scintillation index

$\overline{(\Delta\Phi)^2}$ (Radians^2)	Range in Kilometers			
	0.05	1	2	4
10^2	0.004	0.007	0.014	0.04
10^3	0.04	0.07	0.17	0.38
10^4	0.33	0.55	0.87	1.10
10^5	1.19	1.21	1.17	1.15
10^6	1.25	1.19	1.15	1.09
10^7	1.20	1.14	1.08	1.05
10^8	1.10	1.08	1.06	1.04

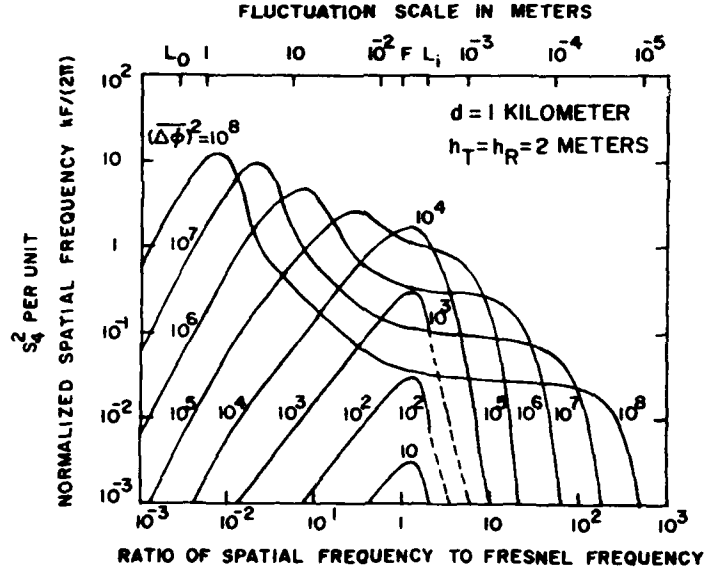

Fig. 1: Illustrating the spatial spectrum of intensity fluctuations for a range of 1 kilometer.

Successive unit increase of $(\Delta\phi)^2$ cause these deviations to add up on a root-mean-square basis (Booker et al 1985). This leads to an accumulated rms scattering angle of the order of $(\lambda/2\pi l)$ where, for the Kolmogoroff spectral index, the value of l is given by

$$l = 0.6 \frac{L_o}{[\overline{(\Delta\phi)^2}]^{3/5}}$$

Diffractive scattering dominates refractive scattering so long as the accumulated refractive scattering angle is less than the diffractive scattering. Thus, when $(\Delta\phi)^2$ is large enough the refractive scattering dominates and character of the intensity spectrum changes. BV provided a detailed procedure for the estimation of the key scintillation parameters, these are easily calculated from the formulae when the following quantities are specified : (i) the rms fluctuation of temperature which is related to the rms fluctuation of refractive index at optical frequencies (Crain and Gerhardt 1952), (ii) the height of the terminals which decides the outer scale of the irregularities (iii) the range, and (iv) the wavelength. Consider a rms fluctuation of temperature of 1^0 C, terminal heights of 2 meters and propagation ranges of 1, 2, 4 and 8 kilometers. Table 2 shows the key scintillation parameters for a He-Ne laser operating on a wavelength of 6.33×10^{-7} meter.

References

Booker H.G. and H.O. Vats (BV)
Radio Science 20, 833, 1985 (References therein).

Booker H.G. and G. MajidiAbi, JATP, 43, 1199, 1981.

Booker H.G., J. Ferguson and H.O. Vats, JATP, 47, 381, 1985.

Crain C.M. and Gerhardt J.R.
Proc. Inst. Rad. Eng. 40, 50, 1952.

Table 2. Scintillation parameters for transmission at a wavelength of 6.33×10^{-7} meter between terminals at a height of 2 meters in atmosphere with a rms temperature fluctuation of 1° C.

Parameter \ Kms:-	1	2	4	8
Outer scale (meters)	2.0	2.2	1.8	1.4
Fresnel scale (meters)	7.1×10^{-3}	1.0×10^{-2}	1.4×10^{-2}	2.0×10^{-3}
RMS Phase fluctuation (radians)	8.8×10^{2}	1.2×10^{3}	1.7×10^{3}	2.1×10^{3}
Intensity correlation scale (meters)	3.5×10^{-4}	2.3×10^{-4}	1.5×10^{-4}	8.7×10^{-5}
Twinkling scale (meters)	0.14	0.44	1.4	4.6
RMS fluctuation in arrival angle (radians)	2.9×10^{-4}	4.4×10^{-4}	6.8×10^{-4}	1.2×10^{-3}
Fractional correlation bandwidth	2.4×10^{-3}	5.3×10^{-4}	1.1×10^{-4}	1.9×10^{-5}
Actual correlation bandwidth (Hz)	1.2×10^{12}	2.5×10^{11}	5.2×10^{10}	8.9×10^{9}
Fading rate for 1 m/s cross wind (Hz)	9.1×10^{2}	1.4×10^{3}	2.1×10^{3}	3.7×10^{3}
Twinkling rate for 1 m/s cross wind (Hz)	2.2	0.73	0.23	0.069

Statistics of Laser Beam Propagation through a Turbulent Atmosphere

by R.H. Clarke, P. Kara and H-Y. E. Ng.
Imperial College of Science and Technology, London

Introduction

The beam propagation method is amenable to both analysis and simulation. Its application to the analysis of laser-beam propagation through a turbulent atmosphere, using Papoulis' optical ambiguity function [1], was presented by Clarke [2]. A computer simulation of essentially the same phenomenon had been given earlier by Inggs and Clarke [3].

The Beam Propagation Method

When diffraction, whether random or regular, can be described as "forward scatter" or "narrow angle", then the parabolic equation approximation applies and the beam propagation method can be used. This divides the medium into a series of slab-like sections at right angles to the direction of the beam. Then each section is traversed twice. The first time, on the assumption that it is uniform, diffraction is allowed to occur. Then the accumulated phase, due to rays passing through the irregularities contained within the section, is calculated and imposed all at once at the exit plane of the section.

The beam propagation method can be expressed mathematically as follows, in the two-dimensional $(x-z)$ space with the laser beam launched at the plane $z=0$ into the region $z>0$. If the width of the first slab section is Δz_1, then any one of the electromagnetic field components can be written,

$$f(x, \Delta z_1^+) = f(x, \Delta z_1^-) \exp\{j\Phi(x)\} \qquad (1)$$

in which $f(x, \Delta z_1^-)$ is the field diffracted in the slab (assumed momentarily to be uniform) arising from the field $f(x, 0)$ over the entry plane. The phase $\Phi(x)$ superimposed at the exit plane of the section is given in terms of the departure $n_1(x, z)$ of the refractive index from its mean value by

$$\Phi(x) = -k \int_0^{\Delta z_1} n_1(x, z)\, dz \qquad (2)$$

where k is the mean wavenumber and a time dependence $exp(j\omega t)$ is assumed. In this first section the field over the entry plane will be the fundamental-mode laser transmitter output

$$f(x,0) = f_0 \exp\left\{-\frac{x^2}{w_0^2}\right\}. \qquad (3)$$

Simulation

Fig. 1 shows the results of a simulation [3] based on the beam propagation method. The simulation was aimed at elucidating the behaviour of a microwave beam in very strong turbulence. (The results are however applicable to a laser beam propagating several kilometres through atmospheric turbulence). The field distribution of the original microwave beam is Gaussian, as in eqn. (3), with w_0 = 3.6 m. The wavelength λ = 1 cm and the field is allowed to diffract over slabs of width Δz = 1 km. Fig. 1(a) shows the development of the beam intensity profile over the planes at 2,4,6,8 and 10 km. from the transmitter in the absence of turbulence. In Fig. 1(b) profiles are shown over the same planes when turbulence is present. The turbulence induces a random phase which is imposed over the exit planes of each 1-km slab, in accordance with equ.(1). It is assumed to be a Gaussian process (by the Central Limit Theorem), to have an r.m.s. value for each slab of 0.28 rads., and to have a lateral scale size of 50 cm.

Statistics of the Field

Theory [2] says that the mean (i.e. coherent) field will be reduced below the field in the absence of turbulence by the factor $\exp(-\sigma_\phi^2/2)$ where σ_ϕ is the r.m.s. phase fluctuation, in each slab. Thus in the simulation of Fig. 1 this factor accumulated over 10 slabs is 0.676. The evidence of this can be seen in the final profile of Fig. 1(b), where the signal level, though random, is at a higher level in the region of the original beam. The phase fluctuation, in traversing the beam, over the exit plane of the final slab in the same simulation as in Fig.1, is shown in Fig.2. The phase fluctuates much less within the beam. Detailed examination shows that the field is Rayleigh - distributed with uniformly distributed phase in $(-\pi, \pi)$ outside the beam, but has a Nakagami-Rice distribution within it.

Mean Intensity Profile

The formulas for the mean intensity (and autocorrelation) of the field [2,4] have been evaluated by numerical integration. They have been applied to the geometry of B.G. King's experiment [5] for which the transmitted laser beam had a waist w_c of 8 cm. Fig. 3 shows the dependence of beam waist on distance from the transmitter, both in the presence and absence of turbulence. In the presence of turbulence the inital Gaussian profile becomes

modified with increasing distance, as Fig. 1(b) shows. But eventually, when the coherent part has become insignificant, the beam acquires an average Gaussian shape, as King observed.

The turbulence parameters were adjusted [6] to fit King's measured beam-waist value of about 3 m at a distance of 37 km. This implied that $\sigma_\chi = 1$ rad. after a distance of 1 km, and the associated turbulence parameters were an r.m.s. refractive-index fluctuation of 3×10^{-6} and a scale size of 1 cm.

Conclusion

Simulations of a propagating laser beam and numerical integration of a formula for mean intensity have served to clarify the picture of the statistical structure of the beam in the presence of statistically uniform turbulence. Within the original beam, out to a distance of 1 or 2 km, the field is represented by a Rayleigh-distributed phasor plus a constant (the coherent part of the field). Outside this region the field is simply Rayleigh-distributed. However, if the turbulence is non-stationary, which will certainly be true over tens of kilometers, the complex-Gaussian character of the field will change to being lognormal [7,8].

References

1. A. Papoulis, "Ambiguity Function in Fourier Optics", J. Opt Soc. Amer., 64, No.6, June 1974, pp. 779-88.

2. R.H. Clarke, "Analysis of Laser Beam Propagation in a Turbulent Atmosphere", A.T. and T. Tech. J., 64, No.7, September 1985, pp. 1585-1600.

3. M.R. Inggs and R.H. Clarke, "A Computer Simmulation of Propagation through a Tenuous Random Medium", Proc. IEEE-URSI Symp., Seattle, Washington, June, 1979.

4. A. Ishimaru, "The Beam Wave Case and Remote Sensing", in "Laser Beam Propagation in the Atmosphere", J.W. Strohbehn, ed., Springer, 1978.

5. B.G. King, P.J. Fitzgerald and H.A. Stein, "An experimental Study of Atmospheric Optical Transmission", Bell System Tech. J., 62, No.3, March 1983, pp. 607-29.

6. R. H. Clarke, "On the Interpretation of Laser Propagation Experiments", Proc. IMA Conference on Wave Propagation and Scattering, Cambridge, April, 1984. B.J. Uscinski, ed. To be published by Reidel, 1986.

7. M. Nakagami, "The m - Distribution - a General Formula of Intensity Distribution of Rapid Fading" in Statistical Methods in Radio-Wave Propagation", W.C. Hoffman, ed., Pergamon, 1960.

8. J. Kanellopoulos and R.H. Clarke, "Prediction of Cross-Polarigation Discrimination Statistics for Propagation through Spatially Non-Uniform Rain", Radio Science, 16, No.2, February, 1981, pp. 203-11.

Fig. 1

Beam amplitude profiles.
(a) No turbulence.

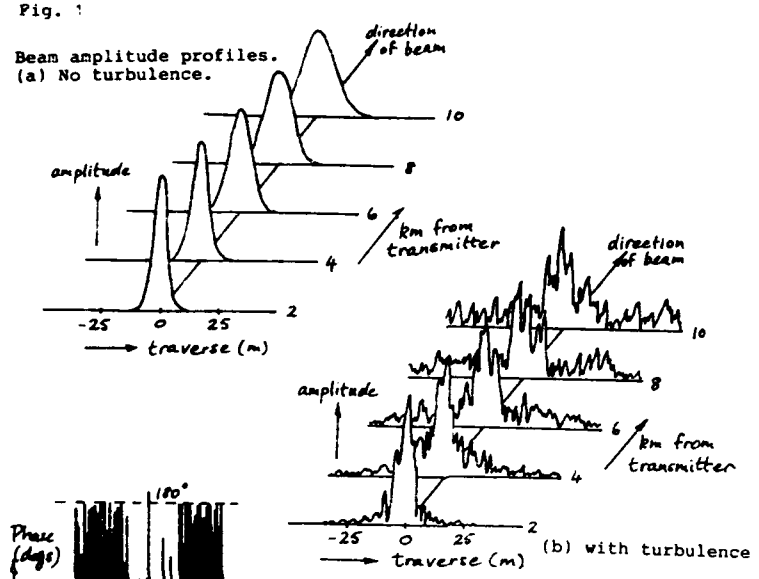

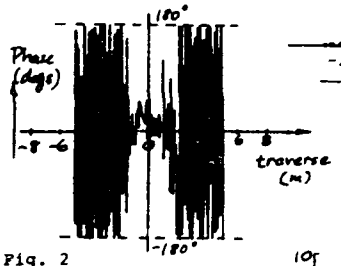

Fig. 2

Beam phase profile.

Fig. 3 Beam waist vs. distance.

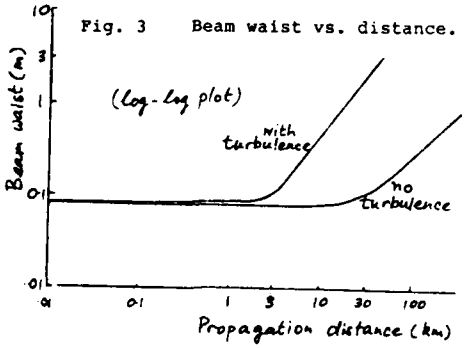

STRONG SCINTILLATION MEASUREMENTS CORRECTED FOR THE APPARATUS SATURATION P5

A. Consortini
Dipartimento di Fisica - Sezione di Fisica Superiore - Università di Firenze
Via S. Marta, 3 - 50139 Firenze, Italy - Tel. 55/470596-499828

G. Conforti
Istituto di Ricerca sulle Onde Elettromagnetiche IROE/CNR
Via Panciatichi, 64 - 50127 Firenze, Italy - Tel. 55/4378512

Intensity-fluctuation moments are measured in small and strong atmospheric scintillation. They are corrected for saturation of detecting system and compared with those of log-normal and Furutsu distributions.

The results of measurements of intensity moments of laser radiation, after a 1800 m path through the atmospheric turbulence over the city of Florence, are described. The path connects the tops of two buildings one of which is on a hill. The altitude varies considerably along the path. A beam from a 15 mW, 6328 Å, He-Ne c.w. laser, with a divergence of about 1 mrad, propagates in the atmosphere. In order to avoid the averaging effect of the aperture the intensity at a point in the central region of the propagated beam is collected by a small-aperture receiver. In practice a diaphragm, 2÷5 mm in diameter, is placed on one side of a tube ~1 m long. A detector is placed on the opposite side of the tube. The interior of the tube is black and a red glass filtre is placed in front of the diaphragm. However the background radiation is not completely removed and has to be taken into account during the elaboration of the data. The data are digitized by a 12-bit AD converter and stored on the disc of a small computer system, at the rate of ~65 samples/s. The computer is suitably programmed to speed the storage velocity.
Each measurement consists of five steps. First, a set of 5000 data of only the background radiation is collected (80 s), then three sets of 15000 data each are collected (each lasting 4 min) and finally another set of 5000 background data is collected.
The data are subsequently elaborated by the same computer to obtain the first five moments $\langle I^n \rangle$ (n=1 to 5) of the laser intensity, ([1]).
These measurements are made with a double purpose: the first purpose is to characterize the real situations which are encountered in practice when the measurements are not made in special locations such as the desert or the steppes or the laboratory. The second purpose is to investigate whether the results can be interpreted by means of the existing theoretical distributions valid for homogeneous turbulence, or if they require new theoretical efforts.
The measured moments are compared with those expected in the case of homogeneous turbulence, namely the log-normal and Furutsu distributions. We recall that the log-normal distribution is valid in the case of small scintillation, while the Furutsu distribution is one recently proposed for the case of intermediate and strong scintillation, ([2,3]). The log-normal distribution is a one-parameter distribution, generally the second normalized moment M_2. All moments of log-normal distribution

can be expressed by means of M_2. The n-th normalized moment $M^n = \langle I^n \rangle / \langle I \rangle^n$ is given by

1) $$M_n = M_2^{n(n-1)/2}$$

The Furutsu distribution is a two parameters distribution namely M_2 and Δ'. It has a cut-off value I_c, of the intensity I, above which the probability density vanishes. The cut-off intensity depends on Δ' through the relation $I_c = \langle I \rangle M_2^{(1-\Delta')/2\Delta'}$, where $\langle I \rangle$ denotes the mean intensity.
The n-th normalized moment of Furutsu's distribution is given by

2) $$M_n = M_2^{\frac{n(n-1)(1-\Delta')}{2[1+\Delta'(n-3)]}}$$

When $\Delta'=0$ the moments of the log-normal distribution are obtained. In previous works we showed [3,4] that measurements of high order moments require a system with a very large dynamic range, that is very large values of the ratio α_{DS} between saturation intensity I_{DS} and mean value $\langle I \rangle$ to be measured. Typical values are of the order of one hundred. Our system has a value of about fourty and introduces a non negligible deterioration of the moments. Such a deterioration does not spoil the information and can be considered as a sort of systematic error. We have developed an a - posteriori procedure which allows one to remove these errors from the measured moments. The procedure was developed both for Furutsu's and log-normal distribution and consists of two subsequent steps. The first step is to evaluate, theoretically, how much the intensity moments are deteriorated by the system saturation [3,4]. These moments are referred to as "deteriorated moments" and denoted by $\langle \overline{I^n} \rangle$. The second step consists of a comparison between measured and "deteriorated moments". Fig. 1 shows a comparison

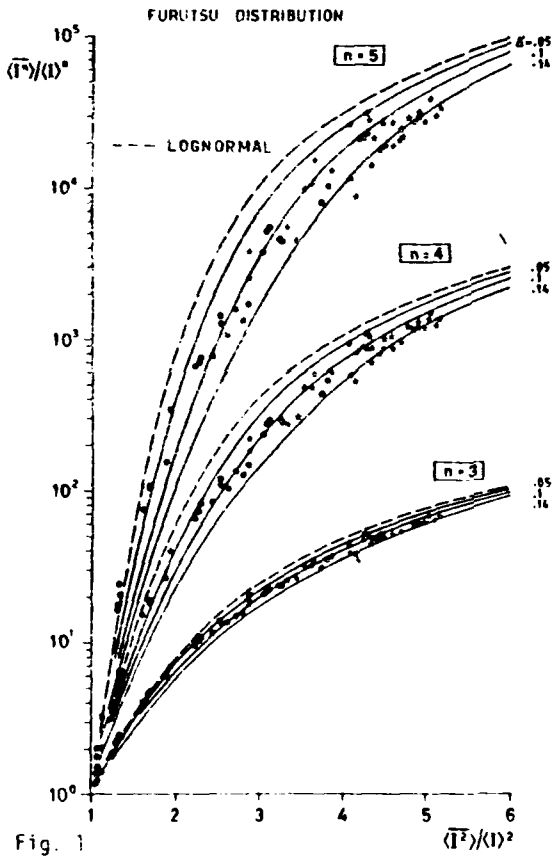

Fig. 1

between normalized "deteriorated moments" (solid and dashed curves) corresponding to $\alpha_{DS}=40$ and experimental data (dots and stars). For this value of α_{DS} one has $\sqrt{I} = \sqrt{I}$. In practice for each measurement the quantity α_{DS} is determined by using the measured mean value of the intensity and the known value of the apparatus saturation intensity. Then a fitting is carried out between the measured moments and the deteriorated moments evaluated by using the above value of α_{DS}. The fitting consists of finding the values of the parameters (M_2 and Δ' for Furutsu's or M_2 for log-normal distribution) which minimize a suitably defined fitting error. The value of the fitting error represents a test of the validity of the assumed distribution.

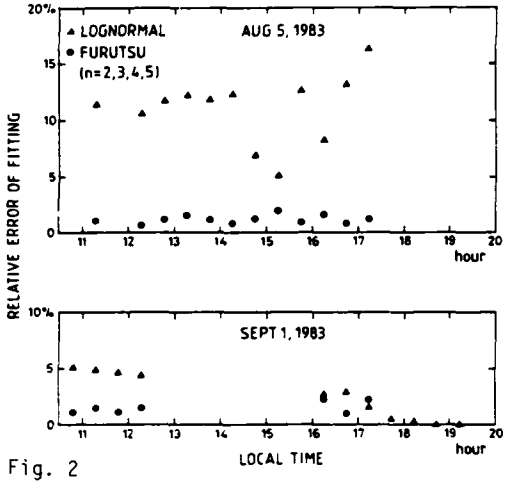

Fig. 2

In fig. 2 the fitting error is represented versus time for both Furutsu's and log - normal distribution. The fitting was carried out by using the normalized moments of order from 2 to 5. The two figures refer to two different days. During the first day and the first half of the second day strong scintillation conditions occurred. From the figures it appears that Furutsu's distribution can generally be fitted with an error much smaller than that of the log-normal distribution. Toward the end of the second day the log-normal error decreases indicating that the distribution becomes log-normal.

The main results of our investigation can be summarized as follows. The two distributions considered seem suitable to describe the intensity fluctuations also in the case of inhomogeneous turbulence. The log-normal distribution is suitable for small values of the normalized second order moment (not larger than ~ 1.8). For increasing values of the normalized second moment (from 1.8 up to ~ 5) the Furutsu distribution yields a small fitting error, much smaller than the log-normal one, and therefore appears to be an appropriate one in this range. The measured moments range in the region of strong fluctuations but do not reach the region of very strong fluctuations, the so called supersaturation region, where the normalized second moment M_2 diminishes and tends to the limiting value of 2. Furutsu's distribution does not include this region. For measurements in the region of very strong fluctuations different distribution need to be considered such a the I-K distribution recently introduced by Phillips and Andrews ([5]). This distribution seems to be a suitable candidate for all ranges of fluctuations.

REFERENCES

1- G. Conforti, A. Consortini: "Measurements of atmospheric turbulence strenght by coherent optical scintillation". Il Nuovo Cimento. C8, N° 6, 698, 1985.

2- V.I. Tatarski: "Wave propagation in a turbulent medium", Mc Graw-Hill , New York, 1961.

3- K. Furutsu: "Theory of irradiance distribution function in turbulent media. Cluster approximation" J. Math. Phis. 17, 1252, 1976. See also S. Ito and K. Furutsu: "Theoretical analysis of the high-order irradiance moments of light waves observed in turbulent air". J. Opt. Soc. Am. 72, 760, 1982.

4- A. Consortini, G. Conforti: "Detector saturation effect on higher-order moments of intensity fluctuations in atmospheric laser propagation measurements". J. Opt. Soc. Am. A1, 1075, 1984.

5- A. Consortini, E. Briccolani. G. Conforti: "Strong-scintillation statistics-deterioration due to detector saturation". J. Opt. Soc. Am. A3, 101 , 1986.

6- L.C. Andrews and R.L. Phillips: "I-K distribution as a universal propagation model of laser beams in atmospheric turbulence". J. Opt. Soc. Am. A2, 160, 1985. See also R.L. Phillips and L.C. Andrews: Universal statistical model for irradiance fluctuations in a turbulent medium. J. Opt. Soc. Am. 72, 864, 1982.

BEAM WANDERING DUE TO A THICK TURBULENT LAYER ALONG THE PATH

P6

A. Consortini, M. Mantovani
Dipartimento di Fisica - Sezione di Fisica Superiore - Università di Firenze
Via S. Marta, 3 - 50139 Firenze, Italy - Tel. 55/470596-499828
G. Conforti
Istituto di Ricerca sulle Onde Elettromagnetiche IROE/CNR
Via Panciatichi, 64 - 50127 Firenze, Italy - Tel. 55/4378512

Wandering and correlation of wandering of two laser beams, after their crossing of a thick layer of atmospheric turbulence along their paths, are theoretically investigated. An experimental laboratory test is reported.

A layer is considered to be thick if its thickness is much larger than the scale of the turbulence. The correlation and structure functions of the wandering of two beams are theoretically evaluated within the limits of the geometrical optics.For the sake of simplicity the beams are assumed to be parallel, the layer is assumed to be normal to the path and the path outside the layer is assumed to be free of turbulence.Reference is made to a coordinate system having x and y axes in the plane of the rays and x axis in the propagation direction , Fig.1. The two beam sources lie on the y axis at a distance d apart. Let P_1 denote the point where beam 1 crosses the plane x=L at the end of the path, in the absence of the turbulent layer. In presence of the layer the point $\bar{P}_1$ of the crossing fluctuates around P_1. The fluctuating differences $\eta_1 = \bar{y}_1 - y_1$ and $\zeta_1 = \bar{z}_1 - z_1$ between the coordinates of $\bar{P}_1$ and P_1 describe the wandering. In the geometrical optics approximation, one has (see e.g.ref.1):

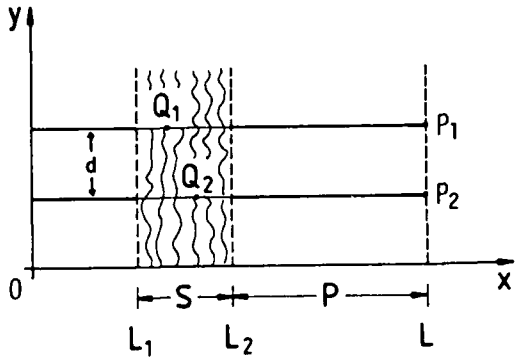

Fig.1

$$1) \qquad \eta_1 = \int_{L_1}^{L_2}\int_{L_1}^{x} \frac{\partial \mu(Q_1)}{\partial y_1}\, ds_1\, dx_1 + (L - L_2)\int_{L_1}^{L_2} \frac{\partial \mu(Q_1)}{\partial y_1}\, dx_1$$

where, (Fig.1), $\mu(Q_1)$ denotes the refractive index fluctuation at a point Q_1 along the ray. L_1 and L_2 denote the layer boundaries. Derivatives and integrals are to be evaluated along the unperturbed ray. Analogous expressions can be found for the corresponding fluctuation η_2 of beam 2, and for γ_1 and γ_2. By multipying the two expressions of η_1 and η_2 and averaging one can find the correlation function of the fluctuations η_1 and η_2 as a sum of multiple integrals:

$$2) \qquad B_y(P_1,P_2) = \langle \eta_1 \eta_2 \rangle = \int_{L_1}^{L_2}\int_{L_1}^{L_2}\left\{\int_{L_1}^{x_1}\int_{L_1}^{x_2} \mathfrak{D} B_n\, ds_2 ds_1 + P\int_{L_1}^{x_1} \mathfrak{D} B_n ds_1 + \right.$$

$$\left. + P\int_{L_1}^{x_2} \mathfrak{D} B_n\, ds_2 + P^2 \mathfrak{D} B_n \right\} dx_2\, dx_1$$

where $P = L - L_2$ and

$$3) \qquad \mathfrak{D} B_n = \frac{\partial^2 B_n(Q_1,Q_2)}{\partial y_1 \partial y_2}$$

and $B_n(Q_1,Q_2)$ denotes the correlation function of the refractive index fluctuations.

We have chosen the correlation function B_n in the form given by Beckman, which allows to describe anisotropic turbulence ([1]):

$$4) \qquad B_n(Q_1,Q_2) = \langle \mu^2 \rangle \exp - \frac{(x_1-x_2)^2}{R_{ox}^2} - \frac{(y_1-y_2)^2}{R_{oy}^2} - \frac{(z_1-z_2)^2}{R_{oz}^2}$$

where R_{ox}, R_{oy} and R_{oz} represent the dimensions of the inhomogeneities in the three directions, respectively, and $\langle \mu^2 \rangle$ denotes the mean square fluctuation of the refractive index.

By introducing Eq.4 into Eq.2 and by evaluating derivatives and integrals one obtains B_y in finite terms. In the case of a thick layer (thickness $S \gg R_{ox}$) one obtains the simple expression:

5) $$B_y = \sqrt{\pi}\, M\, S\, R_{ox}\, \frac{S^2}{3} + PS + P^2$$

where the quantity

6) $$M = \frac{2\langle \mu^2 \rangle}{R_{oy}^2}\left(1 - 2\,\frac{d^2}{R_{oy}^2}\right)\exp\left(-d^2/R_{oy}^2\right)$$

is independent of the layer thickness and position.
The corresponding structure function D_y can be immediately obtained from Eq.s 5 and 6.
The first term in the brackets of Eq.5 represents the contribution to the correlation function due to the layer. In the case when the turbulent medium fills all the path, the quantity P is zero and Eq.5 reduces to a known formula[2].The second term represents a crossed contribution of the layer and the subsequent empty space. Finally the last term represents the contribution of the empty space. Note that the rays emerge from the layer at a fluctuating angle with the unperturbed direction.

An experimental test has been made in the laboratory. Two laser beams propagate along parallel horizontal paths, at a distance 5.4 cm apart, and cross a layer of turbulence produced by a heater. The layer thickness is about 30 cm. After propagation each beam impinges on a position sensor connected to a small computer that allows automatic acquisition and storage of the data.Measurements are made by placing the heater at different locations along the path. The measured correlation and structure functions are obtained by an a-posteriori elaboration of the data. The correlation function is used to check that the layer thickness is large with respect to the scale R_{ox} of the turbulence. The comparison between experimental and theoretical structure functions, Fig.2, allows the test of the behaviour versus P.

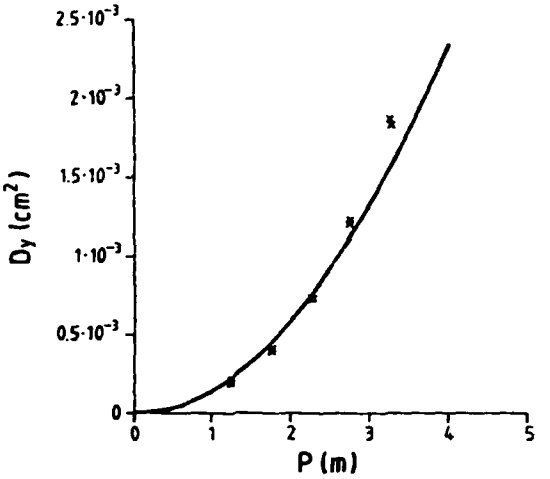

Fig.2

References

1 - P.Beckmann, Radio Sciences J.Res. NBS/USNC-URSI 69D, 629, 1965.
2 - A.Consortini, L.Ronchi and L.Stefanutti, Applied Optics 9, 2453, 1970.

LONG PATH ATMOSPHERIC TRANSMITTANCE MEASUREMENTS: 27

TECHNIQUE, INSTRUMENTATION AND RESULTS

A.D. Devir, A. Ben-Shalom, S.G. Lipson, U.P. Oppenheim and E. Ribak

Department of Physics, Technion - Israel Institute of Technology, Haifa, Israel

For several years we have been conducting measurements of atmospheric transmittance. These measurements were carried over long optical paths (up to 44 km) in the 2.8-13.6 micron wavelength region. The aim of these measurements was to compare our experimental results with the predictions of the late versions of the LOWTRAN computer codes. In this paper we want to present our technique, the instrumentation used in the experiments and our results.

The experimental technique used by us had been modified since we published our preliminary results (1). It is based upon the radiometric measurement of the spectral radiant intensity of a collimated and chopped beam of radiation coming from an infrared source. The measurements are performed at two distances from the source: a short distance of 1-1.5 km and a long distance of 5-44 km. Before and after each measurement the spectroradiometer used is calibrated to check that its sensitivity is constant. The ratio between these two measurements is not equal to the atmopsheric transmittance over the path difference between the corresponding two distances, as assumed in our preliminary report (1). Instead, the spectral radiant intensity of the source is calculated from the signal measured at the short distance. Of course, that calculation is based on the predicted values of the atmopsheric transmittance, but these calculated values are assumed to be accurate enough (especially in wavelength intervals where the transmittance is high) and any residual error can be found later. The measured relative values of the spectral radiant intensity of the source (which is measured in the laboratory) are used to complete the calculations in those wavelengths intervals where the transmittance is too low to be predicted with very small error. Since the spectral radiant intensity of the source is kept constant during all the measurements, the measured values of the atmospheric transmittance can be found from the signal measured at the long distance from the source (2).

The source of the infrared radiation is a hollow graphite rode heated by a controlled current of 400 Ampere to temperature of 2400 K. The rode is held in a windowless chamber flushed with nitrogen to prevent it from burning. The reflecting walls of the chamber, which are serving as radiation shield, are cooled by water. The electrodes which hold the rode and carry the current are also water cooled. The rode is located at the focus of Cassegrain optics with an aperture of 64 cm which produced a beam collimated to 6 mrad. Chopping of the beam at 400 cps is obtained by an air turbine.

At the other end of the optical path, we place our dual-channel spectroradiometer. The spectral resolution of this instrument is 1-2% and is obtained by the use of circular-variable-filters (CVF). The field of view of

the spectroradiometer is 2 mrad. The signal detected is amplified by lock-in amplifiers which are phase locked to the chopping frequency. The reference signal is transmitted by VHF channel. The amplified signals are averaged by a computer which controls the position of the CVF, or the wavelength at which the measurement is taking place. As a result a good S/N ratio is obtained even at optical paths of 44 km.

Our experiments have been carried out in different geographical regions and at various seasons of the year so as to obtain as wide range of parameters as possible. Consequently, air temperatures between 7 and 38 C were investigated, and the use of different altitudes allowed the air pressure to be varied between 0.89 and 1.05 atm. Particular attention was given to attaining conditions with very low and very high water vapour partial pressures (5 to 17 torr).

In this paper we present our results of the contribution of the water vapour continuum to the total atmospheric transmittance. The water continuum in the 4.3-5.5 micron spectral region was not included in the LOWTRAN 5 computer code and its contribution in the 8-14 micron spectral region was incorrectly included in the LOWTRAN 6 (3). Errors in the determination of its contribution will affect the prediction of the atmospheric transmission under high humid conditions or along long horizontal paths.

The transmittance contribution τ_c due to water-vapour at wavenumber ν can be expressed as:(3,4)

$$-\ell n\tau_c = R \cdot D \cdot C_s(\nu) \cdot [P_w + \gamma \cdot (P_t - P_w)] \qquad (1)$$

where R is the distance between source and observer, D the water-vapour content in the air, P_w the water-vapour partial pressure and P_t the total atmospheric pressure.

In the wavelength region 4.3-5.5 μm (2220-1820 cm^{-1}) we find that $\gamma = 0.016 \pm 0.005$, independent of ν, and $C_s(\nu)$ is given in Fig. 1. The curve interpolates data recently published by Burch (7) for other wavelengths. However, we should point out that the structure observed in the data seems not to be a reflexion of the structure predicted by the LOWTRAN calculations, the contribution of which is divided out of the measured total transmittance τ. These results represent data from 22 independent experiments. These values of C_s are close to those included in LOWTRAN 6.

In the wavelength region 8-14 μm (710-1250 cm^{-1}) we found the expression in LOWTRAN 4 and 5 describing the water vapour continuum to be too high by approximately 20%. Therefore, we replaced that expression (5)

$$C_s(\lambda,T) = [1.25 + 1670 \cdot \exp(-7.87/\lambda)] \cdot 10^{-22} \text{ molec}^{-1} \text{ cm}^2 \text{ atm}^{-1} \qquad (2)$$

which is shown as dots in Fig. 2, by an empirical term $C_s'(\lambda,T)$ the value of which was edetermined from the experimental results. The frequency-dependence of $C_s'(\lambda,T)$, measured at approximately T = 296°K, is shown as a solid line in Fig. 2 and is similar to that measured by Burch (6) at 392°K. These values of $C_s'(\lambda,T)$ are close to those reported lately by Burch et al. (7) only above 9.5 m but lower than the values used in LOWTRAN 6. The temperature-dependence of C_s can be derived from the expression (5)

$$C_s'(\lambda,T) = C_s'(\lambda,T') \cdot \exp(T_o(\frac{1}{T} - \frac{1}{T'})) \qquad (3)$$

for T_o = 1610°K, by the use of the two results: our at 296°K and Burch's at 392°K.

REFERENCES

1. A. Ben-Shalom, D. Cabib, A.D. Devir, D. Goldschmidt, S.G. Lipson and U.P. Oppenheim, "Spectral Characteristics of Infrared Transmittance of the Atmosphere in the Region 2.8-14 μm - Preliminary Measurements", Infrared Physics 20, 165 (1980).

2. A. Ben-Shalom, A.D. Devir, S.G. Lipson, U.P. Oppenheim and E. Trakhovsky, "New Developments in Instrumentation for Long Path Atmospheric Transmittance and Radiance Measurements", Proc. SPIE 356, 98 (1982).

3. D.R. Cutten, "Extension of the Water Vapour Continuum Absorption to the 4.5-5.0 μm Region", Infrared Physics 19, 663 (1979); "Atmospheric Broadband Transmission Measurements and Prediction in the 8-13 Micron Window: Influence of Water Continuum Absorption Errors", Appl. Optics 25, 1085 (1985).

4. A. Ben-Shalom, A.D. Devir, S.G. Lipson and U.P. Oppenheim, "Absorption of Infrared Radiation by Atmospheric Water Vapor in the Region 4.3-5.5 μm - Preliminary Measurements", Optical Engineering, 20, 746 (1981).

5. R.E. Roberts, J.E.A. Selby and L.M. Biberman, "Infrared Continuum Absorption by Atmospheric Water Vapor in the 8-12 μm Window", Appl. Optics 15, 2085 (1976).

6. D.E. Burch, "Continuum Absorption by H_2O", Air Force Geophysics Laboratory Report AFGL-TR-81-0300 (1982).

7. D.E. Burch and R.L. Alt, "Continuum Absorption by H_2O in the 700-1200 cm^{-1} and 2400-2800 cm^{-1} Windows", Air Force Geophysics Laboratory Report AFGL-TR-84-0128 (1984).

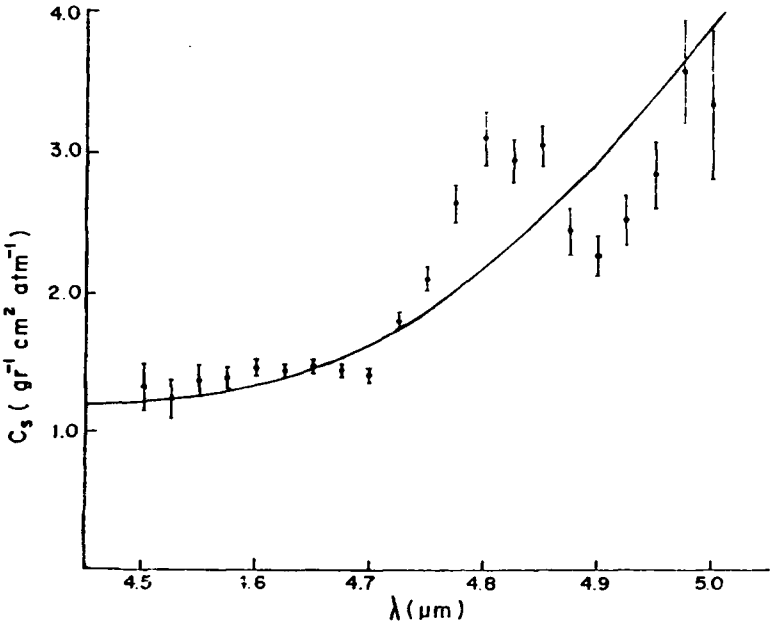

Fig. 1: The experimental results of C_s at 296 K.

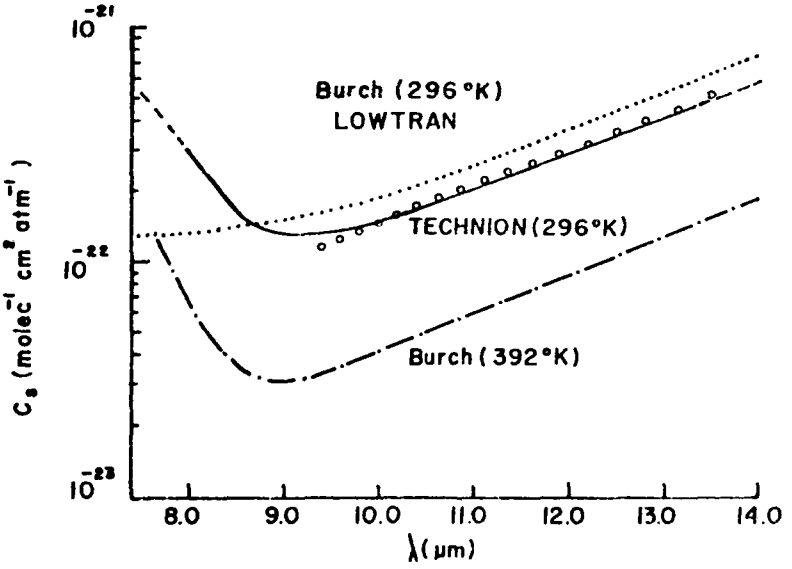

Fig. 2: Our results (solid line) of C_s at 296 K in comparison with the known values (dots) and those measured by Burch (1982) at 392 K (dash-dot). The updated results of Burch et al. (1984) at 296 K are shown by circles.

Analytical Error Estimates for the Time-Dependent Radiative Transfer Inverse Method for Estimating Single-Scattering Parameters

P8

T. Duracz and N.J. McCormick
Department of Nuclear Engineering
University of Washington
Seattle, Washington 98195 USA

Analytical error estimates are developed for an approximate inversion method [J. Opt. Soc. Am. 72, 756 (1982)] to infer the albedo of single scattering and Legendre moments of the angular scattering function from the asymptotic dieaway of the backscattered radiance following a pulse on an optically thick slab target. The errors analyzed are the effects of assuming that a finite slab is infinitely thick, the pulse width is infinitesimally short, and the detector is perfectly oriented.

1. THE INVERSION ALGORITHM

A method has been proposed for estimating the albedo of single scattering and the Legendre angular moments of the monochromatic angular scattering function in an optically thick slab target from measurements of the backscattered radiance at long times after the initial pulse.[1,2] This approximate inverse radiative transfer method uses separate Fourier moments about the azimuthal direction to estimate the unknowns. The method has been numerically tested under conditions with simulated random errors and has shown promise of enabling the albedo of single scattering, and perhaps the asymmetry factor and a third factor, to be estimated.[3] A preliminary experimental test of the method also has been completed.[4]

The inversion method is based on an inverse solution of the radiative transfer equation for radiance $B(\phi;t)$, the radiant energy backscattered at

time t and azimuthal angle ϕ from the illuminated surface of the slab target at a fixed polar angle taken with respect to the inward surface normal. The incident illumination is assumed to be a pulse non-normally incident on the target. The objective of the inversion method is to estimate the set of coefficients $\{f_n\}$ in the single scattering function. The two coefficients of most interest are f_0, the albedo of single scattering, and $f_1/f_0 = g$, the asymmetry factor.

Fourier moments of the radiance,

$$B_m(t) = [\pi(1 + \delta_{m0})]^{-1} \int_0^{2\pi} B(\phi;t) \cos m\phi \, d\phi, \qquad (1)$$

are needed for the inversion algorithm

$$B_m(t) \simeq C_m G_m(t) \exp(-\gamma_m t), \quad m = 0,1,2\ldots, \; t \gg 0, \qquad (2)$$

where C_m depends on the polar angle but is independent of time and γ_m is a function of the unknowns to be estimated, i.e.,

$$\gamma_m = v(1 - f_m), \qquad (3)$$

where v is the speed of light in the target; for a target of finite thickness X, $G_m(t)$ depends also on X, but for a semi-infinite target,

$$G_m(t) = t^{-3/2}. \qquad (4)$$

From Eq. (2) the unknown γ values can be estimated in terms of an ordinary time derivative as

$$\gamma_m = d_t \ln[C_m G_m(t)/B_m(\mu,t)] \; . \qquad (5)$$

2. THE SEMI-INFINITE THICKNESS APPROXIMATION

In an actual experiment, the slab thickness may not be accurately known, or one may wish to avoid using the complicated form of G(t) for a slab; then if one obtains an estimate, $\hat{\gamma}$, by using Eqs. (4) and (5), the difference of the correct γ and the estimated value, $\Delta\hat{\gamma}_m = \gamma_m - \hat{\gamma}_m$, can be shown to be

$$\Delta\gamma_m = -6t^{-1}\left\{\sum_{n=1}^{\infty} \exp[-n^2X^2(2m+3)(\gamma_{m+1}-\gamma_m)/t]\right\}^2 + O(t^2) \quad . \quad (6)$$

For a typical forward scatterer the factor $(\gamma_{m+1} - \gamma_m)$ will be positive and tend to zero as m becomes large, and then $\Delta\gamma_m$ is $O(t^{-1})$ for long times. For this reason the target can be assumed semi-infinitely thick.

3. THE INFINITESIMALLY-SHORT PULSE APPROXIMATION

Inversion algorithm (2) was derived for a Dirac delta function incident pulse. If the incident pulse has a magnitude of A(t), $-t_o < t < t_o$, then a moment of the backscattered radiance is given as

$$B(t) = C \int_{-t_o}^{t_o} ds\ (t-s)^{-3/2}\ e^{-\gamma(t-s)}\ A(s), \quad t >> t_o. \quad (7)$$

(Here the subscript m has been suppressed).

The error $\Delta\gamma_m$ in the estimated coefficient $\hat{\gamma}$ is then found to be

$$\Delta\gamma_m = \hat{\gamma} - \gamma$$

$$= \frac{3}{2}\frac{F_1(\gamma)}{F_0(\gamma)}\,t^{-2} + \frac{3}{4}\frac{1}{F_0^2(\gamma)}\,[5F_0(\gamma)F_2(\gamma) - 3F_1^2(\gamma)]t^{-3} + \ldots \quad (8)$$

where

$$F_n(\gamma) = \int_{-t_o}^{t_o} ds\ s^n e^{\gamma s}\ A(s). \quad (9)$$

Thus it follows that the precise shape of the incident pulse affects the determination of γ only in a term of $O(t^{-2})$.

4. THE PERFECTLY-ORIENTED DETECTOR APPROXIMATION

It was assumed in the derivation of inversion algorithm (2) that the detector was perfectly oriented with respect to the target normal and the

incident pulse. In the event this is not true, then the uncoupling of the Fourier moments implied in Eq. (5) is no longer true, and the estimate $\hat{\gamma}_m$ depends on all the γ_m values. In the limit of $t \to \infty$,

$$\hat{\gamma}_m \to \min \gamma_m, \; m = 0 \text{ to } N. \tag{10}$$

The practical implications of this result for experiments may vary for different experimental situations, however, because effects from random errors will tend to make it difficult to estimate γ_m, $m \geq 3$, for very long times.[3]

5. CONCLUSIONS

For purposes of estimating the albedo of single scattering and other Legendre moments of the angular scattering function, it can be assumed that the backscattered radiance long after the illumination of an optically-thick homogeneous slab target by a brief pulse at $t = 0$ comes from a semi-infinite target illuminated by an instantaneous pulse. The errors in the coefficients made by assuming the slab is infinitely thick are $O(t^{-1})$, while those made by assuming the pulse is infinitesimally brief are $O(t^{-2})$. Also, it is important that the detector be carefully oriented.

Acknowledgment

This work was supported by the U.S. Army Research Office.

References

1. N.J. McCormick, 'Remote characterization of a thick slab target with a pulsed laser,' J. Opt. Soc. Am. 72, 756-759 (1982).

2. N.J. McCormick, 'Inverse methods for remote determination of properties of optically thick atmospheres,' Appl. Opt. 22, 2556-2558 (1983).

3. K.K. Hunt and N.J. McCormick, 'Numerical test of an inverse method for estimating single-scattering parameters from pulsed multiple-scattering experiments,' J. Opt. Soc. Am. A, 2, 1965-1971 (1985).

4. R.A. Elliott, N.J. McCormick, and T. Dursch, 'Preliminary experimental test of the time-dependent radiative transfer inverse method for estimating single-scattering parameters,' Int. Conf. Opt. Millimeter Wave Propag. and Scatt. in the Atmos. (Florence, Italy, May 27-30, 1986.)

Preliminary Experimental test of the Time-Dependent Radiative Transfer Inverse Method for Estimating Single-Scattering Parameters

R.A. Elliott
Oregon Graduate Center
19600 N.W. Van Neumann Drive
Beaverton, Oregon 97006-1999 U.S.A.

and

N.J. McCormick and T. Duracz
Department of Nuclear Engineering
University of Washington
Seattle, Washington 98195 U.S.A.

Time resolved backscattered radiance measurements are used to estimate the albedo of single-scattering of an optically thick system of scatterers using an approximate inversion method [J. Opt. Soc. Am. 72, 756 (1982)] that is based on the long-time dieaway of the radiance following a short pulse. The estimated albedo agreed with the correct value to within <2%.

1. THE INVERSION ALGORITHM

A method has been proposed for estimating the albedo of single scattering and the Legendre angular moments of the monochromatic angular scattering function in an optically thick slab target from measurements of the backscattered radiance at long times after the initial pulse.[1,2] This approximate inverse radiative transfer method uses separate Fourier moments about the azimuthal direction to estimate the unknowns. The method has been numerically tested under conditions with simulated random errors and has shown promise of enabling the albedo of single scattering, and perhaps the asymmetry factor and a third factor, to be estimated.[3] An experiment to validate the method and some preliminary experimental radiance measurements have been described elsewhere[4], and analytical error estimates for the inversion method also have been derived.[5]

The inverse method is based on an inverse solution of the radiative transfer equation for radiance $B(\phi;t)$, the radiant energy backscattered from the planar surface at time t and azimuthal angle ϕ measured with respect to the radiant beam, and at a fixed polar angle taken with respect to the inward surface normal. The long-time dieaway of the radiance following a non-normally incident pulse at time t = 0 is needed for the inversion algorithm.

Here we shall be interested in estimating only the albedo of single scattering of a system of scatterers, f_0, using the algorithm

$$v(1 - f_0) = d\{\ln[t^{-3/2}/B(t)]\}/dt, \qquad (1)$$

where B(t) is the azimuthal average of $B(\phi;t)$,

$$B(t) = (2\pi)^{-1} \int_0^{2\pi} B(\phi;t)\, d\phi \simeq (2\pi)^{-1} \sum_{i=1}^{I} w(\phi_i) B(\phi_i;t) \qquad (2)$$

where the weights $w(\phi_i)$ are calculated with the scheme of Ref. 6. Because the long-time dieaway of the radiance asymptotically becomes azimuthally symmetric, it is also possible to estimate f_0 using any one of the set of radiances at specific azimuthal directions, i.e.,

$$B(t) \simeq B(\phi_i;t) , \quad i = 1 \text{ to } I. \qquad (3)$$

2. THE EXPERIMENT

The experimental set up to measure the backscattered radiance required for the inversion algorithm used a frequency doubled, passively mode-locked Nd:YAG laser and a Pockels cell single pulse selector that produced 50 μJ, 25 psec duration pulses of 532 nm light. Two beam expanding telescopes enlarge the laser beam to 5 cm diameter and collimate and direct it through a Cornu depolarizer and into a scattering cell that is a 15 cm diameter by 15 cm silvered glass cylinder with an AR coated window on the front face and a black anodized aluminum rear face to simulate a semi-infinite medium.

A pellicle beam splitter was used to divert a portion of the laser pulse through a delay line to provide a reference event for precise timing and normalization. The detector used was a Hamamatsu model C979 streak camera capable of resolving events separated in time by <10 psec. The streak camera provided a digital readout of radiation intensity versus time for subsequent numerical analysis.

The time resolved backscattered radiance was measured at seven azimuthal angles (45°, 90°, 135°, 180°, 225°, 270°, and 315°) for two polar angles (20° and 28°) from a dispersion of 91 nm diameter latex spheres in water for which f_0 is essentially unity corresponding to no absorption; the concentration of spheres was 0.54 vol% which gave an optical mean free path between scatterings of ~1.2 mm. An example of the measured radiance is shown in Fig. 1.

3. TEST OF THE ALGORITHM

The data from Fig. 1 and the other six azimuthal angles was combined with Eq. (2) to obtain B(t) for use in inversion algorithm (1) to estimate f_0 and the percent errors are illustrated in Fig. 2. In the interval 70 to 160 psec after the pulse the estimated f_0 was within <2 % of the correct value. The early-time errors (t < 70 psec) arise because the asymptotic dieaway required for the algorithm had not yet begun, while the long-time errors (t > 160 psec) arise because of the small signal to noise ratio.

The data from only Fig. 1 was also used with Eq. (3) to estimate f_0, and the percent errors are shown in Fig. 3. The results indicate that it was possible to get nearly as good as estimate of f_0 as before without measuring the backscattered radiance in more than one direction.

Acknowledgment

This work was supported by the U.S. Army Research Office.

References

1. N.J. McCormick, 'Remote characterization of a thick slab target with a pulsed laser,' J. Opt. Soc. Am. 72, 756-759 (1982).

2. N.J. McCormick, 'Inverse methods for remote determination of properties of optically thick atmospheres,' Appl. Opt. 22, 2556-2558 (1983).

3. K.K. Hunt and N.J. McCormick, 'Numerical test of an inverse method for estimating single-scattering parameters from pulsed multiple-scattering experiments,' J. Opt. Soc. Am. A, 2, 1965-1971 (1985).

4. R.A. Elliott, 'Multiple scattering of optical pulses in particulate media,' Symp. Mult. Scatt. Waves in Random Media and Random Rough Surfaces (University Park, Penn., July 29 - Aug. 2, 1985).

5. T. Duracz and N.J. McCormick, 'Analytical error estimates for the time-dependent radiative transfer inverse method for estimating single-scattering parameters,' Int. Conf. Opt. Millimeter Wave Propag. and Scatt. in the Atmos. (Florence, Italy, May 27-30, 1986).

6. N.J. McCormick, 'Inverse methods for remote determination of properties of optically thick atmospheres,' Appl. Opt. 22, 2556-2558 (1983).

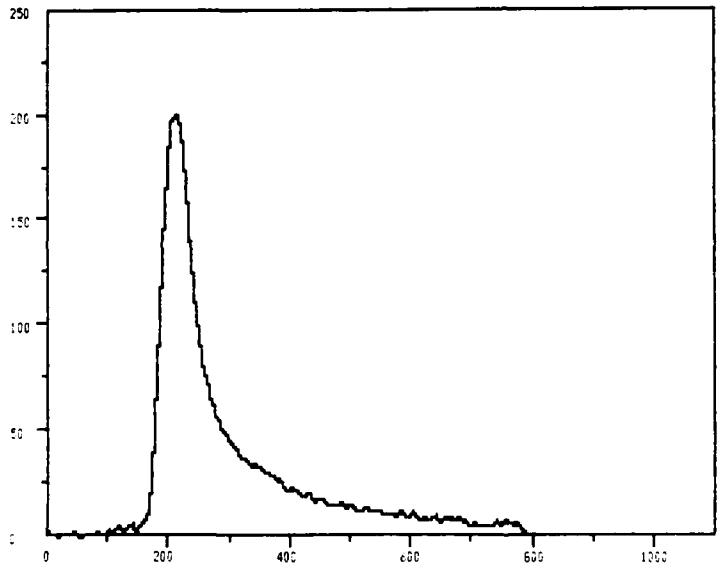

Fig. 1. Normalized backscattered radiance versus time in psec at outgoing polar and azimuthal angles of 20° and 180° and ingoing angles of 52° and 0°, respectively.

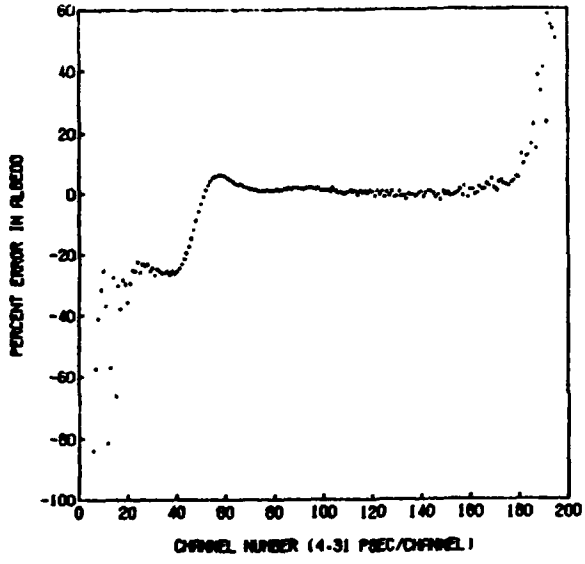

Fig. 2. Estimated percent errors in f_0 versus time for B(t) calculated from 7 azimuthal angles.

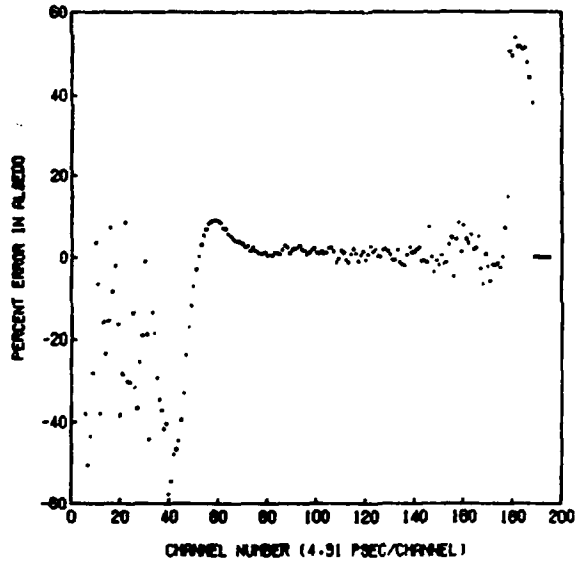

Fig. 3 Estimated percent errors in f_0 versus time for B(t) calculated from single azimuthal single azimuthal angle of 180°, shown in Fig. 1.

Variations in Atmospheric Refractive Index Associated with Ground Turbulence at the Mauna Kea Observatory

P10

D. Andre Erasmus
Institute for Astronomy, 2680 Woodlawn Drive, Honolulu, HI 96822

1. Introduction

Mauna Kea is recognized internationally as one of the world's best locations for astronomical observations. A number of scientific institutions have constructed or are planning construction of telescope facilities in the summit area. The quality of astronomical "seeing" at these facilities is determined by the magnitude and distribution of refractive inhomogeneities caused by turbulence in the atmosphere. There are three main types of turbulent motion that affect seeing quality.

i) Turbulence in the atmospheric boundary layer.
ii) Turbulence in the free atmosphere.
iii) Turbulence in and around the telescope dome.

Within the boundary layer, the effects of turbulence occurring directly above the ground are of particular importance. Temporal and spatial variations in atmospheric refractive index within this layer (the surface boundary layer), determine preferred locations and ground-heights for telescope facilities. In the surface boundary layer, wind speed increases exponentially with height. Wind shear and turbulence intensity will, consequently, decrease with height. Since the ground is a heat source during the day and a heat sink at night, the magnitude of microthermal activity is usually a maximum near the surface. Differences in surface roughness, thermal forcing and topography determine the temporal and spatial variations of microthermal activity.

2. Theoretical Background

Roddier (1981) and Coulman (1985) have written reviews of the theory of wave propagation through a turbulent medium. When a plane wave of light with uniform amplitude propagates through a refractively nonuniform medium, such as the atmosphere, it will exhibit amplitude and phase fluctuations. When such a wave front is focused, the resulting image will vary in intensity, sharpness, and position. These variations are commonly referred to as scintillation, image blurring, and image movement, respectively. The combined effect of these variations are directly related to the refractive-index-structure parameter (C_n^2) which is a measure of the average variability of the refractive index of light in the atmosphere. Image degradation increases as C_n^2 increases. For optical wavelengths, C_n^2 is related to the temperature structure parameter (C_T^2) as follows (Wyngaard et al. 1971):

$$C_n^2 = [(8 \times 10^{-5} P)/T^2]^2 \, C_T^2 \qquad (1)$$

where P is the pressure in mb and T is the temperature in °K. At separations of the order of inertial subrange scales, C_T^2 in a locally isotropic field has the form:

$$C_T^2 = \overline{[T(\underline{x}) - T(\underline{x} + \underline{r})]^2}/r^{2/3} \qquad (2)$$

where $\underline{x}$ and $\underline{r}$ are the position vectors and the overbar indicates a time average. Variations in atmospheric refractive index can therefore be determined by measuring the high frequency temperature fluctuations associated with atmospheric turbulence.

3. Instrumentation and Data Collection

Pairs of high frequency response temperature sensors (microthermal sensors), with separators of about 1-m, were used to monitor microthermal activity within the surface boundary layer. These sensors were mounted at three levels (6.6-m, 11.6-m, 27.5-m) on meteorological towers. Two of the towers are located in the cinder cone complex, one on the summit ridge and one on Poliahu, an isolated hill (Fig. 1). The third tower is located on the lava rock shield to the north of the summit (13 North).

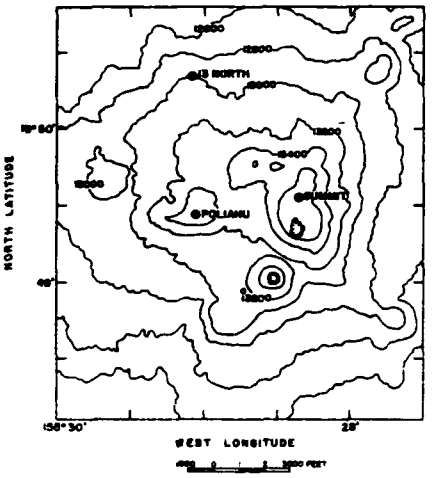

Fig. 1 - Topography and site locations in the summit area of Mauna Kea, Hawaii.

Data were collected over a six-month period from June through November 1985. The signal from the microthermal sensors was filtered to include frequencies between 1 and 25 Hz. The root mean square of the filtered signal was then taken using an averaging time of 6 seconds. This quantity was sampled every minute and the hourly means, maxima and minima were logged. An independent measurement of the temperature fluctuations spectrum was made to determine whether the filtered data were biased because of lack of spectral coverage.

4. Results

The mean daily cycles of C_T^2 for the different sites are shown in Fig. 2. Notice the similarity of the three profiles for the 6.6-m level (Fig. 2a). At the 11.6-m and 27.5-m levels, however, the values for C_T^2 are quite different at the three sites, especially during the day. The vertical jprofiles of C_T^2 also exhibit these differences (Fig. 3). During the day (10h00 - 16h00 LST), the standard profile of C_T^2 with height is reversed at 13 North. At night (22h00 -

04h00 LST) the values of C_T^2 are about two orders of magnitude smaller than the daytime values. At the summit ridge and Poliahu the daytime and nightime profiles are similar but at 13 North they are very different.

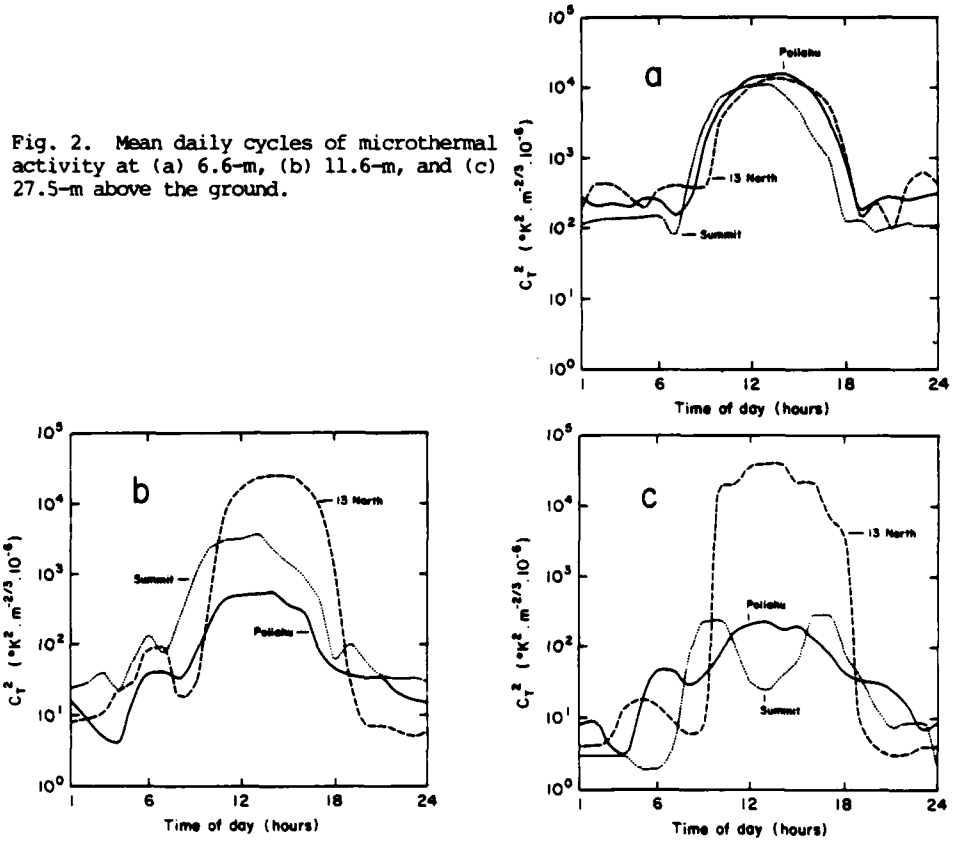

Fig. 2. Mean daily cycles of microthermal activity at (a) 6.6-m, (b) 11.6-m, and (c) 27.5-m above the ground.

The microthermal structure of the turbulence in the suface boundary layer on Mauna Kea can be explained in terms of the thermal effects of the surface and the nature of the flow at each of the sites. At poliahu and the summit ridge, thermal effects are similar but the wind speed gradient is larger on the summit ridge. This indicates that the air is forced to flow over the summit ridge, deepening the mixed layer, but at Poliahu the air tends to flow around the isolated hill. At 13 North there is no local topographic forcing. The lava rock surface heats strongly during the day, encouraging convective mixing and deeping of the mixed layer. At night, rapid cooling of the surface stabilizes the surface boundary layer and suppresses turbulence.

The spectral density functions of $(\Delta T)^2$ were obtained for the filtered and unfiltered data at each of the three towers. It was found that C_T^2 is, at worst, a factor of 3 too small due to lack of spectral coverage. Correcting for this bias, the relative contributions of ground turbulence tot he degredation of image quality under different seeing conditions were determined. At night, when

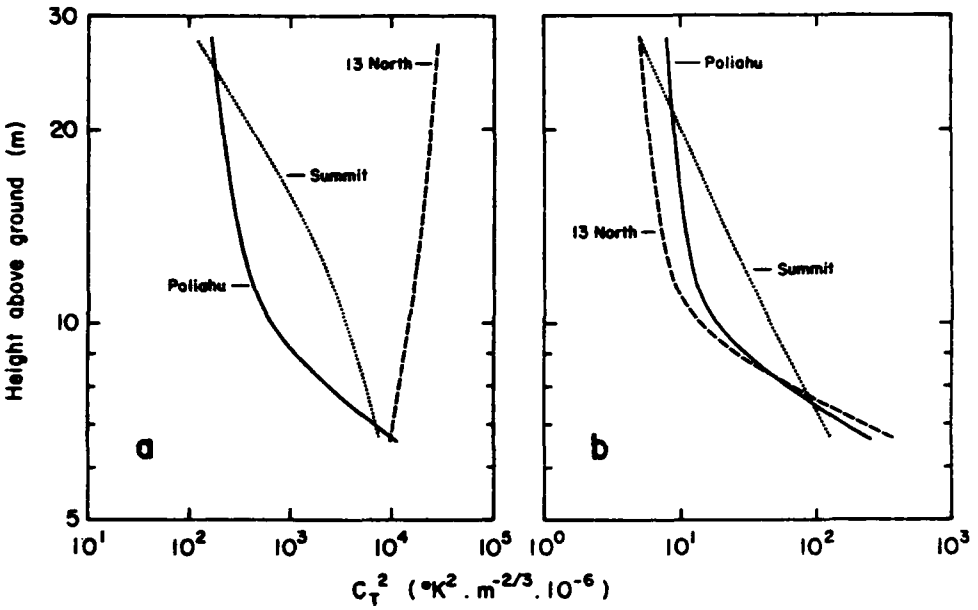

Fig. 3. Mean vertical profile of C_T^2 (a) during the day and (b) at night.

the profiles of C_T^2 at the three sites are similar, this contribution is 0.15%. At night, therefore, effects of ground turbulence are insignificant. During the day the profiles of C_T^2 are very different. At 13 North the mixed layer extends above the top of the tower so that an exact measurement of the ground effects is not possible. At the summit and Poliahu the contribution of the ground turbulence is between 2% and 3% at 1.0 arcsecond seeing. Because of the rapid drop-off of C_T^2 with height, even during the day, at Poliahu, the ground turbulence would constribute about 0.3% tot he total seeing if the telescope were placed above 11.6-m.

5. Conclusion

Within the surface boundary layer at the summit of Mauna Kea, C_n^2 exhibits strong spatial variability during the day and weak spatial variability at night. At night the ground effects at all three sites surveyed are not significantly different. During the day the ground effects are very strong at 13 North, weak at the summit and nearly negligible at Poliahu.

References

Coulman, C. E., Ann. Rev. Astron. Astrophys., Vol 23, pp 19-57, 1985.
Roddier, F., Prog. in Optics XIX, pp 282-376, E. Wolf, Ed. 1981.
Wyngaard, J. C., Izumi, Y., and Collins, S. A., J. Opt. Soc. Amer., Vol. 61, pp 1646-1650, 1971.

Effect of a Phase Screen on Imaging with Light of Arbitrary Spatial Coherence

P11

Ronald L. Fante
Avco Systems Division
Wilmington, MA 01887 USA

In this paper we have considered the imaging of an object located an arbitrary distance behind a random phase screen for the cases when the object has an arbitrary state of surface roughness and the incident radiation has an arbitrary degree of spatial coherence.

Multiple applications of the Huygens-Fresnel principle have been applied to the geometry in Figure 1 and solutions obtained under the following assumptions: 1) all wavelengths in the incident radiation are very small in comparison with the physically meaningful spatial scales such as the object size, object surface-correlation length, phase-screen spatial coherence length, etc., 2) the wavelength is sufficiently small that cross polarization can be ignored, 3) the scattering of radiation by the object can be characterized by a spatially-dependent reflection coefficient defined in a plane just above the object, 4) the backscatter by the random phase screen is negligible and the principal effect of the phase screen is ot simply add a random phase shift ϕ to any incident wave, 5) the characteristic response time of the imager is long in comparison with the temporal coherence time of the source that produces the incident radiation; thus the imager does not follow random temporal fluctuations of the source, 6) for the limit of a diffuse object, its reflection coefficient is a complex Gaussian random variable, and 7) in the limit of a strong phase screen the transmission function $\exp(\gamma\phi)$ of the screen is a Complex Guassian random variable.

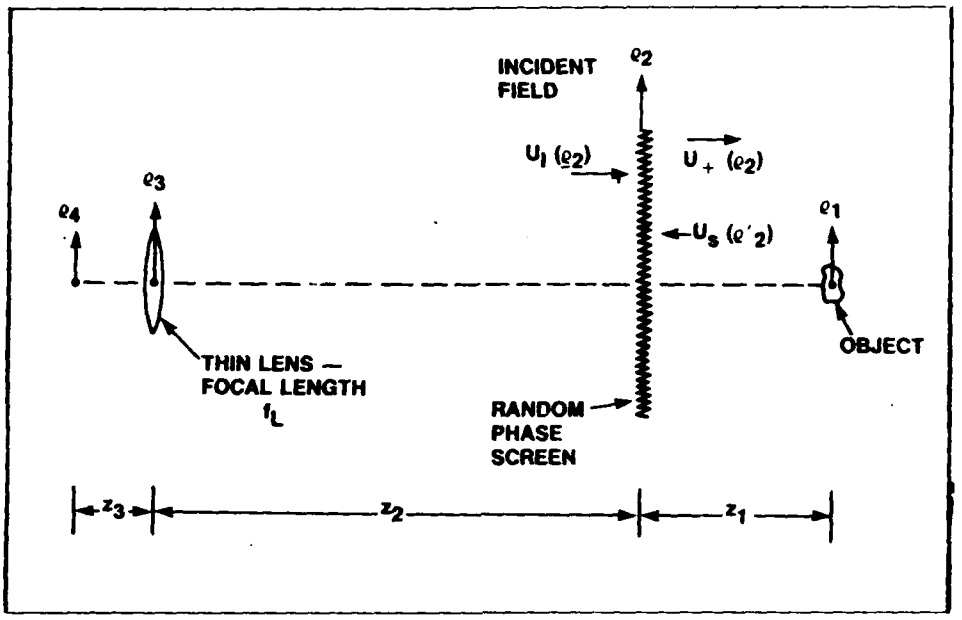

Figure 1: Imaging of an Object Behind a Phase Screen

Results have been obtained for both the image plane irradiance distribution and speckle contrast. Some approximate forms of these results for the speckle contrast are shown in Table 1. From Table 1 we see that imaging with coherent light is virtually impossible. For example, when imaging a diffuse object behind a strong phase screen, one can get values of σ^2 as large as seven even if the illuminating (incident) radiation passes through different phase screen inhomogeneities than the image (reflected) radiation, and even higher values of σ^2 if the incident and reflected rays pass through the same inhomogeneities.

Thus, imaging is possible only with incoherent radiation (spatial coherence length of incident radiation small in comparison with both the object and phase scren coherence lengths). In that case, it is easily shown that the spatial frequency spectrum of the ensemble averaged image plane irradiance is

$$\langle \hat{I}(\underline{f}) \rangle = K \hat{R}(-M\underline{f}) \hat{F}(M\underline{f}) \hat{H}(\lambda z_1 M \underline{f}) \quad , \qquad (1)$$

where $\langle\ \rangle$ denotes an ensemble average, K is a constant, $\hat{R}$ is the spatial Fourier transform of $\langle |R|^2 \rangle$, R is the object reflection coefficient, $\hat{H}$ is the spatial Fourier transform of $\langle \exp[j\phi(\underline{\rho}) - j\phi(\underline{\rho}+\underline{s})] \rangle$, $\hat{F}$ is the optical transfer function of the imager, $\underline{f}$ is the spatial frequency, λ = wavelength, and M is the magnification. An analysis of Eq.(1) shows that a spatial frequency f_o in the object can be imaged if $\lambda z_1 f_o < \ell_p$ where ℓ_p is the spatial correlation length of the phase screen fluctuations. This result is the "shower curtain" effect which states that any spatial frequency f_c can be imaged (to within the diffraction limit of the optics) as long as the distance z_1 between the object and the phase screen is made sufficiently small.

Table 1: Normalized Variance (Square of Speckle Contrast σ) for Object Behind a Strong Phase Screen (for $\gamma_1 \ll \gamma_2$)

Incident Radiation Type	Smooth Object	Diffuse Object
Incoherent	$\sigma_{sm}^2 = \dfrac{1}{1 + \frac{1}{2}\left(\dfrac{L_{res}}{\ell_p}\right)^2}$	$\sigma^2 = \sigma_{sm}^2 + \dfrac{1}{\sigma_{sm}^{-2} + \left(\dfrac{\ell_{res}}{\ell_o}\right)^2} + \dfrac{1}{1 + \left(\dfrac{\ell_{res}}{\ell_o}\right)^2}$
Coherent	Expression very complex but σ^2 usually greater than unity	Expression complex but $\sigma^2 \geq 1$ with $\sigma^2 \to 1$ when $L_{res} >> \ell_p$ and $\ell_{res} >> \ell_o$

ℓ_{res} = Resolution length at object plane

L_{res} = Resolution length at phase screen plane

ℓ_p = phase screen correlation length

ℓ_o = object surface correlation length

National New Technology Telescope Site Survey Instrumentation

P12

F. F. Forbes
Advanced Development Program
National Optical Astronomy Observatories
P. O. Box 26732, Tucson, Arizona 85726-6732

The characterization of atmospheric turbulence at and above the two candidate sites for the NNTT 15-Meter Telescope has resulted in the development of specialized techniques. The equipment used to measure astronomical seeing, microthermals, water vapor and temperature is discussed along with the sample data and calibration results. By using instruments whose altitude coverage overlap, it has been possible to "bookkeep" quantitatively the sources of image degradation due to all causes, especially near the ground.

Introduction

The goals and initial conception for the 15-Meter National New Technology Telescope (NNTT) Site Evaluation Program have been discussed and only an instrumentation elaboration is within the scope of this paper. By exact duplication of instruments at the two sites under investigation, it was intended that the sites could be readily compared and where possible, absolute site parameters could be obtained to afford ranking with other sites presently being studied. The degree of site development dictated, to some extent, the choice of survey instrumentation principally because the Arizona site is a wilderness area, allowing only temporary facilities. Figures 1-10 show the instrumentation and samples of data obtained. The following table summarizes the program instrumentation.

Facility	Instrument	Data Type
Micrometeorological Tower	Anemometer	Windspeed and direction
	Temperature probes	Temperature at 5-tower heights to 30m.
	Microthermal probes	Microthermal activity, C_t^2
Seeing Monitor Tower	ICID Seeing Monitor	Differential image motion
	Microthermal probes	Dome microthermal activity
	IR sky monitor	IR sky emissivity and water vapor
Acoustic Sounder	Echosonde[2]	C_n^2 vs. altitude, 20-150m.

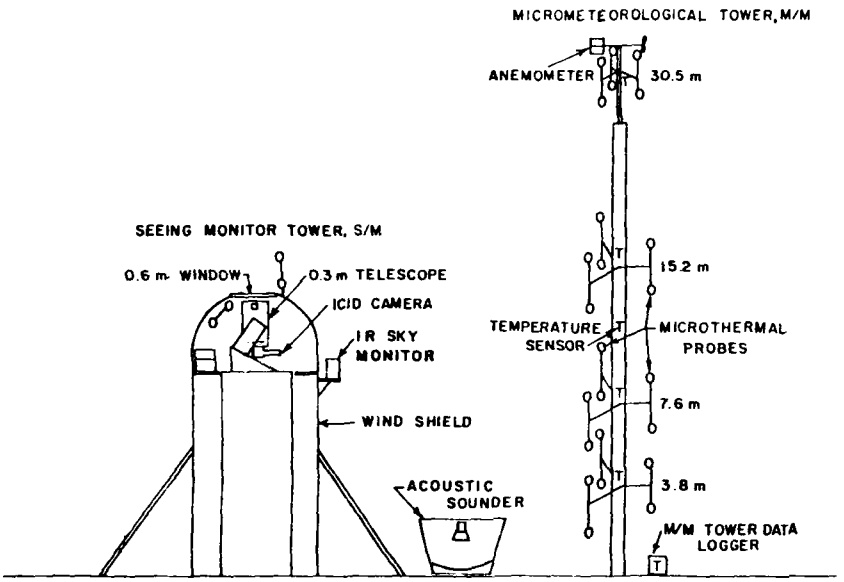

Figure 1. Site survey equipment arrangement.

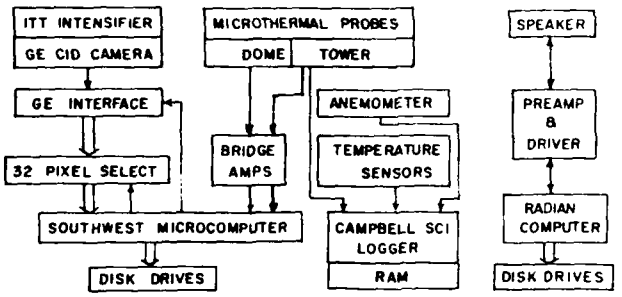

Figure 2. Data collection electronic block diagram.

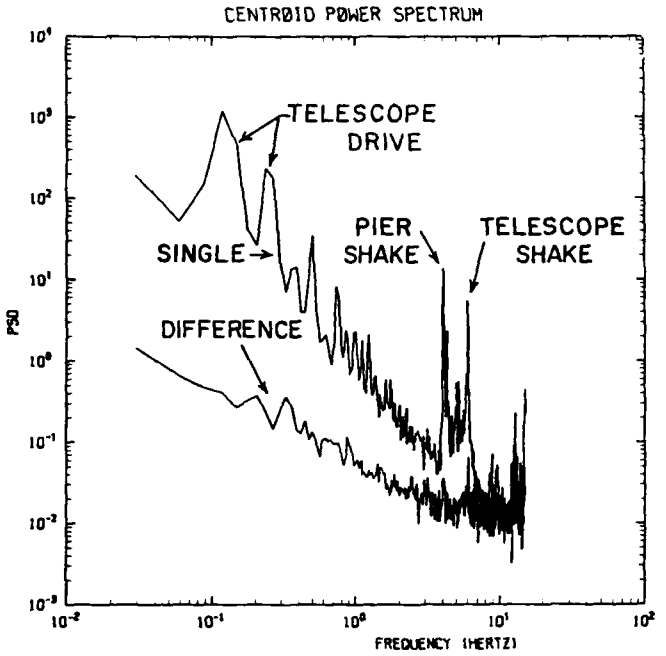

Figure 9. Seeing monitor image motion power spectral density vs. frequency for a single image and the difference motion. Telescope drive periodic errors and resonances in the pier and telescope excited by wind shake are also noted.

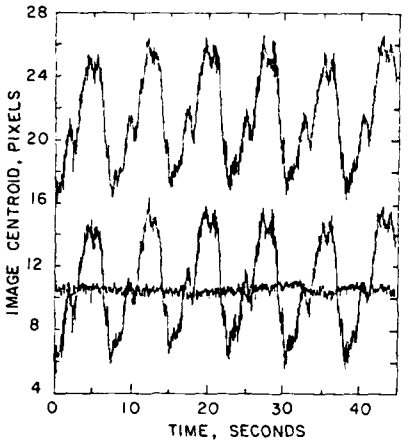

Figure 10. Seeing monitor image centroid motion for two separated images together with their difference motion.

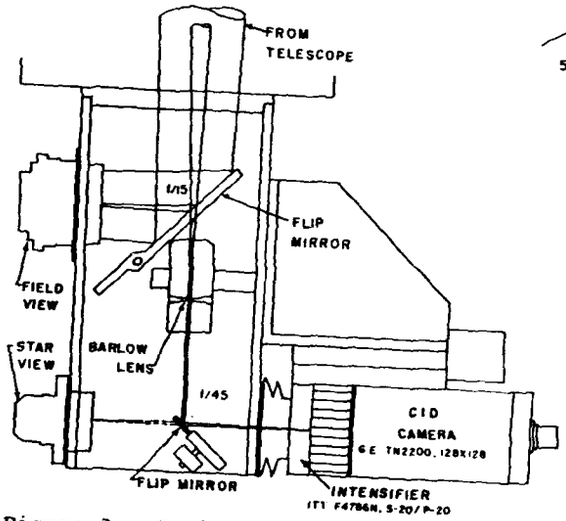

Figure 3. Seeing monitor camera optical layout.

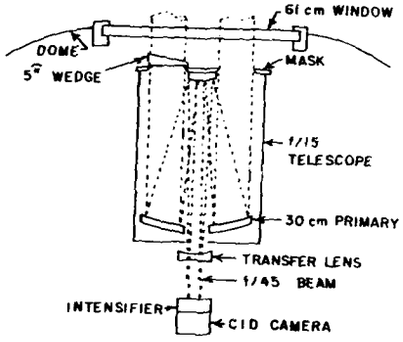

Figure 4. Arrangement of seeing monitor optical elements in the dome.

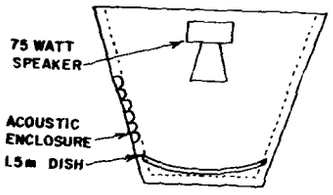

Figure 5. Acoustic sounder

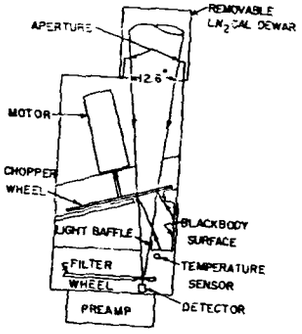

Figure 6. Infrared sky monitor.

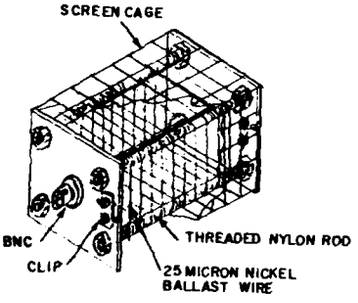

Figure 7. Microthermal probe construction

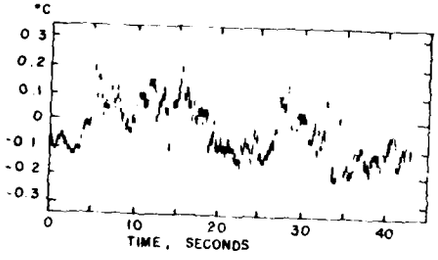

Figure 8. Typical digitized microthermal record.

MILLIMETER-WAVE SCINTILLATION DUE TO ATMOSPHERIC SURFACE-LAYER TURBULENCE

P13

R. J. Hill, S. F. Clifford, and J. T. Priestley
Wave Propagation Laboratory
National Oceanic and Atmospheric Administration
Boulder, Colorado 80303 USA

R. A. Bohlander and R. W. McMillan
Georgia Institute of Technology
Atlanta, Georgia 30332 USA

The fluctuations of intensity and phase difference of a diverged millimeter-wave beam were measured. The beam was propagated 1.4 km at a height of 4 m above exceptionally flat farmland. Figure 1 shows the layout of the experiment. The intensity was measured at each of four horizontally spaced antennas. The phase difference was measured between antenna pairs. The minimum spacing between antennas was 1.43 m, between antennas 1 and 2, and the maximum spacing was 10 m, between antennas 1 and 4. Antenna 5 was not used for the measurements reported here. There were five experiment sessions encompassing summer, fall, winter, and spring conditions. Data were collected during conditions of clear-air turbulence, rain, fog, snow, and ground blizzards. Only the clear-air turbulence data taken during the summer of 1983 are reported here. These data were taken using a millimeter wave frequency of 173 GHz.

A variety of meteorological measurements were obtained simultaneously with the millimeter-wave data. Figure 1 shows the optical propagation paths that give optical refractive-index structure parameter as well as the cross-path component of the wind. Figure 1 also shows the optical rain gauge, optical drop size disdrometers, and the weighing bucket rain gauges. The two micrometeorological stations shown are 4-m-high instrumented towers. At these stations the mean temperature and humidity were recorded, a prop-vane gave wind speed and direction, a three-axis sonic anemometer gave the fluctuating components of the wind vector, platinum resistance-wire thermometers gave the fluctuating temperature, and Lyman-α hygrometers recorded the humidity fluctuations. The millimeter-wave signals, resistance-wire temperature, and Lyman-α humidity were digitized at 100 Hz. The sonic anemometers were digitized at 25 Hz. The other instrument's signals were digitized at 0.39 Hz. The table shows the great variety of clear-air micrometeorological statistics available from our instrumentation.

Figure 2 shows a probability density function (PDF) of the measured intensity; it is compared with lognormal and Gaussian PDFs. At such small intensity variances (0.02) there is little difference between lognormal and Gaussian PDFs, but the data definitely favor the lognormal PDF. Figure 3 shows the PDF of phase difference obtained from antennas 2 and 3 which have a separation of 2.9 m. This PDF is clearly Gaussian. In addition, we find that intensity and phase difference are uncorrelated.

Figure 4 shows the structure function of phase for each of our antenna pairs (separations). The structure function is definitely less steep than the slope of 5/3 that would be expected based on the inertial range prediction. This is

caused by the outer scale. A very simple prediction that includes the outer scale is shown as a solid curve for a horizontal outer scale of 14 m. The mutual coherence function (second moment of the field) is shown in Fig. 5. Since the log-intensity and phase difference are both Gaussian and uncorrelated, it follows that the mutual coherence function should be equal to $\exp[-.5(D_\chi + D_\phi)]$ where D_χ and D_ϕ are the log-amplitude and phase structure functions; we find that this formula predicts the values in Fig. 5 to within 0.5%.

In Fig. 6 we show the normalized variance of intensity versus the inertial range prediction for a spherical wave. Here the radio C_n^2 is obtained from the micrometeorological data. We see that the intensity variance is somewhat underestimated by the inertial-range prediction. This is likely caused by difficulties in calibrating the Lyman-α hygrometer.

Table .--Summary of micrometeorological data from tape 24, taken at 11:30 a.m., July 1983

Average Values	
Humidity	19 g/m^3
Temperature	32°C
Wind speed	5.3 m/s
Wind angle	10°
Pressure	993 mb
Solar flux	94% of full sun
Wind stress	-0.14 $(m/s)^2$
Humidity flux	0.1 $(g/m^2)/s$
Temperature flux	0.03°C m/s
Stability	-0.03
Square Roots of Variances	
Humidity	0.72 g/m^3
Temperature	0.35°C
Wind speed	1.2 m/s
Wind angle	11°
Streamwise wind component	1.1 m/s
Cross-stream wind component	1.0 m/s
Vertical wind component	0.54 m/s
Structure Parameters	
C_n^2 from optical scintillometers	2×10^{-13} $m^{-2/3}$
C_T^2 from optical C_n^2	0.03°C^2 $m^{-2/3}$
C_T^2 from resistance wires	0.03°C^2 $m^{-2/3}$
C_q^2 from Lyman-α hygrometers	0.2 $(g/m^3)^2$ $m^{-2/3}$
C_{Tq} from resistance wires and Lyman-α hygrometers	0.075°C (g/m^3) $m^{-2/3}$
C_n^2 for radio frequencies*	5.9×10^{-12} $m^{-2/3}$

*Obtained from Eq. (79), using C_T^2, C_q^2, and C_{Tq} from the resistance-wire thermometer and Lyman-α hygrometer with A_T and A_q obtained from the radio refractive-index equation.

Acknowledgment: Support was provided by ARO MIPR 122-85.

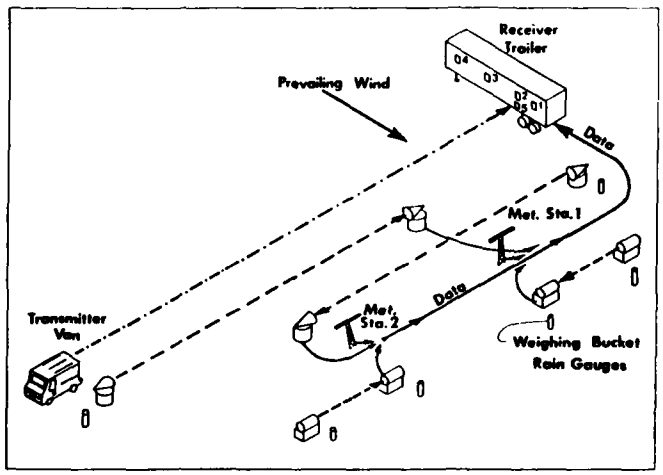

Figure 1.--The instrument positions at the experiment site. The dashed and dotted line denotes mm-wave propagation path (1.4 km); the long-dashed lines, the optical propagation paths (1 km each); and the short-dashed lines, the optical rain gauge paths (50 m each). Solid lines show the flow of micrometeorological data to the data aquisition system in the receiver trailer. Antennas are numbered 1 to 5 in the receiver trailer.

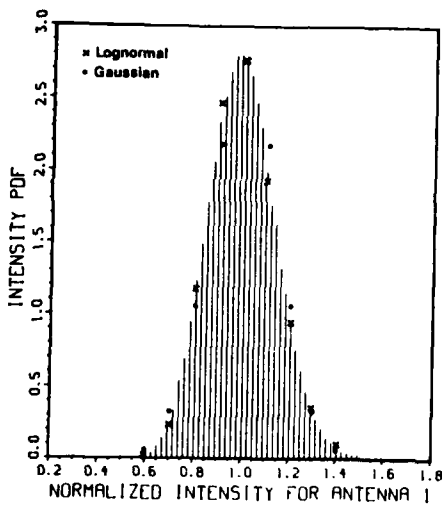

Figure 2.--Probability distribution function of intensity for antenna 1. Normalized intensity is scaled to unit mean value.

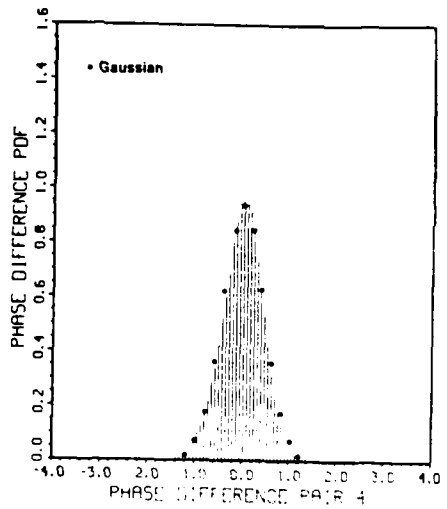

Figure 3.--Probability distribution of phase difference in radians

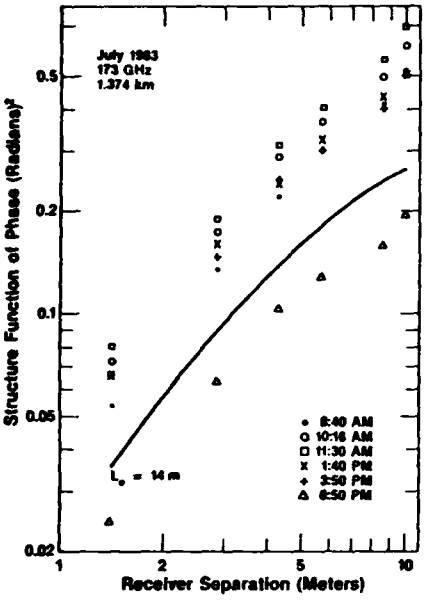

Figure 4.—The structure function of phase. The solid line represents a theoretical prediction for the 6:50 p.m. data

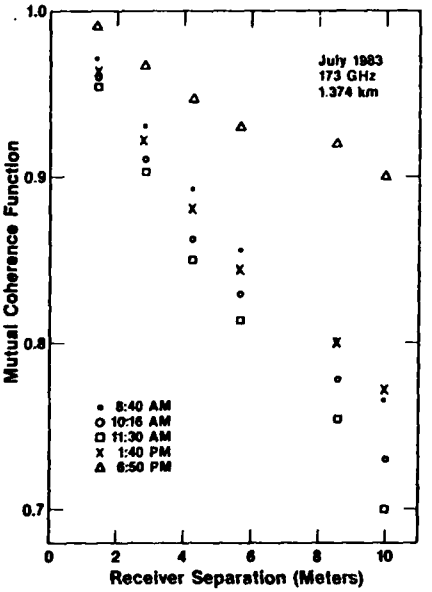

Figure 5.—The modulus of the mutual coherence function.

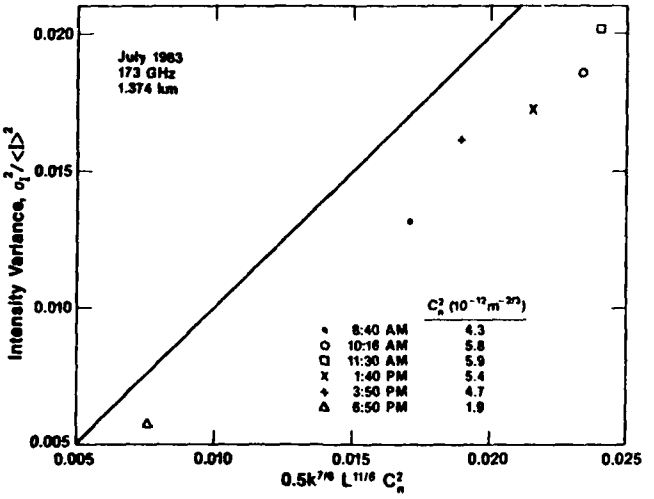

Figure 6.—The normalized variance of intensity versus its inertial-range formula. The straight line shows theoretical calculations.

MEASUREMENTS OF LASER SCINTILLATION IN STRONG TURBULENCE RELEVANT TO LASER EYE SAFETY

P14

R. J. Hill and J. H. Churnside
Wave Propagation Laboratory
National Oceanic and Atmospheric Administration
Boulder, Colorado 80303 USA

The ANSI exposure standard for laser light in the wavelength range 0.4 to 0.7 μm is

$$\tau^{1/4} I < 1.8 \quad s^{1/4}\ mW/cm^2 ,$$

where I is the irradiance in milliwatts per square centimeter and τ is the duration of exposure in seconds.[1] This limit applies for 2×10^{-5} s $< \tau <$ 10 s. The dark-adapted human pupil diameter of 7 mm is the standard for these exposure limits. However, eye damage is insensitive to the pupil diameter, so the daylight-adapted pupil diameter of 3 mm is also of interest.

The irradiance of a laser beam that has passed through the turbulent atmosphere consists of bright scintillation patches that move as the cross-path wind moves the refractive fluctuations. Do these spikes of irradiance exceed the exposure limits, and what are the appropriate irradiance statistics to be measured to define the exposure limits for scintillating laser light? We present measurements and novel statistics directed toward these questions.

We recorded the time series of scintillating irradiance of diverged He-Ne laser radiation (0.633 μm wavelength) propagated a distance of 1 km at a height of 2 m above flat, uniform grassland. Receiver apertures of 7 mm and 3 mm were used. Simultaneous measurements of propagation path-averaged refractive-index structure parameter, C_n^2, and cross-path wind component were carried out using the method of large-aperture scintillometers.[2,3] The following table gives basic information for the experiment runs:

Run	Sampling rate s^{-1}	Aperture size mm	Recorded duration s	Cross wind m/s	C_n^2 $10^{-12}\ m^{-2/3}$	Coherence length mm
A	2500	7	650	1.3	1.1	1.8
B	2500	7	650	2.2	1.0	1.7
C	2500	7	650	2.0	1.1	1.6
D	5000	3	650	3.6	1.2	1.4
E	2500	3	650	3.5	1.2	1.5
F	5000	3	325	1.6	0.70	3.3
G	5000	7	325	2.4	0.60	2.2

We calculated the irradiance probability density function (PDF) for each run. For all runs the irradiance PDFs were lognormal as shown in Fig. 1; the lognormal distribution having the same irradiance variance as the data is shown as circles surrounding dots. Our measurements are within the saturation regime such that the runs of lesser C_n^2 have greater irradiance variance. The greatest

observed intensities were "clipped" by the amplifier at 85 times the mean intensity.

By recording the irradiance time series we can obtain the joint statistics of irradiance and duration. We set thresholds of irradiance I_t at a variety of multiples of the mean irradiance $\langle I \rangle$ and determined the durations τ for which $I > I_t$ in each spike of irradiance. This was used to determine the conditional probability density $p(\tau | I > I_t)$ of duration τ conditional on $I > I_t$. We then integrated this from given threshold duration τ_t to ∞ to obtain the conditional probability distribution $P(\tau > \tau_t | I > I_t)$. We integrated the irradiance PDF to obtain the probability $P(I > I_t)$. From Bayes theorem we obtained the joint probability distribution $P(\tau > \tau_t, I > I_t)$ of duration $\tau > \tau_t$ and $I > I_t$ from the product

$$P(\tau > \tau_t, I > I_t) = P(\tau > \tau_t | I > I_t) \cdot P(I > I_t) .$$

A contour plot of this joint probability is presented in Fig. 2. The dashed line is a $\tau^{-1/4}$ exposure limit. Vertical displacement of the dashed line first crosses the probability contours at $\tau = 8 \times 10^{-4}$ s, indicating that spikes of this duration are most hazardous; longer duration spikes are less hazardous because of their lower probability of large irradiance. Given a value of $\langle I \rangle$ a line parallel to the dashed line exists such that $\tau_t^{1/4} I_t = 1.8\ s^{1/4}\ mW/cm^2$. Events above this line exceed the safety limit.

We find that Taylor's hypothesis does not hold; that is, the spikes of irradiance formed and vanished in a time much shorter than the time for them to have been swept across the receiver aperture. The spikes must move only about 1 mm in the duration they appear in our measured irradiance. Taylor's hypothesis would hold if the wind were as a solid body rotation about the transmitter. Of course it is not so, nor is the cross-wind component uniform along the propagation path.

We define a danger function at time t as follows

$$D(t) = \frac{1}{4\langle I \rangle} T^{-1/4} \int_{t-T}^{t} I(\tau) (t-\tau)^{-3/4} d\tau ,$$

where T is the temporal extent of the filter. We used T = 5.2 s and 2.6 s for sampling rates of 2500 s^{-1} and 5000 s^{-1}, respectively. The average of the danger function is unity, and it weights a spike in the irradiance with the 1/4 power of the spike duration. Thus a value D(t) = 2 implies an eye hazard twice that of a nonscintillating irradiance equal to $\langle I \rangle$. In Fig. 3 we present the probability distribution that D(t) exceeds a given value D_t. Danger function values as great as 12 were encountered in our experiment.

References

1. D. Sliney and M. Wolbarsht, Safety with Lasers and Other Optical Sources, Plenum Press, New York.

2. Ting-i Wang, G. R. Ochs, and S. F. Clifford, J. Opt. Soc. Am. 68, 334, 1978.

3. Ting-i Wang, G. R. Ochs, and S. F. Clifford, Appl. Opt. 20, 4073, 1981.

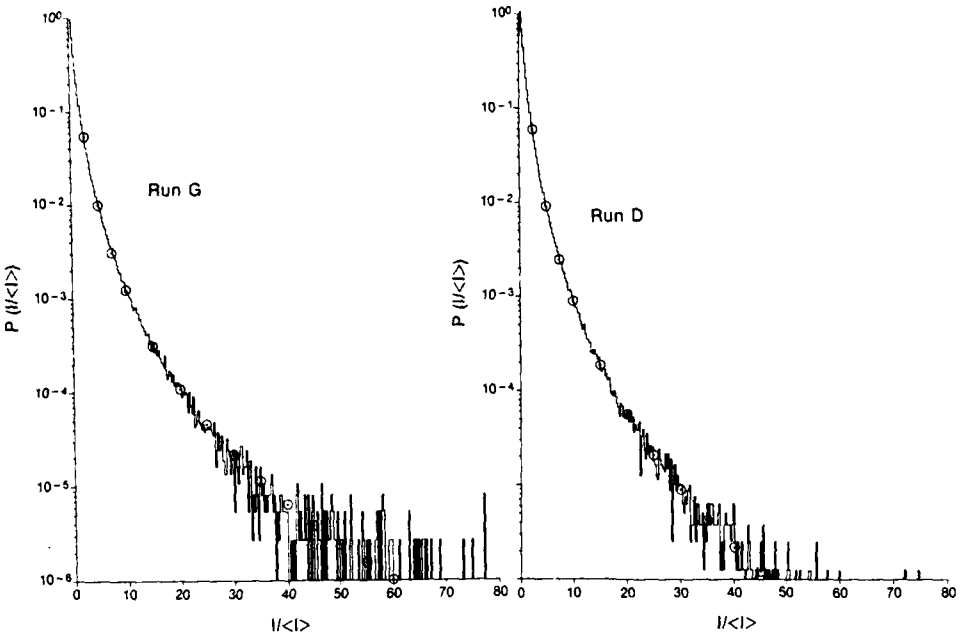

Figure 1. Probability density of irradiance normalized by the mean irradiance.

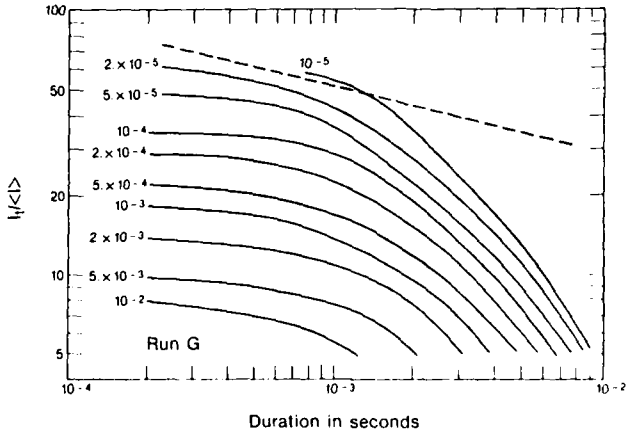

Figure 2. Contours of the joint probability distribution of $\tau > \tau_t$ and $I > I_t$. The dashed line has the -1/4 slope of the exposure limit.

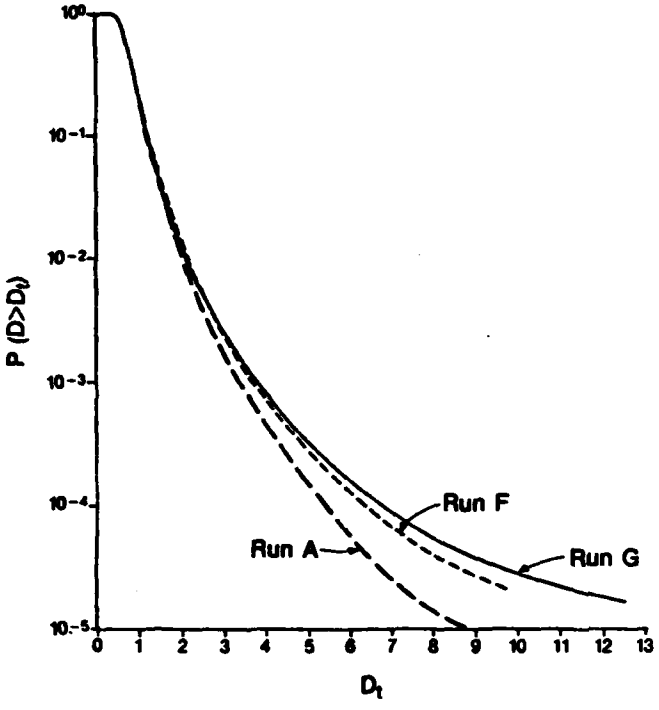

Figure 3. Probability distribution of $D > D_t$ for the danger function.

On the use of a CO_2 laser scintillometer for the investigation of heat transfer between a sea surface and the atmosphere* P15

W. Kohsiek

Royal Netherlands Meteorological Institute (KNMI),
De Bilt, The Netherlands

Introduction

The behaviour of the atmospheric boundary layer is largely influenced by the inputs of heat and water vapour at the surface. A potentially viable method for measuring these inputs is offered by optical scintillation observations. A beam of light (light is to be taken in a broad sense and the wavelength can range from visible to millimeter radiation) is directed horizontally over the surface and detected at some distance from the emitter. The observed radiation will show intensity fluctuations originated by temperature and humidity irregularities in the atmosphere, with relative contributions that depend on the wavelength of the radiation. Temperature and humidity fluctuations are coupled to the vertical surface fluxes of heat (sensible heat flux) and water vapour (latent heat flux) by semi-empirical relations to be discussed below. This paper focusses on the use of a CO_2 laser scintillometer for determining the latent heat flux from sea. In this application the advantage of the scintillation method is not so much its spatial averaged measuring, but its relative insensitivity to flow distortion and sea salt spray as compared to in-situ sensors mounted to a heavy platform some meters above the sea surface.
The CO_2 laser scintillometer was part of the HEXOS (Humidity Exchange Over Sea) pilot experiment in November 1984. HEXOS is an international research program with the ultimate goal to extend parameterization schemes for evaluating vertical water vapour flux over sea, emphasizing conditons with high wind speed. The HEXOS measurements are concentrated on a Dutch measuring platform in the North Sea, with significant contributions from research airplanes, ships, buoys, etc. In the fall of 1986 the main experiment will take place.

The scintillometer

The optical path of the scintillometer was between a lighthouse on the coast, where the CO_2 laser was installed, and the measuring platform. It covered a distance of 9.7 km at an average height of 15 m above the sea surface. The 2W laser beam was chopped mechanically at a rate of 1.6 kHz. On the platform, the radiation was focussed by a 2 cm diameter Germanium lense onto the surface of a liquid nitrogen cooled HgCdTe detector. The detector's output voltage was amplified, demodulated and bandpass filtered between 1.5 and 400 Hz; the resulting signal, that reflects the logarithm of the intensity fluctuations, was measured by a root-mean-square voltmeter. In this way the variance of the logarithm of the received intensity, $\sigma^2_{\ln I}$, was observed.

* This paper is published as HEXOS paper No. 1.

Other observations

On the platform several meteorological instruments were mounted, partly routine instruments for measuring quantities like the wind speed, air temperature and humidity, partly special instruments for observing the fast fluctuations of these quantities. In the context of this paper the routine observations are of interest including the measurement of the sea water temperature.

Theory

For a point source and point receiver and if $(\lambda L)^{\frac{1}{2}}$ is a length scale within the inertial range (Tatarski, 1961),

$$\sigma^2_{\ln I} = 0.50\, k^{7/6}\, L^{11/6}\, C_n^2 \,, \tag{1}$$

where L is the path length and $k = 2\pi/\lambda$ the wavenumber of the radiation. C_n^2 is the refractive-index structure parameter, and can be decomposed like

$$C_n^2 = \frac{A_T^2}{T^2} C_T^2 + \frac{A_Q^2}{Q^2} C_Q^2 + 2\,\frac{A_T A_Q}{TQ} C_{TQ} \,. \tag{2}$$

A_T and A_Q are dimensionless parameters that are given by Hill et al. (1980). T is the temperature in Kelvin and Q the absolute humidity in, e.g., kg m^{-3}. The first term of the right-hand side of Eq.(2) reflects the contribution of temperature fluctuations to C_n^2, the second that of humidity fluctuations and the third term gives the contribution of correlated temperature-humidity fluctuations. C_T^2, C_Q^2 and C_{TQ} are the structure parameters of temperature, humidity, and their correlated fluctuations, respectively. The relation between C_T^2 and the temperature flux is from Wyngaard et al. (1971):

$$\frac{C_T^2\, z^{2/3}}{T_*^2} = 4.9[1 - 7(z/L_M)]^{-2/3} \,, \tag{3}$$

where

$$L_M = u_*^3 T/kg(Q_o + 0.61\, TE_o/\rho). \tag{4}$$

In these equations, Q_o is the vertical flux of temperature (K m s^{-1}), E_o that of water vapour (kg m^{-2} s^{-1}), k = 0.4 the von Kármán constant, g the acceleration of gravity, ρ the air density, u_* the friction velocity, z the height of observation above the surface and T_* the temperature scaling parameter defined by $T_* = -Q_o/u_*$. We assume that an equation similar to (3) holds for the humidity structure parameter, viz.

$$\frac{C_Q^2\, z^{2/3}}{Q_*^2} = 0.8 \times 4.9\,[1 - 7(z/L_M)]^{-2/3} \,, \tag{5}$$

where $Q_* = -E_o/u_*$. The factor 0.8 has been found experimentally by Fairall et al., 1980; however, it should be noted that Eq.(5) has not been thoroughly tested so far. From Eqs.(3) and (5) it follows that

$$\frac{\rho c_p Q_o}{L_v E_o} = (0.8)^{\frac{1}{2}}\, \frac{\rho c_p}{L_v}\, (C_T^2/C_Q^2)^{\frac{1}{2}} \,, \tag{6}$$

which expresses that the Bowen ratio, that is the ratio of the sensible heat flux, $\rho c_p Q_o$ (c_p is the specific heat of air at constant pressure), to the latent heat flux, $L_v E_o$ (L_v is the latent heat of vaporization of water) is directly proportional to $(C_T^2/C_Q^2)^{\frac{1}{2}}$. Relation (6) will be used beneath. We

conclude from (3), (4) and (5) that the sensible and latent heat flux can be calculated from C_T^2, C_Q^2, u_* and L_M.
In order to infer the structure parameters C_T^2 and C_Q^2 from observations of C_n^2 we have to put in two more relations in addition to Eq.(2). The first relation is

$$\frac{Q_o}{E_o} = \frac{c_T}{c_E} \frac{T_s - T_a}{Q_s - Q_a} , \qquad (7)$$

where T_s is the sea surface temperature, T_a the air temperature at some height, Q_s the saturated humidity at temperature T_s, and Q_a the humidity at the same height as T_a; c_T and c_E are the bulk transfer coefficients for temperature and humidity, respectively. It is assumed that $c_T = c_E$ (Large and Pond, 1982). Combining Eqs.(6) and (7), a relation between C_T^2 and C_Q^2 is obtained with parameters T_s, T_a and Q_a. The second relation is

$$C_{TQ} = 0.8(C_T^2 \, C_Q^2)^{\frac{1}{2}} . \qquad (8)$$

It is equivalent to stating that the correlation coefficient between temperature fluctuations and humidity fluctuations with spatial scales within the inertial range is 0.8. There is evidence in the literature that the correlation is as high as this if the fluxes of temperature and humidity have equal directions (Antonia et al., 1978; Fairall et al., 1980; Friehe et al., 1975; Wyngaard et al., 1978) . For one of the runs to be discussed in the next section, the Bowen ratio was negative and a correlation coefficient of -0.5 was assumed instead of 0.8. The set of equations (2), (6), (7) and (8) allows one to calculate C_T^2 and C_Q^2 from the observations of C_n^2, T_a, Q_a and T_s. Then Q_o and E_o can be calculated from Eqs.(3) and (5) if u_* and L_M are kown. The final step is

$$u(z) = \frac{u_*}{k} [\ln \frac{z}{z_o} - \psi_m(\frac{z}{L_M})], \qquad (9)$$

the well-known flux-profile relationship. For a discussion of this relation in relevance to a marine environment we refer to Large and Pond (1982); according to these authors, $z_o = 4.9 \times 10^{-5}$ m is assumed. Given the wind speed u(z) at level z, u_* and L_M can be calculated from Equation (9) if Q_o and E_o are known, because L_M is a function of Q_o and E_o (Eq.(4)). Equation (9) has thus to be solved by iteration. In case of the examples to be shown below, the iteration proved to be very fast because of the small absolute values of the stability parameter z/L_M.

Results and Discussion

Data were obtained on 3 days in November 1984 under favourable conditions, i.e. westerly winds (on-shore). Eight runs of approximately 45 min duration each were analysed. Humidity fluxes were calculated from the scintillation observations by means of the procedure outlined in the foregoing section, and also from the observations of air temperature, humidity, sea water temperature and wind speed by using bulk transfer coefficients published by Large and Pond (1982). The results are shown in the Table. It follows that the humidity fluxes derived from the scintillation observations are about 20% lower than the ones calculated with the bulk method, which means a reasonable good agreement.
It should be mentioned again that the scintillation observations alone were not sufficient to calculate E_o. Additional information was needed, viz. the Bowen ratio, the temperature-humidity correlation coefficient and the friction velocity. One may therefore wonder how sensitive these water

vapour fluxes are to the additional quantities. As to the first six runs of the Table, it was found that an increase of the Bowen ratio by 10% gives a -7% change of E_o, and a 10% increase of the correlation coefficient a -2% change of E_o. The last run but one is insensitive to such variations because the Bowen ratio is zero, whereas for the last run the changes are 5% and -5%, respectively. The sensitivity of E_o to the friction velocity depends on the stability parameter z/L_M; for small positive values of $-z/L_M$, E_o is nearly directly proportional to u_*, whereas for large positive values of $-z/L_M$, E_o tends to be insensitive to u_*. It should also be mentioned that E_o depends on the empiricially determined stability function in Eq.(5).

Table Comparison between humidity fluxes calculated with the scintillometer, and calculated with the bulk aerodynamic method. B = Bowen ratio, u_a = wind speed. Also shown are the contributions to C_n^2 of the C_Q^2 term and the C_{TQ} term of Eq.(2) relative to that of C_T^{2n}.

Date	Start time (GMT)	u_a (m s^{-1})	B	L_M (m)	C_n^2 ($10^{-15} m^{-2/3}$)	rel. contr. C_Q^2	rel. contr. C_{TQ}	L_vE_o scint. (Wm^{-2})	L_vE_o bulk (Wm^{-2})
Nov. 6	13:56	7.3	0.23	-129	0.42	0.11	0.53	31	38
	15:31	6.8	0.21	-124	0.34	0.13	0.57	28	38
	16:48	5.1	0.15	-80	0.23	0.24	0.79	24	30
Nov. 20	14:00	9.5	0.18	-152	0.89	0.18	0.68	69	86
	15:24	8.5	0.17	-135	0.71	0.20	0.72	59	74
	16:46	9.7	0.15	-174	0.76	0.24	0.79	71	82
Nov. 21	10:18	13.0	0	-1179	0.076	∞	-	75	81
	16:00	12.1	-0.07	∞	0.066	1.06	-1.03	63	67

References

Antonia, R.A., A.J. Chambers and C.A. Friehe, 1978: Statistical Properties of Optical Refractive Index Fluctuations in the Marine Boundary Layer. Bound.-Layer Meteor., 15, 243-253.

Fairall, C.W., G.E. Schacher and K.L. Davidson, 1980: Measurements of the Humidity Structure Function Parameters, C_q^2 and C_{Tq}, over the Ocean. Bound.-Layer Meteor., 19, 81-92.

Friehe, C.A., J.C. La Rue, F.H. Champagne, C.H. Gibson and G.F. Dreyer, 1975: Effects of Temperature and Humidity Fluctuations in the Optical Refractive Index in the Marine Boundary Layer. J. Opt. Soc. Amer., 65, 1502-1511.

Hill, R.J., S.F. Clifford and R.S. Lawrence, 1980: Refractive-Index and Absorption Fluctuations in the Infrared caused by Temperature, Humidity and Pressure Fluctuations. J. Opt. Soc. Amer., 70, 1192-1205.

Large, W.G., and S. Pond, 1982: Sensible and Latent Heat Flux Measurements over the Ocean. J. Phys. Oceanogr., 12, 464-482.

Tatarski, V.I., 1961: Wave Propagation in a Turbulent Medium. McGraw-Hill, New York, 285 pp.

Wyngaard, J.C., W.T. Pennel, D.H. Lenschow, and LeMone, 1978: The Temperature-Humidity Covariance Budget in the Convective Boundary Layer. J. Atmos. Sci., 35, 47-58.

Wyngaard, J.C., Y. Izumi, and S.A. Collins, Jr., 1971: Behavior of the Refractive-Index Structure Parameter near the Ground. J. Opt. Soc. Amer., 61, 1646-1650.

LIDAR DETERMINATION OF THE HORIZONTAL AIR MOTION VELOCITY IN THE ATMOSPHERIC BOUNDARY LAYER

P16

Kolev I.N., O.P.Parvanov, R.P.Avramova, V.N.Naboko, B.K.Kaprielov
Institute of Electronics - Bulgarian Academie of Sciences

Lidar technique for wind velocity determination has been widely adopted lately in the atmospheric boundary layer investigations. Derr and Little (1970) [1], Eloranta et all.(1975) [2], Armstrong et all. (1976) [3], Zuev et all. (1977) [4], Sasano et all. (1982) [5], Kolev et all. (1984) [6] etc., have remotly measured the wind velocity by means of correlation analysis of aerosol backscattering profiles obtained from lidar.

The results of sounding presented in this paper are obtained employing the scheme shown on Fig.1. Sounding in vertical direction using a three-beam lidar is energeticly the optimal condition for obtaining the elevation profile of the investigated parameters.

The method used in this paper for the determination of the wind velocity is based on the correlation of optical signals backscattered from aerosol inhomogenities passing through the observed space volumes. The method essentially requires the estimation of the bias time τ_m of the cross-correlation functions maximum

$$R_{xy}(\tau) = \lim_{T\to\infty} \frac{1}{T} \int_0^T X(t)\,Y(t-\tau)\,dt$$

where X(t) and Y(t) denote the time sequences of the aerosol backscatterring coefficient values recieved from each pair of the three observed space volumes, τ is the bias when determining the correlation function and T is the time of measurement.
Proceeding from the assumption (valid in most cases) that the aerosol inhomogenities are entirely carried along by the wind their drift velocity (i.e. wind velocity) is determined using the

classic relation $\zeta = V \cdot \tau_m$

where ζ is the dimension of the measuring base and V is the wind speed.

The remote measurements of the wind velocity were conducted during clear nights, early and late hours of the day.using the lidar designed at the Institute of Electronics-Bulgarian Academie of sciences. The lidar uses a Q-switched YAG:Nd^{3+} laser emitting second harmonic light pulses of 35 mJ with variable repetition rate from 3 to 12,5 Hz as the transmitter and 0,15 m dia. telescope as the reciever. 64 Kbytes RAM computer controls the operation of the lidar electronic part and stores the data on a floppy disc.

To determine the wind velocity time sequences with different lengths providing the time dependence of the aerosol backscattering coefficient value from the three selected directions were used. The typical measurements were carried out with time averaging from 2 to 10 minutes and for inhomogenities with 30 to 300 meters dimension. Fig.2 shows a typical three cross-correl relation functions usually computed for every sounded height. When slight trends in the time sequences existed they were filtered, when it was required the correlation functions were filtered too. Curves shown on Fig.2 have not undergone filtering.

Lidar experimets accompanied by conventional measurements of the wind velocity - theodolite and radar. Theodolite measurements were conducted almost simultaneously (within 5 to 30 minutes) at a distance of several meters from the lidar. In the radar case the data were taken from regular sounding provided by meteorology service 100 to 200 meters from the lidar within 2 hours of the lidar measurements. The results are summarized on Fig.3. In any case the determined directions of the wind velocity

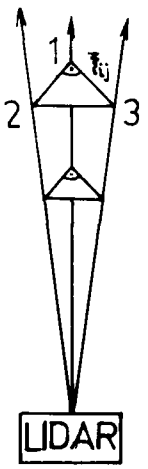

FIG.1 The geometry used for lidar wind measurements.

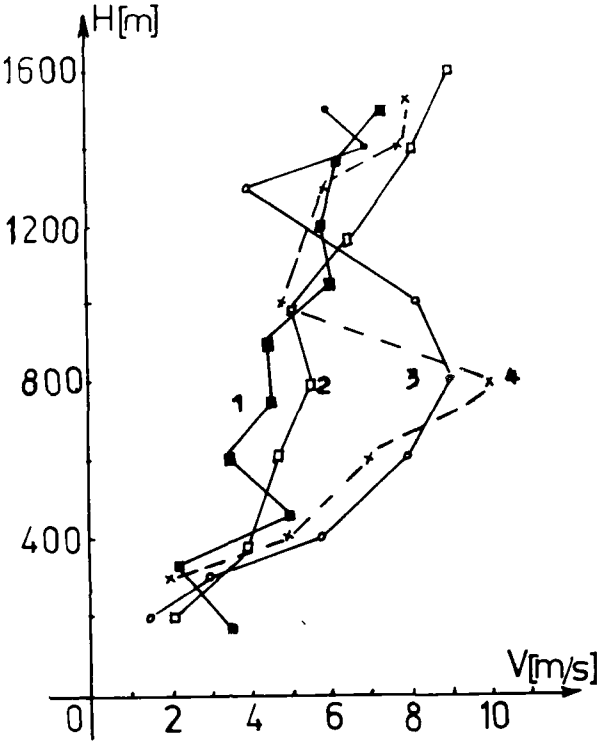

FIG.3 A comparison of lidar (2,3) and pilot balloon (1), radar-tracked pilot balloon (4) wind measurements.

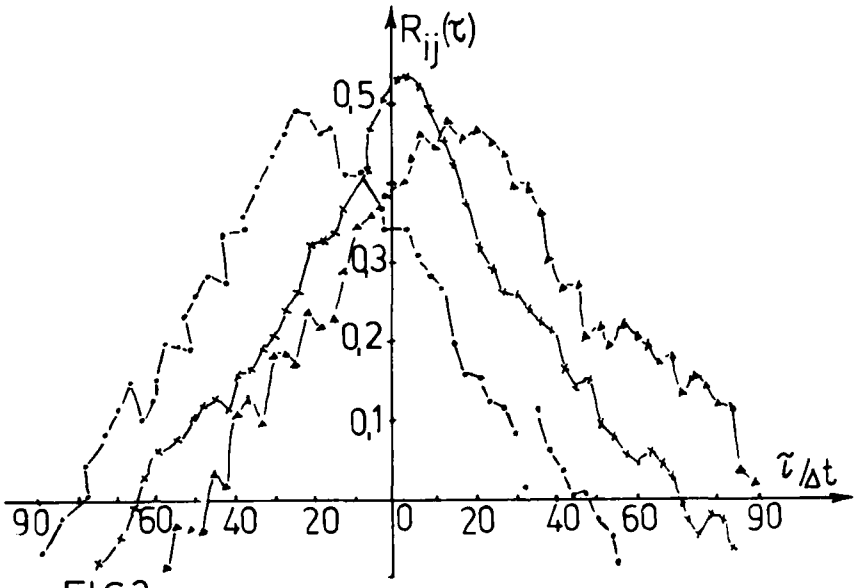

FIG.2 Cross-correlation functions
$R_{12}(\tau)$ -·-, $R_{13}(\tau)$ -·-, $R_{23}(\tau)$ ---

coincided within 10 to 15 degrees.

However, the comparison of the obtained wind velocity values is quolitative since in the case of theodolite and radar measurements the pilot balloons fly through the measured height in 10 to 20 seconds while the lidar observes the signature volumes for several minutes. The results of the comparison considerably depend on time and spatial coincidence of measurements since in the atmospheric boundary layer the wind velocity ubruptly changes.

Experimental results and their comparison with conventional methods demonstrate the ability of vertical sounding to determine the mean wind velocity in the boundary layer using aerosol inhomogenities as natural tracers. The range of the inhomogenities dimension from 30 to 300 m was found to contain the most useful wind information.

In conclusion, it should be noted that the obtained lidar data contained also information about: the inhomogenities spatial dimensions, existence of the temperature inversions, the height of the lower boundary of the clouds, the presence of the wave processes in the atmosphere and their parameters as well, etc. which all are dependent on the sinoptic situation.

References:

1. Derr V.E., C.G.Little, 1970, Appl. Opt., 9, p. 1982.
2. Kloranta E.W., J.M.King, J.A.Weinman, 1975, J.Appl.Meteor., 14, p.p. 1485-1489.
3. Armstrong R.L., J.B.Mason, T.Barber, 1976, Appl.Opt., 15,2891.
4. Zuev V.E., Y.M.Vorevodin, G.G.Matvienko et all.,Appl.Opt., 16, p.p. 2231-2235.
5. Sasano Y., H.Hirokara, T.Yamasaki et all.,1982, J.Appl.Meteor., 21, p.p. 1516-1523.
6. Kolev I., O.P.Parvanov, B.Kaprielov, 1984, 12-th Intern.Laser Radar Conf.,Aix-En-Provence, France, p.p. 399-402.

ANGULAR RESOLUTION OF AN OPTICAL RECEIVER IN A TURBULENT ATMOSPHERE FOR A WIDE RANGE OF THE APERTURE DIAMETERS

I. Gert and Y. Weissman

Soreq Nuclear Research Center, Yavne 70600, Israel P17

An optical wave propagating through a turbulent atmosphere has a distorted wavefront due to different phase shifts along different propagation paths. This distortion randomly changes the angle of arrival, both in space and in time, and increases the effective spot size of the focused beam. The theory of the light wave distortion by a turbulent atmosphere was presented by Tatarski [1]. This theory was used for the study of the angle of arrival fluctuations in numerous studies, mainly for limited intervals of the aperture diameter [2-6]. The aim of the present work was to obtain the expression for the angle of arrival variance for a wide range of aperture diameters. The consideration was restricted to the case of a plane wave propagating perpendicular to the objective plane.

The correlation function of the angle of arrival was determined by Tatarski as

$$B_j(\rho) = \langle \alpha_j(\vec{r})\alpha_j(\vec{r}+\vec{\rho}) \rangle = \begin{cases} \frac{1}{2k^2}\left|\frac{\partial^2 D_s}{\partial \rho^2}\right|, & j = 1 \\ \frac{1}{2k^2\rho}\left|\frac{\partial D_s}{\partial \rho}\right|, & j = 2 \end{cases} \qquad (1)$$

where $\langle \ldots \rangle$ stands for averaging over the time or the statistical assembly, the indices $j=1,2$ stand for the angle of arrival deviations from the normal to the objective plane, along and perpendicular to the vector ρ, respectively, k is the wave number, and $D_s(\rho)$ is the structure function of the phase. The structure function D_s is known for three intervals of ρ: $\rho \ll \ell_o$, $\ell_o \ll \rho \ll \rho_F$, $\rho_F \ll \rho \ll L_o$, where ℓ_o and L_o are correspondingly the inner and the outer scales of the turbulence and ρ_F is the radius of the first Fresnel zone [5]. Substituting the functions D_s in (1), one obtains the expressions for B_j $(j=1,2)$ valid for the intervals quoted above. These expressions are as follows:

$$B_j(\xi) = B_o = AC_n^2 x \ell_o^{-1/3}, \quad \xi \ll 1 \qquad (2)$$

$$B_j(\xi) = b_j B_o \xi^{-1/3}, \quad 1 << \xi << \xi_F, \quad \sigma_1^2 < 0.6 \tag{3}$$

$$B_j(\xi) = 1.5\, b_j B_o \xi^{-1/3}, \quad 1 << \xi << \xi_F, \quad \sigma_1^2 > 25 \tag{3'}$$

$$B_j(\xi) = 2\, b_j B_o \xi^{-1/3}, \quad \xi_F << \xi << L_o/\ell_o \tag{4}$$

where

$$\xi = \rho/\ell_o, \quad \xi_F = \rho_F/\ell_o \tag{5}$$

σ_1 is a propagation parameter, C_n^2 is a turbulence structure constant, x is the propagation distance, A = 1.225, b_1 = 0.661, b_2 = 0.996.

The expressions (2)-(4) were fitted by an interpolation function

$$B_j(\rho) = B_o\left[\frac{1 + g_j^{(+)}\xi^2}{(1+\xi^2)^{7/6}} + \frac{g_j^{(-)}\xi^2}{(\xi_F^2+\xi^2)^{7/6}}\right] \tag{6}$$

$$g_j^{(\pm)} = b_j[1 \pm \sigma_1^2/(10 + 2\sigma_1^2)] \tag{7}$$

For a long exposure, the angle of arrival average is zero, so the variance is $\langle \alpha^2 \rangle = B_o$. The short exposure variance is $\langle (\bar{\alpha})^2 \rangle$, where the upper line stands for the aperture overaging

$$\langle (\bar{\alpha})^2 \rangle = \frac{1}{\pi^2 R^4} \int d\vec{r}_1 \int d\vec{r}_2 [B_1(\rho)\cos^2\psi + B_2(\rho)\sin^2\psi] \tag{8}$$

where $\vec{\rho} = \vec{r}_2 - \vec{r}_1$, R is the aperture radius, and ψ is an angle between $\vec{\rho}$ and a fixed direction (x axis, for example). The integration can be performed numerically. The results of calculations for ℓ_o = 5 mm are presented in Fig. 1, together with the Fried's angle of arrival variance [2] and the diffraction angle. The difference between the long and short exposure angles of arrival is significant when the aperture diameter is smaller than $\sim 10\,\ell_o$. However, for very small diameters (D < 1 cm) the diffraction broading becomes more important than the turbulence fluctuations.

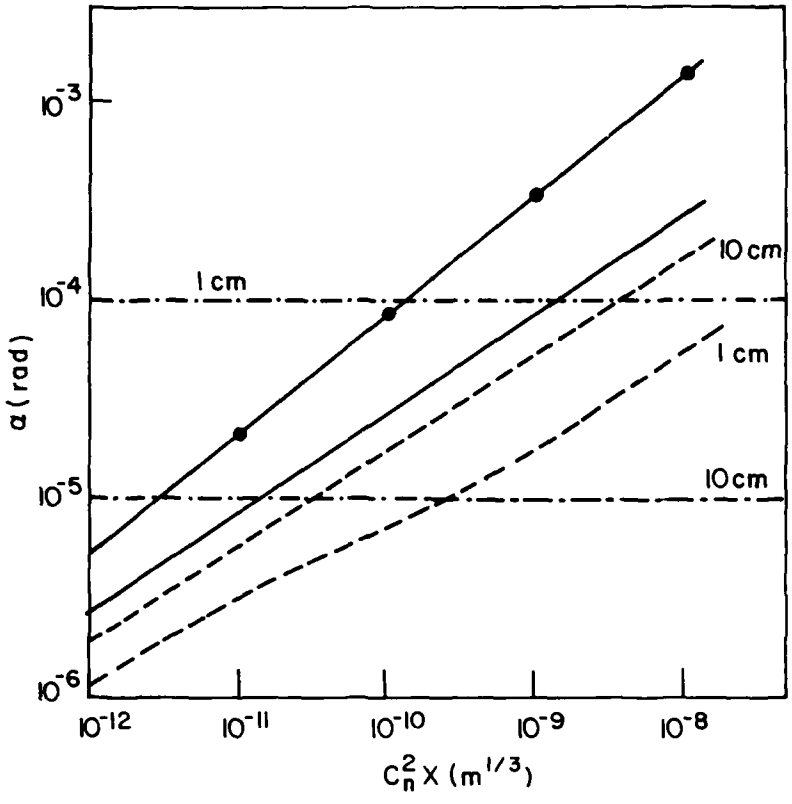

Fig. 1

Angle of arrival variance as a function of the product $C_n^2 x$. ℓ_o = 5 mm, λ = 5 μm. The numbers on the curves stand for aperture diameters.

—— angle of arrival variance, long exposure

---- angle of arrival variance, short exposure

-•- diffraction limit of angular resolution

—•— Fried's angle of arrival variance, long exposure

REFERENCES:

[1] Tatarski, V.I., The effects of the Turbulent Atmosphere on Wave Propagation, Israel Program for Scientific Translations, Jerusalem, 1971.

[2] Fried, D.L., J. Opt. Soc. Am. 55, 1427 (1965).

[3] Lawrence, R. S. and Strohbehn, J. W., Proc. IEEE 58, 1523 (1970).

[4] Lutomirski, R. F. and Buser, R. G., Appl. Opt. 13, 2869 (1974).

[5] Fante, R.L., Proc. IEEE, 63, 1669 (1975).

[6] Gurvich, A. S., Kallistrova, M. A. and Time, N. S., Radiophys. Quant. Electron. 11, 771 (1968).

The Propagation of Optical Pulses through Dense Scattering Media P18

H.Leelavathi and J.P.Pichamuthu
National Aeronautical Laboratory
Bangalore 560017, India.

We develop a simple diffusion model to explain and predict pulse shapes both in scale model and actual cloud propagation experiments. The source-free diffusion equation for a scattering medium of one-dimensional geometry is[1]:

$$D\,\partial^2 I/\partial x^2 = \partial I/\partial t$$

where I is the net intensity and D is the diffusion coefficient.

However we consider the photons to propagate simultaneously both by one-dimensional and three-dimensional diffusion with diffusion coefficients D_1(=b'c) and D_3(=b'c/3) respectively; b' is the diffusion length, c is the velocity of light.

The transmitted pulse is the superposition of the two solutions of the above equation obtained separately using the diffusion coefficients D_1 and D_3.

A lumped RC electrical transmission line model (Fig.1 inset) of the above equation using RC=b'/c, and RC=3b'/c for one-dimensional and three-dimensional diffusion respectively, simplifies the treatment of the problem. Each T-section (shown boxed in Fig.1 inset) represents one diffusion length b' of the medium. The current i(t) through the short circuit in the final section is the analogue of the intensity emerging into free space. The impulse response of the network for various numbers of sections is also shown in Fig.1. The response of a cloud of diffusion thickness τ_D ($\equiv$L/b' where L=geometric thickness) is the superposition of the response of two networks each containing τ_D sections but with RC values b'/c and 3b'/c. For non-integral values of τ_D, the solutions are obtained by interpolation. The response i(t) of the medium to any arbitrary input is easily obtained by convolving the given impulse response h(t) with the input source function S(t), ie. i(t) = h(t)*S(t). The impulse response may directly be used when S(t) is impulse-like.

Pulse shapes obtained experimentally[2-4] are compared with our predictions in Figs.2-5. Curves A and B represent solutions to the diffusion equation using D_1 and D_3 as the diffusion coefficients. E is the experimental pulse. The amplitudes of A and B are chosen so that the curve (A+B) fits the experimental curve. For scale model clouds (Figs.2-4), S(t) has a FWHM of $\sim$ 25 psec, and the values of τ_D are calculated from the expression $\tau_D = g\tau$, using tabulated[2] values of g and τ ($g = 1-\cos\theta$, and τ is the optical thickness). For the real cloud, (Fig.5)[4], the value τ_D=4 fits the experimental curve. The one-dimensional component can be isolated using a small field of view.

The model gives a satisfactory fit to the experimental pulse shapes observed for both real and simulated clouds of $\tau_D \gtrsim 4$. The agreement with experiment indicates that the inclusion of one-dimensional (in addition

to three-dimensional) diffusion is necessary to describe pulse propagation through dense media. For media of $\tau_D < 4$ (Fig.3), in addition to the response predicted by our model, a temporally compact source-like part (S_p) appears in the output pulse. This is the predicted[5] multiple forward scatter component.

Given an impulse like source function and narrow field of view one-dimensional diffusion dominates in the received pulse. Then, b' for the medium can be directly estimated (for $\tau_D > 4$) from $b' \simeq 8.2\ t_p^{-1.85}\ \tau_D\ c$, where t_p is then approximately the instant of peaking of the received waveform. If a wide field of view is used, $b' \simeq 2.7\ t_p^{-1.85}\ \tau_D\ c$.

The present lumped model can also be extended to describe pulse propagation through inhomogeneous (layered) media by adding sections with values of RC appropriate to each layer.

References

1. S. Ito and K. Furutsu, J. Opt. Soc. Am., **70**, 366 (1980)
2. R.A. Elliott, Appl. Opt., **22**, 2670 (1983)
3. R.A. Elliott, (unpublished)
4. G.C. Mooradian and M. Geller, Appl. Opt., **21**, 1572 (1982)
5. R.M. Lerner and J.D. Summers, Appl. Opt. **21**, 861 (1982)

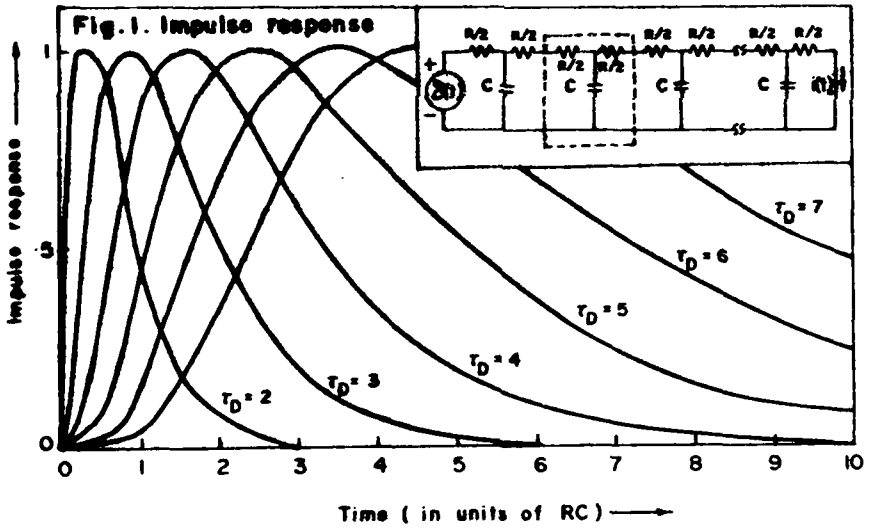

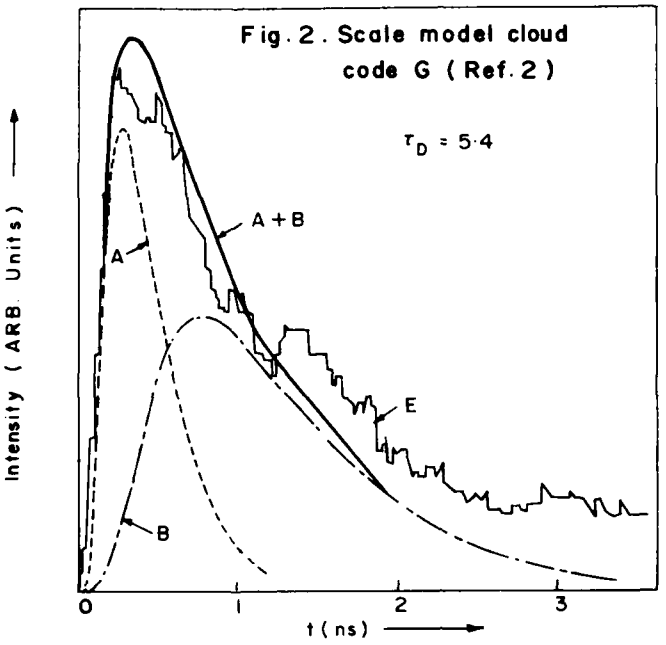
Fig. 2. Scale model cloud
code G (Ref. 2)
τ_D = 5·4
A+B
A
B
E
Intensity (ARB. Units)
0
1
2
3
t (ns)

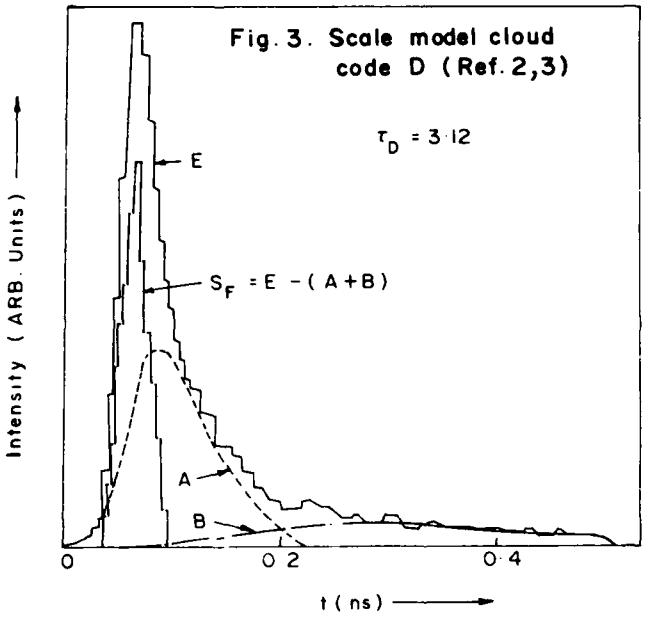
Fig. 3. Scale model cloud
code D (Ref. 2,3)
τ_D = 3·12
E
S_F = E − (A+B)
A
B
Intensity (ARB. Units)
0
0·2
0·4
t (ns)

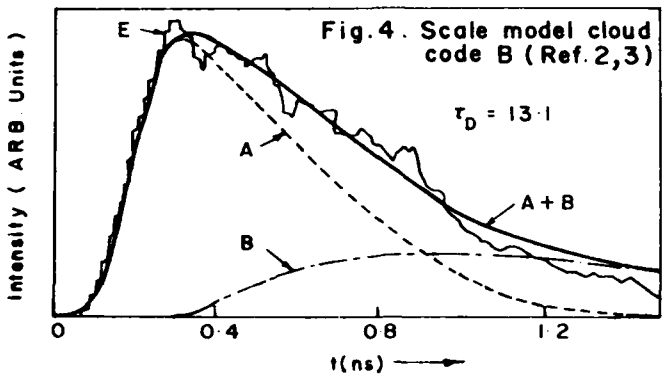
Fig. 4. Scale model cloud code B (Ref. 2,3)
τ_D = 13·1
E
A
A+B
B
Intensity (ARB. Units)
0
0·4
0·8
1·2
t(ns)

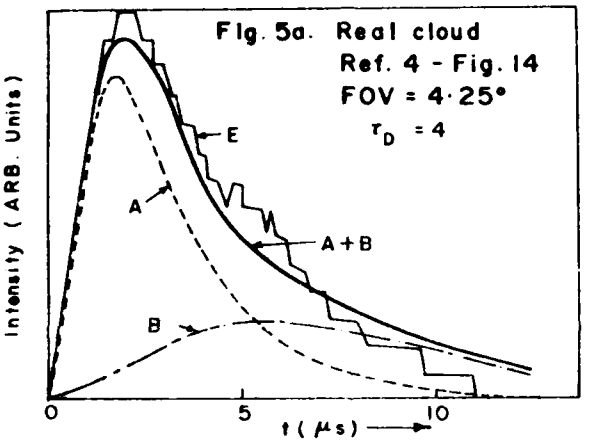
Fig. 5a. Real cloud
Ref. 4 - Fig. 14
FOV = 4·25°
τ_D = 4
E
A
A+B
B
Intensity (ARB. Units)
0
5
10
t (μs)

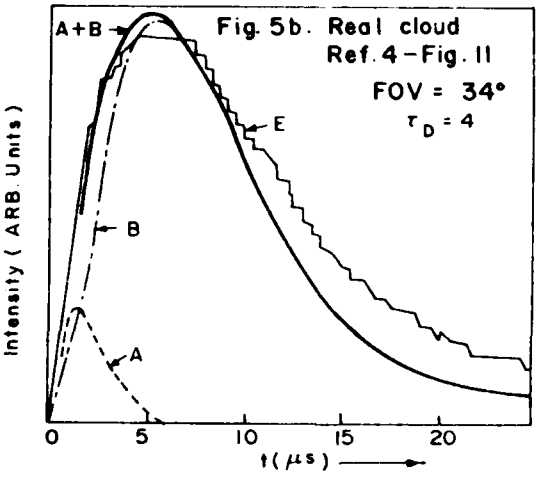
Fig. 5b. Real cloud
Ref. 4 - Fig. 11
FOV = 34°
τ_D = 4
A+B
E
B
A
Intensity (ARB. Units)
0
5
10
15
20
t (μs)

I. MAIGNIAL[1] - J.L. BRENGUIER[2] - P.F. COMBES[3] - C. POUIT[4]

INTRODUCTION

A radiometric system is being studied to measure the temperature of the air, locally, in clouds, from an aircraft. Probes currently used: contact sensors or I.R. radiometers generally fail in clouds. Water drops impacts on sensor sensitive element can be avoided by using protective housings, but this substancially increases the response time, excluding small scale measurements along the flight trajectory. In I.R. radiometry, the dimensions of water droplets are not negligible compared with the wavelength λ (Mie region: $2\pi r/\lambda \simeq 1$, where r is the droplet radius);the droplet signature is then a complex expression due to diffraction. These remarks lead us to a non-contact measurement in the Rayleigh region ($2\pi r/\lambda \ll 1$) where droplets dimensions are very small with regard to λ.

I. DEVICE ANALYSIS

The device (fig.1) uses a 60 GHz radiometer coupled with a cavity resonator. The resonator is a two spherical mirrors open cavity tuned on the molecular resonance of oxygen at 60 GHz. Power radiated by air and the mirrors, filtered by the cavity bandwidth and measured by the microwave radiometer is expressed by :

$$P_R = kT_RB \quad (1)$$

where T_R is defined as the radiometric temperature of the cavity, k is the Boltzmann's constant, and B is the system bandwidth.

1 Thesis student -Université Paul Sabatier-ONERA/CERT 31055 Toulouse.
2 Engineer at the C.Nat.Rech.Met. 31057 Toulouse
3 Professor at the Université P. Sabatier Toulouse
4 Head of the microwave department - ONERA/CERT- 31055 Toulouse

T_R can be calculated , by taking into account noise spectral densities of different elements of the cavity: the oxygen (T_g,Q_g), the mirrors or any kind of radiation source inside the cavity, like the cloud particles (T_m,Q_m):

$$T_R = \frac{\beta}{\beta+1}\left\{\frac{T_g}{1+Q_g/Q_m} + \frac{T_m}{1+\frac{Q_m}{Q_g}}\right\} \quad (2)$$

where β = coupling factor,

T_g= gas temperature

T_m= mirror or cloud particles temperature

Q_g= Q factor relative to gas losses

Q_m= Q factor relative to mirrors or cloud particles losses.

Then, the temperature of the air (T_g) expresses as a function of the cavity temperature measured by the radiometer as:

$$T_g = \frac{\beta+1}{\beta} T_R + \frac{Q_g}{Q_m}\left(\frac{\beta+1}{\beta} T_R - T_m\right) \quad (3)$$

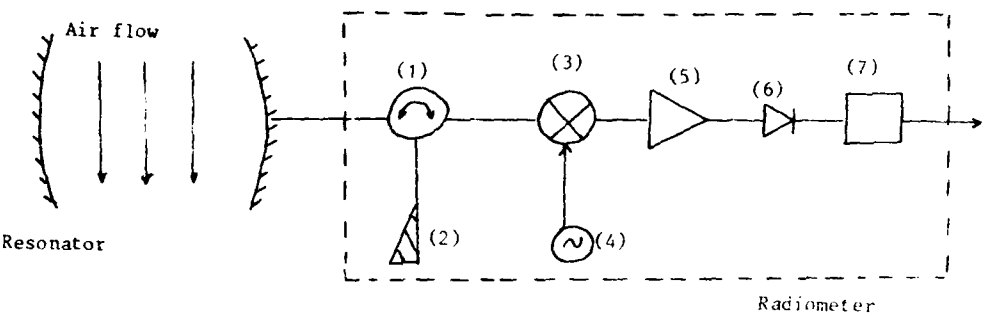

Figure 1 : Experimental set-up

(1) Switch
(2) Reference load
(3) Mixer
(4) Local oscillator
(5) IF amplification
(6) Square law detector
(7) Low pass filter

II. RADIOMETER RESOLUTION

T_{sys} is defined as the system input noise temperature, including T_R and the receiver equivalent input noise temperature T_{rec} : $T_{sys} = T_R + T_{rec}$ (4)

The radiometer parameter of merit, given by the product of the resolution ΔT_R by the time response square root $\sqrt{\tau}$, is for a Dicke radiometer :

$$\Delta T_R \sqrt{\tau} = 2 \frac{T_{sys}}{\sqrt{B}} \quad (5)$$

where B is related to the cavity resonance frequency f_r :

$$B = \frac{f_r}{Q_{pr}} (1+\beta) \qquad (6)$$

where $1/Q_{pr} = 1/Q_g + 1/Q_m$

Relations (3,5 and 6) express that the cavity must be largely overcoupled with the radiometer (β maximum) so that

-most of the power radiated by the oxygen is transmitted to the radiometer ($\frac{\beta+1}{\beta}$ minimum $\simeq 1$) and

-the cavity bandwidth is large for a better parameter of merit.

III. EXPERIMENTAL SET-UP

The dimensions of this device have been choiced in order to permit its mounting on aircraft wings; the corresponding specifications follow:

Cavity resonator

Distance between mirrors $d=0,3$ m

mirrors conductivity $\sigma = 5.10^7\ \Omega^{-1}m^{-1}$

60 GHz O_2 loss angle $tg\,\delta = 2,74.10^{-6}$

Q factors : $Q_g = \frac{1}{tg\,\delta} = 364\ 964$

$$Q_m = \frac{10^5 d}{\sqrt{\lambda}} = 424\ 264$$

$$Q_{pr} = \frac{Q_g Q_m}{Q_g + Q_m} = 196\ 193$$

Coupling factor $\beta = 2000$

Radiometer

Transmission losses before mixer : $L_T = 1,6$ dB

Mixer 10/1000 MHz : gain $G_M = 30$ dB

noise figure $F_M = 2,5$dB (for 20K)

If amplification : gain $G_{IF} = 40$ dB

noise figure $F_{IF} = 2$dB

$\Rightarrow$ $T_{rec} = 160K$; $T_{sys} = T_R + T_{rec} = 460K$

$$\Delta T_R \sqrt{\tau} = 0.04 \quad (7)$$

IV. SENSOR PROJECTED ACCURACY

The experimental objective of the meteorologists is to measure the cloud air temperature with a spatial resolution better than 50 m. Because of the aircraft velocity (80 m/s) this resolution is obtained for a sampling frequency around 2 Hz. The radiometer resolution is then from (7):

$$T_R = 0.06 \text{ K}$$

To improve the existing sensor performances, the accuracy must be better than 0.5 K. Relation (3) shows that, if the mirrors or the other radiation sources and the air are at the same temperature, the system presented here allows an accuracy better than 0.1 K. In fact the mirrors and the cloud particles temperatures can differ from the air temperature by more than 1 K and a differential measure outside of the oxygen resonance frequency is necessary. The radiometer resolution then falls to 0.08 K and the accuracy estimated from (3) becomes: $T_g = 3 \; T_R = 0.23 K$.

In the preceeding section, Q_m has been supposed to be constant. If droplet deposits on the mirrors can not be avoided, the coefficient Q_g/Q_m can change by more than 10%, lowering the accuracy of the system by a factor :

$$(T_R - T_m) \; Q_m/Q_m .$$

V. CONCLUSION

To avoid perturbations by droplets in temperature measurements in clouds, a new device, based on microwave radiometry, has been proposed. Two points make this method more valuable than IR radiometric measurements:

- the measure is local, since the sampling volume is limited to the resonator volume
- the choice of millimeter waves, corresponding to the Rayleigh region, allows us to correct for the droplets contribution by differencial measurements.

Laboratory tests are now performed to avoid droplet deposits on the mirrors in order to satisfy the objectives of the meteorologists with an accuracy better than 0.5 K and a sampling frequency higher than 2 Hz.

An Approach to the Optical Measurement of Humidity Flux P20

R.J. Millington and M.J. Goodspeed

CSIRO Division of Water and Land Resources
GPO Box 1666, Canberra ACT 2601, Australia

INTRODUCTION

Evaporative loss is an important component in the water balance of hydrologic watersheds (Eagleson, 1970) and the assessment of the magnitude of this loss from regions with areas in the range 25 km^2 to 1000 km^2 is a long-standing problem in hydrology.

Several techniques exist for measuring evaporation at a point (Brutsaert, 1982), but estimation of losses over an area involves uncertain assumptions and extrapolations.

Development of a technique for measuring net upward humidity flux as a function of distance along a profile would permit much more accurate assessment of evaporative loss on a regional scale.

Approaches to this problem have employed models of boundary layer turbulence, using optical techniques to measure parameters of the turbulence field and inferring humidity flux from the magnitude of these parameters (Wyngaard and Clifford, 1978; Hill, 1982). Subsequently these measurements have been extended to the millimetre-wave band.

In this paper we propose a method based on measurement of water vapor content, firstly by long-path absorption (Svanberg, 1978) and then by differential absorption Lidar (DIAL) techniques (Hardesty, 1984; Collis and Russell,1976), which appears to offer a more direct approach to the measurement of humidity flux.

LONG-PATH ABSORPTION

This is an active technique in which light is propagated over a distance of the order of kilometres and returns to the vicinity of the source after reflection from a retro-reflector. Absorption by water vapor (or other

molecules) is measured, yielding an estimate of the average concentration over the path covered. Following Svanberg (1978, p.59), we have

$$\ln(I_o(\nu)/I_t(\nu)) = 2R(\Sigma\sigma_i(\nu)N_i+K_{ext})$$

where the symbols have their usual interpretation. When non-water absorbers are present in significant amounts, measurements must be made at a number of wavelengths to separate their effects. This method can also be applied using a non-coherent light source (Ochs, pers. comm.) in a band where water vapor is the dominant absorber.

DIFFERENTIAL ABSORPTION LIDAR

This well-established technique differs from that previously described in that back-scattered light is detected from atmospheric aerosol particles along the propagation path and, by comparison of returned energy levels on and off absorption lines, a range-resolved water content profile can be obtained. Following Collis and Russell (1976) we have

$$P_r(R) = P_o(c\tau/2)\beta(R)A_rR^{-2}\exp[-2\int_o^R \alpha(r)dr]$$

where, again, the symbols have their usual interpretation.

PROPOSED METHOD FOR HUMIDITY FLUX MEASUREMENT

The basis of the method (see Fig. 1) is:

- The propagation of a horizontal laser beam to measure average humidity along a profile by long-path absorption
- The movement of this beam vertically, parallel to itself, at a constant speed of the same order as the vertical mass flux, recording the pattern of average humidity observed
- Comparison of the patterns recorded from two such beams, one scanning upward and one downward.

The rationale is that average humidity along the profile will exhibit fluctuations due to turbulence and any particular fluctuation feature

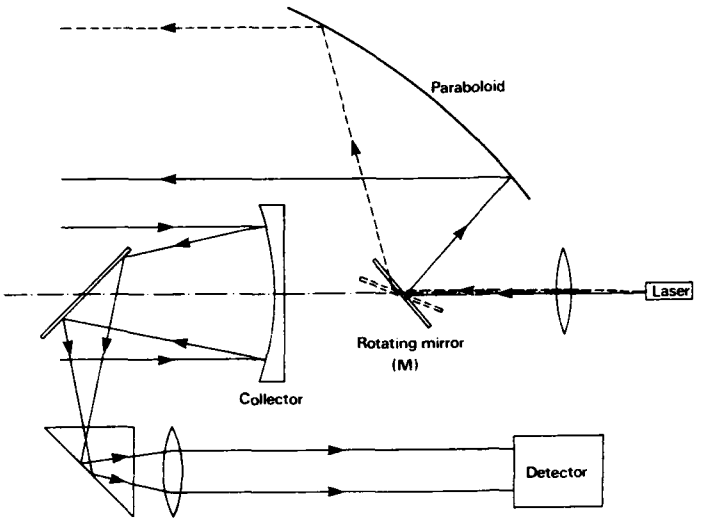

Fig. 1. Schematic diagram of proposed transmitter/receiver geometry.

will be present in the beam for a longer time when the scan moves upward, following the mean motion, than when it moves downward against it.

Let w_h be the mean vertical velocity component of the humidity field, v_s the speed at which the vertical beam-scan is driven. If we assume, simplistically, that a turbulence cell of length 1 in the vertical direction moves upward with the mean velocity w_h then it will be present in the upward-moving beam for time $t_u = 1/(v_s - w_h)$ and in the downward-moving beam for time $t_d = 1/(v_s + w_h)$. Eliminating 1, we obtain $w_h = (t_u - t_d)/(t_u + t_d)$.

In practice, the pattern is evolving in the same time scale as it is moving upwards and it is necessary to consider the complete patterns recorded and adjust the time scales to optimise the fit between them. Contracting the upward-moving time scale and expanding the downward-moving scale both by the factor a, we expect the cross-correlation between the two records to be a maximum for

$$a^2 = t_u/t_d = (v_s+w_h)/(v_s-w_h),$$

giving $$w_h = v_s\,(a^2-1)/(a^2+1). \qquad (1)$$

If both humidity and the vertical velocity component can be assumed to be approximately uniform along the profile then long path absorption is an adequate technique and mean humidity flux is simply obtained as their product. Otherwise we require range-resolved DIAL measurements of humidity and must evaluate the vertical velocity component separately for a number of segments of the profile before computing the flux.

SIMULATION OF THE METHOD

Clearly a number of simplifying assumptions about turbulent humidity flux are implied in the arguments leading to equation 1. Complete analysis is forbiddingly complex and we have adopted the approach of incorporating these assumptions explicitly in a stochastic model of atmospheric turbulence, on which the measurements outlined have been simulated. Currently the atmospheric model is quite simple, involving only uniform vertical movement and dispersion of humidity concentrations along with this movement. More realistic elaboration of this model, to incorporate vorticity for example, is being studied.

PHYSICAL IMPLEMENTATION

As presently envisaged the system will employ an off-axis paraboloid mirror for transmission, mounted coaxially with a spherical mirror for collection (Fig. 1). The rotating plane mirror M sweeps the narrow laser beam stepwise across the paraboloid causing the outward beam to be shifted vertically over a total distance of about 1 m. Returning energy is collected and detected conventionally. Sufficient data registers will be required to store approximately 20 complete profiles for analysis during the interval between sweeps. A pulse repetition frequency around 20 Hz from a sealed CO_2 laser is envisaged, permitting a complete sweep sequence in 1-2 seconds.

REFERENCES

Brutsaert, W.H. (1982). Evaporation into the Atmosphere. (Reidel : Dordrecht.)

Collis, R.T.H. and Russell, P.B. (1976). Lidar measurement of particles and gases by elastic backscattering and differential absorption. In 'Laser Monitoring of the Atmosphere', ed. E.D. Hinkley, pp. 71-151. (Springer-Verlag : Berlin.)

Eagleson, P.S. (1970). Dynamic Hydrology, pp. 211-41. (McGraw-Hill : New York.)

Hill, R.J. (1982). Theory of measuring the path-averaged inner scale of turbulence by spatial filtering of optical scintillation. Appl. Opt. 21, 1201-11.

Lloyd, C.R., Shuttleworth, W.J., Gash, J.H.C. and Turner, M. (1984). A microprocessor system for eddy correlation. Agric. For. Meteorol. 33, 67-80.

Svanberg, S. (1978). Fundamentals of atmospheric spectroscopy. In 'Surveillance of Environmental pollution and Resources by Electromagnetic Waves', ed. T. Lund, pp. 37-66. (Reidel : Dordrecht.)

Wyngaard, J.C. and Clifford, S.F. (1978). Estimating momentum, heat and moisture fluxes from structure parameters", J. Atmos. Sci. 35, 1204-11.

Some Observations of Spherical-Wave Covariance in Strong Refractive-Index Turbulence

P21

Gerard R. Ochs

NOAA/ERL/Wave Propagation Laboratory
325 Broadway
Boulder, Colorado 80303

Introduction

The phenomenon of the saturation of the scintillation of a light wave propagated through strong turbulence in the atmosphere has been observed and studied experimentally and theoretically for over 20 years. During this time, a reasonably complete understanding of the phenomenon has evolved. Recent work in this field is exemplified by references 1,2, and 3. A few questions remain, however, and one of these involves the nature of the very small details in the scintillation pattern, that is, those around the inner scale and smaller. Figure 1 is an example of such a pattern. Some additional observations of this region, with concurrent measurements of inner scale ℓ_o and the refractive-index structure parameter C_n^2, have been made that may contribute to a better understanding of this region of the scintillation pattern.

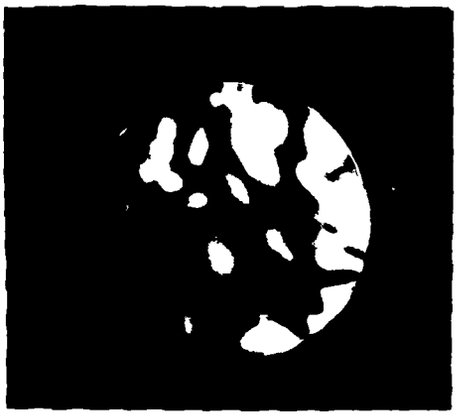

Figure 1. Intensity-scintillation pattern of a 0.63-μm spherical wave 1012 m from its source. The pattern is 50 mm in diameter, the exposure is 1/2000 s with winds less than 1 m/s, and $C_n^2 = 3 \times 10^{-13}$.

Experimental Procedure

The measurements were made on an east-west optical path 1012 m long and 2 m above the grass-covered surface of Table Mountain, a flat mesa approximately 12 km north of Boulder, Colorado. For most of the tests, a continuous-wave He-Ne

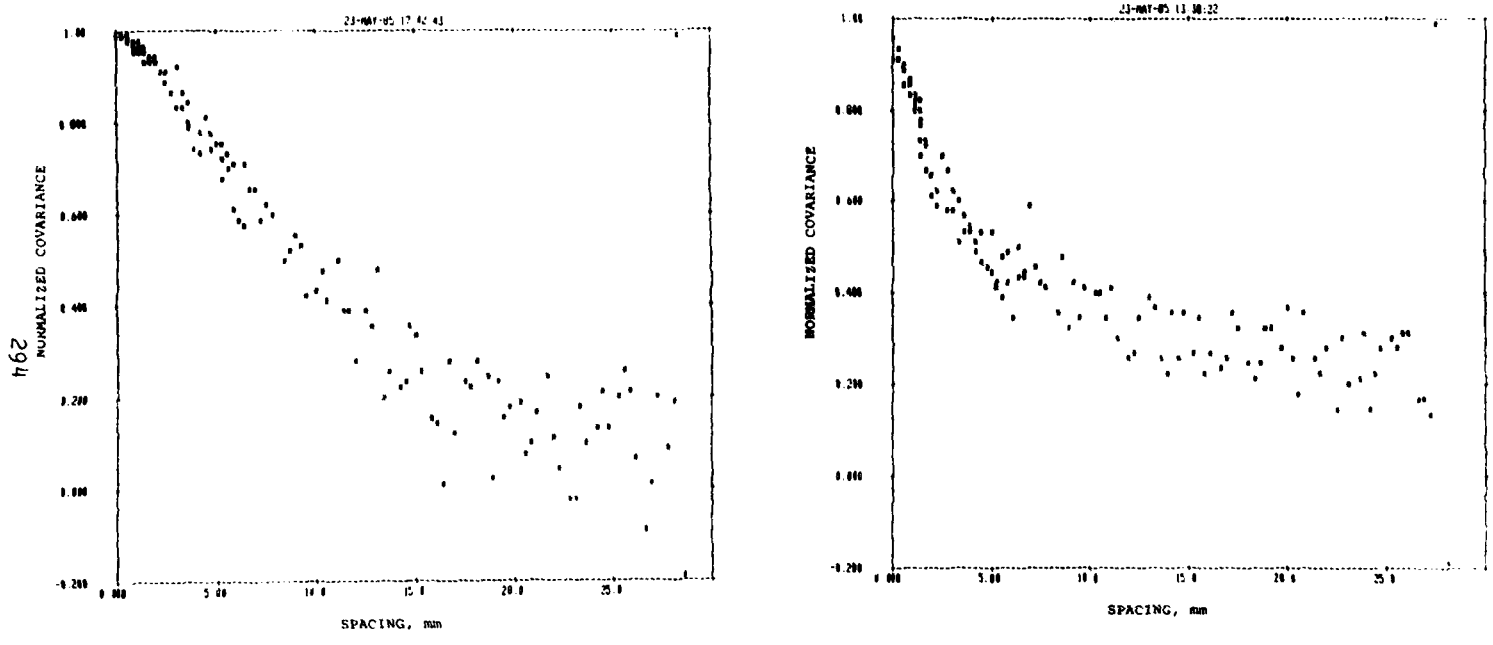

Figure 2. Examples of log-intensity covariance functions measured 1012 m from a spherical-wave 0.63-μm-wavelength laser. The plot on the left was made when $C_n^2 = 1.1 \times 10^{-13}$ $m^{-2/3}$ and $\ell_o = 5.6$ mm. For the plot on the right, $C_n^2 = 1.1 \times 10^{-12}$ $m^{-2/3}$ and $\ell_o = 5.9$ mm.

laser having a 4-mW single-mode output at 0.6328-μm wavelength was used. A negative cylindrical lens expanded the beam slightly in the vertical direction so that the detectors were illuminated regardless of day-to-night changes in regular refraction. In some of the tests of shorter duration, a He-Ne laser having approximately 20 mW of single-mode continuous output was employed.

Photomultiplier tube detectors were used to measure the irradiance of two 1-mm diameter apertures. Interference filters of 1-nm bandwidth were used and the signal fluctuations were observed over a 10 kHz bandwidth. By means of a moving beamsplitter, the spacing of the two apertures could be changed from 0 to 30 mm. The signals were preprocessed by passing them through logarithmic amplifiers and then digitized at the rate of 10 per second. A 1-bit correlator technique was used to measure the normalized log-intensity covariance, and this output was also digitized at a 10 per second rate. A signal-amplitude distribution must be assumed to calibrate the 1-bit correlator. In this case, however, log-normal signal distribution was assumed, which of course was not quite the case. Both experimental and analytical analyses indicate that the error is slight, especially at the close spacings that are of interest here.[4]

An independent measurement of C_n^2, and inner scale ℓ_o, was obtained from several incoherent-light scintillometers[5] and an optical inner scale instrument,[6] all having light paths parallel to the laser path.

Two modes of operation were employed. In one, the space covariance function was obtained by continuously cycling the aperture separation from 30 mm to zero spacing and back out to approximately 8 mm, in 125 seconds, digitally sampling 10 times per second. In the other mode, a 2.2-mm spacing was maintained, and the covariance at this spacing was continuously measured over periods of several days.

Results

Examples of two covariance functions, measured in low and high integrated turbulence, are shown in Figure 2. The strong-turbulence case (right) shows the characteristic increase in irregularity scales smaller and larger than Fresnel zone size.

Perhaps a better way to assess the relative contribution of C_n^2, and inner scale, to the shape of the covariance function, especially the width at small spacings, is to maintain a fixed detector spacing and observe the change in covariance over time. In the following test, a 2.2-mm spacing was used and consecutive 10-min averages of covariance, C_n^2, and inner scale were taken for 41 hours. The quantity $1/(1-C)$, where C is covariance, was compared rather than covariance, since this quantity is approximately equal to the width of the covariance function, for small changes in covariance. The correlation coefficients for the total of the 10-min averages is as follows:

	1/(1-C)	ℓ_o	C_n^2
1/(1-C)	1	.41	-.61
ℓ_o	.41	1	-.06
C_n^2	-.61	-.06	1

Most of the data was taken when the coherence length ρ_o was less than the inner scale. There is some change in the statistics if the data for which $\rho_o < \ell_o$ is removed, as shown in the following table.

	1/(1-C)	ℓ_o	C_n^2
1/(1-C)	1	.66	-.53
ℓ_o	.66	1	-.22
C_n^2	-.53	-.22	1

Thus it appears that under saturated conditions, ℓ_o and C_n^2 (or ρ_o) have approximately equal effects upon the width of the covariance function at 2.2 mm.

Acknowledgments

R. J. Hill and S. F. Clifford suggested and encouraged these measurements. I appreciate the helpful discussions and study of the experimental techniques by J. H. Churnside.

References

1. R. J. Hill, J. Opt. Soc. Am., 72, 212-222 (1982).

2. W. A. Coles and R. G. Frehlich, J. Opt. Soc. Am., 72, 1042-1048 (1982).

3. R. J. Hill, J. Opt. Soc. Am., 2, 445-453 (1985).

4. J. H. Churnside, Appl. Opt., 24, 2488-2489 (1985).

5. Ting-i Wang, G. R. Ochs, and S. F. Clifford, J. Opt. Soc. Am., 68, 334-338 (1977).

6. G. R. Ochs and R. J. Hill, Appl. Opt., 24, 2430-2432 (1985).

SCATTERING FROM RANDOMLY ORIENTED FIBERS IN THE RAYLEIGH-DEBYE-GANS APPROXIMATION.

P22

A.J. PATITSAS,
Department of Physics, Laurentian University,
Sudbury, Ontario, Canada P3E 2C6

In Fig. 1, the direction of the axis of the fiber (a right circular cylinder of finite length) is characterized by the polar and azimuthal angles β, γ respectively, the direction of the incident beam is denoted by $\hat{k}$ which is along the z axis and the direction of the scattered wave is denoted by $\hat{r}$ which has polar and azimuthal angles θ, ϕ respectively. The fiber is assumed to have uniform refractive index m relative to the surrounding medium. The expression for the amplitude of the form factor $F(\theta, \phi)$ is (Van de Hulst (1), Saito and Ikeda (2))

$$F(\theta,\phi)=4a^2L \frac{J_1(u_1)}{u_1} \frac{\sin u_2}{u_2} \qquad [1]$$

where a is the radius of the fiber, L is the length, J_1 is the Bessel function of order one.

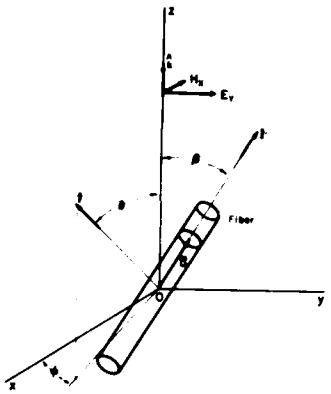

Fig. 1. Typical scattering diagram.

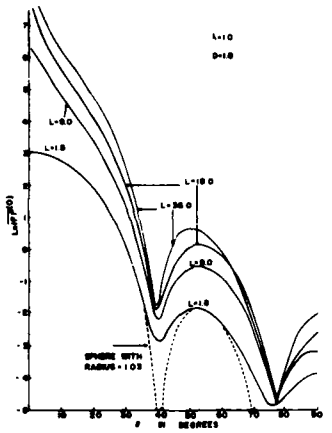

Fig. 2. The natural logarithm of the form factor averaged over all orientations of a fiber is plotted versus the scattering angle for fixed fiber diameter D and for various fiber lengths L.

The parameters u_1, u_2 are given as follows,

$$u_1=2ka \sin\frac{\theta}{2}\sin\delta \qquad u_2=kL \sin\frac{\theta}{2}\cos\delta \qquad [2]$$

δ being the angle between the axis of the fiber and the vector $\underline{c}=\hat{r}-\hat{k}$.
It can be shown easily that

$$\cos\delta=(2-2\cos\theta)^{-\frac{1}{2}}(\sin\theta\cos\phi\sin\beta\cos\gamma + \sin\theta\sin\phi\sin\beta\sin\gamma-(1-\cos\theta)\cos\beta). \qquad [3]$$

It is also obvious that

$$\cos\delta=\frac{1}{c}(\cos\alpha-\cos\beta)$$

where α is the angle between $\hat{r}$ and the fiber axis. The function $L\frac{\sin u_2}{u_2}$ behaves like a δ-function as $\frac{\pi L}{\lambda}$ becomes large. It follows that for a very long fiber the function $F(\theta,\phi)$ and thus the scattered intensity are different from zero only on a cone whose axis coincides with the fiber axis and whose apical angle equals 2β. This behaviour of the scattered intensity is the same for the case of the infinite circular cylinder using the exact boundary value method to obtain the scattered intensity (Kerker (3)). It is clear that when $\hat{r}$ lies on the scattering cone, then $\hat{r}-\hat{k}$ is normal to the fiber axis and since the relative phase change is $\frac{2\pi}{\lambda}(\hat{r}-\hat{k}).\underline{r}'$, where $\underline{r}'$ is the vector position of a scattering volume inside the fiber, one can argue that the validity of the Rayleigh-Debye-Gans theory depends strongly on the diameter and weakly on the length of a long fiber. The explanation to this effect by Koch(4) for the case of randomly oriented elongated particles failed to take into account the scattering cone and is rather vague. The same kind of argument can be used in the case of the disk whose diameter is large compared to the wavelength. In this case it is the function $\frac{a}{\lambda}\frac{J_1(u_1)}{u_1}$ which behaves like a δ-function as $\frac{a}{\lambda}$ becomes very large. This implies that the angle δ in eq. [2] equals zero i.e. the vector $\underline{c}=\hat{r}-\hat{k}$ is now along the normal to the disk as in the case of specular reflection. Thus, the effective relative phase $\frac{2\pi}{\lambda}(\hat{r}-\hat{k}).\underline{r}'$depends strongly on the width and weakly on the diameter of the disk. In order to calculate the average intensity from a system of randomly oriented fibers, the function $|F(\theta,\phi)|^2$

has to be averaged over all β,γ. Since u_1 and u_2 depend on the angle δ, it is normal to introduce a polar axis along the vector $\underline{c}=\hat{r}-\hat{k}$. It is easy to show that

$$\overline{|F(\theta,\phi)|^2}^{(0)} = 16a^4L^2\int_0^{\frac{\pi}{2}}\left(\frac{J_1(u_1)}{u_1}\right)^2\left(\frac{\sin u_2}{u_2}\right)^2 \sin\delta d\delta \qquad [4]$$

where the bar at the top and the superscript 0 indicate average over all orientations. Essentially the same result was obtained by Koch(4) by taking the polar axis along the bisectrix of $\hat{r}$ and $\hat{k}$. In Fig. 2. the natural legarithm of $\overline{|F|^2}^{(0)}$ is plotted versus θ for $\lambda=1.0$, $D=1.8\lambda$ for various values of the fiber length. The interval $d\delta$ was set equal to 2.0° in the numerical evaluation of the integral in eq. [4] using Simpson's rule. The error was less then one in 10^4 in the cases tested. The interesting feature of these plots is that the angular positions of the first two minima, close to 38° and 78°, and to a lesser extent that of the first maximum, in the vicinity of 50°, are quite independent of the aspect ratio R down to R=1.0. Similar results were obtained by Koch(5) for randomly oriented ellipsoids of revolution and Malmon (6). The sphere with radius equal to 1.03λ has the same volume as the fiber with length equal to 1.8λ. The plots for these two cases are very close for the angles θ shown in the figure except for θ near the minima where the form factor for the sphere becomes zero. A quick calculation shows that with $\delta=90°$ and $D=1.8\lambda$ in the expression for u_1, the first zero of $|J_1(u_1)|^2$ is at $\theta=40°$, the second is at $\theta=77°$ and the first maximum is at $\theta=56°$. Thus, in the case of identical fibers randomly suspended and randomly oriented, the diameter can be determined quite accurately from measurement of the angular positions of the minima, for aspect ratios as low as unity. If the fibers are oriented along the y axis, broadside incidence, then $\frac{\sin u_2}{u_2}$ in eq. [1] equals one and the positions of the extrema can be utilized to determine the fiber diameter even more accurately than for random orientations. It can be further noted that the ratio of the intensities for the plots with $L=1.8\lambda$, $L=9.0\lambda$ is close to 3.7 for θ in the range 20° to 30° and for θ in the vicinity of the first maximum. The corresponding ratios for the plots with $L=9.0\lambda$, $L=18.0\lambda$, and with

$L=18.0\lambda$, $L=36.0\lambda$ are close to 2.0. As expected the ratio is equal to R^2 for $\theta=0.0°$. It may be concluded that apart for θ near zero where there is total constructive interference and for θ near the angular positions of the minima of the scattered intensity where there is a high degree of destructive interference, the intensities from the various normal slices of the randomly oriented fiber tend to add. Thus the phases of the wavelets originating at the various normal slices are very well randomized even for R close to one, excepting the angular intervals stated above. Thus, the plots in Fig. 2. suggest that the validity of the Rayleigh-Debye-Gans theory is quite independent of the fiber length even for values of R near one. Can one assume that the dependance of the validity of the theory on the fiber diameter is close to that for a very long fiber Since the effect of the fiber ends on the scattered intensity occurs at large θ where the Rayleigh-Debye-Gans theory is most likely not applicable, the answer to this question is most likely in the affirmative. Computations based on the derivation of the scattering amplitude for long cylinders (Van de Hulst (1)), are underway in order to arrive at a quantitative answer to this question.

REFERENCES

1. Van de Hulst, H.C., "Light Scattering by Small Particles." Wiley, New York, 1957.
2. Saito, N., and Ikeda, Y., J. Phys. Soc. Japan, 6, N°5, 305, (1951).
3. Kerker, M., "The Scattering of Light and Other Electromagnetic Radiation." Academic Press, New York, 1969.
4. Koch, A.L., J. Theoret, Biol, 18, 133 (1968).
5. Koch, A.L., Biochimica et Biophysica Acta, 51, 429 (1961).
6. Malmon, A.G., Acta Cryst. 10, 639 (1957).

Stochastic model for turbidimetric parameters evaluation against observed values.

I. Porceddu, V. Quesada
Cagliari Astronomical Observatory

P23

The knowledge of the real incidence of solar radiation incoming over a given area is indispensable for the correct use of the different energy systems and constitutes a basic element for the evaluation of the energy budget on a local scale (on microscale) and also on a larger scale.

The various models used for the determination of solar radiation can be grouped into two large categories: the so called analogical or parametric models based on indirect processes and those based on direct numerical procedures. However, direct methods appears best for the calculation of incident solar radiation on a given surface. Using our direct method, it is necessary to know how the phenomena of diffusion and absorption (atmospheric attenuation) interact with the cloudiness (shape, kind and coverage) for the solar radiation extinction. The aim of our paper is to present a feasibility study, a work-design which use a software tool for radiative processes emulation.

This tool simulate the atmospheric radiative processes which are made by aerosols particles; in other words, we select the aeros. density (gr/cm**3) and dimensions

(particles, radius) parameters, the radiation parameters and the atmospheric components.

The software tool use a Monte - Carlo procedure for radiative processes emulation, with a plane - parallel atmospheric geometry. A NIP (Near Infrared Photometer) is used to determine the surface incoming radiation on three spectral zones.

By means of NIP (and Volz) photometer, we compare the observed values with the stochastic results.

Preliminary results will be issue in a short time.

AD-A170 393 DIGEST - INTERNATIONAL CONFERENCE ON OPTICAL AND MILLIMETER WAVE PROPAGAT..(U) OREGON GRADUATE CENTER BEAVERTON DEPT OF APPLIED PHYSICS AND E... R A ELLIOTT

UNCLASSIFIED MAY 86 ARO-23498.1-EL-CF DAAL03-86-G-0008 F/G 4/1 NL

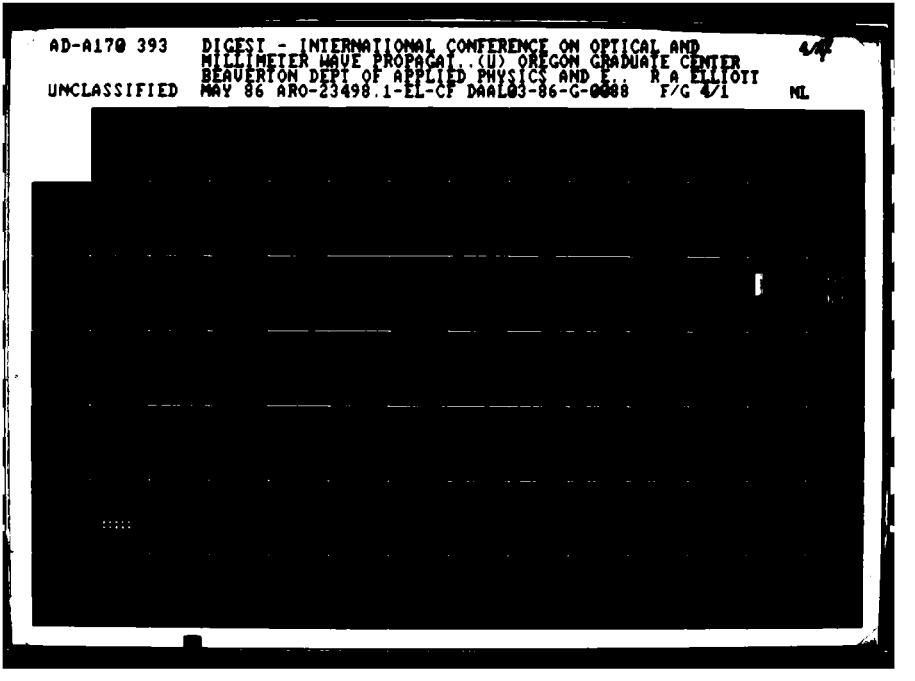

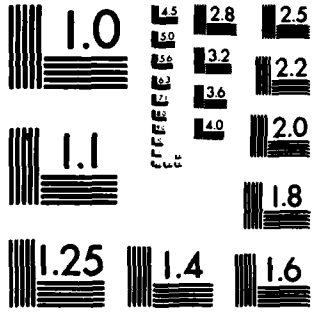

MICROCOPY RESOLUTION TEST CHART
NATIONAL BUREAU OF STANDARDS-1963-A

Atmospheric Turbulence Measurements With a Microwave Refractometer

P24

S.B.S.S. Sarma and P.K. Pasricha
Radio Science Division, National Physical Laboratory,
New Delhi 110 012, India.

1. INTRODUCTION

The scattered power in a tropo-scatter system depends upon the spatial spectral distribution of refractive index fluctuations. The spectral distribution (power spectral, in general) is characterised by two parameters : spectral intensity and slope to the high frequency region. The spectral intensity is given in terms of the well-known Tatarskii's structure constant, C_n^2, which is a measure of the severity of refractive index fluctuations. The spectral slope determines the (scale) size of the inhomogeneities in the turbulent medium. In the absence of in-situ measurements, Kolmogorov's, spectral slope of -11/3 (three dimensional, -5/3 one dimensional) is assumed to hold good. A typical estimate of C_n^2 in a height interval of 1 to 2 km lies in the range of 10^{-15} to 10^{-14} $m^{-2/3}$ [1].

The atmospheric turbulence parameters may be determined by in-situ measurements of refractive index with an air-borne microwave refractometer. In order to collect accurate refractive index information over the Indian subcontinent, an air-borne solid-state digital microwave refractometer has been designed, fabricated, and flight-tested successfully. The variance of the refractive index $\langle \Delta n^2 \rangle$ values were computed at different heights. In an initial exercise, six such sorties were carried out during day time in June, 1983, and another

six in January, 1985. The mean height profiles of C_n^2 for the summer and the winter conditions are computed from the $<\Delta n^2>$ values. Power spectral analysis of the refractive index fluctuations gives the spectral slope at different height levels in the turbulent atmosphere.

2. HEIGHT PROFILES OF C_n^2

The refractive index structure constant C_n^2 is given by

$$C_n^2 = K <\Delta n^2> L_o^{-2/3}, \qquad (1)$$

$<\Delta n^2>$ being the variance of the refractive index at a given height, L_o the size of the largest inhomogeneity (called the outer scale of turbulence) and K a normalization constant. The theoretical value of K equal to 2 is found satisfactory for line-of-sight optical wave propagation through the turbulence atmosphere [2]. The outer scale of turbulence L_o may be taken as $\sim$2 m. The troposcatter experiments, in the S-band and at higher frequencies, are characterized by an outer scale of turbulence such that $L_o >> (\lambda L)^{1/2}$. Here, λ is the observing wavelength and L the radio path length; for L $\sim$ 100 Km, L_o may be taken as 1 Km [3]. The height profiles of $<\Delta n^2>$, obtained by microwave refractometer, and labeled as

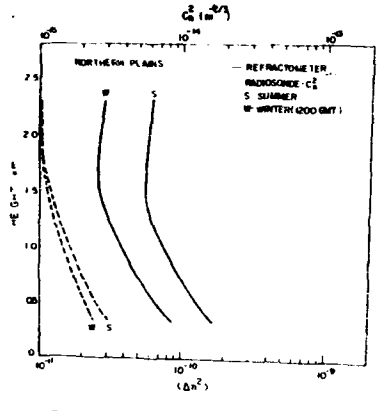

Fig.1 Height profiles of variance ($<\Delta n^2>$ of refractive index fluctuations measured with the refractometer for summer and winter conditions (solid curves). The corresponding profiles from radiosonde are marked dotted.

'summer' and 'winter' are given in Fig.1. A typical value of C_n^2 as 5×10^{-15} $m^{-2/3}$ at 1.5 km for summer conditions was adopted to fix the normalization constant K in expression (1). Putting in $\langle \Delta n^2 \rangle$ as 5.0×10^{-11} $m^{-2/3}$ at 1.5 km and the remaining parameters in (1), the constant K is obtained as $\sim 10^{-2}$. This value of the normalization constant $K \sim 10^{-2}$ is very much lower compared to the theoretically implied value ~ 2. At present, no explanation is offered for such a difference in the value of K. The factor $K.L_0^{-2/3} \sim 10^{-4}$ gives a constant scaling factor to convert $\langle \Delta n^2 \rangle$ values into C_n^2 values as shown in Fig.1. The summer C_n^2 values are consistently higher than the winter period. A similar result was reported by Gossard [1].

3. SPECTRAL ANALYSIS

Power spectral analysis of the temporal variations in refractive index fluctuations are performed to compute the slope of the high frequency fall-off, and the (scale) size of the turbulent structures involved. The spectral slope values, in general, lie between -9/3 to -13/3 for samples in the height range of 700 m to 2 km. A value of spectral slope -15/3 is consistently obtained at 500 m. With the limited data available, no clear variation of the spectral slope with height or season is evident. Representative power spectra plot at 1.5 km obtained from one of the sorties in January 1985 is presented in Fig.2.

A Gaussian description of turbulence gives the scale size r_0 as

$$r_0 = \frac{1}{w} \frac{V}{f_0} , \qquad (2)$$

V being the mean wind speed and f_0 a break-point frequency marked in Fig.2. The simultaneous radiosonde flights in winter give mean wind speed as 4 ms^{-1} in the region from 500 m to 2 km. A typical value of f_0 from Fig.2 may be taken as 5 x 10^{-2} Hz. The average scale size r_0 from (2) is deduced to be $\sim$25 m.

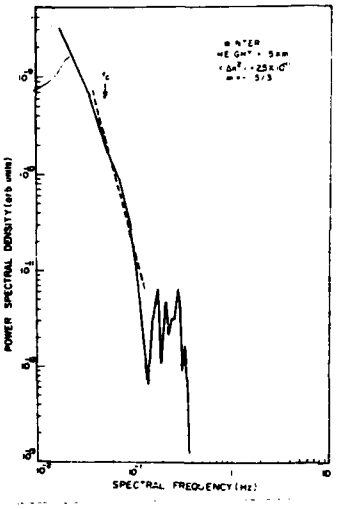

Fig.2 Power spectra of refractive index fluctuations at 1.5 km. The spectral slope, to the high frequency region, marked dotted, is -11.5/3.

4. CONCLUSIONS

A microwave refractometer gives an accurate description of the refractive index distribution in the turbulent atmosphere. A limited number of refractometer measurements were made in the summer and the winter periods in India. With the hypothesis of frozen-in turbulence, the temporal variations in refractive index have been analysed to compute structure constant and spectral slope (thus scale size) of atmospheric turbulence.

REFERENCES

1. E.E. Gossard, Radio Sci., vol.12, pp.89-105, 1977.

2. J.W. Strohbehn, IEEE Proc., vol.56, pp.1301-1318, 1968.

3. A. Ishimaru, IEEE Trans. Antennas and Propagation, vol. AP-20, pp. 10-19, 1972.

Atmospheric Optics

John B. Smyth
Smyth Research Associates
San Diego, California 92123

A wide variety of optical phenomena are associated with light transmission through the earth's atmosphere. These range from exotic rainbows, mirages, and pilot's halos to all aspects of twinkling starlight which have been amalgamated into a single concept entitled scintillation. A good eye observing starlight decerns variations in intensity, in directions of arrival, in color and in size of the image. The magnitude of these scintillations decrease with the elevation above sea level, presumedly disappearing altogether outside the earth's atmosphere.

In 1893, Lord Rayleigh[1] published a paper entitled "On The Theory Of Stellar Scintillation" in which he summarized the important investigations by Respighi[2]. Rayleigh's paper dealt mainly with Respighi's astounding observation that the spectra of stars near the horizon in the east exhibit dark and light bands moving progressively through the spectrum from violet to red. For stars in the west, the movement of the bands is just the opposite: That is, from the red end of the spectrum to the violet. Rayleigh demonstrated that atmospheric dispersion would require violet light to propagate along a path at a higher elevation than the red light, with the intermediate frequencies arriving along appropriate ray paths. It is clear that for rising stars the transmission path for the violet light will encounter atmospheric irregularities first, with ray paths of the longer wavelengths following in proper sequence. For stars setting in the west the ray path associated with red light will encounter a given index of refraction perturbation first, with the electromagnetic effect observed passing through the gamut of higher frequencies. The objective of this paper is to present an approach to a quantitative description of this phenomenon, which at the same time describes other scintillation phenomena.

Rayleigh[1] states, "In the preceding discussion the refracting obstacles have for the sake of brevity been spoken of as throwing sharp shadows. This of course cannot happen, if only in consequence of diffraction; -------." In an investigation of the transmission and reflection of plane acoustic waves from a plane interface between two homogeneous media, Rayleigh[3] extended this study to the case of a non-plane corrugated interface. As a particular case he considered a sinusodial corrugation with space frequency $2\pi/\lambda$ along the x-axis and space frequency equal to zero along the y-axis, where λ is the spatial wavelength of the corrugation along the x-axis. Although general boundary conditions may not be represented by the superposition of sinusoidals as implied, the special case considered depicts how spatial phase modulation of a single space frequency generates sidebands and redistributes the energy of the carrier among these diffraction orders. Since the equations representing the acoustic field are linear, superposition of sinusodials to represent the periodic function describing the field is acceptable. For the case being considered, the sinusoidal surface representing the interface is replaced by

the original plane interface and the acoustic field is assumed to be of constant amplitude with a sinusoidal variation of the phase with the same spatial period as the perturbed interface surface. It can be shown[4] that the first order effect of a field penetrating an inhomogenous region is a change of phase. A well known example of this is the light field in the plane immediately behind a lens of an optical system. Another example is light passing through an acoustic beam where the periodic variations in the dielectric constant of the medium associated with the density fluctuations produced by the sound wave acts like phase grating. Raman and Nath[5] were able to describe the main observables of this phenomenon by assuming that the first order effect on the light transmitting the acoustic beam was a perturbation of the phase in the plane perpendicular to the direction of propagation. Accepting this premise, the diffraction orders and the distribution of energy among the spectra may be computed by the method developed by Rayleigh[3]. The major features of the diffraction phenomenon such as the diffraction angles, the doppler shifts of the various orders, and the fact that the diffraction pattern is not symmetric about the zeroth order when the electromagnetic wave is not incident normally on the acoustic beam, are rather easily found. Although the quantitative evaluation of the intensity in the diffraction orders is not so easily made and, in fact, has been done for only a fairly limited number of cases, these include most of the cases for which quantitative measurements have been made. This phenomenon has been studied mainly for liquids and solids where it is easily observed. In the case of gases the effect is extremely small due to the small acoustic impedance of gases: For example, the ratio of the impedance of water to that of air is 3600.

Even so, the distance traveled through the earth's atmosphere is quite large and the integrated phase along adjacent ray paths may be different. There are studies which indicate that the "dancing" of stellar images is a discontinuous change in direction of arrival of light[6]: a phenomenon which might be explained in terms of Fermat's principle where one stationary path becomes extinct while another quite different one comes into being. This is seen quite readily in the case of light diffracted by an acoustic beam in water: changing the intensity of the sound field diffracts energy from one order into another without light passing through any of the diffraction nulls. This spatial phase modulation redistributes energy among the space frequencies in just the same way energy is redistributed among the time frequencies when a time signal is phase modulated. This assumed spatial modulation of the phase in the wavefront will produce the major observables of astronomical seeing: glinting of stellar direction; flucuation of intensity of light arriving from a given direction; dilation of image size; and color banding.

Electromagnetic properties of the atmosphere are mapped on the starlight arriving at the earth's surface. And, perhaps, it is possible to use the observed time and space scintillation of starlight to say something about the earth's atmosphere. Von Neumann's statement made many years ago that "The hydrodynamics of meteorology presents without doubt the most complicated series of interrelated problems not only that we know of, but that we can imagine." is just as true today.

For example: the fact that the eye never sees a star resolve into two or more distinct images places a bound on the minimum scale size of the spatial phase modulation. Likewise, the cessation of twinkling of an exterrestrial source such as a planet, when its angular size reaches 10^{-4} radians corroborates this information. When an aperture of a telescope located at sea

level is open to a size greater than four inches, the scintillation of the intensity of the image vanishes. Astronomers frequently evaluate the quality of "seeing" by counting the number of diffraction rings that may be seen for a given aperture opening. On nights of excellent astronomical seeing an aperture opening of four inches at the Lowell Observatory[6], (2200 meters) will exhibit many well defined rings; whereas, the Naval Observatory (89 meters) will at best yield one diffraction ring. The spatial distance over which starlight twinkling is correlated is a function of elevation. Many years ago the author used two small mirrors mounted on two parallel tracks, four feet long, separated by the distance between his eyes. The two mirrors were on blocks at 45° with the track which could be moved independently along each track. This double track was mounted on a camera tripod and made perpendicular to the direction to some star. With the two mirrors placed side by side in the middle of the track, light from the star could be observed by both eyes simultaneously via the two mirrors. By separating the two mirrors, along the two tracks spatial correlation of the scintillation could be observed. The intensity variations became uncorrelated at about four inches at sea level, fifteen inches at three thousand feet and twenty-six inches at the mile high Palomar Observatory.

Ronchi[7] in a delightful book entitled "Optics -The Science of Vision", points to enlightment through the return of philosophy as the basic benchmark for all science. At best, physical reality is described, not explained.

REFERENCES

1 Rayleigh, Lord. Philosophical Magazine, 36, 129-142, 1893
2 Respighi Atti Nuovi Lincei, 21, 1868
3 Rayleigh, Lord. Theory of Sound, Dover, Vol. 2, 89-96, 1945
4 Smyth, J.B. Journal of Research, 65D, 293-297, 1961
5 Raman, C.V. and N.S.N. Nath, Proc. Incian Acad. Sci. 3, 459- ,1936
6 Mikesell, A.H. J.O.S. 41, 689-695, 1951
7 Ronchi, V. Optics The Science of Vision, New York University Press, 1957

MINIMUM VARIANCE ESTIMATOR OF FOURIER INTENSITIES DEGRADED BY ATMOSPHERIC TURBULENCE

P26

C.C. Wackerman and J.R. Fienup

Environmental Research Institute of Michigan
P.O. Box 8618
Ann Arbor, Michigan 48107 USA

1. Introduction

When imaging with large earth-bound optical telescopes atmospheric turbulence degrades the resolution to approximately one second of arc, which is many times worse than the diffraction limit set by the telescope aperture. The situation can be improved by gathering Fourier intensity data. Labeyrie showed [1,2] that if one takes a number of short-exposure images, one can combine their Fourier intensities to form an estimate of the object's Fourier intensity that has energy out to the diffraction limit of the telescope. How to combine the information from these short-exposure images to get the best estimate of the object's Fourier intensity (what we mean by best will be defined in Section 3) is the topic of this paper. In Labeyrie's traditional stellar speckle interferometry the Fourier intensities are averaged. It will be shown that although this technique works well for higher spatial frequencies of the Fourier plane, it works poorly for low spatial frequencies. A new method which is more accurate at low spatial frequencies will be described in Section 3.

In order to have a general model for these discussions, let $o(\alpha,\beta)$ be the object we wish to image and $h_k(\alpha,\beta)$ be the kth point spread function which includes both atmospheric and telescope effects. Then [3, p. 259]

$$g_k(\alpha,\beta) = o(\alpha,\beta) * h_k(\alpha,\beta) \tag{1}$$

where $g_k(\alpha,\beta)$ is the kth of N images of the object we record and * is the convolution operator. If we let upper case letters represent Fourier transforms of lower case letters, from (1) we have

$$\left|G_k(u,v)\right|^2 = \left|O(u,v)\right|^2 \left|H_k(u,v)\right|^2, \quad k = 1, \ldots, N \tag{2}$$

where (u,v) represents the Fourier (spatial frequency) plane. For a given Fourier plane location, (u,v), the N real values that we have measured, $|G_k(u,v)|^2$ are the data values we need to combine to produce an estimate for $|O(u,v)|^2$. In this paper we are considering the effects of the fluctuations due to atmospheric turbulence but not the effects of noise.

In Section 2 we derive the joint probability density function for our N data values. In Section 3 we derive estimators for $|O(u,v)|^2$ based on this density function. Section 4 will state conclusions.

2. Derivation of Joint-Density Function

Assuming that the atmosphere produces negligible amplitude fluctuations, the optical transfer function, H(u,v), described above can be written as [4, p. 404]:

$$H(u,v) = \frac{\iint P(x,y)P^*(x-\lambda fu,y-\lambda fv)\exp(i[\phi(x,y)-\phi(x-\lambda fu,y-\lambda fv)])\,dxdy}{\iint |P(x',y')|^2\,dx'\,dy'} \tag{3}$$

where λ is the wavelength of the propagating field, f is the focal length of the optical system, P(x,y) is the complex pupil function of the optical system which includes telescope aberrations and $\phi(x,y)$ represents phase fluctuations caused by the atmosphere. Under the Rytov approximation to the solution of the wave equation [4, Section 8.4.2], $\phi(x,y)$ is zero-mean Gaussian. The integrand of Eq. (3) is a complex number $A\exp[i\Psi]$ where

$$A = \frac{P(x,y)P^*(x-\lambda fu,y-\lambda fv)}{\iint |P(x',y')|^2\,dx'\,dy'}$$

and

$$\Psi = \phi(x,y) - \phi(x - \lambda fu, y - \lambda fv).$$

Since $\phi(x,y)$ is zero-mean Gaussian so is Ψ. The variance of Ψ, var(Ψ), is $E[(\phi(x,y) - \phi(x - \lambda fu, y - \lambda fv))^2]$ (where $E[\bullet]$ denotes expected value) which is the wave structure function, $D(\Delta x,\Delta y)$, evaluated at offset $(\lambda fu,\lambda fv)$. Work by Kolmogorov [5] gives a form for this function as [4, p. 413]

$$D(\Delta x,\Delta y) = 2.91(4\pi^2/\lambda^2)C_n^2 L(\Delta x^2 + \Delta y^2)^{5/6} \tag{4}$$

where we have assumed that the wave is propagating along the z axis through an atmosphere of thickness L and C_n^2 is the structure constant of the atmospheric refractive index fluctuations. Since integrating is just adding up the function over a large number of points, we can estimate Eq. (3) for some specific location (u,v) as

$$H(u,v) = \sum_{j=1}^{M} A_j \exp[i\Psi_j] \tag{5}$$

where M is some large integer. Assuming that the random process $\phi(x,y)$ is spatially correlated only over an area that is much smaller than the aperture of the imaging system [4, Section 8.6.3] we can assume that the Ψ_j's are almost always independent. By the Central Limit Theorm the real and imaginary parts of Eq. (5), denoted by R and I respectively, are Gaussian distributed with statistics:

$$E[R] = \exp[-0.5\ \mathrm{var}(\Psi)]\ P_1$$

$$\mathrm{Var}(R) = 0.5(1 - \exp[-\mathrm{var}(\Psi)])^2\ P_2$$

$$E[I] = 0$$

$$\mathrm{Var}(I) = 0.5(1 - \exp[-2\ \mathrm{var}(\Psi)])\ P_2 \tag{6}$$

where

$$P_1 = \left[\iint |P(x,y)|^2\ dx\ dy\right]^{-1} \iint P(x,y)P^*(x - \lambda fu, y - \lambda fv)\ dx\ dy$$

and

$$P_2 = \left[\iint |P(x,y)|^2\ dx\ dy\right]^{-2} \iint [P(x,y)P^*(x - \lambda fu, y - \lambda fv)]^2\ dx\ dy.$$

For the random variable $s = |H(u,v)|^2$, the probability density function is [6, Chapter 7]

$$P_s(s) = \frac{1}{2\pi\sqrt{\mathrm{Var}(R)\ \mathrm{Var}(I)}} \int_0^{\pi} \exp - \left[\frac{(\sqrt{s}\cos\phi - E[R])^2}{2\ \mathrm{Var}(R)} + \frac{(s \sin^2\phi)}{2\ \mathrm{Var}(I)}\right] d\phi. \tag{7}$$

We actually make measurements of the random variable t,

$$t = |G(u,v)|^2 = |O(u,v)|^2 |H(u,v)|^2 = cs$$

where $c = |O(u,v)|^2$ is the constant we are trying to estimate. From Eq. (7) we have [7, Chapter 6]

$$P_t(t) = (c)^{-1}\ P_s(t/c)$$

Finally, since we are making N independent measurements the joint density function is

$$P_t(t_1, \ldots, t_N) = (c)^{-N}\ P_s(t_1/c)\ P_s(t_2/c) \ldots P_s(t_N/c). \tag{8}$$

3. Derivation of Estimators

We wish to derive estimators which are unbiased and which have the smallest variance of all unbiased estimators. We shall refer to these as uniformly minimum variance unbiased (UMVU) estimators [12, Chapter 4; 7 Chapter 8]. First note that for all locations of the Fourier plane where $\mathrm{Var}(\Psi)$ is large enough so that $\exp[-0.5\ \mathrm{Var}(\Psi)]$ is approximately zero then, by Eq. (6), $E[R] = 0$ and $\mathrm{Var}(R) = \mathrm{Var}(I) = 0.5\ P_2$. Under these conditions the joint density function in Eq. (8) reduces to the joint density function of N independent expotenially distributed numbers. The UMVU estimator is well known for that case [12, Chapter 5], which we will denote by c, as:

$$c = (NP_2)^{-1} \sum_{i=1}^{N} t_i \tag{9}$$

which is essentially the traditional Labeyrie averaging [1]. To find where this assumption is applicable, we set some small value, δ, such that $\exp[-0.5\ \mathrm{var}(\Psi)]$ will be taken as zero if it is less then δ. Using Eq. (4) and solving for d, the distance from the origin in the Fourier plane to the point $(\lambda fu, \lambda fv)$, we have:

$$d > \left[\frac{-0.687\ln(\delta)\lambda^2}{(2\pi)^2 C_n^2 L}\right]^{3/5}$$

For locations in the Fourier plane that are closer to the origin then d, Eq. (9) is no longer UMVU. For these locations the density function in Eq. (8) should be used and no known closed form estimator exists. Considering Eq. (8) as a function of the N data values measured and the constant c we are estimating, for some given set of measurements we can iteratively find the value of c that maximizes Eq. (8). This is the maximum-likelihood estimator [12, pp. 99-107; 9, pp.290-298; 10, pp. 65-72] and since the problem is one-dimensional, techniques such as the Fibonaci search or the golden section search [11, Section 29.4] can be used. Examples showing the increased accuracy of this method will be presented in the talk. Although maximum-likelihood estimators are not guaranteed to be UMVU, in most cases they are [10, p. 68]. Also, if the number of measurements is large, all maximum-likelihood estimators become UMVU asymptotically [9, p. 298; 10, p. 71].

4. Conclusion

We have shown that to estimate the Fourier intensity of an object imaged through the atmosphere we must divide the Fourier plane into two regions: the high frequency region for which the traditional method is accurate, and the low frequency region where an iterative maximization of Eq. (8) is more accurate.

The authors gratefully acknowledge the contributions to this work by T.R. Crimmins and J.M Cederquist. This research was supported by the U.S. Air Force Office of Scientific Research under Contract F-49620-82-K-0018.

References

1. Labeyrie, A., Astron. Astophs., vol. 6, p. 85 (1970).
2. Gezari, D.Y., A. Labeyrie, R.V. Stachnik, Astrophys. J. Lett., vol. 173, L1 (1972).
3. Dainty, J., Laser Speckle and Related Phenomena, Ch. 7, 2nd edition, Springer Verlag, (1983).
4. Goodman, J. Statistical Optics, Wiley-Interscience, New York, (1985).
5. Kolmogorov, A., in Turbulence, Classic Papers on Statistical Theory (S.K. Friedlander, L. Topper, editors), Wiley-Interscience, (1961).
6. Beckman, P., A. Spizzichino, The Scattering of Electomagnetic Waves from Rough Surfaces, The Macmillan Co., (1963).
7. Davenport, J., Probability and Random Processes, McGraw-Hill Inc., (1970).
8. Fried, D.L., J. Opt. Soc. Am., vol. 50, p. 1380, (1966).
9. Meyer, P., Introductory Probability and Statistical Applications, 2nd edition, Addison-Wesley Publ. Co., (1970).
10. Van Trees, H., Detection Estimation and Modulations Theory, John Wiley and Son's Inc., (1968).
11. Gellert, W., H. Kustner, M. Hellwich, H. Kastrer (eds.), The UNR Concise Encyclopedia of Mathematics, Van Nostrand Reinhold Co., (1975).
12. Bickel, P., K. Doksum, Mathematical Statistics: Basic Ideas and Selected Topics, Holden-Day Inc., (1977).

Behaviors of Beam Wander in the Turbulent Near-earth Atmosphere P27

Song Zhengfang

Anhui Institute of Optics and Fine Mechanics, Academia Sinica,

P. O. Box 25, Hefei, Anhui, P. R. C

There have been many theorelical studies and experimental measurements on light beam wander in a turbulent atmosphere since 1960s. These researches are all but concered with weak turbulence. The theoretical study related to strong turbulence is very littel. Experiments performed by our lab indicate that there exists saturation phenomenon of beam wander in strong turbulence and the classical theories are not suitable for explaining the phenomenon. Therefore it is necessary to develope a theory explained satisfactorily the phenomenon. Using Markov approximation and Ehrenfest principle, and asuming that complex amplitude of wave field is normal statistics. Zhang et al [1] derived a general expression of beam wander suited whole region of turbulence. The expression predicts correctly the behaviors of beam wander even in the staturation region.

The general equation of beam wander variance is given by

$$\sigma_\rho^2=\langle \rho_c^2\rangle = \iint(\vec{\rho}_1,\vec{\rho}_2)\langle I(\vec{\rho}_1)I(\vec{\rho}_2)\rangle d\vec{\rho}_1 d\vec{\rho}_2 \Big/ \left(\int I(\vec{\rho})d\vec{\rho}\right)^2 \qquad (1)$$

where $\langle I(\vec{\rho}_1)I(\vec{\rho}_2)\rangle$ is intensity correlation function. The function involves terms of 5/3 power as the Kolmogorov spectrum or modified van Karman spectrum is used. Hence the function can not be solve strictly. If a quadratic approxiamtion is used to solve the function, some factors of it, such as beam spreading, will be neglect. In order to avoid this

difficult problem, we assume that the field statistics is Ganssian. It can then be shown as

$$\langle I(\vec{\rho}_1) I(\vec{\rho}_2) \rangle = \langle I(\vec{\rho}_1) \rangle \langle I(\vec{\rho}_2) \rangle + |\Gamma_2(\vec{\rho}_1, \vec{\rho}_2)|^2 \qquad (2)$$

where $\Gamma_2(\vec{\rho}_1, \vec{\rho}_2)$ is mutual coherence function. The right side of Eq(2) no longer involves fouth-roder term, the quadratic approximation can then be used reasonably. After certain processing one have

$$\sigma_\alpha^2 = \sigma_\rho^2 / L^2 = 0.651 C_n^2 L \alpha_0^{-2} \int_0^1 d\eta (1-\eta)^2 \left\{ \alpha_0^2 K_0^{-7/6} \left(\frac{\alpha_0 g}{2} \right)^{-7/12} \exp\left(\frac{K_0^2 \alpha_0^2 g}{4} \right) \right.$$
$$\left. \times W_{-\frac{12}{12}, \frac{1}{12}} \left(\frac{K_0^2 \alpha_0^2 g}{2} \right) + \frac{1}{2} V^{-1} K_0^{-7/6} \left(\frac{g}{4V} \right)^{-7/12} \exp\left(\frac{g K_0^2}{8V} \right) W_{-\frac{12}{12}, \frac{1}{12}} \left(\frac{g K_0^2}{4V} \right) \right\} \qquad (3)$$

where the modified van Karman spectrum was used, Cn is index of refraction structure constant, L is path length, α_0 is source size, $K_0 = 1/L_0$, L_0 is outer scale of turbulence, Wm, n (x) is whittaker function, and

$$g = (1 - \frac{\eta L}{F})^2 + (1 + \xi + \xi^2) f^{-2}$$
$$V = 2\left[3(1 - \frac{\eta L}{F}) + (\frac{\eta L}{F})^2 + (f^{-2} + \xi^{-1}) \xi^2 + \xi^{-1} + (1 + \frac{3}{4}\xi) f^{-2} \right] \rho_0^{-1}$$

where F is radius of beam curvature, $f = k\alpha_0^2 / L$, $k = 2\pi/\lambda$, λ is wave length, $\xi = \alpha_0 / \rho_s$, $\xi = 4\alpha_0 / \rho_0$, ρ_0 is coherence length for a spherical wave, and ρ_s is coherence length.

When $K_0 \to 0$ and the weak turbulence is taken into account, Eq.(3) can be reduced as

$$\sigma_\alpha^2 = 1.92 C_n^2 L (2\alpha_0)^{-1/3} \qquad (4)$$

It is in agreement with the common formula [2].

We have been carring out a series of beam-wander experiments for many years. Fig. 1 and 2 present comparision of the measuremental data with the calculated results. The theoretic values of σ_α are calculated by Eq. (4) in Fig. 1 and Eq. (3) in Fig. 2. It can be seen in Fig. 1 that there exists obviously saturation phenomenon of beam wander as

$\sigma_{\alpha theo.} \geq 40$ μrad. All the experimental values of σ_α are less then 50 μrad, while the calcualted values may well come to 80 μrad and more. As the general expression (3) is used, the measured and calculated beam-wander angle is fairly consistent. The correlation coefficient between them is 0.85. Fig. 3 indicates a typical record of σ_α and Cn measured simultaneously. The scale of Cn is drawed in the same scale as σ_α. As shown in Fig. 3 the day-night change of beam wander is quite evident as well as the turbulent intensity. The correlativity of them is very well when $Cn < 1 \times 10^{-7} cm^{-1/3}$. When $Cn > 1.5 \times 10^{-7} cm^{-1/3}$, however, σ_α is not relative to Cn. The saturation phenomenon is then emereged in this case.

Probability distribution and temporal spectrum of beam wander are also measured in the experiments. The results is accordant with theoretic prediction. Besides, a relationship between beam wander and scintillation is considered.

REFERENCES

1. Zhang Yixin, Song Zhengfang, Gu Weiyu, and Gong Zhiben, Acta Optica sinica (in the press).
2. R. L. Fante, Proc. IEEE, Vol 68 (1980) No. 11, PP. 1424-1443.

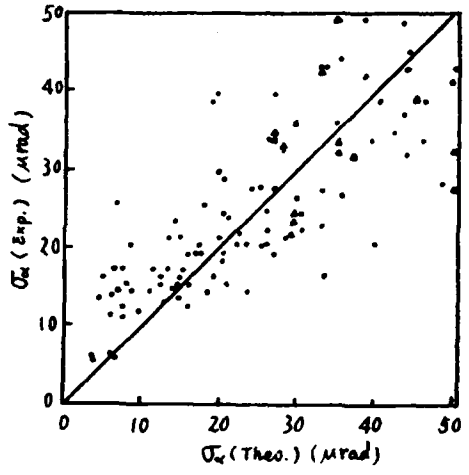

Fig 1. Comparison between measured and calculated σ_α by Eq.(3).

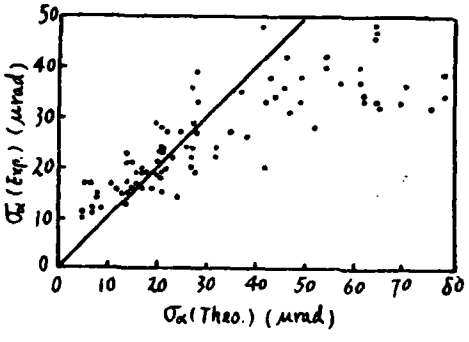

Fig. Comparison between measured and calculated σ_α by Eq. (4).

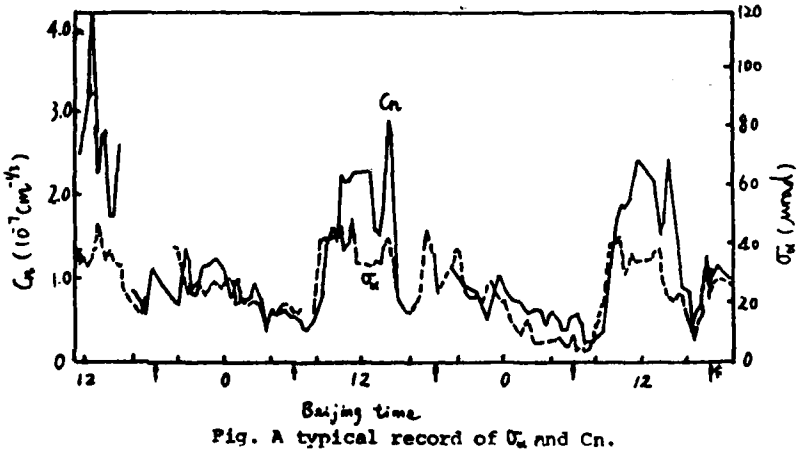

Fig. A typical record of σ_α and Cn.

REMOTE SENSING

Optical Remote Wind Measurement Using Speckle-Turbulence Interaction[1]

J. Fred Holmes
Oregon Graduate Center
Department of Applied Physics and Electrical Engineering
19600 N.W. Von Neumann Drive
Beaverton, Oregon 97006-1999

(invited)

Speckle-turbulence interaction has the potential for allowing single ended, remote sensing of the path averaged, vector crosswind. If a laser transmitter is used to illuminate a target, the resultant speckle field generated by the target is randomly perturbed by the atmosphere as it propagates back to the receiver. This creates a scintillation pattern at the receiver; and, if a crosswind is present, this pattern will move across the field of view of the receiver. Consequently, the time delayed statistics of the speckle field at the receiver are dependent on the crosswind velocity and can be used to determine the vector crosswind in a plane perpendicular to the propagation direction.

Remote crosswind sensing utilizing speckle-turbulence interaction has been accomplished using a polychromatic source and direct detection and also using a monochromatic source and optical heterodyne detection. The polychromatic work was done in the near infrared utilizing a Nd:YAG laser operating at 1.06 microns. With a direct detection receiver, a pulsed transmitter is required; and furthermore, in order to measure the time delayed statistics, the transmitter must be double pulsed. This resulted in a complicated and very expensive transmitter that was plagued by beam alignment, beam jitter, stability and reliability problems. Nevertheless, some good experimental data was obtained which indicates that the speckle-turbulence technique has merit.

An example of this data is shown in Figure 1. The data was taken at the Biggs Optical Test Range (BOTR) in El Paso, Texas. In situ instrumentation consisted of a linear array of 20 propeller anemometers spaced evenly along the path. Their outputs were added without weighting to provide the solid trace. The output of the pulsed system is shown by the dashed lines. A four second averaging time was used.

The key features of the direct detection system were: Pulsed Laser; Polychromatic; Direct Detection; 1.06 Microns Wavelength. Although good results were obtained with this system, it had a fatal flaw. Because of the limited pulse repetition rate, the only usable processing technique was the slope of the time lagged covariance function at zero time delay. Unfortunately the slope is proportional to both the crosswind and the strength of turbulence. Since the strength of turbulence is not known a priori, the system will not be useful until there are significant improvements in pulsed laser technology that will allow other signal processing methods to be used.

[1]This material is based in part upon work supported by the Army Research Office under Contract DAA G29-83-K-0077 and DAA L03-86-K-0022.

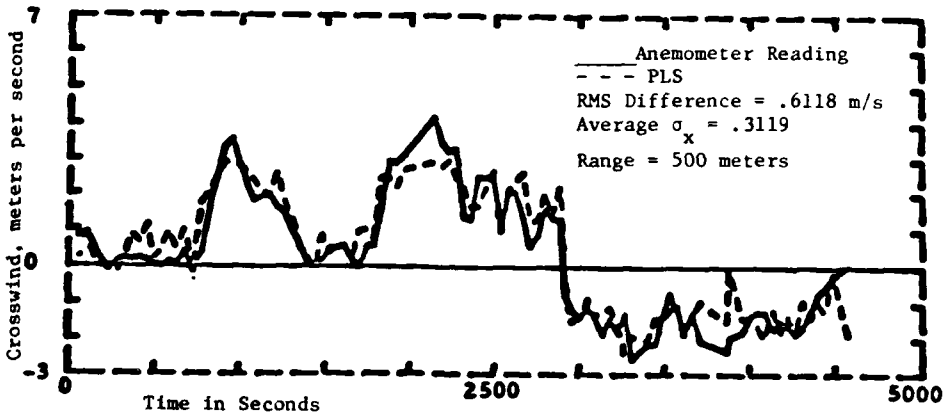

Figure 1. Wind measurement, pulsed laser system.

A continuous wave (cw) laser transmitter of modest power level (one watt) in conjunction with optical heterodyne detection can also be used to exploit the speckle-turbulence interaction and measure the crosswind. The key features of such a system are: Continuous Wave; Monochromatic; Heterodyne Detection; 10.6 Microns Wavelength.

The use of a cw transmitter at 10.6 microns and optical heterodyne detection has many advantages over direct detection and a double pulsed source in the visible or near infrared. These advantages include the availability of compact, reliable and inexpensive transmitters; better penetration of smoke, dust and fog; stable output power; low beam pointing jitter; and considerably reduced complexity in the receiver electronics. In addition, with a cw transmitter, options exist for processing the received signals for the crosswind that do not require a knowledge of the strength of turbulence.

From previous work, the time lagged covariance (TLC) function using the joint Gaussian assumption is given for the focused case by

$$C_I(\bar{P},\tau) = \langle \big(I(\bar{P}_2,t_2) - \langle I \rangle \big)\big(I(\bar{P}_1,t_1) - \langle I \rangle \big) \rangle \qquad (1)$$

$$= \langle I \rangle^2 \exp\Big[- \frac{P^2}{2a_o^{\,2}} - \frac{32}{3\rho_o^{\,5/3}} \int_0^1 \big| (1-w)\bar{P} - \bar{v}\tau \big|^{5/3} \, dw \Big] \qquad (2)$$

where $\bar{P}_i$ designates the location of a detector in the receiver plane; $\bar{P} = \bar{P}_2 - \bar{P}_1$; $\tau = t_2 - t_1$; a_o = Transmitter Beam Radius; ρ_o = Transverse Phase Coherence Length; $\bar{V}$ = Vector Wind Velocity;

and W = Normalized Path Length from the Transmitter-Receiver to the Target. As can be seen from Eq.(1), if two detectors are separated by a vector distance $\bar{P}$, the time delayed covariance can be measured; and from Eq.(2) it can be seen that the measured quantity will be a function of the crosswind velocity.

With a cw system there are several options for processing the data to obtain the wind. Some of these methods are illustrated in Figure 2. The Briggs method measures the time delay, τ_B, at which the autocovariance and the time-lagged covariance curves cross. The delay to peak method, measures the time delay, τ_p, where the time-lagged covariance reaches its peak value. The width of the autocovariance method measures the time delay, τ_W, at which the autocovariance curve decreases to 67% of its peak value. the slope method measures the slope, S, of the time-lagged covariance function at zero time delay. All of these methods have been used for the line of sight case and appear to have applicability to remote wind sensing using speckle turbulence interaction. Assuming uniform wind and turbulence, the wind velocity using these methods is given by

Briggs Method $V = P/(3.1056\,\tau_B)$; Delay to Peak Method $V = P/(2\tau_p)$;

Width of Autocovariance Method (67%) $V = 0.1395\,\rho_o/\tau_W$;

Slope $V = 3\rho_o^{5/3}\, S/\left(32\, P^{2/3}\, C_I(\bar{P},o)\right)$.

Although the above methods are useful, some new methods have been developed that use both the autocovariance function and the time lagged covariance. Formulation for these quantities are functions of both the crosswind and ρ_o the transverse phase coherence length. By combining them and also averaging the results for several different time delays, both the crosswind and ρ_o can be measured. One result for the crosswind which was used to process the data presented in Figures 3 and 4 is

$$V = \frac{1}{N}\sum_{i=1}^{N}\frac{P}{\tau_i}\left[\frac{\ln C_{IN}(o,\bar{v}\,\tau_i)}{\ln C_{IN}(\bar{P},o) + p^2/2\alpha_o^2}\right]^{3/5} \qquad (3)$$

where τ_i = i^{th} time delay; C_{IN} = Normalized (to the mean squared) time lagged covariance; N = Number of time delays used; and where the direction of the crosswind is determined by the skewness of the TLC. Figures 3 and 4 show some experimental data taken using a diffuse target at 500 meters and 1000 meters range and two second time averages. The in situ data was taken using a Campbell Scientific, CA-9, path averaging anemometer.

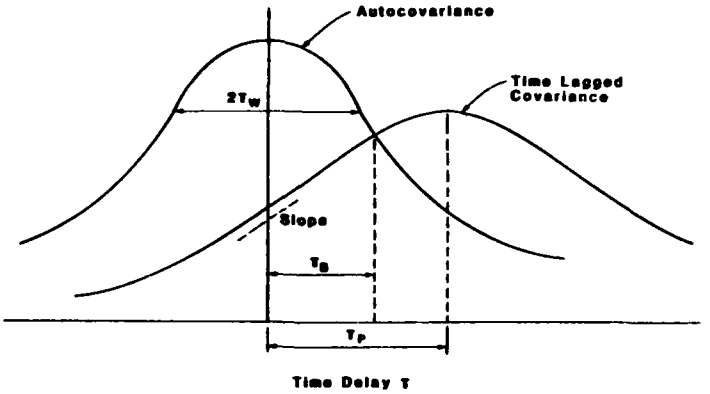

Figure 2. Processing Methods

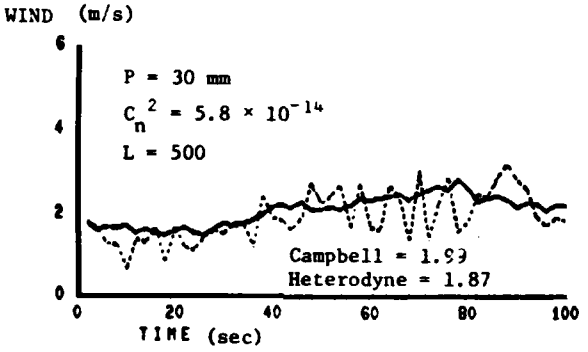

Figure 3. 500 meter Experimental Data
Wind = 1.99 m/s

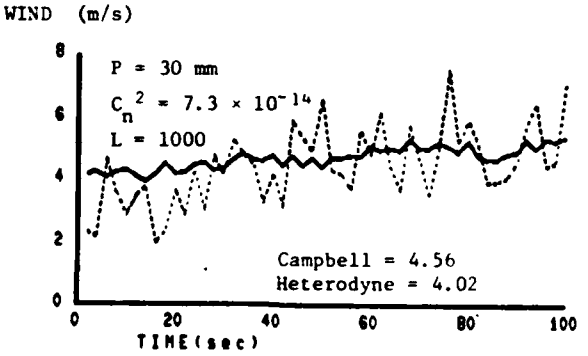

Figure 4. 1000 meter Experimental Data
Wind = 4.56 m/s

SYNTHETIC APERTURE SPATIAL FILTERING OF SCINTILLATION: A NEW TECHNIQUE FOR MEASURING OPTICAL REFRACTIVE TURBULENCE PROFILES

S. F. Clifford
J. H. Churnside
NOAA/ERL/Wave Propagation Laboratory
Boulder, Colorado 80303

(invited)

INTRODUCTION

There have been many attempts to derive profiles of optical refractive turbulence in the atmosphere using both in situ and remote sensors. In situ sensors generally provide poor data continuity in time. Because of the expense and difficulty of launching balloons or aircraft, they are by their nature strictly intermittent probers of the turbulent state of the atmosphere. On the other hand, in situ sensors provide very high spatial resolution, with the caveat for balloon-borne sensors that they are transported by the local wind velocity, which makes their trajectories unpredictable. Remote sensors such as the existing optical scintillometers have much poorer resolution and work with the highest efficiency at night. They do, however, provide nearly continuous monitoring of the atmosphere with minimum expense.

We propose here a technique that combines most of the best features of in situ and remote sensors. It involves an elevated point source of light translating across the field of view of a ground-based passive optical system. The light source may be on dedicated airplanes, airplanes of opportunity, or remotely powered vehicles. It could be designed to work with tower-mounted or balloon-borne retroreflector arrays, with a laser on the ground providing the velocity. All that is required is that the source speed be much faster than the atmospheric motion intervening between the source and ground.

OPERATIONAL PRINCIPLE

Figure 1 illustrates the geometry of the synthetic aperture spatial filter concept. A point source of light at height h above the ground translates across the field of view of a ground-based, sinusoidal, receiver array. The source is moving parallel to the array length with a speed V_o that is much faster than typical atmospheric motions ($V_o \gg 50$ m/s). Because of the rapid translation we may ignore the intrinsic speed of the medium V_g; then, to the observer on the ground, the atmosphere appears to have a velocity profile that rotates about the receiver, that is, $V(z) = V_o(z/h)$.

From Fig. 2 we can determine how the spatial filter interrogates the turbulent medium. As a spherical wave propagates through the atmosphere from z = h

to z = 0, it encounters turbulent irregularities that perturb the phase front. Eventually, at the ground there will be fluctuations in the received irradiance as a function of position (scintillation pattern) at nearly all spatial frequencies. If the receiver spatial filter has a wavenumber K_R, it will respond only to those irregularities in the scintillation pattern at or very near the wavenumber K_R. Each path position will contribute to the detected signal, but a different wavenumber of the refractive turbulence K will contribute for each path position. From our diagram: if the wave encounters a Fourier component of refractive turbulence of wavelength $\ell = 2\pi/K$ at position z, the pattern detected on the ground will be larger by an amount $\ell_R = \ell/(1 - z/h)$. In wavenumber space this corresponds to the relation $K_R = K(1 - z/h)$. In addition, when the refractive turbulence component at z moves its wavelength, the image it produces in the receiving plane will move its wavelength resulting in a magnified velocity given by $V_R = V(z)/(1 - z/h)$.[1] If, in addition, we observe the filtered signal through a narrow passband temporal filter at frequency ω_o, we find that the response will be due only to those wavenumbers that satisfy $\omega_o = K_R V_R = KV$. Note that although the scale size and velocity of the refractive turbulence are each geometrically magnified, their ratio is not and the frequency is invariant.

The final processed signal is the response of refractive turbulence at a position z that simultaneously satisfies the equations

$$\begin{aligned} K_R &= K[1 - z/h] \\ \omega_o &= KV \\ V(z) &= V_o z/h \ . \end{aligned} \tag{1}$$

Solving Eq. (1), we obtain

$$\begin{aligned} K_o &= K_R + \omega_o/V_o \\ z_o/h &= [1 + (K_R V_o/\omega_o)]^{-1} \ , \end{aligned} \tag{2}$$

where K_o and z_o are respectively; the wavenumber and height to which the system is sensitive.

CONCLUSION

Our result Eq. (2) illustrates that by spatially and temporally filtering the scintillation pattern observed on the ground, we are able to profile refractive turbulence strength and spectral slope. The resulting equations show that the filtered signal S, where

$$S(\omega_o, K_o) \propto \Phi_n(K_R + \omega_o/V_o) \tag{3}$$

---

[1] These arguments are based on a single scatter propagation model valid for weak refractive turbulence, which is observed in near-vertical propagation of optical waves. Also, we use quite simple geometric optics arguments to explain the details of the concept. Including the effects of diffraction is not difficult and indeed is included in our mathematical model.

where Φ_n is the spectrum of the refractive index fluctuations. Equation (3) and (2) imply that we may interrogate the medium at a height z_o and wavenumber K_o and thereby infer the refractive index structure parameter $C_n^2(z_o)$. In addition, Eq. (2) shows that we may vary z_o and K_o independently, thereby opening up the possibility of both profiling C_n^2 as a function of height and observing the strength of the spectrum $\Phi_n(K)$ at a fixed height. A detailed analysis indicates that if the spatial filter limits the resolution, which is likely the case, the resolution of such a system would be $\delta z = h[4K_R x]^{-1}$, where x is the length of the spatial filter.

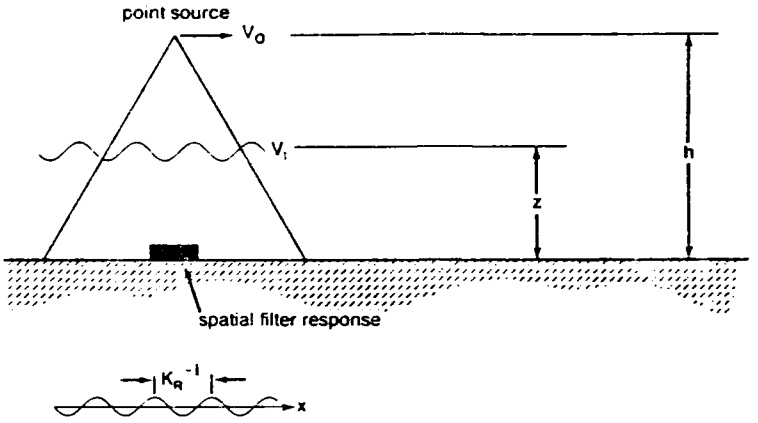

For a diverging source moving with velocity V_o the atmosphere appears to have a velocity profile

$$V(z) = V_o\left(\frac{z}{h}\right)$$

If $V(z) >> V_t$ we can ignore V_t

Figure 1. Schematic of the use of an airborne light source to measure profiles of refractive turbulence.

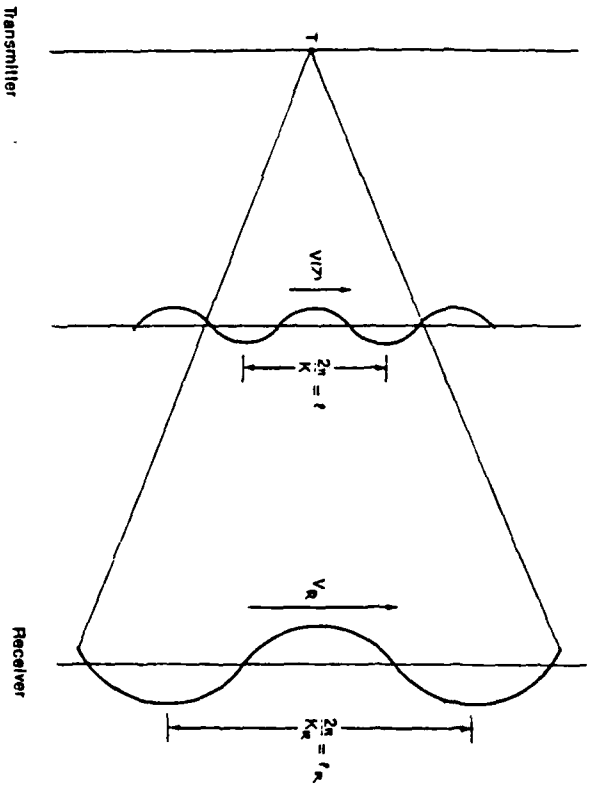

Figure 2. Schematic of the interaction of a spherical wave with a single Fourier component of turbulence.

Remote Sensing of Heat and Moisture Fluxes by Optical and Millimeter Wave Scintillation

W. Kohsiek

Royal Netherlands Meteorological Institute (KNMI)
De Bilt, The Netherlands

(invited)

Introduction

If a light source is observed through a turbulent medium like the atmosphere, rapid fluctuations of the received radiation intensity (scintillations) are noted due to fluctuations of the refractive index. A thorough quantitative description of the phenomenon was first given by Tatarski (1961). Commonly, the scintillation strength is expressed as the variance of the logarithm of the amplitude of the radiation received, σ^2_{lnA}. Tatarski showed that, for a horizontal transmission path in a homogeneous and isotropic atmosphere, σ^2_{lnA} is directly proportional to the refractive-index structure parameter C_n^2 at the height of the path above the surface, provided that

$$\ell_o << \sqrt{\lambda L} << L_o, \tag{1}$$

where λ is the wavelength of the radiation, L the length of the transmission path, L_o the outer scale of the turbulence and ℓ_o the inner scale of the turbulence. Typically, L_o is of the order of the height of the path, and ℓ_o varies from a few millimeters to one cm. C_n^2 is defined by

$$C_n^2 = \frac{\overline{[n(\vec{r}_1) - n(\vec{r}_2)]}^2}{|\vec{r}_1 - \vec{r}_2|^{2/3}}, \qquad \ell_o << |\vec{r}_1 - \vec{r}_2| << L_o, \tag{2}$$

where n is the refractive index, $\vec{r}_1$ and $\vec{r}_2$ are two locations in space and the overbar denotes an ensemble average.
Refractive-index fluctuations are mainly due to fluctuations of the temperature and the humidity (other sources, like pressure fluctuations, may be left out here), and consquently C_n^2 can be decomposed as

$$C_n^2 = a_\lambda C_T^2 + b_\lambda C_Q^2 + 2a_\lambda b_\lambda C_{TQ}. \tag{3}$$

The coefficients a_λ and b_λ depend on pressure, temperature and humidity, and on wavelength (Hill et al., 1980). The structure parameters C_T^2 and C_Q^2 are defined analogous to C_n^2, and
$C_{TQ} = [T(\vec{r}_1) - T(\vec{r}_2)]\,[(Q(\vec{r}_1) - Q(\vec{r}_2)]\,/\,|\vec{r}_1 - \vec{r}_2|^{2/3}$.
In the lower parts of the atmosphere (this will be specified in the next section), C_T^2 and C_Q^2 are coupled to the vertical surface fluxes of heat and moisture. In principle, one could infer C_T^2, C_Q^2 and C_{TQ} by observing σ^2_{lnA} at three different wavelengths, and next calculate the surface fluxes from C_T^2 and C_Q^2. However, in practice it is difficult to find suitable radiation sources and useful transmission paths where the coefficients a_λ and b_λ are sufficiently different at the respective wavelengths. If one only has scintillation observations at one or two wavelengths, then additional relations between C_T^2, C_Q^2 and C_{TQ} are wanted in order to infer each structure parameter separately. The extra relations are often based on micrometeorological theory or experiments. Such relations will be discussed below, as well as the relations between the surface fluxes of heat and moisture and C_T^2, C_Q^2 and C_{TQ}. The paper will be concluded with some

examples of measuring moisture fluxes by means of the scintillation phenomenon.

Structure parameters and the fluxes of heat and moisture

We will restrict the discussion to the unstable atmosphere (that is, if the transport of heat is directed from the surface to the atmosphere) for two reasons: firstly, the fluxes of heat and moisture are an order of magnitude larger in the unstable atmosphere than in the stably stratified atmosphere, and thus more important from a practical point of view, and secondly, relations between structure parameters and fluxes have far better been explored for the unstable atmosphere.

Micrometeorologists often discriminate a shallow atmospheric layer above the earth's surface where the vertical transports of momentum, heat etc. change little with height; it is called the atmospheric surface layer. It is found that this layer has a typical thickness of some tens of meters. Another much used conception is that of the atmospheric boundary layer; it is the layer bounded by the earth's surface at one end, and the temperature inversion at the other. In this layer a thorough mixing of all kinds of quantities is attempted by eddies of many different scales. The depth of the boundary layer is of the order of a few hundred meters up to ~ 2 km. Relations between structure parameters and fluxes originally were derived for the surface layer. E.g., for temperature (Wyngaard et al., 1971):

$$\frac{C_T^2 \, z^{2/3}}{T_*^2} = 4.9[1 - 7(z/L_M)]^{-2/3} \, . \qquad (4)$$

Here, z is the height above the surface and $T_* = - Q_o/u_*$ where Q_o is the surface flux of heat and u_* the friction velocity. The latter quantity is related to the momentum transport τ and the air density ρ by $\tau = \rho u_*^2$. L_M is the Monin-Obukhov length and is a function of u_* and Q_o . (We ignore the effect of the moisture flux on L_M here.) In case of an unstable atmosphere, $-L_M$ varies from some meters up to some hundreds of meters; the smaller $|-L_M|$ is, the more unstable is the atmosphere. For $-z/L_M >> 1$, Eq.(4) reduces to

$$C_T^2 = 2.67 \, z^{-4/3} \, (\frac{g}{T})^{-2/3} \, Q_o^{4/3} \, , \qquad (5)$$

where g is the acceleration of gravity and T the temperature in K. Eq.(5) provides for a relation between C_T^2 and Q_o that is of particular interest to practical applications because of its simplicity. The condition $-z/L >> 1$ may be relaxed down to $-z/L > 0.5$, a condition which is often met if, e.g., z = 20 m.

Two questions may now be addressed: (i) do relations similar to Eq.(4) exist for C_Q^2 and C_{TQ}, and (ii) can relations of the type of Eq.(4) or (5) be used above the surface layer.

As to the first question, there is evidence that there are relations for C_Q^2 and C_{TQ} that differ from the one for C_T^2 only by the value of the numerical constant 4.9 (for relevant references, see Kohsiek (1982)). Moreover, the ratio $C_{TQ}/(C_T^2 C_Q^2)^{\frac{1}{2}}$ has typical values of 0.8 to 0.9, because of the high correlation between temperature and humidity fluctuations. The answer to the second question is not a simple one. It is commonly observed that C_T^2 behaves as $z^{-4/3}$, as expressed by Eq.(5), some way above the surface layer, but the decrease diminishes and eventually is turned into an increase as one approaches the inversion. The actual fraction of the boundary layer up to which Eq.(5) is still valid is not yet well understood from the modeler's point of view (Wyngaard and LeMone, 1980; Burk, 1980,

1981); it presumably depends on z_i/L_M, where z_i is the height of the inversion, and on characteristics of the inversion itself such as the jumps of temperature and humidity. These conditions may be very different for e.g. a marine and a land environment. From observations, the fraction appears to be ~ 0.1 for weakly mixed boundary layers such as often occur over sea, and 0.5 for well-developed convective boundary layers over land (see Frisch and Ochs (1975), Wyngaard and LeMone (1980) and Fairall et al. (1980) for observations over sea, and Tsvang (1969), Kaimal et al. (1976), Kunkel and Walters (1981) and Dubloscland (1982) for over-land data). Broadly speaking, the same can be said on the behaviour of C_Q^2 with height; consequently, C_T^2/C_Q^2 appears to be fairly independent on height in the lower parts of the boundary layer. This is no longer true in the upper parts, however, where C_T^2 and C_Q^2 are known to behave differently (Wyngaard and LeMone, 1980; Druilhet et al., 1983). Even more reserve should be exercized as to C_{TQ} since the T-Q correlation is observed to change sign in the midst or upper parts of the boundary layer (Wyngaard et al., 1978; Druilhet et al., 1983). However, it seems warranted to adopt a constant value of $C_{TQ}/(C_T^2C_Q^2)^{\frac{1}{2}}$ for the lower tenth of the boundary layer. Summarizing, we conclude that C_T^2, C_Q^2 and C_{TQ} all obey relations of the kind of Eq.(4) up to at least one tenth of the inversion height. As a consequence, in that layer $(C_T^2/C_Q^2)^{\frac{1}{2}}$ is independent of height and proportional to the ratio of the sensible heat flux and the latent heat flux (moisture flux), or Bowen ratio, and $C_{TQ}/(C_T^2C_Q^2)^{\frac{1}{2}}$ has a value close to 1.

Examples of moisture fluxes inferred from scintillation observations

Two examples of inferring moisture fluxes by means of scintillation observations at one wavelength will be discussed. Essential information on the experiments, and results are to be found on the next page. We may add some comments:
The 30 GHz experiment has been described by Kohsiek and Herben (1983). Because scintillation was observed at one wavelength only, two extra relations between C_T^2, C_Q^2 and C_{TQ} had to be added to Eq.(3). The one for $(C_T^2/C_Q^2)^{\frac{1}{2}}$ is equivalent to assuming a Bowen ratio of 0.6. The bottom figure illustrates the relative contributions of the three terms of Eq.(3) to C_n^2 on a particular day. Moisture fluxes from scintillation (L_vE_o) were referred to fluxes calculated with the Priestley-Taylor formula ($L_vE_o^{ref}$). The other example is pertinent to an exeriment over the North Sea where a CO_2 laser scintillometer was used. Here, $(C_T^2/C_Q^2)^{\frac{1}{2}}$ was related to the Bowen ratio calculated from observations of air temperature (T_a) and humidity (Q_a), and sea water temperature (T_s). Moisture fluxes were calculated independently by using bulk exchange coefficients. As shown by the bottom figure, the contribution of C_{TQ} to C_n^2 is comparable to that of C_T^2. This is because of the small values of the Bowen ratio; over land, the contribution of C_{TQ} would typically be 30% of that of C_T^2. With both examples a reasonable agreement is found between moisture fluxes calculated with and without the use of scintillation measurements. (The exception on June 25 at 07:15 GMT is probably due to a low morning inversion.)

Conclusion

The technique of measuring the vertical fluxes of heat and moisture by means of scintillation is based on relations between the fluxes and the structure parameters C_T^2, C_Q^2 and C_{TQ}. Such relations are reasonably well established for the unstable surface layer, but improvement of our knowledge is to be sought for the weakly mixed boundary layer.

Example 1

λ = 1 cm (30 GHz radio wave)
L = 8.2 km
z = 60 m (average)
land (agriculture, woods)
$(C_T^2/C_Q^2)^{\frac{1}{2}} = 1.33$
$C_{TQ}/(C_T^2C_Q^2)^{\frac{1}{2}} = 0.87$

Date (1982)	Time (GMT)	Q^* (Wm^{-2})	$L_v E_o$ (Wm^{-2})	$L_v E_o^{ref}$ (Wm^{-2})	$\frac{L_v E_o}{L_v E_o^{ref}}$
May 26	10:45	509	329	339	0.97
	11:45	524	310	354	0.88
	12:45	491	290	331	0.88
	13:30	482	351	325	1.08
	14:15	405	292	277	1.05
June 25	07:15	201	297	119	2.50
	08:15	313	229	194	1.18
	09:15	408	320	257	1.25
	10:15	482	325	308	1.06
	11:15	531	385	344	1.12

Q^* is the net radiation
run length 15 min.

Example 2

λ = 10.6 um (CO_2 laser)
L = 9.7 km
z = 15 m
sea
$(C_T^2/C_Q^2)^{\frac{1}{2}} \sim (T_s - T_a)/(Q_{sat}(T_s) - Q_a)$
$C_{TQ}/(C_T^2/C_Q^2)^{\frac{1}{2}} = 0.8$, except the last run (= -0.5)

Date (1984)	Time (GMT)	B	$L_v E_o$ (Wm^{-2})	$L_v E_o^{ref}$ (Wm^{-2})	$\frac{L_v E_o}{L_v E_o^{ref}}$
Nov. 6	13:56	0.23	31	38	0.84
	15:31	0.21	28	38	0.74
	16:48	0.15	24	30	0.78
Nov. 20	14:00	0.18	69	86	0.81
	15:24	0.17	59	74	0.79
	16:46	0.15	71	82	0.87
Nov. 21	10:18	0	75	81	0.93
	16:00	-0.07	63	67	0.95

B is the Bowen ratio
run length approx. 45 min.

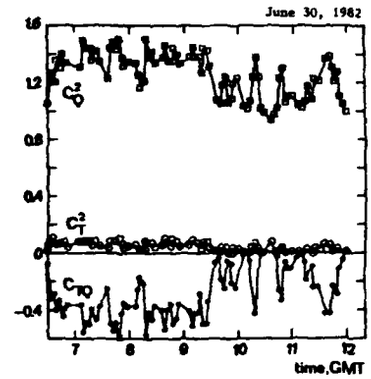

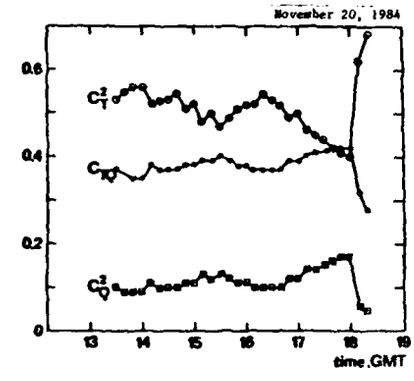

Relative contributions to C_n^2

References

Burk, S.D., 1980: Refractive Index Structure Parameters: Time-Dependent Calculations Using a Numerical Boundary-Layer Model. J. Appl. Meteor., 19, 565-576.

Burk, S.D., 1981: Comparison of Structure Parameter Scaling Expressions with Turbulence Closure Model Predictions. J. Atmos. Sci., 38, 751-761.

Druilhet, A., J.P. Frangi, D. Guedalia and J. Fontan, 1983: Experimental Studies of the Turbulence Structure Parameters of the Convective Boundary Layer. J. Climate Appl. Meteor., 22, 594-608.

Dubosclard, G., 1982: A Solar Study on the Temperature Structure Parameter in the Convective Boundary Layer. Bound.-Layer Meteor., 22, 325-334.

Fairall, C.W., R. Markson, G.E. Schacher and K.L. Davidson, 1980: An Aircraft Study of Turbulence Dissipation Rate and Temperature Structure Function in the Unstable Marine Atmospheric Boundary Layer. Bound.-Layer Meteor., 19, 453-469.

Frisch, A.S., and G.R. Ochs, 1975: A Note on the Behavior of the Temperature Structure Parameter in a Convective Layer Capped by a Marine Inversion. J. Appl. Meteor., 14, 415-419.

Hill, R.J., S.F. Clifford and R.S. Lawrence, 1980: Refractive-Index and Absorption Fluctuations in the Infrared caused by Temperature, Humidity and Pressure Fluctuations. J. Opt. Soc. Amer., 70, 1192-1205.

Kaimal, J.C., J.C. Wyngaard, D.A. Haugen, O.R. Coté and Y. Izumi, 1976: Turbulence Structure in the Convective Boundary Layer J. Atmos. Sci., 33, 2152-2169.

Kohsiek, W., 1982: Measuring C_T^2, C_Q^2 and C_{TQ} in the Unstable Surface Layer, and Relations to the Vertical Fluxes of Heat and Moisture. Bound.-Layer Meteor., 24, 89-107.

Kohsiek, W., and H.H.A.J. Herben, 1983: Evaporation derived from Optical and Radio-Wave Scintillation. Appl. Optics, 22, 2566-2570.

Kunkel, K.E., and D.L. Walters, 1981: Behavior of the Temperature Structure Parameter in a Desert Basin. J. Appl. Meteor., 20, 130-136.

Tatarski, V.I., 1961: Wave Propagation in a Turbulent Medium. McGraw-Hill, New York, 285 pp.

Tsvang, L.R., 1969: Microstructure of Temperature Fields in the Free Atmosphere. Radio Sci., 4, 1173-1177.

Wyngaard, J.C., Y. Izumi and S.A. Collins, Jr., 1971: Behavior of the Refractive-Index Structure Parameter near the Ground. J. Opt. Soc. Amer., 61, 1646-1650.

Wyngaard, J.C., W.T. Pennell, D.H. Lenschow and M.A. LeMone, 1978: The Temperature-Humidity Covariance Budget in the Convective Boundary Layer. J. Atmos. Sci., 35, 47-58.

Wyngaard, J.C., and M.A. LeMone, 1980: Behavior of the Refractive Index Structure Parameter in the Entraining Convective Boundary Layer. J. Atmos. Sci., 37, 1573-1585.

REMOTE SENSING OF ATMOSPHERIC TURBULENT LAYERS

J. VERNIN, J-L. CACCIA

Département d'Astrophysique de l'I.M.S.P. - U.A. 709 du C.N.R.S.
Université de Nice - Parc Valrose - 06034 NICE CEDEX - FRANCE

(invited)

I - INTRODUCTION :

Vernin and Azouit[1] have shown that a statistical and spatio-temporal study of atmospheric speckle patterns produced by the light of a single star permits the wind velocities in the turbulent layers to be obtained. The purpose of this paper is to show, in a first step, that using an a-priori knowledge of theoretical shapes of spatio-temporal correlations of atmospheric speckle patterns we can also determine the altitude and the C_N^2 of each turbulent layer.

II - SPATIO-TEMPORAL CORRELATION OF ATMOSPHERIC SPECKLE PATTERN :

1 - Atmospheric speckles

A plane wave arriving from a star traverses the atmosphere, which is supposed to be a discrete superposition of thin turbulent layers, which exhibit refractive index fluctuations[2]. Assuming the small perturbation approximation we can show that we observe at the ground level the sum in intensity of speckle patterns created by each layer. The characteristics of each speckle pattern are the following :

i) the coherence width of the speckles is proportionnal to $\sqrt{\lambda h}$, where λ is the wavelength of light and h the altitude of the layer[1].

ii) the motion of the speckles follows the velocity of the wind in the layer which has created them.

iii) the variance of intensity fluctuations is proportionnal to $C_N^2(h)\Delta h$ where Δh is the layer thickness[3].

Thus, we have to treat the speckle pattern created by each of the turbulent layers statistically and separately in order to obtain the altitude and the C_N^2 of each.

2 - Spatial autocorrelation

The autocorrelation of speckles at the ground level after the light has traversed the atmosphere can be written, using the formalism of Roddier[3] :

$$(1) \qquad C(x,y) = \int_0^\infty C_N^2(h)\, C_0(x,y,h)\, dh$$

with :

$$(2)\quad C_o(x,y,h) = 3.9\ 10^{-2}k^2 \left[\int_{-\infty}^{+\infty}\int_{-\infty}^{+\infty} \left[f_x^2 + f_y^2\right]^{\frac{-11}{6}} \ \mathrm{Sin}^2\left[\pi\lambda h(f_x^2 + f_y^2)\right] \times \right.$$
$$\left. \times \exp\left[-2i\pi(xf_x + f_y)\right]\ df_x df_y \right]$$

where (f_x,f_y) are the spatial frequency components and k is the wave vector modulus.

The expression (2) combines the turbulence spectral law of Kolmogorov[4] and a Fresnel filtering term. Considering a discrete superposition of N turbulent layers indexed i each having a width Δh in the atmosphere, the integral (1) can be written :

$$(3)\quad C(x,y) = \sum_{i=1}^{N} C_N^2(h_i)\ C_o(x,y,h_i)\ \Delta h$$

Figure 1 shows four examples of autocorrelations corresponding to four different altitudes.

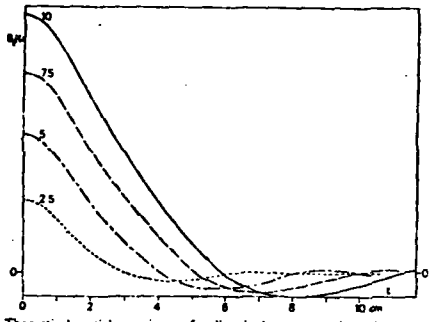

. Theoretical spatial covariance of stellar shadow patterns in arbitrary scale, assuming a thin turbulent layer at the altitude indicated in km on each curve (2.5, 5, 7.5 and 10 km). The integral $\int dh \cdot C_N^2(h)$ over the layer thickness is assumed to be the same in each case.

Figure 1 : (from reference 3)

We note in figure 1 that if we take the sum of these four curves we lose the detailed information on each layer because we obtained a unique correlation peak at the origin. This peak contains only infromation integrated over all the atmosphere. Evidently we cannot use only a pure spatial study for obtaining tha parameters related to each layer, thus we need to use a multidimensional analysis.

3 - Spatio-temporal correlation

We suppose the Taylor assumption is verified, i.e. each turbulent layer has a translational velocity vector $\vec{V}_i(u_i,v_i)$ and each turbulent element moves without distortion during the analysis time.

We calculate the cross-correlation of two speckle pictures taken with a temporal shift τ :

$$(4)\quad C(x,y,\tau) = \sum_{i=1}^{N} C_o(x - u_i\tau, y - v_i\tau, h_i)\ C_N^2(h_i)\ \Delta h$$

In this expression we see that the correlation peaks corresponding to each turbulent layer are no longer stacked at the origin as in previous paragraph, but they are at the points which have the coordinates equal to (x_i,y_i) , so that : $x_i = u_i\tau$ and $y_i = v_i\tau$.

Thus, it is sufficient that the centers of the peaks are well separated, one from another, to permit the extraction of the parameters related to each turbulent layer.

III - METHOD FOR CALCULATING PARAMETERS :

1 - The nature of the problem :

The experiment described by Vernin and Azouit[1] consists of bidimensional spatio-temporal correlation estimations of atmospheric speckle-patterns with the possibility to adjust the integration time ΔT and the delay τ. The problem is to detect and to analyse correlation peaks in a noisy background which is a classical problem of extraction of signal from noise.

2 - Calculation of atmospheric parameters :

The method consists of finding locally the best possible fit by the method of least squares, of an experimental peak to a theoretical peak which is calculated numerically. The position (x_i, y_i) where the fit is the best permit the vector coordinates (u_i, v_i) of the wind velocity to be obtained : $v_i = x_i / \tau$ and $v_i = y_i / \tau$; and then the altitude parameter h_i defining the correlation peak making this fit is the altitude of the layer. The $C_N^2(h_i)\Delta h_i$ value is directly derived from the altitude value when this last value is correctly estimated.

IV - EXPERIMENTAL RESULTS AND DISCUSSION :

The period concerned was the night from December 3 to 4, 1981 between 1.15 and 2.00 AM, the star observed was Capella (almost at the zenith) and the instrument was the 1m93 telescope of the Observatoire de Haute-Provence. The results presented are obtained from correlations with ΔT = 5 mn 30 s, τ= 6 ms and the exposure time of the speckle patterns θ = 0.5 ms.

Table of the results :

Wind velocity		Alt.
mod. m/s	dir. °	km
16	47	8
31	42	14
50	54	20
58	48	?
18	4	38
10	-33	42

Six peaks were detected and five gave indications about the altitude, the sixth being defined by a too few pixels ; it is in the upper right part of figure 2.

With these values of wind speed and direction we can make a hodograph and compare it with the hodograph from the meteorological station of Nîmes(*). Figure 2 shows these two curves.

We clearly see in figure 2 that our hodograph is in good agreement with that of Nîmes (Nîmes is wbout 100 km from the O.H.P. and the hodograph was made at 0.00 AM) but our altitude values are overestimated in respect of those of Nîmes.

(*)with acknowledgements to : Service d'Aëronomie, Réduit de Verrières
91370 Verrières le Buisson, B.P. n°3 - FRANCE

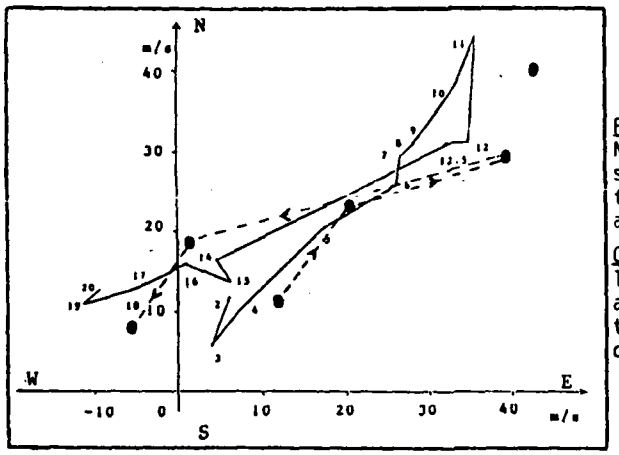

Figure 2 : Hodograph of Nîmes : full-line ; the small numbers along the full-line represent the altitude scale.

Our hodograph : dotted-line with arrows showing altitude increasing through the five well-determined points.

As shown in II, 1, i, the altitude of the layer is sensitive to the width of the correlation peak. Unfortunately, several experimental conditions lead to spread the correlation function : size of the pixels, fluctuations of the wind velocity vector during the integration time ΔT^5 and blurring of the speckles during the exposure time θ . Thus, the estimated altitude shown in the table, are over-estimated. These preliminary results will be very soon corrected from the above mentioned effects.

V - CONCLUSION :

We have shown the possibility of extracting correct information about the relative altitudes of turbulent layers from bidimensional spatio-temporal cross correlation analysis of atmospheric speckle patterns.

We expect to obtain the absolute altitudes as soon as the deconvolution problem is solved.

This is an essential point because the correct $C_N^2(h)\Delta h$ values are directly derived from the absolute altitudes.

REFERENCES :

1. Vernin J;, Azouit M; : Traitement d'image adapté au speckle atmosphérique : II - Analyse multidimensionnelle appliquée au diagnostic à distance de la turbulence. - J. of Optics (Paris) (1983), 14, 131-142.

2. Tatarskii V.I. : Wave propagation in a turbulent medium. - Dover Publications, New-York (1961).

3. Roddier F. : The effects of atmospheric turbulence in optical astronomy. - Progress in Optics, E. Wolff ed. (1981) Vol. XIX, 281-376.

4. Kolmogorov A.N. : Local structure of turbulence in incompressible fluids with very high Reynolds numbers (1941), Dan SSSR, 30, 229.

5. Little L.T. and Ekers R.O. : A method for analysing drifting random patterns in astronomy and geophysics. - Astron. Astrophys. (1971) 10, 306-309.

Meteorological Parameters Derived from Scintillation Measurements

Gerd Ortgies, Forschungsinstitut der Deutschen Bundespost,
D-6100 Darmstadt, Federal Republic of Germany

Extensive theoretical and experimental work has been carried out to understand the nature of amplitude scintillations which occur on satellite-earth links under clear air conditions. In this context, the description of the scattering medium by the structure parameter α is of particular interest. Vilar and Haddon /1/ have derived this parameter from a spectral analysis of amplitude scintillations. However, the disadvantage of their method was that they had to derive the transverse wind velocity of the scattering medium relative to the propagation path from meteorological measurements carried out 44 miles away from the receive station.

In this contribution it will be shown that the structure constant, the altitude of the turbulent layer and the transverse wind velocity can be derived from scintillation measurements performed simultaneously with two antennas of different diametres. Such measurements were carried out with the OTS satellite at 11.786 GHz at the Deutsche Bundespost experimental ground station Leeheim from June to December 1983 using antennas with diametres of 3 m and 8.5 m /2,3/. From the measured data, concurrent power density spectra of amplitude scintillations were calculated for time intervals of six minutes in every 2-h period for the measuring interval June to September 1983. These spectra can be well approximated by two asymptotes which intersect at the corner frequency f_c. The power density is nearly constant at frequencies below the corner frequency, whereas above it follows a power law with exponent (n-1), n being the exponent of the Kolmogorov spectrum /4,5/.

From a comparison of spectra measured concurrently with the two antennas, it has been found that, in general, the spectral density beyond the corner frequency decreases faster for the 8.5-m antenna than for the 3-m antenna (Fig. 1). This experimental result is in good agreement with theory /6,7/. Rücker /6/ showed that the parameter n derived from the spectrum measured with the 3-m antenna deviates only slightly from the corresponding value derived for a point aperture. Thus, for the following considerations n is taken from the spectrum measured with the smaller antenna. It further follows from the experiment that the corner frequencies are independent of the antenna diametre (see Fig. 2). This is also in good agreement with theoretical work /6/.

The variance of the amplitude fluctuations is the integrated power density spectrum. Due to an averaging effect, the variance depends besides other parameters on the antenna radius R /2/. Under the assumption of a homogeneous structure of the scattering medium along the propagation path up to a distance L, the variance is

given by /6/

$$\sigma^2 = \pi^2 \alpha k^{(6-n)/2} L^{n/2} \left[\Gamma\left(-\frac{n}{2}\right)\left[-\frac{n}{2}\left(\frac{k}{L}a^2\right)^{(n-2)/2} + \left(1+\frac{k^2}{L^2}a^4\right)^{n/4} \sin\left(\frac{n}{2}\arctan\frac{L}{k\,a^2}\right)\right]\right] \qquad (1)$$

where $a=0.5\sqrt{\eta}\ R$; η : antenna efficiency; α: structure parameter; k: wave number corresponding to the beacon frequency.

Hence, L can be determined from the ratio of the variances measured simultaneously with the two antennas and from n. Results are given in Fig. 3 for more than 200 evaluated spectra. With the information on L and the measured corner frequency the transverse wind velocity v_t can be calculated for a small antenna /1,6/ via

$$f_c = \frac{v_t}{2\pi}\sqrt{\frac{k}{L}}\left[\frac{\sqrt{\pi}\,\Gamma\left(\frac{n}{2}\right)}{2\,\Gamma\left(\frac{n+3}{2}\right)\Gamma\left(\frac{n-1}{2}\right)\sin\left(\frac{5-n}{4}\pi\right)}\right]^{\frac{1}{1-n}} \qquad (2)$$

For measured corner frequencies in between 0.05 and 1Hz, transverse wind velocities were found in the range of 0.9 to 12 m/s.

With n and L known, the structure parameter α , which depends on the inhomogeneity of the refractive index, on the inner and outer scale sizes of the scattering medium and on the exponent of the Kolmogorov spectrum, can be calculated from eq.(1). The measured distribution of α is depicted in Fig. 4 on a logarithmic scale. The results are in good agreement with measurements of Vilar and Haddon /1/.

Fig. 5 shows that α and L are well correlated, the latter being proportional to the layer height. For low altitudes of the turbulent layers high values were found for α decreasing rapidly with increasing L. This behaviour can be easily understood, as α depends mainly on the variance of the refractive index which itself is a function of temperature and humidity. Therefore, an attempt was made to correlate α with the water vapour pressure at distance L. The water vapour pressure was calculated from the measured temperature and humidity at ground level, assuming a vertical temperature gradient of 1°C per 200 m. The results are shown in Fig. 6 for the measuring period June 1st to July 19th, 1983, and seem to indicate a linear relationship on a semi-logarithmic scale.

It has been shown that meteorological parameters like transverse wind velocity, altitude of the turbulent layer and structure parameter of the turbulence can be derived directly from power density spectra measured concurrently with two antennas of different sizes. Other methods, however, resort to assumptions on either the transverse wind velocity or on the altitude of the turbulent layer in calculating the structure parameter /1/. Therefore, additional meteorological measurements are necessary if only one antenna is available.

Because of the huge amount of data, it seems impractical to sample data for a continuous off-line spectral analysis in order to get statistical results on the structure parameter. This difficulty can be overcome when assuming for n the theoretical value of 11/3 valid for the Kolmogorov spectrum. This value was found to coincide well with the mean value derived from the spectral slope of the spectra measured with the 3-m antenna. From continuously measured variances, statistics can be derived for α or for the more often used structure constant C_n^2 which is uniquely related to α /1,6/.

References

/1/ E. Vilar, J. Haddon, IEEE Trans. Antennas Propagat., AP-32, 340-346, (1984)
/2/ F. Rücker, F. Dintelmann, Electron. Lett., 19, 1032-1034, (1983)
/3/ G. Ortgies, F. Rücker, Electron. Lett., 21, 143-145, (1985)
/4/ A. Ishimaru, IEEE Trans. Antennas Propagat., AP-20, 10-19 (1972)
/5/ G. Ortgies, Electron. Lett., 21, 771-772, (1985)
/6/ F. Rücker, Technischer Bericht Nr. 445 TBr 77 des Forschungsinstitutes der DBP, (1985), (available from Fernmeldetechnisches Zentralamt, Dept. B-ZDI-DrV, D-6100 Darmstadt)
/7/ M.J.M. van Weert, AGARD Conf. Proc. 159, 27-1...27-9, (1975)

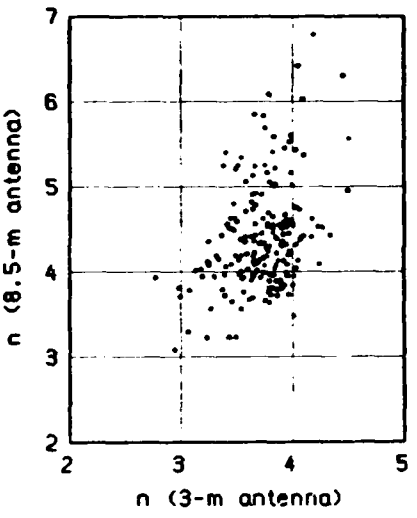

Fig.1: Scattergram of concurrently measured values n for the 3-m and 8.5-m antenna.

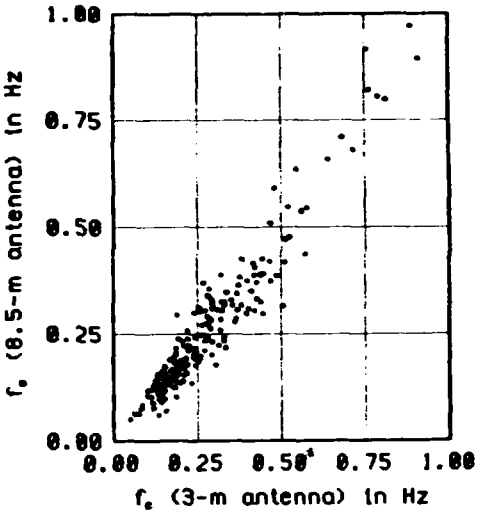

Fig.2: Scattergram of concurrently measured corner frequencies.

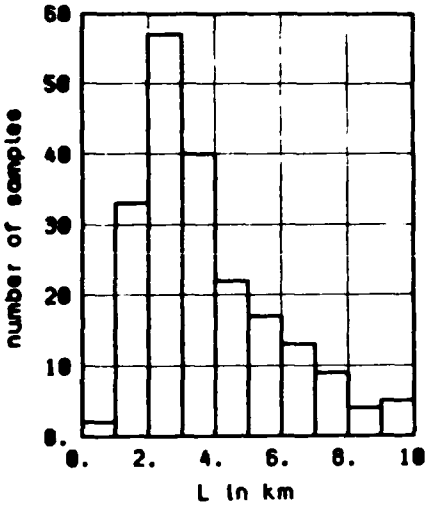

Fig.3: Distribution of L.

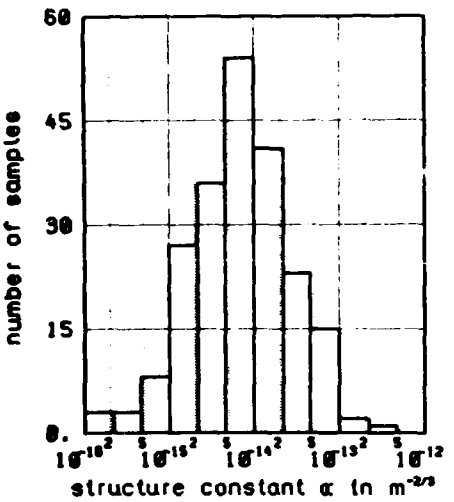

Fig.4: Distribution of α.

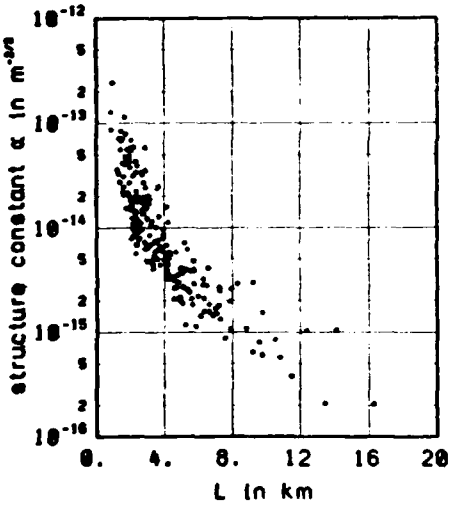

Fig.5: Correlation between α and L.

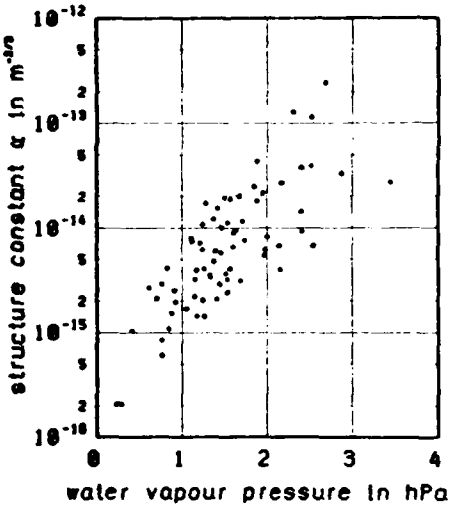

Fig.6: Correlation between α and water vapour pressure.

Comparisons of Meteorological and Structure Parameters in Complex Terrain

W. Porch, L. Rosen

Lawrence Livermore National Laboratory

Livermore, California 94550, U.S.A.

W. Neff

NOAA/WPL

Boulder, Colorado 80303, U.S.A.

In two field experiments in The Geysers geothermal region of Northern California and one experiment in the oil-shale region of Eastern Colorado, acoustic sounders and cross-wind sensors were collocated within and across the valley, respectively. This arrangement allows comparison of the temperature structure parameter C_T derived from the acoustic sounder with the index of refraction structure parameter C_n from the optical turbulence used by the cross-wind sensor to derive the speed. Comparison of the spatial/temporal averaging associated with acoustical, optical and point measurements is also of interest in complex terrain.

The variability of tethersonde determination of the lapse-rate compared to spatially averaged optical refraction measurements demonstrate the difficulty associated with spatial representativeness of point measurements in complex terrain. Fig 1 shows the optically determined lapse-rate comparison with temperature gradients from tethersonde data from temperatures just above and just below the optical path is reduced when the average gradient throughout the drainage layer is used. Also included in Fig. 1 are the standard deviation of light intensity (related to C_n) and the acoustic sounder record for the same period. Some correspondence is seen between the peak in optical turbulence and the rise and fall of the drainage layer around 2000 PST shown in the sounder record. Also, the

general rise in the drainage layer and the lapse-rate throughout the night, though possibly circumstantial, may be related.

The data from a 600m optical path and the associated monostatic doppler sounder below the path were digitized together from which 1 minute averaged values were constructed of acoustic signal, vertical doppler shift, optical turbulence and cross-wind speed. A comparison can be made for C_n and C_T determined from acoustic backscatter and optical scintillation at the height the acoustic beam intersects the optical path. Fig. 2 a) and b) shows the time series comparison for C_n and C_T, respectively. Here the long period correspondence is not as good as for a wind speed comparison derived from a tracer adjacent to the optical path and the cross-wind sensor. This is due in part to the harsher scale requirements necessary for comparison of turbulent quantities. A larger contributor, is probably the effect of wind noise on the acoustic receiving sensor. The relatively high sea breeze related winds of 3-4 m/s occur at just the time ($\sim$ 1700 PST) when sunset isothermal conditions would imply and the optical turbulence shows a substantial decrease in C_n and therefore C_T. In spite of the relatively smaller long period correspondence of the optical and acoustic turbulence, there is a better correspondence of the higher frequency behaviour. A quantitative comparison of these correspondences was found in the coherence spectra between the optical cross-winds and tower down-valley wind component and between C_n and C_T.

Representative values of meteorological parameters measured during the experiments described above under a variety of conditions will be used as input to coupled electromagnetic and hydrodynamic numerical model. The goal will be to access the relative importance of different meteorological parameters and conditions on high energy laser propagation.

This work was performed under the auspices of the U.S. Department of Energy by the Lawrence Livermore National Laboratory under Contract W-7405-Eng-48.

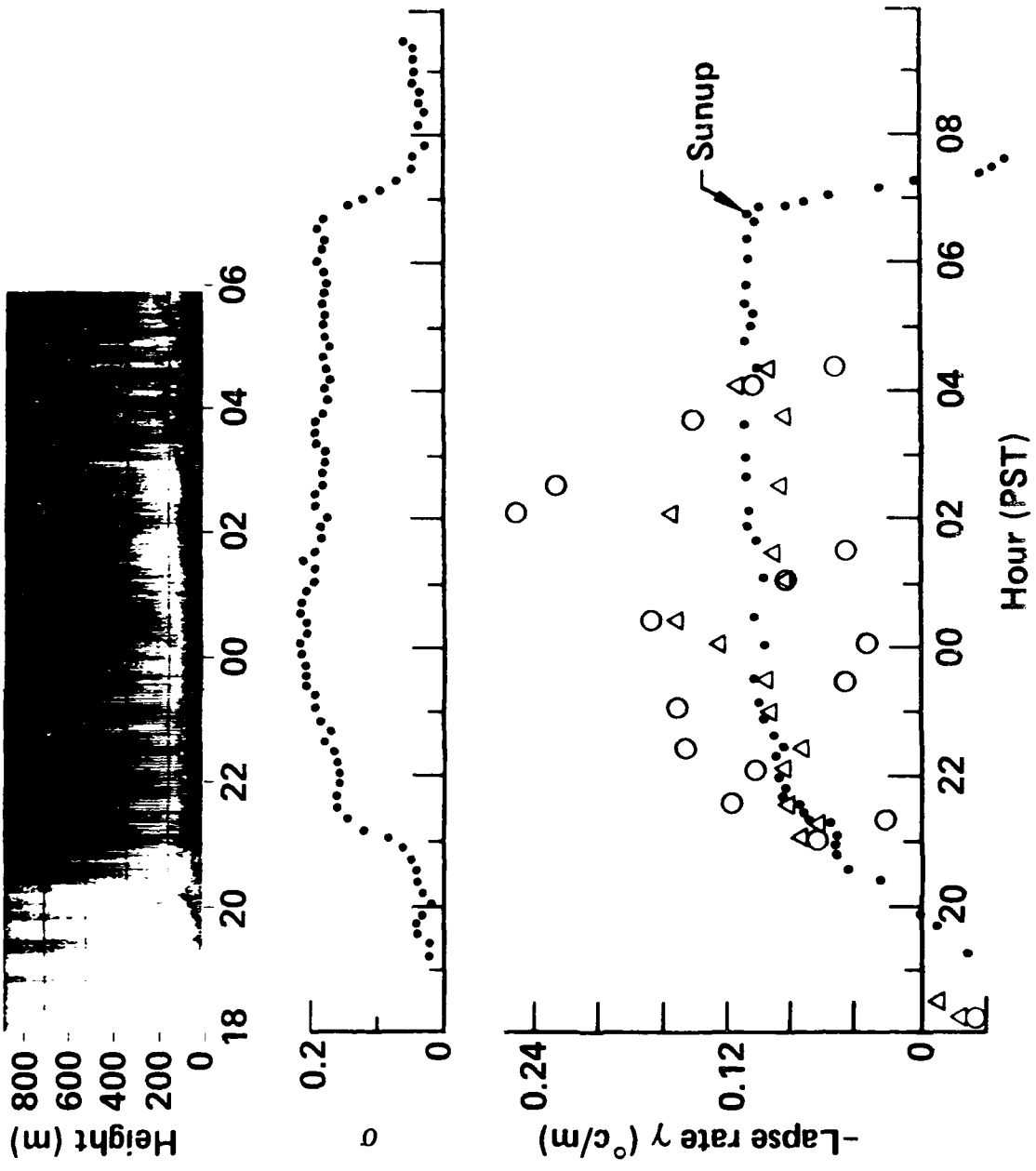

Figure 1. Meteorological Parameters in Complex Terrain

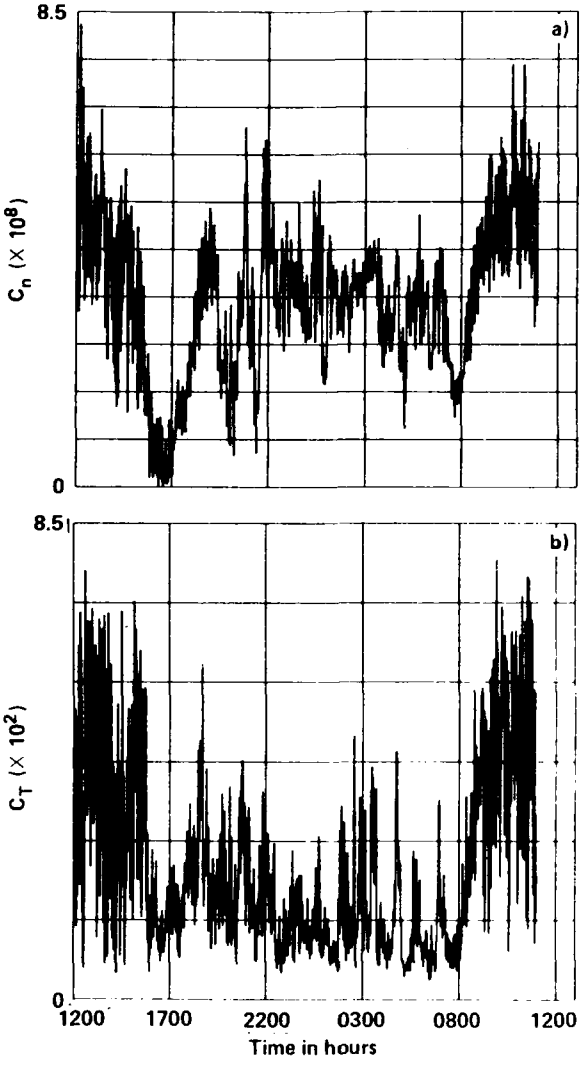

Figure 2. Comparison of optical (a) and acoustic (b) turbulence measured at the same location.

Remote Sensing of Atmospheric Water Vapor Profiles from Simulated Millimeter Wave Moisture Sounder Data

R. G. Isaacs, G. Deblonde, R. Worsham, and L. D. Kaplan
Atmospheric and Environmental Research, Inc.
840 Memorial Drive, Cambridge, Massachusetts 02139, U.S.A.

V. J. Falcone
Air Force Geophysics Laboratory
Hanscom Air Force Base, Massachusetts 01731, U.S.A.

1. Introduction

This paper summarizes the results of a study to investigate the retrieval of atmospheric water vapor profiles over land and ocean from several combinations of millimeter wave frequency channels. A millimeter wave region water vapor absorption feature with sufficient line strength for this application is the $3_{13}-2_{20}$ rotational line located at 183.31 GHz (Shaerer and Wilheit, 1979). Channel selection has been investigated by including various subsets of frequencies in the vicinities of 183, 150, 90, 50, 37, 22, and 19 GHz. Studies of the millimeter wave moisture retrieval problem to date have generally focused on clear sky simulations (Rosenkranz et al., 1982; Kakar, 1983). In order to determine the possible effects of beam filling cloud on the quality fo water vapor retrievals, these calculations compare the accuracy of clear and cloudy cases. Retrievals are based on a statistical regression method which minimizes the mean square error between the estimated and observed water vapor profiles. The necessary retrieval statistics are calculated from an a priori sample of temperature and water vapor profiles and corresopnding sensor data simulations.

2. Technical Approach

Water vapor profile retrievals were obtained by first calculating synthetic channel brightness temperatures using a recently developed sensor simulation model (Isaacs et al., 1985). This radiative transfer code utilizes: (a) a set of channel frequencies for each hypothetical sensor instrument, (b) radiosonde profiles of atmospheric moisture and temperature, (c) cloud models consisting of liquid water content and vertical extent, (d) surface emissivity data, and (3) sensor physical characteristics including noise and scanning geometry. A total of 14 potential channel frequencies were selected. These are summarized in Table 1. Simulated sensor brightness temperatures were calculated for each channel set and atmospheric profile using the radiative transfer equation (Waters, 1976):

$$T_B = T_{B1} + \{\varepsilon\, T_s + (1-\varepsilon)T_{B2}\}\, \exp(-\tau)$$

where T_{B1} is the upward emission from the atmosphere alone, ε is the surface emissivity = (1-R), R is the surface reflectivity, T_s is the surface temperature, T_{B2} is the downward emission from the atmosphere plus the attenuated cosmic background emission, and τ is the total opacity of the atmosphere along the line of sight. The quantities T_{B1} and T_{B2} are line integrals along the sensor line of sight given by:

$$T_{B1} = \int_o^H T(z)\ \gamma(z)\ \exp\ [-\int_z^H \gamma(z')\ dz']dz,$$

$$T_{B2} = T_c\ e^{-\tau} + \int_o^H T(z)\ \gamma(z)\ \exp[-\int_o^z \gamma(z')\ dz']dz.$$

Here H is the effective height of the atmosphere (taken as 50 km), $\gamma(z)$ is the total extinction profile equalling the sum of gas absorption and cloud attenuation, and T_c is the cosmic background temperature. Millimeter wave cloud attenuation properties used in the simulation were from Falcone et al. (1979).

Vertical moisture profile retrievals were obtained from independent samples of simulated sensor brightness temperatures using a statistical inversion technique based on Gaut et al. (1975). The scheme chooses, in a statistical sense, the most probable combination of atmospheric and surface properties which produces the set of measured radiometric data values. An individual retrieval of the absolute abundance of water vapor (molecules cm^{-2} in six layers corresponding to 0-200, 200-300, 300-500, 500-700, 700-850 mb, and 850-1000 mb, respectively, from n channel brightness temperatures was obtained from $\hat{u} = Dt$, with $D = (UT^t)\hat{T}^*\Lambda^{*-1}\ T^{*t})$, where $\hat{u}$ is a vector giving an estimate of the profile of integrated water vapor in each of the six layers, t is a vector whose components are n brightness temperatures, U_{rs} is water vapor at six levels for s atmospheric samples (r=6), T_{ns} are brightness temperatures for n channels for s samples, T^* are selected eigenvectors of TT^t, and Λ^* is a diagonal matrix whose elements are corresponding eigenvalues. Retrieval accuracy was assessed by comparing inferred layer water vapor abundances to those in the actual profiles and evaluating the fractional root mean square (RMS) error over the ensemble of retrievals. The RMS error for each layer k evaluated over the set of N = 100 independent soundings was defined as:

$$RMS(k) = \frac{1}{\bar{u}(k)} \{N^{-1} \sum_{j=1}^{N} [\hat{u}(k,j) - u(k,j)]^2\}^{1/2},$$

where $\hat{u}(k,j)$ and $u(k,j)$ are, respectively, the retrieved and actual water vapor amounts for the k^{th} layer and j^{th} sounding and $\bar{u}(k)$ is the layer mean value. For comparison, the same statistic was evaluated assuming the mean of the ensemble as the best estimate climatological retrieval for each sounding, i.e., by replacing $\hat{u}$ by $\bar{u}$ itself.

3. Results

Over the tropical ocean for the sample set investigated, water vapor profile retrieval results in clear cases are encouraging. All of the sample instruments tested in simulation provide retrievals with less than 15 percent fractional RMS error in the lower troposphere (below 700 mb) and between 20 and 30 percent in the middle troposphere (between 300 and 700 mb). These retrieval accuracies may be compared with that of climatological variance for these layers, 28 to 38 percent and 55 percent, respectively (see Figure 1). The effect of cloud on the simulated millimeter wave moisture retrievals is dramatic and independent of either the background surface or the selected channel set. For cloudy cases over the ocean, for example, the RMS fractional error for the SSM/T-2 instrument (Figure 2), is increased by a factor of one half. Over land, results are not quite as drastic except perhaps near the surface, but only because retrievals are not that good for clear cases (see Figure 3). Based on the results of our retrieval simulations, it is evident that millimeter wave vertical moisture profile retrievals over land will be degraded in quality in comparison to those potentially obtainable over the

oceans. Further details can be found in a report by Isaacs and Deblonde (1985).

4. Acknowledgement

This work was sponsored by the Air Force Systems Command, Air Force Geophysics Laboratory, under contract F19628-84-C-0134.

5. References

Falcone, V. J., L. W. Abreu, and E. P. Shettle, 1979: AFGL-TR-79-0253.

Gaut, N. E., M. G. Powler, R. G. Isaacs, D. T. Chang, and E. C. Reifenstein, III, 1975: AFCRL-TR-75-0007.

Isaacs, R. G., and G. Deblonde, 1985: AFGL-TR-85-0095

Isaacs, R. G., G. Deblonde, R. D. Worsham, M. Livshits, 1985: AFGL-TR-85-0040.

Kakar, R. K., 1983: J. Clim. and Appl. Meteorol., 22, 7, 1282-1289.

Rosenkranz, P. W., M. J. Komichak, and D. H. Staelin, 1982: J. Appl. Meteorol., 21, 1364-1370.

Schaerer, J., and T. T. Wilheit, 1979: Radio Sci., 14, 321-375.

Waters, J. W., 1976: Methods of Experimental Physics, 12, Part B, Academic Press, pp. 142-176.

Table 1
Simulated Frequencies

GHz	SSM/T-2	4 Channel	5 Channel	9 Channel	10 Channel	14 Channel
183+/-7	X		X	X	X	X
183+/-3	X		X	X	X	X
183+/-1	X		X	X	X	X
90.0			X	X	X	X
150.0	X		X	X	X	X
50.5		X		X		X
53.2		X		X		X
54.35		X		X		X
54.9		X		X		X
19.35(H)					X	X
19.35(V)					X	X
22.24(V)					X	X
37.0(H)					X	X
37.0(V)					X	X

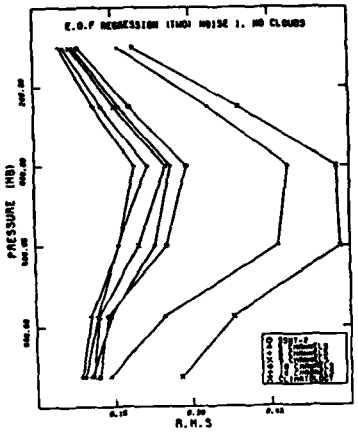

Figure 1: RMS error DMSP mission sensor channel sets, clear cases over the ocean.

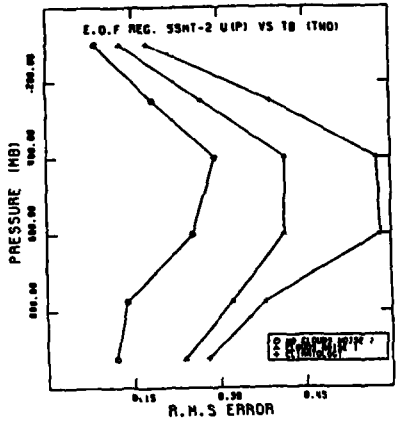

Figure 2: RMS error,SSM/T-2 instrument,cloudy vs clear, over the ocean.

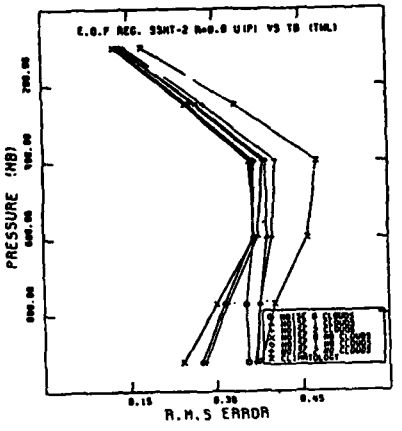

Figure 3: RMS error,SSM/T-2 instrument, cloudy vs clear, over land with various sensor noise levels in K.

Remote Sensing of Wind by Electrooptic Phase Modulation of Atmospheric Emissions

Daniel J. McCleese, David M. Rider, Jack S. Margolis and John T. Schofield

Jet Propulsion Laboratory, California Institute of Technology, Pasadena, California, USA 91109

INTRODUCTION

A new instrumental approach to measurements of upper atmospheric parameters is being developed for the upcoming NASA Eos near-Earth orbital spacecraft. This approach is a novel application of electrooptic phase modulation to gas correlation spectroscopy (McCleese and Margolis, 1983; McCleese, Margolis and Ballard, 1984). The atmospheric measurements to be made include the vector wind field, the concentrations of minor and trace species, and atmospheric temperature and pressure in the stratosphere and mesosphere. These measurements are to be made globally, and with complete coverage of the dayside and nightside.

In this paper we focus on the technique employed for the remote sensing of wind in the 20 to 120 km altitude range. Winds are a major factor in controlling the global distribution of many atmospheric species including ozone. Yet, wind velocities in the upper atmosphere have never been measured globally. Recent work has shown that techniques using the geostrophic approximation to infer winds from temperature data appear to work well in deducing the mean, long time-scale wind field; however, they do not do well when inferring non-linear disturbances known to be important in species transport in the upper atmosphere. Additionally, winds derived from remotely sensed temperature data from polar orbiting spacecraft suffer from limitations in spatial and temporal sampling. Because it is the horizontal thermal gradient which is of interest in deducing winds, the potential for sampling baises is of considerable concern. Without direct measurements of the wind field we can not be certain of the correctness of our present view of upper atmospheric transport.

MEASUREMENT APPROACH

Work just completed in the laboratory has demonstrated a new approch to gas correlation spectroscopy that enhances the technique to include the capability of measuring the wind-induced Doppler shift in the naturally occuring infrared thermal emission features of stratospheric and mesospheric gases. This enhancement is made possible by utilizing electrooptic phase modulation. Crystals, such as cadmium telluride, exhibit a large electrooptic effect; that is, by applying a voltage across a properly cut crystal the refractive index of the crystal is altered (see Yariv, 1975). Light passing through an electrooptic crystal, to which an oscillating voltage is applied, experiences a modulation of its phase (equivalent to frequency modulation). This is shown schematically in Fig. 1 together with a diagram representing the action of an electrooptic phase modulator (EOPM) upon a single spectral emission line. In

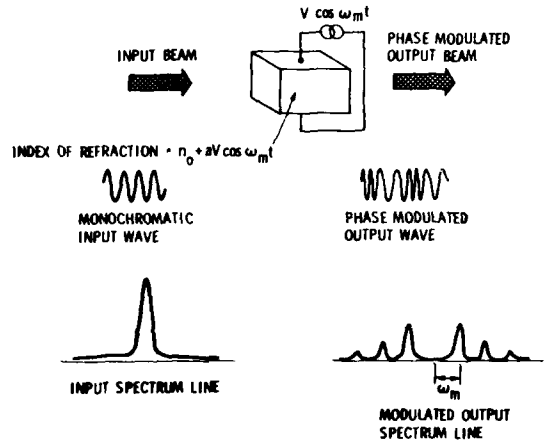

Figure 1. Electrooptic phase modulation is illustrated showing the effect of phase modulation upon a spectral line.

a gas correlation spectrometer, a cell containing an atmospheric gas provides a frequency reference with which observed atmospheric emission spectra are compared. Figure 2 illustrates the configuration of a limb viewing correlation spectrometer employing an EOPM. In Fig. 3 we show the spectroscopic principles of the measurement technique. The top part of Fig. 3a shows the unmodulated atmospheric emission and the reference cell spectrum with no relative velocity between the instrument and atmosphere. In the lower portion of Fig. 3a, the atmospheric spectrum is phase modulated at a frequency ω_m with the EOPM modulation index chosen to produce zero carrier amplitude. The phase modulation, in this example, eliminates the absorption of the atmospheric emission by the reference cell. In Fig. 3b, the emission spectra are Doppler shifted. The modulation frequency ω_m in this figure corresponds to the Doppler shift produced by the relative velocity between the reference cell and atmosphere. Figure 3c is the spectrum of the radiant flux from the atmosphere as seen by the detector when the modulation frequency equals the Doppler shift. In Fig. 3d, the variation of the radiant flux, for a fixed relative velocity, is shown as a function of EOPM modulation frequency. The minimum measured flux occurs at the modulation frequency which is equal to the Doppler shift of the spectrum.

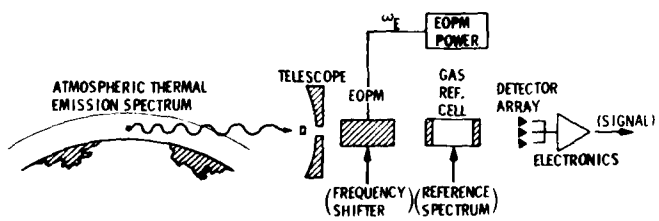

Figure 2. Schematic of Stratospheric Wind Infrared Limb Sounder, a gas correlation spectrometer employing electrooptic phase modulation.

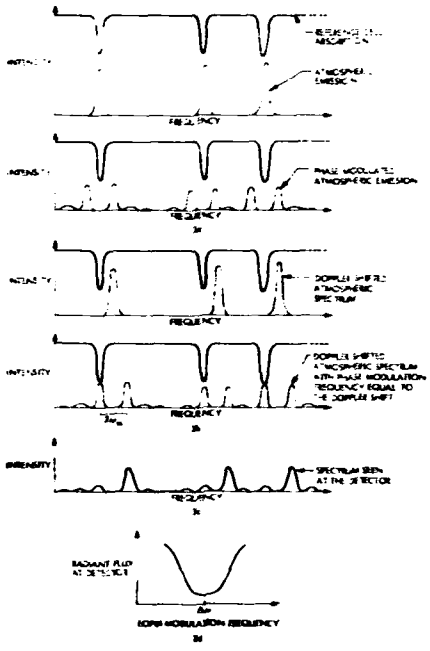

Figure 3. The principle of operation of the EOPM in measuring winds is shown.

LABORATORY DEMONSTRATION

In order to demonstrate the instrument approach described above, we have assembled a laboratory breadboard of an EOPM gas correlation spectrometer. This breadboard has been used to examine the characteristics of cadmium telluride EOPMs operating near 8 μm wavelength, and at modulation frequencies 100 to 500 MHz. The measurements outlined below have also been used to verify the numerical models we have developed to compute the transfer function of the instrument and to predict the performance of a spaceborne sensor in measuring winds, species abundances, and atmospheric temperature and pressure.

Figure 4 shows one result of our laboratory tests. Using the breadboard instrument, we have simulated the measurement of the concentration of N_2O in an atmospheric limb path. N_2O is of particular interest since it is the tracer species of choice for wind measurements in the 20 to 50 km altitude range. The figure shows the response of the laboratory instrument to a range of pressures of N_2O in a sample cell. This measurement is performed by alternately switching on and off the RF power applied to the EOPM (i.e., alternating between the conditions shown in the top and bottom parts of Fig. 3a). For this example, the instrument reference cell contained 3 torr of N_2O.

For convenience, the experiment was performed in absorption. Also plotted in the same figure is the calculated instrumental response using our numerical model. In practice, the line-of-sight amounts of N_2O in the atmosphere correspond to the 0 to 2 torr range of Fig. 4. At greater pressures in the sample cell, the effects of line saturation reduce the magnitude of the correlation signal. This can be appreciated by referring to Fig. 3a and considering the case of a spectral line in the atmosphere whose effective width is comparable to the EOPM modulation frequency. The 1σ noise in this measurement between 0 and 1 torr is 0.01 torr.

Laboratory verification of the measurement of Doppler shifts with the instrument is now underway. Current estimates of the performance of the flight sensor suggest that winds will be determined to better than $\pm$ 5 m/s over the entire 20 to 120 km range with a vertical resolution of 3 to 5 km.

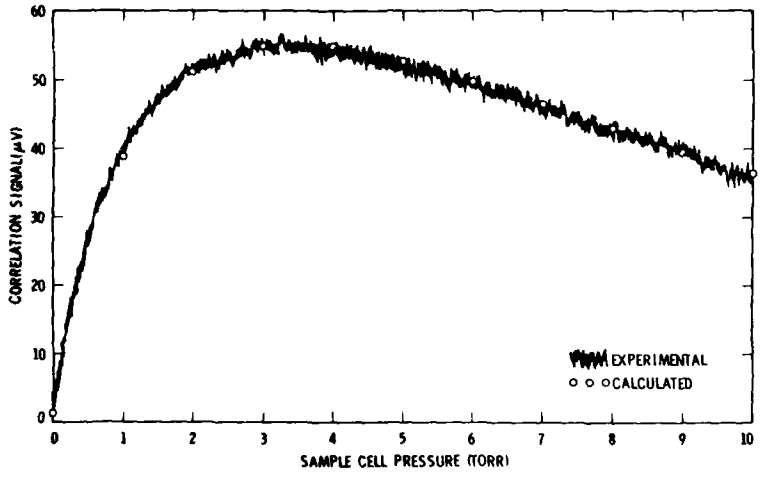

Figure 4. Experimental results are shown demonstrating the performance of the breadboard instrument in species measurements. The instrument reference and sample cells are 1 cm in length.

ACKNOWLEDGEMENTS

The research described in this paper was performed by the Jet Propulsion Laboratory, California Institute of Technology, under contract with the National Aeronautics and Space Administration.

REFERENCES

D. J. McCleese and J. S. Margolis, Appl. Opt. 22, 2528 (1983).

D. J. McCleese, J. S. Margolis and J. Ballard, Appl. Opt. 23, 527 (1984).

A. Yariv, Quantum Electronics, 2nd Ed. (John Wiley & Sons, New York, 1975), Chap. 14.

PARTICLE SCATTERING

MULTIPLE SCATTERING EFFECTS IN THE OFF-AXIS PROPAGATION OF LASER RADIATION

A. Zardecki and S. A. W. Gerstl
Theoretical Division, MS P371
Los Alamos National Laboratory
Los Alamos, NM 87545, U.S.A.

(invited)

Recent results of Battistelli et al[1,2] demonstrate the significance of multiple scattering in the on-axis laser beam propagation through turbid media. When the mean size of particles is larger than or comparable to the wavelength of radiation, the small-angle approximation provides an adequate interpretation of on-axis experimental data. For the off-axis configuration, we show that the small-angle approximation remains valid when the scattering angles are of the order of the angular spread of the scattering phase function. In addition, by combining the small-angle and diffusion approximations, the range of validity of our description can be extended considerably.

Under the small-angle approximation and with the z axis chosen along the direction of the incident beam, the equation of radiative transfer[3,4] reads:

$$\left(\vec{\phi}\cdot\frac{\partial}{\partial\vec{r}}+\frac{\partial}{\partial z}+\sigma\right)I(\vec{\phi},\vec{r},z)=\sigma_s\int P(\vec{\phi}-\vec{\phi}')I(\vec{\phi}',\vec{r},z)d\vec{\phi}' \quad , \qquad (1)$$

where $I(\vec{\phi},\vec{r},z)$ is the spectral radiance function of a monochromatic beam wave at a point with coordinates $(\vec{r},z)$ along a direction whose unit directional vector $\vec{\Omega}$ has a projection $\vec{\phi}$ transverse to the beam axis. The volume extinction and scattering coefficients are denoted σ and σ_s, respectively. The normalization condition for the scattering phase function $P(\vec{\phi})$ is

$$\int P(\vec{\phi})d\vec{\phi}=1 \quad . \qquad (2)$$

We assume that the incident laser beam can be represented by a Gaussian function in both spatial distribution and angular divergence; i.e.

$$I_o(\vec{\phi},\vec{r})=\frac{\beta^2\gamma^2}{\pi^2}\exp(-\beta^2\vec{\phi}^2-\gamma^2\vec{r}^2) \quad , \qquad (3)$$

and that the phase function is

$$P(\vec{\phi}) = \frac{\alpha^2}{\pi} \exp(-\alpha^2 \vec{\phi}^2) \quad . \tag{4}$$

With the aid of the Fourier transform technique the solution to Eqs. (1-4) can be written[3] in the form of a series expansion in powers of σ_s. This method is most appropriate to treat the case of an open detector. On the other hand, the finite field-of-view (FOV) effects are conveniently quantified with the appoach of Dolin and Fante.[4]

In the work of Fante,[5] which applies to sharply peaked phase functions, $I(\vec{\phi}', \vec{r}, z)$ in the integrand on the right-hand side of Eq. (1) is expanded in a Taylor series about $\vec{\phi}' = \vec{\phi}$. After truncating the series at the second term, a system of two equations for the unscatterred radiance, $I^{(o)}$, and the scattered portion, $I^{(s)}$, is obtained. This theory leads to the expression for $I^{(s)}$ in the form of a one-dimensional integral. As the inclusion of the FOV effects requires integrations over both the detector area and the receiving angle, Fante's formulation seems to be most practical.

To determine how well our model predicts scattering effects, the results of our computations were compared with the irradiance measurements[6] of the optical scattering by high density hydrosols. A He-Ne laser beam was passed through a tank containing polystyrene spheres of (2.26±0.07) μm diameter, suspended in water. The profile of the light at the exit surface of the tank was measured for different optical depths and detector FOV, and compared with the calculated results of our model. Figures 1 and 2 show the irradiance as a function of the distance from the beam axis for the detector's half angle FOV = 0.357 deg. The phase function parameter α, equal to 8.46 rad^{-1} according to Mie theory, was adjusted to $\alpha = 10.85$ rad^{-1}. This increases the scattered part $I^{(s)}$, thus leading to a better agreement with experimental data.

For an open detector, FOV = 90 deg, the radiance distribution function $I(\vec{\Omega}, r, z)$ is represented as a sum of the small-angle approximation solution $I^{(s.a)}$ and the solution $I^{(d)}$ due to diffusion approximation,[7] i.e.

$$I(\vec{\Omega}, \vec{r}, z) = I^{(s.a)}(\vec{\phi}, \vec{r}, z) + I^{(d)}(\vec{\Omega}, \vec{r}, z) \quad . \tag{5}$$

Here $I^{(s.a)}$ satisfies Eq. (1), whereas $I^{(d)}$ is a solution to the steady state diffusion equation.

If we assume that the dominant part of the forward scattering is accounted for by the Gaussian phase function of Eq. (4), the remaining part of scattering can be described in terms of isotropic diffusion. Consequently, the general scattering phase function $P(\vec{\Omega},\vec{\Omega}')$ is split into two parts according to the formula

$$P(\vec{\Omega},\vec{\Omega}') = \kappa_1 P_1(\vec{\Omega},\vec{\Omega}') + \kappa_2 P_2(\vec{\Omega},\vec{\Omega}') \quad , \tag{6}$$

where P_1, corresponding to small-angle scattering, is given by Eq. (4) after we let $P_1(\vec{\Omega},\vec{\Omega}') \rightarrow P(\vec{\phi} - \vec{\phi}')$, and where

$$P_2(\vec{\Omega},\vec{\Omega}') = \frac{1}{4\pi} \quad . \tag{7}$$

Our normalization condition, which sets the integral of the phase function over $d\vec{\Omega}'$ to unity, implies that $\kappa_1 + \kappa_2 = 1$; therefore the κ's can be regarded as relative weights of small-angle and diffusion scatterings.

In Figs. 3 and 4, where $\kappa_1 = 0.9$ and $\kappa_2 = 0.1$, $I^{(s.a)}$ is represented as a sum of unscattered and scattered contributions, whereas $I^{(d)}$ is denoted by the label "diffuse". We note that this approach acounts only for about 50% of the scattered energy. A further improvement could be achieved by representing the scattering phase function as a combination of two or more Gaussian peaks[8] supplemented by a uniform part. However, a satisfactory description of experimental data, valid for any value of r, would require the rigorous solution of the three-dimensional transport equation.

References

1. E. Battistelli, P. Bruscaglioni, A. Ismaelli, and G. Zaccanti, J. Opt. Soc. Am. 2, 903 (1985).
2. E. Battistelli, P. Bruscaglioni, A. Ismaelli, and G. Zaccanti, Opt. Acta 32, 717 (1985).
3. W. G. Tam and A. Zardecki, Appl. Opt. 21, 2405 (1982).
4. A. Zardecki and W. G. Tam, Appl. Opt. 21, 2413 (1982).
5. R. L. Pante, IEEE Trans. Antennas Propag. AP-21, 750 (1973).
6. N. E. Elliott, D. M. Stupin, G. M. Stokes, and W. P. Unruh, to be published.
7. W. G. Tam and A. Zardecki, Appl. Opt. 19, 2822 (1980).
8. J. A. Weinman, J. Atm. Sc. 33, 1763 (1976).

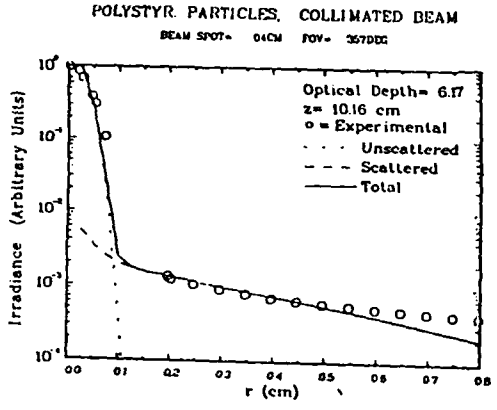

Figure 1

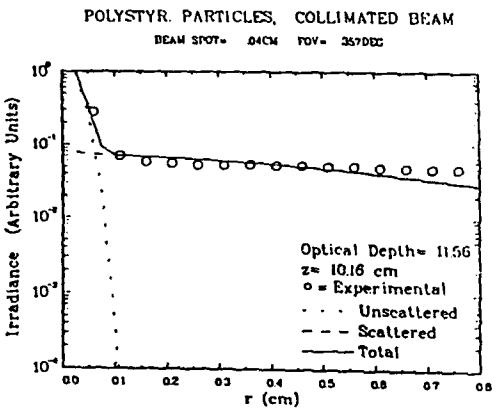

Figure 2

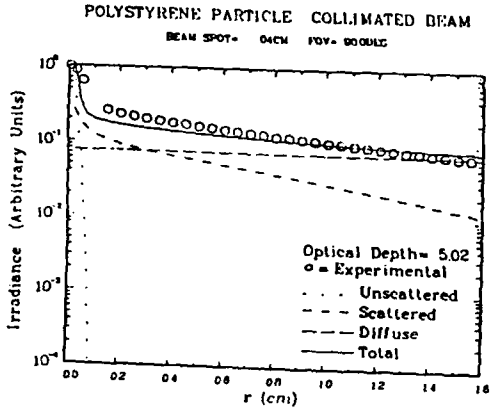

Figure 3

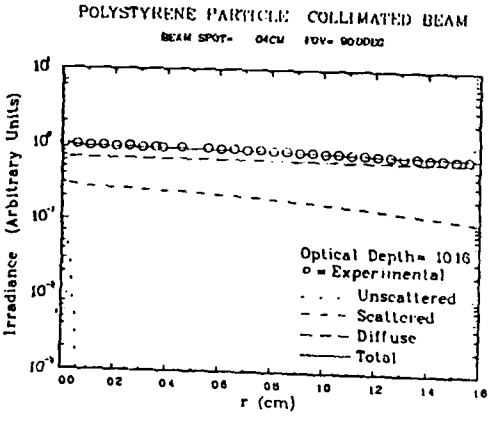

Figure 4

EFFECTS OF MULTIPLE SCATTERING AND NON-SPHERICAL STATISTICS IN DISCRETE RANDOM MEDIA

V. V. VARADAN AND V. K. VARADAN
Laboratory Department of Engineering Science and Mechanics and
The Pennsylvania State University Park
University Park, PA 16802 **(invited)**

ABSTRACT

The effect of multiple scattering between the discrete, random inhomogeneities, statistical correlation in the position of the scatterers, details of the geometry, size and properties of the inhomogeneity via the T-matrix are considered. In previous studies, the Quasi - Crystalline Approximation which was used to truncate the infinite hierarchy of equations for the coherent field required a knowledge of the two body correlation function. Although the T-matrix of a non-spherical scatterer can be calculated in a straight forward manner, only spherical statistics were available even for non-spherical scatterers, via the Percus Yevick equation or Monte Carlo simulation for hard spheres. Recently, we have been able to simulate the positional, angle dependent correlations of non-spherical particles using Monte Carlo simulation and an expansion of the two scatterer correlation function in Legendre polynomials.These values are used in calculating the effective wavenumber of the coherent field for media containing aligned spheroidal scatterers and will be compared with previous results using spherical statistics.The first order approximation of the incoherent intensity will also be calculated.

INTRODUCTION

The average or effective properties of a random medium containing inclusions of one material or voids distributed in some fashion in a second material called the host or matrix material can be conveniently studied by analyzing the propagation of plane waves in such materials and solving the resulting dispersion equations. Since waves propagating in such a two phase system will undergo multiple interactions with the scatterer phase, it becomes natural to consider multiple scattering theory and ensemble averaging techniques if the distribution of the inclusion phase is random.

In this paper, a multiple scattering theory is presented that utilizes a T-matrix to describe the response of each scatterer to an incident field. The T-matrix is simply a representation of the Green's function for a single scatterer in a basis of spherical or cylindrical functions. In this definition, it simply relates the expansion coefficients of the field that excites a scatterer to the expansion coefficients of the field scattered when both fields are expanded in the same spherical wave basis [1].

The formalism presented is generally applicable to acoustic electromagnetic and elastic waves. Good agreement has been obtained with available experimental results for all three types of waves for a wide range of wavelengths, scatterer concentration and properties [2,3]. The theory presented here most closely resembles the work of Twersky [4],[5].The infinite hierarchy of equations that results in a multiple scattering formalism when the exciting filed is averaged has usually been truncated by using the Quasi Crystalline Approximation first proposed by Lax [6]. In this approximation, which is shown to be completely equivalent to a partial resummation of the multiple scattering

series, only a knowledge of the two body correlation function is required. In previous studies [7,8], we relied on spherical statistics for hard spheres, generated by Monte Carlo simulation or by the Percus-Yevick approximation even for non-spherical scatterers. Essentially, this increased the exclusion volume surrounding the non-spherical scatterer, and artificially restricted us to smaller concentrations in order to prevent the statistical spheres from overlapping. In the present study, these restrictions are removed by using a new Monte Carlo simulation developed by Steele [9] for non-spherical scatterers, that is based on expanding the two body correlation functions in Legendre polynomials. This permits us to consider the angular correlations that exist for non-spherical oriented scatterers.

Numerical results will be presented for aligned and randomly oriented oblate and prolate spheroids using the new correlation functions and compared with previous calculations for spheroids that used spherical statistics. We forsee important applications of these new results to electromagnetic wave propagation through aerosols, which are non-spherical and often consist of aggregates and also in other cases where non-spherical scatterers are involved. The approach is summarized in this extended summary and results will be presented at the meeting.

EFFECTIVE WAVENUMBER FOR THE AVERAGE FIELD IN A DISCRETE RANDOM MEDIUM

Let the random medium contain N scatterers in a volume V such that $N \to \infty$, $V \to \infty$ but $n_o = N/V$ the number density of scatterers is finite. Let u, u^o, $u^e{}_i$, $u^s{}_i$ be respectively the total field, the incident or primary plane, harmonic wave of frequency ω, the field incident or exciting the i-th scatterer and the field which is in turn scattered by the i-th scatterer.These fields are defined at a point $\mathbf{r}$ which is not occupied by one of the scatterers. In general, these fields or potentials which can be used to describe them satisfy the scalar or vector wave equation. Let Re ϕ_n and Ou ϕ_n denote the basis of orthogonal functions which are eigenfunctions of the Helmholtz equation. The qualifiers Re and Ou denote functions which are regular at the origin (Bessel functions) and outgoing at infinity (Hankel functions) which are respectively appropriate for expanding the field which is incident on a scatterer and that which it scatters. Thus, we can write the following set of self-consistent equations:

$$u = u^o + \sum_{i=1}^{N} u^s{}_i = u^e{}_i + u^s{}_i \equiv u^o + \sum_{i \neq j} u^s{}_j + u^s{}_i \qquad (1)$$

$$u^o(\mathbf{r}) = p \exp(ik\mathbf{k}_o \cdot \mathbf{r}) = \Sigma_n \alpha_n \text{ Re } \phi_n^i(\mathbf{r}-\mathbf{r}_i) \qquad (2)$$

$$u^e_i = \Sigma_n \alpha_n^i \text{ Re } \phi_n(\mathbf{r} - \mathbf{r}_i); \qquad a < |\mathbf{r}-\mathbf{r}_i| < 2a \qquad (3)$$

$$u^s_i = \Sigma_n f_n^i \text{ Ou } \phi_n(\mathbf{r} - \mathbf{r}_i); \quad |\mathbf{r}-\mathbf{r}_i| > a \qquad (4)$$

where α_n^i and f_n^i are unknown expansion coefficients. We observe in Eqs.(3) and (4) that "a" is the radius of the sphere or cylinder (for 2-D problems) circumscribing the scatterer and that all expansions are with respect to a coordinate origin located in a particular scatterer.

The T-matrix by definition simply relates the expansion coefficients of

u^e_i and u^s_i provided $u^e_i + u^s_i$ is the total field which is consistent with the definitions in Eq. (1). Thus [1],

$$f^i_n = \sum_{n'} T^i_{nn'} \alpha^i_{n'} \tag{5}$$

and the following addition theorem for the basis functions is invoked

$$Cu\ \phi_n(r-r_j) = \sum_{n'} \sigma_{nn'}(r_i-r_j)\ Re\ \phi_{n'}(r-r_i) \tag{6}$$

Substituting Eqs. (2) - (6) in Eq. (1), and using the orthogonality of the basis functions we obtain

$$\alpha^i = a^i + \sum_{j\neq i} \sigma(r_i-r_j)\ \alpha^j \tag{7}$$

This is a set of coupled algebraic equations for the exciting field coefficients which can be iterated and leads to a multiple scattering series.

For randomly distributed scatterers, an ensemble average can be performed on Eq. (7) leading to

$$\langle \alpha^i \rangle_i = a^i + \langle \sigma(r_i-r_j)\ T^j \langle \alpha^j \rangle_{ij} \rangle_j \tag{8}$$

where $\langle\ \rangle_{ijk\ldots}$ denotes a conditional average and Eq. (8) is an infinite hierarchy involving higher and higher conditional expectations of the exciting field coefficients. In actual engineering applications, a knowledge of higher order correlation functions is difficult to obtain, usually the hierarchy is truncated so that at most only the two body positional correlation function is required.

To achieve this simplification the quasi-crystalline approximation (QCA), first introduced by Lax [6] is invoked, which is stated as

$$\langle \alpha^j \rangle_{ij} \approx \langle \alpha^j \rangle_j \tag{9}$$

Then, Eq. (8) simplifies to

$$\langle \alpha^i \rangle_i = a^i + \langle \sigma(r_i-r_j)\ T^j \langle \alpha^j \rangle_j \rangle_i \ ; \tag{10}$$

an integral equation for $\langle \alpha^i \rangle_i$ which in principle can be solved. We observe that the ensemble average in Eq. (10) only requires $P(r_j|r_i)$, the joint probability distribution function. In particular, the homogeneous solution of Eq. (10) leads to a dispersion equation for the effective medium in the quasi-crystalline approximation. Defining the spatial Fourier transform of $\langle \alpha^i \rangle_i$ as

$$\langle \alpha^i \rangle_i = \int e^{iK\cdot r_i}\ X^i(K)\ dK \tag{11}$$

and substituting in Eq. (10), we obtain for the homogeneous solution

$$X^i(K) = \sum_{j\neq i} \int \sigma(r_i-r_j)\ T^j\ P(r_j|r_i)\ e^{iK\cdot(r_i-r_j)}\ dr_j\ X^j(K) \tag{12}$$

If the scatterers are identical

$$X^i(K) = X^j(K) = X(K) \tag{13}$$

and thus for a non-trivial solution to $\langle \alpha^i \rangle_i$, we require

$$\left| I - \sum_{j \neq i} \int \sigma(\mathbf{r}_i - \mathbf{r}_j)\, T^j \; P(\mathbf{r}_j | \mathbf{r}_i)\, e^{i \mathbf{K} \cdot (\mathbf{r}_i - \mathbf{r}_j)} \; d\mathbf{r}_j \right| = 0 \qquad (14)$$

In order to perform the integration in Eq. (14), we need a model for the pair distribution function. For non-spherical scatterers, the pair distribution function depends not only on the length of the vector connecting the centers of the scatterers, but also on the direction of this vector and the orientation of each scatterer. If the scatterers are spherical, then there is no dependence on direction and orientation and the statistics are said to be spherical or isotropic. In both cases, the scatterers are not allowed to overlap, i.e. an infinite repulsive potential is assumed between scatterers. In the statistical mechanics literature, several schemes are available for calculating the pair distribution function of ' hard ' particles. For spherical hard particles, analytical results can be obtained for sparse concentrations in the form of a density expansion or virial series, and for higher concentrations the Percus-Yevick, the self-consistent approximation, and Monte Carlo simulations have all been used for distributions of spheres, see [7,8]. Results, explicitly for non-spherical scatterers are not readily available, and in previous calculations, we artificially surrounded the non-spherical scatterer by a transparent sphere that enclosed it, or considered a sphere of equivalent volume. In the first approximation, the non-overlap of the statistical spheres severely limited the concentrations that we could consider, and the second approximation, although better than the first did not lead to satisfactory results at volume fractions exceeding 10%.

In recent years, considerable progress has been made in Monte Carlo simulations for non-spherical hard particles by Steele [9]. He has expanded the joint probability functions in a series of spherical harmonics and radial functions with unknown coefficients. The coefficients are evaluated directly in the Monte Carlo simulation. For aligned prolate and oblate spheroids, these results have just become available. The excluded volume for these geometries is also spheroidal. The hole correction integral can only be done numerically, and the resulting matrix is no longer diagonal. This is being implemented now, and results will be ready at the time of the meeting. We also plan to implement these statistics in calculations of the incoherent intensity and compare with previous results using spherical statistics.

REFERENCES

1. V. K. Varadan and V. V. Varadan, Acoustic, Electromagnetic and Elastic Wave Scattering - Focus on the T-matrix Method, Pergamon Press, NY (1980).
2. V. K. Varadan, V. N. Bringi, V. V. Varadan, and A. Ishimaru, Radio Science 18, 321 (1983).
3. V. V. Varadan, Y. Ma and V. K. Varadan, J. Opt. Soc. Am., in press.
4. V. Twersky, J. Math. Phys. 19, 215 (1978).
5. V. Twersky, J. Acoust. Soc. Am., 64, 1710 (1978).
6. M. Lax, Phys. Rev. 88, 621 (1952).
7. V. N. Bringi, V. V. Varadan and V. K. Varadan, IEEE Trans. Antennas and Propagation, AP-30, 805 (1982).
8. V. N. Bringi, V. K. Varadan and V. V. Varadan, IEEE Trans. Antennas and Propagation, AP-31, 371 (1983).
9. V. N. Kabadi and W. A. Steele, Ber. Bunsenges. Phys. Chem., 89, 2 (1985).

MODEL AND LABORATORY SIMULATION OF MULTIPLE SCATTER EFFECT ON LASER FORWARD- AND BACKSCATTERING

Luc R. Bissonnette

Defense Research Establishment, Valcartier
P.O. Box 8800, Courcelette, Quebec, Canada G0A 1R0
(invited)

The paper describes a multiple-scattering propagation model and compares predictions with measurements performed in laboratory-generated water droplet clouds. The solutions are applicable to the inversion of lidar returns affected by multiple-scattering contributions.

Model

The propagation medium is treated stochastically as the random spatial, temporal and size distributions of the suspended particles constitute a space-time random field for the refractive index. The equations for the statistical moments (average amplitude and average irradiance) are derived from the wave equation of electromagnetic propagation. There results an unclosed hierarchy of equations which is truncated through the hypotheses of quasi-homogeneity and quasi-isotropy of the random amplitude and phase function in the plane normal to the main direction of propagation. The validity of these assumptions is to be verified a posteriori. Reference 1 gives the basic developments.

The resulting governing equations for the case of a collimated beam are

$$\frac{\partial A}{\partial z} + \frac{1}{2}(\alpha_m + \alpha_a + \alpha_s^+ + \alpha_s^-)A - \frac{i}{2k}\nabla_\perp^2 A = 0, \qquad (1)$$

$$\frac{\partial I^+}{\partial z} + (\alpha_m + \alpha_a + \alpha_s^-)I^+ - D^+\nabla_\perp^2 I^+ = \alpha_s^+ AA^* + \alpha_s^- I^-, \qquad (2)$$

$$-\frac{\partial I^-}{\partial z} + (\alpha_m + \alpha_a + \alpha_s^-)I^- - D^-\nabla_\perp^2 I^- = \alpha_s^- AA^* + \alpha_s^- I^+, \qquad (3)$$

where AA^*, I^+ and I^- are respectively the reduced, forward-scattered and backscattered irradiance, z is the coordinate along the beam axis, r is the radial coordinate, and $\nabla_\perp^2$ is the Laplacian operator in the transverse plane.

The parameters α's and D's constitute the bulk properties of the random medium. They are formally related to the properties of the

particles and surrounding medium through the closure relations. However, complete determination of the α's and D's has not been possible yet because of mathematical difficulties. The convenient but heuristic alternative adopted here is to apply the independent Mie solutions to the physical definitions of the α's and D's. Thus, α_a is the aerosol absorption coefficient calculated from the average Mie absorption efficiency function; α_s^+ is the aerosol forward-scattering coefficient obtained by integrating the average scattering efficiency function over the forward hemisphere; α_s^- is the aerosol backscattering coefficient calculated by integrating over the backward hemisphere; and α_m is the gaseous absorption coefficient assumed given. Finally, the diffusion coefficients D^+ and D^- are modeled as follows:

$$D^+ = (z-z') \frac{\int_0^{\pi/2} p(\theta)\sin\theta d\theta}{\int_0^{\pi/2} p(\theta)d\theta} \; ; \quad D^- = (z'-z) \frac{\int_{\pi/2}^{\pi} p(\theta)\sin\theta d\theta}{p(\pi)} \quad (4\text{-}5)$$

where $p(\theta)$ is the phase function and $(z-z')$, the distance from the point of scattering. The linear z-dependence is suggested from the asymptotic form of the closure relations in the limit of small $(z-z')$. The proportionality functions are averages of the sine of the scattering angle. The normalization constants were chosen for best fit with data. Although the formal closure relations indicate that D^+ and D^- should saturate with increasing $(z-z')$, calculations have shown that the saturation has only marginal effects for the conditions investigated to date.

The solutions of eqs. 1-3 are irradiance solutions. The field-of-view effect is accounted for by multiplicative factors derived from geometric considerations.

Experiment

The experiment was carried out under controlled laboratory conditions (Ref. 2). Water droplet clouds were generated by ultrasonic nebulizers in a chamber of adjustable length. The size distribution of the drops produced by these nebulizers is reasonably invariant and the density can be changed by regulating the nebulizers output flow into and out of the chamber. After sufficient settling time and through gentle stirring, a homogeneous concentration can be maintained for as long as needed. The drop sizes are distributed between ~ 0.1 and 15 μm with a peak near 1.0 μm. The concentrations were varied from 0 to ~ 5 g/m^3 which corresponds to an extinction coefficient at 0.63 μm between 0 and ~ 3 m^{-1}.

Scattering measurements were performed with 3 lasers: 0.63, 1.06 and 10.6 μm. The transmitted beam profiles were obtained with sufficient dynamic range to detect beam broadening by forward scatter. These measurements were done for two fields of view (20 and 350 mrad)

and two cloud depths (1.5 and 2.6 m). The radiation backscattered by the cloud was also measured at 10.0, 8.8 and 5.6 m from the cloud boundary for the 3 wavelengths, two fields of view (10 and 15 mrad) and two cloud depths (1.5 and 2.6 m).

Results

Typical 0.63-μm beam profiles showing beam broadening at 2 fields of view are compared with the model predictions in Fig. 1. The agreement is very good. The corresponding backscatter data is plotted in Fig. 2. The single-scattering solution obtained by integration of the lidar equation is also drawn for comparison. As illustrated, the multi-scatter contributions are significant and well accounted for by our model. Additional results will be presented and discussed.

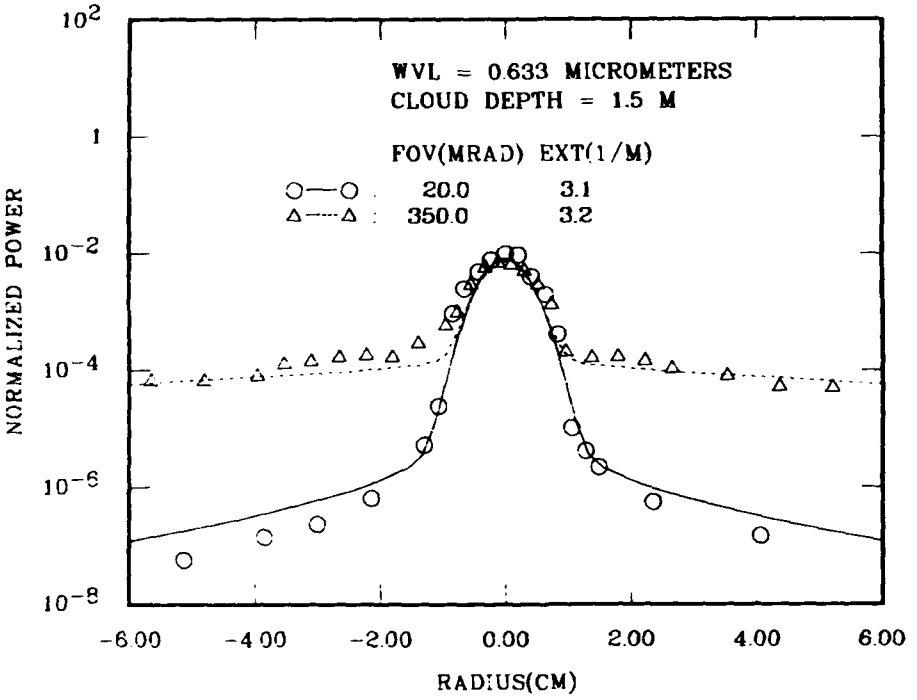

Fig. 1 - Measured and calculated flux density profile of a laser beam transmitted through laboratory generated water droplet clouds. Curves are calculations and symbols, measurements.

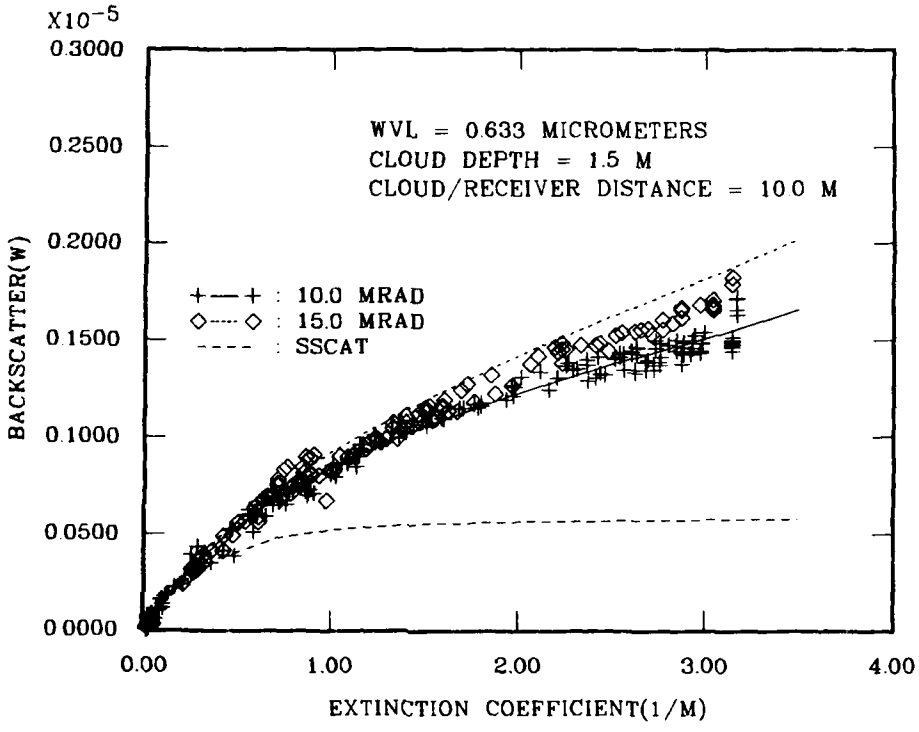

Fig. 2 - Measured and calculated backscattered power from laboratory-generated water droplet clouds as a function of cloud extinction coefficient. Curves are calculations and symbols, measurements. SSCAT is single-scattering solution.

The model solutions have an interesting application to the inverse lidar problem. They provide a potential means of exploiting the information contained in the multi-scatter contributions to resolve the indetermination created by the presence of two unknowns in the lidar equation, i.e. the extinction and backscatter coefficients.

Reference

1. Bissonnette, L.R., "Laser Forward- and Backscattering in Particulate Media", DREV R-4351/85, March 85, available through NTIS.

2. Smith, R.B., Houston, J.D., Ulitsky, A., Carswell, A.I. and Sutherland, P.B., Optech Inc, Downsview, Ont., private communication.

A Multiple Scattering Layer Model for Propagation in Discrete Random Media

Charles L. Rino - SRI International
333 Ravenswood Avenue, Menlo Park, CA 94025

We take advantage of the fact that the scattering medium is linear. Thus, all wave-field interactions can be treated as superpositions of plane waves. Starting with the complex scattering function for a single particle, we derive the general form of the scattering operator that characterizes the scattering of a single plane wave by a random distribution of scatterers over a plane. To date, we have considered only single scattering within the elemental scattering plane, which limits the present theory to tenuous particle distributions. Two scattering functions result: One characterizes the scattering of waves in the same direction that they are propagating (forward scatter), the other characterizes the scattering of waves in the opposite direction that they are propagating (backscatter).

By using the scattering functions, we can derive coupled difference equations for an arbitrary incident spectrum of waves interacting with a succession of scattering planes, as illustrated in Figure 1. Between the scattering planes, the waves propagate freely, which is easily characterized. The equations that result are shown in Figure 2. The model is based entirely on elementary characterizations of forward scattering, backward scattering, and free-space propagation. The tortuous multiple interactions of waves with the individual particles is fully accommodated in this formalism, but it is unnecessary to consider these interactions explicitly. In the limit as ΔL approaches zero, the equations are equivalent to the differential equations derived by H. Bremmer ["General Remarks Concerning Theories Dealing with Scattering and Diffraction in Random Media," Radio Sci., Vol. 8, No. 6, pp. 511-534 (June 1973)], and V. I. Gel'fgat ["Reflection in a Scattering Medium," Sov. Phys. Acoust., Vol. 22, No. 1 (January-February 1976)].

The ultimate usefulness of any formalism, however, depends on the ease with which it yields useful results. Thus, ultimately we must obtain tractable formulas for the signal moments. These formulas follow directly from the difference equations for the complex wave fields, but they involve averages that contain mixed products of the wave fields and the scattering functions. Nonetheless, by using the Markov approximation, the averages over products can be evaluated as products of averages over the wave-field terms and averages over the scattering-function terms. There results a system of equations that are fully specified in terms of the second-order statistics of the scattering functions. These statistics can be calculated from the distribution of the particle attributes.

With appropriate limiting operations, coupled first-order differential equations can be derived. For scatterers whose average scattering characteristics depend only on the difference between the incident- and scattered-wave vectors, the differential equations have multiplicative coefficients and are easily solved. For example, for a slab of length L, we can compute the mutual coherence functions for the forward scattered wave field at $z = L$ and the backward scattered wave field at $z = 0$ as

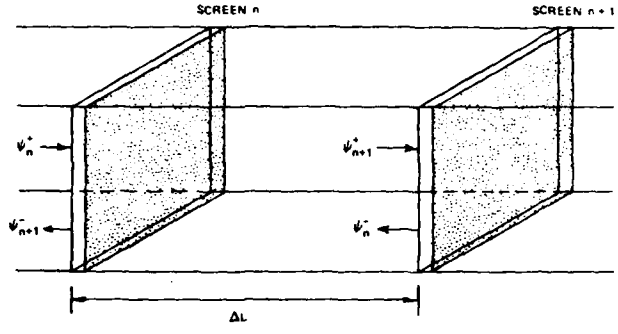

FIGURE 1 SPECTRAL DOMAIN ITERATION FOR INCREMENTAL SLAB

$$\hat{\psi}_{n+1}^{+} = \{\hat{\psi}_n^{+} + \tilde{\psi}_n^{+} @ H_n^{f}\} P^{+} + [\hat{\psi}_n^{-} P^{-}] @ H_n^{b} P^{+}$$

DIRECT WAVES | FORWARD SCATTERED WAVES | BACKWARD SCATTERED WAVES

$$\hat{\psi}_{n+1}^{-} = \{\hat{\psi}_n^{-} P^{-} + [\hat{\psi}_n^{-} P^{-}] @ H_n^{f}\} + \hat{\psi}_n^{+} @ H_n^{b}$$

$\hat{\psi}_n^{\pm} @ H_n^{f,b}$ represents the forward (f) or backward (b) scattering of the wave-field incident from the left (+) or right (-) by the nth scattering plane, as shown in Figure 1

$P^{\pm}$ represents the free-space propagation from the nth to (n+1st layer)

FIGURE 2 COUPLED DIFFERENCE EQUATIONS RELATING THE FORWARD-PROPAGATING WAVE FIELD, $\hat{\psi}_n^{+}$, AND THE BACKWARD-PROPAGATING WAVE FIELD, $\hat{\psi}_n^{-}$, BEFORE AND AFTER WAVE-FIELD INTERACTION WITH THE *nth* SCATTERING LAYER.

$$R^{+}(\Delta\rho) = \exp\{-\beta(\Delta\rho)z\}\ \{1 - \xi(\Delta\rho)^2 \exp\{2\beta(\Delta\rho)[z-L]\}\}D(\Delta\rho) \qquad (1)$$

and

$$R^{-}(\Delta\rho) = \xi(\Delta\rho) \exp\{-\beta(\Delta\rho)z\}\ \{1 - \exp\{2\beta(\Delta\rho)[z-L]\}\}D(\Delta\rho) \qquad (2)$$

where

$$D(\Delta\rho) = [1 - \xi(\Delta\rho)^2 \exp\{-2\beta(\Delta\rho)L\}]^{-1} \quad . \qquad (3)$$

The functions $\xi(\Delta\rho)$ and $\beta(\Delta\rho)$ depend on the inverse Fourier transforms of the forward, $S(\Delta K)$, and backward, $F(\Delta K)$, scattering functions for the scattering planes and the forward extinction coefficient Γ_0; that is, $2\Gamma_0$ is the exponential attenuation rate of the coherent intensity in the absence of backward scattering. The remaining terms are defined as

$$\beta(\Delta\rho) = [(2\Gamma_0 - S(\Delta\rho))^2 - F(\Delta\rho)^2] \qquad (4)$$

and

$$\xi(\Delta\rho) = F(\Delta\rho)/[\beta(\Delta\rho) + (2\Gamma_0 - S(\Delta\rho))] \quad . \qquad (5)$$

If the scatterers are lossless,

$$2\Gamma_0 = S(0) + F(0) \qquad (6)$$

and $\beta(0) = 0$; however, Equations (1) and (2) admit well-defined limits for lossless media.

If the scattering functions of the individual particles and their distributions are known, Γ_0, S, and F can be evaluated. To illustrate the results with a specific example, we have used an ensemble of dielectric spheres for which the scattering functions admit exact solutions. Figure 3 shows the coherent and total intensities as a function of layer thickness for lossless spheres. Note that as L approaches infinity, all the incident power is backscattered. Figure 4 shows the corresponding quantities for lossy spheres. Here, the backscattered intensity saturates at a constant value equal to $\xi(0)$. These results are discussed and compared with the cumulative forward-scatter single-backscatter approximation [D. A. de Wolf, "Electromagnetic Reflection from an Extended Turbulent Medium: Cumulative Forward-Scatter Single-Backscatter Approximation," IEEE Trans. Antennas Propagat., Vol. AP-19, No. 2 (March 1971); S. Ito and S. Adachi, "Multiple Scattering Effect on Backscattering from a Random Medium," IEEE Trans. Antennas Propagat., Vol. AP-25, No. 2 (March 1977); R. L. Fanté, "Generalization of the Booker-Gordon Formula to Include Multiple Scattering," Radio Sci., Vol. 17, No. 6, pp. 1521-1530 (November-December 1982)]. This last approximation also predicts the backscatter correlation function.

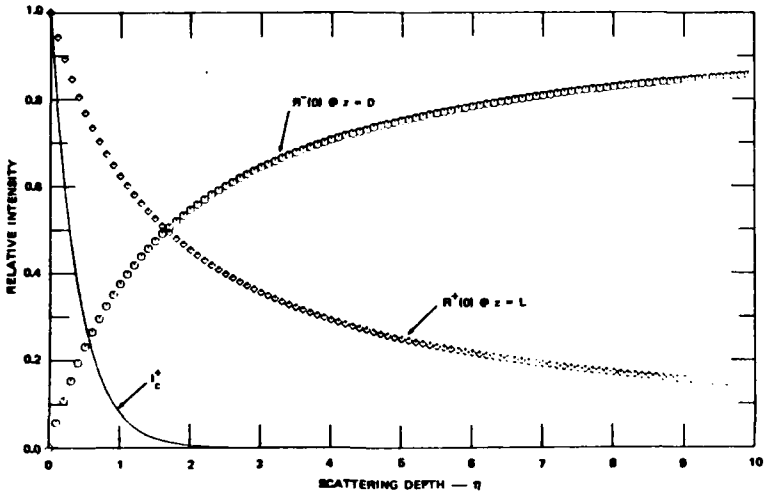

FIGURE 3 PLOT OF THE COHERENT INTENSITY, I_c^+, AND THE INTENSITY OF THE TOTAL WAVE FIELD, $R^+(0)$, MEASURED AT THE EXIT PLANE OF A SLAB OF LOSSLESS SPHERES (ka = 10), TOGETHER WITH TOTAL BACKSCATTERED INTENSITY AT THE ENTRY PLANE OF THE SLAB $R^-(0)$. (The depth parameter is defined as $\eta = \pi a^2 DL$, where a is the sphere radius, D is its density, and L is the layer thickness.)

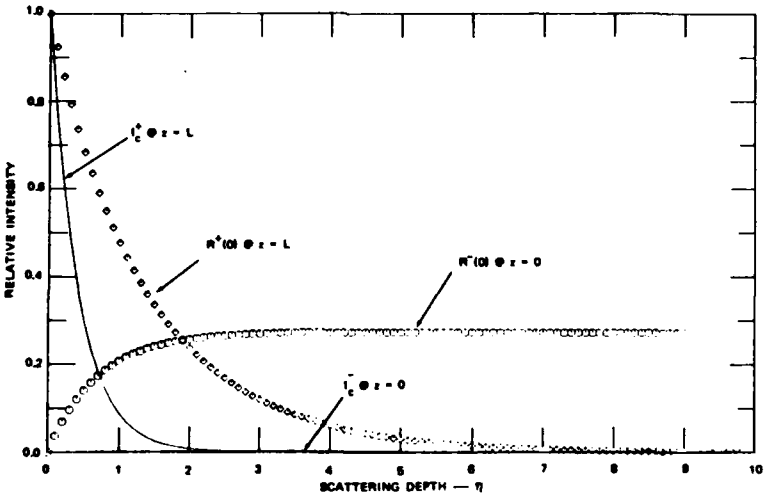

FIGURE 4 SAME PLOT AS FIGURE 3, BUT FOR ABSORBING SPHERES (ϵ = 4.0 - i0.01)

MULTIPLE SCATTERING EFFECTS ON THE PROPAGATION OF A LIGHT BEAM IN AN INHOMOGENEOUS MEDIUM

G. Zaccanti, P. Bruscaglioni, P. Pili

Dipartimento di Fisica - Universita' di Firenze -
Via S. Marta, 3 - 50139 Florence - Italy

The effect of multiple scattering on the propagation of light beams in a turbid medium has been the object of many theoretical studies. On the other hand few published comparisons between the results of numerical computations and measurements in controlled situations are to be found in the literature.

The aim of this paper is to present the results of laboratory measurements pertaining to the transmission of a collimated light beam (HeNe source, 10 mW) through suspensions of latex spheres in water, and to make a comparison with the predictions of calculations.

The transmitted power was measured by an optical receiving system whose Field of View was varied in 6 steps between $\alpha = 0.5^{o}$ and $\alpha = 3^{o}$ (semiaperture). The optical depth of the suspensions was also varied during the measurements. The suspensions were obtained from monodispersions of polystyrene spheres, with radii ranging from 0.15 μm to 7.85 μm.

The dependence of the received power, P_r, on the F.O.V. semiaperture α and on the optical depth τ was analyzed.

The part of the received power pertaining to the direct attenuated beam was not dependent on α, in our ranges of F.O.V. apertures, due to the high collimation of the laser beam. The received scattered power depended on α. Thus, by analysing P_r as a function of α, with τ fixed, we were enabled to separate the contribution P_o pertaining to the attenuated beam (1).

The presence of inhomogeneities of the medium interposed between a source and a receiver can cause the amount of received scattered power to vary, with respect to the case of a homogeneous medium with the same optical depth. This effect was shown by the results of numerical computations, which indicated that, given the optical depth, when the extinction coefficient is larger in the proximity of the receiver, the relative contribution of forward scattering to the received power increases.

This paper aims particularly to give an experimental verification of this effect.

The simple scheme of the measurements is shown in the last figure of this paper (Fig. 3). For each vaue of the optical depth of the suspension, measurements were repeated with differen

values of the distance D between the vessel containing the suspension and the receiver.

Fig. 1 gives four examples of a comparison between measured and calculated ratio P_s/P_o (scattered received power divided by attenuated beam power) plotted versus τ . The figure refers to polystyrene spheres with average radius 7.85 μm. The crosses connected by the continuous lines in Fig. 1a, b, c, d, indicate the measured ratios. The squares indicate the ratios calculated by taking into account ten orders of scattering (Semi-Monte Carlo code whose scheme is explained in (2)).

A comparison between the data of Fig. 1a, b, c, d, shows that the predicted effect is verified. The increase of received scattered power, occurring when the suspension is nearer the receiver, is more pronounced when α is larger, as was also predicted by calculations (3). Fig. 2 gives an example of this latter effect, as it shows that the decrease of P_s/P_o when D increases is steeper for $\alpha = 3^o$ than for $\alpha = 1.5^o$.

To have a more detailed comparison with the results of calculations an analysis was made, aiming at examining the contributions of first and second ordersof scattering separately. This was possible since, under assumption of validity of the small angle approximation, the ratio P_s/P_o can be represented (for a given geometry) by a polynomial in τ (see for instance ref. (4) eq. 10, or also ref. (1)). Thus one can write, for α and D fixed:

$$P_s/P_o = K_1(\alpha)\tau + K_2(\alpha)\tau^2 + \ldots\ldots$$

where the term $K_m(\alpha)\tau^m$ corresponds to the contribution of mth order of scattering.

The Table at the end of the paper gives examples of the values of the coefficients K_1 and K_2 deduced by analyzing the dependence on τ of the measured ratio P_s/P_o, compared with the values calculated theoretically by taking into account measurements geometry and the scattering properties of the suspended spheres.

(1) E. Battistelli, P. Bruscaglioni, G. Zaccanti. "Separation and analysis of forward scattered power in laboratory measurements of the transmittance of light beam". In press (Applied Optics, Feb. 1986).
(2) E. Battistelli, P. Bruscaglioni, A. Ismaelli, G. Zaccanti. J. Opt. Soc. Am. A, 2, 903 (1985).
(3) E. Battistelli, P. Bruscaglioni, A. Ismaelli, G. Zaccanti. Optica Acta, 32, 717 (1985).
(4) W.G. Tam, A. Zardecki. Appl. Opt. 21, 2405 (1982).

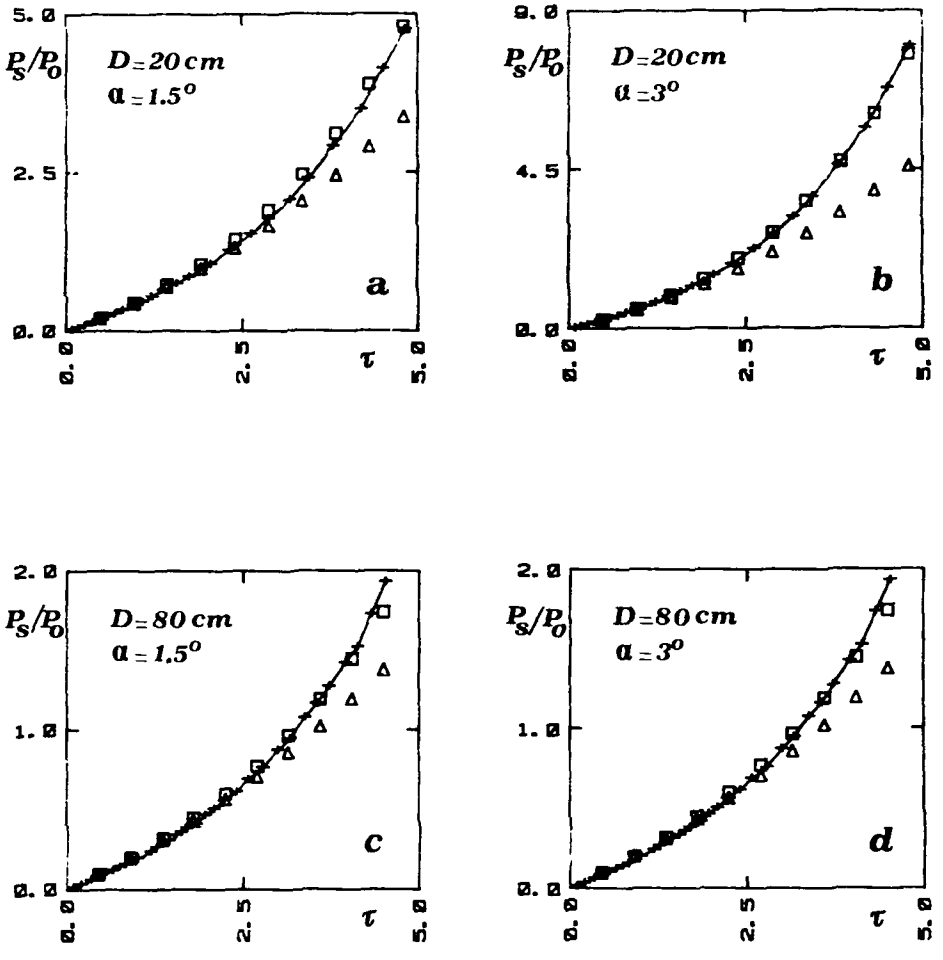

Fig. 1 - Comparison between calculated (squares) and measured (crosses connected by a continuous line) ratios P_S/P_O between the received scattered power and the direct beam attenuated power. The ratios are plotted versus the optical depth τ. The triangular marks indicate the summed contributions of the first two orders of scattering.
Spheres with average radius 7.85 μm. Receiver's area radius 1 cm. The cases a, b, c, d differ in the geometrical parameters of the measurements (see Fig. 3).
Note that at the larger distance: D = 80 cm, an early saturation of the scattered received power with the angle α occurs, so that the results for $\alpha = 1.5^\circ$ and $\alpha = 3^\circ$ nearly coincide.

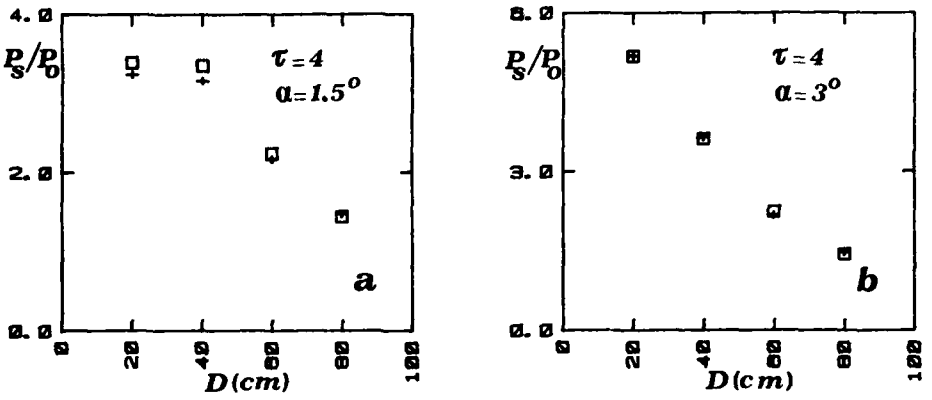

Fig. 2 - Ratio P_S/P_O plotted versus D. Crosses: measured ratios. Squares: calculated ratios. Spheres with average radius 7.85 μm. a: $\alpha = 1.5^o$, b: $\alpha = 3^o$.

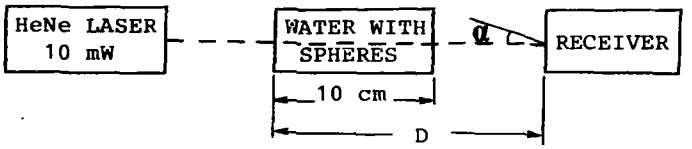

Fig. 3 - Scheme of the measurements. The container with the suspension of latex spheres in water is placed at different distances (D) from the receiver. α: semiaperture of the receiver's F.O.V.

TABLE - Measured (K_1^m, K_2^m) and computed (K_1^t, K_2^t) values of the first two coefficients of the polinominal in τ representing P_S/P_O. Spheres with radius 7.85 μm.

α	D = 20 cm				D = 80 cm			
	K_1^t	K_1^m	K_2^t	K_2^m	K_1^t	K_1^m	K_2^t	K_2^m
0.5°	.096	.08	.011	.016	.096	.08	.011	.009
1.0°	.28	.23	.038	.043	.19	.17	.025	.019
1.5°	.39	.35	.066	.070	.19	.17	.025	.023
2.0°	.42	.41	.085	.096	.19	.17	.025	.024
2.5°	.44	.43	.097	.11	.19	.17	.025	.024
3.0°	.45	.43	.10	.12	.19	.17	.025	.025

Scattering from Nonspherical "Chebyshev Particles"

Alberto Mugnai
Istituto di Fisica dell'Atmosfera, Consiglio Nazionale delle Ricerche
00044 Frascati, Italy

Warren J. Wiscombe
Laboratory for Atmospheric Sciences, NASA/Goddard Space Flight Center
Greenbelt, Maryland 20771, USA

Scattering of radiation by atmospheric particles is important in a wide variety of meteorological studies. In most practical applications the scattering particles are assumed to be spherical, regardless of their real shape. It is the purpose of our study to search, theoretically, for the main differences between spherical and nonspherical aerosol scattering.

To this end, using the 'exact' Extended Boundary Condition Method (EBCM) [1, 2], we have computed the phase function, as well as the scattering and absorption efficiencies (denoted by Q_{sca} and Q_{abs}, respectively), the single-scattering albedo ω, the asymmetry factor g, and the backscattered fraction for isotropically incident radiation $\bar{\beta}$ (see Wiscombe and Grams [3]), for a rather general class of rotationally-symmetric nonspherical particles (which we call "Chebyshev particles") of the form $r = r_o[1 + \varepsilon T_n(\cos\vartheta)]$, where ε is a deformation parameter and T_n a Chebyshev polynomial of order 'n'.

The scattering calculations have been carried out for 23 different particles with refractive index $\tilde{m} = 1.5\text{-}0.02i$ and equal-volume-sphere size parameters x = 1 to 25 (in steps of 1), that were obtained by taking 'n' = 2, 3, 4, 6, 8 and 20, and ε = -0.2 to 0.2 in steps of 0.05. Some of the Chebyshev particles considered in this study are shown in Fig. 1.

Un-shape-averaged and shape-averaged nonspherical single-scattering quantities have then been compared with corresponding un-size-averaged and size-averaged (over $\Delta x = 0.1x$) spherical results. The bulk of our scattering calculations are published in a Compendium [4] together with a description of the EBCM numerical procedures. A tiny subset of *all* that data was examined at the beginning of this research [5]. A detailed analysis of all our results will be published in a pair of forthcoming papers [6, 7], of which the present

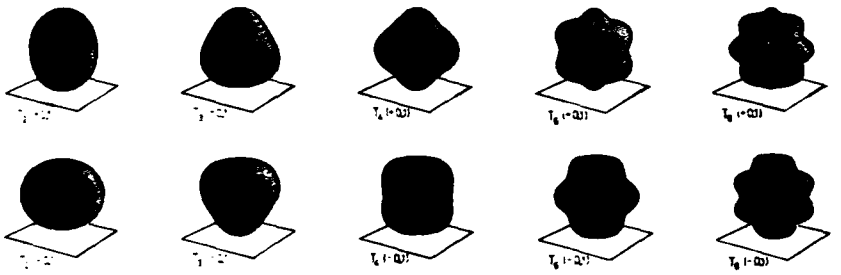

FIG. 1 3-D representation of the Chebyshev particles with $|\varepsilon| = 0.1$ used in this study. $T_n(+e)$ and $T_n(-e)$ indicate Chebyshev particles with waviness parameter 'n' and deformation parameter ε = +e and -e, respectively.

one constitutes a short summary.

Fig. 2 shows the percent differences of Q_{sca}, Q_{abs}, ω, g, and $\bar{\beta}$, for randomly-oriented Chebyshev particles $\langle T_n \rangle$ from corresponding size-averaged spherical results. No attempt has been made in this figure to identify, for each set $\langle T_n \rangle$, the results corresponding to the various ε values. It is quite evident that nonsphericity always increases Q_{abs} for size parameters larger than about 10, while it decreases g -- and, correspondingly, increases $\bar{\beta}$ -- in the size range x = 8 to 15. Less definite, on the other hand, is the effect of nonsphericity on Q_{sca} and ω ; Q_{sca}, however, seems to be 'on the average' somewhat larger for nonspherical particles, while ω tends to be smaller. In addition, concavity almost always enhances the nonspherical-spherical differences.

Fig. 3 shows nonspherical and spherical phase functions for four different size parameters covering the range of sizes explored in this study. It is evident that the spherical-nonspherical variation may be largely reduced when the size-averaged spherical phase function is considered, rather than that for the equal-volume-sphere; in the near-forward scattering region (scattering angle $\theta = 0^{\circ}$-60°), the former mimics rather well the phase function for the mixture of all $\langle T_n \rangle$ particles. Differences, however, may become large in the side- and back-scattering regime ($\theta = 60^{\circ}$-180°), for this region is most sensitive to particle shape, as the spread of the results for the various $\langle T_n \rangle$ particles clearly shows; the back-scattering, in particular, shows a dramatic sensitivity to particle shape. Finally, side-scattering is definitely enhanced by nonsphericity for x>10, while, for the larger sizes, all nonspherical phase functions tend to be smaller for θ less than about 100°.

Acknowledgments

Computer time for this study was provided by the National Center for Atmospheric Research, which is sponsored by the National Science Foundation. One of us (A.M.) wishes to thank the Cooperative Institute for Research in the Atmosphere at Colorado State University, Fort Collins, Colorado, USA, for its hospitality and generous financial support while most of this work was being carried out. Financial support to this research was also provided by Progetto Strategico CNR "Clima e Ambiente dell' Area Mediterranea".

References

[1] P.C. Waterman, "Matrix Formulation of Electromagnetic Scattering," Proc. IEEE 53, 805 (1965).

[2] P. Barber and C. Yeh, "Scattering of Electromagnetic Waves by Arbitrarily Shaped Dielectric Bodies," Appl. Opt. 14, 2864 (1975).

[3] W.J. Wiscombe and G.W. Grams, "The Backscattered Fraction in Two-Stream Approximations," J. Atmos. Sci. 33, 2440 (1976).

[4] W.J. Wiscombe and A. Mugnai, "Single Scattering from Nonspherical Chebyshev Particles: a Compendium of Calculations," NASA Tech. Memo. (NASA/GSFC, Greenbelt, Md, in press).

[5] A. Mugnai and W.J. Wiscombe, "Scattering of Radiation by Moderately Nonspherical Particles," J. Atmos. Sci. 37, 1291 (1980).

[6] A. Mugnai and W.J. Wiscombe, "Scattering from Nonspherical "Chebyshev Particles". I. Cross Sections, Single-Scattering Albedo, Asymmetry Factor and Backscattered Fraction," Appl. Opt. (submitted).

[7] W.J. Wiscombe and A. Mugnai, "Scattering from Nonspherical "Chebyshev Particles". II. Phase Function and Degree of Polarization," (In prepar.).

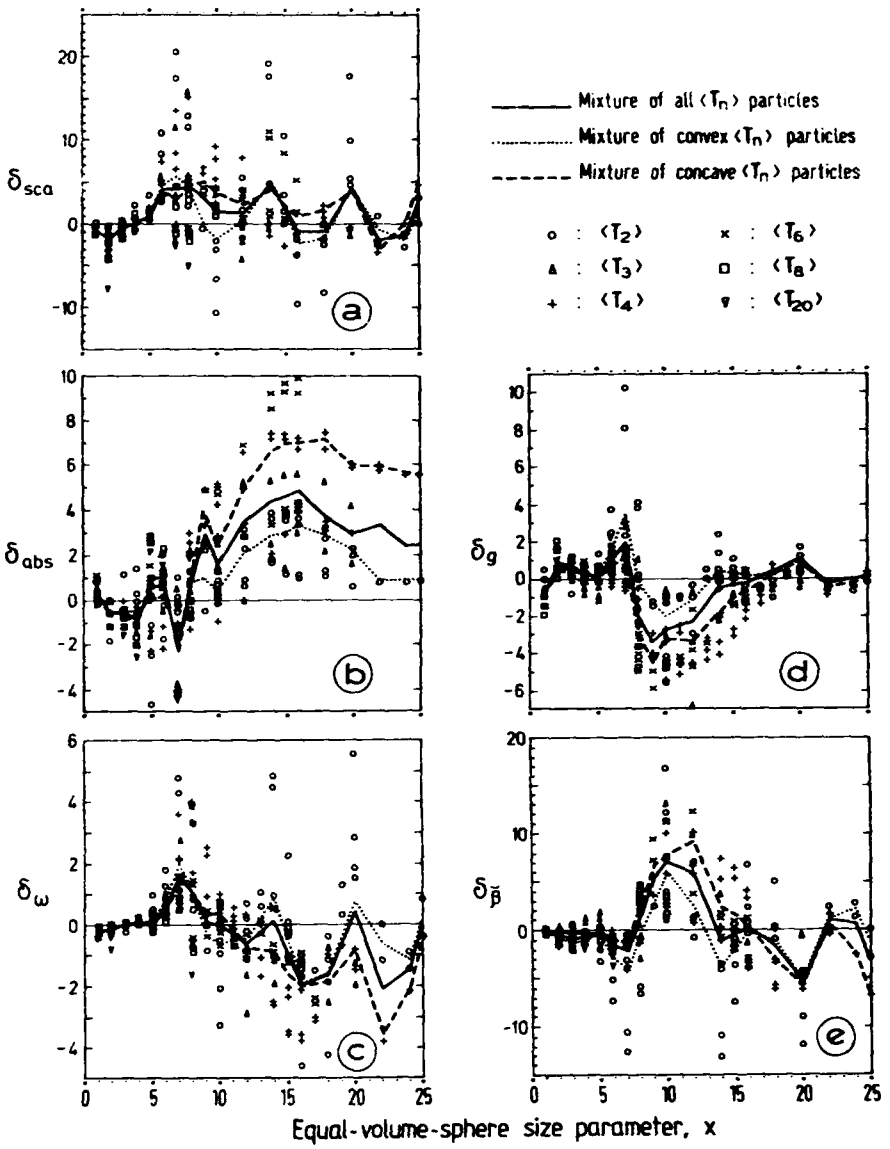

FIG. 2 Percent differences δ_{sca}, δ_{abs}, δ_{ω}, δ_{g}, and $\delta_{\bar{\beta}}$, between nonspherical and size-averaged (over $\Delta x = 0.1x$) spherical Q_{sca}, Q_{abs}, ω, g, and $\bar{\beta}$, respectively, versus equal-volume-sphere size parameter, x. All randomly-oriented Chebyshev particles $\langle T_n \rangle$ considered in this study are represented, as well as the three indicated different 'mixtures' of them.

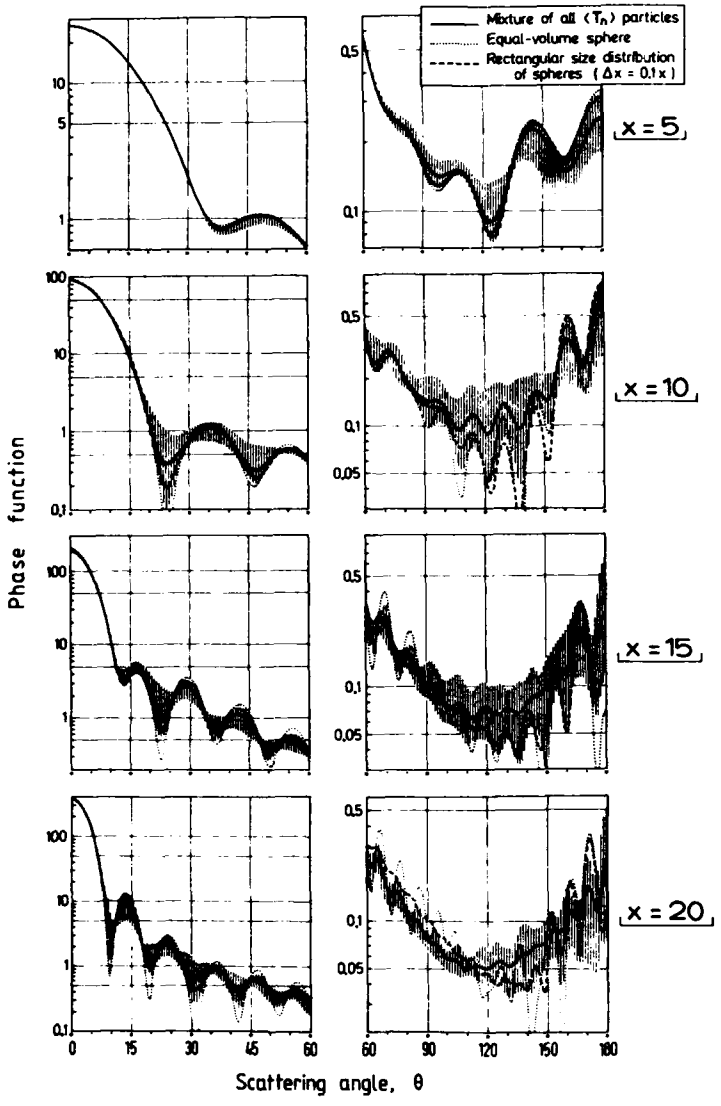

FIG. 3 Phase function in the near-forward scattering regime (left column) and in the side- and back-scattering regime (right column) versus scattering angle, θ, for the mixture of all randomly-oriented Chebyshev particles, $\langle T_n \rangle$, and for equal-volume-sphere size parameters x = 5,10,15,20. Un-size-averaged and $\Delta x = 0.1x$ size-averaged spherical phase functions are also shown for comparison. The shaded areas -- that are bounded by the lower and upper envelopes of the phase functions for all individual $\langle T_n \rangle$ particles -- represent the range of variation of the nonspherical phase function.

Light Scattering by Multi-Layered Particles

by

M. Kleiman, A. Cohen*, I. Ariel, and S. Egert

Department of Environmental Physics, Israel Institute for Biological Research, Ness - Ziona, 70450 , Israel

*Department of Atmospheric Sciences
The Hebrew University of Jerusalem
Jerusalem,91904,Israel

Introduction

The Mie scattering coefficients are generally presented only in terms of the complex refractive index assuming that the permeability $\mu = 1$. This is especially true for the derivation of the scattering coefficientsof multi-layered particles[1] or in the case of coated spheres the permeability is assumed for simplicity to be the same for all layers.[2]

Below we present the general solution for a multiple layered sphere for which each layer is permitted to acquire any desired complex refractive index and a permeability as well.

Algorithm

Let us consider the case of a sphere composed of a core of radius a, coated by layers of radii $a_2, a_3, \cdots, a_{\ell+1}$,correspondingly. Each layer has an electric susceptibility[3]

$$\chi_E^j = \left(\frac{i\varepsilon\omega}{c} + \frac{\sigma}{c} \right)_j \quad , j = 1, \cdots, \ell+1$$

and a magnetic susceptibility

$$\chi_M^j = \left(\frac{i\mu\omega}{c} \right)_j$$

for which we define $k_j^2 = -\chi_E^j \chi_M^j$ (k_0 is used for the surrounding medium).

The complex refractive index m_j is given by

$$m_j = (\varepsilon_j \mu_j)^{1/2}$$

Solving for the boundaries between two consecutive layers of dirrent χ_E and χ_m we can write the final scattering coeffcients in a form similar to the known Mie coefficient as follows

$$A_n^E = \frac{k_{\ell+1}\chi_E^0 S_n'^{E,\ell}\psi_n(k_0 a_{\ell+1}) - k_0 \chi_E^{\ell+1} S_n^{E,\ell}\psi_n'(k_0 a_{\ell+1})}{k_{\ell+1}\chi_E^0 S_n'^{E,\ell}\xi_n(k_0 a_{\ell+1}) - k_0 \chi_E^{\ell+1} S_n^{E,\ell}\xi_n'(k_0 a_{\ell+1})}$$

and

$$A_n^M = \frac{k_{\ell+1}\chi_M^0 S_n'^{M,\ell}\psi_n(k_0 a_{\ell+1}) - k_0 \chi_M^{\ell+1} S_n^{M,\ell}\psi_n'(k_0 a_{\ell+1})}{k_{\ell+1}\chi_M^0 S_n'^{M,\ell}\xi_n(k_0 a_{\ell+1}) - k_0 \chi_M^{\ell+1} S_n^{M,\ell}\xi_n'(k_0 a_{\ell+1})}$$

(we note that in the literature we find usually the notations $a_n = A_n^E$ and $b_n = A_n^M$ where E and M denote the electric and magnetic components).

In the above equations

$$S_n^{E,\ell} = \psi_n(k_{\ell+1}a_{\ell+1}) - e_n^{E,\ell}\chi_n(k_{\ell+1}a_{\ell+1})$$

$$S_n'^{E,\ell} = \psi_n'(k_{\ell+1}a_{\ell+1}) - e_n^{E,\ell}\chi_n'(k_{\ell+1}a_{\ell+1})$$

where

$$e_n^{E,\ell} = \frac{k_{\ell+1}\chi_E^{\ell}\psi_n'(k_{\ell+1}a_\ell)S_n^{E,\ell-1} - k_\ell \chi_E^{\ell+1}\psi_n(k_{\ell+1}a_\ell)S_n'^{E,\ell-1}}{k_{\ell+1}\chi_E^{\ell}\chi_n'(k_{\ell+1}a_\ell)S_n^{E,\ell-1} - k_\ell \chi_E^{\ell+1}\chi_n(k_{\ell+1}a_\ell)S_n'^{E,\ell-1}}$$

and similarly for $S_n^{M,\ell}$, $S_n'^{M,\ell}$, $e_n^{M,\ell}$ where all functions involving the notation E should be replaced by the corresponding function for M. For $\ell = 0$ $e_n^{E,0} = e_n^{M,0} = 0$ or $S_n^{E,0} = \psi_n(k_1 a_1)$.

Thus, when a sphere composed of a core and 2 additional layers is considered, $\ell = 2$. It is useful to note that if k_j is the same for all layers, $e_n^{E,\ell}$ vanishes for all values of ℓ and $S_n^{E,\ell}$ becomes $\psi_n(k_{\ell+1}a_{\ell+1})$. Hence A_n^E and A_n^M are exactly the known Mie coefficients.

This algorithm allows a simple treatment for computer calculations.

Examples of Results

We used the algorithm to calculate the sensitivity of extinction by a layered particle to small changes in the coated material depth for several susceptibility values. An example is given in Fig. 1 where a sharp maximum (two orders of magnitude difference) appears when small changes are assumed in the coated layer relative depth (a corresponding change of $(a_2 - a_1)/\lambda \approx 10^{-3}$) for a particle composed of two layers.

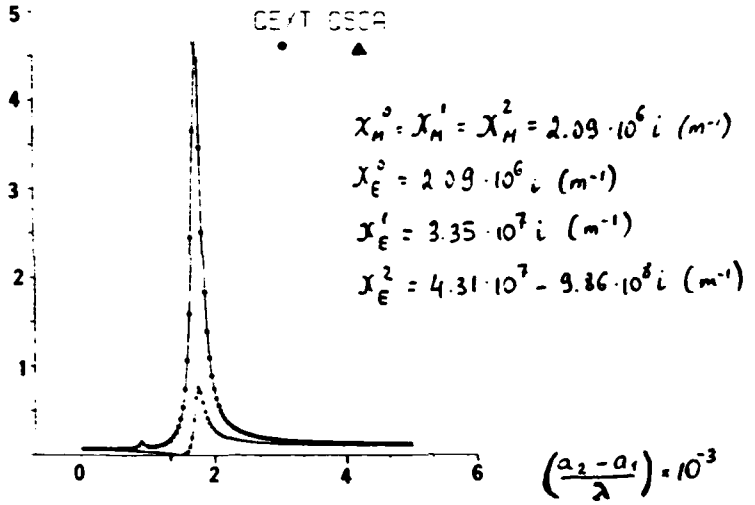

Fig.1. The extinction and scattering efficiencies as a function of the coated layer relative depth.

References

1. M. Kerker, The Scattering of Light, (Academic Press, N.Y.) 1969.

2. C. Bohren and D.Huffman, Absorption and Scattering of Light by Small Particles , (John Wiley, N.Y.)1984.

3. P.Debye,Ann. Physik (4) 30, 57, 1909.

Higher-order Temporal Moments of Picosecond Optical Pulses in a Laboratory-simulated Multiple Scattering Atmosphere

Arun K. Majumdar
Lockheed-California Company
Kelly Johnson Research & Development Center
P.O.Box 551, Burbank,California 91520
U.S.A

We report new results on higher-order temporal moments of picosecond laser pulses transmitted through multiple-scattering media. Effects of optical depth and the receiver field-of-view (FOV) on these temporal moments were studied to analyze the broadening of non-Gaussian pulses.

Ultrashort picosecond optical pulses (~10-25 ps) were generated from a very low threshold (~18 mA), high efficient, single spatial mode GaAlAs laser diode (λ=0.837 μm) by the method of current modulated gain switching. A continuous train of optical pulses separated by 100 MHz was produced. The collimated beam was transmitted through a scattering cell containing uniform latex microspheres suspended in water. The scattering cell simulated low-visibility atmosphere in a laboratory scale for performing optical communication experiment in a controlled environment.[1,2] The variable iris at the exit window of the cell provided the receiver FOV to vary from 0.22 to 2.1 degree. The scattered light was collected by a combination of lens system, suitable for the diode laser wavelength, and focused to a detector. The detector was a high speed GaAlAs/GaAs p-i-n photodiode, with a typical rise time of 50 ps, 3 dB bandwidth of greater than 7 GHz, and quantum efficiency of 65%.

The temporal intensity profiles of the multiple-scattered pulses, obtained from the detector system, were recorded with sampling oscilloscope with fast sampling sweep units and sampling head with a resolution of 25 ps risetime. The output data curves from the photographs were digitized and placed into a computer graphics system to provide proper scalings and generation of points and to

store the information on computer tapes for further processing.

We measured the temporal moment of the broadened pulse shape, f(t), defined as follows. The n th temporal moment, $<t^n>$ is given by

$$<t^n> = \int_0^\infty t^n f(t)\, dt \Big/ \int_0^\infty f(t)\, dt \qquad (1)$$

We have measured higher-order moments upto n=8. The effects of impulse response of the detector and the sampling units are taken into account. Figure 1 shows the plot of the higher-order temporal moments as a function of optical depth, τ . The moments seem to increase with τ at the beginning at a faster rate and then still increase but at a slower rate. Figure 2 shows the higher-order moments with increasing FOV for optical depth of $\tau = 10.31$. As the FOV is increased, they seem to reach limiting values. The pulse-width broadening, $<\Delta t^2>^{1/2}$, is shown in the Figure 3 as a function of optical depth τ for different values of FOV. As the FOV is increased, it is seen that the broadening tends to attain a limiting value for larger FOV's.

1. A.K. Majumdar, IEEE Journal of Quantum Electronics, Vol. QE-20, NO.8, pp 919-932, August, 1984.
2. A.K. Majumdar, Applied Optics, Vol.24, pp3659-3665, November 1, 1985.

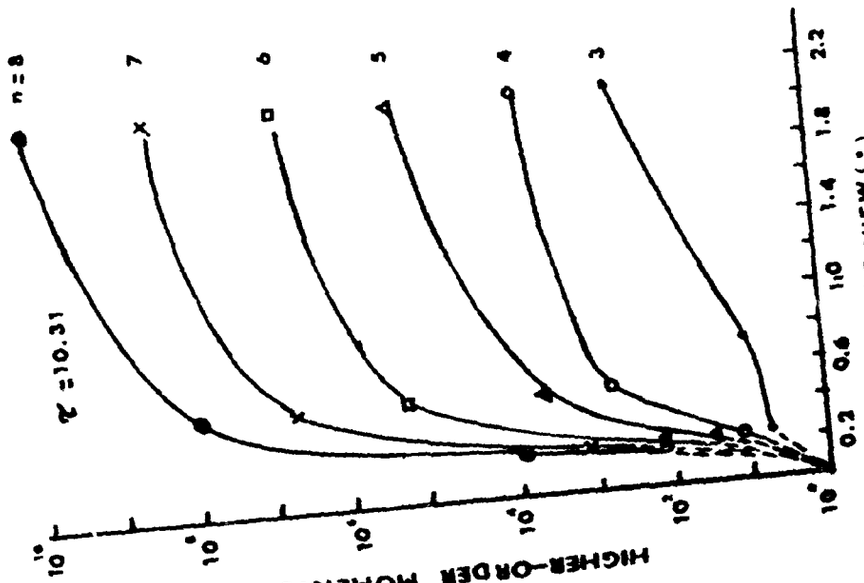
n=8
7
6
5
4
3
τ =10.31
HIGHER-ORDER MOMENTS
FIELD-OF-VIEW (°)

FIG. 2

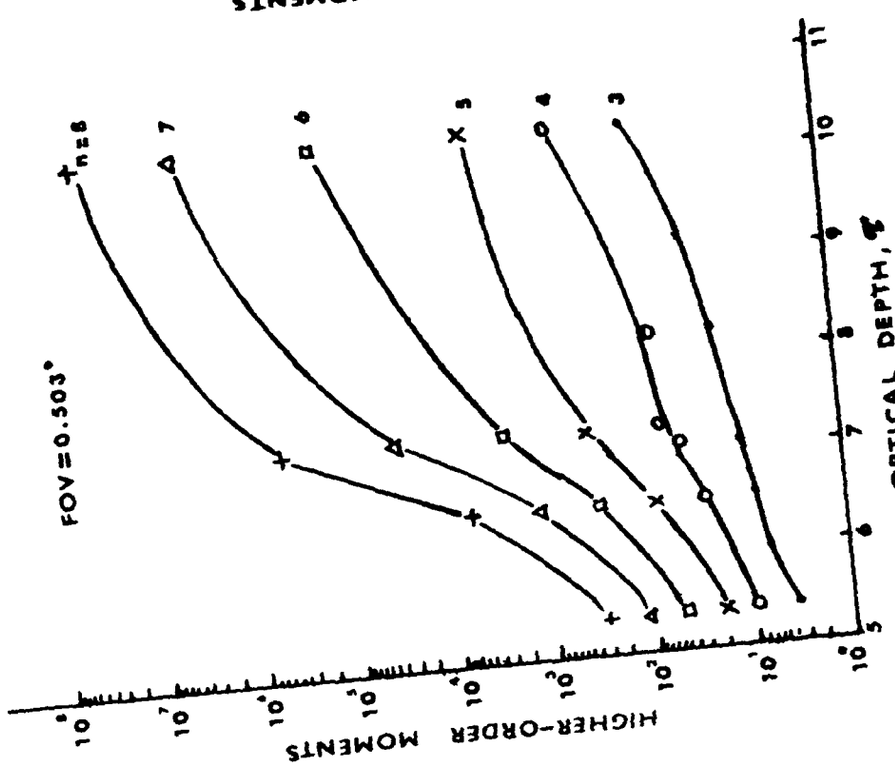
n=8
7
6
5
4
3
FOV=0.503°
HIGHER-ORDER MOMENTS
OPTICAL DEPTH, τ

FIG. 1

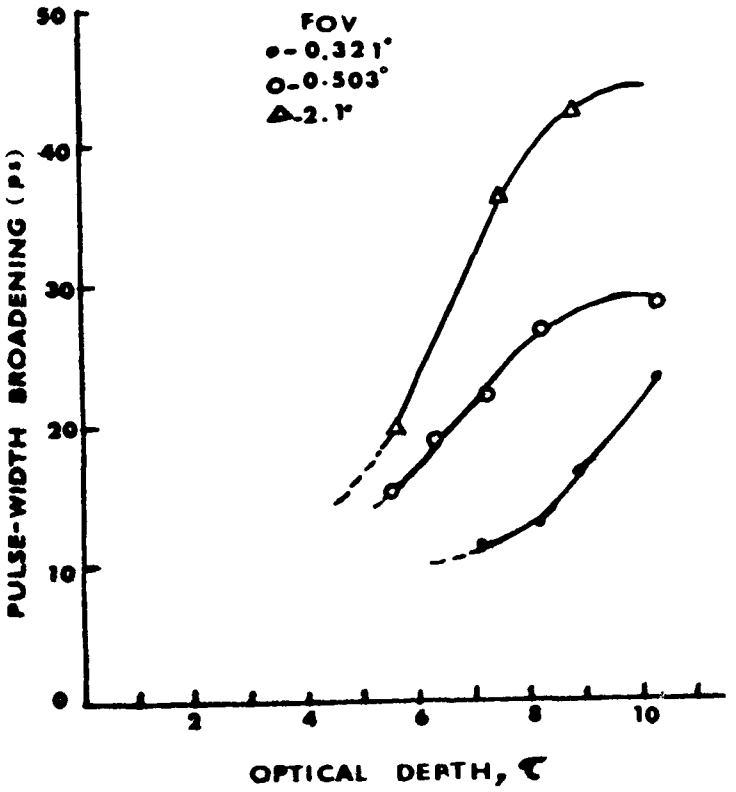
FOV
●-0.321°
○-0.503°
△-2.1°
PULSE-WIDTH BROADENING (ps)
50
40
30
20
10
0
2
4
6
8
10
OPTICAL DEPTH, τ

FIG. 3

DETERMINATION OF THE OPTICAL CHARACTERISTICS OF ATMOSPHERIC PARTICLES SEPARATED BY SIZE

F. Prodi, V. Levizzani and G. Casarini
Istituto FISBAT-CNR, Reparto Nubi e Precipitazioni,
Via De' Castagnoli 1, 40126 Bologna, Italy

The volume extinction coefficient of a layer of atmospheric particles depends on several parameters, such as the concentration, shape, size distribution and optical characteristics (complex refractive index) of the particles. Usually the complex refractive index at a given wavelength is taken constant for the whole distribution, while in reality the distribution itself results from the superposition of different particle populations, each whith its own optical characteristics. Realistic extinction models should be developed on the basis of complex refractive indexes valid in each size class of the distribution. Instead, experimental determinations of the optical characteristics by various authors were performed on integral samples of the particles and such information on the size effect is lacking; these studies were in fact conducted either by analyzing an airborne dispersion of particles or their deposit on filter from integral samplings, or in an aerosol impactor (Grams et al. 1974; Tanaka et al. 1983). In all cases the light beam in the nephelometer hits regions where particles are polydispersed.

The present determination of the optical characteristics of the particles takes advantage of the size separation of the aerosol particles while airborne and their deposition on a single filter (Prodi V. et al 1979). Therfore in our optical apparatus, which is essentially a polar nephelometer as in the previously mentioned experiments, the beam hits particles onto the filter in a carefully determined size range. The scattered intensity signal at the different angles is recorded and processed in a data system composed by a/d converters and a computer for obtaining fast and accurate angular scannings.

The procedure to evaluate the optical characteristics of the particles from the scattered intensity is the following.

At a given θ angle the output signal of the photomultiplier is proportional to the scattered intensity

$$V_{OUT} = h \cdot I_{SCATT,TOT} = \left[\frac{h S I_0}{K^2 R^2} \right] \cdot \int_{r_{min}}^{r_{max}} i_1 (\theta, m, x) \cdot n(r)\, dr$$

where I_o is the intensity of the incident wave, which is polarized perpendicularly to the scattering plane, S is the filter surface area hit by the laser beam, h is an apparatus sensitivity coefficient, k is the wavenumber, R the distance from the particles to the photomultiplier, n(r) is the particle distribution function per unit area of the filter, i_1 is the element of the "transformation matrix" (Van de Hulst, 1957) relative to the component of the incident wave perpendicular to the scattering plane at the angle θ, m the complex refractive index, and $x = 2\pi r/\lambda$ is the size parameter. In the following K will indicate the expression in brackets and β the integral.

For each angle θ_i an average value $V_o(\theta_i)$ is determined from the measuremnts. Due to the measurement errors the difference between measured and computed values:

$$V_o(\theta_i) - K \cdot \beta(\theta_i, m)$$

is $\neq 0$.

Therefore a quantity χ^2 is defined:

$$\chi^2 = \sum_{i=1}^{N} \frac{[V_o(\theta_i) - K \cdot \beta(\theta_i, m)]^2}{\sigma_i^2}$$

and the complex refractive index m is determined from the couple of (m_{re}, m_{im}) minimizing χ^2.

In particular the measurements have been taken on Sahara dust particles, obtained from deposits of muddy rains at the ground and subsequently aerosolized, on rural + antropogenic aerosols and on latex spheres as test on spheres of known index of refraction.

The results are discussed.

References

Grams, G.W., I.H.Blifford, Jr.,D.A. Gillette and P.B. Russel, 1974: Complex index of refraction of airborne soil particles. J. Appl. Met.,13, 459-471.

Prodi, V., C.Melandri, G.Tarroni, T. De Zaiacomo, M.Formignani and D. Hochrainer, 1979: An inertial spectrometer for aerosol particles. J.Aerosol Sc.,101, 411-419.

Tanaka, M., T. Takamura and T. Nakajima, 1983: Refractive index and size distribution of aerosols as estimated from light scattering measurements. J.Cl.Appl.Met., 22,1253-1261.

Van de Hulst, H.C., 1957: Light scattering by small particles, J.Wiley and Sons, New York, 470 pp.

OPTICAL PROPAGATION AND COMMUNICATION THROUGH CLOUDS

G. Lee, J. Rockway, B. Speer, and G. Mooradian
Titan Systems Inc., P.O. Box 12139, La Jolla, CA 92037

Low data rate optical communications from satellites or aircraft offers the potential for jam resistant, relatively covert communication links which can perform many desirable functions. To provide high availability all weather optical communications, it is necessary to penetrate clouds. Clouds not only attenuate the optical beam but also cause substantial temporal and spatial dispersion of the beam in a very non-uniform manner. The design and operation of all weather links require the solution to three related, but different, problems: (1) Given a physical description of a given cloud, determine the effect on optical communication performance, (2) for a given receiver location and time of year, compute the probability distribution of cloud loss so that system availability can be estimated as a function of transmitter and receiver parameters, and (3) Develop a simple remote sensor that in real time can estimate the total link loss due to clouds (reflection, spot spreading, pulse stretching, absorption, etc.) so that the system can use the maximum allowable spot area that will still allow communication. The transmitter often does not know the exact location of the receiver so that large spot sizes allow the transmitter to cover the area of uncertainty quickly.

An experimental and theoretical program has been in progress since 1979 to study these problems and to develop communication hardware. This paper will discuss the results of several recent experiments and studies. Experiments have been performed in a wide range of cloud conditions which include stratus clouds off the California coast, winter frontal clouds in Oregon and tropical cumulus clouds on the wet side of two Hawaiian Islands. Each experiment was different but, in general, an airborne

*This work was supported by contracts from DARPA and Naval Ocean System Center, San Diego.

visible laser was used and simultaneous measurements were made of the received pulse energy, pulsewidth and receiver S/N at a ground station while various kinds of in-situ cloud measurements were performed. The in-situ cloud measurements included airborne Knollenberg probes, a nephelometer, up and down looking radiometers as well as pilot observations and pictures. Solar irradiance was also measured at the ground station and used to infer cloud optical thickness τ . During some experiments solar transmission was also measured at the ground station both on and off the oxygen absorption band to estimate total pulse path delay in the cloud and thus infer pulse stretching. Later experiments also used both visible and IR satellite pictures from GOES and DMSP to estimate cloud tops, cloud reflectance and τ .

In parallel with the experiments, analytical models for cloud propagation losses were developed using Monte-Carlo simulations. The model assumes uniform plane parallel clouds with some τ , physical thickness, top altitude, albedo and $\langle \cos \theta \rangle$. A data base of the distribution of cloud optical thickness for wide regions of the northern hemisphere was developed using the USAF Global 3D NEPH analysis data base of satellite cloud observations. This required a model for extinction length as a function of cloud type which was taken from the literature and is shown in Table 1.

Although the results of these studies are not yet complete, a number of preliminary conclusions can be drawn.

(1) Values of τ inferred from measurements of solar irradiance using the Monte-Carlo propagation model and in-situ measurements from the airborne nephelometer compared very well given the difficult spatial and temporal sampling problem. On the other hand, values of τ inferred from measurements of cloud droplet spectrums by the Knollenberg probes were typically a factor of two lower than the values inferred from solar irradiance.

(2) Values of τ estimated from using Table 1 and cloud physical thickness reports were less by up to a factor of 5 to 10 than the values inferred from solar irradiance for thick clouds

in Oregon. For instance, stratus clouds with physical thickness of 30000 feet and τ <20 were observed. This may be due to the fact that very thick winter clouds contain large amounts of ice and thus have smaller extinction coefficients. This may also explain why earlier satellite measurements of τ were often less than expected.

Table 1

CLOUD TYPE	EXTINCTION LENGTH b(m)	CLOUD TYPE	EXTINCTION LENGTH b(m)
CUMULONIMUMBUS	25	ALTOCUMULUS	65
NIMBOSTRATUS	55	CUMULUS	50
STRATUS	15	CIRROSTRATUS	350
ALTOSTRATUS	45	CIRROCUMULUS	350
STATOCUMULUS	20	CIRRUS	350

(3) When predictions of pulse stretching and spot spreading using the values of τ inferred from solar irradiance and pilot estimates of physical cloud parameters were compared with measurements, they were the same within less than a factor of two for stratus clouds. However it is clear that some technique for remotely sensing cloud physical thickness is necessary for non-stratus clouds.

(4) The use of ground based solar transmission measurements off and on the oxygen absorption band to estimate pulse delay and stretching appears to compare well with model predictions for large values of τ but more propagation measurements are necessary to determine accuracy.

(5) Inference of τ from satellite estimates of reflectance were compared with the airborne and ground measurements. The accuracy of present methods are limited for large values of τ by sensor error in measuring reflected energy and for small values of τ by the sensitivity of the reflectance function to sun and satellite angle.

(6) The overall cloud propagation model appears to agree well with the measurements for stratus clouds. Two cases of irregular cumulus clouds were found where the model under predicted laser pulse energy by an order of magnitude for small spots. The reason is unclear.

Figure 1 shows a typical plot of measured versus predicted received laser energy density per pulse at the ground station for stratus clouds of $10 \leq \tau \leq 20$. The variation in received pulse energy is due to both variations in cloud conditions and beam divergence of the airborne transmitter. The model predictions use values of τ inferred from solar irradiance and physical cloud parameters from pilot observations.

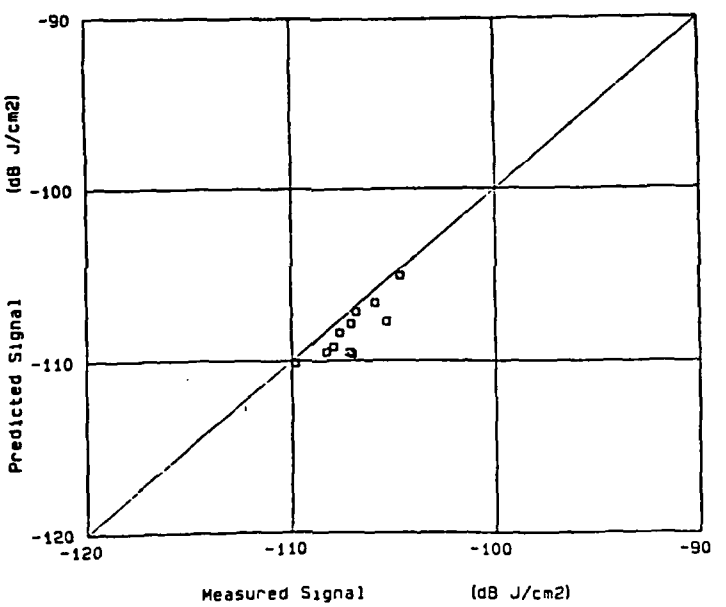

Figure 1. Comparison of Experimental Data and Model

Monte' Carlo Simulation of an Optical Scatter Channel: Use of Variance Reducation Techniques

Hari M. Gupta*
Department of Electrical and Computer Engineering, Drexel University, Philadelphia, PA 19104

1. Introduction

Optical communications through atmosphere has received a considerable importance in recent years. However, the tranmission medium, at times, consists of water drops, aerosols and clouds. The overall effect of the above is to produce multiple scattering of the incident optical wave [1]. In this paper we study simulation of an optically scatter channel when the transmission medium is cloud. The simulations are carried out on a computer using random walks. We use the variance reduction techniques to reduce the statistical fluctuations.

2. Channel Model

A plane, parallel, fixed and homogeneous cloud is considered as the channel. The scatterers are assumed to be spherical water droplets of random size and distributed randomly within the cloud. The incident optical signal is step in time and impulse in space and is considered as a stream of monoenergetic photons. Each of the incident photon undergoes multiple scattering thus executing a random walk. Three characteristic parameters of the cloud i.e. average extinction coefficient, $\bar{\beta}_{ex}$, average albedo of single scattering, $\bar{\omega}$, and average normalized phase function, $\bar{p}(\psi)$, are calculated using Mie formalism [2]. The output signal beneath the cloud is incoherent and dispersive in space, angle and time. The purpose of the simulation is to determine above dispersions with reduced statistical fluctuations.

3. Simulation Procedure

In the simulation a photon is always vertically incident on the cloud and starts its trajectory in zero azimuthal plane with unit weight. The direction after scattering is fixed by the selection of angle of scattering ψ and the azimuthal angle ξ. The former is selected from a probability density function corresponding to $\bar{P}(\psi)$ and the latter is chosen to be uniformly distributed between $-\pi$ and $+\pi$ radians. The trajectory of a photon is followed in all the three dimensions and the expected intensity weight is estimated after each scattering. The intensity weights are recorded in proper space, angular and temporal arrays. Detailed simulation steps are described by Gupta [3].

---

* On leave of absence from Department of Electrical Engineering, Indian Institute of Technology, New Delhi, 110016, INDIA

4. Variance Reduction Techniques

The output signal invariably fluctuates because of statistical nature of simulations. These fluctuations can be reduced by using large number of photon histories and thus using large computer time. Alternatively, variance reduction techniques can be used to reduce the computer time. Two such techniques used in the simulation are Russian Roullete and forced collision.

In Russian Roullete small angle scattering events are enhanced and photons with large scattering angles are killed probabilistically. Let $0 \leq \psi < \alpha$ is the important region. Then an importance ratio X_α, with value less than 1, is chosen. An uniformly distributed random number Z is tested against X_α and the following modifications in the photon weight are incorporated,

(i) If $0 < \psi \leq \alpha$ the photon history is continued as usual.
(ii) If $\alpha \leq \psi \leq \pi$ and $Z > X_\alpha$ then photon history is terminated but counted for final averaging.
(iii) If $\alpha \leq \psi \leq \pi$ and $Z \leq X_\alpha$, the weight of the photon is increased by a factor of $(1/X_\alpha)$

Thus an extra weight is attached to photons which survive in unimportant region. For example, when $X_\alpha = 0.2$ then 80% of photons in unimportant region are killed and the weight of rest 20% is increased by 5.

In forced collision the intercollision distance is chosen using truncated exponential distribution. Thus a photon is not allowed to escape the medium. The output weight is corrected to keep the estimator unbiased [3].

5. Results of Simulation

Simulations have been carried out at 0.7 micron wavelength for cumulus clouds with 100 scatterers per cubic cm. Results are obtained for two values of optical thicknessess i.e. $\tau = 5$ and $\tau = 10$.

It is found that the use of variance reduction techniques cut computer time by 50% to 70%. Figure 1 shows the variance vs computer time for a simulation run showing the efficacy of techniques. However, it is observed that simulated results are dependent on the choice of X_α. Figure 2 shows the time dispersion curves for three values of X_α i.e. 0.2, 0.4 and 0.5.

REFERENCES

1. E.A. Bucher, "Computer Simulation of Light Pulse Propagation for Communication Through Thick Cloud", App. Opt., Vol. 12, 2391-2400, 1973.

2. H.M. Gupta, "Multiple Scattering of Electromagnetic Waves in Clouds at Optical Frequencies", Jour. Inst. Elect. and Telecom. Engrs, Vol. 23, 141-144, 1977.

3. H.M. Gupta, "Space-Time Response of a Cloud Communication Channel to an Optical Signal" Opt. and Quant. Elect., Vol. 12, 499-509, 1980.

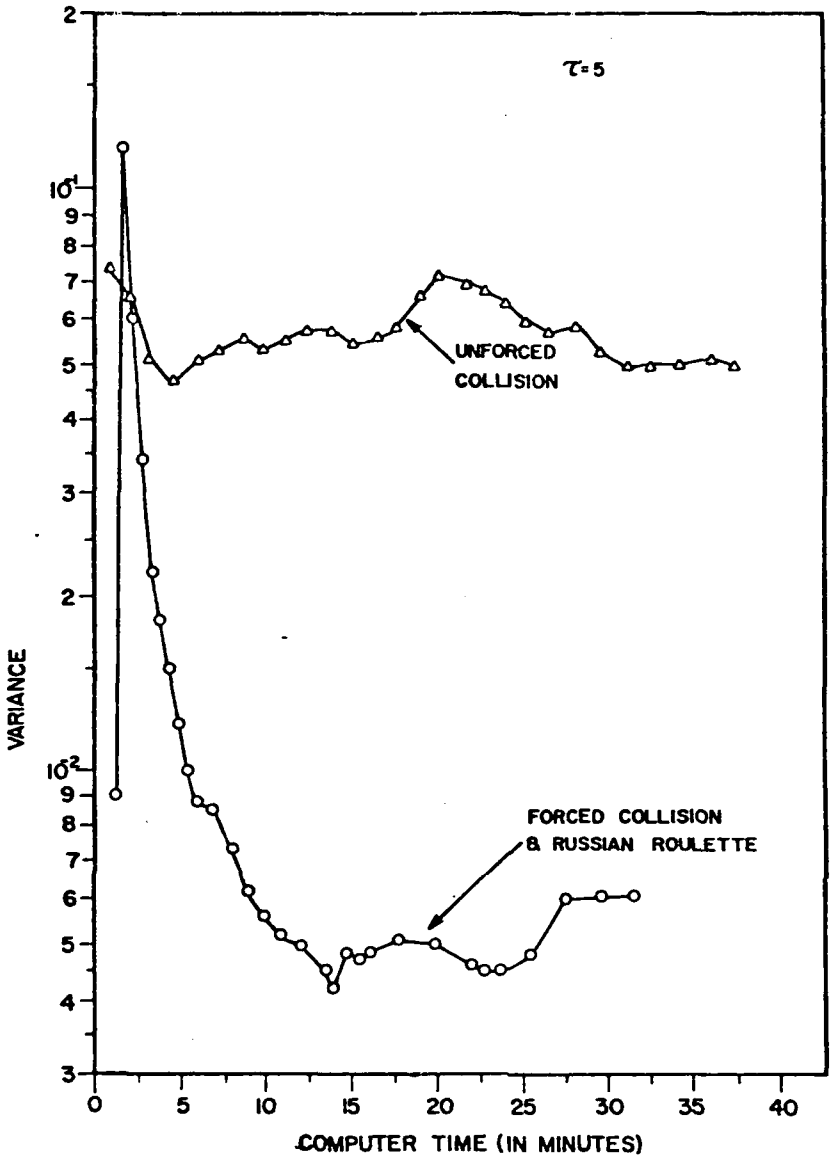

Fig. 1 - Variance in time dispersion vs computer time

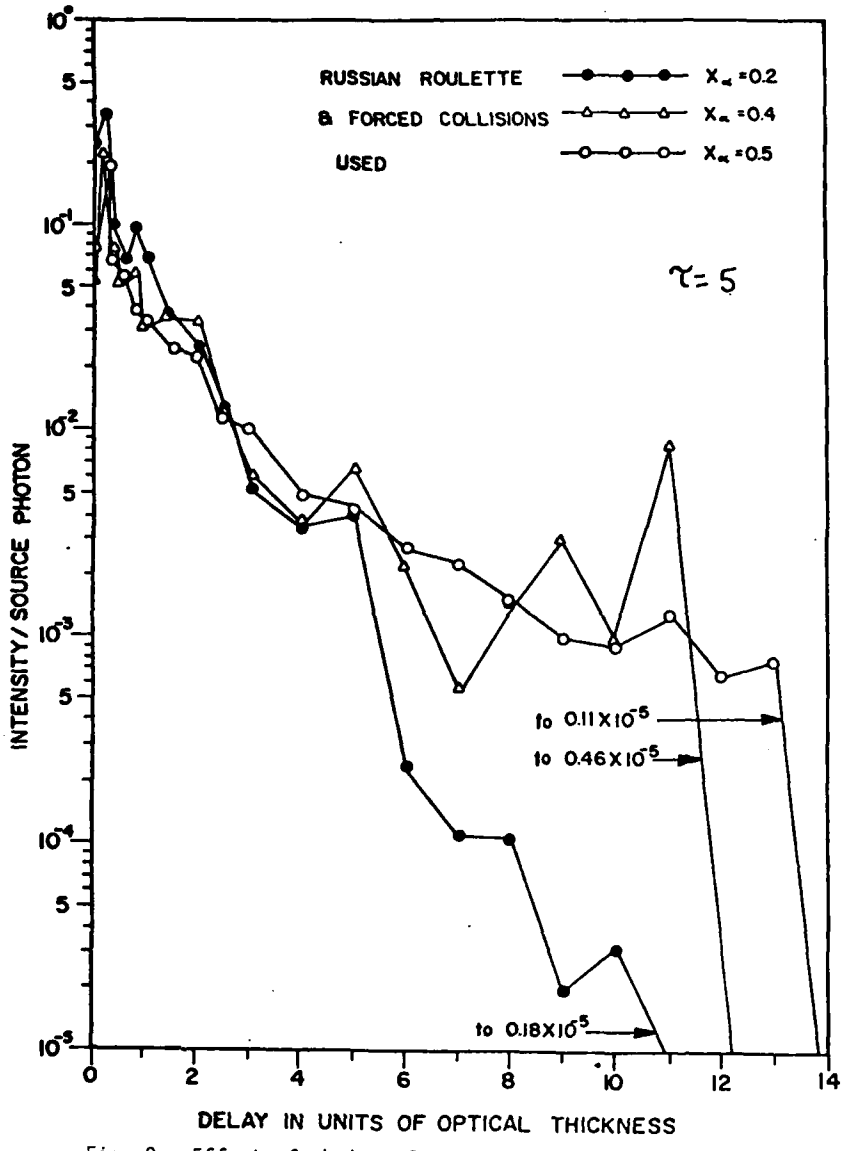

Fig. 2 - Effect of choice of X_α on time dispersion (delay)

AIME C. 55
AITKEN G.J.M. 63
ANDREWS L.C. 179
ARIEL I. 383
ARMSTRONG R.L. 143
AVRAMOVA R.P. 271
AZAR Z. 35,211
AZOULAY E. 35,211

BAARS E.P. 115,161
BANAKH V.A. 19
BARBINI R. 215
BASILI P. 71
BEN-SHALOM A. 235
BEN-YOSEF N. 39
BERTOLOTTI M. 165
BISSONNETTE L.R. 367
BOHLANDER R.A. 259
BOOKER H.G. 219
BRENGUIER J.L. 283
BRUSCAGLIONI P. 375
BUECHTEMANN W. 97

CACCIA J.L. 333
CASARINI G. 391
CHANG R.K. 137
CHURNSIDE J.H. 185,263, 325
CIOTTI P. 71
CLARKE R.H. 223
CLIFFORD S.F. 259,325
COHEN A. 383
COLE R.S. 157
COMBES P.F. 283
CONFORTI G. 227,231
CONSORTINI A. 227,231
COSTALES J. 207
CRESCENTINI L. 153

D'AURIA G. 71
DAINTY J.C. 51
DE AMICI G. 207
DE LEEUW G. 101
DEBLONDE G. 349
DEVIR A.D. 235
DURACZ T. 239,243

EBERT R. 97
EDNER H. 93
EGERT S. 383
ELLIOTT R.A. 243
ERASMUS D.A. 247
ESSEN H. 115

FALCONE V.J. 349
FANTE R.L. 251
FELSEN L.B. 15
FERRAZZOLI P. 71
FIENUP J.R. 311
FIOCCO G. 153
FIONDA E. 67
FLATTE' S.M. 11
FORBES F.F. 255

FURUTSU K.	111	KLEIMAN M.	383
		KOHNLE A.	191
		KOHSIEK W.	267,329
GALLE B.	93	KOLEV I.N.	271
GARDNER C.S.	107	KOLOSOV V.V.	133
GERSTL S.A.W.	359	KOPYTIN Yu.D.	129
GHIGO A.	215		
GIORGI M.	215		
GOCHELASHVILI K.S.	43,151	LAPINSKAS M.	345
GOLDNER E.	39	LAST I.	275
GOODSPEED M.J.	287	LAX M.	147
GOZANI J.	23	LEE G.	393
GUPTA H.M.	397	LEELAVATHI M.	279
		LEVIN S.	207
		LEVIZZANI V.	391
HARLEY A.S.	119	LIEBE H.J.	203
HILL R.J.	185,259,	LIPSON S.G.	235
	263		
HOLMES J.F.	321		
HOUTMAN R.	63	McCLEESE D.J.	353
		McCORMICK N.J.	239,243
		McMILLAN R.W.	259
ISAACS R.G.	349	MAIGNIAL I.	283
IYER K.N.	215	MAJUMDAR A.K.	387
		MANTOVANI M.	231
		MARGOLIS J.S.	353
JAKEMAN E.	171	MAZAR R.	15
JOHNSON R.	63	MEGIE G.	89
JUNDT H.	191	MENDEZ E.R.	119
		MERLO U.	67,71
		MILLINGTON R.J.	287
KAPLAN L.D.	349	MIRONOV V.L.	19
KAPRIELOV B.K.	271	MOORADIAN G.	393
KARA P.	223	MUGNAI A.	379

NABOKO V.N. 271
NEFF W. 341
NEUWIRTH R. 191
NG N-Y.E. 223
NIETO-VESPERINAS M. 79

O'DONNELL K.A. 119
OCHS G.R. 185,293
OPPENHEIM U.P. 235
ORTGIES G. 337

PALUCCI A. 215
PARABONI A. 195
PARVANOV O.P. 271
PASCALAR H. 207
PASRICHA P.K. 303
PATITSAS A.J. 297
PETRACCA S.P. 175
PHILLIPS R.L. 179
PICHAMUTHU J.P. 279
PILI P. 375
PINTO I.M. 175
POGODAEV A.A. 129
PORCEDDU I. 301
PORCH W. 341
POUIT C. 283
PRIESTLEY J.T. 259
PRODI F. 391
PROKHOROV A.M. 151

QUESADA V. 301

RADJABOV T.S. 43
RIBAK E. 235
RIBEZZO S. 215
RIDER D.M. 353
RINO C.L. 371
ROCKWAY J. 393
ROSEN L. 341

SAINT-DENIS R. 345
SARMA S.B.S.S. 303
SCHIFFER R. 123
SCHOFIELD J.T. 353
SHISHOV V.I. 43,151
SIBILIA C. 165
SINEV S.N. 133
SMOOT G. 207
SMYTH J.B. 307
SOLIMINI D. 71
SPEER B. 393
STARODUMOV A.N. 151
STEFFENS W. 191
SUNESSON A. 93
SVANBERG S. 93

THIELHEIM K.O. 123
THOMAS C.D.V. 31
TUR M. 35,211

Cancelled

UNEUS L. 93
UPHOFF L. 345
UZUNOV I.M. 43

VARADAN V.K. 363
VARADAN V.V. 363
VATS H.O. 219
VERNIN J. 333

WACKERMAN C.C. 311
WALLIN S. 93
WANG J. 67
WEISSMAN Y. 275
WEITZ A. 39
WENDT W. 93
WHITMAN A.M. 27
WILKERSON T.D. 85
WINKER D.M. 59
WISCOMBE W.J. 379
WITEBSKY C. 207
WOLF E. 77
WORSHAM R. 349

YUDANIN B. 147
YURA H.T. 7

ZACCANTI G. 375
ZARDECKI A. 359
ZEMLYANOV A.A. 129,133
ZHENGFANG S. 315
ZUEV V.E. 19,129,133

The Organizing Committee would like to thank most sincerely for their assistance and cooperation:

COMUNE DI FIRENZE

ENTE PROVINCIALE PER IL TURISMO DI FIRENZE

ENTE PROVINCIALE PER IL TURISMO DI SIENA

and for their contribution:

OFFICINE GALILEO

SEGNALAMENTO MARITTIMO ED AEREO (S.M.A.)